UNIVERSITÉ DU LUXEMBOURG

PhD-FSTM-2023-21
The Faculty of Science, Technology and Medicine

DISSERTATION

Defence held on 09/03/2023 in Luxembourg

to obtain the degree of

DOCTEUR DE L'UNIVERSITÉ DU LUXEMBOURG

EN SCIENCES DE L'INGÉNIEUR

by

Taygun Fırat Yolaçan
Born on 22 March 1990 in Altındağ, (Turkey)

CONNECTION TECHNOLOGIES FOR FAST ERECTION OF STEEL STRUCTURES FOR BUILDINGS (FEOSBUILD)

Dissertation defence committee

Prof. Dr. Markus Schäfer, Dissertation Supervisor
Professor, Université du Luxembourg

Prof. Dr. Christoph Odenbreit, Chairman
Professor, Université du Luxembourg

Prof. Dr. Slawomir Kedziora, Vice Chairman
Professor, Université du Luxembourg

Prof. Dr. Jean-François Demonceau
Assoc. Professor, Université de Liège, School of Engineering, Urban and Environmental Engineering

Dr. François Hanus
Business Manager Steligence Fabrication Center, ArcelorMittal Luxembourg

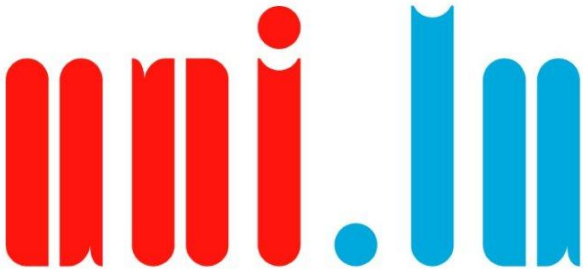

UNIVERSITÉ DU
LUXEMBOURG

Taygun Fırat Yolaçan
fratyolacan@yahoo.com
ORCID iD: 0000-0002-8456-9936

ACKNOWLEDGMENTS

This thesis was written under the FEOSBuild research project, which was executed at the University of Luxembourg. The FEOSBuild research project is funded by Luxembourg National Research Fund (FNR), grant reference: 2018-1-12651094 and co-founded by ArcelorMittal Belval Differdange S.A.

The steel plates used for the slip-factor determination tests for CNC-cut saw-tooth surfaces were provided by ArcelorMittal Belval Differdange S.A.

PREFACE

Since the beginning of my professional career, I have always been eager to face new engineering problems related to my subjects of interest. My intention has been to foresee new coming challenges and achieve success despite any sort of difficulties. FEOSBuild research project allowed me to spend my last four and a half year on very intensive experimental, numerical and analytical investigations to develop state-of-the-art structural joint configurations to be use in steel-concrete hybrid building frames. I have faced many challenges during the development, execution and the dissemination of this research project however I believe that I also developed my professional, intellectual and personal skills under these difficulties.

This thesis is the result of academic research activities conducted between 15 November 2018 to 14 November 2022 at the Department of Engineering at the University of Luxembourg under the FEOSBuild research project which is funded by Luxembourg National Research Fund (FNR) with a grant reference: 2018-1-12651094 and co-founded by ArcelorMittal Belval Differdange S.A.

First and foremost, I would like to express my sincere gratitude to my doctoral supervisor Prof.Dr.-Ing Markus Schäfer for offering me the opportunity to be part of his research team to pursue my doctoral studies at the University of Luxembourg. His continuous support and patient guidance both in my research activities and personal life made this thesis to be complete. In addition, most importantly, he provided me free and comfortable research environment where I can speak, discuss and act without any limitations for the development of this thesis.

I would like to express my profound appreciation to my thesis supervision committee members Prof.Dr.-Ing Christoph Odenbreit and Dr. François Hanus for their support and their constructive critics during the development and execution of this research project.

I would like to express my true gratitude to John Frederik Gurski and Tolja Munser from the structural laboratory at the University of Wuppertal. Their patience and very valuable guidance for many of the experimental investigations presented in this thesis made this work possible. Our discussion on the technical subjects, their very kind attitude towards to me starting from the first day of our collaboration and their expertise in structural testing are truly acknowledged and respected. I also appreciate their entire structural laboratory team for their contributions to the experimental test campaigns conducted at the University of Wuppertal.

I would like to express my special thanks to the laboratory members of the University of Luxembourg, Gilbert Klein, Ken Adam, Marc Seil, and Ed Weyer for their kind effort dedicated to my research project. Their guidance and their continuous support on any technical requirement made all of the experimental investigations presented in this thesis to be perfectly conducted within the

limited period of this research project. I also appreciate the entire laboratory team of the University of Luxembourg.

I appreciate my colleagues Özgun Ergün, Qingjie Zhang, Jovan Fodor, Pellumb Zogu, Maxence Paoletti and Nejati Shain for all of our discussions on many different subjects which allowed me to evolve both technically and personally. Their continuous support as friends and colleagues made possible this work to be finalized. I especially appreciate Qingjie Zhang and Jovan Fodor for their friendship from the first day of my arrival in Luxembourg as both a young researcher and most importantly as an expat in a new country without a friend or a family member.

I am extremely thankful to all my friends who have supported me during my journey from the beginning of my academic studies until the finalization of thesis. Their support will be never forgotten.

I appreciate Dr. Ferdinand Reif and Spannverbund Luxembourg S.A. for their contribution and flexibility in the material supply for a part of the experimental investigations conducted under this thesis.

I would like to express my true gratitude to Daniel Holigagues and Kiehne GmbH for their very kind support for the production of several experimental test specimens tested under the scope of this thesis. Their expertise in computer numerical control machining, their guidance for the development of the structural details and their patience in the production of the test specimens are appreciated.

I am grateful to my parents Sebahat Danıştı Yolaçan and Orhan Yolaçan for their continuous support from the beginning of my academic posts to the finalization of this thesis. I would like to also express my special thanks to my brothers, Tugay Süphan Yolaçan and Muharrem Meriç Yolaçan, for all of the good times we have spent and for all of the hard times we have overcome together.

In the end, I would like to express heartfelt thanks, my appreciation and all my respect to my wife Beyza Özçolak. I would not have completed my doctoral thesis without her continuous support over the past years. Her belief and trust in me, and her patience during the endless working hours of this study kept me motivated to continue my research even during the most critical physical, psychological and financial hard times that we faced together. Therefore, I would dedicate this thesis to my lovely wife Beyza Özçolak.

TABLE OF CONTENTS

LIST OF FIGURES

FIGURE

LIST OF TABLES

TABLE

LIST OF ANNEXES

LIST OF ABBREVIATIONS

2D Two Dimensional

3D Three Dimensional

BC Boundary Condition

CAD Computer Aided Design

CNC Computer Numerical Control

CoV Coefficient of Variation

Dim Dimension

DAMAGEC Compressive Damage Variable

DAMAGET Tensile Damage Variable

DT Linear Variable Displacement Transducer

FE Finite Element

FEM Finite Element Model

FEA Finite Element Analysis

GJSFB Grouted Joints for Continuous Composite Slim-floor Beams

NA Neutral Axis

LC Load Cell

PEEQ Equivalent Plastic Strain

Plug-inC Bolt-less Plug-in Connection for Steel-concrete Hybrid Building Frames

SMIBC Saw-tooth Mechanical Interlock Bolted Connection

WAAM Wire Arc Additive Manufacturing

LIST OF SYMBOLS

A	Percentage elongation of a steel coupon
A	Area
A_s	Stress area of a bolt; total stress area of reinforcements
$A_{s,re}$	Stress area of a reinforcement
D_p	Damage parameter
E	Elastic Modulus
E_s	Elastic modulus of a steel material
E_{cm}	Secant modulus of elasticity of concrete
E_{mean}	Mean elastic modulus of a material
F	Force
F_N	Force in the direction of a surface or a line normal
F_b	Tension force in a bolt
$F_{b,u}$	Ultimate strength of a bolt
$F_{b,y}$	Yield strength of a bolt
F_{Clamp}	Clamping force
F_f	Machine force at the rupture of a steel coupon
F_{lr}	Linear rotation threshold force for Plug-inC
$F_{lr,mean}$	Mean linear rotation threshold force for Plug-inC
F_m	Machine force attaining the ultimate strength of a steel coupon
$F_{p,C}$	Bolt pre-tension force
$F_{p,C,initial}$	Initial nominal bolt pre-tension force
F_{si}	Individual slip-load
F_{sm}	Mean slip-load
F_{Test}	Applied load from a testing machine or a hydraulic-jack
$F_{th,u}$	Ultimate strength of a threaded-rod
$F_{th,y}$	Yield strength of a threaded-rod
F_u	Ultimate load-bearing capacity of a structural connection or a joint
$F_{u,analytical}$	Estimated load-bearing capacity of a structural connection or a joint
$F_{u,exp}$	Expected ultimate load-bearing capacity of a structural connection or a joint
$F_{u,mean}$	Mean ultimate load-bearing capacity of a structural connection or a joint
$F_{u,Test}$	Maximum applied load from a testing machine or a hydraulic-jack
F_y	Elastic load-bearing capacity

$F_{y,mean}$	Mean elastic load-bearing capacity
$F_{Ø}$	Axial Force in a steel reinforcement or a headed-fastener
G_F	Fracture energy of concrete
I_b	Moment of inertia of a beam
K_c	Concrete damage plasticity parameter
L_b	Span length of a beam
$L_{j,eff}$	Effective joint length
L_o	Original gauge length
L_{span}	Span length of a beam
L_t	Total length of a steel coupon
M	Moment
$M_{b,pl}$	Plastic moment resistance of a beam cross-section
$M_{b,pl,hogging}$	Hogging plastic moment resistance of a beam cross-section
$M_{b,pl,Rd}$	Design plastic moment resistance of a beam cross-section
$M_{b,pl,sagging}$	Sagging plastic moment resistance of a beam cross-section
M_{ext}	External moment action
M_{int}	Internal moment reaction
M_j	Joint Moment
$M_{j,Ed}$	Design moment at a joint
$M_{j,pl}$	Plastic moment resistance of a joint
$M_{j,Rd}$	Design resistance of a joint
N	Tension force
N_{Ed}	Resultant design tension force on a fastener or a group of fasteners
$N_{Rd,i}$	Design tension resistance of an individual anchorage component
$N_{Rm,i}$	Mean tension resistance of an individual anchorage component
$N_{Rm,u,re}$	Mean ultimate axial resistance of a steel reinforcement
N_{Test}	Resultant actual tension force on a fastener or a group of fasteners
R_d	Design resistance
R_{eH}	Upper yield strength of a steel coupon
R_{eL}	Lower yield strength of a steel coupon
R_m	Mean resistance; Tensile strength of a steel coupon
R_p	Proof strength
S	Rotational stiffness
S_{ini}	Initial rotational stiffness
$S_{ini,mean}$	Mean initial rotational stiffness
S_j	Rotational stiffness of a joint
$S_{j,ini}$	Initial rotational stiffness of a joint
$S_{j,ini,EN1994-1-1}$	Initial rotational stiffness of a joint according to EN1994-1-1
S_{mean}	Mean rotational stiffness

S_o	Original cross-sectional area of a steel coupon
S_{sec}	Secant rotational stiffness
V	Shear force
V_{Ed}	Design shear force
$V_{Rd,i}$	Design shear resistance of an individual anchorage component
$V_{Rm,i}$	Mean shear resistance of an individual anchorage component
V_{Test}	Actual shear force
V_r	Coefficient of variation for a probabilistic model
V_{rt}	Coefficient of variation of a resistance function
V_δ	Coefficient of variation of error (Data vs Estimation)
Z	Percentage reduction of the cross-sectional area of a steel coupon
a_o	Original gauge thickness of a rectangular steel coupon
b_{eff}	Effective width of a steel-concrete composite beam
b_o	Original gauge width of a rectangular steel coupon
cc	Center of compressive stress block
d_o	Original gauge diameter of a cylindrical steel coupon
e	Load eccentricity
e_{actual}	Actual load eccentricity achieved during an experimental test
f_{b0}	Initial equibiaxial compressive yield stress for concrete damage plasticity
f_c	Compressive strength of concrete
f_{c0}	Initial uniaxial compressive yield stress for concrete damage plasticity
$f_{c,cylinder}$	Cylinder compressive strength of concrete
$f_{c,cube}$	Cubic compressive strength of concrete
f_{cm}	Mean value of concrete cylinder compressive strength
f_{ctm}	Mean value of axial tensile strength of concrete
$f_{ctm,fl}$	Mean value of flexural tensile strength of concrete
f_f	Stress at the rupture or fracture of a material
f_s	Yield strength of a steel reinforcement material
f_u	Ultimate strength of a material
f_{ub}	Characteristic ultimate strength of bolt material
$f_{u,m}$	Mean ultimate strength of a material
f_{ur}	Reduced ultimate strength of a material
f_y	Yield strength of a material
f_{yr}	Reduced yield strength of a material
g_k	Weight per unit area; Weight per unit length
h	Height
h_{ef}	Effective height of a headed-fastener
$h_{connection}$	Total connection height of two components
k	Translational stiffness

$k_{d,n}$	Design fractile factor
$k_{d,\infty}$	Design fractile factor for test number >= 100
k_{ini}	Initial translational stiffness
$k_{ini,mean}$	Mean initial translational stiffness
k_{mean}	Mean translational stiffness
k_n	Characteristic fractile factor
k_∞	Characteristic fractile factor for test number number >= 100
n	Number of tests; Number of data points; Number of area
n_{bolts}	Number of bolts
q_k	Characteristic value of a uniformly distributed load or a line load
rc	Center of rotation
r_d	Design value of resistance
r_k	Characteristic value of resistance
r_m	Resistance value calculated using the mean values of the basic variables
s_s	Standard deviation for the distribution of the slip loads
s_μ	Standard deviation for the distribution of the slip-factors
t	Thickness
u	Displacement
u_x	Displacement in x-axis direction
u_y	Displacement in y-axis direction
u_x	Displacement in z-axis direction
w	Width; Crack width; Uniformly distributed loading
w_c	Crack width for $\sigma_{ct} = 0$
α	Exponent for tension-shear interaction equation of an anchorage
γ_M	Partial factor for resistance
$\delta_{creep,criterion}$	Creep criterion of EN1090, Annex G
$\delta_{criterion}$	Slip criterion of EN1090, Annex G
δ_{gap}	Machining tolerance between hub and dovetail components
δ_i	Individual slip of each faying surface
δ_{slip}	Relative slip between two different components
δ_m	Testing machine displacement attaining the tensile strength of a steel coupon
δ_x	In-plane horizontal relative displacement
δ_y	In-plane vertical relative displacement; Slip; Deflection
δ_z	Out-of-plane horizontal relative displacement
ε	Strain
ε_c	Compressive strain in the concrete
ε_{c1}	Compressive strain in the concrete at the peak stress
ε_{cu}	Ultimate compressive strain in the concrete
ε_{ctm}	Mean value of axial tensile cracking strain of concrete

$\varepsilon_{ctm,fl}$	Mean value of flexural tensile cracking strain of concrete
ε_f	Rupture strain of a material
ε_{lim}	Pre-defined strain limit for a material
ε_u	Necking strain of a material
ε_y	Yield strain of a material
$\varepsilon_{y,f}$	Yield strain of a beam flange
$\varepsilon_{y,w}$	Yield strain of a beam web
η	Stiffness modification factor
θ	Rotation angle; bend angle of a reinforcement; dovetail angle
κ	Beam curvature
μ	Coulomb friction coefficient; Slip-factor
μ_i	Individual slip factor
$\mu_{i,nominal}$	Individual slip factor based on initial bolt pretension load
$\mu_{i,actual}$	Individual slip factor based on actual bolt pretension load
ν	Poisson's ratio
ρ	Density
σ	Normal stress
σ_c	Compressive stress in concrete
σ_{ct}	Tensile stress in concrete
σ_s	Stress in steel
σ_v	Von mises stress
τ	Shear stress
Φ	Rotation
Φ_j	Joint rotation
$\Phi_{j,failure}$	Joint rotation recorded at failure instant of an test specimen
$\Phi_{j,pl}$	Joint rotation at plastic moment resistance of a joint
$\Phi_{j,max-record}$	Maximum joint rotation recorded in an experimental test
$\Phi_{j,u}$	Ultimate rotation capacity of a joint
φ	Slope angle
π	Mathematical constant
$\emptyset$	Diameter of a steel reinforcement or a headed-fastener

ABSTRACT

Steel-concrete hybrid building systems offer sustainable and effective structural solutions for multi-story and high-rise buildings considering that steel is a completely recyclable material and that the most advantageous mechanical properties of steel and concrete could be used simultaneously against the effects of tension and compression stress resultants. On the other hand, a small percentage of multi-story buildings and a small number of high-rise structures are actually constructed using steel-concrete hybrid building technologies. This is mostly a result of general contractors' orientation toward the completion of construction projects using traditional reinforced-concrete construction techniques. Therefore, they generally do not employ a sufficient and competent workforce to execute labor-intensive and complex on-site manufacturing activities such as welding of fin plates and pre-tensioning applications for high-strength bolts required to assemble steel beams and reinforced-concrete columns and walls of steel-concrete hybrid building systems. In order to reduce labor-intensive on-site tasks, general construction contractors typically utilize conventional construction approaches using only reinforced concrete building systems. As a result, the structural and environmental benefits of steel-concrete hybrid building systems could not be widely adopted by the construction industry. This research project proposes three different novel structural joint configurations with cutting-edge saw-tooth interface mechanical interlock bolted connection, bolt-less plug-in connection, and grouted joint details for beam-to-column joints of steel-concrete hybrid building systems. The proposed joint configurations eliminate on-site welding and enable the accommodation of construction and manufacturing tolerances in three spatial directions to achieve fast erection strategies for the construction of steel-concrete hybrid building systems. Therefore, the outcomes of the research project make it possible for general construction contractors to use their existing workforce to complete construction tasks for steel-concrete hybrid building systems without the requirement of specialized tools or training. In this study, a total of six separate experimental test campaigns were established to determine the load-deformation behaviors of the proposed joint configurations and to identify their load-bearing components. In order to show that the suggested joint configurations are appropriate for mass production without the utilization of special equipment or machinery, the experimental test prototypes of the proposed joint configurations were produced in partnership with commercial producers. The experimental test campaigns were simulated with numerical models by means of advanced computer-aided finite element analyses for the identification of the ultimate deformation limits of the proposed joint components and to clarify their progressive failure mechanisms under quasi-static loading conditions. A set of analytical resistance models were developed to estimate the load-bearing capacities of the proposed joint configurations based on

the failure modes identified by the observations made during the experimental tests and in accordance with the output results of the numerical simulations. Based on the analytical expressions, the most significant, in other words, the basic variables impacting the load-bearing capacities of the proposed joint configurations were identified. Additionally, the load-deformation behaviors of the proposed joint configurations were further investigated with numerical parametric studies by parametrizing the basic variables to understand their impact on the load-deformation behaviors of the proposed joint configurations. To verify the accuracy of the analytical resistance models of the proposed joint configurations, the estimations of the analytical expressions were compared with the output results of the numerical parametric studies. Based on the distribution of the estimations of the analytical expression against the output result of the numerical parametric studies, characteristic and design partial safety factors were established according to EN1990, Annex D for the analytical resistance models of the saw-tooth interface mechanical interlock bolted connection and bolt-less plug-in connection. The estimations of the analytical resistance model of grouted joint details for beam-to-column joints of steel-concrete hybrid building systems were also compared with the output results of a numerical parametric study but no partial safety factor was established for this joint detail.

CHAPTER 1

Introduction

1.1 Research motivation

The current practice in the construction sector investigates the industrialization of the construction fields by reducing on-site activities such as the standardization of the structural joint details to develop fast erection strategies for more efficient and economical construction process while achieving high reliability for the assembly techniques [5, 6, 7]. It is a fact that pre-fabricated and partially cast-in-place structural elements such as precast reinforced concrete columns and steel-concrete composite slim floor slab systems have recently gained importance to reduce the labour intensive on-site activities of conventional construction methodologies [8, 9] and they paw the way to develop fast erection and dismantling strategies for civil engineering structures [10, 11, 12]. On the other hand, the structural detailing between the horizontal and vertical members of the load-bearing building frames has not yet been fully evolved by means of the structural continuity and integrity. Especially there is a lack of knowledge and practical solutions for the beam-to-column connections of steel-concrete hybrid building systems [13] compared to the developments in the production of the structural elements [14].

Although various solutions have been proposed for the connections between the horizontal and the vertical members of reinforced-concrete precast systems [15, 16, 17, 18], structural joints between the steel beams and the reinforced-concrete columns and walls have not yet been fully optimized to realize fast erection strategies for the load-bearing frames of steel-concrete hybrid buildings [13, 19, 20] and bridges [21]. Therefore, the current applications for the construction fields of the steel-concrete hybrid building systems designed with reinforced-concrete bracing systems and steel beams mainly depend on the availability of the craftsmen to perform labour-intensive on-site activities such as welding of fin plates and extended end-plates [22], and application of additional in-situ grouting to guarantee structural integrity between the joint components [21].

Additionally, the steel components of the steel-concrete hybrid building systems are often produced in steel workshops and delivered to the construction sites as finished products while the reinforced-concrete components are produced at the construction sites. Therefore, it becomes necessary to have adjustable assembly techniques to accommodate the construction and the manufacturing tolerances that arise due to the different production procedures, tolerance limitations

and the dimensions of the steel and reinforced-concrete components. However, the application of adjustable assembly techniques has not yet been the mainstream for the construction industry because of their expensive manufacturing costs compared to the conventional joint detailing such as the reinforcement bars for reinforced-concrete structures, fin-plates for steel structures and the combination of embedded anchor plate with fin-plates for steel-concrete hybrid building systems.

Furthermore, during the last decades, the construction contractors started to use steel formwork systems instead of individual wooden plates to benefit from the reuse-ability, assembly and dismantling speeds, safety and robustness of the steel formwork systems [9]. However, these formwork systems are generally not customizable for the needs of the construction fields by means of the application of the novel joint configurations between steel beams and reinforced-concrete columns and walls. Therefore, it is mostly required to install steel anchor plate to be flash to the formwork and to perform labour-intensive welding operations of fin plates or brackets to the anchor plate after the dismantling of steel formwork systems to be able to assembly the steel beams with the reinforced-concrete columns and walls [13, 23, 24].

Consequently, construction contractors tend to adopt conventional construction methodologies [9, 16] with solely reinforced-concrete building frames to avoid the labour-intensive on-site activities and costly assembly techniques of steel-concrete hybrid building systems described in the previous paragraphs. As a result, the construction industry could not fully benefit from the superior load-bearing behaviour of the steel-concrete hybrid building systems [20].

Therefore, a research project - FEOSBuild, *Fast Erection of Steel Structures for Buildings*, co-funded by *Luxembourg National Research Fund (FNR) and ArcelorMittal & Differdange SA* was established by 15th November 2018 and comprises of an interdisciplinary approach to develop novel adjustable structural beam-to-column connections between steel beams and reinforced-concrete columns or walls of steel-concrete hybrid building systems.

It is the fact that the global site operation optimization for the fast erection of structural elements is challenging as it requires achieving reliable structural joint detailing while aiming to minimize overall project duration and maximizing construction site safety. Therefore, state-of-the-art technologies are required to be used to establish novel structural joint configurations for steel-concrete hybrid building systems. The FEOSBuild research project proposes to eliminate on-site welding of fine-plates and brackets for the bolted connections with saw-tooth interface mechanical interlock connection, bolt-free plug-in connection and grouted joints for continuous steel-concrete composite slim-floor beams. Thereby, the labour intensive and costly on-site activities could be eliminated to assemble steel beams and reinforced-concrete columns and walls of the hybrid building systems which will paw the way to achieve fast erection strategies with minimized craftsmanship and increased construction field organization.

To summarize, the main motivation of the FEOSBuild research project and this thesis is the achieve the fast erection strategies for steel-concrete hybrid building systems by eliminating labor-intensive assembly of the structural joints using pre-fabricated on-site weld-free and bolt-free joint configurations.

1.2 Scope and limitation of the thesis

The scope of this study is to develop three different novel adjustable structural joint configurations to assemble steel beams and reinforced-concrete columns and walls of steel-concrete hybrid building systems for the development of fast erection strategies in construction sites. The name and the corresponding abbreviations for the proposed joint configurations are defined with the following items. Fig. 1.1 presents the overall views of the proposed joint configurations;

1. *Saw-tooth Interface Mechanical Interlock Bolted Connection (SMIBC)*
2. *Bolt-less Plug-in Connection (Plug-inC)*
3. *Grouted Joints for Continuous Composite Slim-floor Beams (GJSFB)*

In this study, the load-deformation behaviors and the load-bearing mechanisms of the proposed joint configurations are determined with experimental, numerical and analytical investigations for quasi-static loading conditions. The accidental loading actions, e.g. earthquake and fire, and the fatigue behavior of the proposed joint components are not in the scope of this study.

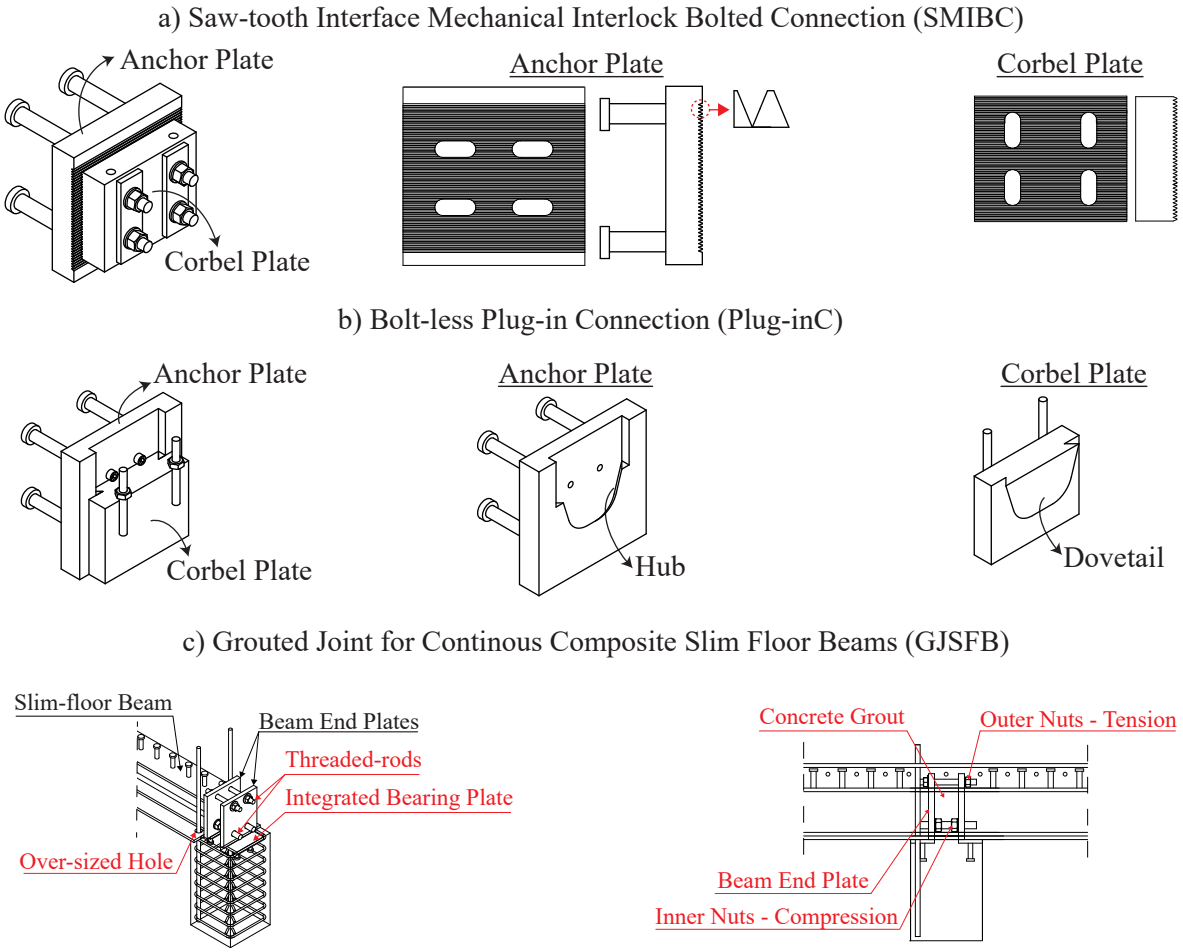

Figure 1.1: Proposed joint configurations and their components

1.3 Research methodology

Despite the fact that each joint configuration requires a separate investigation through literature review, prototyping of the joint components, development of experimental test campaigns, production of test specimens, preparation and validation of numerical simulation models, and derivation of analytical equations, a unique and systematic research methodology was used to be able to develop the three different novel joint configurations.

Initially, the existing literature regarding the development of novel structural joint configurations was reviewed to determine the requirements and the limitations for the development of on-site weld-free and bolt-less joint components that enable the fast erection of steel beams with reinforced-concrete columns and walls of steel-concrete hybrid building systems. Additionally, specific literature reviews are presented for the unique requirements of the load-bearing mechanisms and the structural response of each joint configuration under the corresponding chapters.

Having defined the adjustability requirements for the fast erection strategies by means of the accommodation of the construction and the manufacturing tolerances, preliminary 3D-CAD drawings of the proposed joint components, which enable the accommodation of the aforementioned tolerances and could be assembled without on-site welding, were prepared. Thereafter, the preliminary CAD drawings were shared with industrial producers to receive expert reviews with respect to the limitations of the production tools for the preliminary geometrical details of the proposed joint components. By this means, it was intended to manufacture the suggested joint components using existing production tools without the need for specialized equipment or technology. Thereby, it was ensured that the proposed joint configurations could be mass produced using the equipment and methods now in use by industrial production facilities. This process was crucial because one of the key objectives of the research effort is to integrate a sizable market for the proposed joint configurations.

Once the production techniques of the proposed joint components had been verified based on the producer feed-backs, the preliminary numerical simulations were performed with computer-aided finite element analyses to estimate the approximate ultimate load-bearing capacities and the approximate ultimate deformation limits of the proposed joint configurations. In addition, the preliminary finite element analyses were used to determine the principal load-bearing mechanisms of the joint components. Thereby, it became possible to optimize the geometrical parameters for the load-bearing mechanisms of the proposed joint components with respect to the minimum required design load-bearing resistance and the maximum deformation limits of the structural systems in which the proposed joint configurations are designed to be used. Consequently, based on the optimized geometrical details and the expert reviews from the producers, the 3D-CAD drawings of the proposed joint components were finalized.

To determine the load-bearing behaviors of the proposed joint configurations, experimental test campaigns were established based on the scaled version of the proposed joint configurations by means of the geometrical symmetry or the isolated joint configurations without the existence of

the full-scale building frames. The output results of the aforementioned preliminary finite element analyses were also used to design the experimental test set-ups by means of the required loading capacity of the testing machines and/or hydraulic jacks, the minimum required resistance of the test frames and the measurement ranges of the instrumentation. The experimental test campaigns were conducted under quasi-static loading conditions. The experimental test results were investigated in detail to define the load-deformation behaviors of the proposed joint configurations and to understand the reasons behind failure mechanisms of the joint components. Furthermore, the test results were used to define the principle load-bearing mechanisms of the proposed joint configurations. In line with the experimental test campaigns, the material properties of the test specimens were determined with material characterization tests to calibrate the preliminary finite element models and to be able to evaluate the estimations of the analytical expressions against the test results.

All of the experimental tests conducted to determine the load-deformation behaviors of the proposed joint configurations within the scope of this thesis were simulated with computer-aided finite element analyses to be able to estimate the ultimate deformation limits of each joint component, to clarify the load distribution between the joint components and to be able to present the progressive failure mechanisms of the joint components. The finite element modelling methods and the solution schemes of the finite element analyses of the experimental tests were validated against the test result.

According to the observations made during experimental tests, the outcomes of those tests, and the estimations from the finite element analyses, a set of analytical resistance models were developed to estimate the load-bearing capacities of the proposed joint configurations. Estimations of the analytical expressions were first compared with the test results for the validation of the analytical expressions. Consequently, it became possible to identify the basic variables that define the load-bearing capacities of the proposed joint configurations through the analytical expressions. Thereby, numerical parametric studies were performed using the proven finite element modelling methods and the solution schemes by parametrizing the basic variables of the joint components to investigate the impact of the basic variables on the load-deformation behaviors and the load-bearing capacities of the proposed joint configurations. Furthermore, the output results of the numerical parametric studies provided additional simulation-based data to evaluate the accuracy of the analytical resistance model developed to estimate the load-bearing capacities of the proposed joint configurations. According to the comparison of the estimations of the analytical resistance models against the output results of the numerical parametric studies and the experimental tests, partial safety factors were defined through a statistical evaluation procedure in order to enable the analytical expressions to be used for the ultimate capacity approximations of the proposed joint configurations.

Fig. 1.2 presents the flow chart of the research methodology adopted in this thesis according to the details presented in the previous paragraphs.

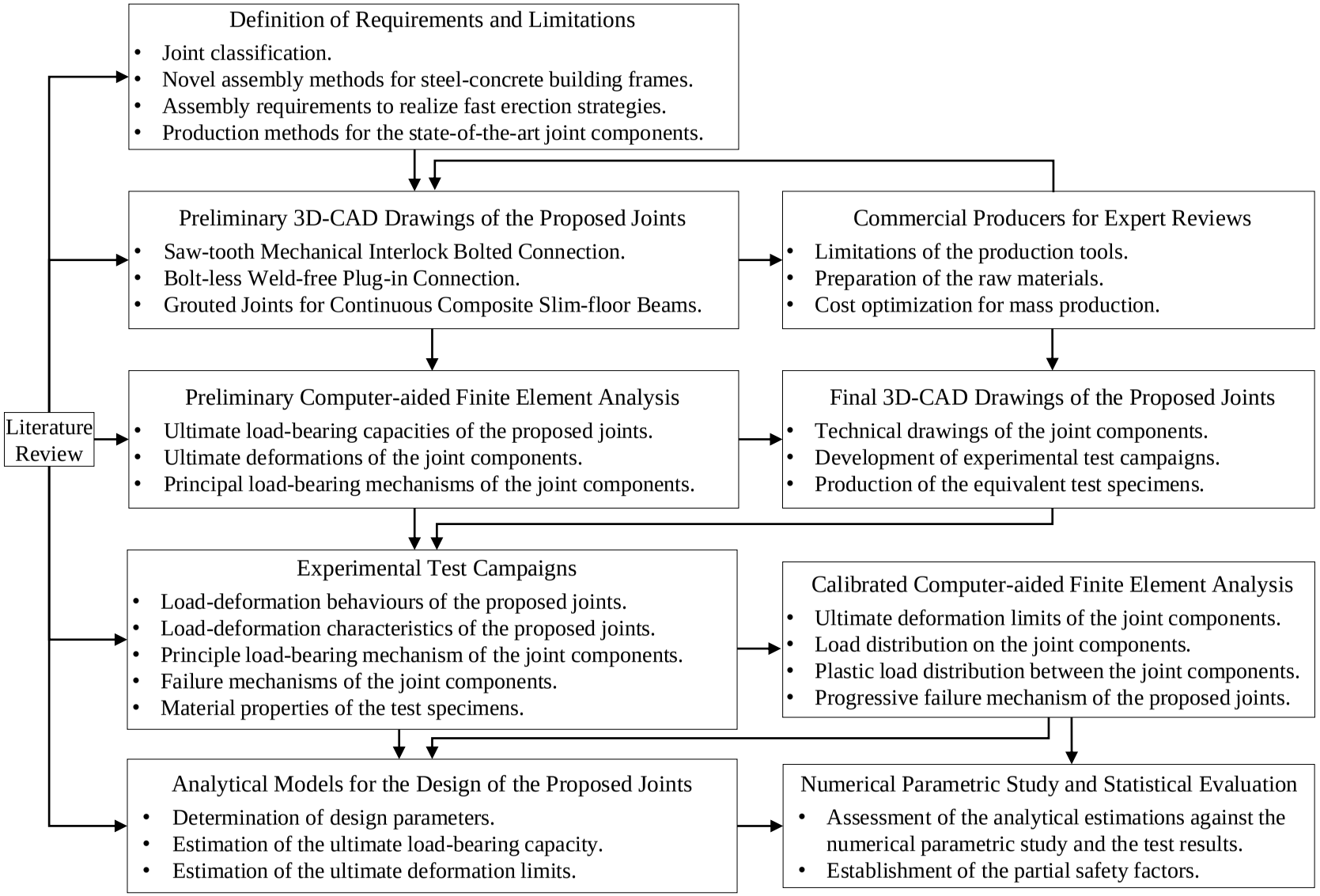

Figure 1.2: Flow chart of the research methodology

1.4 Structure of the thesis

This thesis comprises of six chapters. Fig. 1.3 summarize the structure of the thesis.

CHAPTER – 1

Introduction

Research motivation, scope and limitations of the research and structure of the thesis are presented.

CHAPTER – 2

State of the art

The selected literature is presented for development of novel structural joint configurations.

CHAPTER – 3

Saw-tooth Interface Mechanical Interlock Bolted Connection

Technical drawings, production methodology, and experimental, numerical and analytical investigations for the load-deformation behaviors of *Saw-tooth Interface Mechanical Interlock Bolted Connection* are presented. *S*tructural joint configurations of *Saw-tooth Interface Mechanical Interlock Bolted Connection* with reinforced-concrete columns are presented

CHAPTER – 4

Bolt-less Plug-in Connection for Steel-concrete Hybrid Building Frames

Technical drawings, production methodology, experimental, numerical and the analytical investigations for the load-deformation behaviors of *Bolt-less Plug-in Connection* are presented.

CHAPTER – 5

Grouted Joints for Continuous Slim-floor Beams

Technical drawings, production methodology, experimental, numerical and analytical investigations for the load-deformation behaviors of *Grouted Joints for Continuous Slim-floor Beams* are presented.

CHAPTER – 6

Conclusion, Summary and Recommendations for Further Research

Conclusions remarks and the outlook of the thesis are presented together with the recommendations for further research on the proposed joint configurations.

Figure 1.3: Structure of the thesis

CHAPTER 2

State of the art

2.1 Literature Review

The development of novel structural joint configurations to connect steel beams and reinforced-concrete columns of steel-concrete hybrid building systems are essential to increase the market share of steel-concrete hybrid building systems in the construction industry. On the other hand, it is a complex task to develop a novel structural joint as it requires to determine the load-deformation behaviors of the joints under various loading conditions to be able to establish reliable, durable and economical solutions by satisfying both the needs of the structural demand by means of the resistance, rigidity and ductility and the needs of the construction fields by means of tolerance accommodation for fast erection of building frames. Furthermore, according to EN1993-1-8 [25], structural joints are classified based on their strength, i.e. moment resistance, and their rotational stiffness with respect to the strength and the stiffness of the structural members that the joints connect. The classification of the structural joints plays a crucial role for the calculation of the internal actions and overall deformations within a structure as the level of the structural indeterminacy imposed by the structural joints determines the distribution of the internal forces required to be calculated to perform the design of the structural members. Additionally, ultimate load-bearing capacity of the structural joints determines the limit states for the external actions that can be resisted by a structure. Overall, load-deformation behaviors and load-deformation characteristics of the structural joints shall be well defined if novel structural joints will be established. Therefore, this chapter presents a comprehensive literature review to summarize the experimental, numerical and analytical investigations performed to develop novel structural joint configurations in order to create basis for the development of the proposed structural joint configurations of the FEOSBuild research project.

Kuhlmann et al. [13] recently proposed nominally-pin and rigid joint details for steel-to-concrete hybrid building systems using cast-in-place anchor plates within the scope of *"INFASO"* research project. Although their solution requires on-site welding of a corbel plate with an anchor plate, they showed that their joint details are successful to accommodate construction tolerances for the fast erection of steel beams with reinforced-concrete walls. They satisfied the flexural rigidity of their rigid joint detail by elongating the longitudinal steel reinforcements of the composite slab

into the reinforced-concrete wall with coupler connections to resist the tension stresses and by positioning a contact plate between the cast-in-place anchor plate and the steel beam to resist the compression stresses. As the longitudinal steel reinforcements of the composite slab are taken into account for the calculation of the resistance and the stiffness of their rigid joint detail, they also nominated their rigid joint as a composite joint based on the definition provided by EN1994-1-1 [2]. According to the results of their experimental test program for the nominally-pin joint detail, they showed that the ultimate load-bearing capacity of their nominally-pin joint detail is limited to pry-out failure of the cast-in-place anchor plate for small eccentric loading condition. For larger load-eccentricity, they concluded that the failure mode of their nominally-pin joint detail switches to concrete cone failure. They also highlighted that additional steel reinforcements positioned next to the anchor plate increase the resistance of their nominally-pin joint configuration and satisfy high ductility compared with those tested without the additional steel reinforcement. According to their experimental test program with their rigid joint detail, they concluded that the load-bearing capacity of their rigid joint depends on the ratio of the longitudinal steel reinforcement of the concrete slab elongated in the concrete wall. Ozbolt et al. [26] also presented analytical models based on component method [25] for the estimations of the load-deformation behaviors of the nominally-pin and the rigid joint details developed under *"INFASO"* research project and they proposed new components related to the anchorage in concrete which is not yet defined in the current design codes [2, 25]. Additionally, Henriques et al. [27] performed numerical studies to present the details of computer-aided finite element modelling techniques for the rigid joint configuration proposed by *"INFASO"* research project [13]. They concluded that Von Mises plasticity model could be used for the constitutive material law of steel components of the composite joints and the failure of the joint could be detected by monitoring the material strain limit for longitudinal steel reinforcements. In addition, Henriques et al. [27] also highlighted the importance of the bond model for numerical simulation between the steel reinforcements and the concrete volume of the composite joints.

Konertz et al. [28] proposed a structural joint detail to connect steel beams to reinforced-concrete columns and walls with cast-in-place anchor channels by means of a bolted connection to offer a simple solution for the accommodation of construction tolerances without on-site welding. They used fiber-optic measurement technology to investigate the load-distribution between the anchorage of the channels subjected to longitudinal shear force. Thereby, they were able to demonstrate that each anchor contributed the applied loading to be transferred to the concrete. Thus, their outcome showed that the ultimate load-bearing capacity of the cast-in-place anchor channels might be estimated by considering the plastic distribution of the longitudinal shear force between the anchors. However, according to the loading limitation and the scope of their experimental test program, the maximum loading applied even for the largest anchor channel in their test program was less than 70kN which is far more less than the required design resistance for a structural joint of steel beam having span length of 12m to 16m for multi-storey and high-rise building frames. Therefore, although their solution provides practical and on-site weld-free application for the fast erection of steel beams with reinforced-concrete columns and walls, it does

not provide sufficient load-bearing capacity for the action effects that may develop for the general span length of steel-concrete hybrid building systems and requires further research.

A commercial establishment, HALFEN, proposes several on-site weld-free bolted connections with cast-in couplers for beam-to-column joints of the steel-concrete hybrid building systems [29]. Although these solutions could be accepted as a good fit to connect steel beams and reinforced-concrete columns and walls of steel-concrete hybrid building systems, the cast-in position of the couplers may not provide practical strategies to accommodate the construction tolerances for the erection stages of the steel beams.

Another commercial established, Peikko, proposes a structural joint configuration named as *PCs® Corbel* [30, 31] to connect steel, cast-in-place or precast reinforced-concrete columns with steel or precast concrete beams. *PCs® Corbel* consists of cast-in anchor plate and bolted corbel plate. The anchor and the corbel plates of *PCs® Corbel* are connected with each other through serrated steel surfaces and high-strength pre-tension bolts. There exist over-sized bolt holes on the corbel plate, thus the position of the corbel plate could be adjusted with respect to the position of the columns through the over-sized bolt holes and serrated surfaces of the anchor and corbel plates to accommodate construction and the manufacturing tolerances. *PCs® Corbel* do not occupy the space beneath concrete beams unlike traditional concrete corbels and they are integrated inside the beam which enables to increase compartment volumes by eliminating the beam down-stand under the floor. By means of the accommodation of the construction tolerances and enabling fast erection strategies for steel-concrete hybrid building systems *PCs® Corbel* could be accepted as an ideal solution. On the other hand, the connection between beams and *PCs® Corbel* requires a utilization of a special steel-concrete composite beam known as *DELTABEAM®* [32, 33] or a beam shoe [34] to be installed into the precast reinforced-concrete beams. Consequently, to the best of the author's knowledge, the application of this innovative solution for the fast erection of standard hot-rolled steel beams and reinforced-concrete columns and walls has not yet been proposed. Furthermore, although there have been numerous applications of this commercialized solutions, only limited number of the literature is available regarding to the load-deformation behaviors and characteristics of this solution. Bujnak et al. [17] presented results of experimental tests conducted to evaluate the mechanical behaviour of *PCs® Corbel* with three reinforced-concrete columns having 280mmx280mm cross-section and they concluded that for all of the experimental tests the failure of the joint was due to the separation of *PCs® Corbel* from concrete columns. However, they did not present further details regarding to the load-deformation behavior, the deformations of the *PCs® Corbel* and the failure mode of the anchorages. Fiala et al. [35] conducted experimental test program with precast columns from high performance concrete material to show experimental verification of *PCs® Corbel* under simultaneous action of tension and shear loads. According to their experimental test program, the failure mechanism of *PCs® Corbel* was recorded to be as the shear failure, in other words the yielding of the serrated steel topology and the mean ultimate load bearing capacity of *PCs® Corbel* was recorded to be higher than 650kN for all of the experimental tests. Kvist and Näkne [36] performed numerical simulations to investigate the load-bearing mechanism of *PCs®*

Corbel under fire conditions. Although, they concluded that *PCs® Corbel* to have sufficient fire performance for the gravitational design loading of *PCs® Corbel*, they did not included the serrated steel surfaces of the anchor and the corbel plates in their numerical models, thus their findings should be carefully investigated.

Perreira et al. [37, 38] proposed a beam-to-column connection known as ATLSS which facilitates the erection of structures through self-alignment and self-locking properties. The emphasis of their design was to use their innovative solution to automate production of structural joints and the construction fields by minimizing human assistance during the erection procedures of the building frames. The load bearing mechanism of ATLSS connection was evolved from dovetail geometry. The basic configuration of ATLSS connection is a tenon mounted on a beam which slips into a mortise welded on a column [39]. The shapes of the tenon and the mortise are designed to be conical to facilitate the erection and make the joint self-guiding. The possibility of manufacturing the tenon and mortise out of steel plates with CNC machining was evaluated but cast steel was selected as a more economical solution. For beam-to-column joint configuration of ATLSS connection, the mortise is shop-welded to the column flange or web and the tenon is already bolted to the beam through slotted holes, thus construction tolerances along the longitudinal axis of the beams could be accommodated before the delivery of the beams on the construction site. Consequently, ATLSS connection allows beams and columns to be assembled in construction site with no need for on-site welding or structural bolting. The load-deformation behaviors of ATLSS connection were investigated in detail with comprehensive experimental testing program developed for various loading conditions. According to the initial shear test results of their experimental program, Fleischman et al. [40] showed that load-bearing mechanism of ATLSS connection to be activated once fitting tolerances between the tenon and the mortise were closed by rigid body motion of the tenon in the mortise. They noted this behaviour as unacceptable for the integrity of the connection. The failure mode of the connection under pure shear load was recorded once the arms, e.g. side edges, of the mortise were completely opened and allowed the tenon to freely push all the way through. Consequently, they revised their design and added stiffeners to the side edges of the mortise and seating at the bottom of the mortise to increase stiffness of the mortise and to prevent free sliding of the tenon in the mortise if the side edges of the mortise yields. In addition, contact surfaces of the tenon and mortise were machined for the revised version of ATLSS connection to minimize the impact of the fitting tolerances on the load-deformation behavior. However, they highlighted the machining of the contact surfaces to be as uneconomical. Fleischman et al. [40] determined moment-rotation behavior of ATLSS connection with a separate test campaign and they noted the rotational ductility of the connection to be excellent as the connection was able to rotate 0.286 radian before losing its load-bearing capacity. However, they also mentioned that the moment-resistance of the connection to be about 10-15% of the plastic moment resistance capacity of the connected beam. Therefore, they defined the connection as a simple, in other words, as a nominally-pin connection. On the other hand, different joint configurations of ATLSS connection with semi-rigid load-bearing characteristics was proposed for steel-concrete composite building

frames [41, 42, 43]. This novel connection also applied in an actual building as a case study to demonstrate the ease of erection and demountability achieved by ATLSS connection [40].

A commercial establishment, Anstar Oy, proposes on-site weld-free and bolt-less connection for beam-to-column/wall or beam-to-beam joints of precast reinforced-concrete building frames and steel-concrete hybrid building systems consist of a special steel-concrete composite beam nominated as *A-BEAM*® [44]. This innovative connection is named as *AEP*® *steel bracket* [45] and consists of a machined bridge plate, which is similar to a corbel plate, hidden cast-in sockets positioned in a beam and a column or a wall. The classification for the joint configuration of *AEP*® *steel bracket* is defined as a nominally-pin connection. On the other hand, it is noted in the design manual [45] that the bracket acts as a swivel joint against torsional actions subjected to the beam and transfers the torsional bending moment to the column without support in case of unsymmetrical slab installation. This innovative solution enables to accommodate $\mp$30mm and $\mp$1.5°construction tolerances along the longitudinal axis of the beam, and to accommodate $\mp$20mm and $\mp$2.0°construction tolerances along the longitudinal axis of the column or the wall. To the best of the author's knowledge, there is no available literature regarding to the load-deformation behaviors and characteristics of *AEP*® *steel bracket*. *AEP*® *steel bracket* could be accepted as a robust solution to achieve fast erection strategies for steel-concrete hybrid building systems. However, neither joint details nor design guides or technical approval is available for the utilization of this solution with standard hot-rolled steel beams. Therefore, the utilization of this solution for steel-concrete hybrid building systems depends on the availability of the special beam (*A-BEAM*® [44]) and this restraint limits the application of the solution.

Recently, an innovative on-site weld-free full-strength moment connection nominated as *ConXTech*® *ConXL*^{TM} *moment connection - ConXL* is approved by the connection prequalification review panel of the American Institute of Steel Construction (AISC) - ANSI/AISC 358s1-18 [46]. This connection allows the assembly of hot-rolled wide-flange steel beams to concrete filled square HSS or built-up box columns using high-strength bolts. In addition, *ConXL*^{TM} solution can also be used in steel-concrete composite building frames with reinforced-concrete slab. The configuration of *ConXL*^{TM} comprises collar corner assemblies shop-welded to HSS or built-up column and collar flange assemblies shop-welded to steel beam. Thereby, the steel beam could be positioned on the column by sliding the collar flange assemblies in the collar corner assemblies [39]. Finally, high-strength bolting of collar flange and corner assemblies guarantees the structural integrity of the connection. Rezaeian et al. [47] and Yang et al. [48] performed numerical studies with computer-aided advanced finite element analysis and they showed that the seismic behavior of *ConXL*^{TM} rigid connection is also appropriate for box-columns without concrete fill. Thus, the limitations of ANSI/AISC 358s1-18 [46] for the utilization of *ConXL*^{TM} only with concrete filled square HSS or built-up box columns could be extended with further research effort and it may be possible to use this innovative solution for the beam-to-column connections of steel-concrete hybrid-building frames.

In 2021, Shemshadian et al. [49] proposed a novel intermeshed connection for beam-to-beam and

beam-to-column joints of steel building frames. Two different configurations of the connection with two different puzzle strip like topologies were prepared using computer numerical control (CNC) plasma and water-jet cutting of the steel beams. This novel connection facilitates the erection of steel structures by eliminating the need for structural bolting and on-site welding. The first connection configuration is nominated as *Front-intermeshed* connection and it consists of multiple CNC cut dovetail-socket pairs on the upper and the lower flanges of the steel beam and CNC cut serrated surface along the height of the web. Thereby, the *Front-intermeshed* connection enables to assemble adjacent steel beams through the dovetail-socket pairs at the upper and at the lower flanges of the positioning one of the beam on the other one at the location of the dovetail-socket. The dovetail joints at the upper and the lower flanges are envisaged to resist the tension and compression forces resulting from the bending moment at the connection and the serrated surface of the web is envisaged to resist the shear force. However, based on the output results of the numerical studies performed by Shemshadian et al. [49] it was shown that the *Front-intermeshed* connection has relatively low flexural moment resistance and it is classified as non-ductile according to EN1993-1-1 [50]. Furthermore, Shemshadian et al. [49] also highlighted that the *Front-intermeshed* connection does not also provide flexibility for the accommodation of the construction tolerances. Therefore, in order to improve the load-bearing capacity of their proposal they also proposed *Side-intermeshed* connection which comprises tooth-shaped CNC cut notches (tooths) at the edges of beam flanges and an angle with holes (sockets) which has identical topology with the notches. Thereby, two separate beams could be connected at their flanges via the angles at each sides. In addition, *Side-intermeshed* connection also comprises a pair of shear plates bolted to the web of the beams for shear transfer. Shemshadian et al. [49] determined the load-deformation behavior of *Side-intermeshed* connection with four full-scale experimental tests and they demonstrated that *Side-intermeshed* connection has sufficient ductility and load-bearing capacity as the plastic load-bearing capacity of the tested beams were attained without significant damage in the connection. Additionally, they also noted that the test specimens were assembled quickly without any special skills.

Socketed steel joints have a vast practical application in grid shell structures [51]. For instance, Mashrah et al. [52] proposed a novel dovetail connection for grid shells application which is easy to assemble and has a lower cost to build in comparison to common bolted and welded joints for grid shells. Their solution shows similarities to ATLSS connection proposed by Perraira et. al [37, 38] and also eliminates both on-site welding and bolting. Mashrah et al. [52] developed two different configurations for this connection; the first configuration comprises conventional dovetail and socket (key-way) components and the other one consists of dovetail and socket components with added teeth patterns. The dovetail component of the connection is shop-welded to steel beam and the socket is prepared on a hub ring. The structural joint configuration of their connection mechanism completes when the dovetail is set inside the socket (key-way) machined on the hub ring and the upper and lower surfaces of the hub ring are closed with cover plates with a screw bolt passing through a hole in the center of the hub ring. In order to determine the mechanical response of their connection configurations for quasi-static loading condition, Mashrah et al. [52] conducted

an experimental test campaign with four large-scale tests and they noted that the load-bearing mechanism of their dovetail connection actives after the initial sliding of the dovetail in the key-way due to the existence of the production tolerances required to achieve easy erection of the connection components. The failure mode of their first connection configuration without the teeth patterns was the flexural tensile failure of the edges of the key-way. The bending load-bearing behavior of their first connection configuration was identified to have trilinear behavior having elastic, elastic-plastic and plastic stages. The failure mode of their second connection configuration with the teeth patterns was again the flexural tensile failure of the edges of the key-way. However, they concluded that the connection containing teeth patterns showed more than twice higher yield and ultimate bending-moment capacity compared to the connection without the teeth patterns. They classified both of their connection configurations as semi-rigid joint according to stiffness classification boundaries of EN1993-1-8 [25]. Mashrah et al. [52] also performed numerical parametric study with 3D finite element analysis of their connection configurations to understand the impact of the geometrical design parameters on the load-bearing capacity of their connection configurations. According to their parametric study, they showed that the load-bearing capacity of their connection configurations are mostly influenced by the height of the socket, thus the dovetail, and the ring thickness of the hub. Mashrah et al. [52] proposed simplified analytical resistance model to estimate the yield bending moment capacity of their connection configurations. The estimations of their analytical model showed excellent agreement with the results of their test campaign and their numerical parametric study, thus their connection configurations could be adapted for different dimensions and load-bearing requirements of grid shells structures without the need for advanced computer-aided numerical models and time inefficient experimental test campaigns.

In addition to the novel connection details developed for steel-to-steel and steel-to-concrete beam-to-column joints of civil engineering structures presented in the previous paragraphs, variety of innovative connection details have been proposed by many researchers for precast concrete construction technology to reduce on-site construction tasks and to increase construction efficiency by means of both time and cost. Therefore, it is essential for the scope of the FEOSBuild research project to investigate these novel connection details. Following paragraphs present some of the most attractive connection details proposed for precast concrete building technology.

Choi et al. [53] proposed bolted hybrid connection for beam-to-column connection of precast concrete frames. Their proposal mainly consists of bolting steel plates integrated into a precast concrete beam and a precast concrete column together with application of high-performance cast-in-situ fibre-reinforced cement at the joint region after the bolting. They suggested the application of high-performance fibre-reinforced cement to provide an efficient stress transfer mechanism between disconnected precast members. Thereby, the connection between the precast frame components is provided with a ductile steel connector and high-performance cement as a simple yet robust and reliable solution. As there exists in-situ cement application, their connection could be nominated as *wet connection* for precast frames. They did not provide information regarding to accommodation of construction and manufacturing tolerances with their connection details. However, due to

geometry of the bolt holes presented in their study, their connection would not be expected to accommodate the tolerances. They determined the seismic performance of their connection with an experimental test campaign. According to the results of their experimental campaign, they concluded that their pre-cast beam-to-column connection performed similarly to the monolithic reinforced-concrete connection and they highlighted that the high-performance cast-in-situ fibre-reinforced cement provided full structural integrity for the stress transfer between the beams and the columns. Therefore, they defined the seismic performance of their connection as excellent.

Ghayeb et al. [54] also introduced novel hybrid precast reinforced concrete beam-to-column connections for precast structural members. Their connection comprises of steel plates, tubes, couplers, reinforcements and cast-in-situ concrete (*wet connection* for precast frames). They investigated the seismic performance of their novel hybrid beam-to-column connections against a regular precast reinforced concrete beam-to-column connection and they concluded that the hybrid connections comprises structural steel and cast-in-situ concrete components are superior by means of strength and ductility to the regular connections that comprise cast-in-situ concrete and steel reinforcements for precast concrete moment resisting frames.

Zhong et al. [55] proposed a novel precast concrete beam-to-column connection with bolted steel plates and rubber layers. Their solution eliminates cast-in-situ concrete to increase construction efficiency and known as a type of *dry connection*. They conducted an experimental test program to determine the seismic performance of their novel joint mechanism for precast concrete frame against the seismic performance of an identical dimensions monolithic cast-in-place reinforced-concrete frame. The results of their experimental program showed that the ultimate load-bearing capacities of the precast concrete frames assembled with their novel joint mechanism were nearly identical with the corresponding monolithic concrete frame. However, the location for the plastic-hinge formation for the pre-cast frames with their novel joint mechanism was noted to be different with respect to the monolithic frame and it was highlighted that the energy dissipation capacity of the monolithic frame was higher than the pre-cast frames. Furthermore, they also noted that the rubber layer that was installed between the two separate components of the pre-cast frames, which were the beam and the column, highly impacted the seismic performance of their novel connection. Consequently, it could be stated that although the advantages of the dry-connection for pre-cast concrete frames by means of the construction efficiency further development is required to increase their seismic performance.

In 2020, Esmaeili and Ahooghalandary [56] introduced an innovative hybrid beam-to-column connection with high seismic performance for fast assemble of precast concrete frames. Their connection configuration eliminates on-site welding and structural bolting and requirement for the utilization of on-site formwork. Thus, it increases efficiency of construction sites by reducing labour-intensive on-site construction tasks. In addition, their connection includes seat plates, which function similar to a corbel plate, shop-welded to a steel box positioned in the column during the pre-casting of the column. Thereby, the precast beam could be simply laid on the seat plates during the erection phase; thus, their connection also eliminates the need for temporary supports (e.g.

scaffolding) required during the assembly of the frame components, and enables accommodation of the construction tolerances. The precast beam in this connection has two parts; the lower part of the beam is prefabricated, which makes their proposal to be considered as *dry connection*, and the upper part of the beam is made of cast-in-situ concrete after the placement of hollow core slab elements. Before the in-situ casting of the upper beam part, machined steel reinforcing bars with threaded ends are positioned next to the beam-to-column joint and connected with the precast column through holes prepared at both surfaces of the column to anchor the reinforcing bars to the column. Thereby, the upper part of the precast beam provides semi-monolithic load-deformation behavior. They determined the seismic performance of their connection with experimental test program. In addition, they performed computer-aided finite element analyses to estimate the impact of the fundamental parameters such as the compressive strength of concrete, axial column force, beam concrete confinement and the dimensions of the steel plates on the seismic performance of their connection. According to the result of their experimental program, they showed that their connection has a relatively high flexural capacity with comparable ductility and energy dissipation properties concerning the regular monolithic reinforced-concrete beam-to-column connections. The result of their numerical analyses showed that the initial stiffness of their connection is nearly independent of the selected parameters and the ultimate load-bearing capacity of their connection showed to have a relatively low dependency on the selected parameters. Thus, their experimental results might be accepted to be valid for various axial loading conditions of the precast columns and the different geometrical and material configurations of the connection components.

According to the previous studies presented for the beam-to-column connection of precast concrete frames, it could be concluded that the *wet connection* details have superior load-deformation behaviour under seismic actions compared to *dry connection* details. It is important to highlight that the seismic behaviours of the proposed structural joint configurations are out-of-the-scope of the FEOSBuild research project and this thesis. For the development of *Grouted Joints for Continuous Composite Slim-floor Beams (GJSFB)* presented in Chapter 5 also cast-in-situ concrete application (*wet connection* detail) was adopted to achieve structural integrity between the continuous composite slim-floor beams and reinforced-concrete columns/walls of the steel-concrete hybrid building systems. Additional literature reviews regarding the load-deformation behaviors of the continuous composite beams are presented in Chapter 5.

This section presented considerable research effort dedicated to develop innovative and novel beam-to-column and beam-to-beam connection details for steel-concrete hybrid, steel-steel, and precast concrete building frames. Regarding the cutting-edge solutions presented in this chapter, it is possible to define several conclusions for the requirements to develop novel structural joint configurations for fast erection of steel structures for buildings (FEOSBuild).

First of all, to develop novel beam-to-column connections for steel-concrete hybrid building systems, it is required to conduct experimental, numerical and analytical investigations to determine the load-deformation behaviors and the fundamental parameters affecting these behaviors of the novel connections. Thereby, it might be possible to achieve large-scale market integration of the

novel connections. On the other hand, only three of the presented research outputs have shown to be commercially available for large-scale implementation in construction industry. These commercially available solutions are *PCs® Corbel* [30, 31], *AEP® steel bracket* [45] and *ConXTech® ConXL™* [46]. It is important to highlight that two of these solutions have been technically approved to be implemented in engineering structures by satisfying the required details for structural design and applications [31, 46]. However, the commercialization and the technical assessment of the structural joint configurations presented in this thesis were not the target of the FEOSBuild research project.

Secondly, it is shown with the existing literature that on-site welding needs to be eliminated and the use of structural bolts should be minimized to increase the efficiency of the construction sites by reducing the labour-intensive construction tasks which require special tools and trained workers. In addition, it is demonstrated that accommodation of construction and manufacturing tolerances is crucial for the fast erection of structural frame components. State-of-the-art has shown that oversized and slotted bolt-holes, and serrated surface topologies to be excellent solutions for the structural details of connection components in order to accommodate the tolerances. Furthermore, it is also shown that joint configurations consisting of corbel plates to position steel beams without the need of temporary supports such as scaffolding greatly improve the efficiency of construction site operations by providing more space for workers and storage while enabling tower cranes to be mobilized for other construction tasks after the beam has been placed on the corbels. Therefore, the joint configurations proposed in this thesis also eliminate on-site welding and minimize the use of structural bolts having structural corbels to achieve fast erection strategies in construction sites. Accordingly, the joint configurations suggested in this thesis are designed to eliminate on-site welding and to minimize the use of structural bolts while including corbel plates or corbel-like joint configuration for the efficiency of construction site operations.

Thirdly, it has been proven with many other researchers that dovetail-socket type structural connection details are good candidates for eliminating on-site welding and bolting for the assembly of building frame components. Although the connection components with dovetail-socket details require special production techniques and show non-linear load-deformation behaviors due to their complex geometry, material non-linearities and non-linear contact interactions between the dovetail-socket surfaces, it is important to consider that the recent developments in modern industrial machinery allow fast, optimized and economical production of connection components with complex geometries. For instance, technologies such as 3D-printing with Wire Arc Additive Manufacturing (WAAM) technique for steel construction [57] or cutting methods such water jet and computer numerical control (CNC) machining of steel plates can be used for the fabrication of complex geometries. Furthermore, the other challenge which ATLSS research group [37] dealt in 1994 for geometrical and material nonlinearities is now less pronounced. Thanks to more capable computational resources these nonlinear behaviours can be considered in numerical models and thereby providing better prediction for the mechanical behavior of dovetail-socket type structural connections under various loading conditions. Additionally, this better precision render parametric analysis more reliable and erase the need for experimental tests with prohibitive costs. On the

other hand, the load-bearing mechanism of dovetail-socket type structural connections has not yet been fully understood and there is a lack of practical knowledge for the market integration of these solutions in the construction industry. Therefore, further research is required to develop analytical resistance models for the estimation of the ultimate load-bearing capacities of these types of structural connection mechanisms. In addition, partial safety factors are required to be established for the engineering design calculations of dovetail-socket type structural connection details.

To conclude, in the light of the available literature, the most of the research effort presented in this thesis focused to develop novel structural joint configurations that eliminate on-site welding and minimize use of structural bolts to enable fast erection of steel beams of steel-concrete hybrid building systems. As consisted with the presented literature, load-deformation behaviors and load-deformation characteristics of the proposed joint configurations were determined with experimental, numerical and analytical investigations.

CHAPTER 3

Saw-tooth Interface Mechanical Interlock Bolted Connection

3.1 Introduction

The current advancements in Computer Numerical Control (CNC) technologies may offer novel solutions for the design and the execution of the structural joints for steel-concrete hybrid building systems to realize fast erection strategies by accommodating construction and manufacturing tolerances with on-site weld free joint components. However, by the best of the knowledge of the author, limited solutions with these technologies were introduced up to the date for the steel-to-concrete interfaces of the hybrid building systems [17, 45]. In this chapter, a novel saw-tooth interface mechanical interlock bolted connection, here-on named SMIBC, is proposed to enable the fast erection of steel beams to RC-columns/walls by accommodating manufacturing and construction tolerances for the load-bearing frames of the hybrid building systems. The mechanical interlock mechanism of SMIBC was achieved by CNC cut steel saw-tooth topology and high strength T-head bolts.

The proposed joint configuration of SMIBC enables construction contractors to use their steel formwork systems without any on-site customization and to assembly steel girders with RC-columns/walls without on-site welding while allowing the accommodation of the construction and the manufacturing tolerances in three spatial directions. Fig. 3.1 illustrates the overall configuration of the joint assembly and the components of SMIBC with the nominal dimensions.

T-head high-strength bolts (T-bolts) are selected to assemble the anchor and corbel plates. Thus, the interlock mechanism between the saw-tooth surfaces is secured with a simple yet robust and reliable connection method. The horizontal slotted holes on the anchor plate enable to position the T-bolts within $\mp$12mm horizontal range with respect to the centre of the horizontal slotted holes. The vertical slotted holes drilled on the corbel plate and the saw-tooth surfaces enable accommodation of $\mp$12mm construction tolerances in the vertical direction with respect to the centre of the horizontal slotted holes. Thereby, it becomes possible to accommodate construction tolerances in horizontal and vertical directions independently. This feature brings high flexibility to the construction field against the conventional construction techniques of the steel-concrete hybrid multi-storey and high-rise buildings [23]. The assembly of the proposed joint configuration is also illustrated in Fig. 3.1d in which the longitudinal slotted holes positioned at the bottom

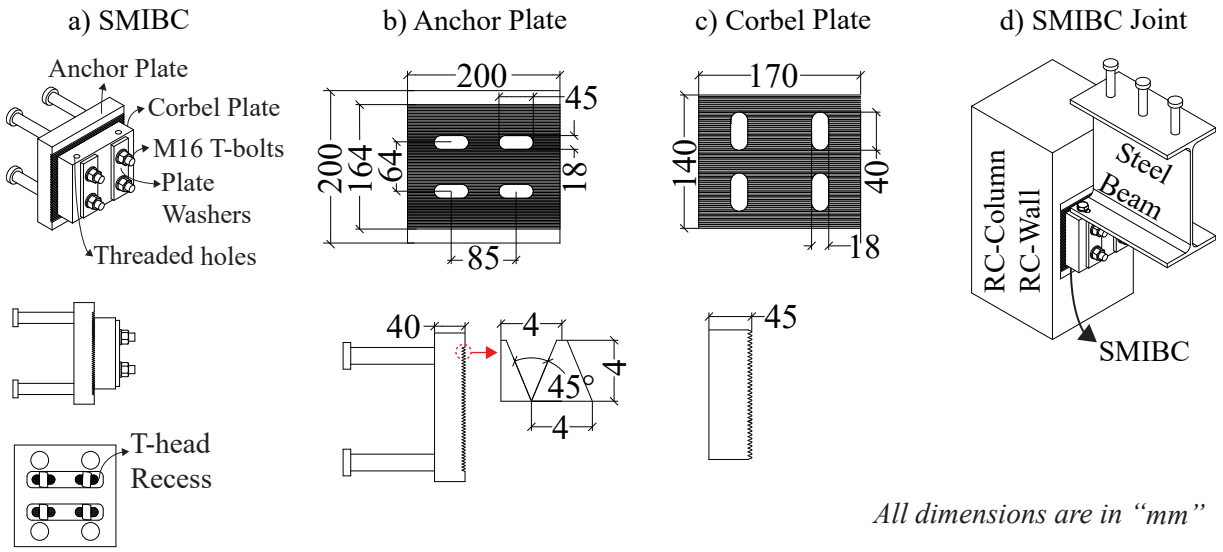

Figure 3.1: Saw-tooth interface mechanical interlock bolted connection (SMIBC).

flange of the steel beam allows accommodating the construction tolerances along the longitudinal direction of the steel beam. The steel beam could be connected with SMIBC through the threaded holes positioned at the top surface of the corbel plate by using high-strength bolts to resist possible torsional actions during the construction stages. It is also possible to variate the arrangement to connect the steel beam and the corbel plate, such as by shop-welding vertically aligned threaded rods to the back surface of the corbel plate. The detailed technical drawings and the images for the prototype production of SMIBC components are presented in Section 3.3 together with the examination for the accommodation of the construction and the manufacturing tolerances with SMIBC for RC-column configuration. In addition, Fig. 3.2 shows the production of the saw-tooth interface by means of the CNC cutting procedure and the coupling of the saw-tooth surfaces. Further images regarding to the coupling of the saw-tooth surfaces of SMIBC components are presented in Section 3.3.

Four different experimental test campaigns were established to investigate the load-bearing mechanism and the load-deformation behaviors of SMIBC and SMIBC joint in RC-column configurations.

Initially, the load-bearing mechanisms of SMIBC was investigated with isolated test configurations of equivalent SMIBC components for non-eccentric and eccentric loading conditions under two different test campaigns. Section 3.2 presents these experimental test campaigns, corresponding numerical simulations, a numerical parametric study, an analytical resistance model of SMIBC and the statistical assessment of the analytical resistance model with respect to the output results of the numerical parametric study based on EN1990, Annex D [58]. Furthermore, the frictional resistance between the saw-tooth surfaces of the anchor and the corbel plates was investigated with a separate test campaign performed according to EN1090-2, Annex G [59]. Annex-A of this thesis presents the results of the slip-factor determination tests performed to determine the slip-factor

a) CNC-production of Saw-tooth Surfaces b) Coupling of Saw-tooth Surfaces

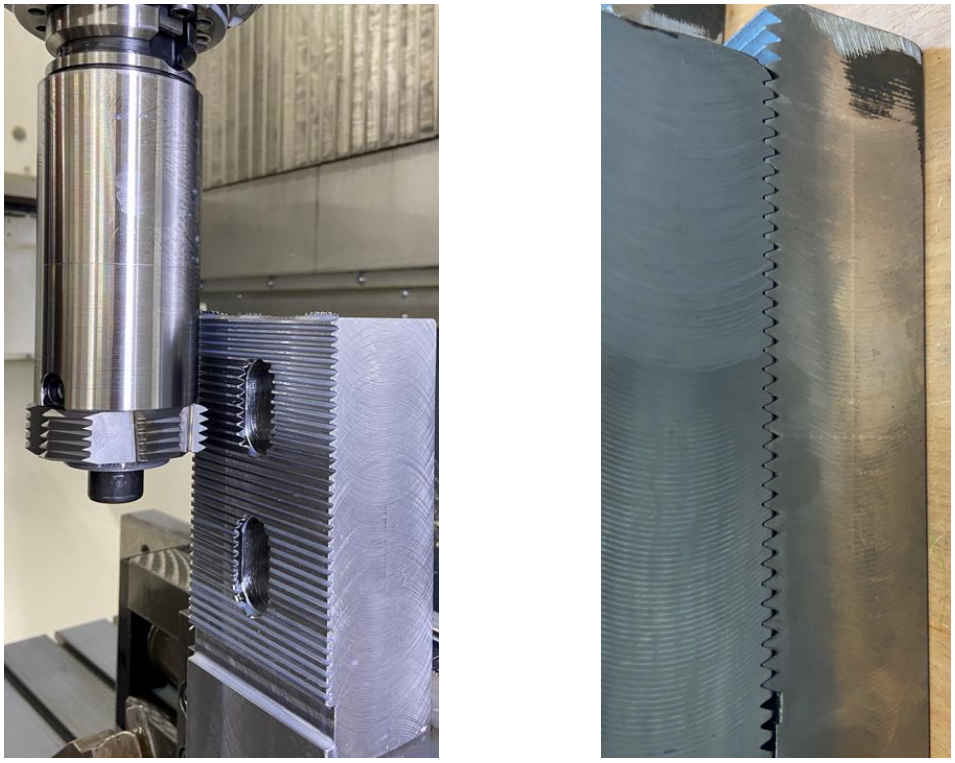

Figure 3.2: Production of the saw-tooth surfaces and their coupling.

between the saw-tooth surfaces of SMIBC components.

Additionally, the load-deformation behaviors of SMIBC joint in RC-column configurations which were detailed with different steel reinforcement next to the anchor plate of SMIBC were investigated with another experimental test campaign. Section 3.3 presents the details of the test campaign performed for SMIBC joint in RC-column configurations together with the corresponding numerical simulations, the design calculations and a modified design methodology for the anchorage of SMIBC in the RC-column configurations in accordance with EN1992-4 [1].

3.2 Load-deformation behavior of SMIBC

This section presents experimental, numerical and analytical investigations performed to establish the load-deformation behaviors and the ultimate load-bearing capacity of SMIBC. To be able to solely focus on to the load-bearing mechanisms of SMIBC, isolated configurations of SMIBC components without reinforced-concrete structural members were investigated.

Two different test campaigns were executed to determine the load-displacement and moment-rotation behaviours of SMIBC for non-eccentric and eccentric loading conditions;

- The first test campaign, here-on named SMIBC-E0, consisted of two test series, and it was designed to determine the load-displacement behaviour of SMIBC under non-eccentric monotonic loading condition to investigate the load-bearing mechanism and to determine the ultimate load capacity of the saw-tooth interface.
- The second test campaign, here-on named SMIBC-E1, consisted of three test series, and it was designed to determine the load-displacement and moment-rotation behaviours of SMIBC under monotonic loading with eccentricity.
- For both of the test campaigns, the initial bolt pretension level was selected as the variable test parameter between the test series. Table 3.1 summarizes the test campaigns and the variable test parameters.
- Due to the loading capacity limitations of the available testing machines, the test campaigns were executed with only the horizontal symmetric half of SMIBC. Although the initial deformation profile resulted from the clamping force (bolt pretension load) along the saw-tooth interface could not be represented by the half geometry of the connection, a set of computer-aided finite element analyses (FEAs) was performed prior to the tests to analyze the impact of the initial deformation profile on the ultimate capacity by comparing the output results of FEAs performed with and without symmetric boundary conditions. As a result, it was shown that the horizontal half-symmetric configuration of SMIBC is sufficient to determine the load-displacement and moment-rotation behaviours. The details of the aforementioned FEAs performed prior to the experimental test campaigns are presented in Section 3.2.3.1.

Thereafter, the experimental test campaigns were simulated by means of FEAs to further investigate the failure mechanisms of SMIBC under non-eccentric and eccentric loading conditions. The output results of the FEAs were validated against to the test results. Thereby, the selected FE-modelling and solution techniques were used to perform a numerical parametric study to understand the impact of the load-eccentricity, the material strength and the static-friction coefficient between the saw-tooth surfaces of SMIBC components on the ultimate load-bearing capacity of SMIBC.

Finally, based on the investigation of the experimental test results and the output results of the FEAs, an analytical resistance model was established to estimate the ultimate load-bearing capacity of SMIBC. The estimation of the analytical resistance model against to the output results of the numerical parametric study was evaluated based on the statistical evaluation procedure of EN1990, Annex D [58] and partial safety factors were established for the utilization of the analytical resistance model in engineering approximations for the capacity estimation of SMIBC.

Table 3.1: Summary of the parameters for the isolated SMIBC test campaigns.

Test Campaign	Test ID	Load-eccentricity (e) [mm]	Bolt Pre-tension[1] ($F_{p,C}$) [kN]
SMIBC-E0	E0-1-01	0	22
	E0-1-02	0	22
	E0-1-03	0	22
	E0-2-01	0	70
	E0-2-02	0	70
	E0-2-03	0	70
SMIBC-E1	E1-1-01	30	22
	E1-1-02	30	22
	E1-1-03	30	22
	E1-2-01	30	44
	E1-2-02	30	44
	E1-2-03	30	44
	E1-3-01	30	70
	E1-3-02	30	70
	E1-3-03	30	70

[1] The level of the pre-tension load was identical for both the upper and lower M16-bolts.

3.2.1 SMIBC capacity tests without load-eccentricity, SMIBC-E0

SMIBC-E0 test campaign was executed to determine the load-bearing capacity of the saw-tooth interface under non-eccentric monotonic loading. Therefore, a symmetric test frame was designed with a configuration adopted from the principles of the standard push tests defined by EN1994-1-1 Annex B [2]. Fig. 3.3 shows the overall geometry of the test set-up with the technical drawings and the images of the main set-up components. The height of the saw-tooth interface was kept identical to the connection assembly presented in Fig. 3.1. However, as indicated earlier, the width of the saw-tooth interface was arranged to be equal to the horizontal half symmetric width of the connection assembly. The dimensional details of the test specimens are also given in Table 3.2 together with the ordered material grades. The M20 threaded-rods shown in Fig. 3.3 were designed to achieve additional stiffness against the separation of the saw-tooth interface. Thus, it was aimed to determine the ultimate load-bearing capacity of the saw-tooth interface without any separation between the saw-tooth surfaces of the inner and cover plates, which may be triggered due to the unique shape of the saw-tooth threads, as later explained in Section 3.2.4. Furthermore, additional nuts were installed to the upper M20-threaded rods at the outer web surfaces of the U-profiles to resist rotation that may occur due to the eccentricity between the loading and the support reactions.

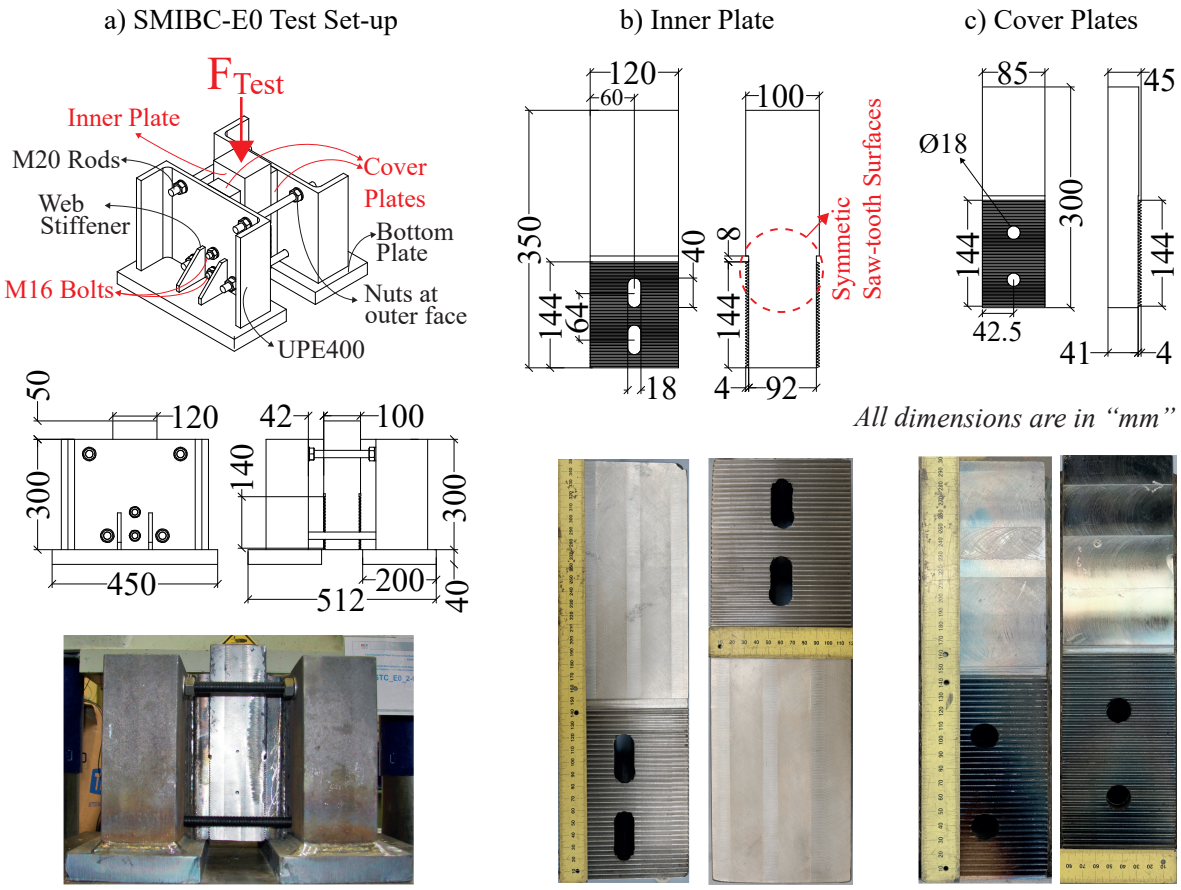

Figure 3.3: SMIBC-E0 test set-up and the technical drawings of the main set-up components.

Table 3.2: Overall details of the test specimens for SMIBC-E0 test campaign.

Component Name	Dimensions [in mm]	Ordered Grade	Norm
Inner Plates	350x120x100	S235	EN10025-2 [60]
Cover Plates	300x85x45	S235	EN10025-2 [60]
Bottom Plates	450x200x40	S460	EN10025-2 [60]
U-Profiles	UPE400	S355	EN10025-2 [60]
M16-bolts	M16x260	8.8	ISO4014 [61]
M20 Threaded-rods	M20x400	10.9	DIN976 [62]

To assemble the test specimens, the bottom plates, web stiffeners and the cover plates were welded to the UPE-profiles. Thereafter, the inner plate was assembled with the cover plates in a vertical position that the M16-bolts were in contact with the bottom surface of the slotted holes of the inner plate. In addition, the flat contact surfaces of the inner and the cover plates were greased. Thereby, the applied loading was guaranteed to be resisted by only the saw-tooth interface without bolt-shearing and frictional resistance.

3.2.1.1 Material properties of the test specimens

The mechanical material properties of the inner plates, cover plates and UPE-profiles were determined with steel coupon tests performed according to EN ISO 6892-1 [63]. 3 coupon samples were manufactured from the aforementioned components after the experimental tests. Table 3.3 summarizes the results of the material characterization tests for SMIBC-E0 test campaign. The detailed results are also presented in Annex-B.

Table 3.3: Material properties of the main test specimens for SMIBC-E0 test campaign.

Specimen Name	Order	Sample ID	E^1 [GPa]	f_y [MPa]	f_u [MPa]	A[2] [%]
Inner Plate	S235	SMIBC-E0-1-01 (IP-1)	195	218	406	35.5
		SMIBC-E0-2-01 (IP-2)	196	181	406	36.0
		SMIBC-E0-1-03 (IP-3)	194	181	406	40.0
		Mean Values	195	193	406	37.2
Cover Plate	S235	SMIBC-E0-1-01 (CP-1)	207	253	463	33.0
		SMIBC-E0-2-01 (CP-2)	208	309	474	31.5
		SMIBC-E0-1-03 (CP-3)	207	268	459	35.0
		Mean Values	207	277	465	33.2
UPE-Profile	S355	SMIBC-E0-1-01 (UPE-1)	205	380	534	28.5
		SMIBC-E0-2-01 (UPE-2)	205	381	535	32.5
		SMIBC-E0-1-03 (UPE-3)	205	386	537	29.0
		Mean Values	205	382	535	30.0

[1] Elastic modulus (E) was determined according to EN ISO 6892-1 Method A1 [63].

[2]The term A corresponds to percentage elongation of the steel coupon after the fracture [63].

3.2.1.2 Instrumentation of the test specimens

Fig. 3.4 shows the test set-up together with the layout of the measurement equipment. In total, six linear variable displacement transducers (DTs) were used to measure the relative displacements between the inner plate and the cover plates. In addition, two load-cells (LCs) were installed under the nut of the M16-bolts to be able to apply the initial bolt pre-tension load (see Table 3.1) with high precision and to measure the variation of the tension stress resultants in the M16-bolts during the tests. Furthermore, two additional LCs were also installed under the nuts of the lower row of the M20 threaded-rods to measure the total force resisted against the separation of the saw-tooth interfaces by the threaded-rods. The measurement ranges and the measurement alignments of the displacement transducers and the load-cells are summarized in Table 3.4.

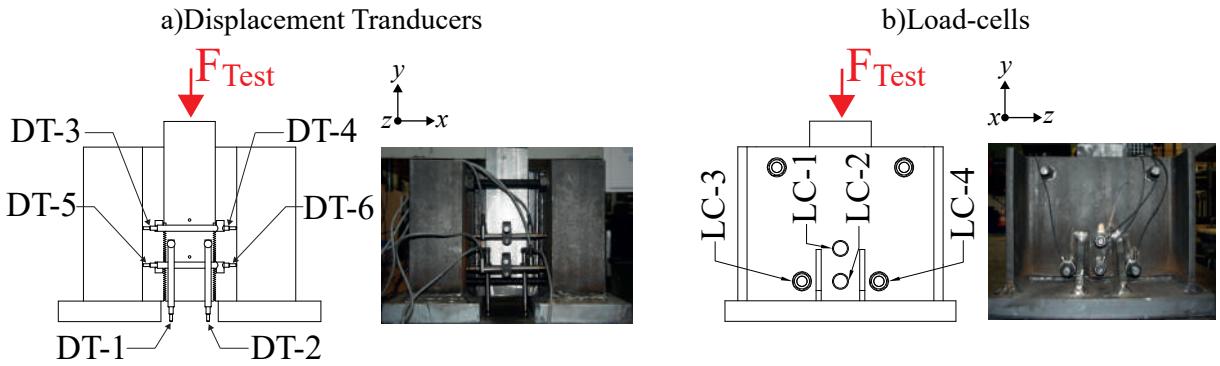

Figure 3.4: Displacement transducers (DT) and load-cells (LC) / SMIBC-E0 test campaign.

Table 3.4: Summary of the displacement-transducers and the load-cells / SMIBC-E0 test campaign.

Sensor ID	Direction	Measurement Range
DT-1	Vertical (*y-axis*)	10mm
DT-2	Vertical (*y-axis*)	10mm
DT-3	Horizontal (*x-axis*)	10mm
DT-4	Horizontal (*x-axis*)	10mm
DT-5	Horizontal (*x-axis*)	10mm
DT-6	Horizontal (*x-axis*)	10mm
LC1	Horizontal (*x-axis*)	200kN
LC2	Horizontal (*x-axis*)	200kN
LC3	Horizontal (*x-axis*)	400kN
LC4	Horizontal (*x-axis*)	400kN

3.2.1.3 Loading procedure and the execution of SMIBC-E0 test campaign

Fig. 3.5 illustrates the loading procedure of the experimental tests having the following steps;

- Monotonically load up to 5% of the expected test capacity - $F_{u,exp}$ (Displacement-controlled 0.12mm/min).
- Cycling loading period between 5% - 40% of the expected test capacity (Force-controlled 0.01Hz - 25Cycles).
- Monotonically load until the ultimate test capacity - $F_{u,Test}$ (Displacement-controlled 0.12mm/min).

For the first test of each test series, the expected ultimate test capacity ($F_{u,exp}$) was estimated with FEA performed prior to the experimental tests with the characteristic material properties [50]

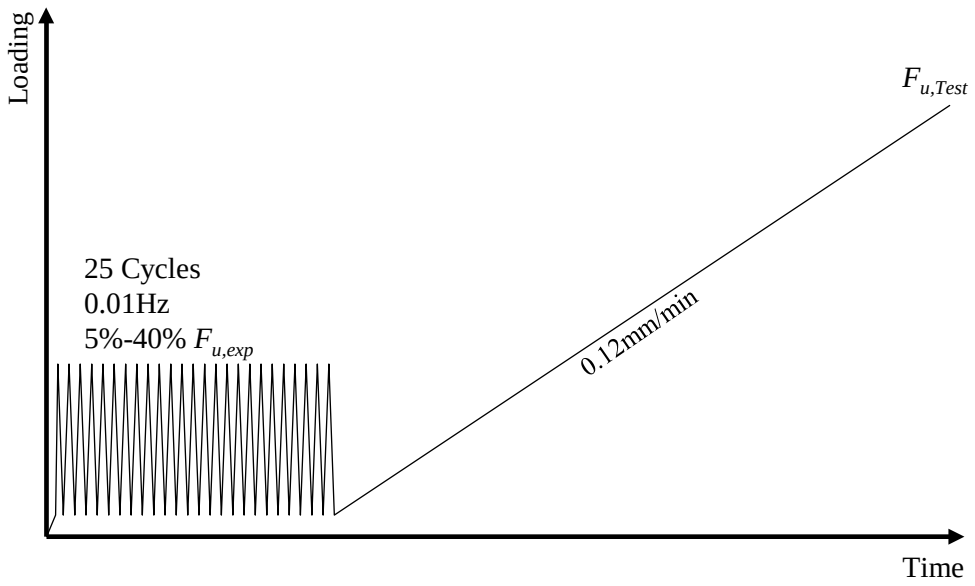

Figure 3.5: Loading procedure of SMIBC-E0 test campaign.

of the ordered material grades listed in Table 3.2. The FE-model is presented in Section 3.2.3.2. For the second and the third tests of each test series the expected ultimate test capacity was taken as the ultimate test load of the first test of the corresponding test series.

The tests were executed in The Structural Laboratory for The University of Wuppertal with a 10MN capacity uni-axial compression testing machine. The force from the testing machine and the data from the measurement devices presented in Section 3.2.1.2 were continuously recorded with 1000Hz data acquisition speed during the tests.

3.2.1.4 Results and discussions

Fig. 3.6a shows load-displacement curves of each test performed under SMIBC-E0 test campaign. The load values in Fig. 3.6a are given as half of the applied load (F_{Test}) as the test set-up; thus, the saw-tooth interfaces were symmetric with respect to the vertical central axis of the test set-up. The relative displacement between the inner and the cover plate (δ_y) was calculated as the arithmetic mean of the data recorded by DT-1 and DT-2 (see Fig. 3.4a) as presented in Eq. 3.1. The summary of the test results is presented in Table 3.5. The ultimate test loads ($F_{u,Test}$) listed in the table correspond to the maximum load recorded from the test machine while the ultimate load-bearing capacity of each symmetric saw-tooth interface is denoted as F_u in the table.

$$\delta_y = \frac{DT_1 + DT_2}{2} \tag{3.1}$$

As the horizontal half-symmetric configuration of SMIBC was tested, the ultimate load-bearing capacity of the full SMIBC configuration for non-eccentric monotonic loading condition could be determined by multiplying the ultimate load-levels presented in Fig. 3.6a by a factor of two.

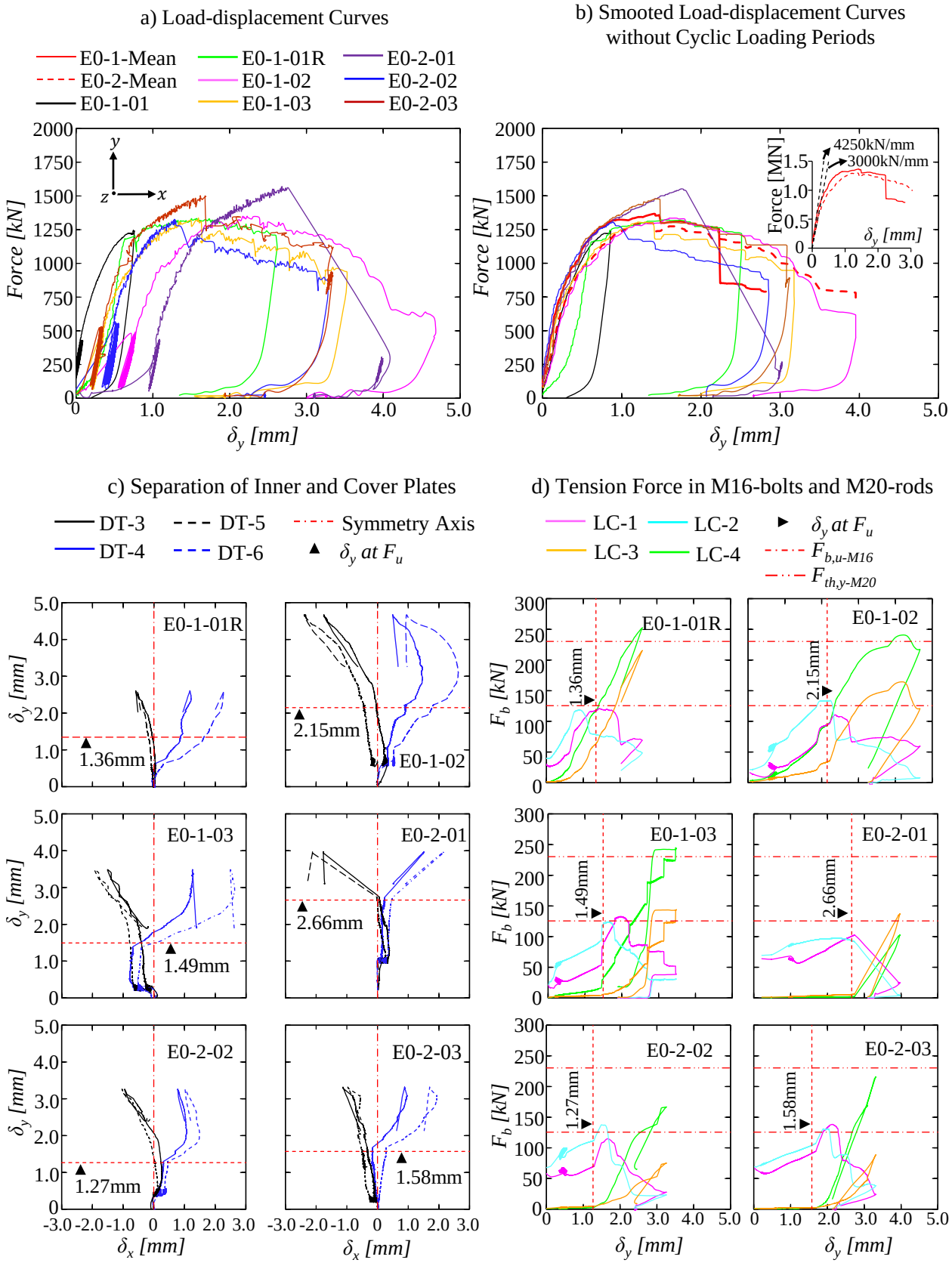

Figure 3.6: Test results of SMIBC-E0 test campaign.

Table 3.5: Summary of the test results for SMIBC-E0 test campaign.

Test Series	Test ID	$F_{u,Test}$ [kN]	F_u [kN]	$\delta_{y,at\ F_u}$ [mm]	$F_{b,M16\text{-}1\ at\ F_u}$ [kN]	$F_{b,M16\text{-}2\ at\ F_u}$ [kN]
SMIBC-E0-1	E0-1-01R	2666	1333	1.36	117	78
	E0-1-02	2700	1350	2.15	95	134
	E0-1-03	2674	1337	1.49	84	118
	Mean Values	2680	1340	1.67	99	110
SMIBC-E0-2	E0-2-01	3138	1569	2.66	101	93
	E0-2-02	2650	1325	1.27	65	108
	E0-2-03	3006	1503	1.58	91	104
	Mean Values	2931	1466	1.84	86	102

Two different test results are presented for the initial test of the first test series, which are identified as E0-1-01 and E0-1-01R in Fig. 3.6a-b. Because the first test, E0-1-01, was repeated, and the repetition is labelled as E0-1-01R. The initial attempt (E0-1-01) was conducted with a 2.5MN universal testing machine, and no failure was recorded at the maximum load capacity of the testing machine. Therefore, the test specimens were carefully carried in an assembly form to a 10MN uni-axial compression testing machine and the test was repeated. It could be detected from Fig. 3.6a that nearly all of the deformation except the part that belongs to the cycling loading period was recovered during the unloading path of the initial attempt. Therefore, the repetition (E0-1-01R) was executed without the cycling loading period. In addition, it could be noticed from Fig. 3.6a that the unloading period of the initial attempt and the loading period of the repetition show similar load-displacement characteristics; thus, it could be indicated that the test specimens did not damage during the transportation between the testing machines. However, the test E0-1-01R was deliberately terminated at an instant that corresponds to about a 10% load drop after reaching the maximum test load due to safety concerns. On the other hand, the other tests were not terminated before having a 25% load drop after attaining the ultimate test loads.

In Fig. 3.6b, the smoothed load-displacement curves for each test are presented excluding the cycling loading period to have a clear comparison of the test results. The smoothing operations were performed over the median of the data points for each of the curves presented in Fig. 3.6a. In addition, the mean load-displacement curves of each test series are given in Fig. 3.6b with the initial translational elastic stiffness values for each test series. Based on the mean curves, it is evident that the increase in the initial pre-tension load of the M16-bolts from 22kN to 70kN (see Table 3.1) resulted in approximately 42% higher the initial elastic stiffness for the saw-tooth interface. In addition, the ultimate load-bearing capacity of the saw-tooth interface was also enhanced by about 10%. The increase in the initial elastic stiffness and the ultimate capacity could be attributed to the better coupling of the saw-tooth surfaces which may be impacted by the cutting imperfections. The

impact of the bolt pre-tension on the load-bearing capacity and the initial elastic stiffness of SMIBC is also discussed in Section 3.2.3.2 with numerical simulations of the test campaign.

Fig. 3.6c shows the relative horizontal displacements, i.e. separation, between the inner and the cover plates; thus, the saw-tooth interfaces, recorded by DT-3 to DT-6 (see Fig. 3.4a). The separation between the saw-tooth interfaces was less than 1mm for all tests at the ultimate test loads. Accordingly, comparing the level of the separations with the height of the saw-tooth thread (4mm-see Fig. 3.1b) nearly a full-contact condition along the saw-tooth interfaces could be stated before reaching the ultimate test loads. Therefore, it is concluded that the failure of the saw-tooth threads triggered the initiation of the load-drop. In addition, the estimations of the equal load distribution for symmetric saw-tooth interfaces of the test specimens could be justified with Fig. 3.6c as the separations between the inner and the cover plates were similar with respect to the vertical symmetry axis of the test set-up. The only excessive deviation from this observation was recorded for the third test of the first test series (E0-1-03) for which the cover plate positioned at the right side of the test assembly approached about 0.8mm to the inner plate before attaining the ultimate test load. This behaviour could be attributed to the geometrical imperfections of the test specimens. Because the imperfections would cause a gap between the flat surfaces of the inner and the cover plates; as a result, the cover plate would rotate around the out-of-plane direction (*z-axis*) of the test assembly due to the eccentricity between the saw-tooth interface and the position of the support reaction. Consequently, this action would lead the cover plate to approach the inner plate.

Fig. 3.6d shows the variation of the tension forces for the M16-bolts and the bottom row of the M20 threaded-rods. At the ultimate test loads, the tension stress resultants in the M20-threaded rods did not reach their characteristic yield limit ($F_{th,y\text{-}M20}$) calculated based on the material grade listed in Table 3.2. As a result, it could be justified for all of the tests that the saw-tooth interfaces were almost in full-contact condition before attaining the ultimate test load, and the failure of the saw-tooth threads triggered the load-drop. Furthermore, in Fig. 3.6d the sudden increases could be detected for the tension stress resultants in the M16-bolts and the M20 threaded-rods at the instants that correspond to the ultimate test loads. Due to the unique shape of the saw-tooth threads it is the fact that the applied vertical force decomposes to in-plane horizontal stress resultants (*x-axis* direction) along the saw-tooth interfaces and the magnitude of the decomposition in the horizontal direction highly increases around the ultimate test load due to the high deformations, or more specifically due to the out-of-plane (*z-axis* direction) rotation of the saw-tooth threads.

Additionally, it could be noticed in Fig. 3.6d that for the tests E0-1-01R and E0-1-02, the M16-bolts reached their ultimate characteristic capacities ($F_{b_u,M16}$) which was calculated based on the material grade of the M16-bolts listed in Table 3.2, before attaining the ultimate test loads. However, for the test E0-1-03 the variation of the tension forces in the M16-bolts and the M20 threaded-rods shows similar behaviour to those observed in the second test series (E0-2). This difference could be explained by the in-plane horizontal relative displacements recorded between the inner and cover plates for the right side of E0-1-03 test assembly. As described previously, the cover plate at the right side of E0-1-03 test assembly approached the inner plate before reaching the ultimate test

load, and this resulted in additional compressive stress along the saw-tooth interface as similar to the higher clamping forces (i.e. initial bolt pre-tension) applied for the second test series, E0-2. Therefore, the variations of the tension stress resultants in the M16-bolts and the M20-threaded rods of the test E0-1-03 were similar to the second test series.

a) Deformation of a Saw-tooth Surface for the Inner Plate

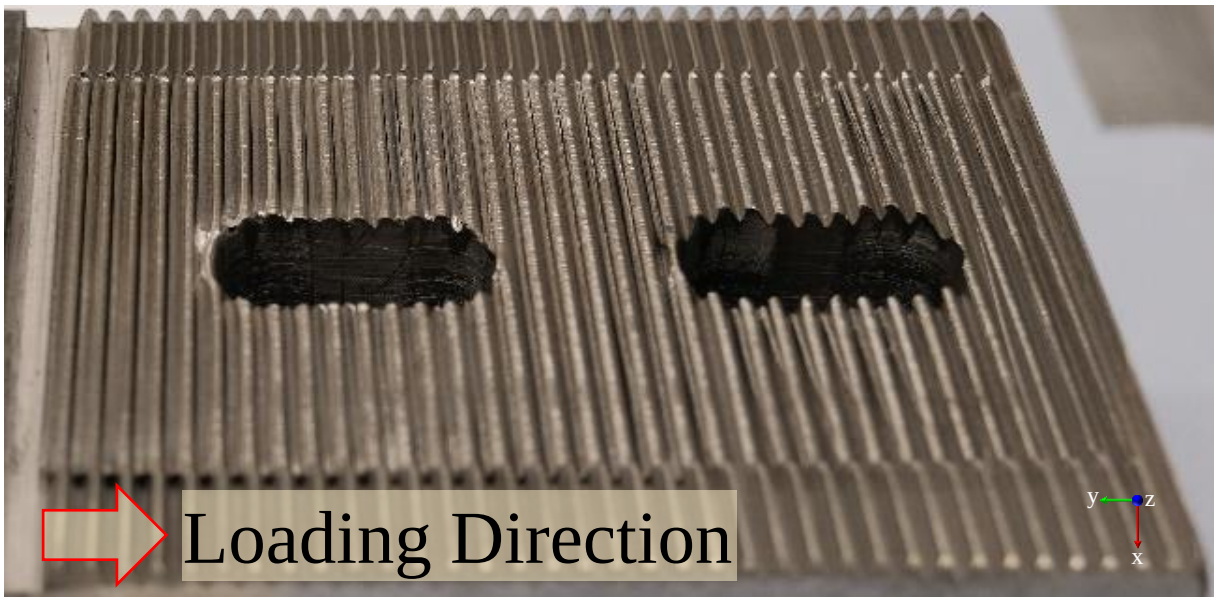

b) Deformation of the Saw-tooth Surface for a Cover Plate

c) Deformation of the M16-bolts

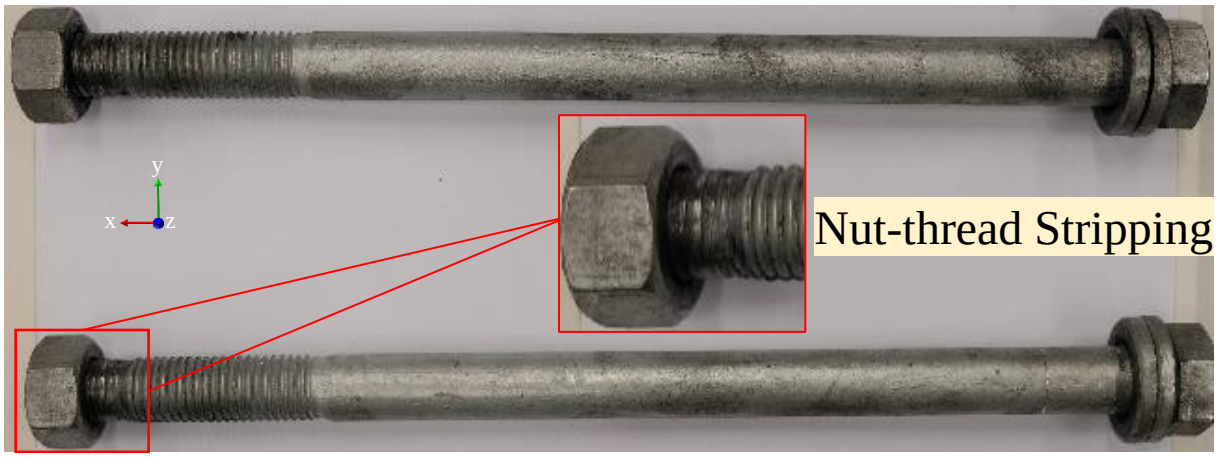

Figure 3.7: Deformations of E0-1-02 test specimens.

Fig. 3.7 shows the deformation profiles for one of the saw-tooth interface and the M16-bolts for E0-1-02 test specimens. The uniform yielding along the entire interface height of the saw-tooth surface is visible for the inner plate. In addition, the rotation of the saw-tooth threads of the cover plate and the damage at the far edge of the saw-tooth surface of the inner plate indicate that the saw-tooth threads close to the load introduction region underwent more deformation than the others. Thus, it could be deduced that the applied loading started to be resisted by the saw-tooth threads close to the load-introduction region and by their yielding the loading successively distributed to the following saw-tooth threads. Furthermore, the rotation of the saw-tooth threads for both the inner plate and the cover plate clearly explains the variation of the tension forces in the M16-bolts and the M20-threaded rods as the rotation of the saw-tooth threads leads to further decomposition of the applied vertical load into in-plane horizontal stress resultants. Although it was observed from Fig. 3.6d that the M16-bolts reached their characteristic ultimate strength, no necking was observed (see Fig. 3.7c). This is because the fact that the selected M16-bolts [61] behave similarly to the HR-type high strength bolts, which lose their load-bearing capacities due to the failure of the bolt threads within the nut [64], i.e. nut-thread stripping, as highlighted in Fig. 3.7c. Additional images after test condition of the test specimens for the other tests of SMIBC-E0 test campaign are presented in Annex-B.

3.2.2 SMIBC capacity tests with load-eccentricity, SMIBC-E1

SMIBC-E1 test campaign was executed to determine the load-displacement and moment-rotation behaviours of SMIBC under monotonic loading condition with load-eccentricity. Fig. 3.8 shows the test set-up together with the technical drawings and the images of the main set-up components of SMIBC-E1 test campaign. As similar to SMIBC-E0 test campaign, the height of the saw-tooth interface was kept identical to the height connection assembly (see Fig. 3.1), and the width of the saw-tooth interface was equal to the horizontal half symmetric width of SMIBC. The dimensional details of the test specimens are also given in Table 3.6 together with the ordered material grades. The load-eccentricity (e) was achieved by the introduction of the load to the cover plates through M36-bolts positioned at the top of the cover plates. The distance between the mid-length of the M36-bolt holes and the saw-tooth surfaces was arranged to be equal to desired load-eccentricity of 30mm (e=*30mm*). In addition, 5mm gaps highlighted in Fig. 3.8a were designed to resist the moment action only with the mechanical interlock components which are the saw-tooth interface and the M16-bolts.

For the preparation of the test set-up, the inner plate was assembled with the cover plates in a vertical position in which the shanks of the M16-bolts were in contact with the bottom surface of the slotted holes of the cover plates. Thereby, the most unfavourable position was selected for the M16-bolts, for which they may be subjected to shear and tension forces simultaneously.

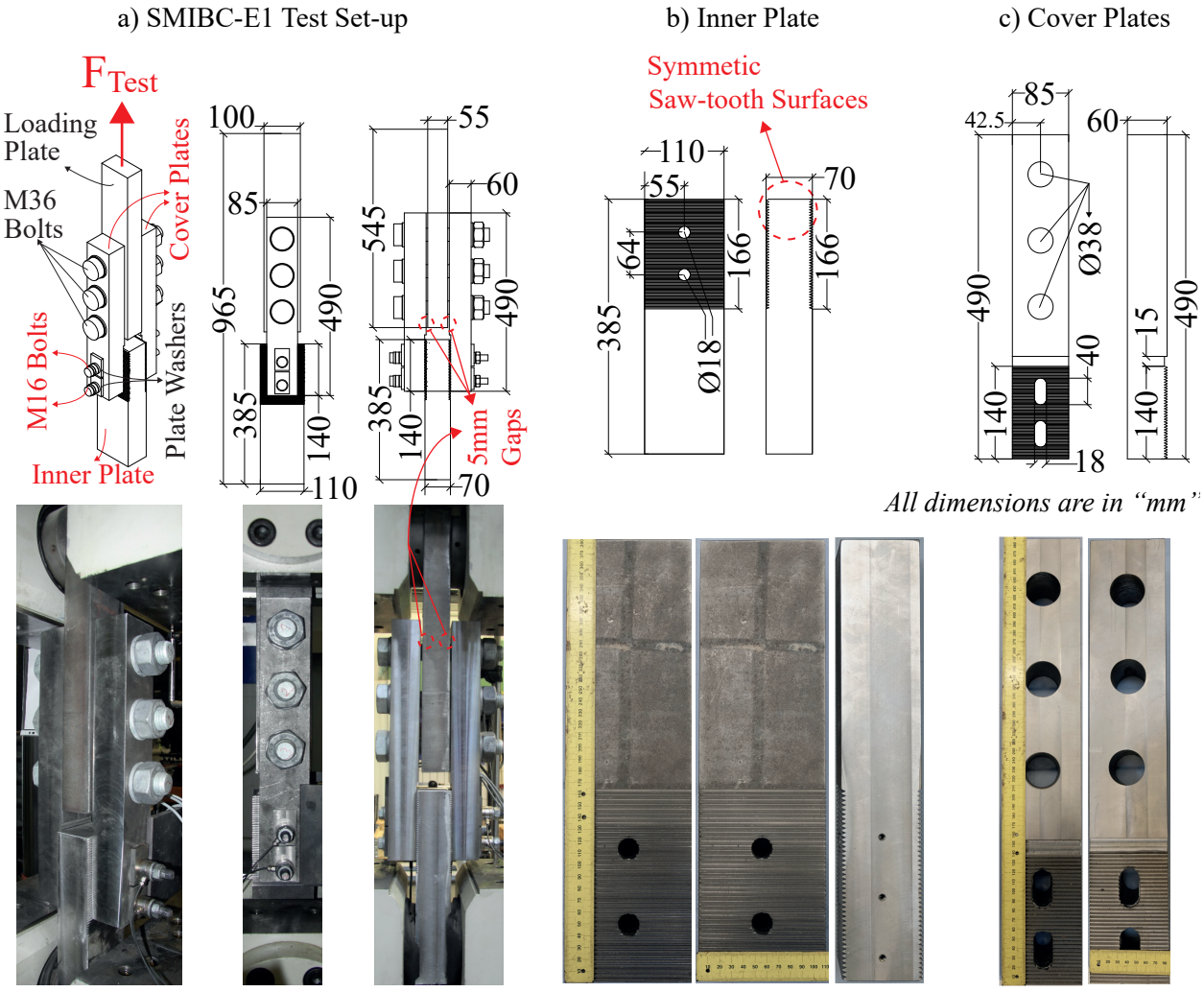

Figure 3.8: SMIBC-E1 test set-up and the technical drawings of the main set-up components.

Table 3.6: Overall details of the test specimens for SMIBC-E1 test campaign.

Component Name	Dimensions [in mm]	Ordered Grade	Norm
Inner Plates	385x110x70	S235	EN10025-2 [60]
Cover Plates	490x85x60	S235	EN10025-2 [60]
Loading Plates	545x100x55	S460	EN10025-2 [60]
M16-bolts	M16x260	8.8	ISO4014 [61]
M36-bolts	M36x240	10.9	EN14399-4 [65]

3.2.2.1 Material properties of the test specimens

The mechanical material properties of the inner plates, cover plates and M16-bolts were determined with steel coupon tests performed according to EN ISO 6892-1 [63]. 3 coupon samples were

manufactured from the inner and the cover plates after the experimental tests. The steel coupons of the M16-bolts were manufactured from unused bolts taken from the same delivery package of the tested bolts. Table 3.7 summarizes the results of the material characterization tests performed for the main components of SMIBC-E1 test campaign. The detailed results are also presented in Annex-B.

Table 3.7: Material properties of the main test specimens for SMIBC-E1 test campaign.

Specimen Name	Order	Sample ID	E^1 [GPa]	f_y [MPa]	f_u [MPa]	A^2 [%]
Inner Plates	S235	SMIBC-E1-1-02 (IP-1)	206	245	386	41.0
		SMIBC-E1-2-02 (IP-2)	204	244	386	40.0
		SMIBC-E1-3-01 (IP-3)	209	244	387	39.0
		Mean Values	206	244	386	40.0
Cover Plates	S235	SMIBC-E1-1-02 (CP-1)	211	259	452	30.5
		SMIBC-E1-2-02 (CP-2)	204	235	451	28.5
		SMIBC-E1-3-01 (CP-3)	204	282	458	28.5
		Mean Values	206	259	454	29.2
M16-bolts	8.8	M16-1	212	869	929	18.5
		M16-2	208	865	923	20.0
		M16-3	215	855	918	19.0
		Mean Values	212	863	923	19.2

[1] Elastic modulus (E) was determined according to EN ISO 6892-1 Method A1 [63].

[2]The term A corresponds to percentage elongation of the steel coupon after the fracture [63].

3.2.2.2 Instrumentation of the test specimens

Fig. 3.9 shows the test set-up and the layout of the measurement equipment. Six displacement transducers (DTs) were installed to measure in-plane relative displacements between the inner and the cover plates. In addition, two load-cells (LCs) were positioned under the nut of the M16-bolts to apply the initial pretension with high precision and to measure the variation of the tension stress resultants in the M16-bolts during the tests. The measurement ranges and the measurement alignments of the displacement transducers and the load-cells are summarized in Table 3.8.

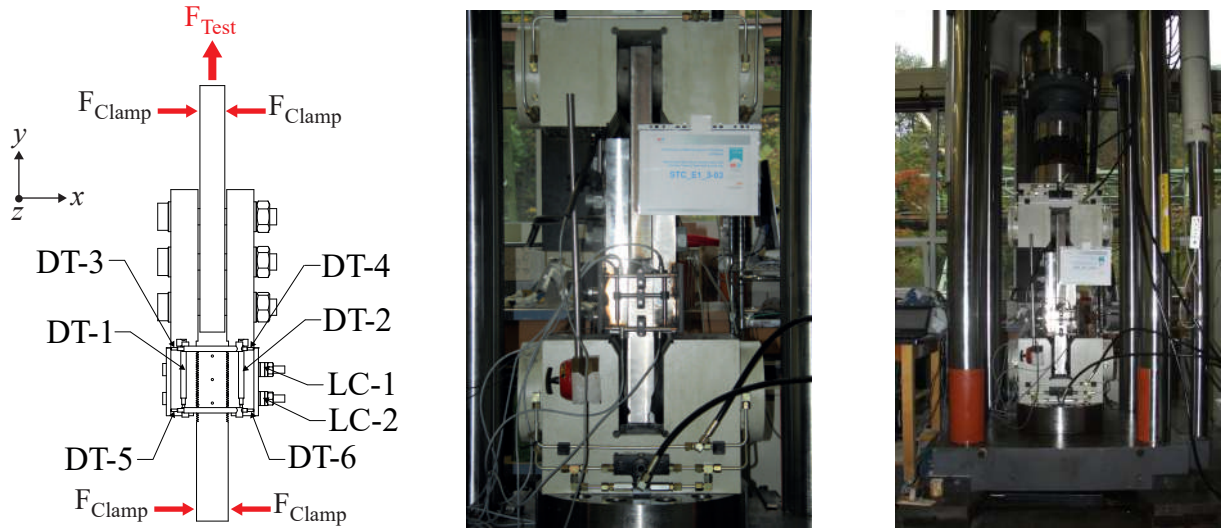

Figure 3.9: Displacement transducers (DT) and load-cells (LC) / SMIBC-E1 test campaign.

Table 3.8: Summary of the displacement-transducers and the load-cells / SMIBC-E1 test campaign.

Sensor ID	Direction	Measurement Range
DT-1	Vertical (*y-axis*)	10mm
DT-2	Vertical (*y-axis*)	10mm
DT-3	Horizontal (*x-axis*)	10mm
DT-4	Horizontal (*x-axis*)	10mm
DT-5	Horizontal (*x-axis*)	10mm
DT-6	Horizontal (*x-axis*)	10mm
LC1	Horizontal (*x-axis*)	200kN
LC2	Horizontal (*x-axis*)	200kN

3.2.2.3 Loading procedure and the execution of SMIBC-E1 test campaign

The loading was applied with a loading procedure identical to the one presented in Section 3.2.1.3. The tests were executed in The Structural Laboratory for the University of Wuppertal with a 2500kN universal testing machine. The force output of the testing machine and the data from the measurement devices presented in Section 3.2.2.2 were continuously recorded with 1000Hz data acquisition speed during the tests. For the first test of each test series, the expected ultimate test capacity ($F_{u,exp}$) was estimated with FEA performed prior to the experimental tests with the characteristic material properties [50] of the ordered material grades (see Table 3.6). The FE-model is presented in Section 3.2.3.2. For the second and the third tests of each test series, the expected ultimate test capacity was defined based on the first test result of the corresponding test series.

3.2.2.4 Results and discussions

Fig. 3.10a shows the load-displacement curves of each test performed in SMIBC-E1 test campaign. Similar to the previous test campaign, the load values given in the figure were presented as half of the applied loading from the testing machine. The relative vertical displacement (δ_y) between the inner and the cover plates was calculated as the arithmetic mean of the data recorded with DT-1 and DT-2 (see Fig. 3.9) with Eq. 3.1. The mean load-displacement curves derived from the test data of each test series are also presented in Fig. 3.10a by highlighting the initial elastic stiffness characteristics of the test series. Due to the data acquisition problems during the third test of the second test series (E1-2-03) and the first test of the third test series (E1-3-01) the force outputs from the testing machine and the load cells were not recorded. Therefore, the related results for these tests are not shown in Fig. 3.10a-c, and they are not considered for the calculations of the mean load-displacement curves.

The moment values were calculated with Eq. 3.2 by multiplying the half of the applied loading with the pre-defined load-eccentricity (*e=30mm*). The out-of-plane (*z-axis*) rotations were calculated with Eq. 3.3. The summary of the test results is given in Table 3.9.

$$M = \frac{F_{Test} \cdot e}{2} \tag{3.2}$$

$$\theta_z = \arctan\left(\frac{\frac{DT_3+DT_4}{2} + \frac{DT_7+DT_8}{2}}{h_{interface} = 140mm}\right) \tag{3.3}$$

The ultimate test loads ($F_{u,Test}$) presented in Table 3.9 corresponds to the maximum loading recorded from the testing machine while the ultimate load-bearing capacity of each symmetric saw-tooth interface is denoted as F_u in the table. As indicated earlier, only the horizontal half-symmetric configuration of the saw-tooth interface was tested.Therefore, the ultimate load-bearing capacity of the entire SMIBC under the pre-defined load-eccentricity (*e=30mm*) could be determined by multiplying the ultimate load-levels shown in Fig. 3.10a by a factor of two.

According to Fig. 3.10a and Fig. 3.10b, there is no significant difference between the test series concerning the load-displacement and moment-rotation curves. However, the initial bolt pretension loads for the M16-bolts were set to 22kN, 44kN and 70kN for the first, the second, and the third test series (see Table 3.1), respectively. Therefore, it could be stated that for a load eccentricity equal to or larger than the selected one (*e*=30mm), the level of the initial bolt pretension load is not significant for the load-displacement behaviour of SMIBC. For all of the tests, the ultimate test loads were recorded at an instant that corresponds to the brittle failure of the lower M16-bolts. The brittle failure characteristic was due to the nut-thread stripping [64].

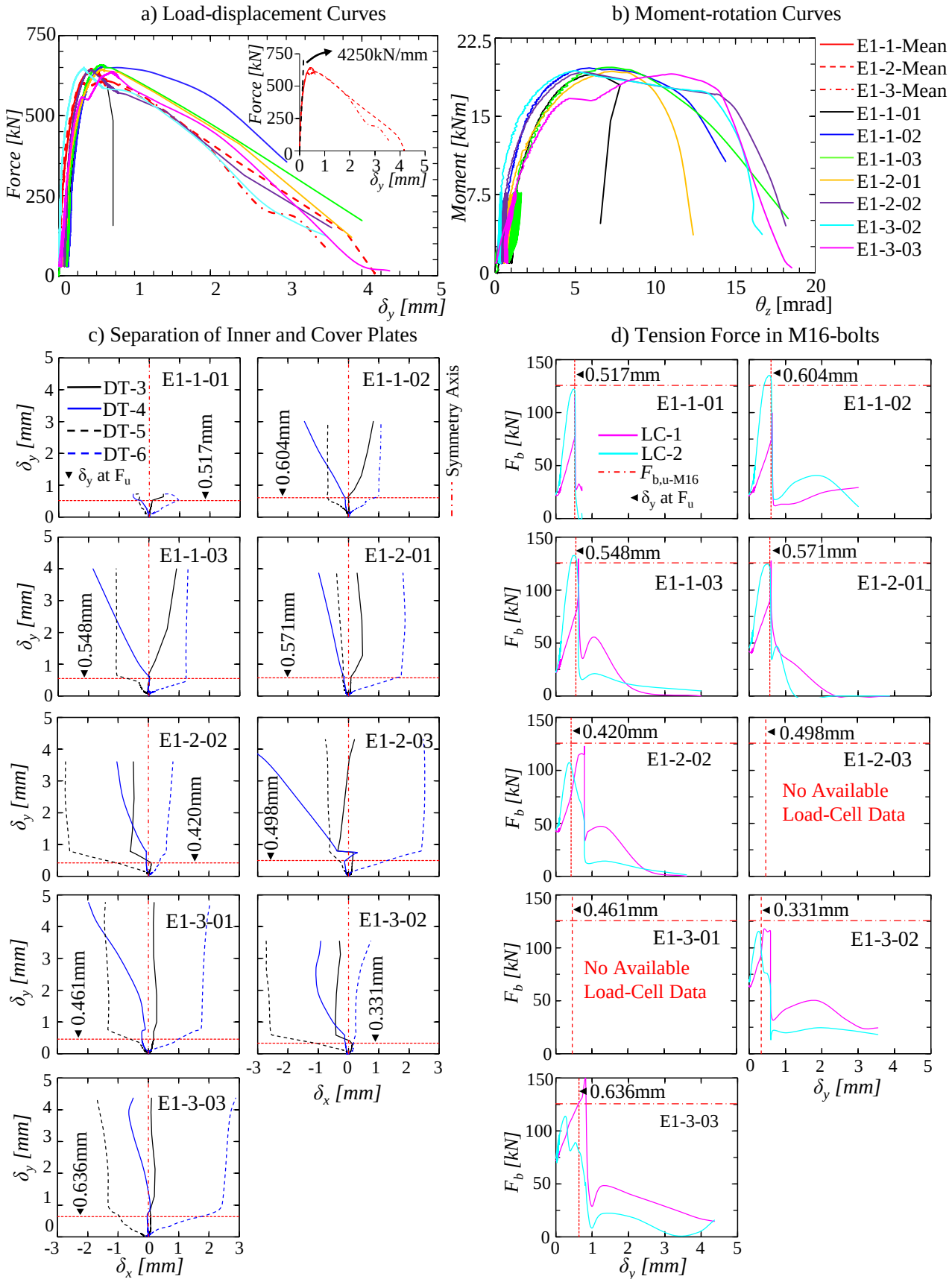

Figure 3.10: Test results of SMIBC-E1 test campaign.

Table 3.9: Summary of the test results for SMIBC-E1 test campaign.

Test Series	Test ID	$F_{u,Test}$ [kN]	F_u [kN]	M_u [kNm]	$\delta_{y,at\ F_u}$ [mm]	$\theta_{z,\text{at } M_u}$ [mrad]	$F_{b,M16\text{-}1\ at\ F_u}$ [kN]	$F_{b,M16\text{-}2\ at\ F_u}$ [kN]
SMIBC-E1-1	E1-1-01	1276	638	19.0	0.52	5.61	115	121
	E1-1-02	1312	656	19.6	0.61	5.44	97	135
	E1-1-03	1318	659	19.7	0.55	6.55	129	133
Mean Values		1302	651	19.4	0.56	5.87	113	130
SMIBC-E1-2	E1-2-01	1292	646	19.3	0.57	6.99	128	125
	E1-2-02	1284	642	19.2	0.42	5.23	122	107
	E1-2-03	N/A	N/A	N/A	0.48	6.29	N/A	N/A
Mean Values		1288	644	19.3	0.49	6.17	125	116
SMIBC-E1-3	E1-3-01	N/A	N/A	N/A	0.46	6.80	N/A	N/A
	E1-3-02	1300	650	19.4	0.33	4.61	117	115
	E1-3-03	1276	638	19.1	0.70	10.45	154	113
Mean Values		1288	644	19.3	0.50	7.29	136	114

For all of the test series executed under SMIBC-E1 test campaign, the mean initial translational elastic stiffness was determined to be equal to 4250kN/mm as presented in Fig. 3.10a. It is important to highlight that, this outcome matches with the initial elastic stiffness of the second test series of the first test campaign presented in Fig. 3.7b. As detailed in Section 3.2.1, the saw-tooth threads close to the load introduction region firstly activate to resist the applied loading. Therefore, the initial elastic stiffness of SMIBC is characterised by the load-deformation behaviour of these threads. In addition, apart from the first test campaign, by introducing the load-eccentricity, additional clamping action developed at the level of the first activated threads as they were in the compression zone due to the out-of-plane rotation (*z-axis direction*) of the cover plates. As a result, the magnitude of this additional action predominated the clamping force, i.e. the initial bolt pretension load, and became decisive for the initial stiffness characteristics. Therefore, this phenomenon resulted in the initial translational elastic stiffness for all of the test series of SMIBC-E1 test campaign to be nearly identical.

Fig. 3.10c shows relative horizontal in-plane displacements for the upper and the lower edges of the saw-tooth interfaces between the inner and the cover plates recorded by DT-3 to DT-6 (see Fig. 3.9). It could be deduced from the figure that the load distribution between the right and the left symmetric saw-tooth interfaces was equal as the relative horizontal displacements between the inner plate and the cover plates were similar with respect to the vertical symmetry axis of the test set-ups. In addition, the level of the separation between the inner plate and the cover plates at the lower edge of the saw-tooth interface was less than 2mm at the ultimate load levels. Thus, upon the

failure, the coupling between the saw-tooth threads of the inner plate and cover plates was more than 50% even for the lowest edge of the interface considering the height of the saw-tooth threads (4mm-see Fig. 3.1b). Therefore, it could be stated that the load-bearing capacity and ductility for the tested SMIBC configuration under the selected load eccentricity could be further increased by replacing higher capacity M16-bolts with ductile failure characteristics such as 10.9 HV-type high strength bolts [64].

Fig. 3.10d shows the tension force variation in the M16-bolts. The failure instants of the bottom M16-bolts coincide with the mean relative displacement that corresponds to the ultimate test loads. Thus, the previous statement linking the failure of the tested SMIBC configuration with the brittle failure of the bottom M16-bolt is justified. In addition, the sudden increase in the tension force for the upper M16-bolts was triggered by the failure of the lower M16-bolts as the entire tension force accumulated in the lower bolt transferred to the upper one, which led to the brittle failure of the tested SMIBC configuration.

Fig. 3.11 shows the deformation profiles for one of the saw-tooth interfaces and the M16-bolts of E1-3-01 test specimens. The yielding and the rotation of the saw-tooth threads at the region close to the load introduction are apparent for the inner and the cover plates. Consequently, it could be deduced that the load-deformation behaviour of these threads determined the initial stiffness characteristics of the tested SMIBC configuration. This observation is consistent with the previous statement that indicates the saw-tooth threads close to the load introduction region activate firstly to resist the applied loading until plastic hinge forms at their tips. Furthermore, the nut-thread stripping which triggered the failure of the M16-bolts is visible for both the upper and lower bolts in Fig. 3.11c. The bending of the bolts could also be noticed, which was due to the position of the cover plates as they were located at the most unfavourable position for the M16-bolts to be subjected to both tension and shear forces simultaneously. Although the visible bending deformations on the M16-bolts, there were neither the indication of the shear failure nor the shank necking for the M16-bolts. This was because the producer limits the failure mode of the bolts as nut-thread stripping by keeping the yield strength of the bolt materials higher than the characteristic ultimate strength of the selected bolt material strength (Grade 8.8 - see Table 3.7). Additional images after test condition of the test specimens for the other tests of SMIBC-E1 test campaign are presented in Annex-B.

a) Deformation of a Saw-tooth Surface for the Inner Plate

b) Deformation of the Saw-tooth Surface for a Cover Plate

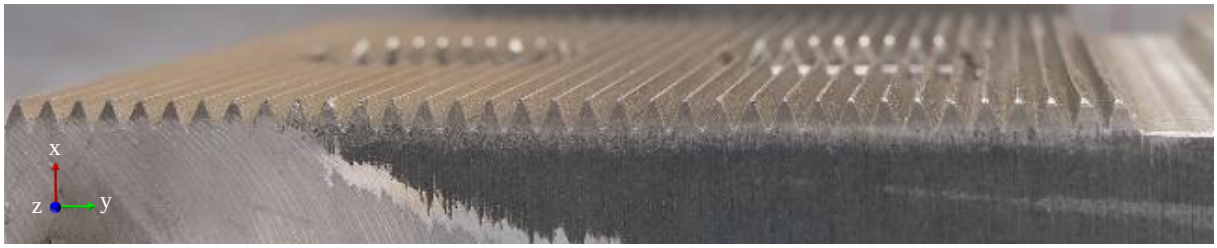

c) Deformation of the M16-bolts

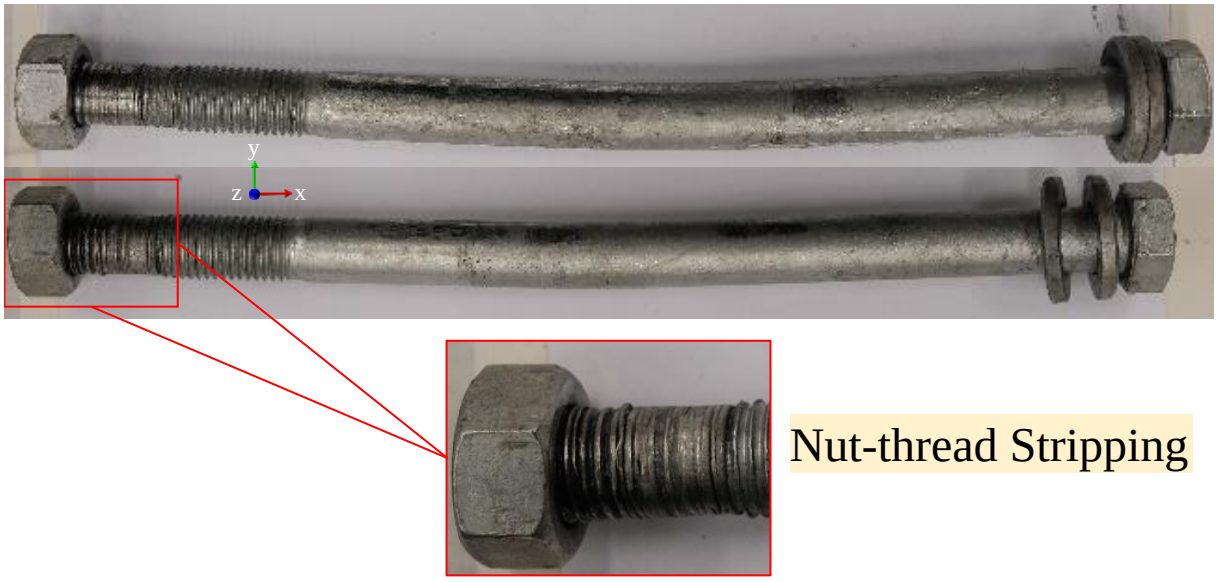

Figure 3.11: Deformations of E1-3-01 test specimens.

3.2.3 FEA simulations

A set of numerical simulations were performed with the commercial FEA software package Abaqus/CAE [66] to design the test set-ups, to clarify the observed failure mechanisms during the experimental tests, to investigate the load distribution along the saw-tooth interface under different parameters for the development of an analytical resistance models and to perform the statistical evaluation of the analytical resistance models with a numerical parametric study.

3.2.3.1 FEAs performed prior to SMIBC test campaigns

Due to the capacity limitation of the available testing machines, the experimental tests were executed with only the horizontal symmetric half of the saw-tooth interface for both of the test campaigns with non-eccentric (SMIBC-E0) and eccentric (SMIBC-E1) loading conditions. On the other hand, it was neither economical nor practical to satisfy symmetric boundary conditions (BCs) for the experimental test set-ups. Therefore, two separate FEAs were performed prior to the design of the test set-ups to analyze if the load-displacement behaviour of SMIBC could be determined with an experimental set-up that consists of only the horizontal symmetric half of the saw-tooth interface.

The horizontal half symmetric geometry of SMIBC was modelled in Abaqus/CAE [66]. The explicit geometry of the saw-tooth threads was included in the model. Two different analyses were performed with and without the symmetric BCs along the vertical symmetry axis of SMIBC to investigate the impact of the symmetric BCs on the load-deformation behaviour of SMIBC. Fig. 3.12a-c shows the symmetry axes of SMIBC, the half symmetric FE-model, the model components, the interaction types and their properties between the model components and the FE-discretization (i.e. meshing). Reduced integration solid brick elements (C3D8R [66]) were selected for the FE-discretization. The material properties assigned to the model components are listed in Table 3.10. The interaction properties assigned between the model components are also summarized in Table 3.11.

The analyses were performed in two solution steps with static and dynamic-implicit solution schemes of Abaqus/Standard. The first step was defined to apply the bolt pre-tensions to M16-bolts

Table 3.10: Material properties of FE-model components.

Component Name	Material Model	E [GPa]	ν	f_y [MPa]	f_u [MPa]	ε_u [%]
Anchor Plate	Bi-linear	210	0.3	235	360	15
Corbel Plate	Bi-linear	210	0.3	215[1]	340[1]	15
Washer Plate	Linear-elastic	210	0.3	N/A	N/A	N/A
M16-bolts	Bi-linear	210	0.3	640	800	5

[1] As the thickness of the corbel plate is larger than 40mm, the yield and the ultimate strengths of the corresponding material model for the corbel plate were reduced according to EN1993-1-1 [50].

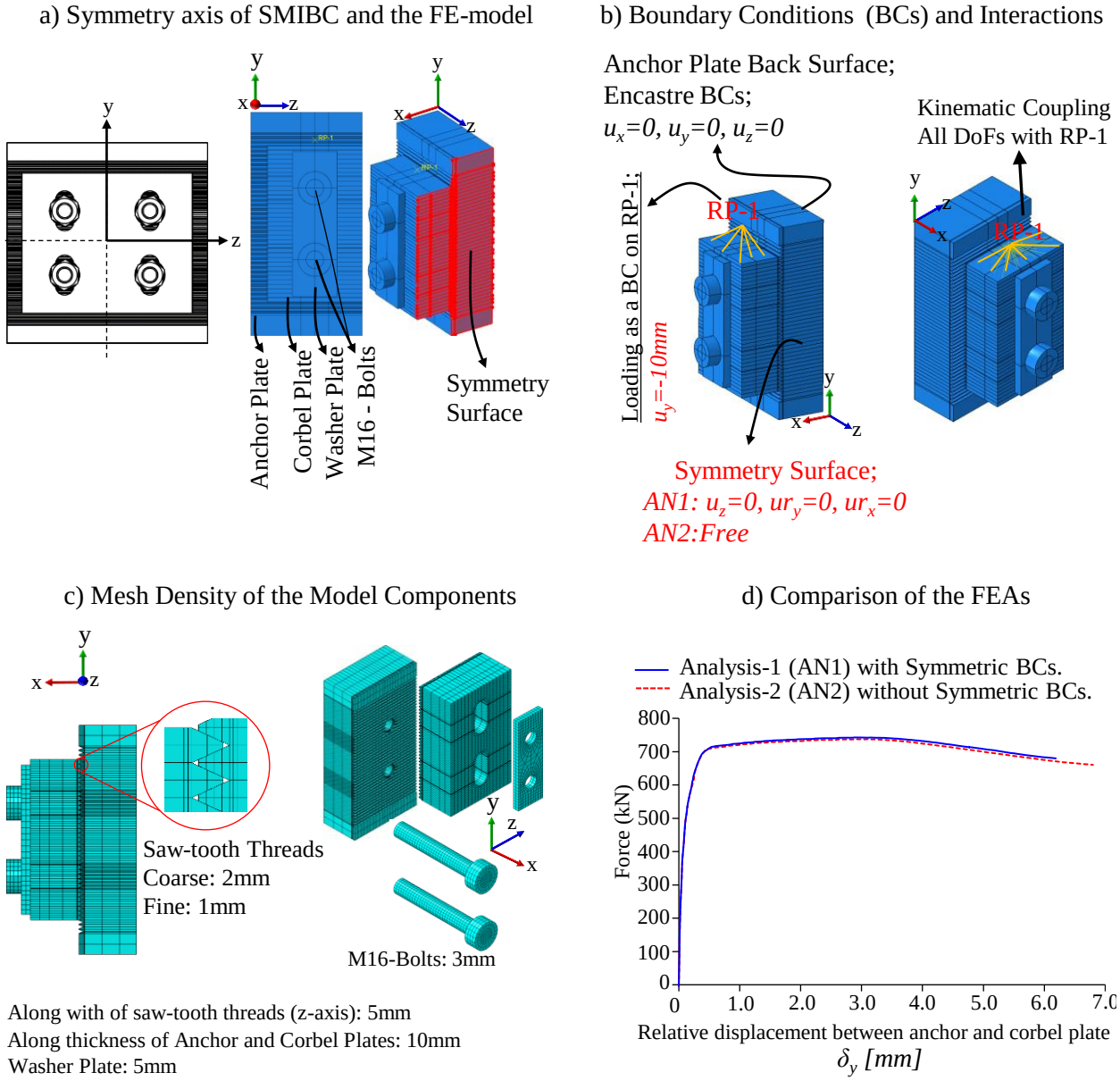

Figure 3.12: Details and the results of the FEAs performed prior to SMIBC test campaigns.

using the bolt load tool of the software [66] with static solution. Thereafter, the loading was applied through the second solution step by introducing 10mm vertical displacement in *(-) y-axis* direction to the reference point kinematically coupled with the top surface of the corbel plate using the smooth step function of the software [66] with dynamic-implicit solution scheme. The applied force was recorded as the *y-axis* support reaction at the back surface of the anchor plate.

According to the output results of the FEAs performed prior to the experimental tests presented in Fig. 3.12d, it was concluded that the impact of the symmetric boundary conditions on the load-displacement behaviour of SMIBC was insignificant. Therefore, the experimental test campaigns were executed with only the horizontal half symmetric configuration of SMIBC.

Table 3.11: Interaction properties between the FE-model components.

Connected Components	Interaction Method	Interaction Properties	
		ND	TD
Anchor Plate to Corbel Plate	Surface to Surface Contact	Hard	Penalty Friction ($\mu = 0.42$[1])
Washer Plate to Corbel Plate	Surface to Surface Contact	Hard	Penalty Friction ($\mu = 0.10$)
M16-bolts to Anchor Plate	Surface to Surface Contact	Hard	Penalty Friction ($\mu = 0.10$)
M16-bolts to Corbel Plate	Surface to Surface Contact	Hard	Penalty Friction ($\mu = 0.10$)
M16-bolts to Washer Plate	Surface to Surface Contact	Hard	Penalty Friction ($\mu = 0.10$)

ND: Normal Direction, TD: Tangential Direction

[1] The magnitude of the static friction coefficient between the saw-tooth surfaces was determined with a separate test campaign presented in Annex-A.

3.2.3.2 FEAs of SMIBC test campaigns

FE-models of SMIBC-E0 and SMIBC-E1 test configurations were developed with the explicit geometries of the set-up components including the saw-tooth threads for the inner and the cover plates. On the other hand, the rolling radius of the steel profile (UPE400), the threaded regions of the M-16 bolts and M20 threaded-rods, and the nuts were not included in the FE-model for the computational efficiency of the analyses. The bolt-heads and washers were modelled with circular geometry to reduce the computational effort.

Fig. 3.13 shows the FE-model of SMIBC-E0 test campaign with the FE-discretization. Only a quarter of the test set-up was modelled with symmetric BCs as the set-up and the loading were symmetric. Reduced integration solid brick elements (C3D8R [66]) were used for the FE-discretization. The material properties assigned to the main model components were defined based on the steel coupon tests presented in Table 3.3. The tri-linear material model used for the main FE-model components is illustrated in Fig. 3.13c and the corresponding properties of the model are listed in Table 3.12.

According to the observations highlighted in Fig. 3.11c and Fig. 3.7c, it was shown that the selected M16-bolts [61] failed due to nut-thread stripping with brittle failure characteristics. Therefore, a notional material modelling technique was adopted to be able to model the load-deformation behaviour of the M16-bolts without explicit modelling of the bolt and the nut threads geometry. In the proposed modelling technique, a bi-linear material law was defined with an notional yield strength which corresponds to the nominal ultimate tensile load capacity of the M16-bolts when multiplied by the nominal stress area of the selected bolt size. The notional material model assigned to M16-bolts is shown in Fig. 3.13d, and the related properties are listed in Table 3.12. A bi-linear material model with strain hardening was used for the bottom plate [67], the web-stiffener and the M20-threaded rods. The material properties of these components were assigned as the characteristic values for the material grades listed in Table 3.6 according to

EN1993-1-1 [50] and ISO 898-1 [68].

The interaction properties of the model components are listed in Table 3.13. The friction coefficient between the saw-tooth surfaces of the inner and the cover plates was determined with a separate testing campaign presented in Annex-A.

a) FE-model and BCs of SMIBC-E0 Test Campaign

b) Mesh Density of the Model Components

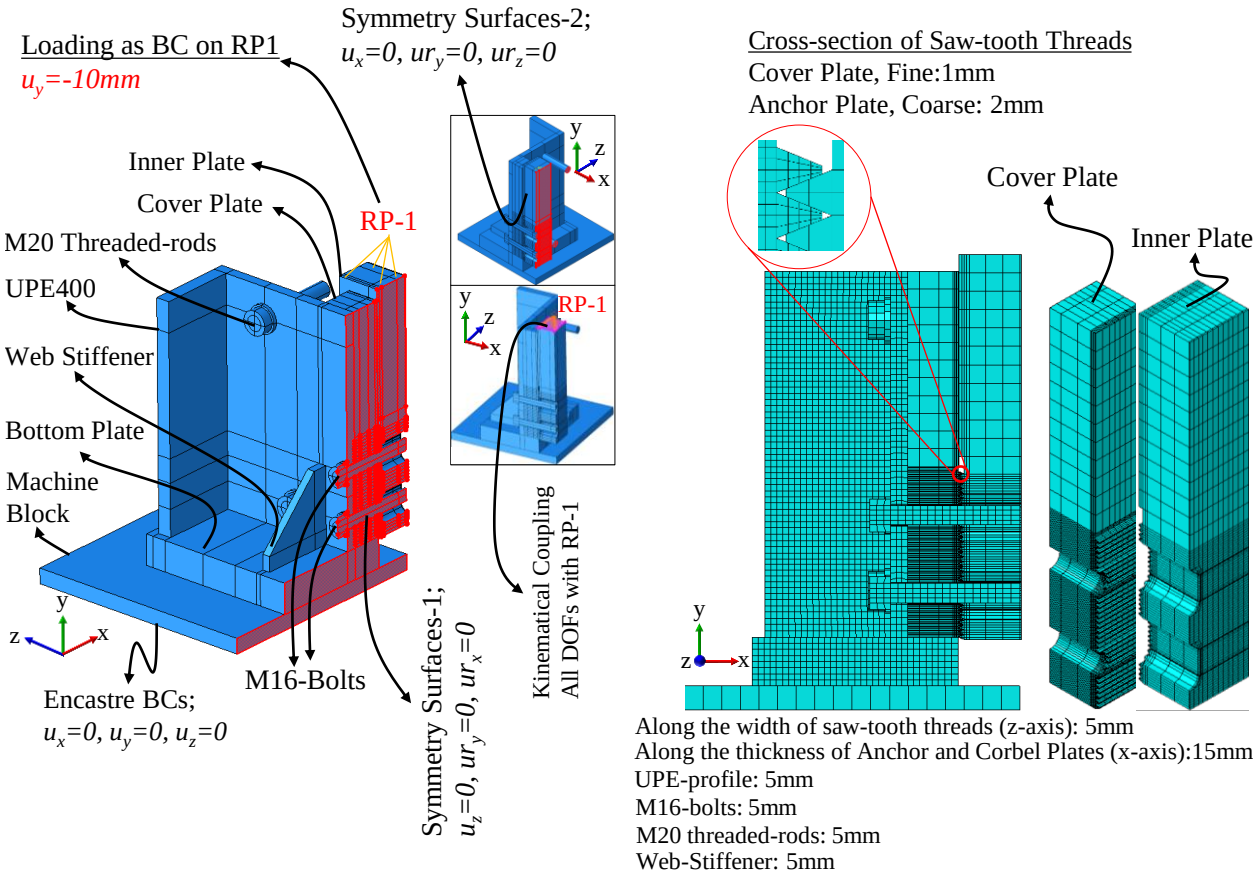

c) Material Model
Inner Plate, Cover Plate and UPE Profile

d) Notional Material Model for M16-Bolts

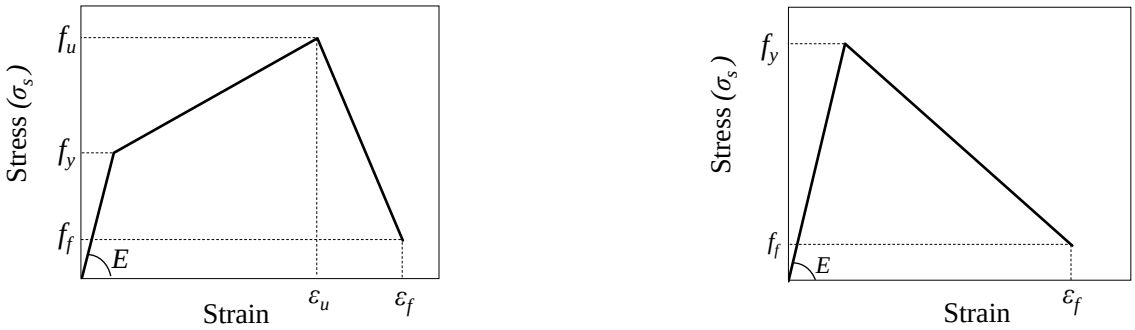

Figure 3.13: FE-model and the material laws for of SMIBC-E0 test campaign.

Table 3.12: Material properties assigned to the FE-model components / SMIBC-E0 test campaign.

Component Name	Material Model	E [GPa]	ν	f_y [MPa]	f_u [MPa]	f_f[1] [MPa]	ε_u[2] [%]	ε_f [%]
Inner Plate	Tri-linear	195	0.3	193	406	20	30	37
Cover Plate	Tri-linear	207	0.3	277	465	20	25	33
Bottom Plate	Bi-linear	210	0.3	460	550	N/A	15	N/A
UPE-profile	Tri-linear	205	0.3	382	535	20	20	30
M16-Bolts[3]	Bi-linear	210	0.3	625	N/A	20	N/A	15
M20 Threaded-rods	Bi-linear	210	0.3	900	1000	N/A	9	N/A
Web Stiffener	Bi-linear	210	0.3	355	490	N/A	15	N/A
Machine Block	Linear-elastic	210	0.3	N/A	N/A	N/A	N/A	N/A

NOTE-1: The elastic modulus (E), yield strength (f_y), ultimate strength (f_u) and the fracture strain (ε_f) for the material models of the inner plate, cover plate and the UPE-profile are assigned as the mean values presented in Table 3.3.

NOTE-2: Due to the absence of the coupon tests for the bottom plates and the web-stiffeners, the material properties of these components are assigned based on the characteristic properties of the selected material grades from EN1993-1-1 [50] and ISO 898-1 [68].

[1]The magnitude of the fracture stress is set to 20MPa for all of the model components having tri-linear material model with material degradation to have a linear approximation for the post necking material behavior.

[2] The calculation of the ultimate strains (ε_u) for the tri-linear material law are presented in Annex-B, they corresponds to the mean values of the coupon tests for the test specimens presented in Table B.1.

[3] A notional material modelling technique was adopted to be able to model the load-deformation behaviour of the M16-bolts without explicit modelling of the bolt and the nut threads geometry as illustrated in Fig. 3.13d.

The analyses were performed in two solution steps. The first step was defined to apply the bolt pre-tensions to M16-bolts using the bolt load tool of the software [66], and it was executed with the general static solution scheme. The second step was performed with the dynamic-implicit solution scheme by introducing 10mm vertical displacement along the *(-)y-axis* direction (push) to the reference point (RP-1) kinematically coupled with the top surface of the inner plate (see Fig. 3.13a) using smooth step function of the software [66]. The force output was recorded as the *y-axis* axis support reaction below the machine block.

Two separate FEAs were performed for SMIBC-E0 test campaign by applying 22kN and 70kN initial bolt pre-tension for the M16-bolts as identical to SMIBC-E0 test campaign (see Table 3.1).

Fig. 3.14a compares the load-displacement curves of the FEAs with the mean test curves of SMIBC-E0 test campaign. Apart from the mean curves, no difference in the initial stiffness and the ultimate capacity was observed between the output results of the FEAs. This outcome could be attributed to the fact that the FE-models were developed with the perfect geometry of the saw-tooth threads; thus, no manufacturing-related imperfection was included in the models. Therefore, for both of the FEAs performed with 22kN and 70kN initial bolt pre-tension applied to M16-bolts, the

Table 3.13: Interaction properties between the FE-model components of SMIBC-E0 test campaign.

Connected Components	Interaction Method	Interaction Properties	
		ND	TD
Saw-tooth Surfaces	Surface to Surface Contact	Hard	Pen. Fric. ($\mu = 0.42$)
Flat Inner and Cover Plate Surfaces	Surface to Surface Contact	Hard	Frictionless
Bottom Plate to Machine Block	Surface to Surface Contact	Hard	Frictionless
M16-bolts to UPE-profile	Surface to Surface Contact	Hard	Pen. Fric. ($\mu = 0.10$)
M16-bolts to Inner Plate	Surface to Surface Contact	Hard	Pen. Fric. ($\mu = 0.10$)
M16-bolts to Cover Plate	Surface to Surface Contact	Hard	Pen. Fric. ($\mu = 0.10$)
Cover Plate to UPE-profile	Tie Constrain	N/A	N/A
Cover Plate to Bottom Plate	Tie Constrain	N/A	N/A
Web-stiffener to UPE-profile	Tie Constrain	N/A	N/A
Web-stiffener to Bottom Plate	Tie Constrain	N/A	N/A

ND: Normal Direction, TD: Tangential Direction, Pen. Fric.: Penalty Friction

saw-tooth threads were in full contact along the interface height while for the test environment the saw-tooth surfaces for the second test series (SMIBC-E0-2) executed with 70kN initial bolt pre-tension could be considered to have higher degree of coupling compared to the first test series (SMIBC-E0-1) performed with 22kN initial bolt pre-tension as the clamping force (i.e. pre-tension) cancel-out the impact of the imperfection of the saw-tooth threads that reduces the degree of the coupling. As a result, it is concluded that 22kN initial bolt pre-tension is not sufficient to achieve the full capacity of the saw-tooth interface for the proposed geometry of SMIBC in real-life conditions due to the manufacturing-related imperfections of the saw-tooth threads.

In addition, Fig. 3.14b-c compares the deformation profiles along the saw-tooth surfaces of the inner plate and the cover plate for FEA-E0-1 against the deformation profiles shown in Fig. 3.7 for the final analysis step of the FEA. Based on the presented details, it could be deduced that the load-displacement behaviour and the deformation profiles along the saw-tooth interfaces estimated by the FEA are consistent with the test results. Furthermore, based on the PEEQ outputs presented in Fig. 3.14b it is validated that the initial five saw-tooth threads close to the load introduction region started to carry the loading and the loading was successively distributed to the following saw-tooth threads by the yielding of the initial threads. As a result, it is deduced that the load-bearing capacity of the saw-tooth interface could be estimated by the summation of the ultimate individual saw-tooth thread capacity if sufficient plastic deformation is satisfied for the saw-tooth threads close to the load-introduction.

Fig. 3.15 show the FE-model of SMIBC-E1 test campaign with the model components and the FE-discretization. Only a quarter of the test set-up was modelled with symmetric boundary conditions. The material model shown in Fig. 3.13c was also used to define the constitutional material laws for the inner and the cover plates with the mean material properties listed in Table 3.7. The material model and the corresponding material properties of the M16-bolts were defined as identical to the FE-model of SMIBC-E0 test campaign (see Fig. 3.13d and Table 3.12). A bi-linear

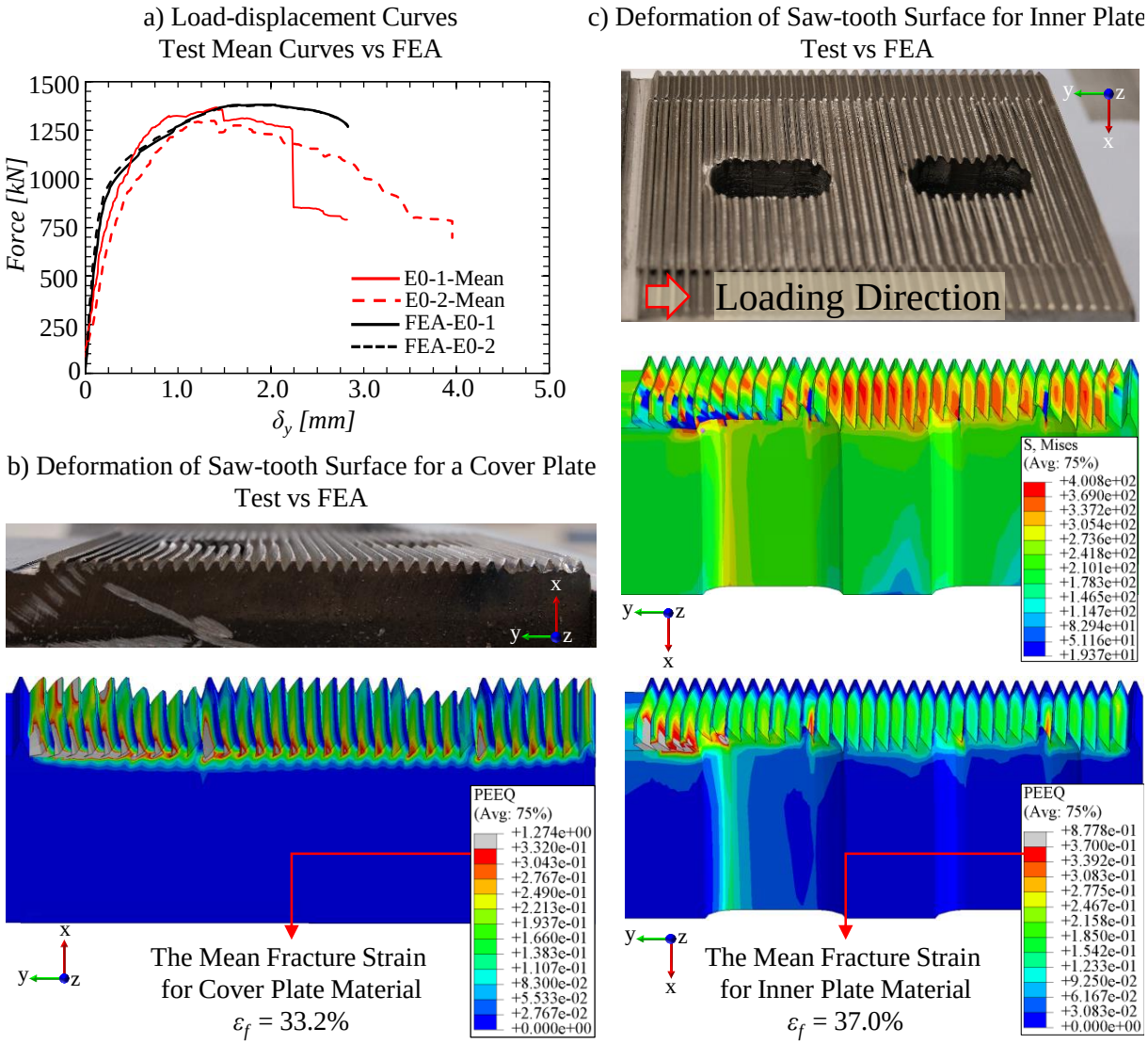

Figure 3.14: Comparison of the test results for SMIBC-E0 test campaign with corresponding FEAs.

material model with strain hardening [67] was used for the loading plate, the plate washers and the M36-bolts. The material properties of these components assigned based on EN1993-1-1 [50] and EN1993-1-8 [25] as the characteristic values of the selected material grades listed in Table 3.6. The interactions between the FE-model components of SMIBC-E1 test campaign is listed in Table 3.15.

Three separate FEAs were performed for SMIBC-E1 test campaign by applying 22kN, 44kN and 70kN initial bolt pre-tension for the M16-bolts as identical to SMIBC-E1 test campaign (see Table 3.1). The analyses were performed in two solution steps identical to the FEAs of SMIBC-E0 test campaign. On the other hand, as consistent with SMIBC-E1 test configuration, the loading was applied as a pull force (see Fig. 3.15a) at a region that corresponds to the surface clamped by the testing machine (see Fig. 3.9). The force output was recorded as the *y-axis* support reactions at the surface region of the inner plate that was restrained in all DOFs (see Fig. 3.15a).

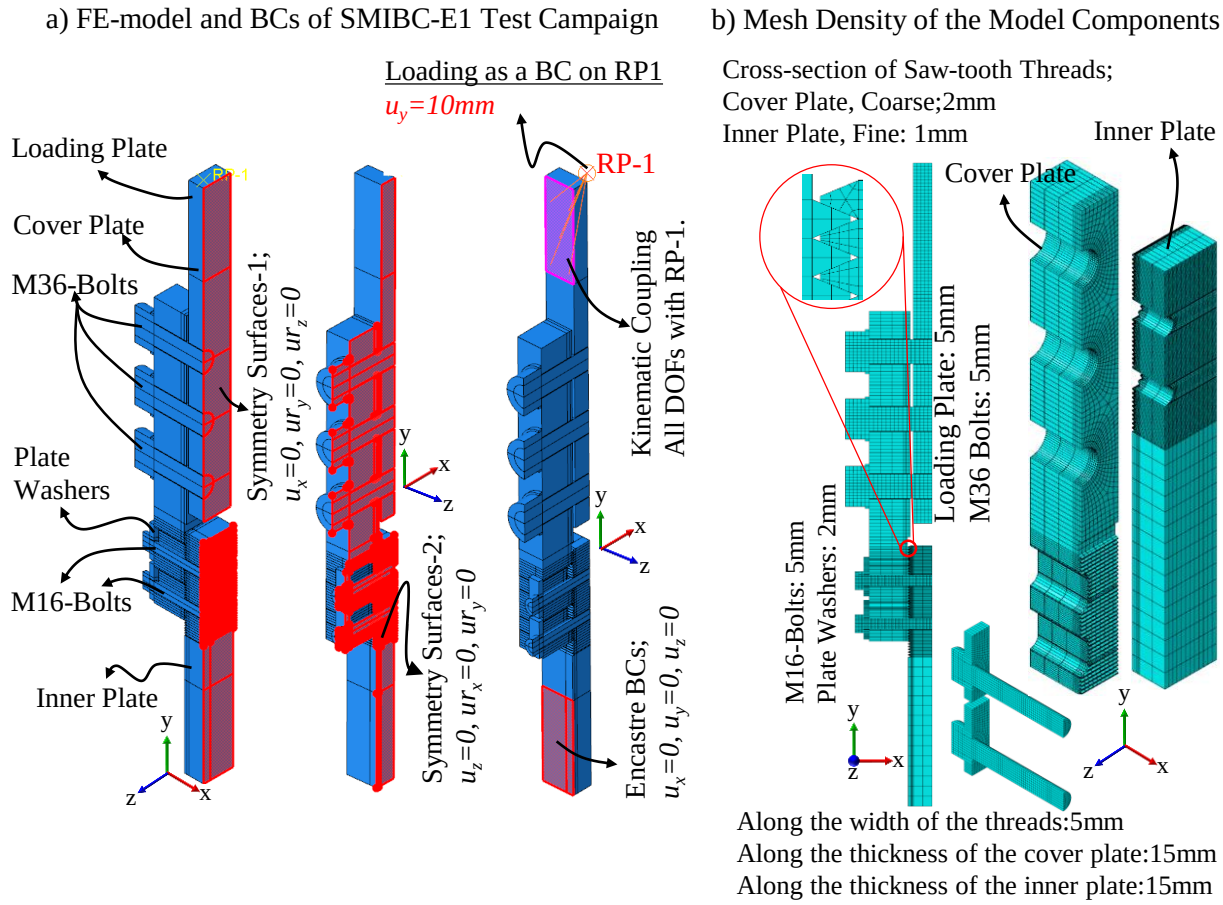

Figure 3.15: FE-model of SMIBC-E1 test campaign.

Table 3.14: Material properties assigned to the FE-model components / SMIBC-E1 test campaign.

Component Name	Material Model	E [GPa]	ν	f_y [MPa]	f_u [MPa]	f_f[1] [MPa]	ε_u[2] [%]	ε_f [%]
Inner Plate	Tri-linear	206	0.3	244	386	20	31	40
Cover Plate	Tri-linear	207	0.3	258	448	20	25	29
Loading Plate	Bi-linear	210	0.3	460	550	N/A	15	N/A
Plate Washers	Bi-linear	210	0.3	460	550	N/A	15	N/A
M36-Bolts	Bi-linear	210	0.3	900	1000	N/A	5	N/A

NOTE-1: The elastic modulus (E), yield strength (f_y), ultimate strength (f_u) and the fracture strain (ε_f) for the material models of the inner plate and the cover plate are assigned as the mean values presented in Table 3.7.

[1]The magnitude of the fracture stress is set to 20MPa for all of the model components having tri-linear material model with material degradation to have a linear approximation for the post necking material behavior.

[2] The calculation of the ultimate strains (ε_u) for the tri-linear material law are presented in Annex-B.

Table 3.15: Interaction properties between the FE-model components of SMIBC-E1 test campaign.

Connected Components	Interaction Method	Interaction Properties	
		ND	TD
Saw-tooth Surfaces	Surface to Surface Contact	Hard	Pen. Fric. ($\mu = 0.42$)
M16-bolts to Washer-plates	Surface to Surface Contact	Hard	Pen. Fric. ($\mu = 0.10$)
M16-bolts to Inner Plate	Surface to Surface Contact	Hard	Pen. Fric. ($\mu = 0.10$)
M16-bolts to Cover Plate	Surface to Surface Contact	Hard	Pen. Fric. ($\mu = 0.10$)
M36-bolts to Loading Plate	Surface to Surface Contact	Hard	Pen. Fric. ($\mu = 0.10$)

ND: Normal Direction, TD: Tangential Direction, Pen. Fric.: Penalty Friction

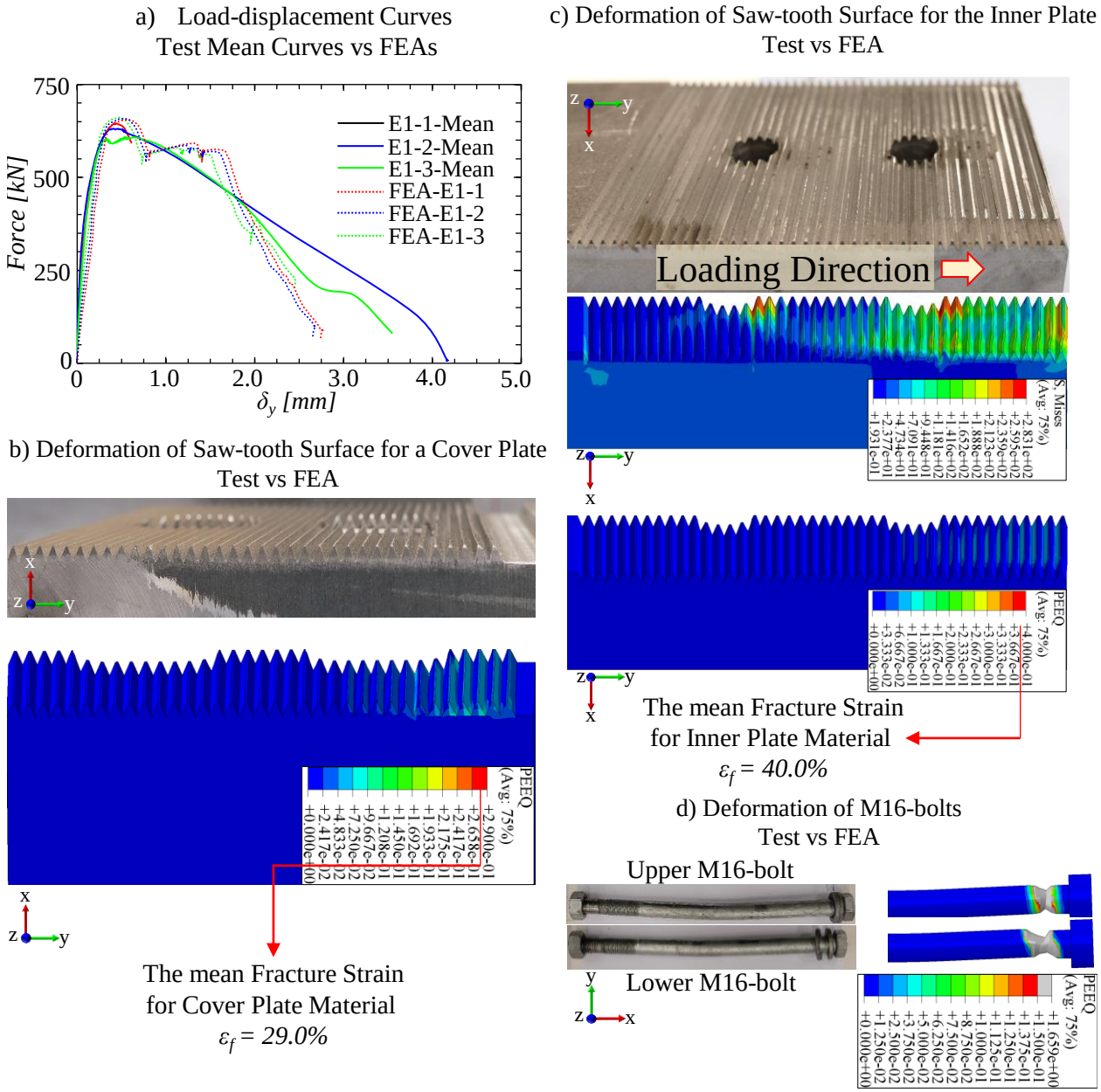

Figure 3.16: Comparison of the test results for SMIBC-E1 test campaign with corresponding FEAs.

Fig. 3.16a, shows the comparison of the load-displacement curves for the FEAs and the mean results of SMIBC-E1 test campaign. The output results of the FEAs are in very good agreement with the mean test results. In addition, Fig. 3.16b,c,d show the comparisons of the deformation profiles on the inner plate, cover plate and M16-bolts between FEA-E1-3 and the test specimens earlier presented in Fig. 3.11 for the final FE-analysis step. As it could be noticed from the figure that the output results of FEA were consistent with the test results and they validate that the failure mode of SMIBC switches from the saw-tooth interface failure (see Fig. 3.14) to the failure of the M16-bolts by the introduction of the load-eccentricity. On the other hand, it is the fact the governing failure mode of SMIBC depends on the magnitude of the load-eccentricity which was indented to be designed as 30mm (e=*30mm*) for SMIBC-E1 test campaign while the actual magnitude of the load-eccentricity for the selected test set-up depends on the bending and the out-of-plane rotation (*z-axis* direction see Fig. 3.9) of the cover plates together with the stress distribution along the length of the M36-bolt holes where the loading was introduced to the cover plates. Therefore, to determine the magnitude of the actual load-eccentricity for SMIBC-E1 test campaign, Fig. 3.17 presents a section cut at the upper edge of the cover plate at an analysis instant that corresponds to the ultimate load-bearing capacity of SMIBC and it shows that the actual load-eccentricity was 20mm (e_{actual}=*20mm*) for SMIBC-E1 test campaign. Consequently, the magnitudes of the moments presented in Fig. 4.7b and Table 3.9 shall be reduced by a factor of 1.5.

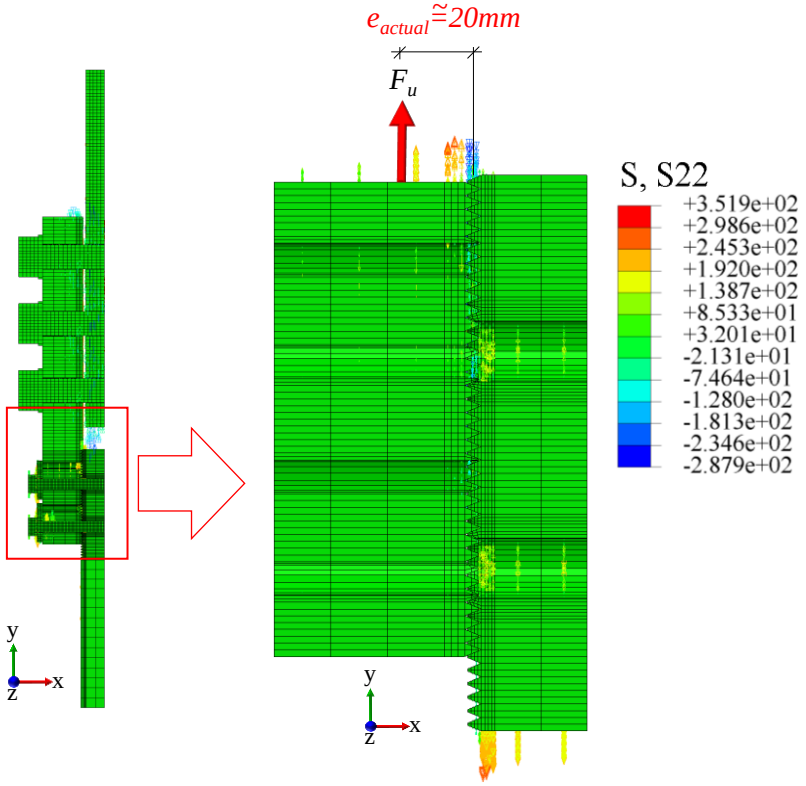

Figure 3.17: Position of the *y-axis* resultant force on a section cut of the cover plate at $F_{u,FEA-E1-3}$.

Furthermore, as the actual load-eccentricity is less than the desired one it is necessary to investigate the load-bearing capacity of SMIBC under different load-eccentricities. This investigation was performed as a numerical parametric study and it is presented in Section 3.2.5.2.

According to the presented results in this section, it is shown that the selected finite element modelling and analysis techniques are capable of simulating the load-displacement behaviour and the failure mechanisms of SMIBC with and without load-eccentricity. Therefore, it is concluded that the selecting finite element modelling and analysis techniques could be used to perform numerical parametric study. The energy balances for the selected analysis scheme are presented in Annex-B.

3.2.4 Analytical investigation for the load-bearing mechanism of SMIBC

This section presents an analytical resistance model to determine the ultimate load-bearing capacity of SMIBC. Fig. 3.18a shows a simplified 2D illustration of SMIBC used to develop the analytical resistance model. The following assumptions were adopted for the analytical resistance model;

- Plane sections remain in plane after the bending of the saw-tooth threads.
- Deformations are small and could be ignored for the analytical calculations.
- The thread angle (θ) is constant during the entire loading history and the corbel plate rotates rigidly in case of eccentric loading.
- The shear stress along the length of a saw-tooth thread (L_{thread}) is uniformly distributed.
- The friction coefficient (μ) between the saw-tooth surfaces is constant.

It is important to mention that although the stress distribution and the displacement along the restrained edge of the saw-tooth threads may be estimated with more complex methodologies such as the Airy stress function approach [69], the assumptions presented above and the beam theory [70] were selected to simplify the analytical resistance model of SMIBC for the estimation of the ultimate load-bearing capacity of SMIBC.

Similar to the order of the test campaigns, initially, the load eccentricity (e) was considered to be equal to zero, and the load-bearing capacity of the saw-tooth interface was estimated with the analytical model.

Fig. 3.18b shows a resultant force (F_N) along the normal direction of the contact surface for an isolated saw-tooth thread belonging to the 2D-illustration of the corbel plate. In addition, Cartesian coordinates decomposition of the resultant force and the free body diagram of the saw-tooth thread for the static equilibrium conditions are illustrated in Fig. 3.18b. The magnitudes of the in-plane horizontal and vertical lever-arms (h_x and h_y) of the resultant force (F_N) with respect to the restrained edge of the saw-tooth thread are also noted in Fig. 3.18b.

The derivations of the Cartesian coordinates decomposition and the reaction forces presented on the free body diagram are formulated by Eqs. 3.4- 3.6, and Eqs. 3.7-3.9, respectively;

$$P_{thread} = F_N \cdot \sin\theta \tag{3.4}$$

$$F_{thread} = F_N \cdot \cos\theta \tag{3.5}$$

$$F_{thread} = P_{thread} \cdot \cot\theta \tag{3.6}$$

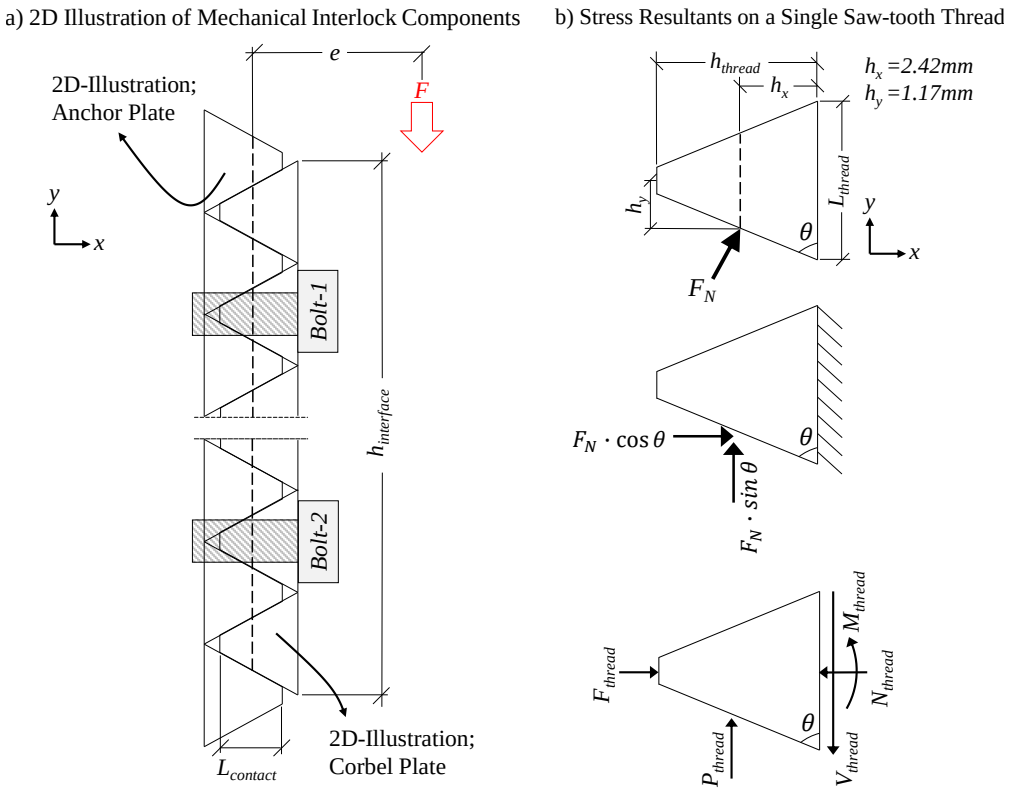

Figure 3.18: 2D-illustration for the load-bearing components of SMIBC

If the static equilibrium is considered together with the lever-arms (h_x and h_y) shown in Fig. 3.18b for an isolated saw-tooth thread;

$$N_{thread} = F_{thread} \tag{3.7}$$

$$V_{thread} = P_{thread} \tag{3.8}$$

$$M_{thread} = P_{thread} \cdot h_x - F_{thread} \cdot h_y \tag{3.9}$$

Introducing Eq. 3.6 into Eq. 3.9, the relation between F_{thread} and M_{thread} can be formulated as Eq. 3.10.

$$M_{thread} = F_{thread} \cdot \left(\frac{h_x}{\cot\theta} - h_y \right) \tag{3.10}$$

In addition, the normal stress distribution at the restrained edge of the saw-tooth thread may be estimated with a strain limited design concept which is generally used in civil engineering practice for the design of the reinforced concrete members under bending moment action [71]. However, apart from the regular strain limited design concept, it is crucial to consider the impact of the shear stress on the load-bearing capacity of a single saw-tooth thread due to the aspect ratio of the saw-tooth threads. Therefore, a notional material model with reduced mechanical properties is proposed for the normal stresses at the restrained edge of the saw-tooth thread. Fig. 3.19a shows a realistic material model for ductile metals together with the approximate material model used for the development of the analytical resistance function. The approximate material model does not consider the degradation of the material strength after the necking of the material (ε_u) to further simplify the procedure for the development of the analytical resistance function. However, it is important to note that the constant plateau stress-strain relation after the necking of the material (ε_u) may lead to overestimating the ultimate load-bearing capacity of SMIBC. Fig. 3.19b illustrates the proposed notional material model with reduced mechanical properties to consider the impact of the shear stress on the load-bearing capacity of a single saw-tooth thread. In addition, Fig. 3.19c presents the strain limited design concept of a saw-tooth thread with the notional mechanical properties for a loading condition illustrated in Fig. 3.18b. It is important to note that the utilization of a notional material law with reduced mechanical properties in case of an excessive shear loading along a cross-section is not a new concept as it has been already proposed by EN1993-1-1 [50] for the cross-sectional analysis of steel beams under the bending moment and vertical shear actions. The reduced mechanical properties for the notional material model are formulated analogical to the Von-mises yield criterion in 2D loading conditions as presented by Eqs. 3.11-3.13.

$$\sigma_v = \sqrt{{\sigma_x}^2 + 3 \cdot {\tau_{xy}}^2} \tag{3.11}$$

$$f_{yr} = \sqrt{{f_y}^2 - 3 \cdot {\tau_{xy}}^2} \tag{3.12}$$

$$f_{ur} = \sqrt{{f_u}^2 - 3 \cdot {\tau_{xy}}^2} \tag{3.13}$$

The unit in-plane shear stress (τ_{xy}) that appears in Eqs. 3.11-3.13 could be formulated with Eq. 3.14 considering the assumptions listed at the beginning of this section and the free body diagram presented in Fig. 3.18b.

$$\tau_{xy} = \frac{P_{thread}}{L_{thread}} \tag{3.14}$$

Furthermore, for a predefined magnitude of F_{thread} that appears in Fig. 3.18b it becomes possible to find the position of the neutral axis (NA) for Fig. 3.19c by satisfying the force equilibrium, in other words, solving Eq. 3.15 for the cross-section at the restrained edge of the saw-tooth thread. Having defined the position of the neutral axis, the resultant magnitude of the moment (M_{thread}) could be determined by solving Eq. 3.16 for the predefined F_{thread}.

$$F_{thread} = \int_0^{L_{thread}} \sigma_x \, dy \tag{3.15}$$

$$M_{thread} = \int_0^{L_{thread}} \sigma_x \cdot y \, dy \tag{3.16}$$

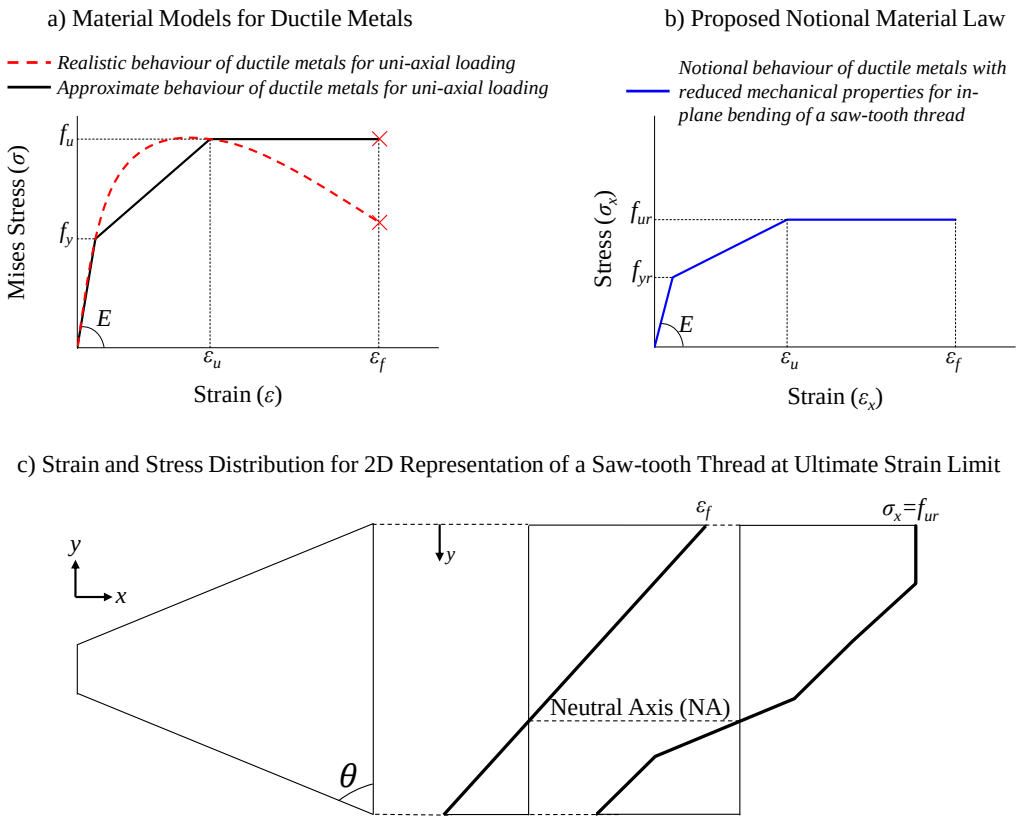

Figure 3.19: Approximate material models for the ductile metals and the corresponding proposed notional material model for the saw-tooth threads with the strain limited design concept of SMIBC.

Repeating the simultaneous solution of Eq. 3.15 and Eq. 3.16 for arbitrary values of F_{thread} ranging from zero to a value that corresponds to the full plastic state under pure compression for the cross section at the restrained edge of the saw-tooth thread, the F_{thread} - M_{thread} curve, which is here on named as the capacity curve, of the saw-tooth thread could be drawn as shown in Fig. 3.20 for the unit width of the saw-tooth thread. Furthermore, as highlighted in Fig. 3.20 the position on the capacity curve which coincide with Eq. 3.10 corresponds to the *x-axis* decomposition ($F_{u,thread}$) of the ultimate normal force ($F_{u,N}$) that could be resisted by a single saw-tooth thread. Having determined $F_{u,\,thread}$, the *y-axis* decomposition of the ultimate normal force on the saw-tooth thread ($P_{u,thread}$) could be determined with Eq. 3.17 analogical to Eq. 3.6.

$$P_{u,thread} = \frac{F_{u,thread}}{\cot\theta} \tag{3.17}$$

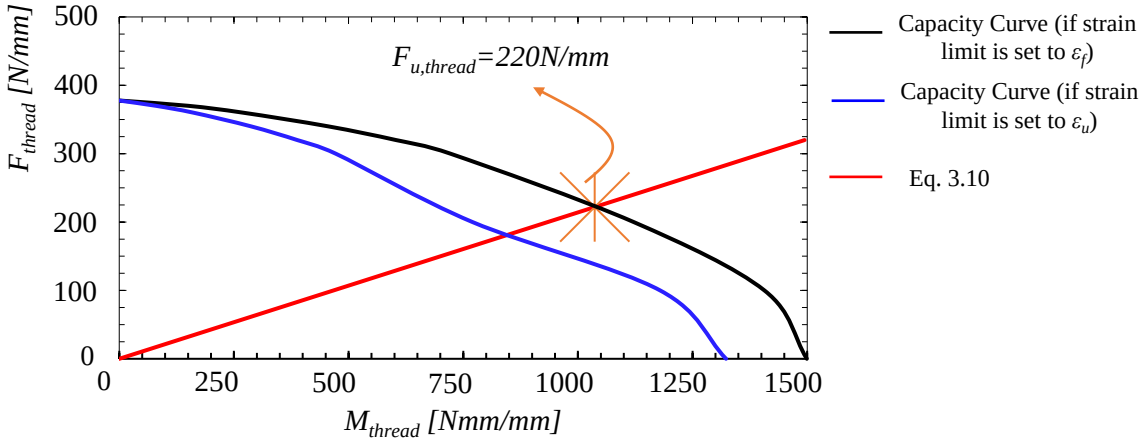

Figure 3.20: The capacity curve of a single saw-tooth thread together with the linear relation formulated by Eq. 3.10.

Additionally, as shown in Fig. 3.7 and Fig. 3.14, the applied load on the inner plate for SMIBC-E0 test configuration is successively distributed along the entire saw-tooth interface height ($h_{interface}$) by the yielding of the saw-tooth threads close to the load-introduction. Therefore, the ultimate load-bearing capacity of SMIBC for non-eccentric loading conditions could be estimated with the proposed analytical resistance model by multiplying the magnitude of $P_{u,thread}$ with the number of the connected threads, which is calculated by dividing the total saw-tooth interface height ($h_{interface}$) to the length of an saw-tooth thread (L_{thread}), and the width of the connected threads, in other words the width of the saw-tooth interface ($w_{interface}$), as formulated in Eq. 3.18.

$$F_{u,analytical} = P_{u,thread} \cdot w_{interface} \cdot \frac{h_{interface}}{L_{thread}} \tag{3.18}$$

The capacity curve presented in Fig. 3.20 was calculated based on the mean material properties for the inner plates of SMIBC-E0 test campaign presented in Table 3.3 (see also Annex-B and Table B.1) and the geometrical detail of the saw-tooth threads presented in Fig. 3.1b. Consequently, the ultimate load-bearing capacity of the saw-tooth interface investigated in SMIBC-E0 test campaign could be estimated with Eq. 3.19 by inputting $F_{u,thread}$ highlighted in Fig. 3.20 and the geometrical parameters of the saw-tooth interface presented in Fig. 3.3 into Eq. 3.18;

$$F_{u,analytical,SMIBC-E0} = \frac{220 \cdot 10^{-3}}{0.414} \cdot 85 \cdot \frac{140}{4} \tag{3.19}$$

$$F_{u,analytical,SMIBC-E0} = 1581kN$$

Table 3.16: Comparison between the analytical estimations and the mean SMIBC-E0 test results.

Test Series	$F_{u,mean}$[1] [kN]	$F_{u,analytical}$ [kN]	Difference [%]
E0-1	1340	1581 (1293)[2]	18.0 (3.5)[2]
E0-2	1466	1581 (1293)[2]	7.8 (11.8)[2]

[1] $F_{u,mean}$ corresponds to the mean ultimate load-bearing capacity for each test series of SMIBC-E0 test campaign presented in Table 3.5.

[2] The values presented in parenthesis are the load-bearing capacity of saw-tooth interface if the ultimate strain limit of the proposed notional material law is set to ε_u instead of ε_f.

Table 3.16 compares the ultimate load-bearing capacity of the saw-tooth interface estimated by Eq. 3.19 with the mean ultimate capacity of the saw-tooth interfaces calculated based on the results of SMIBC-E0 test campaign (see Table 3.5). According to the comparison, it is concluded that the proposed analytical resistance model for non-eccentric loading condition estimates the ultimate load-capacity of the saw-tooth interface for E0-2 test series with only 8% difference on the non-conservative side. The non-conservative estimation could be linked to the approximate material model without consideration of the material degradation after the necking strain (ε_u - see Fig. 3.19). In addition, the estimation of the analytical resistance model is also non-conservative with 18% difference for E0-1 test campaign. However, similar to FEAs presented in Section 3.2.3, the analytical resistance model also considers the perfect geometry for the saw-tooth threads; thus, it assumes the coupling between the saw-tooth threads of the anchor and the corbel plates as full and perfect. Therefore, the higher difference between the output result of the estimations of the analytical resistance model and the mean ultimate load-bearing capacity of the saw-tooth interface for E0-1 test series could be also attributed to the geometrical imperfections of the saw-tooth threads for the test specimens. Furthermore, as shown in Fig. 3.14c, the saw-tooth threads close to the load-introduction lose their load-bearing capacity at the ultimate load-level due to the material degradation. However, the analytical resistance model does not consider the material degradation (see Fig. 3.19a,b) for the simplicity of the proposed methodology. Consequently, the 8% difference in the non-conservative side between the estimation of the analytical model and E0-2 test series could be linked to the approximate material model illustrated in Fig. 3.19a.

It is important to note that due to the non-linearity of the problem as a result of the non-linear material behavior and the relation between the normal and shear stress resultants at the restrained edge of a saw-tooth thread the simultaneous solution of Eq. 3.15 and Eq. 3.16 requires an iterative procedure which may be performed with spreadsheet calculations.

The case of an eccentric loading condition, the analytical resistance model is presented through Eqs. 3.4-3.19 could be further developed by assuming the rigid rotation of the corbel plate and by considering the stress resultants resisted by the bolts. Fig. 3.21 presents the stress resultants on the corbel plate and on the bolts for the 2D-illustration of the mechanical interlock components presented earlier in Fig. 3.18 under an eccentric loading condition by assuming that the height of

the rotation centre is equal to the quarter of the interface height ($h_{interface}$). The stress resultants on the bolts due to the rigid rotation of the corbel plate, i.e. the moment action, are nominated with an asterisk symbol (*) and formulated through Eqs. 3.20-3.23 for the illustration presented in Fig. 3.21.

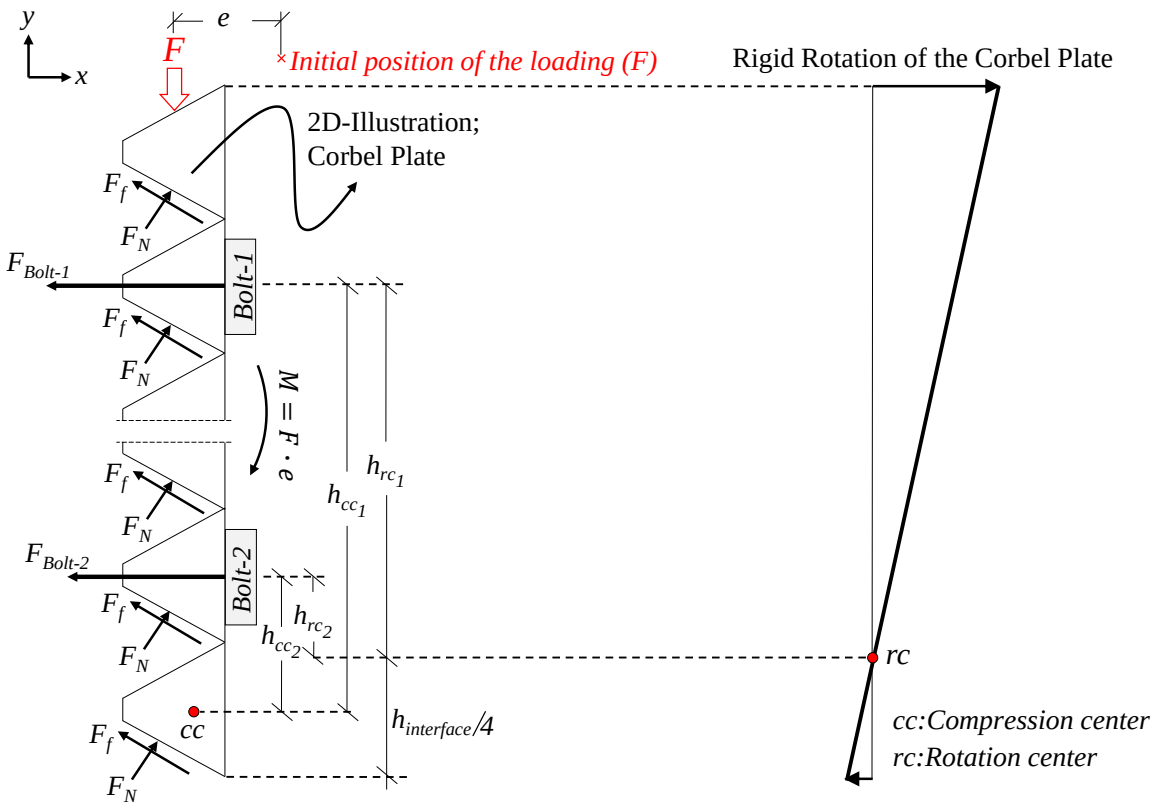

Figure 3.21: 2D Illustration of the stress resultants on the bolts and the saw-tooth threads for the rigid rotation of the corbel plate under eccentric loading.

Defining the static equilibrium condition for the moment action;

$$F \cdot e = F^*_{Bolt-1} \cdot h_{cc_1} + F^*_{Bolt-2} \cdot h_{cc_2} \tag{3.20}$$

In addition, if the triangle similarity is applied with respect to the rotation center of the corbel plate shown in Fig. 3.21, the relation between the resultant forces on the bolts due to the load-eccentricity could be derived as formulated in Eq. 3.21 to Eq. 3.23.

$$F^*_{Bolt-Total} = F^*_{Bolt-1} + F^*_{Bolt-2} \tag{3.21}$$

$$F^*_{Bolt-2} = \frac{F^*_{Bolt-1} \cdot h_{rc_2}}{h_{rc_1}} \tag{3.22}$$

$$F^*_{Bolt-1} = \frac{F \cdot e \cdot h_{rc_1}}{h_{cc_1} \cdot h_{rc_1} + h_{cc_2} \cdot h_{rc_2}} \tag{3.23}$$

Additionally, assuming the horizontal decomposition (*x-axis* direction) of the normal force at the contact surface of the saw-tooth threads to be resisted equally by the upper and the lower bolts at the ultimate limit state the total tensile force on *Bolt-1* could be estimated with Eq. 3.24;

$$F_{Bolt-1} = F^{*}_{Bolt-1} + (F_{thread} - F_N \cdot \mu \cdot \sin\theta) \cdot \left(\frac{w_{interface} \cdot h_{interface}}{n_{bolts} \cdot L_{thread}} \right) \tag{3.24}$$

Furthermore, as similar to Eq. 3.18 if the applied loading assumed to be uniformly distributed along the entire saw-tooth interface for the ultimate limit state it becomes possible to estimate the tension force on *Bolt-1* in terms of P_{thread} as formulated in Eq. 3.25;

$$F_{Bolt-1} = P_{thread} \cdot \frac{w_{interface} \cdot h_{interface}}{L_{thread}} \cdot \left(\frac{e \cdot h_{rc_1}}{h_{cc_1} \cdot h_{rc_1} + h_{cc_2} \cdot h_{rc_2}} + \frac{\cot\theta - \mu}{n_{bolts}} \right) \tag{3.25}$$

Thereby, the ultimate vertical loading on a unit width of a saw-tooth thread ($P_{u,thread}$) could be determined with Eq. 3.26 by inserting the ultimate tensile load capacity of the selected bolt for the mechanical interlock of the saw-tooth interface replacing F_{Bolt-1} in Eq. 3.25;

$$P_{u,thread} = \frac{F_{Bolt-1,u}}{\frac{w_{interface} \cdot h_{interface}}{L_{thread}} \cdot \left(\frac{e \cdot h_{rc_1}}{h_{cc_1} \cdot h_{rc_1} + hcc_2 \cdot h_{rc_2}} + \frac{\cot\theta - \mu}{n_{bolts}} \right)} \tag{3.26}$$

In addition, using the formulations defined by Eq. 3.17 into Eq. 3.25, the horizontal decomposition ($F_{u,thread}$) of the ultimate normal force that could be resisted by a single saw-tooth thread for an eccentric loading condition ($F_{u,N}$) could be formulated with Eq. 3.27.

$$F_{u,thread} = \frac{F_{u,Bolt-1} \cdot \cot\theta}{\frac{w_{interface} \cdot h_{interface}}{L_{thread}} \cdot \left(\frac{e \cdot h_{rc_1}}{h_{cc_1} \cdot h_{rc_1} + hcc_2 \cdot h_{rc_2}} + \frac{\cot\theta - \mu}{n_{bolts}} \right)} \tag{3.27}$$

Consequently, for an eccentric loading condition, the magnitude of the *x-axis* decomposition

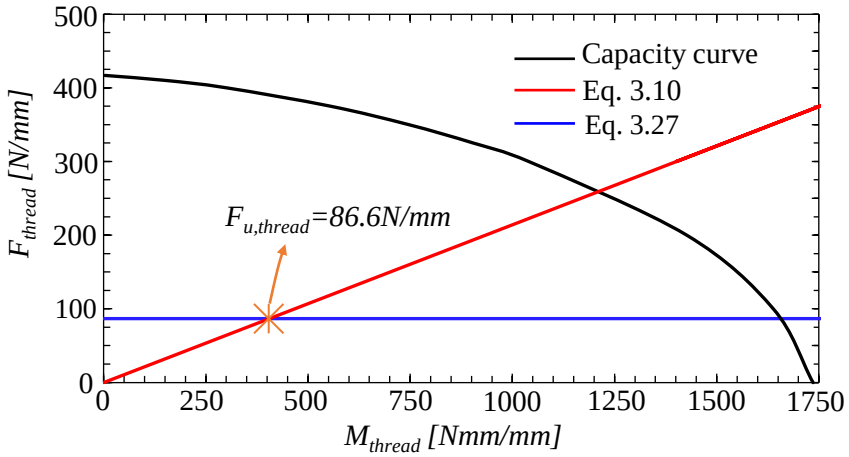

Figure 3.22: The capacity curves of a single saw-tooth thread together with the linear relations between formulated by Eq. 3.10 and Eq. 3.27.

of the ultimate normal force on a saw-tooth thread ($F_{u,thread}$) from Eq. 3.27, the capacity curve of the saw-tooth thread from simultaneous solution of Eq. 3.15 and Eq. 3.16, and the linear relation presented with Eq. 3.10 could be superimposed as shown in Fig. 3.22. Furthermore, the ultimate load-bearing capacity of SMIBC for an eccentric loading condition for which the bolt failure determines the load-bearing capacity of SMIBC could be estimated by combining Eq. 3.18 with Eq. 3.17 and Eq. 3.27 as presented in Eq.3.28;

$$F_{u,analytical} = \frac{F_{Bolt-1,u}}{\left(\frac{e \cdot h_{rc_1}}{h_{cc_1} \cdot h_{rc_1} + hcc_2 \cdot h_{rc_2}} + \frac{\cot\theta - \mu}{n_{bolts}}\right)} \tag{3.28}$$

As a result, according to Fig. 3.22 it could be concluded that if the coincidence of the capacity curve and Eq. 3.10 is above the coincidence of Eq. 3.27 and Eq. 3.10 the failure mode of SMIBC is due to the bolt failure under tension forces instead of the saw-tooth interface failure. This outcome was also earlier derived in Section 3.2.2 and Section 3.2.3 experimentally and numerically.

The results presented in Fig. 3.22 were calculated based on the material properties of the cover plate listed in Table 3.7, the saw-tooth thread shown in Fig. 3.1b, the geometric parameters of the saw-tooth interface presented in Fig. 3.8 using 20mm load-eccentricity (*e=20mm*) as consistent with the actual load-eccentricity achieved by SMIBC-E1 test set-up (see Fig. 3.17) using the characteristic ultimate tensile strength of the selected M16-bolts, which is $F_{b,u\text{-}M16}$=*125.6kN* as also shown in Fig. 3.10d. Thereby, the ultimate load-bearing capacity of SMIBC investigated in SMIBC-E1 test campaign could also be estimated with Eq. 3.29 by inputting the magnitude of $F_{u,thread}$ highlighted on Fig. 3.22 with the geometric parameters of the saw-tooth interface shown by Fig. 3.8 into Eq. 3.18 together with Eq. 3.17.

$$\begin{aligned} F_{u,analytical,SMIBC-E1} &= \frac{F_{u,thread}}{\cot\theta} \cdot w_{interface} \cdot \frac{h_{interface}}{L_{thread}} \\ F_{u,analytical,SMIBC-E1} &= \frac{86.6 \cdot 10^{-3}}{0.414} \cdot 85 \cdot \frac{140}{4} \\ F_{u,analytical,SMIBC-E1} &= 622kN \end{aligned} \tag{3.29}$$

Table 3.17 compares the ultimate load-bearing capacity of SMIBC estimated with Eq. 3.29 and the mean ultimate load-bearing capacities of the test series performed under SMIBC-E1 test campaign. The maximum difference between the estimation of the analytical resistance model and the ultimate mean load-bearing capacity of SMIBC configuration tested in SMIBC-E1 test campaign was only 4% according to the test results presented in Table 3.9 and the estimation was conservative.

To conclude, the presented analytical resistance model is capable to estimate the ultimate load-bearing capacity of SMIBC for both non-eccentric and eccentric loading conditions. In addition, it is graphically shown the switching between the failure modes from the saw-tooth interface failure to bolt failure as consisted with the experimental test results and the FEA simulations.

Table 3.17: Comparison between the analytical estimations and the mean SMIBC-E1 test results.

Test Series	$F_{u,mean}$[1] [kN]	$F_{u,analytical}$ [kN]	Difference [%]
E1-1	651	622	4.4
E1-2	644	622	3.4
E1-3	644	622	3.4

[1] $F_{u,mean}$ corresponds to the mean ultimate load-bearing capacity for each test series of SMIBC-E1 test campaign presented in Table 3.9.

3.2.5 Statistical evaluation of the analytical resistance model

A statistical evaluation was performed according to EN1990, Annex D [58] and based on the output results of a numerical parametric study, which was executed due to the limited number of the experimental test results, to establish partial safety factors for the analytical resistance model presented in Section 3.2.4.

It is the fact that for the joint configuration of SMIBC (see Fig. 3.1d) the loading along the saw-tooth interface could only be applied with a certain level of load eccentricity. Therefore, the numerical parametric study and the statistical evaluation were only executed for SMIBC subjected to eccentric loading conditions.

3.2.5.1 Numerical parametric study

A numerical parametric study was performed with the FE-model presented in Fig. 3.12 including the symmetric boundary conditions (BCs). The material properties of the anchor plate and the corbel plate, the friction coefficient (μ) between the saw-tooth surfaces and the load-eccentricity (e) were selected as the variable parameters of the parametric study. According to the results presented in Fig. 3.14 and Fig. 3.16, it was earlier concluded that the impact of the initial bolt pre-tension applied to the M16-bolts is insignificant for the ultimate load-bearing capacity of SMIBC in FEA as the FE-models do not include the CNC-production imperfections of the saw-tooth threads and the saw-tooth surfaces are fully coupled at the beginning of the analyses. Therefore, the initial bolt pre-tension was not considered as a variable and it was set to 22kN for all of the FEAs performed under the numerical parametric study. The bolts were positioned at the central position with respect to both of the horizontal and the vertical slotted holes of the anchor and the corbel plates respectively (see Fig. 3.1).

The tri-linear material model with material softening presented in Fig. 3.13c was used for the anchor and the corbel plates with four different sets of material properties. The material models and the related properties for the M16-bolts and the washer plate were kept identical to the ones listed in Table 3.12 and Table 3.14, respectively.

Table 3.18 summarizes the input parameters of the parametric study. The yield strength (f_y) and the ultimate strength (f_u) of S235 and S355 grade steels listed in Table 3.18 were assigned according

to EN1993-1-1 [50] as the characteristic values [67]. The ultimate strains (ε_u) of the corresponding material grades (S235 and S355) were calculated according to EN1993-1-5, Annex C [67] using the bi-linear material model with strain hardening based on the characteristic values of the yield and ultimate strengths. In addition, the fracture strains ε_f of the corresponding material grades (S235 and S355) were assigned as the minimum requirement for the elongation of the steel material before fracture according to EN1993-1-1[50].

To summarize, for each material grade listed in Table 3.18, 40 separate FEAs were performed by varying the load-eccentricity (e) and the static friction coefficient (μ) between the saw-tooth surfaces of the anchor and the corbel plates. Thus, in total 160 FEAs were performed.

Table 3.18: Summary of the variable parameters for the numerical parametric study.

Material Grade	Component Name	E [GPa]	ν	f_y [MPa]	f_u [MPa]	f_f [MPa]	ε_u [%]	ε_f [%]	e [mm]	μ
S235	Anchor Plate	210	0.3	235	360	20	6	15		
	Corbel Plate	210	0.3	215[1]	360	20	7	15		
S355	Anchor Plate	210	0.3	355	490	20	7	15	$\begin{bmatrix}15\\20\\25\\30\\35\\40\\45\\50\end{bmatrix}$	$\begin{bmatrix}0\\0.15\\0.30\\0.42\\0.60\end{bmatrix}$
	Corbel Plate	210	0.3	335[1]	470[1]	20	7	15		
SMIBC-E0[2]	Anchor Plate	207	0.3	277	456	20	22	33		
	Corbel Plate	195	0.3	195	406	20	23	37		
SMIBC-E1[3]	Anchor Plate	206	0.3	244	386	20	25	40		
	Corbel Plate	207	0.3	258	448	20	14	29		

[1] As the thickness of the corbel plate is larger than 40mm, the yield and the ultimate strengths of the corresponding material model for the corbel plate were reduced according to EN1993-1-1 [50].

[2] Material properties of the inner and the cover plates of SMIBC-E0 test campaign were used (see Table 3.12).

[2] Material properties of the inner and the cover plates of SMIBC-E1 test campaign were used (see Table 3.14).

Fig. 3.23 compares the results of the numerical parametric analyses for the ultimate load-bearing capacity of the half-symmetric SMIBC. Following conclusions could be drawn based on Fig. 3.23

- If the magnitude of the friction coefficient is less than 0.3 (μ<*0.3*), the relation between the load-eccentricity and the ultimate load-bearing capacity of SMIBC is nearly linear. This outcome is also consisted with the analytical resistance model presented by Eq. 3.28 as the impact of the friction coefficient on the ultimate load-bearing capacity of SMIBC for an

eccentric loading condition diminishes with lower magnitudes of the friction coefficient.

- If the magnitude of the friction coefficient is higher than 0.3 ($\mu > 0.3mm$) the relation between the load-eccentricity and the ultimate load-bearing capacity of SMIBC is highly non-linear.
- If the load-eccentricity is larger than 25mm ($e > 25mm$), the impact of the friction coefficient (μ), and the material properties of the corbel and anchor plates on the ultimate load-bearing capacity of SMIBC becomes nearly insignificant as the load-bearing capacity of the M16-bolts determines the ultimate load-bearing capacity.

In addition, it could be noticed in Fig. 3.23 that the mean ultimate load-bearing capacities of SMIBC-E1 test series very well matches with the output results of the FEAs performed with 20mm load-eccentricity ($e=20mm$) and 0.42 friction coefficient ($\mu=0.42$). Thus, the previous statement that is presented in Fig. 3.17 which indicates that the actual load-eccentricity achieved by SMIBC-E1 test set-up was 20mm further validated. The load-displacement curves for the output results of the parametric study are presented in Annex-B.

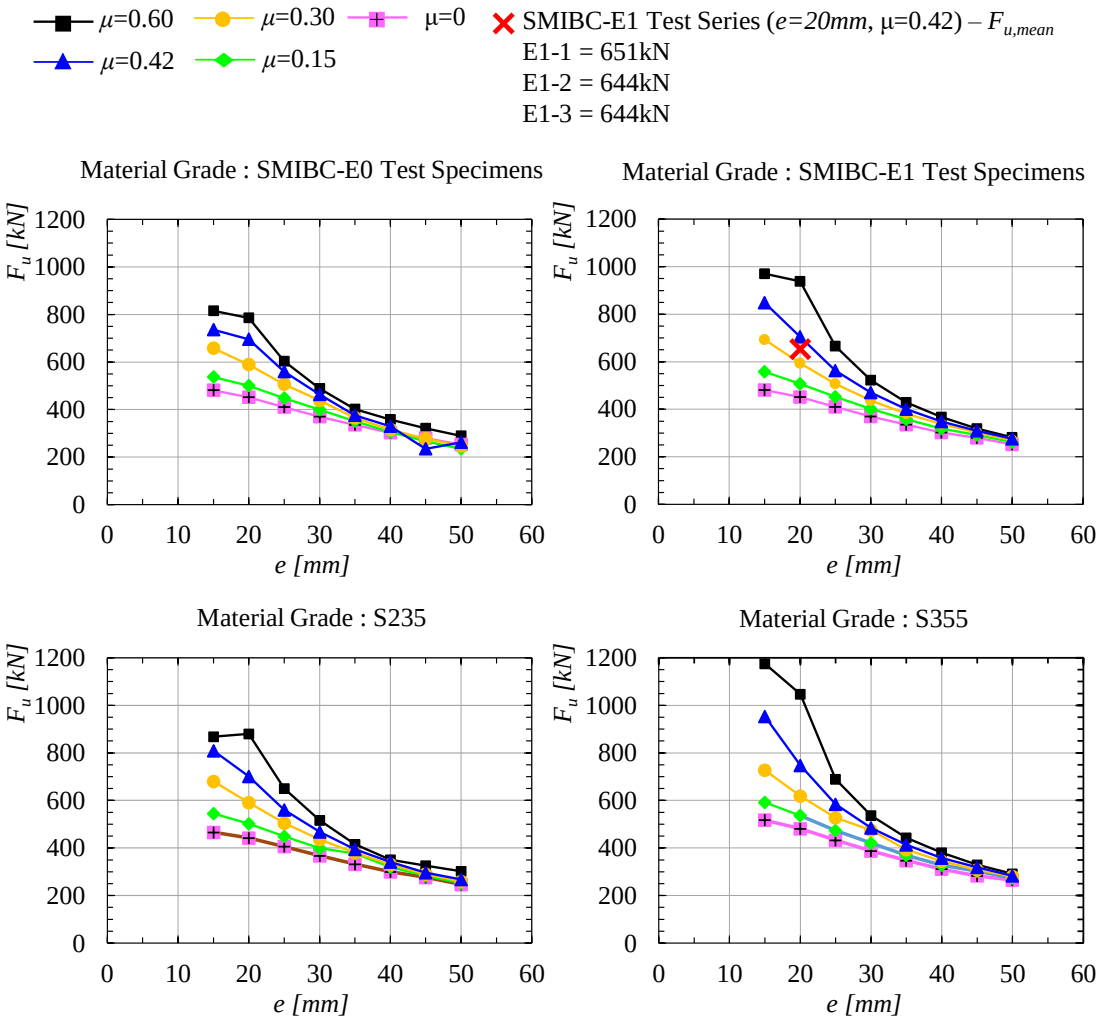

Figure 3.23: Comparisons for the output results of the numerical parametric study.

3.2.5.2 Statistical Evaluation

For all of the FEAs performed under the numerical parametric study, the ultimate load-bearing capacity of SMIBC was limited to the bolt failure as a result of the load eccentricity. Therefore, the statistical evaluation was performed for only the analytical resistance model formulated with Eq. 3.28 which includes the impact of the load-eccentricity on the ultimate load-bearing capacity of SMIBC.

EN1990, Annex D [58] was followed to perform the statistical evaluation based on the output results of the numerical parametric study and the SMIBC-E1 test campaign by means of the ultimate load-bearing capacity of the half symmetric SMIBC configuration. Therefore, Eq. 3.28 is named as the analytical resistance function for the rest of this section.

Fig. 3.24 compares the output results of the numerical parametric study, SMIBC-E1 test campaign and the estimation of the analytical resistance function for the ultimate load-bearing capacity of the half symmetric SMIBC configuration. For the statistical evaluation, the entire data set presented in Fig. 3.24 was used as the scatters of the data points with respect to the load-eccentricity are similar for different material properties and for the different magnitudes of the static friction coefficient (μ). In other words, the data presented in Fig. 3.24 was not separated into the sub-sets [58]. It is crucial to mention that the statistical evaluation performed in this section does not fully conform with EN 1990 Annex D [58] as the evaluation is not only based on the experimental test data but also on the output results of the FEA due to the quantity of the performed tests.

According to EN1990 Annex D [58], the coefficient of variations (CoVs) of the basic variables of Eq. 3.28 need to be known with prior knowledge. However, it is the fact that there is a lack of knowledge regarding the statistical characterizations for some of these parameters such as the mean values and the standard deviations for the saw-tooth thread angle (θ), the thread width (w_{thread}) and the thread length (L_{thread}) defined in Fig. 3.18b. Therefore, these parameters are not considered in the statistical evaluation. However, the anchor and corbel plates of SMIBC are designed to be produced with CNC-cutting technology (see Fig. 3.2). Consequently, very high precision could be expected for the dimensions of these components and the previous assumption not to consider the probabilistic characteristics of these dimensions could be accepted as reasonable.

Consequently, the ultimate tensile capacity of the bolts ($F_{b,u\text{-}M16}$), the static friction coefficient (μ) between the saw-tooth surfaces and the load-eccentricity (e) were considered as the basic variables with normal distributions, while the other parameters were assumed to be deterministic for Eq. 3.28 and equal to the geometrical details for the saw-tooth interface presented in Fig. 3.8. The mean values of the basic variables of Eq. 3.28 ($F_{b,u\text{-}M16}$, μ, e), were assumed to be equal to the values presented in Table 3.18. The coefficient of variation (CoV) of the friction coefficient between the saw-tooth threads was determined with an additional test campaign presented in Annex-A and it was assumed to be identical for all of the magnitudes of the friction coefficient presented in Table 3.18. The CoV for the ultimate tensile capacity of the bolts was determined based on the ultimate tensile force resisted by the M16-bolts recorded during SMIBC-E1 test campaign (see Table 3.9), and the CoV of the load-eccentricities were determined based on non-intented eccentricity of plates for

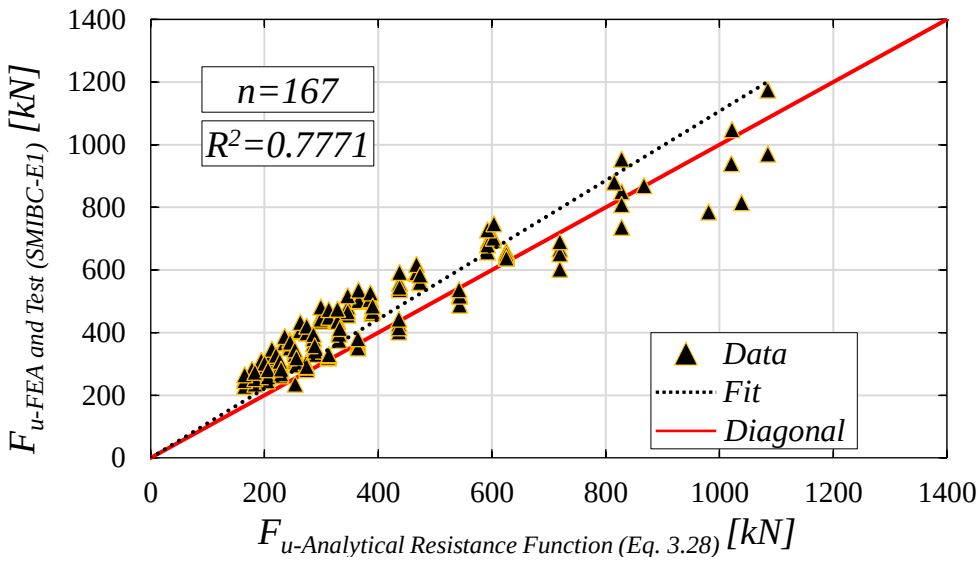

Figure 3.24: The estimation of the analytical resistance function for the ultimate load-bearing capacity of half symmetric SMIBC against the experimental tests and the parametric study.

a horizontal joint defined in EN1090, Annex D [59] by assuming the corresponding non-intented eccentricity to be equal to the standard deviations of the load-eccentricities presented in Table 3.18.

Table 3.19 presents the basic variables, the mean values and the coefficient of variations of the basic variables used for the statistical evaluation of the analytical resistance function of SMIBC.

According to EN1990, Annex D [58], to be able to perform the statistical evaluation of an analytical resistance function, it is required to define the CoV for the estimations of the analytical resistance function. However, it is fact that Eq. 3.28 shows non-linear characteristic with respect to the variation of the basic variables listed in Table 3.19. Therefore, to determine the coefficient of variation of the analytical resistance function, *Monte Carlo* simulations were performed using the statistical parameters listed in Table 3.19. In total, 40 separate *Monte Carlo* simulations were performed and the mean of the CoVs of these simulations was considered as the CoV for the output results of the analytical resistance function. Thereby, it became possible to follow the statistical evaluation procedure defined by EN1990 Annex D [58] to establish the partial safety factors for Eq. 3.28 to be used in engineering calculations.

Table 3.19: Basic variables and their statistical parameters for the statistical evaluation of Eq. 3.29

Basic Variables	Mean Values	Coefficient of Variation (CoV) [%]	Distribution
$F_{b,u\text{-}M16}$ [kN]	121	10.8	Normal
e [mm]	15,20,25,30,35,40,45,50	13.3,10.0,8.0,6.6,5.7,5.0,4.4,4.0	Normal
μ	0[1], 0.15, 0.30, 0.42, 0.60	5.42	Normal

NOTE-1: Nominal values are presented for the basic variables and their coefficient of variations.

[1] The standard deviation for the mean static friction coefficient equal to 0 (μ=*0*) was assumed to be infinitesimal number (e.g. 10^{-10}) to be able to perform the Monte Carlo simulations.

Table 3.20: Input parameters for the statistical evaluation procedure of EN1990, Annex D (n=167 > 100) and the output parameters of the evaluation procedure for Eq. 3.29

Required Input Parameters	Assigned Values
V_δ	0.174[1]
V_{rt}	0.146[2]
k_∞	1.64[3]
$k_{d,\infty}$	3.04[3]
Output Parameters	**Output Results**
r_k	$0.747 \cdot r_t$
r_d	$0.546 \cdot r_t$
$\gamma_M = r_k / r_d$	1.369

[1] Determined according to data set presented in Fig. 3.24.

[2] Determined based on the results of the 40 *Monte Carlo Simulations*.

[3] According to EN1990, Annex D [58].

By the scope of this study, the statistical evaluation procedure of EN1990, Annex D [58] will not be further detailed and only the input and output parameters of the procedure are presented in Table 3.20. Consequently, Fig. 3.24 shows the comparisons for the ultimate load-bearing capacity of the half symmetric SMIBC estimated with Eq. 3.28 against the output results of the numerical parametric study and SMIBC-E1 test campaign together with the characteristic and design values of the estimations. It is important to note that the presented statistical evaluation was performed with respect to the load-deformation behaviour of the 8.8 Grade M16-bolts selected for the experimental test campaigns [61]. Therefore, further experimental and parametric investigations are required to evaluate the analytical resistance function if SMIBC is designed with a different type of bolts.

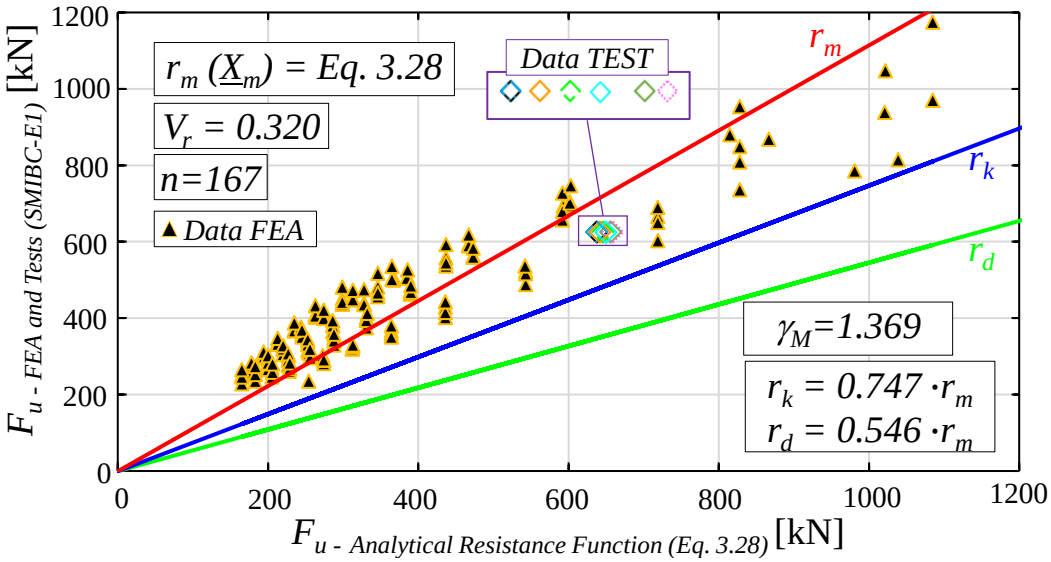

Figure 3.25: The characteristic and design values of the analytical estimations for the ultimate load-bearing capacity of half-symmetric SMIBC under load-eccentricity.

3.2.6 Summary for the investigations of SMIBC

In order to achieve fast erection strategies for high-rise and multi-storey buildings, state-of-the-art structural joint configurations are to be developed to connect load-bearing members of steel-concrete hybrid building systems. CNC-cutting technologies may offer variety of connection details against conventional connection methods. However, these solutions are not common in the construction industry. This section presented an on-site weld-free joint configuration with a novel CNC cut saw-tooth interface for the beam-to-column connection of steel-concrete hybrid building systems.

Two different testing campaigns were executed to determine the ultimate load-bearing capacity, the load-displacement behaviour, and the moment-rotation behaviour of Saw-tooth Interface Mechanical Interlock Bolted Connection (SMIBC) for non-eccentric and eccentric loading conditions. Saw-tooth interface failure and bolt failure by nut-thread stripping were identified for the non-eccentric and the eccentric loading conditions, respectively. Numerical simulations of the testing campaigns were developed to further investigate the load distribution along the saw-tooth interface and to perform a numerical parametric study. The simulations were validated against the test results. It was shown with the numerical simulations that the saw-tooth threads close to the load-introduction region initially resist the loading, and by the yielding of these threads, the loading distributes successively to the following saw-tooth threads.

Furthermore, an analytical resistance model is presented to estimate the ultimate load-bearing capacity of SMIBC for non-eccentric and eccentric loading conditions. The estimations of the analytical resistance model showed a good agreement with the test results. Partial safety factors were established for the analytical resistance model through a statistical evaluation performed for eccentric loading conditions against the results of SMIBC-E1 test campaign and the output results of the numerical parametric study. It should be highlighted that due to the limited number of the experimental tests, the number of the data for the statistical evaluation was mostly based on the output results of the numerical parametric study. Furthermore, some of the statistical variables of the basic parameters for the analytical resistance model were unknown and the statistical evaluation was performed according to several assumptions with respect to these unknown parameters. Therefore, additional experimental tests considering variation of the load-eccentricity, surface finishing of the saw-tooth threads, the geometry of the saw-tooth threads, material properties may be required for further calibration of the analytical resistance model and the corresponding outputs of the statistical evaluation. Additionally, it is also important to mention that if the presented analytical equations will be used for design purposes, the mean material properties that were used for the development of the analytical resistance model against the test results should be replaced with the design material properties (i.e. elastic-modulus, yield strength, ultimate strength and corresponding strain) and design material models (e.g. elastic-plastic material model) of the corresponding design regulations.

It is crucial to mention that the presented analytical resistance model is only valid for the tested geometries of the saw-tooth threads and SMIBC components. Additionally, the models consider

full contact between the saw-tooth surfaces of the inner and cover plates for both non-eccentric and eccentric loading conditions.

Further research may consider different geometry for the saw-tooth thread angle, variation of the bolt positions and their sizes to investigate the accuracy of the analytical resistance model and the statistical evaluation procedure with larger experimental data sets. The last but not the least, this study does not consider possible impacts of the production technique, e.g. flame cutting of the plates, for the load-deformation behaviours of SMIBC.

3.3 Investigation of anchorage details for SMIBC to be used in reinforced-concrete columns

The load-bearing characteristics for the isolated configuration of SMIBC are presented in Section 3.1 with extensive experimental, numerical and analytical studies. However, the joint configuration of SMIBC presented in Fig. 3.1dd also includes reinforced-concrete (RC) columns or walls. A possible joint configuration of SMIBC with RC-structural members is illustrated in Fig.3.26 for a steel-concrete hybrid building frame. As illustrated in Fig. 3.26, the interaction between SMIBC and RC-structural members is designed to be realized with headed-fasteners which are arc-welded to the anchor plate. Therefore, SMIBC-CC testing campaign was established to investigate the load-deformation behaviors of SMIBC joint configuration in RC-columns for different steel reinforcement details around the anchor plate, and to examine the practicality of SMIBC by means of the accommodation of the construction and manufacturing tolerances.

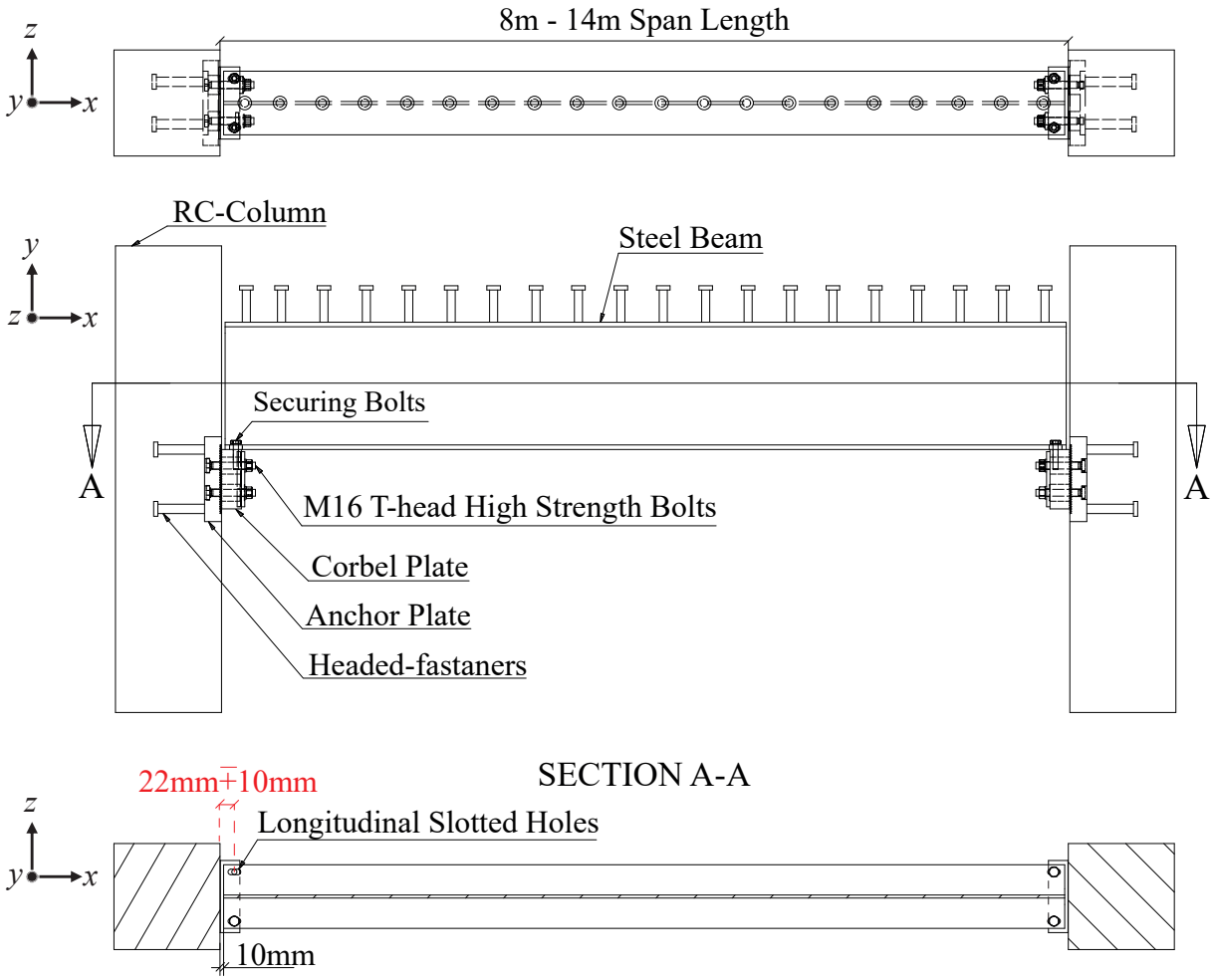

Figure 3.26: SMIBC joint in reinforced-concrete (RC) column configuration.

a) Technical Drawing

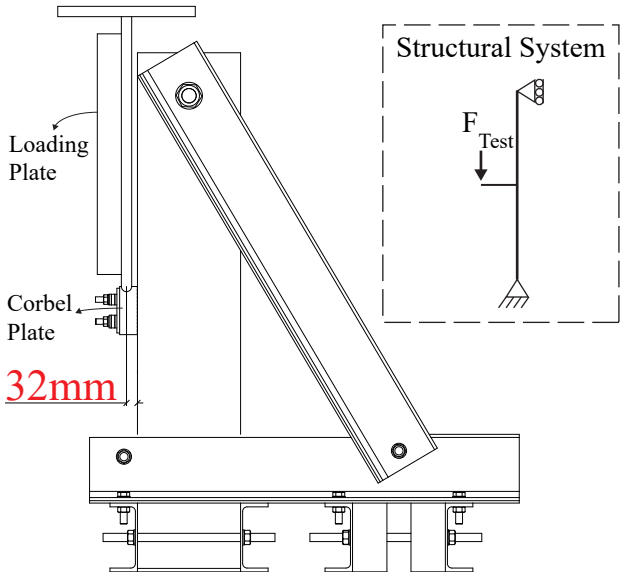

b) Test Environment

Figure 3.27: Overall configuration of SMIBC-CC test set-up.

A testing strategy was developed to focus on the failure mechanisms of the reinforced-concrete load-bearing components next to the anchor plate. Three tests were performed with different reinforcement arrangements around the anchor plate. Fig. 3.27 shows the overall configuration of the test set-up with RC-column and SMIBC. The load-eccentricity highlighted in Fig. 3.27a (e=32mm) was arranged to be equal to the foreseen load-eccentricity that may occur if the steel beam illustrated in Fig. 3.26c is positioned to cover -10mm construction tolerance with respect to the longitudinal beam axis.

The test frame and RC-columns were designed to have higher resistance than the mean ultimate resistance of SMIBC determined through the isolated test campaign presented in Section 3.2.2. By this means, it was guaranteed to have the failure within the vicinity of the anchorage. The RC-columns and the steel components of the test frame were designed according to EN1992-1-1 [72] and EN1993-1-1 [50], respectively.

Fig. 3.28 shows the technical drawings of the set-up components together with the nominal dimensions of the RC-columns. For all three tests the same test frame was used and the global column dimensions were kept identical.

Fig. 3.29 shows the technical drawings and the corresponding images of the main SMIBC components produced for the column tests. For all three tests, identical SMIBC components, which were manufactured with CNC-cutting technique from identical steel plates, were used. In addition, the T-head bolts and the headed-fasteners were taken from the same delivery packages.

a) Overall Configuration of the Test Frame

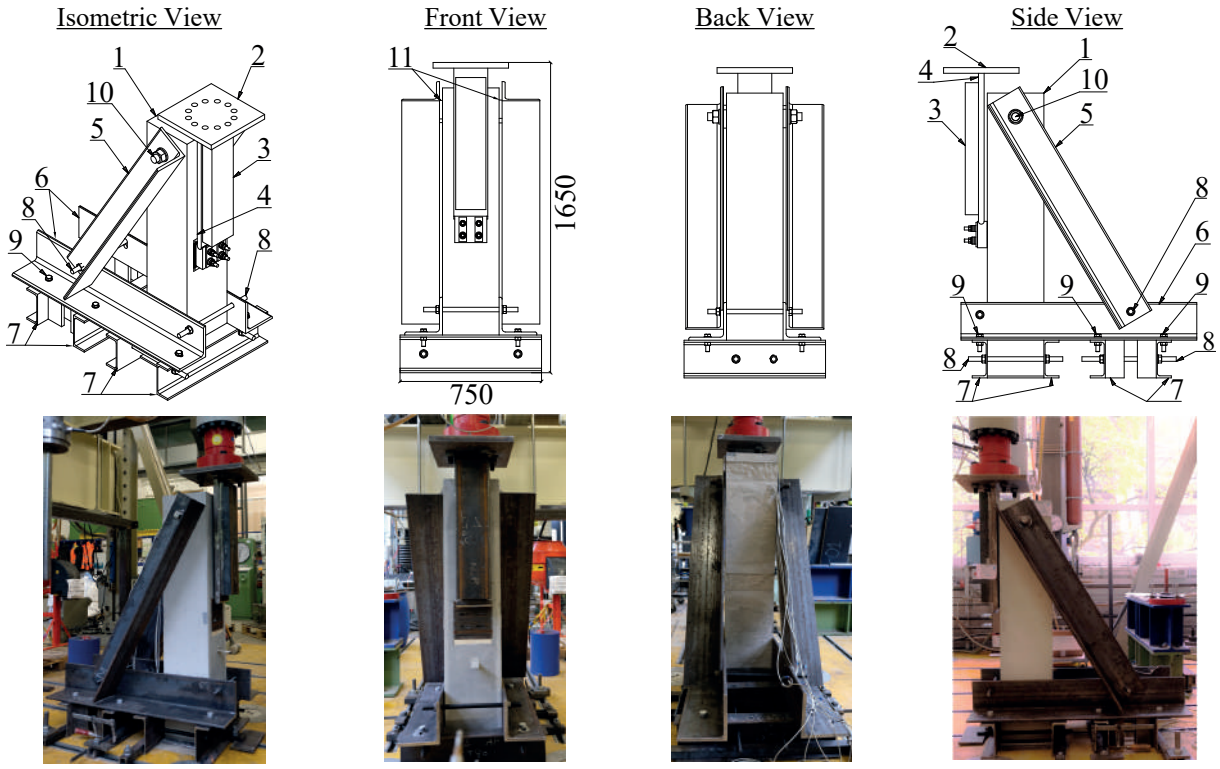

b) Global Dimensions of RC-columns and Technical Drawings of the Frame Componens

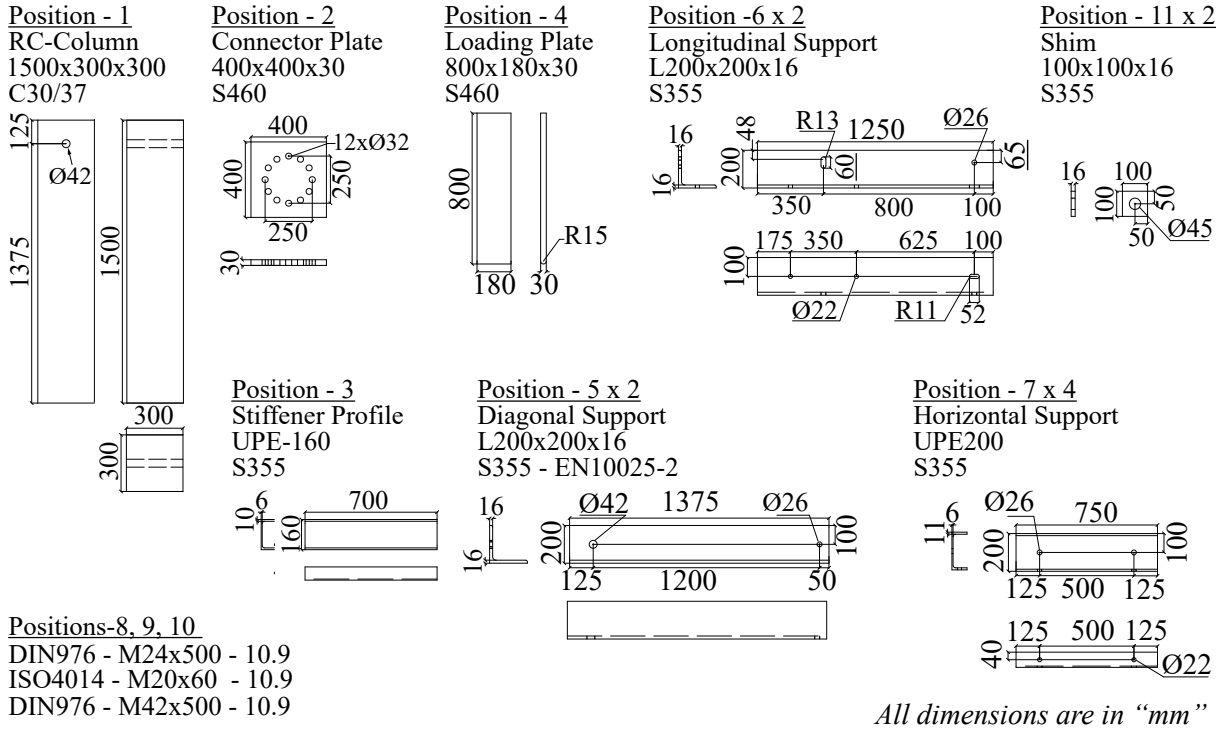

Figure 3.28: Overall configuration and the technical drawings of the test frame.

For the experimental tests, loading was introduced to the corbel plates with a loading plate as shown in Fig. 3.27 instead of a steel beam presented in Fig. 3.26. Therefore, the pin-connection between the corbel plates and the loading plate was achieved by load-introduction recess drilled on the upper surface of the corbel plates (Fig. 3.29b). The distance between the central axis of the load-introduction recess and the front column surface was kept 32mm as identical to the foreseen load-eccentricity (e=32mm). Fig. 3.30 shows the alignment of a corbel plate and the loading plate.

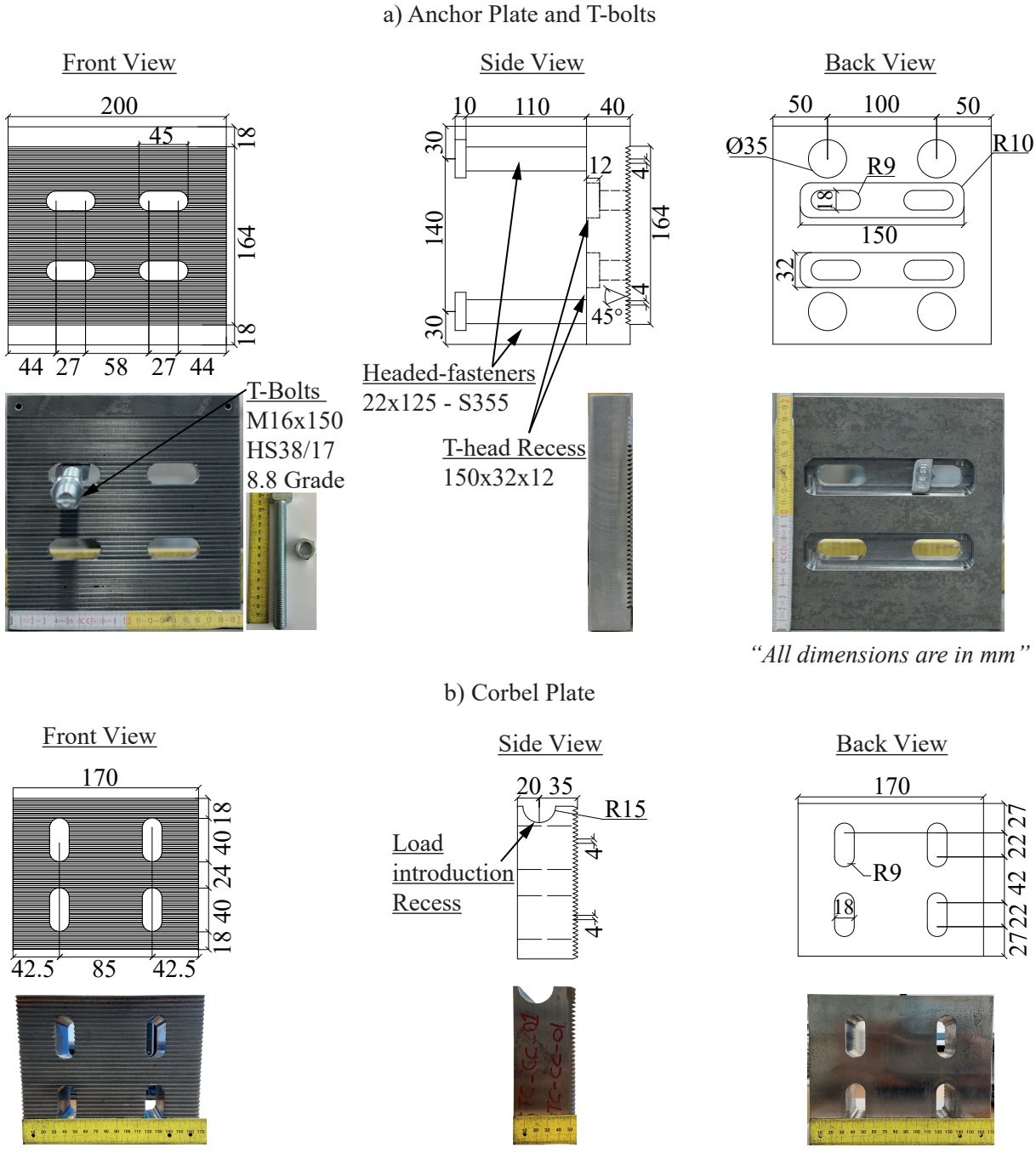

Figure 3.29: Technical drawings of SMIBC components.

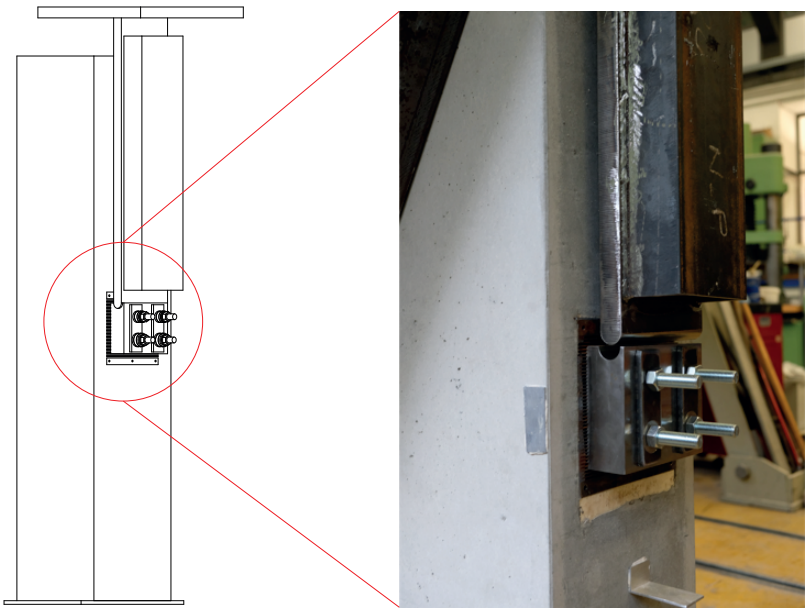

Figure 3.30: Alignment of the loading plate and a corbel plate.

It is crucial to mention that although SMIBC-E1 test campaign (see Table 3.1 and Section 3.2.2) was designed to be performed under 30mm load-eccentricity (*e=30mm*), it was earlier shown in Fig. 3.17 with the output results of FEA that the distance between the resultant vertical force and the saw-tooth interface was 20mm (i.e. *e=20mm*) at the ultimate load limit of SMIBC-E1 test specimens. Therefore, SMIBC-CC testing campaign also provides additional experimental results with 32mm load-eccentricity to verify the analytical resistance model and the statistical evaluation procedure presented in Section 3.2.4 and Section 3.2.5.2.

3.3.1 Accommodation of the construction and manufacturing tolerances

SMIBC components were also assembled before the testing campaign and welding of the headed-fasteners to examine the practicality of SMIBC for the accommodation of the construction and manufacturing tolerances.

In Fig. 3.31a, it is shown that a T-head bolt [73] freely passes from the horizontally aligned slotted holes on the anchor plate and it is possible to position the bolt within $\mp$12mm horizontal range. Furthermore, it could be seen that the bolt head is perfectly fitting the T-head recess. Thus, once the bolt is turned 90°around its longitudinal axis, the bolt head locks to the recess and it becomes possible to apply the required pre-tension load to the bolts to secure the interaction between the saw-tooth surfaces of the anchor and corbel plates.

Fig. 3.31b shows the connection between the corbel plate and the anchor plate in a vertical position for which the corbel plate is at the lowermost level with respect to the anchor plate. It could be seen from the front and the side views that the corbel plate could be positioned $\mp$12mm vertical range with respect to the central axis of the horizontally aligned slotted holes drilled on the

a) Positioning of a T-head Bolt in ±12mm Horizontal Range

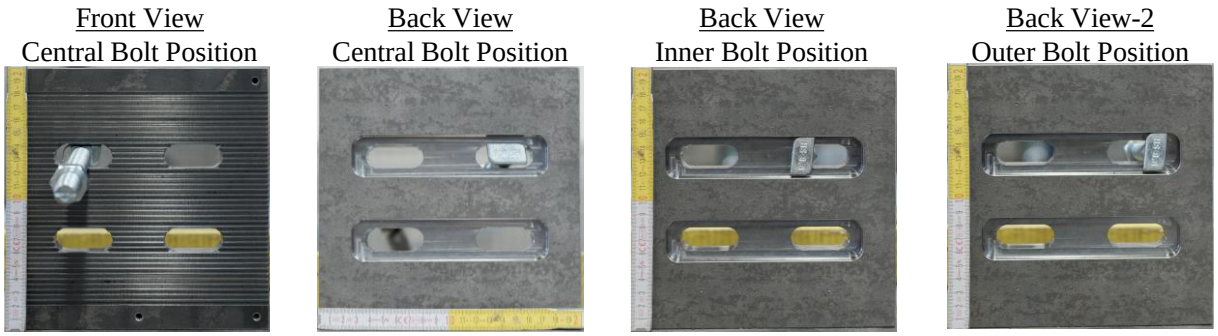

b) Assembly of the SMIBC Components at the Lowermost Position of the Corbel Plate

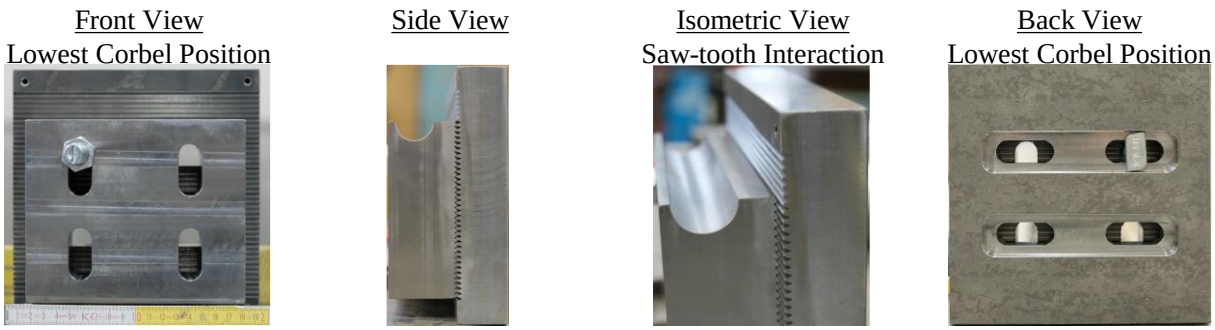

Figure 3.31: Practicality of SMIBC to accommodate construction and manufacturing tolerances.

anchor plate through the saw-tooth surfaces with 4mm intervals as consisted with the geometry of the saw-tooth threads illustrated in Fig. 3.1b.

It is shown in Fig. 3.31 that SMIBC is suitable to accommodate the construction and manufacturing tolerances in ∓12mm horizontal and vertical directions independently. On the other hand, it is important to note that while the accommodation of the horizontal tolerances could be achieved without any limitation by means of the position intervals, the vertical tolerances may be accommodated with 4mm intervals due to the geometry of the saw-tooth threads.

Furthermore, before the experimental tests, the practicality of the SMIBC is also examined for a RC-column configuration. Fig. 3.32 shows the successive steps for the assembly of SMIBC components. The assembly procedure initially begins with positioning of the T-head bolts through the horizontally slotted holes of the anchor plate. Thereafter, the T-head bolts are turned 90°around their longitudinal axes to lock their heads to the T-head recesses. After this, the corbel plate is positioned on the anchor plate through the saw-tooth interface for the desired vertical position with 4mm intervals along ∓12mm vertical range. Finally, the washer plates are installed to close the vertically aligned slotted holes of the corbel plate, and the required bolt pre-tension is applied to the T-head bolts. For all three tests, the central bolt and corbel plate positions were used and 44kN initial bolt pre-tension load ($F_{p,C}$=*44kN*) were applied to the bolts as identical to the SMIBC-E1-2 test series presented in Section 3.2.2.

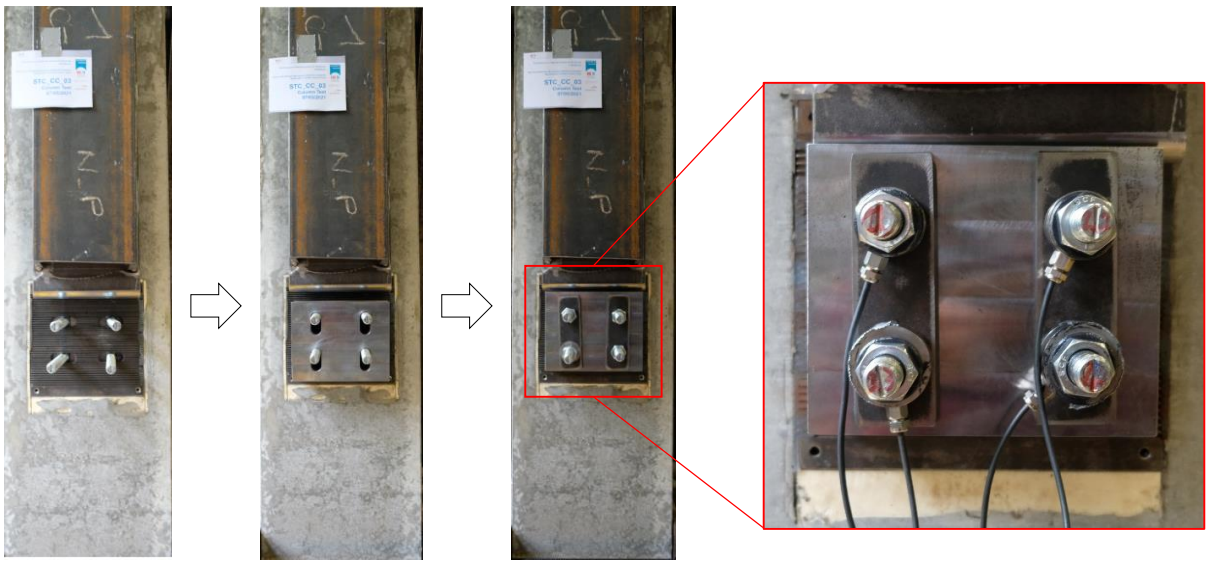

Figure 3.32: Assembly of SMIBC components in RC-column configuration.

3.3.2 Design strategy of the tested anchorages

This section presents the background information and the overall design strategy adopted for the detailing of the steel reinforcements positioned next to the anchor plates. The design capacities against the different failure modes of the anchorages are presented in Section 3.3.8.

Recently, a new Eurocode part has been published for the design of fastenings for use in concrete, EN1992-4 [1], which allows the use of supplementary steel reinforcements in the shape of stirrups and loops against concrete-cone and concrete-edge failure modes. Thus, the design capacity of the anchorages with headed-fasteners used in RC-columns and walls could be enhanced with supplementary reinforcements positioned next to the anchor plates. Fig. 3.33 presents the failure modes of headed-fasteners for use in concrete according to EN1992-4 [1].

On the other hand, it has been shown that EN1992-4 [1] significantly underestimates the resistance of anchorages with headed-fasteners for RC-members [74, 75, 76, 77] as EN1992-4 [1] neglects the simultaneous resistance of the steel reinforcements and the concrete volume around the fasteners against to the applied loading [24, 74, 75, 76, 77]. In addition, EN1992-4 [1] assumes the anchorage length of the supplementary reinforcements to be equal to the part of the reinforcements in the theoretical concrete breakout body without explicit consideration of the hooks of the stirrup reinforcements [74, 76]. Furthermore, EN1992-4 [1] conservatively interacts the tension and shear forces for the design verification [75] due to the lack of test data and closed form mathematical formulation for the stress flow next to the anchorage. Additionally, EN1992-4 [1] does not consider the favourable contributions of the supplementary reinforcements against the pry-out failure mode [13, 24]. The last but not the least, according to EN1992-4 [1], only stirrups and loop shape supplementary reinforcements could be considered to be effective against the tension and shear forces in the anchorage, and any other shape of the steel reinforcements around the fasteners are

not taken into account for the design calculations. Overall, it could be stated that the additional capacity contribution of the steel reinforcements positioned in the anchorage is not fully considered by EN1992-4 [1]. Therefore, SMIBC-CC testing campaign was designed to determine the load-displacement and moment-rotation behaviours of SMIBC joints in RC-column configurations detailed with different reinforcement arrangements around the anchor plate. Consequently, the main research goal was set to understand the failure mechanisms of the reinforced-concrete load-bearing components of the anchorages by investigating the impact of the steel reinforcement arrangements applied next to the anchor plate on the load-bearing capacity of SMIBC joint for RC-column configurations.

To solely focus on the failure mechanisms of the reinforced-concrete components next to the anchor plate, the headed-fasteners were designed to have higher load-bearing capacity than the reinforced-concrete components of the anchorages. In addition, the thickness of the anchor plates was selected to be sufficiently large to have elastic load-deformation behavior for the anchor plates during the entire loading-history. Thereby, it became possible to investigate the impact of the different reinforcement arrangements on the load-displacement and moment-rotation behaviours of SMIBC joint in RC-column configurations. The design capacities of the headed-fasteners are also presented in Section 3.3.8.

The reinforcement arrangement of the first test specimen, which is here on nominated as CC-01 and shown in Fig. 3.34a, was designed without particular supplementary reinforcement next to the anchor plate and the test specimen was detailed with stirrups and longitudinal reinforcements according to EN1992-1 [72] with respect to the mean ultimate test load presented in Table 3.9 for SMIBC-E1-2 test series (see Section 3.2.2). However, to be able to position the stirrups at the mid-height of the column, additional straight reinforcement bars, which are nominated as Pos.3 in Fig. 3.34a, were positioned behind the anchor plate. In addition, the density of the stirrups was increased at to the top and the bottom edges of the test specimen to achieve further resistance at the restrained outer boundaries of the column. The first test is considered to be the reference test and the steel reinforcement arraignment of the first tests was kept identical for the second and the third tests.

For the reinforcement arrangement of the second test specimen, which is here on nominated as CC-02 and presented in Fig. 3.34b, two tension supplementary reinforcements in the shape of stirrup (Pos.-4) were positioned to be in contact with the upper row of the headed-fasteners. In addition, two shear reinforcements in the shape of loops (Pos.-5 and Pos.-6) were positioned directly under the upper and lower rows of the headed-fasteners. The shape and the position of the tension and the shear supplementary reinforcements of the second test specimen were designed based on EN1992-4 [1].

For the reinforcement details of the third test specimen, which is here on nominated as CC-03 and presented in Fig. 3.34c, special shape supplementary reinforcements (Pos.-7) were applied. The bend angle of the special shape supplementary reinforcements is determined to be 45° based on the decomposition of the resultant force on the concrete column introduced by the headed-

fasteners. Thereby, it was aimed to transfer the entire stress resultants introduced by the headed-fasteners to the RC-column through the upper anchorage length of the special shape supplementary reinforcements (Pos.-7). The design calculations regarding to the determination of the bend angle of the special shape supplementary reinforcements are presented in Section 3.3.8. Furthermore, the total stress area of the special shape supplementary reinforcements of CC-03 test specimen was kept identical to the total stress area of the supplementary reinforcements applied for CC-02 test specimen. Thereby, the effectiveness of the special shape supplementary reinforcement was evaluated against the supplementary reinforcements configuration suggested by EN1992-4 [1].

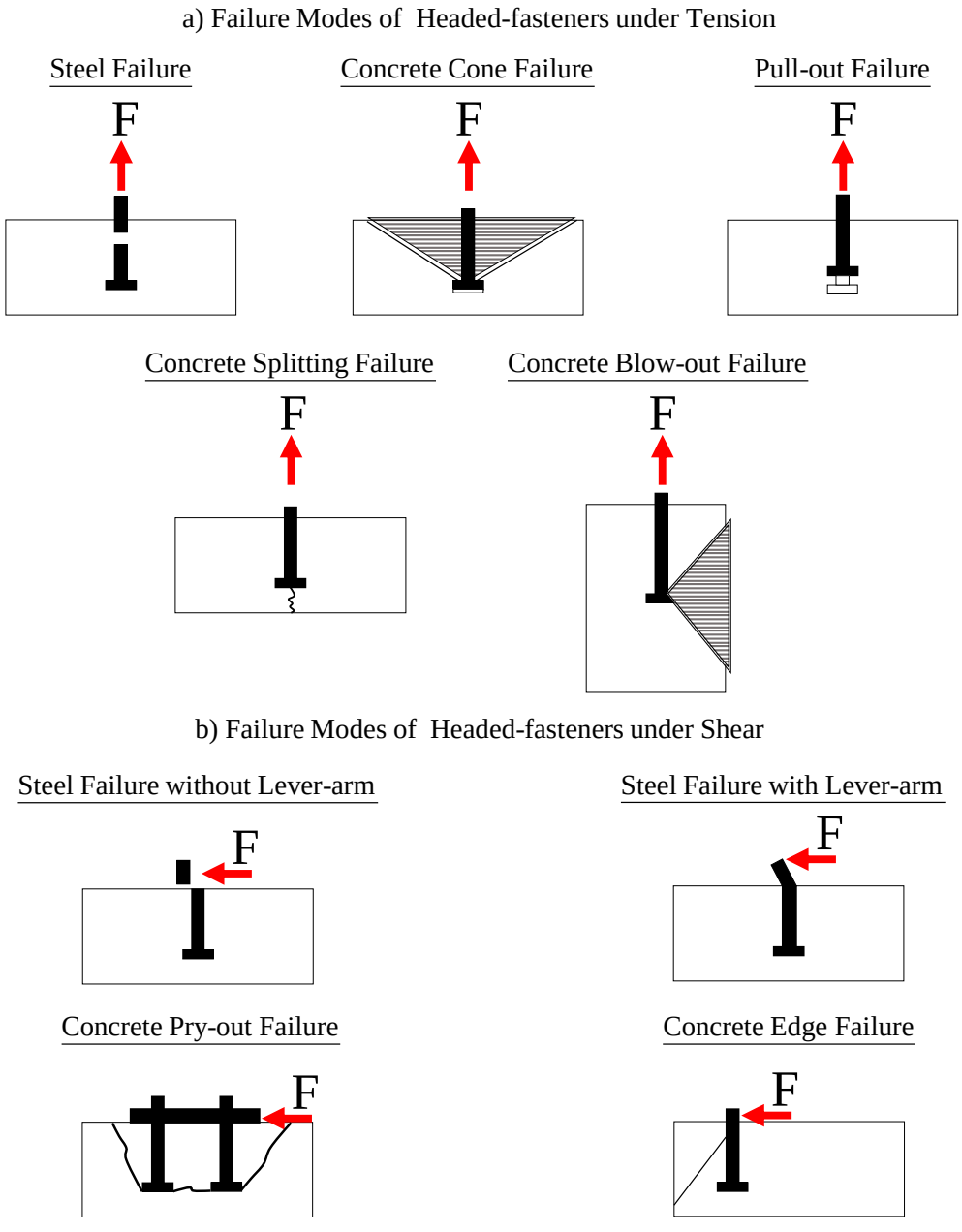

Figure 3.33: Failure modes of headed-fasteners for use in concrete according to EN1992-4 [1].

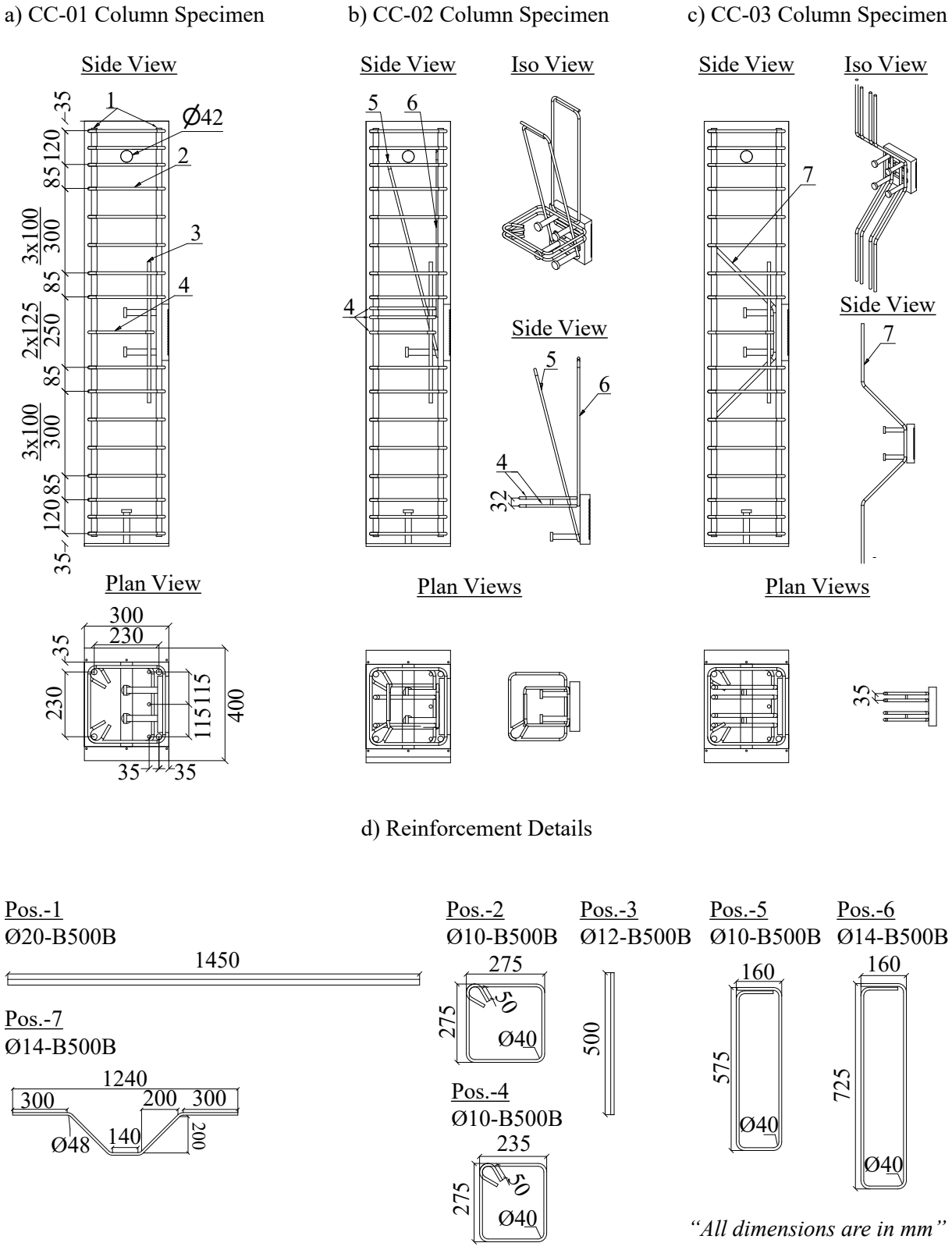

Figure 3.34: Technical drawings of the test specimens and the steel reinforcements.

3.3.3 Material properties of the test specimens

Twelve cylindrical concrete samples (150x300mm) were cast together with the test specimens. The elastic modulus and the compressive strength of the concrete material were determined according to EN12390 [78, 79] at 28 days after the concrete casting and at the test dates. Table 3.21 summarizes the results of the material characterization tests of the concrete samples.

Table 3.21: Material properties of the concrete samples of SMIBC-CC test campaign.

Order Class: **C30/37**	Sample Number	E^1 [GPa]	$f_{c,cyclinder}{}^2$ [MPa]	f_{ctm} [MPa]	ρ [kg/dm^3]
Age:28 Days	1	30.1	31.4	3.05	2.35
	2	29.7	29.9	3.05	2.35
	3	28.9	30.2	3.05	2.35
Mean Values		29.6	30.5	3.05	2.35
CC-01 Age:49 Days	1	31.0	33.6	3.33	2.36
	2	31.6	36.2	3.33	2.37
	3	31.6	36.0	3.32	2.35
Mean Values		31.4	35.3	3.33	2.36
CC-02 Age:51 Days	1	30.9	34.4	3.33	2.36
	2	31.3	34.0	3.33	2.35
	3	31.6	35.9	3.32	2.37
Mean Values		31.3	34.8	3.33	2.36
CC-03 Age:55 Days	1	32.2	35.6	3.33	2.36
	2	30.2	34.9	3.33	2.36
	3	30.1	33.9	3.32	2.35
Mean Values		30.8	34.8	3.33	2.36
Cement		: CEM I 42.5N			
W/C		: 0.54			
Exposition Class		: XC4,XD1,XF1,XA1,XM1(2)			
Consistency Class		: F3			
Aggregate Size		: 8mm			

[1] Elastic modulus (E) was determined based on the testing method presented by EN12390-13 Method A [79].

[2] Compressive strength was determined based on the testing method presented by EN12390-3 [78].

The material properties of the anchor plates and the steel reinforcements positioned next to the anchor plates were determined with steel coupon tests performed according to EN ISO 6892-1 [63]. Three coupon samples were manufactured from the anchor plates and the steel reinforcements for each different diameter of the reinforcements were positioned next to the anchor plates. The steel coupons of the anchor plates were cut after the tests. Table 3.22 summarizes the material properties of the anchor plates and the steel reinforcements, the detailed results are also presented in Annex-C.

Table 3.22: Material properties of the steel specimens of SMIBC-CC test campaign.

Specimen Name	Order	Sample ID	E^1 [GPa]	f_y [MPa]	f_u [MPa]	A^2 [%]
Anchor Plate	S235	AP-1	217	386	486	39.0
		AP-2	221	383	489	36.5
		AP-3	212	381	484	38.5
Mean Values			217	383	486	38.0
Reinforcement-*Ø10*	B500B	*Ø10*-1	251	563	649	26.0
		Ø10-2	199	573	655	23.5
		Ø10-3	198	562	650	25.0
Mean Values			216	566	651	24.8
Reinforcement-*Ø12*	B500B	*Ø12*-1	238	441	593	32.5
		Ø12-2	217	496	605	29.5
		Ø12-3	202	472	613	30.0
Mean Values			219	470	604	30.7
Reinforcement-*Ø14*	B500B	*Ø14*-1	208	579	656	20.5
		Ø14-2	205	574	651	19.5
		Ø14-3	200	536	622	23.0
Mean Values			204	563	643	21.0

[1] Elastic modulus (E) was determined according to EN ISO 6892-1 Method A1 [63].

[2] The term A corresponds to percentage elongation of the steel coupon after the fracture [63].

3.3.4 Production of the test specimens

Fig. 3.35a shows the form-works and the positioning of an anchor plate and a bottom plate in the form-work of a test specimen. The anchor plates were fixed to the formwork in a position that their saw-tooth surfaces were flush with the formwork. It could be noticed that the T-head bolt recesses were closed with a thin steel plate to protect the recesses and the bolt holes from concrete flow. The side surfaces of the anchor plates were covered with styropor to introduce the applied loading to the columns directly with the headed-fasteners by eliminating any contacts between the column and the side surfaces of the anchor plates.

The steel reinforcements were first assembled as a reinforcement cage at the out side of the form-works and they were later positioned in the form-works for all of the test specimens. Fig. 3.35 shows the preparation of the test specimens and their reinforcement details before the concrete casting.

Once all of the test specimens were prepared, their concrete casting was done on the same day with the same concrete delivery from one truck. Fig. 3.36 shows the casting of the test specimens. The test specimens were kept in the laboratory hall until the test dates.

a) Plate Positioning

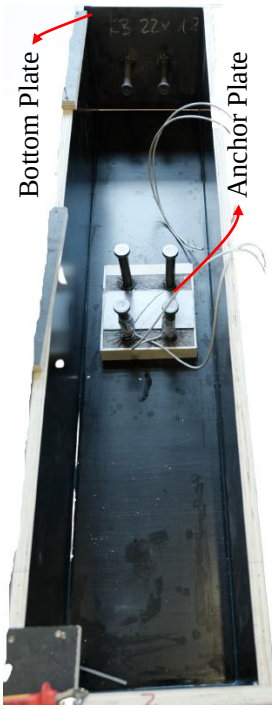

b) CC-01 Column Specimen

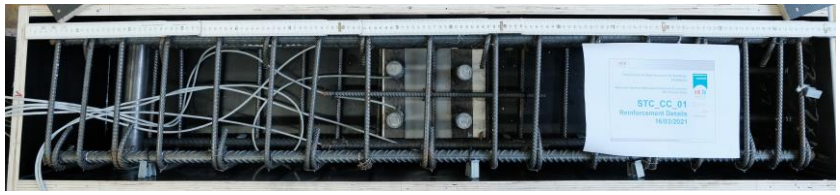

c) CC-02 Column Specimen

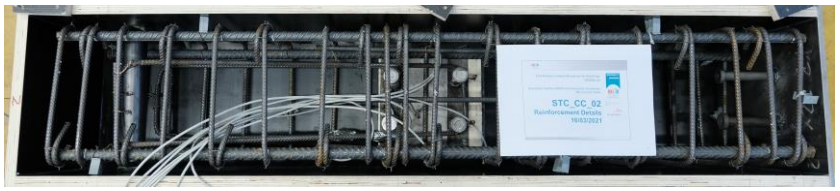

d) CC-03 Column Specimen

Figure 3.35: Form-works, positioning of the anchor and bottom plates and steel reinforcements.

Figure 3.36: Concrete casting.

3.3.5 Instrumentation of the test specimens

To measure the tension and shear stress resultants transferred from the headed-fasteners to the anchorage as a normal force on the steel reinforcements positioned next to the anchor plates, the reinforcements were instrumented with strain-gauges (SGs). Fig. 3.37 shows the position of the strain-gauges on the steel reinforcements and the headed fasteners. Table 3.23 summarizes their measurement orientations.

The test specimens were also equipped with 16 linear variable displacement transducers (DTs) and 4 load-cells (LCs). Fig. 3.38 shows the position of the displacement transducers and the load-cells. Table 3.24 summarizes their measurement orientations and measurement ranges. Identical displacement transducer and load-cell configurations were applied for all three tests.

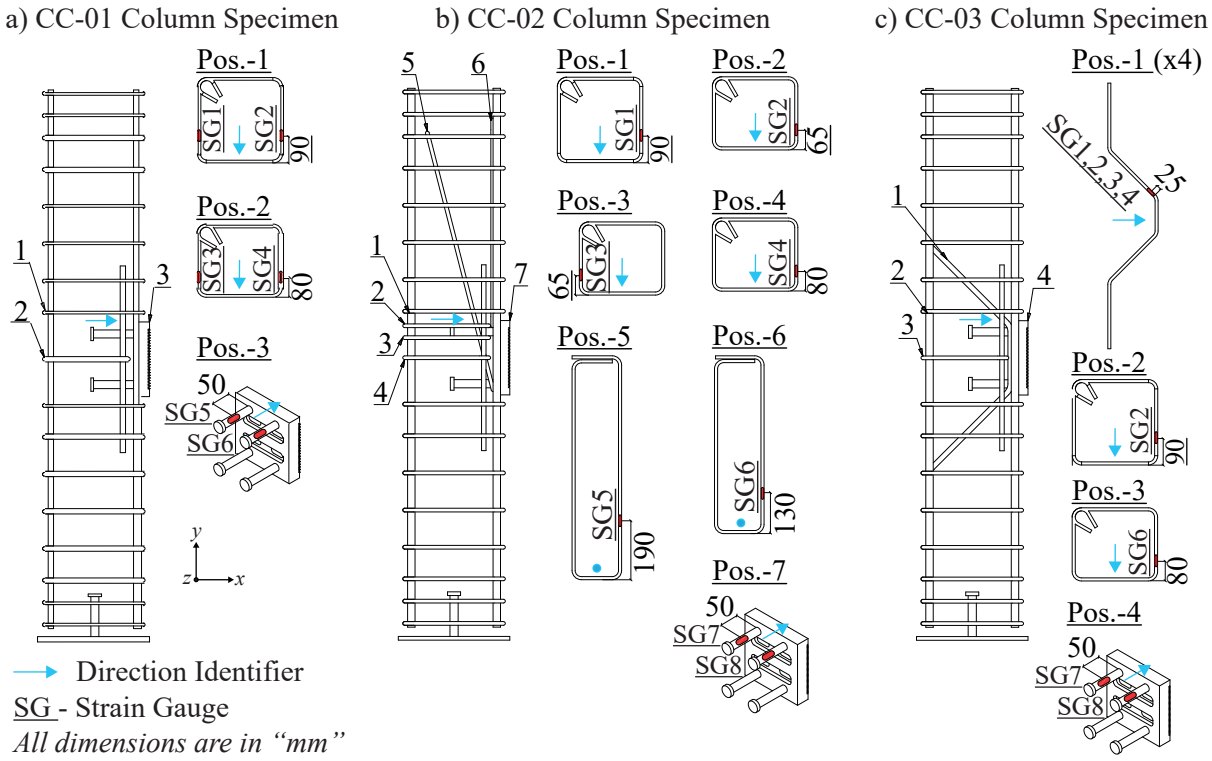

Figure 3.37: Strain-gauge distribution (SG) / SMIBC-CC test campaign.

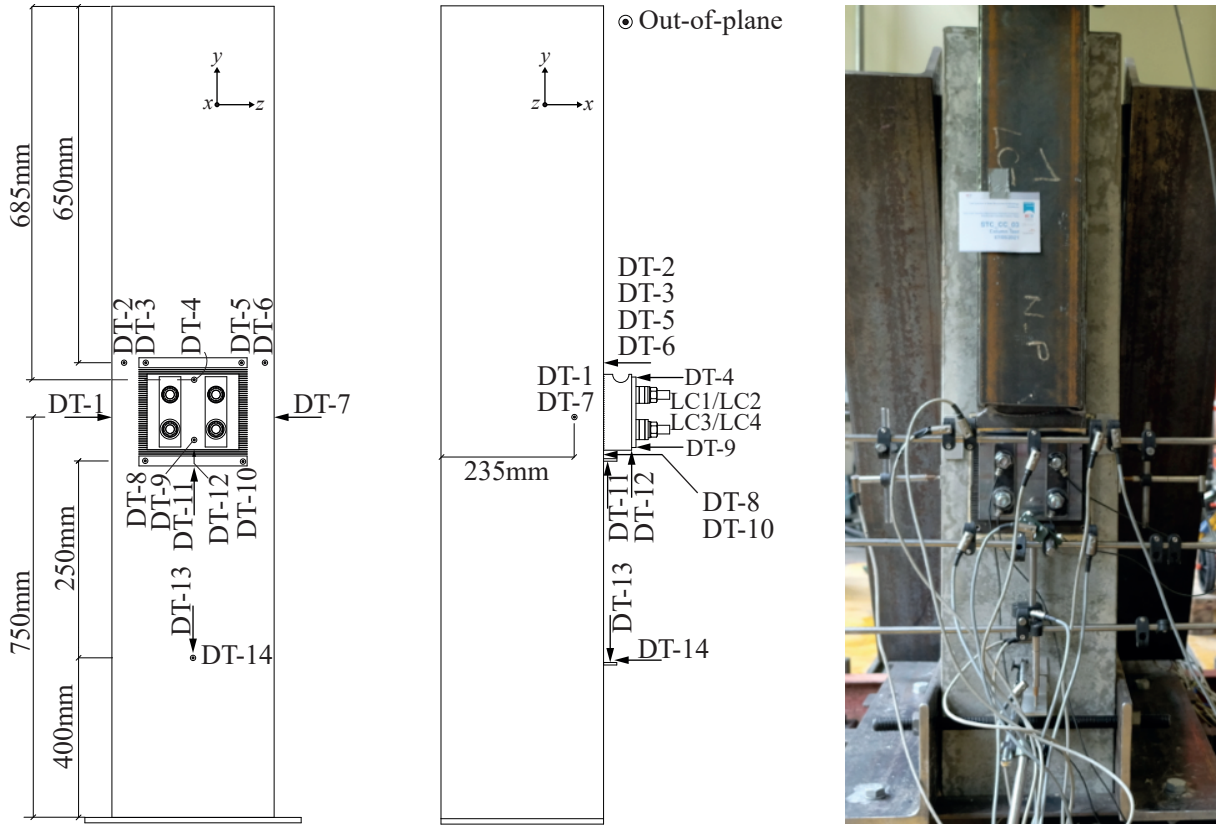

Figure 3.38: Displacement transducers (DT) and load-cells (LC) / SMIBC-CC test campaign.

Table 3.23: Details of the strain-gauges (SG) / SMIBC-CC test campaign.

Test ID	Sensor ID	Position	Direction	Measurement
CC-01	SG-1	Stirrup-1	Horizontal (x-axis)	1D
	SG-2	Stirrup-1	Horizontal (*x-axis*)	1D
	SG-3	Stirrup-2	Horizontal (*x-axis*)	1D
	SG-4	Stirrup-2	Horizontal (*x-axis*)	1D
	SG-5	UL-Fastener	Horizontal (*x-axis*)	1D
	SG-6	UR-Fastener	Horizontal (*x-axis*)	1D
CC-02	SG-1	Stirrup-1	Horizontal (*x-axis*)	1D
	SG-2	Stirrup-2	Horizontal (*x-axis*)	1D
	SG-3	Stirrup-3	Horizontal (*x-axis*)	1D
	SG-4	Stirrup-4	Horizontal (*x-axis*)	1D
	SG-5	Hook-5	Vertical (*y-axis*)	1D
	SG-6	Hook-6	Vertical (*y-axis*)	1D
	SG-7	UL-Fastener	Horizontal (*x-axis*)	1D
	SG-8	UR-Fastener	Horizontal (*x-axis*)	1D
CC-03	SG-1	Special shape-1	Diagonal (*x-axis* and *y-axis*)	1D
	SG-2	Special shape-2	Diagonal (*x-axis* and *y-axis*)	1D
	SG-3	Special shape-3	Diagonal (*x-axis* and *y-axis*)	1D
	SG-4	Special shape-4	Diagonal (*x-axis* and *y-axis*)	1D
	SG-5	Stirrup-2	Horizontal (*x-axis*)	1D
	SG-6	Stirrup-3	Horizontal (*x-axis*)	1D
	SG-7	UL-Fastener	Horizontal (*x-axis*)	1D
	SG-8	UR-Fastener	Horizontal (*x-axis*)	1D

UL: Upper Left, UR: Upper Right, 1D: One Directional measurement along longitudinal axis.

Table 3.24: Displacement-transducers (DT) and load-cells (LC) of SMIBC-CC test campaign.

Test ID	Sensor ID	Contact	Direction	Range
CC-01 CC-02 CC-03	DT-1	Column	Horizontal (*z-axis*)	10mm
	DT-2	Column	Horizontal (*x-axis*)	10mm
	DT-3	Anchor Plate	Horizontal (*x-axis*)	20mm
	DT-4	Corbel Plate	Horizontal (*x-axis*)	20mm
	DT-5	Anchor Plate	Horizontal (*x-axis*)	20mm
	DT-6	Column	Horizontal (*x-axis*)	10mm
	DT-7	Column	Horizontal (*z-axis*)	10mm
	DT-8	Column	Horizontal (*x-axis*)	10mm
	DT-9	Corbel Plate	Horizontal (*x-axis*)	10mm
	DT-10	Column	Horizontal (*x-axis*)	10mm
	DT-11	Anchor Plate	Vertical (*y-axis*)	20mm
	DT-12	Corbel Plate	Vertical (*y-axis*)	20mm
	DT-13	Column	Vertical (*y-axis*)	10mm
	DT-14	Column	Horizontal (*x-axis*)	10mm
	LC1	UL-Bolt	Horizontal (*x-axis*)	200kN
	LC2	UR-Bolt	Horizontal (*x-axis*)	200kN
	LC3	LL-Bolt	Horizontal (*x-axis*)	400kN
	LC4	LR-Bolt	Horizontal (*x-axis*)	400kN

UL: Upper Left, UR: Upper Right, LL:Lower Left, LR:Lower Right.

3.3.6 Execution of SMIBC-CC test campaign

The tests were executed in The Structural Laboratory for the University of Wuppertal with 2000kN hydraulic jack. Fig. 3.39 illustrates the overall configuration of the test specimens with respect to the position of the hydraulic jack from a side view. The force from the hydraulic jack and the data from the measurement devices presented in Section 3.3.5 were continuously recorded with 100Hz data acquisition speed during the tests.

The loading procedure was adopted from Hanswille [80]. Fig. 3.40 presents the loading procedure having the following loading steps;

- Load up to 40% of the expected capacity - $F_{u,exp}$ (Displacement-controlled 0.5mm/min),
- Rest 15 minutes (Displacement-controlled),
- Cycling period between 5% - 40% of the expected capacity (Force-controlled 0.1Hz - 100Cycles),
- Total unload at the end of the cycling period (Displacement-controlled 1mm/min).,
- Load up to 60% of the expected capacity (Displacement-controlled 0.5mm/min),

- Rest 15 minutes (Displacement-controlled).
- Load up to 100% of the expected capacity (Displacement-controlled 0.5mm/min),
- Rest 60 minutes (Displacement-controlled).

1. If there is no failure at the expected capacity (100%);
   (a) Total unload (Displacement-controlled 1mm/min),
   (b) Load up to 120% of the expected capacity (Displacement-control 0.5mm/min),
   (c) Rest 15 minutes (Displacement-control),
   (d) If there is no failure at the 120% of the expected capacity;
      i. Total unload (Displacement-controlled 1mm/min),
      ii. Load until the ultimate load capacity - $F_{u,Test}$ (Displacement-controlled 1mm/min).

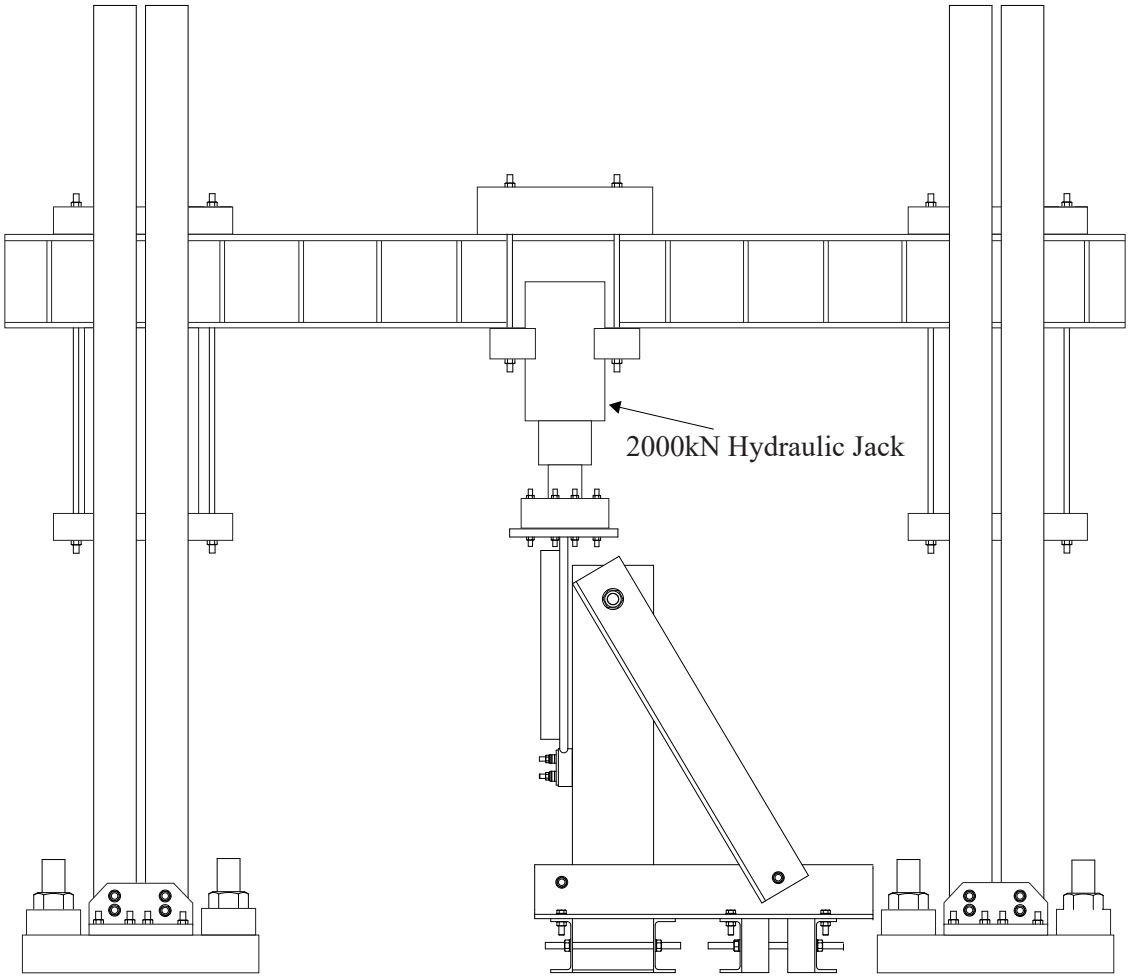

Figure 3.39: Configuration of the test set-up and the test frame.

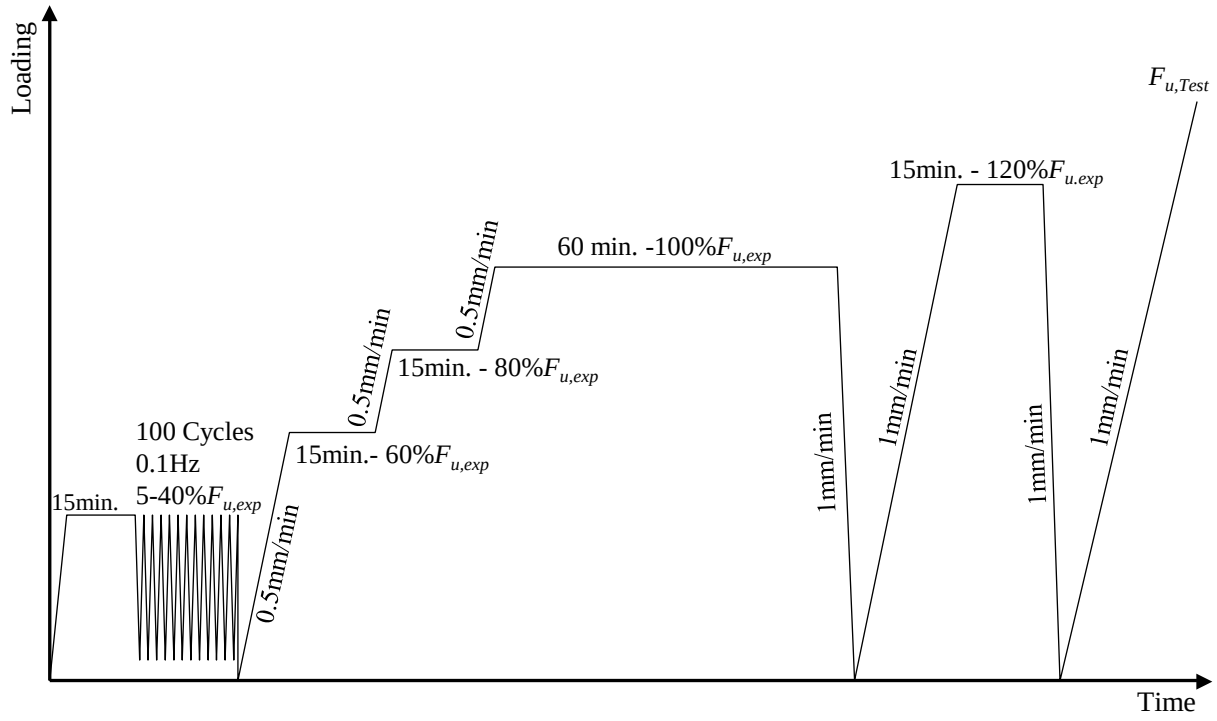

Figure 3.40: Loading procedure of SMIBC-CC test campaign.

The expected capacities were determined with FEAs performed prior to the experimental tests based on the mean material properties of the concrete material and the characteristic material properties of the steel reinforcements determined according to EN1992-1-1 [72], characteristic material properties of the anchor plate determined according to EN1993-1-1 [50], and the characteristic material properties of the headed-studs based on the producer catalog [81]. The FE-models are presented in Section 3.3.7.

3.3.6.1 Test results and discussions / CC-01

Fig. 3.41 shows the vertical displacements of the anchor plate with respect to the applied loading for CC-01 test specimen. Although a relatively stiff testing frame was designed to achieve ideal boundary conditions at the lower and the upper edges of the RC-column (see Fig. 3.28), it was neither practical nor economical to satisfy perfect restrains at the boundaries. Therefore, the impact of the global column displacements on the vertical displacements of the anchor plate were eliminated with Eq. 3.30 based on Fig. 3.38, and the load-displacement behavior of the anchor plate without the impact of the global column displacements is also presented in Fig. 3.42 together with the translational initial elastic and secant stiffness values of the anchorage.

$$\delta_y = DT_{11} - DT_{13} \tag{3.30}$$

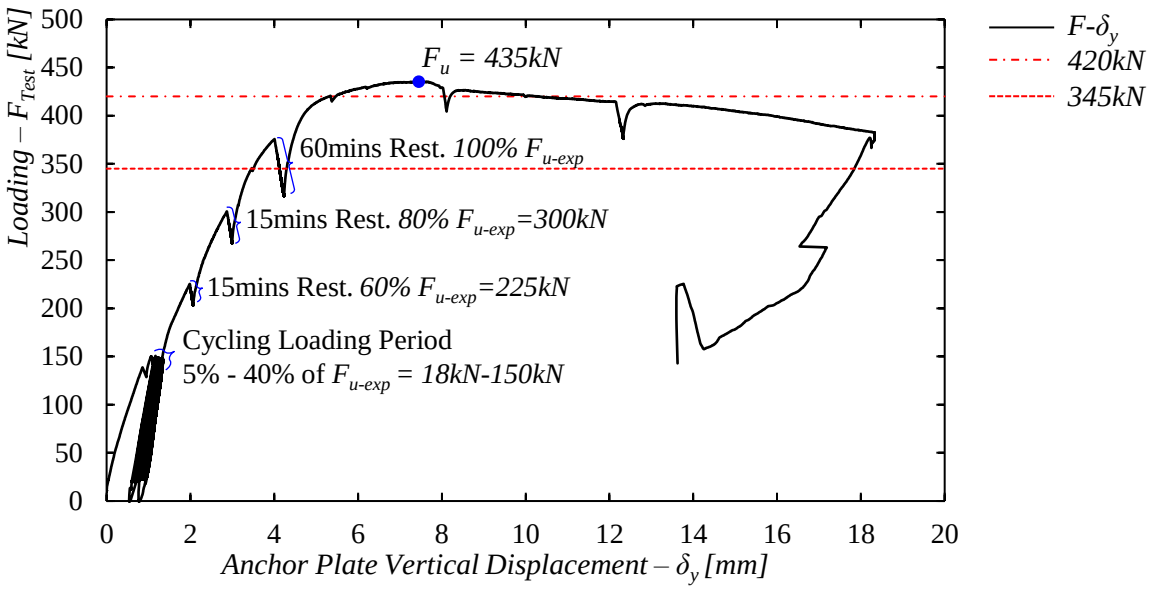

Figure 3.41: Anchor plate load-displacement behavior with the global column behavior / CC-01.

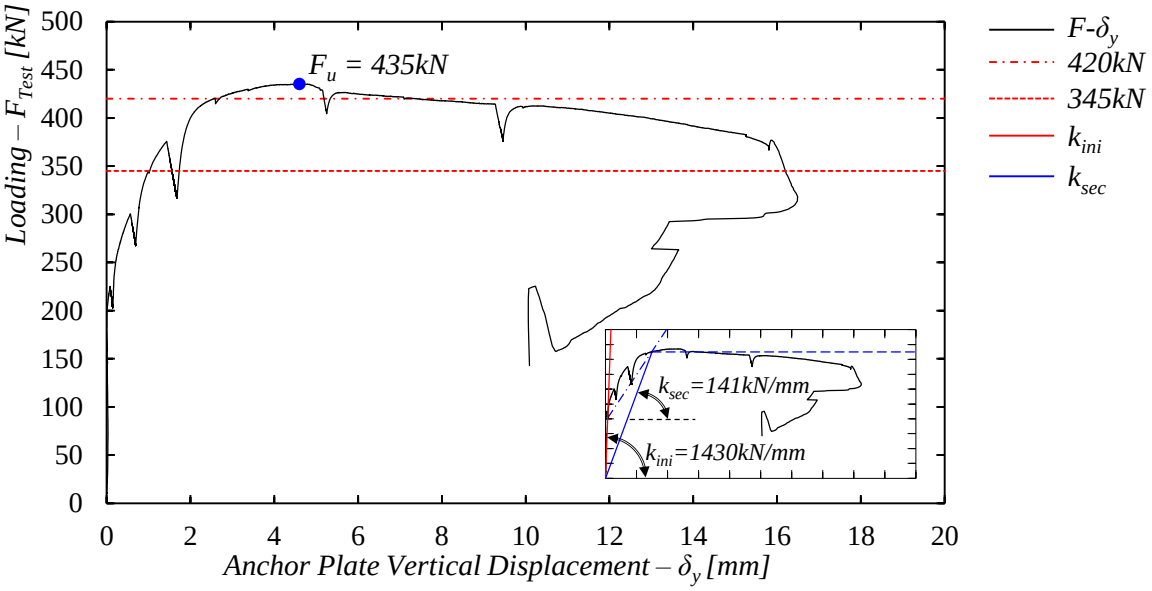

Figure 3.42: Anchor plate load-displacement behavior without the global column behavior / CC-01.

Comparing Fig. 3.41 and Fig. 3.42, it could be concluded that the assembly gaps of the test frame were closed during the initial and the cyclic loading steps. Therefore, the load-displacement behavior presented in Fig. 3.42 is used to investigate the test results. The ultimate load-bearing capacity of CC-01 test specimen ($F_{u,CC\text{-}01}$) could be noticed to be equal to 435kN in Fig. 3.42. However, sudden load-drops at 345kN and 420kN load-levels could also be noticed. The reason behind these drops is investigated in detail to clarify the failure mechanism of the anchorage.

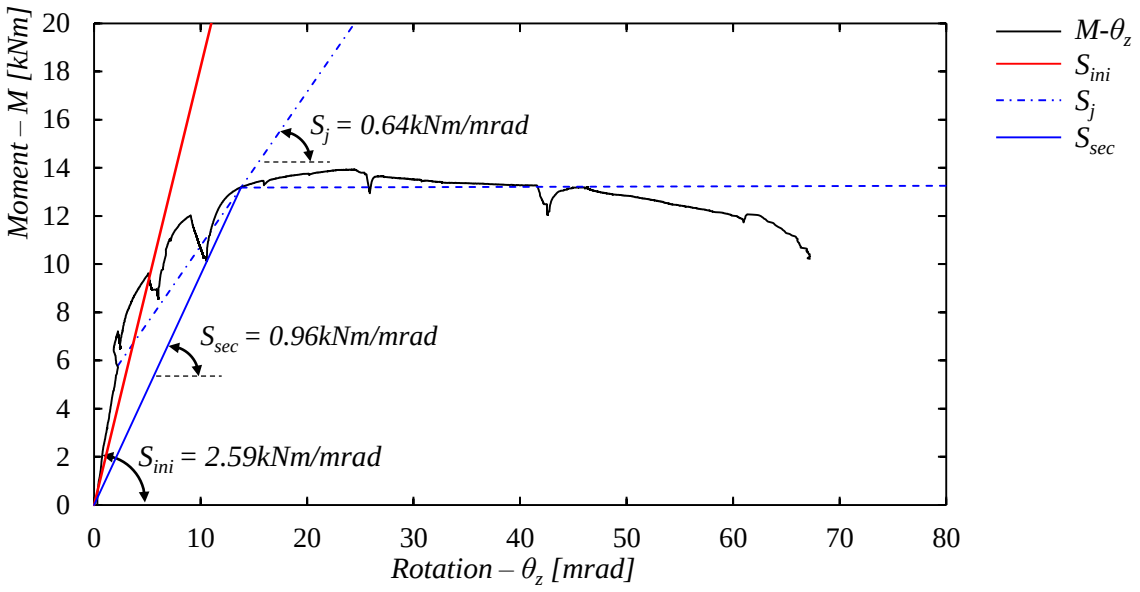

Figure 3.43: Moment-rotation behavior of the anchor plate / CC-01.

Fig. 3.43 shows the moment-rotation behavior of the anchor plate. The cycling loading period and the unloading period after reaching the ultimate test load are not shown in the figure to have clear image of the moment-rotation behavior. The moment values were calculated directly as the multiplication of the applied loading with the pre-defined load eccentricity (e=32mm - see Fig. 3.27a). The rotation values were calculated with Eq. 3.31 according to the configuration of the displacement transducers (DTs) presented in Fig. 3.38.

It is crucial to note that similar to the load-displacement behavior presented in Fig. 3.42, the global horizontal column displacements (*x-axis*) were also subtracted from the horizontal displacements of the anchor plate to precisely determine the rotation of the anchorage. To be able to calculate the global horizontal displacements of the column at the level of the anchor plate, it was assumed that the horizontal column displacements due to the assembly tolerances of the test frame were linear along the height of the column and their magnitude at the anchor plate level was calculated with triangle similarity based on the data collected with DT-14 (see Fig. 3.38).

$$\theta_z = \arctan\left(\frac{\left(\frac{DT_3+DT_5}{2} - \frac{850mm \cdot DT_{14}}{400mm}\right) + \left(\frac{DT_8+DT_{10}}{2} - \frac{650mm \cdot DT_{14}}{400mm}\right)}{h_{anchor-plate=200mm}}\right) \tag{3.31}$$

Before further investigation of the test results, it is important to mention that CC-01 test specimen was detailed without additional supplementary reinforcements (see Fig. 3.34a).

Fig. 3.44 to Fig. 3.49 show the crack propagation on the column with respect to the loading steps of the test procedure. During the cycling loading period, no surface crack was observed, thus no visual inspection shown for the cycling loading period. Furthermore, Fig. 3.50 shows the crack patterns on the test specimen after the disassembly of the set-up components.

Figure 3.44: Crack patterns at 225kN (60% of $F_{u,exp}$) / CC-01.

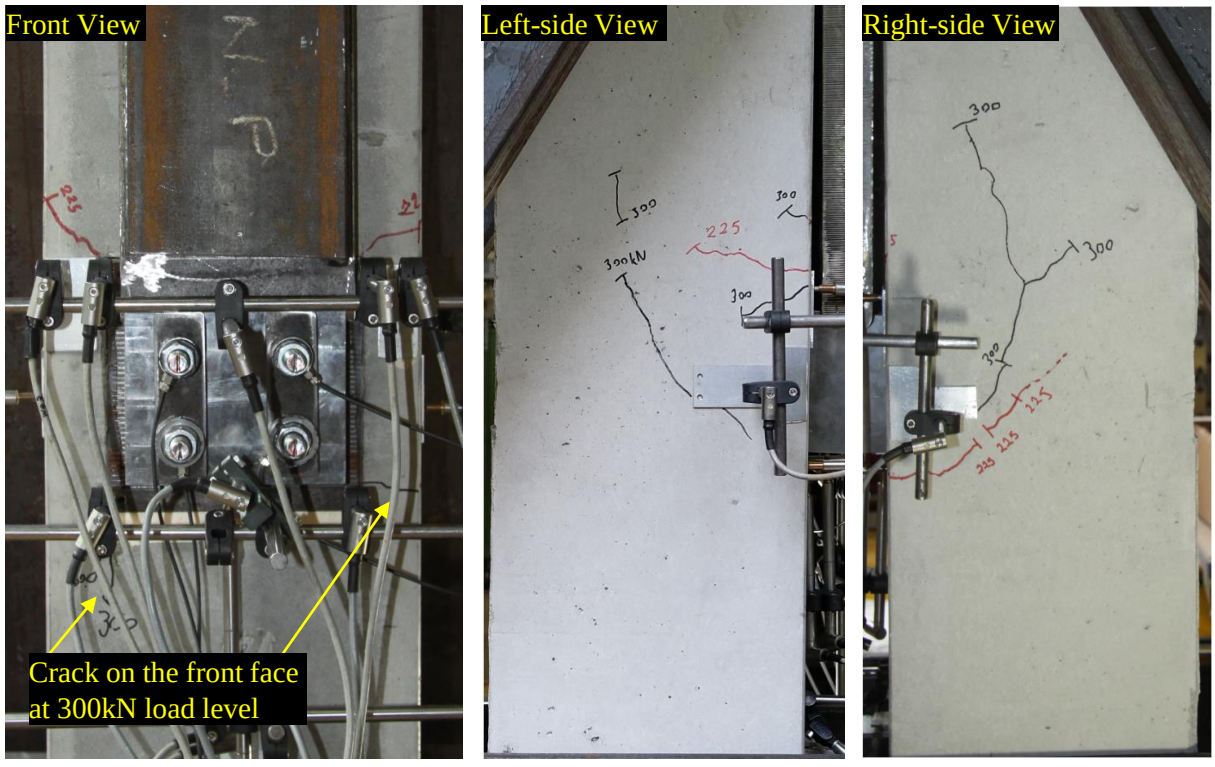

Figure 3.45: Crack patterns at 300kN (80% of $F_{u,exp}$) / CC-01.

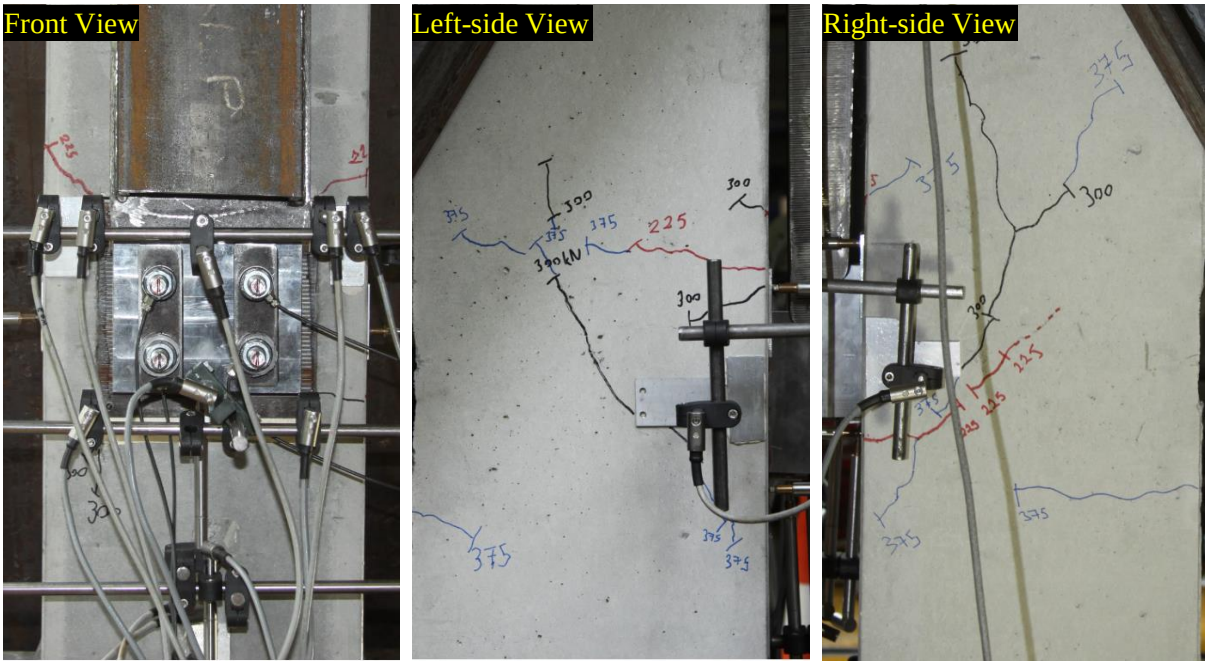

Figure 3.46: Crack patterns at 375kN (100% of $F_{u,exp}$) / CC-01.

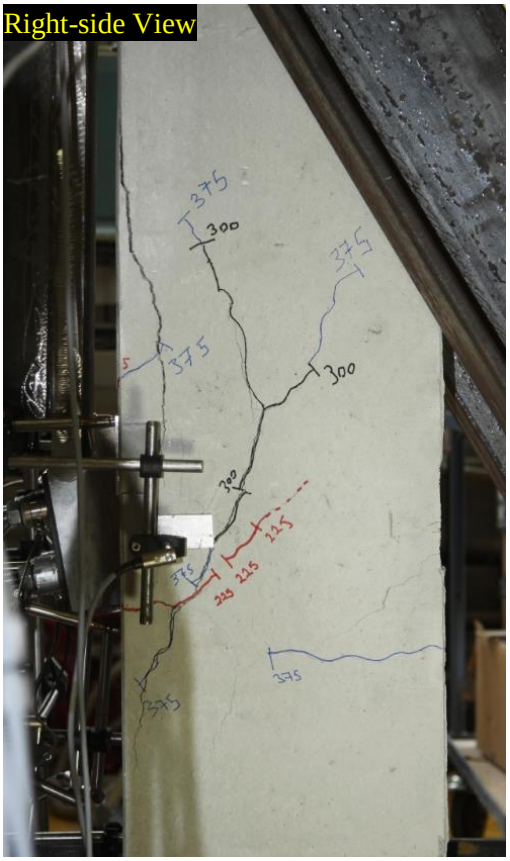

Figure 3.47: Crack patterns at $F_{u,CC\text{-}01}$=*435kN* / CC-01 (due to the safety concerns only the image of the right side view is available).

Dashed black lines indicate cracks identified after the test.

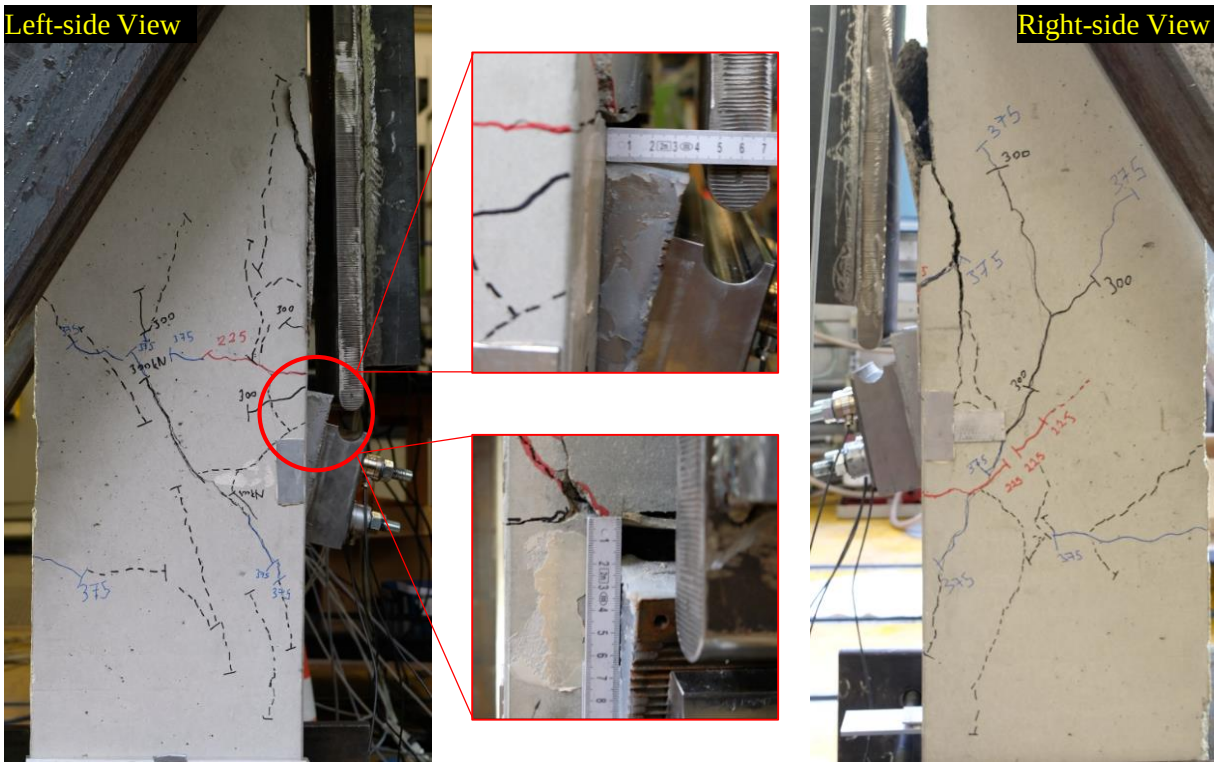

Figure 3.48: Crack patterns at the maximum displacement level / CC-01.

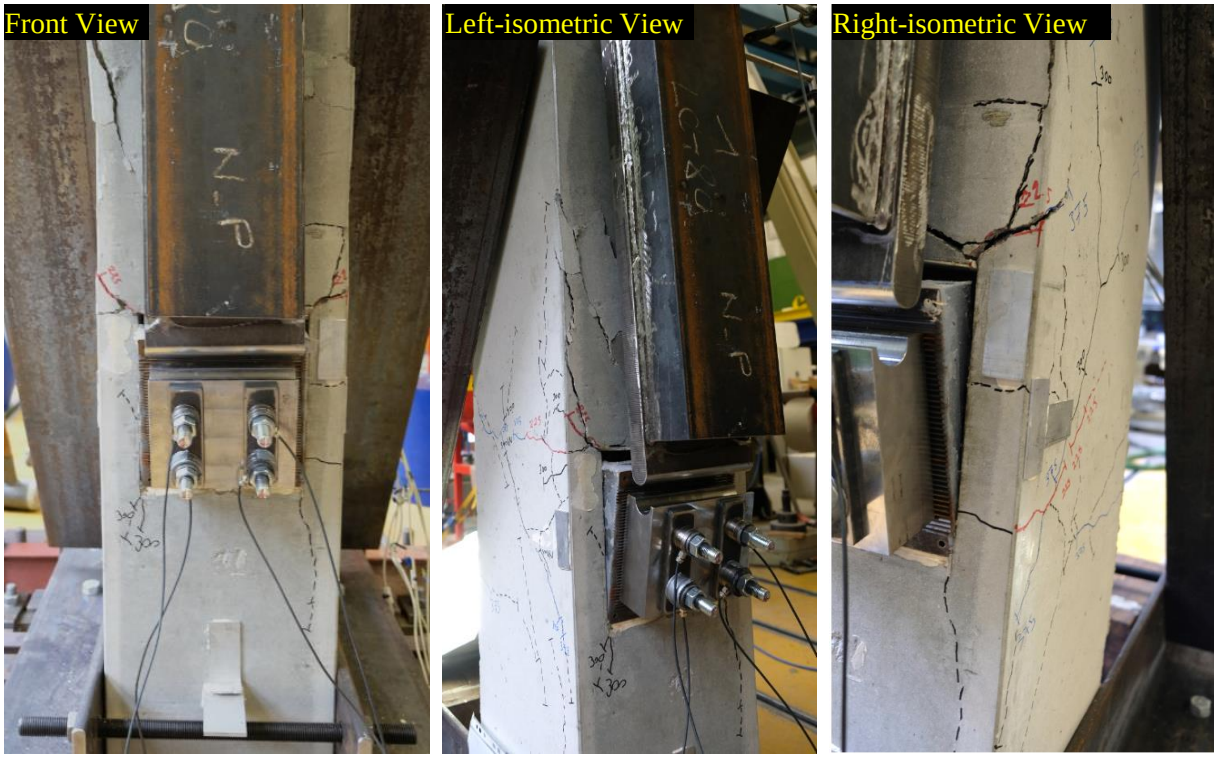

Figure 3.49: Crack patterns at the maximum displacement level - Iso views / CC-01.

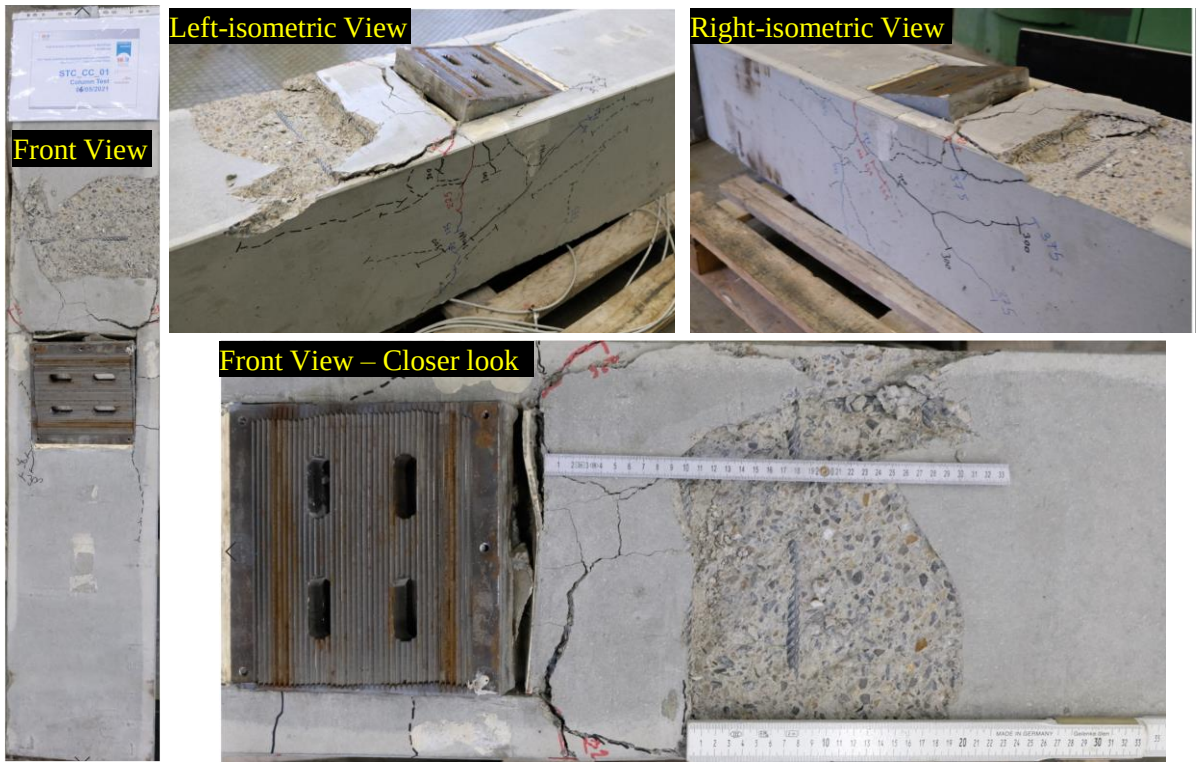

Figure 3.50: Crack patterns after the disassembly of the set-up components / CC-01.

As it could be identified from Fig. 3.44 to Fig. 3.48, the crack patterns along the side views of the column started to grow about 225kN vertical load-level. The propagation of the cracks recorded at the side views could be attributed to the interaction of concrete-cone and pry-out failure modes.

To have better visualization against the interaction between the concrete-cone and pry-out failure modes, Fig. 3.51 highlights the crack patterns along the side-views of the column with respect to the corresponding loading steps. The development of the concrete-cone and pry-out failure modes could be recognized in these figures. However, it is not possible to identify which failure mode initiated first.

Therefore, the stress resultants on the steel reinforcements positioned next to the anchor plate were investigated in Fig. 3.52 to clarify the load-bearing mechanisms of the reinforced-concrete components of the anchorage of CC-01 test specimen. The resultant forces were calculated according to well known Hooke's law as formulated in Eq. 3.32 based on the recorded strains, the mean elastic modulus (see Table 3.22) and the nominal cross-section area (*Ø=10mm*) of the steel reinforcements. The unloading period was excluded from the figure to have clear visualization. The strain gauges nominated as SG-3 and SG-4 were damaged around 10 to 12mm vertical anchor plate displacement (δ_y=10mm-12mm) after attaining the ultimate test load; thus, they were also excluded from the figure after their damage instants.

a) Right Side Views

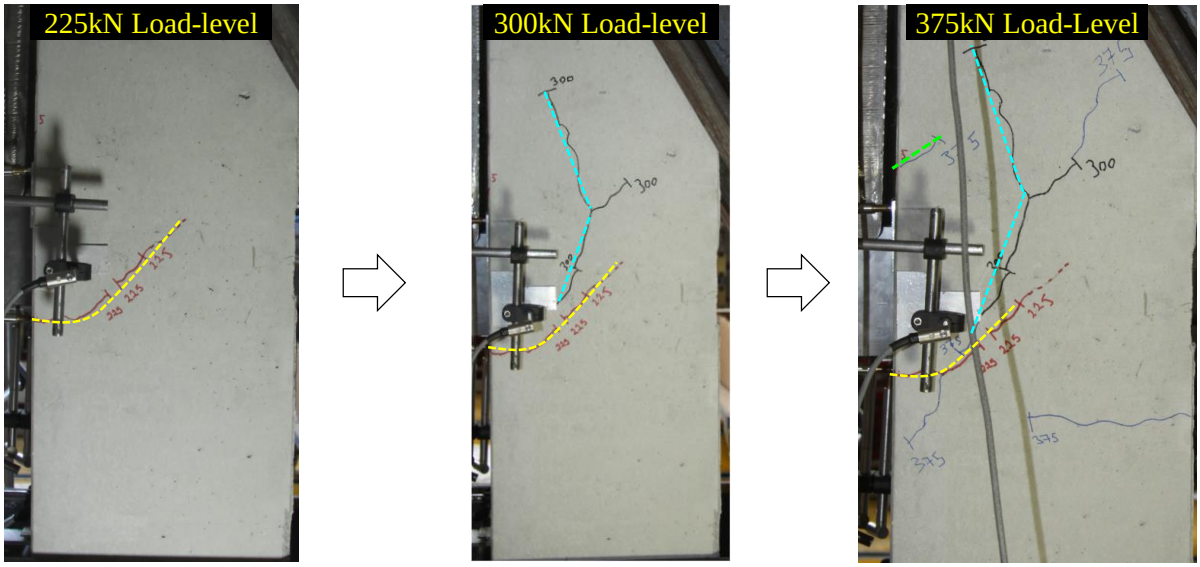

b) Left Side Views

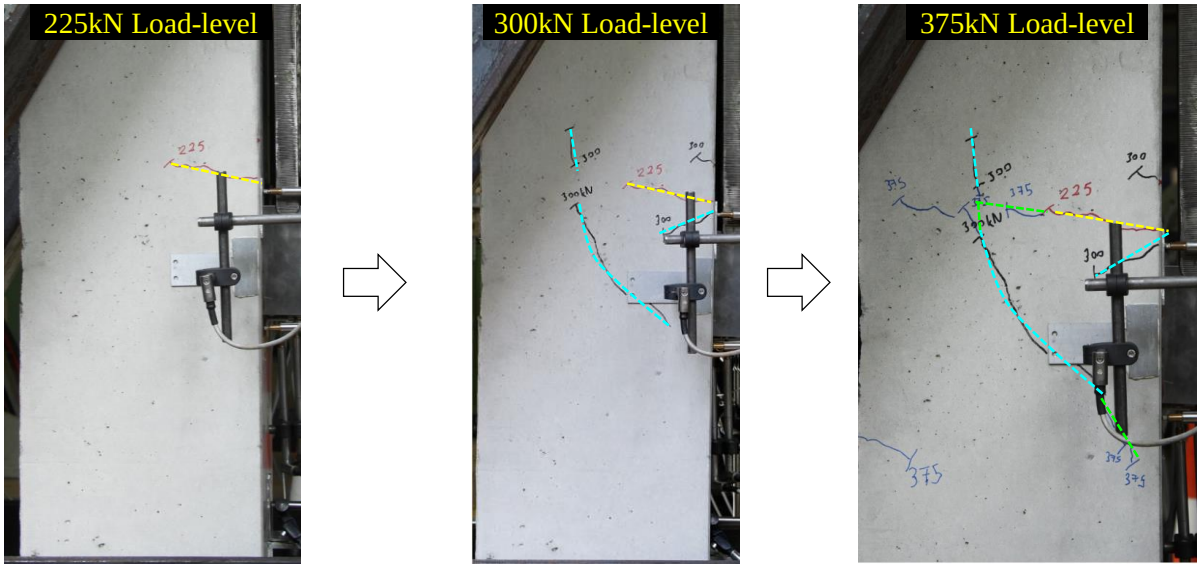

Figure 3.51: Development of concrete-cone and pry-out failure modes / CC-01.

According to Fig. 3.52, the steel reinforcements positioned in the theoretical cone-shaped concrete break-out body (Pos.1 and Pos.2) started to be loaded at 180kN vertical load-level. Thus, this load-level is accepted to correspond the initiation of a cone-shaped concrete breakout. However, at 225kN load-level (60% of the expected capacity – see Fig.3.44) the cone-shaped breakout body was not visible at the side-views of the column. Because by the initiation of the concrete-cone failure, the steel reinforcements (Pos.1 and Pos.2) started to resist the tension stress resultants in the cone-shaped breakout body and the cracks did not propagate up to the side surfaces. Accordingly, it could be stated that the crack pattern highlighted in Fig.3.51 was developed after the initial

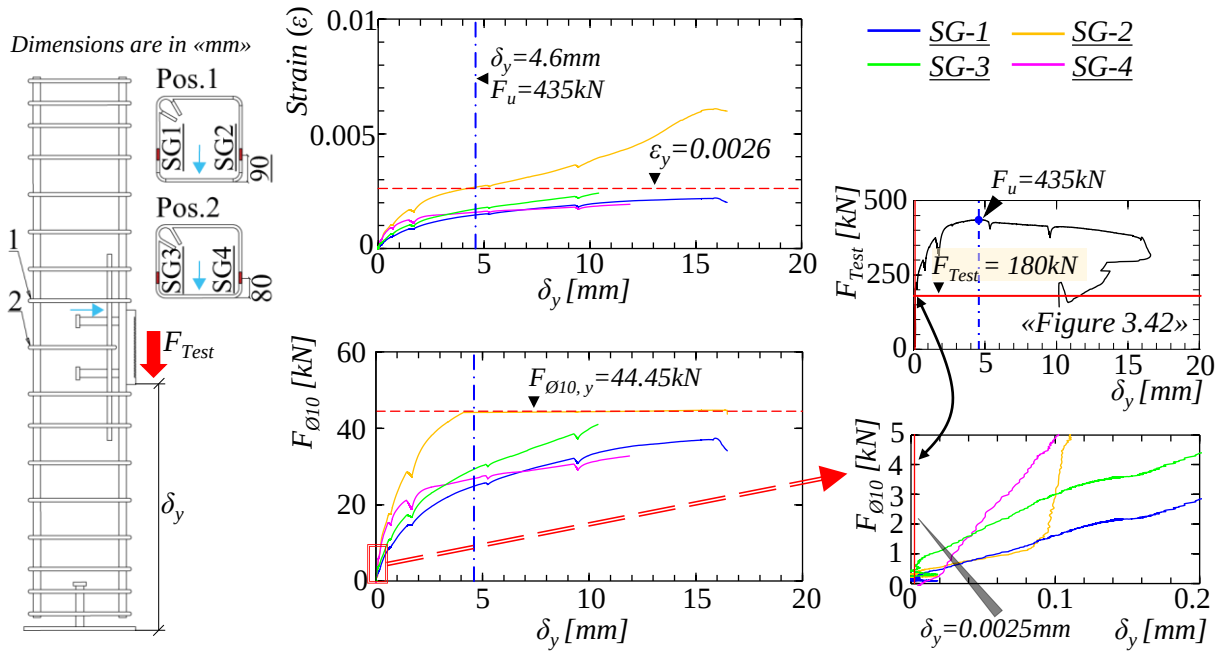

Figure 3.52: Strains and corresponding stress resultants on the reinforcements / CC-01.

formation of the cone-shaped breakout out body and this indicates that the pry-out failure mode developed after the initiation of the concrete-cone failure mode.

$$F_{Ø10} = \begin{cases} \frac{E_{mean} \cdot \varepsilon \cdot (Ø)^2 \cdot \pi}{4} & \varepsilon \leq \varepsilon_y \\ \frac{E_{mean} \cdot \varepsilon_y \cdot (Ø)^2 \cdot \pi}{4} + \frac{\frac{E_{mean}}{100} \cdot (\varepsilon - \varepsilon_y) \cdot (Ø)^2 \cdot \pi}{4} & \varepsilon > \varepsilon_y \end{cases} \tag{3.32}$$

Furthermore, considering the crack patterns shown in Fig. 3.45, it could be concluded that the pry-out concrete breakout body was mostly developed. However, it was still possible to increase the loading as the straight reinforcement bars (see Fig.3.34a - Pos.3) positioned behind the anchor plate were in the theoretical pry-out concrete breakout body and they resisted the applied loading against the pry-out failure mode. The contribution of the straight reinforcement bars against the applied loading later investigated in Section 3.3.8 with numerical simulation of the experimental test.

At the ultimate test load ($F_{u,CC\text{-}01}$=435kN), only the left leg of the steel reinforcement nominated as Pos.1 was yielded. In addition, there was no visible anchorage failure of the steel reinforcement based on the visual inspection presented through Figs. 3.44-3.50. Therefore, the test specimen was cut to clarify the main failure mechanism of the anchorage.

Fig. 3.53 shows a section cut of the column together with the right-side column view presented in Fig. 3.47. As highlighted in Fig. 3.53, a secondary cone-shaped concrete breakout body could be noticed. On the other hand, the secondary breakout body was not visible during the visual inspection at 375kN load-level (see Fig. 3.51). This is mainly due to the fact that the secondary

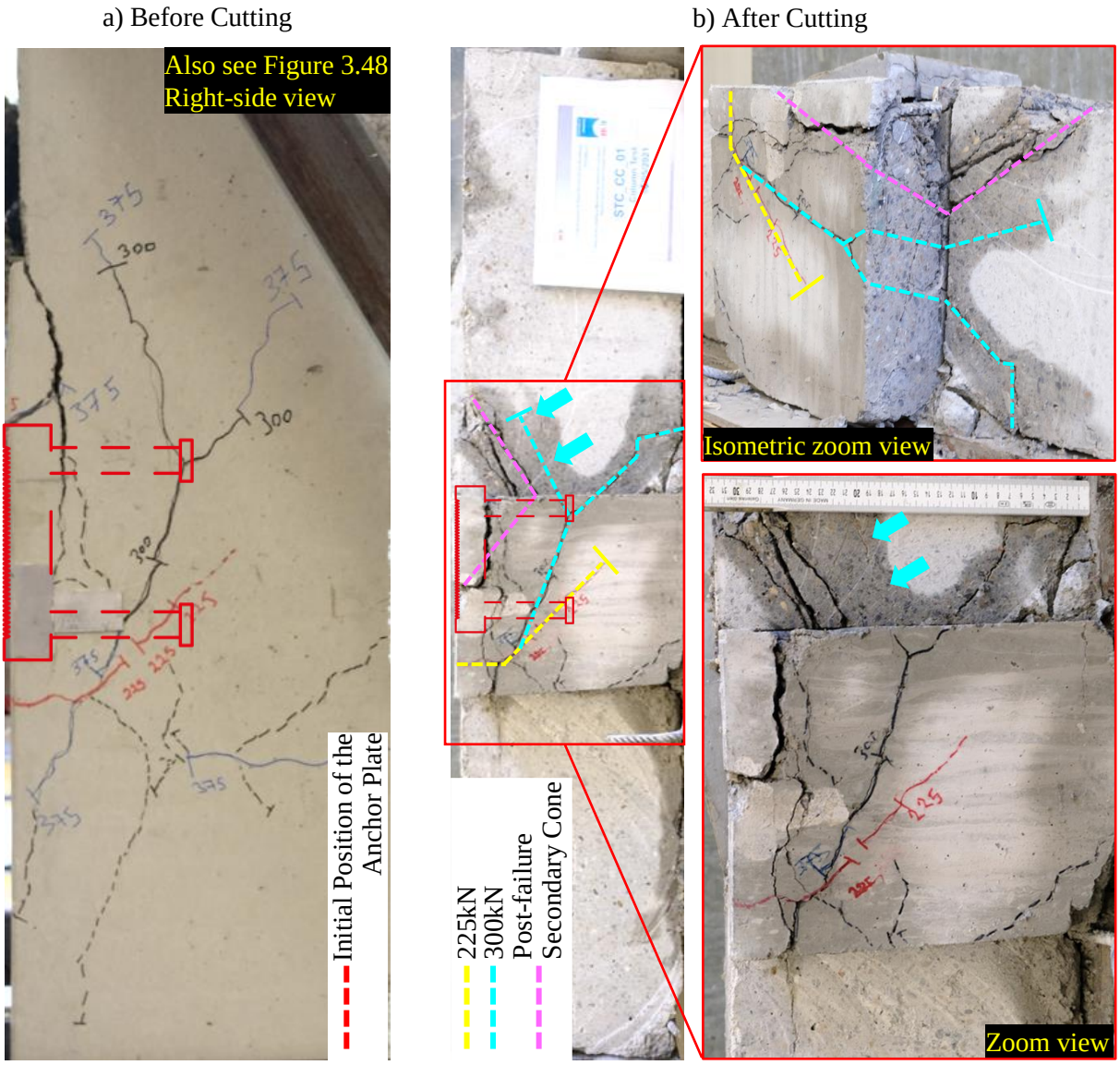

Figure 3.53: Section cut of the test specimen / CC-01.

cone shaped breakout body was formed after the development of the pull-out failure of the upper row of the headed studs at 420kN load-level. Furthermore, from Fig. 3.53b it could be observed that the initial cone-shaped breakout-body did not fully form. Therefore, the limiting value for the ultimate load-bearing capacity of the anchorage ($F_{u,CC\text{-}01}$=*435kN*) could be attributed to neither the concrete-cone nor the pry-out failure modes.

For further clarification of the pull-out failure mode, the horizontal displacements of the column surface and the anchor plate at the height that corresponds to the upper edge of the anchor plate is investigated in Fig. 3.54. It could be noticed that at 345kN load-level, which corresponds to initial load-drop at δ_y=*1.03mm* (see Fig. 3.42), the relative *x-axis* displacements between the anchor plate and the concrete surface started to increase as a result of the pull-out failure initiation. Thereafter, at

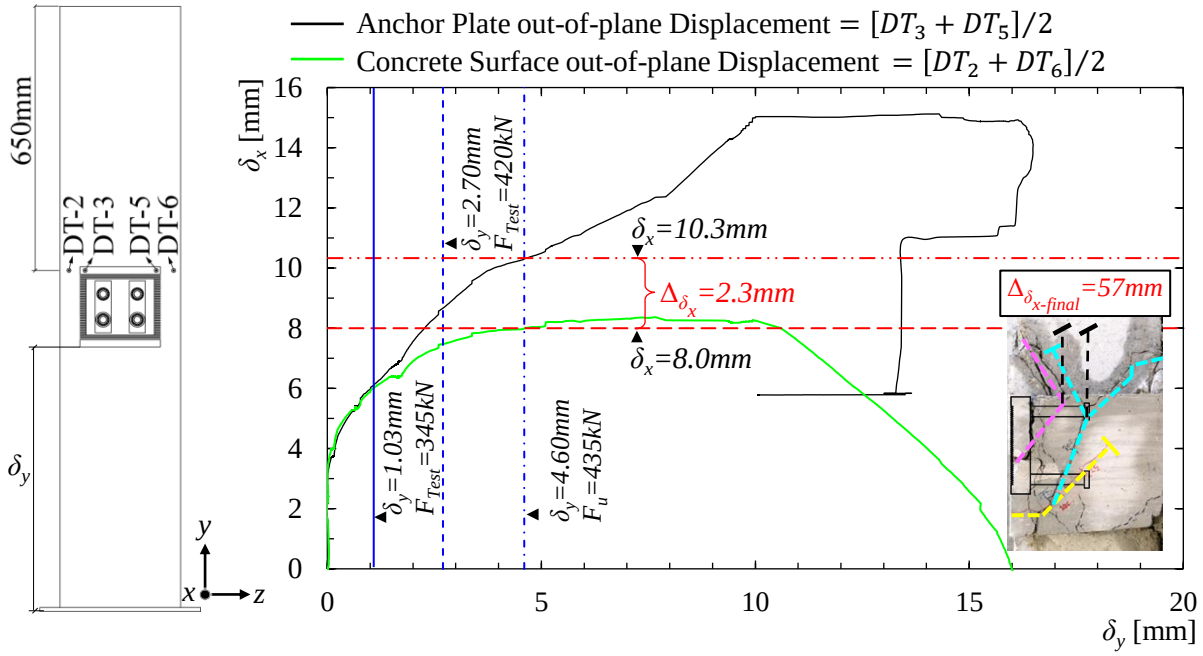

Figure 3.54: Investigation of the pull-out failure / CC-01.

420kN load-level, which corresponds to the second load-drop at δ_y=*2.70mm*, the rate of the relative displacements significantly increased and at the ultimate test load ($F_{u,CC\text{-}01}$=*435kN* at δ_y=*4.6mm*) the anchor plate started to freely displace along the *x-axis* direction as no further displacement on the concrete surface was recorded.

Without the investigation of the section cut and the relative horizontal displacements between the anchor plate and column surface, it could have been stated that the failure of the anchorage was due to the pry-out failure as highlighted in Fig. 3.51. However, the principle reason behind the failure of the anchorage was identified as the pull-out failure. Therefore, it could be stated that the secondary cone-shaped breakout body (see Fig. 3.53) developed during the post failure stage of the anchorage.

As earlier indicated, the headed-fasteners were designed to have larger load-bearing capacity than the reinforced-concrete components of the anchorage. Therefore, as expected, no failure was observed in the headed-fasteners. On the other hand, the lower row of the headed-fasteners under the applied loading. Fig. 3.55 shows the deformed state of the anchor plate after the test together with the strains and corresponding stress resultants at the upper row of the headed-fasteners. The resultant forces were calculated according to Hooke's law based on the recorded strains, the nominal elastic modulus of the headed-fasteners [81] and their nominal cross-section area (*Ø=22mm*) as formulated in Eq. 3.33.

As highlighted in Fig. 3.55, SG-5 was damaged around δ_y=*2.2mm* and SG-6 started to record noncontinuous data after the yielding of the fastener and it was damaged around δ_y=*3.8mm*. Therefore, the data recorded after the damage of the strain-gauges is not shown in Fig. 3.55.

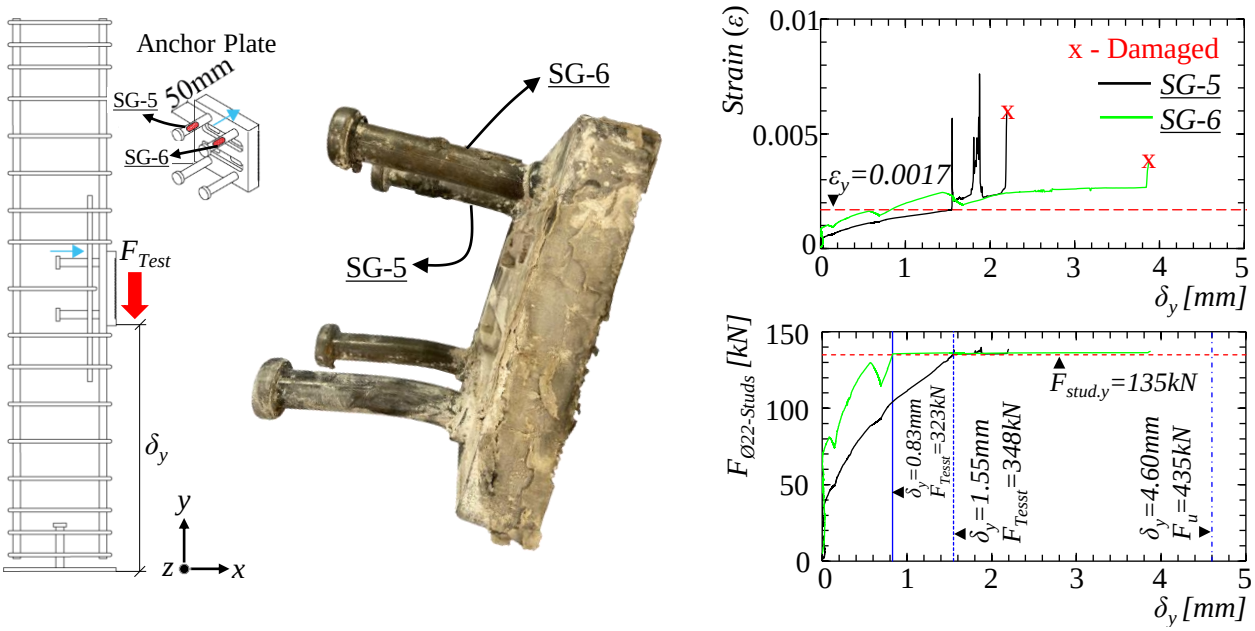

Figure 3.55: Stains and corresponding stress resultants on the upper headed-fasteners / CC-01.

Both of the upper headed-fasteners yielded before the initial load drop at F_{Test}=345kN and they were also slightly bent due to the applied loading. No strain data were recorded from the lower row of the headed-fasteners. However, based on the deformations their yielding is obvious. Due to the large deformation of the lower row of the headed-fasteners it could be stated that the applied vertical load initially resisted by the lower headed-fasteners and by their yielding the upper row of the headed fasteners also subjected to shear force.

$$F_{Ø22-fasteners} = \begin{cases} \frac{E \cdot \varepsilon \cdot 22^2 \cdot \pi}{4} & \varepsilon \leq \varepsilon_y \\ \frac{E \cdot \varepsilon_y \cdot 22^2 \cdot \pi}{4} + \frac{\frac{E}{100} \cdot (\varepsilon - \varepsilon_y) \cdot 22^2 \cdot \pi}{4} & \varepsilon > \varepsilon_y \end{cases} \tag{3.33}$$

As expected, there was no visible deformation along the saw-tooth interface and the T-head bolts at the end of the test. Fig. 3.56 shows the after test conditions of the saw-tooth surfaces of the anchor and the corbel plates. In addition, after test conditions of the T-head bolts and the variation of the tension forces in the bolts are presented in Fig. 3.57. Based on the analytical resistance model presented in Section 3.2.4, the ultimate load-bearing capacity of SMIBC is estimated as $R_{u,SMIBC(e=32mm)}$=774kN for the selected load-eccentricity. Therefore, it is concluded that the analytical resistance model of SMIBC is successful for the estimation of the resistance of SMIBC as no deformation was observed for the load-bearing components of SMIBC, which are the saw-tooth interface and T-head bolts, at the end of the experimental test. Furthermore, according to Fig. 3.57, it is clear that the tension force in the upper row of the T-head bolts was far less than their elastic load-bearing capacity, which was calculated based on the nominal stress area of the bolts (Ø=16mm)

and the characteristic yield strength of the selected bolt material grade (8.8 [25]). The increase of the tension force in the upper row of the M16-bolts after the ultimate load-bearing capacity of the anchorage is attributed to the rotation of SMIBC as it triggered the applied load to be further decomposed along the *x-axis* direction as shown in Fig. 3.57b.

a) Anchor Plate Saw-tooth Surface

b) Corbel Plate Saw-tooth Surface

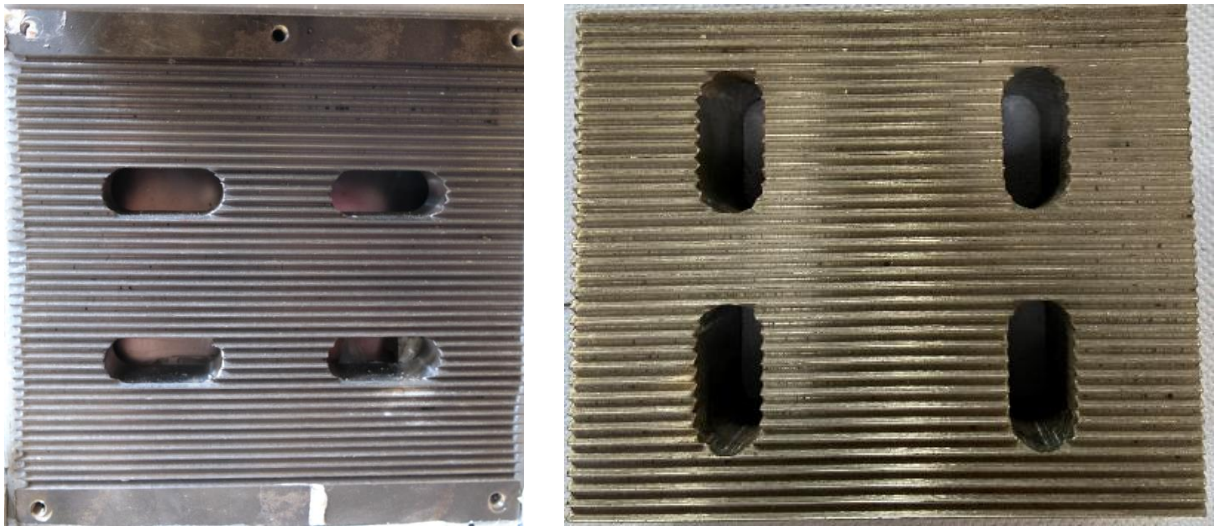

Figure 3.56: After test conditions of the saw-tooth surfaces / CC-01.

a) T-head Bolts and Their Positions

b) Variation of Tension Forces in the Bolts

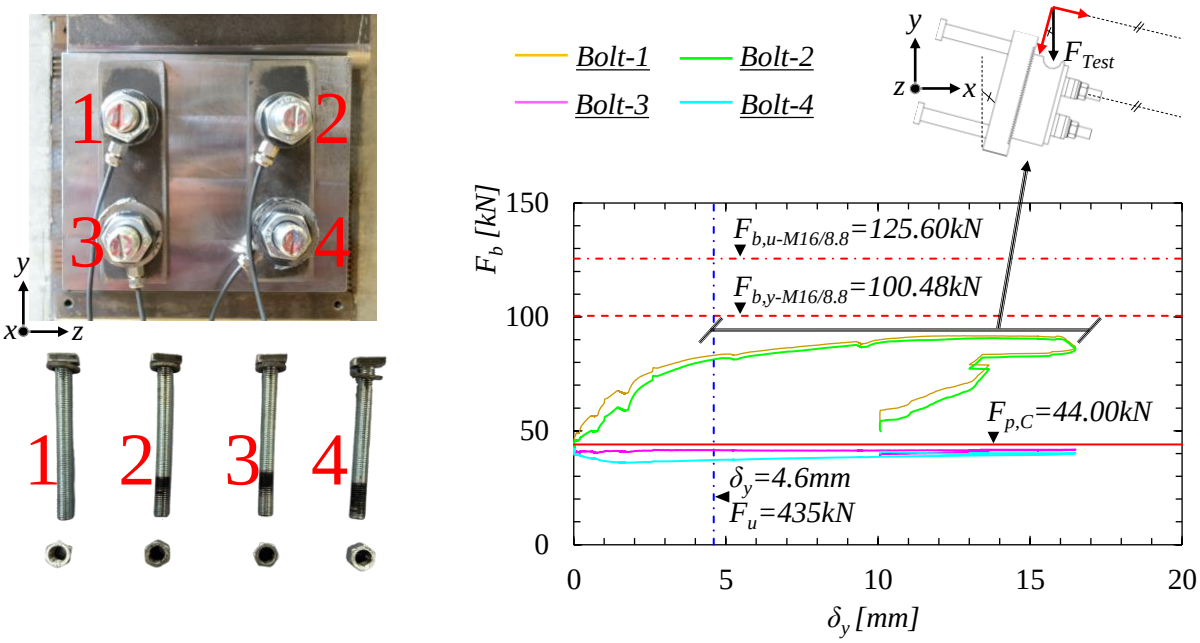

Figure 3.57: After test conditions of the T-head bolts and tension forces on the bolts / CC-01.

Finally, Table 3.25 summarizes the recorded test loads, i.e. F_{Test}, and the vertical anchor plate displacements, i.e. δ_y, successively together with the corresponding individual failure modes identified for the anchorage of CC-01 test specimen.

Table 3.25: Summary of the identified failure modes for the anchorage of CC-01 test specimen.

Position	Failure Modes	F_{Test} [kN]	δ_y [mm]	Identifications
Column	Concrete Cone	180	0.0025	Initiation
Column	Concrete Pry-out	225	0.083	Initiation
UL Headed Stud	Yielding[1]	323	0.83	Fully Developed
Column	Pull-out	345	1.03	Initiation
UR Headed Stud	Yielding[1]	348	1.55	Fully Developed
Column	Pull-out	420	2.70	Partially Developed
Column	Pull-out	435	4.60	Fully Developed
Reinforcement Pos.2	Yielding	435	4.60	Fully Developed

UL:Upper Left, UR:Upper Right.

[1] The yield strength of the headed-fasteners against tensile loading was calculated based on the characteristic material properties given in the product catalog [81]. Thus, they may not reflect the actual yield instant of the fasteners as it was possible to increase the loading after the yielding of both of the upper row of the headed-fasteners.

3.3.6.2 Test results and discussions / CC-02

Fig. 3.58 shows the vertical displacements of the anchor plate with respect to the applied loading. Similar to the first test results, the load-displacement curve presented in Fig. 3.58 includes the global column displacements while they were excluded from Fig. 3.59 based on Eq. 3.30. The initial translational elastic and the secant stiffness values of the anchorage are also noted in Fig. 3.59. The expected ultimate load-bearing capacity of the anchorage in CC-02 test specimen was 500kN ($F_{u,exp}$=*500kN*). Therefore, the loading procedure and related loading steps were defined based on the expected capacity. However, the actual ultimate load-bearing capacity was 460kN ($F_{u.CC\text{-}02}$=*460kN*) to be 8% less than the expected capacity. The expected capacity was estimated based on the numerical simulation performed prior to the experimental test with mean and characteristic material properties where appropriate, and using perfect column geometry. Consequently, this difference could be attributed to the actual material properties and the imperfections imposed during the manufacturing and the assembly of the test specimens.

Comparing Fig. 3.58 and Fig. 3.59, it could be stated that the assembly gaps of the test frame closed during the initial loading step (Up to 40% - $F_{u,exp}$) and the cycling loading period. Therefore, from here on, the load-displacement behavior presented in Fig. 3.59 is used for further investigations of the test results.

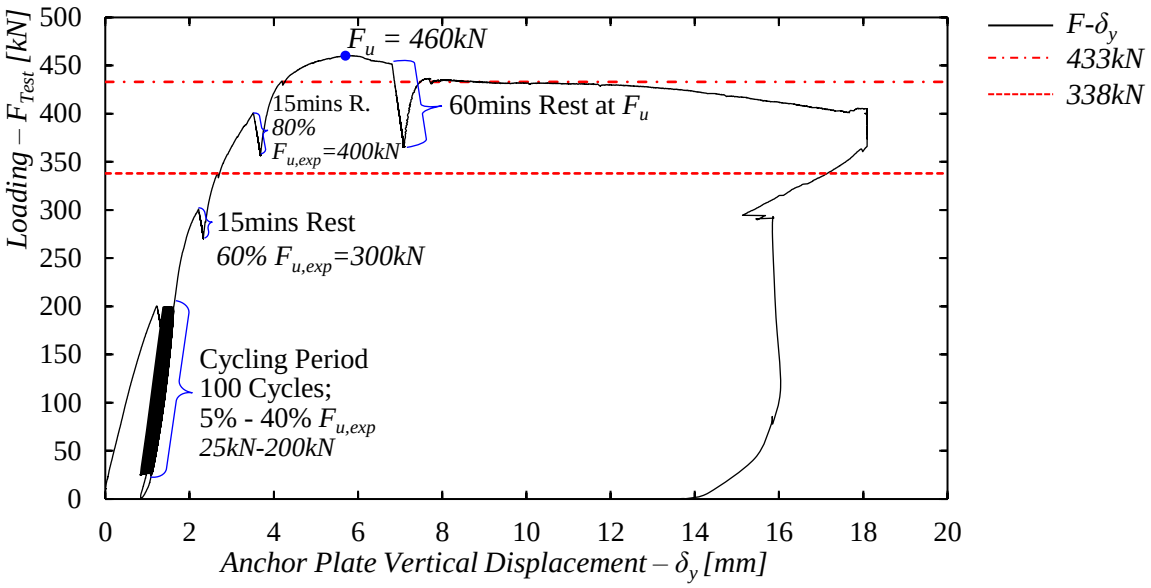

Figure 3.58: Anchor plate load-displacement behavior with the global column behavior / CC-02.

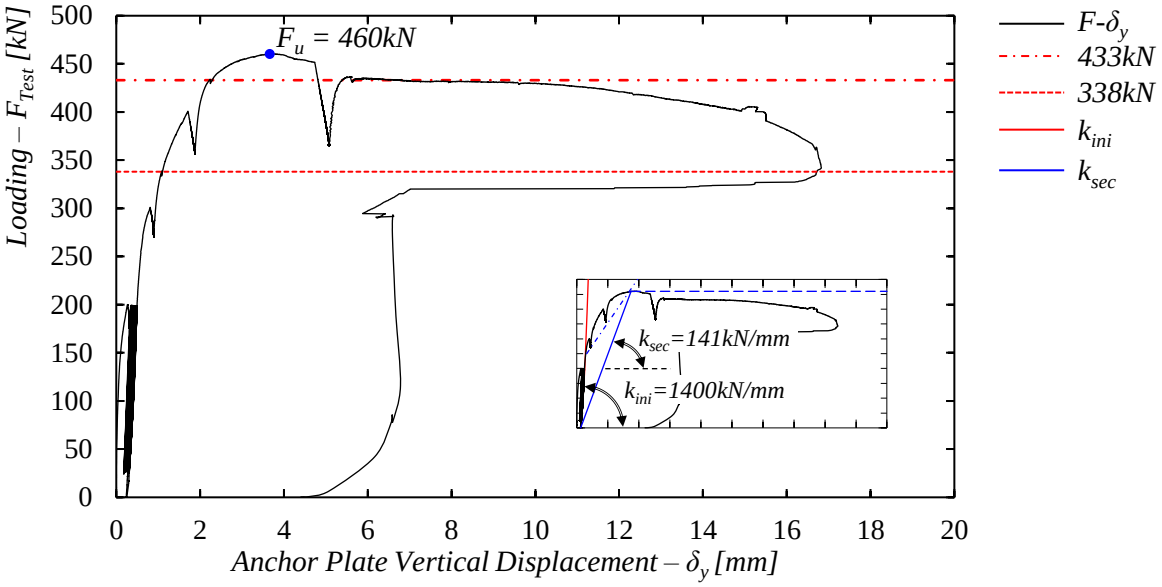

Figure 3.59: Anchor plate load-displacement behavior without the global column behavior / CC-02.

During the unloading period, the displacement transducer that measures the global vertical column displacements (DT-13 see Fig. 3.38) was stuck at the largest measurement range (10mm see Table. 3.24). Therefore, the recovery of the anchor plate vertical displacements during the unloading period that could be noticed in Fig. 3.59 does not represent the real behavior of the anchorage.

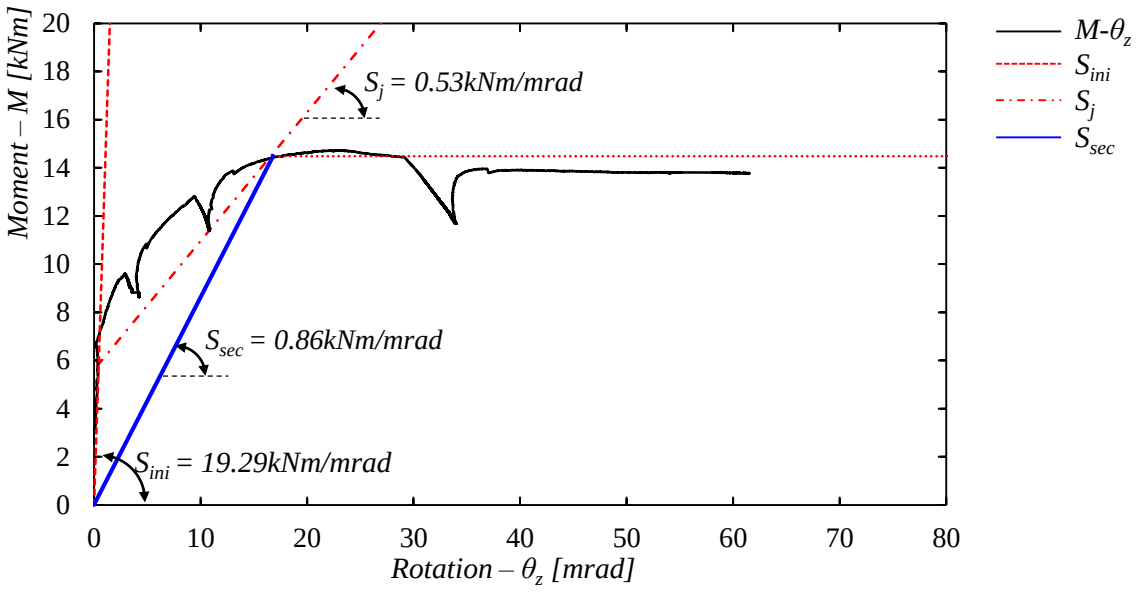

Figure 3.60: Moment-rotation behavior of the anchor plate / CC-02.

According to Fig. 3.59, the ultimate load-bearing capacity of CC-02 test specimen ($F_{u,CC-02}$) was 460kN. On the other hand, at 338kN and 433kN load-levels there were relatively small but sudden load-drops as similar to the first test results. These drops might indicate damage initiation in the anchorage. The reason behind these load-drops are later investigated in detail in this section.

Fig. 3.60 shows the moment-rotation behavior of the anchor plate. The cycling loading period and the unloading period are excluded from the figure for clear visualization of the moment-rotation behavior as the displacement transducers that measures the global column displacements (see Fig. 3.38 DT-13 and DT-14) were stuck during the unloading period. As identical to the first test, the moment values were calculated by the multiplication of the applied loading with the pre-defined load eccentricity (e=32mm) and the rotation values were calculated with Eq. 3.31.

As illustrated in Fig. 3.34b, CC-02 test specimen was detailed with supplementary steel reinforcements according to EN1992-4 [1]. Therefore, the crack patterns were developed at higher load-levels compared to CC-01 test specimen which was detailed without supplementary steel reinforcement around the anchor plate.

Fig. 3.61 to Fig. 3.64 show the crack propagation on the test specimen with respect to the loading steps of the test procedure. During the cycling loading period and at 300kN load-level (60% of the expected capacity - $F_{u,exp}$) no surface crack was observed; thus, these loading steps are not shown in the following figures. Furthermore, Fig. 3.65 shows the crack patterns on CC-02 test specimen after the disassembly of the set-up components.

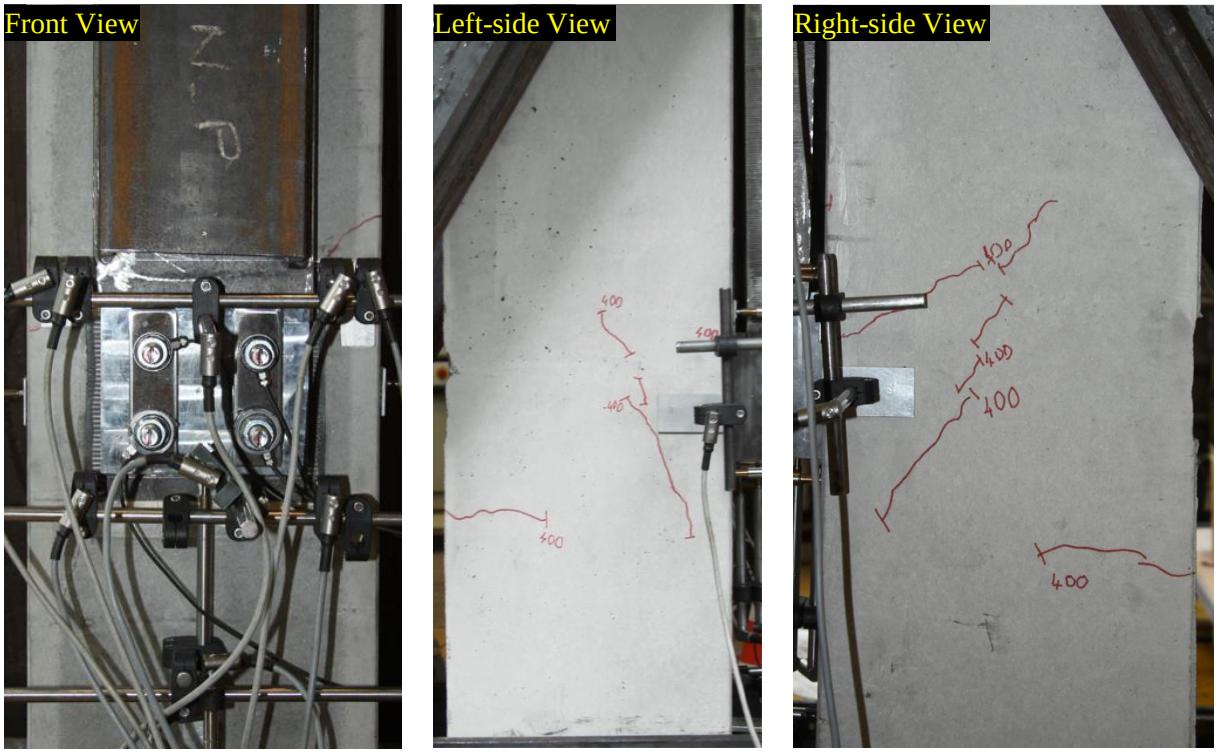

Figure 3.61: Crack patterns at 400kN (80% of $F_{u,exp}$) / CC-02.

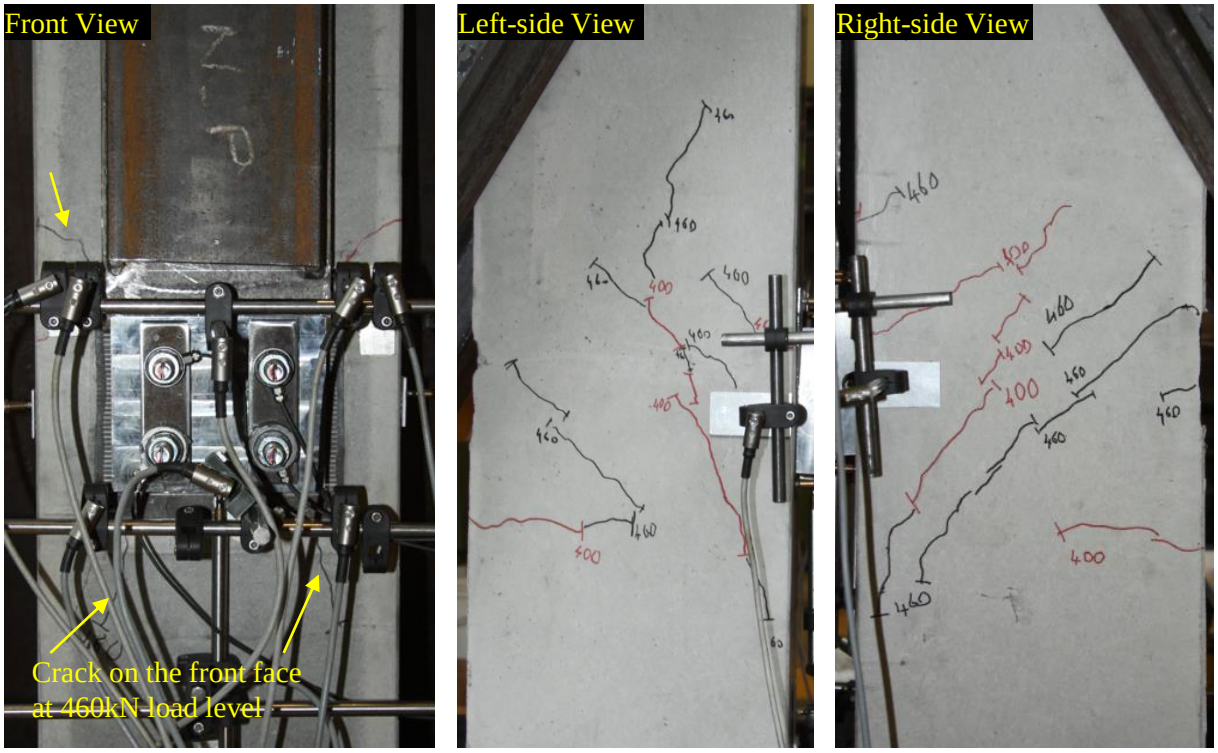

Figure 3.62: Crack patterns at 460kN (F_u) / CC-02.

Dashed blue lines are drawn after the test due to the safety concerns

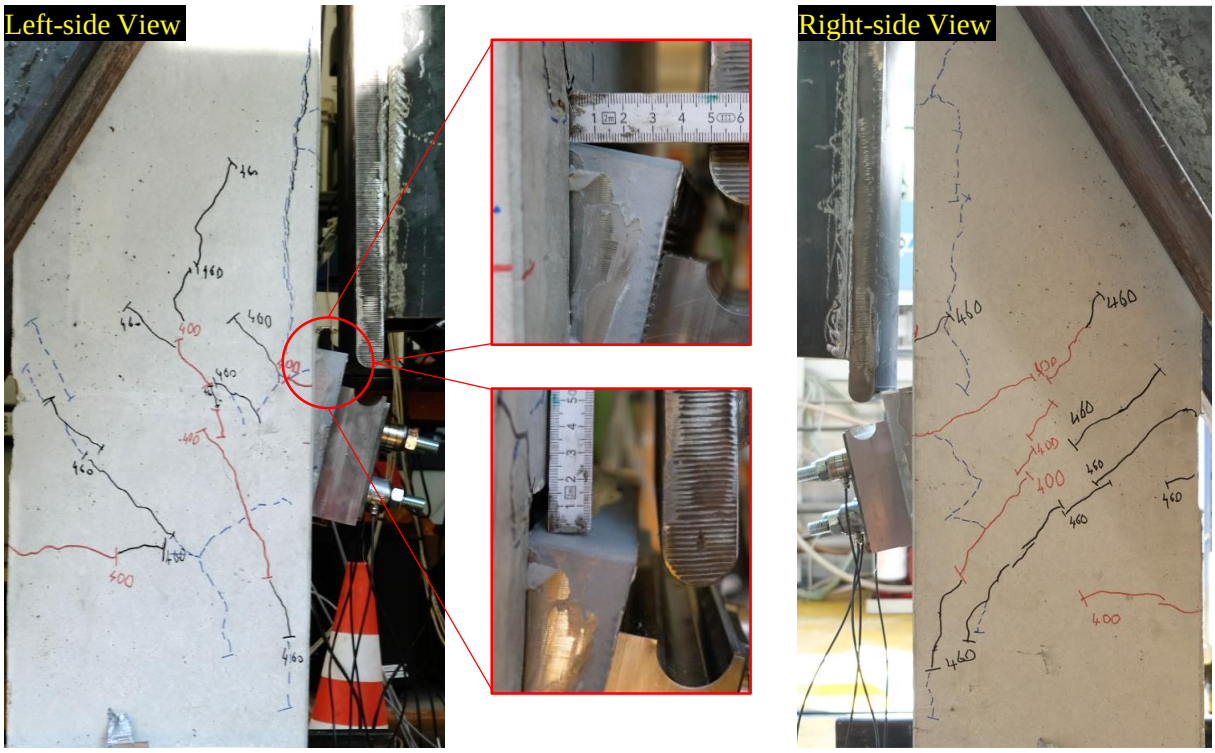

Figure 3.63: Crack patterns at the maximum displacement level / CC-02.

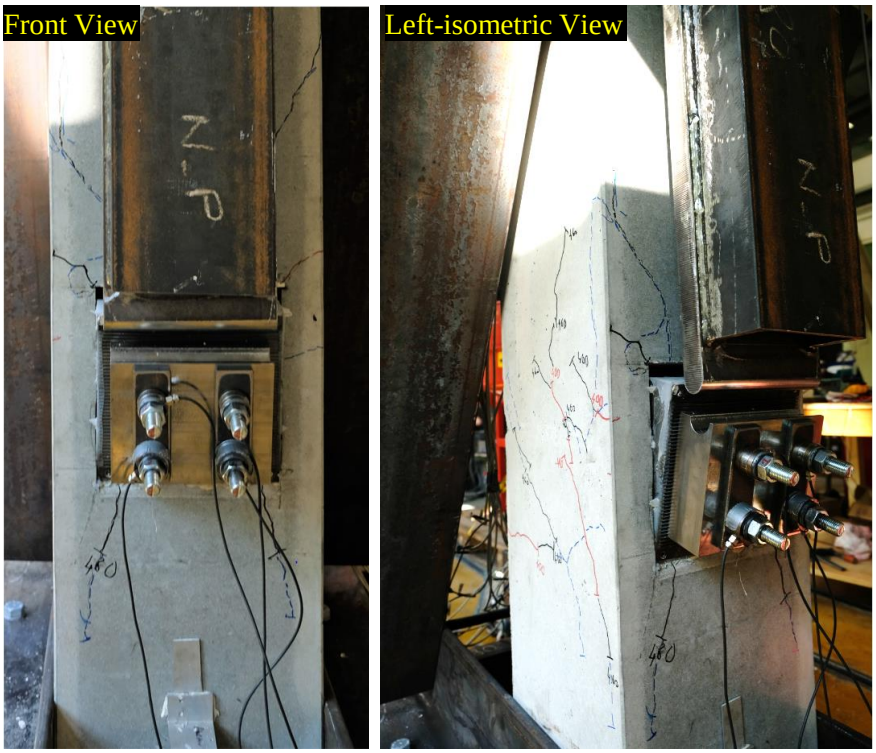

Figure 3.64: Crack patterns at the maximum displacement level - Additional views / CC-02.

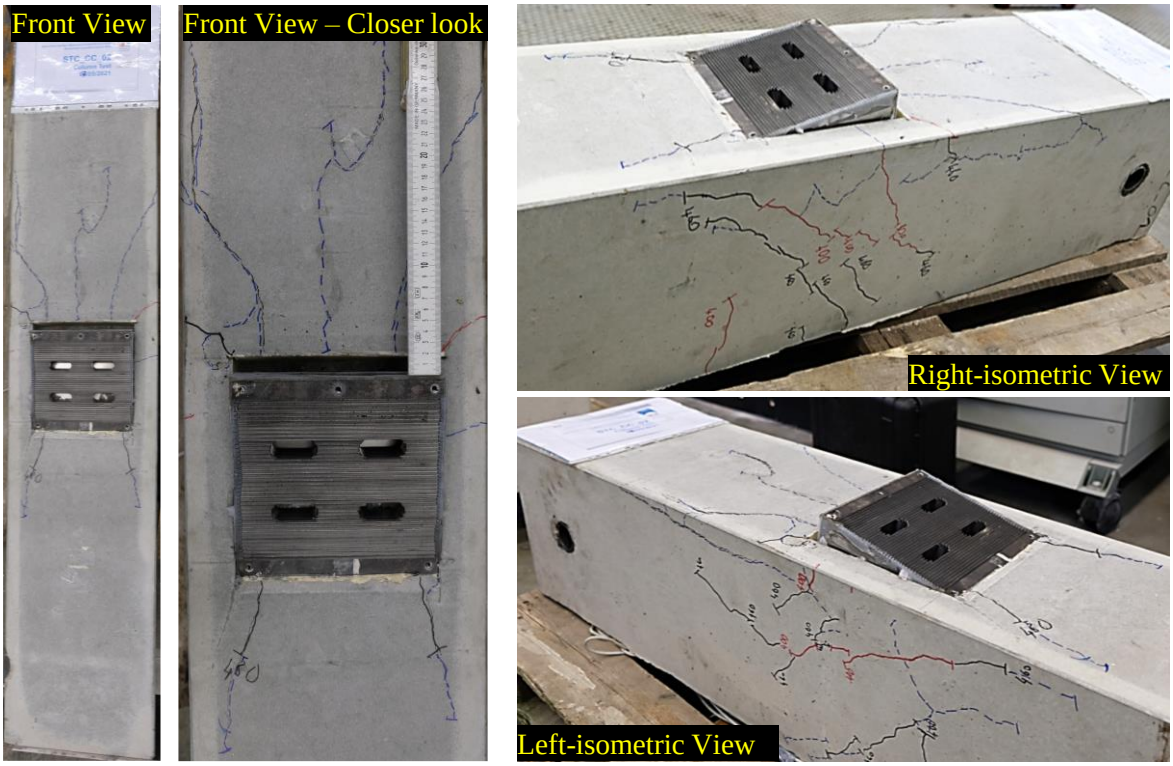

Figure 3.65: Crack patterns after the disassembly of the test set-up / CC-02.

According to the visual inspection presented from Fig. 3.61 to Fig. 3.65, it could be deduced that the crack patterns started to develop around 400kN vertical load-level. These crack patterns may be attributed to concrete-cone failure mode. Apart from the first column test (CC-01 see Fig. 3.51) the pry-out concrete cracks close to the bottom edge of the anchor plate were not observed for the second column test. This result could be linked to the existence of the supplementary steel reinforcements positioned under the headed-fasteners to resist the vertical shear stress resultants (Pos.-5 and Pos.-6 in Fig. 3.34b). Fig. 3.66 highlights the crack patterns along the side-views of the column with respect to the corresponding loading steps to focus the development of the cone-shaped concrete breakout body. Although severe concrete crack patterns could be noticed at the ultimate load limit of the anchorage ($F_{u,CC\text{-}02}$=*460kN*), the cone-shaped break-out body did not fully develop. Thus, the failure mechanism of the anchorage could not be directly attributed to the concrete-cone failure mode. Accordingly, it is concluded that the supplementary steel reinforcements positioned next to the anchor plate (see Fig. 3.34b) provided additional resistance against both the concrete cone and concrete pry-out failure modes.

To investigate the contribution of the supplementary reinforcements for the load-bearing mechanism of the anchorage, the resultant forces on these reinforcements are investigated in Fig. 3.67. The resultant forces were calculated according to Hooke's law as formulated in Eq. 3.32 based on the recorded strains, the mean elastic modulus (see Table 3.22) and the nominal cross-section area (*Ø=10mm*) of the reinforcements. The strain gauges, SG-3 was damaged during the concrete casting,

a) Right Side Views

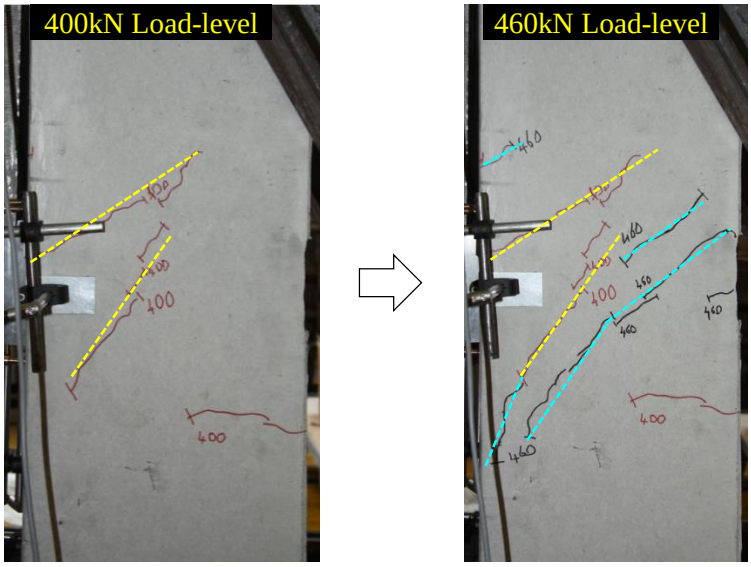

b) Left Side Views

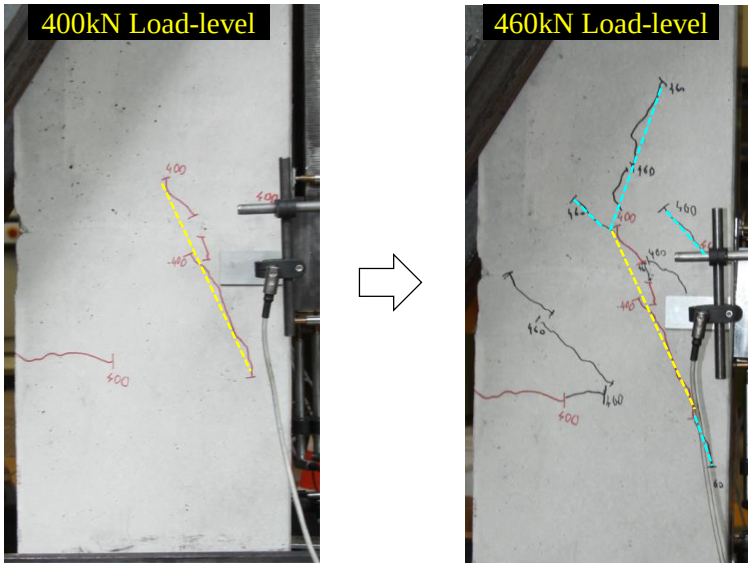

Figure 3.66: Development of cone-shaped concrete breakout body / CC-02.

and SG-5 was damaged around 9mm vertical displacement of the anchor plate (δ_y=9mm); thus, the data after the damage instant of the strain gauges are excluded from the figures. In addition, the unloading period is excluded from the figure for clear visualization.

It is crucial to note that Fig. 3.67 presents the resultant forces on the steel reinforcements only for one of the legs where the strain-gauge was attached. The total forces resisted by the corresponding reinforcements could be calculated by multiplying the given force values with a factor of two.

According to Fig. 3.67, the rate of the resultant forces on the supplementary shear reinforcements positioned under the headed-fasteners (Pos.-5 and Pos.-6) started to increase by about 250kN

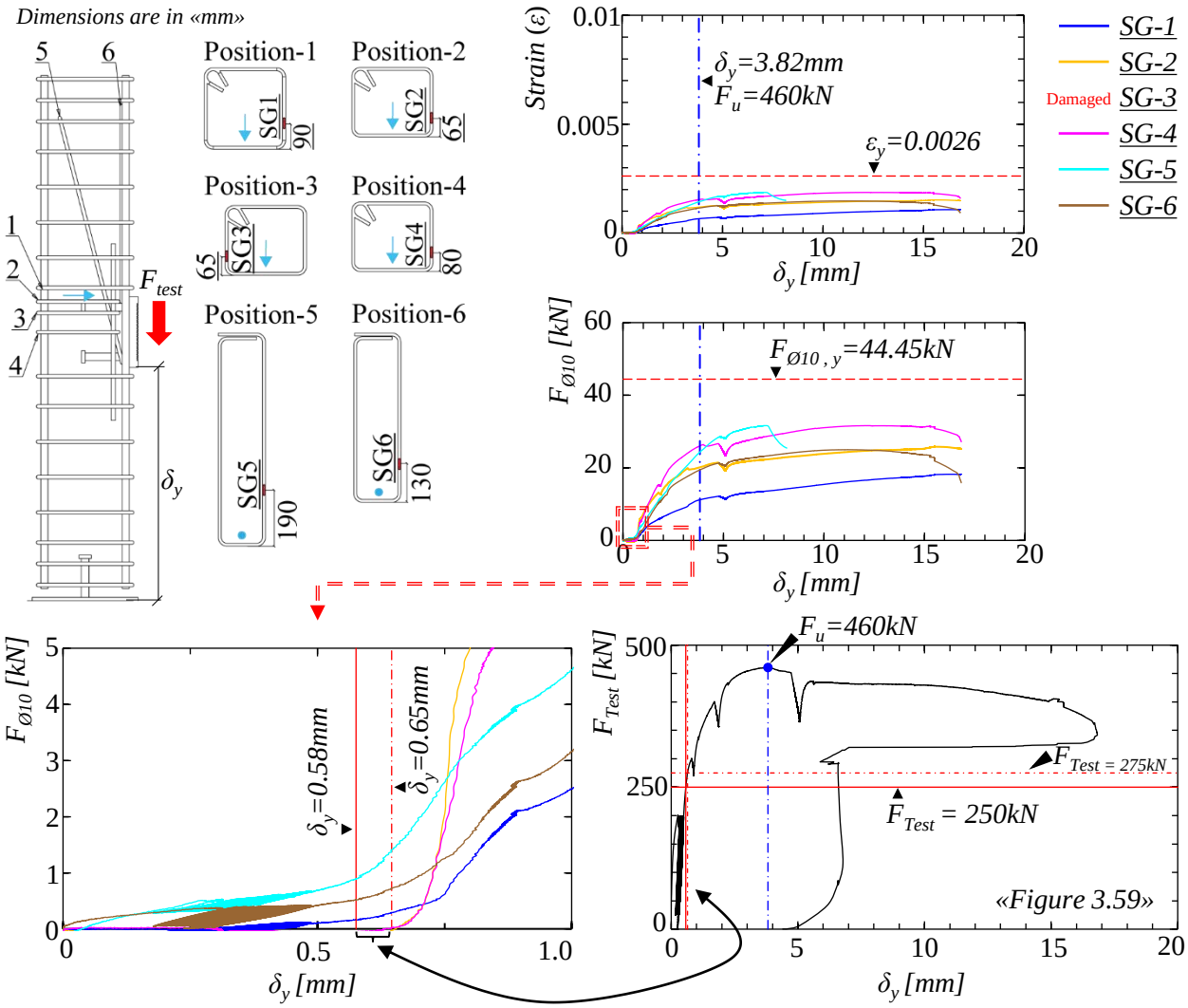

Figure 3.67: Strains and corresponding stress resultants on the reinforcements / CC-02.

vertical load-level. Thus, this load-level could be accepted to correspond the initiation of the pry-out failure mode, or more specifically it could be stated that the concrete volume under the headed-fasteners started to crush due to compression stress resultants transferred by the headed-fasteners to the concrete volume. On the contrary, even at 400kN load-level (80% of the expected capacity – see Figs. 3.61-3.66), the characteristic pry-out concrete cracks close to the bottom edge of the anchor plate were not visually detected; thus it could be stated that the supplementary shear reinforcements (Pos.-5 and Pos.-6) prevented the pry-out failure of the anchorage. However, EN1992-4 [1] does not consider the favorable contribution of the supplementary shear reinforcements against the pry-out failure mode. Therefore, the design calculations of the anchorages with headed-fasteners for RC-column configurations performed according to EN1992-4 [1] are highly conservative even the anchorages are detailed with supplementary shear reinforcements [24, 74]. This phenomenon is further investigated in Section 3.3.8.

As highlighted in Fig. 3.67, the resultant forces on the stirrup reinforcements nominated as Pos.2 and Pos.4 suddenly increased about 275kN load-level. As these reinforcements were mainly resisting the tension stress resultants in the anchorage, it is concluded that concrete-cone failure mode initiated about 275kN applied load-level. However, as earlier indicated that no cone-shaped surface crack was observed before 400kN applied load-level during the visual investigations. Thus, it could be stated that the supplementary reinforcements positioned in the theoretical cone-shaped breakout body (Pos.1 to Pos.4) prevented the development of the concrete cracks. The crack patterns presented in Fig. 3.66 also support this statement as they do not correspond to fully developed cone-shaped breakout body at the ultimate load-limit of the anchorage ($F_{u,CC\text{-}02}$=*460kN*).

Furthermore, at the ultimate load-level, the reinforcements around the anchor plate did not yield. Therefore, the failure of the anchorage could not be attributed to concrete-cone or concrete pry-out failure modes. Consequently, the test specimen was cut to investigate the crack formation next to the headed-fasteners and to clarify the failure mechanism of the anchorage.

Fig. 3.68 shows a section cut of the column together with the right-side column view presented in Fig. 3.63. It could be seen Fig. 3.68b that the crack formations inside the test specimen for the initial position of the anchor plate did not fully develop; thus, neither concrete-cone nor pry-out breakout bodies fully formed at the initial position of the headed-studs. On the other hand, a secondary cone-shaped breakout body could be noticed at the shifted position (δ_x=*33mm*) of the upper headed-fastener. Therefore, similar to the first test, it is concluded that the pull-out failure mode of the upper row of the headed-fasteners was the limiting mechanism for the load-bearing capacity of the anchorage. Furthermore, the crushed concrete volume under the upper row headed-fasteners could be linked to the initiation of the pry-out failure but as indicated earlier this failure mode did not fully develop due to the existence of the shear supplementary reinforcements.

To investigate the development of the pull-out failure mode, the horizontal displacements of the anchor plate and the column surface at the height that corresponds to the upper edge of the anchor plate is investigated in Fig. 3.69. The unloading period is excluded from the figure. At 300kN load-level the relative horizontal displacements between the anchor plate and the concrete surface started to increase as a result of the pull-out failure initiation. However, no load-drop was observed at this load-level according to the load-displacement behavior of the anchor plate (see Fig. 3.59). On the other hand, it could be seen from Fig. 3.69 that the relative displacement between the anchor plate and the concrete surface did not change considerably until 338kN load-level which corresponds to the initial load drop in the load-displacement behavior. After 338kN load-level, the rate of the relative displacements between the anchor plate and the column surface significantly increased. Thereafter, at 400kN load-level, which corresponds to the second load-drop, the rate of the relative horizontal displacements further increased and at the ultimate load-limit ($F_{u,CC\text{-}02}$=*460kN*) the anchor plate started to freely displace along the *x-axis* direction as no further displacement on the concrete surface was identified. Therefore, it is concluded that the failure of the anchorage occurred due to the pull-out failure of the upper row of the headed-fasteners.

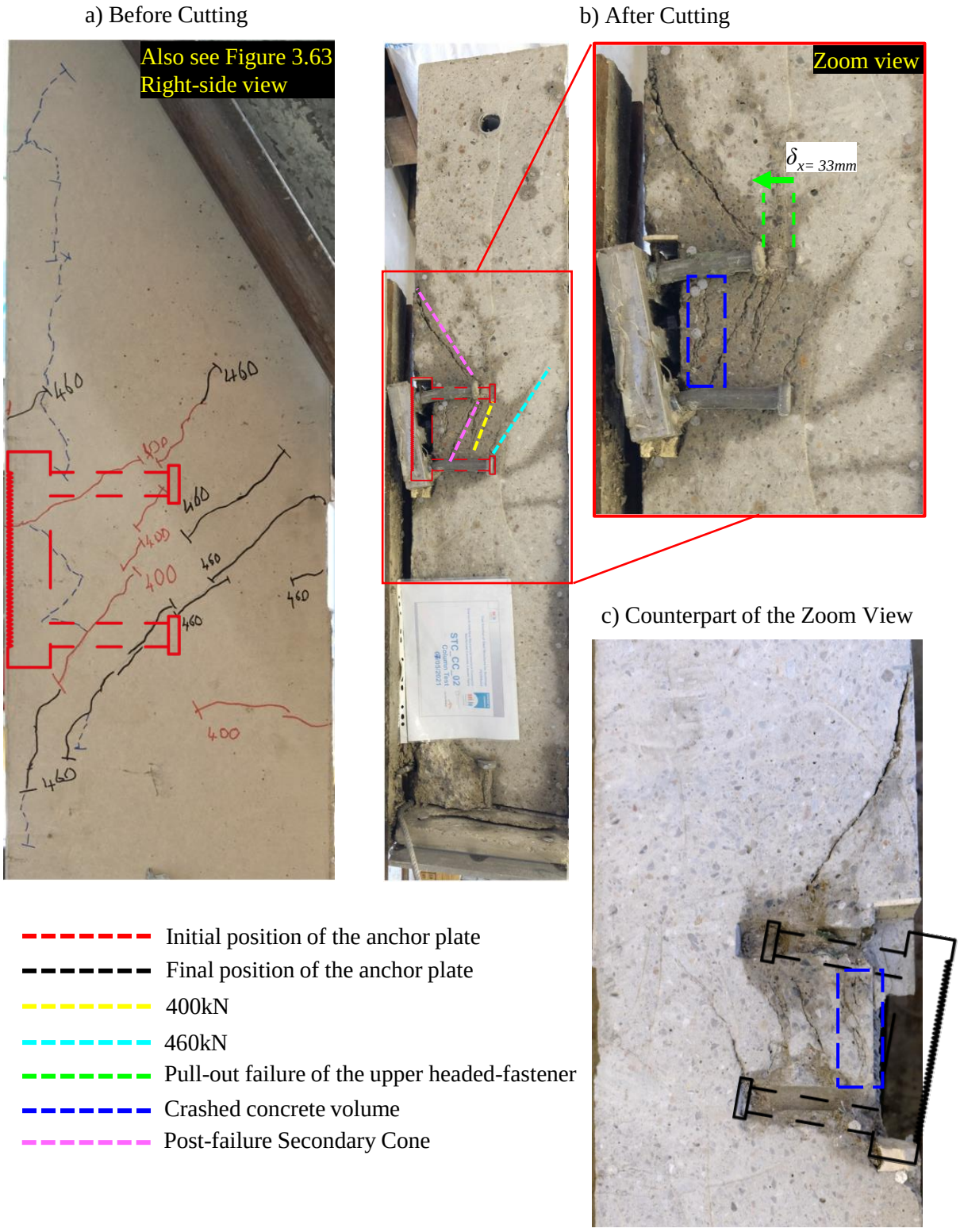

Figure 3.68: Section cut of the test specimen / CC-02.

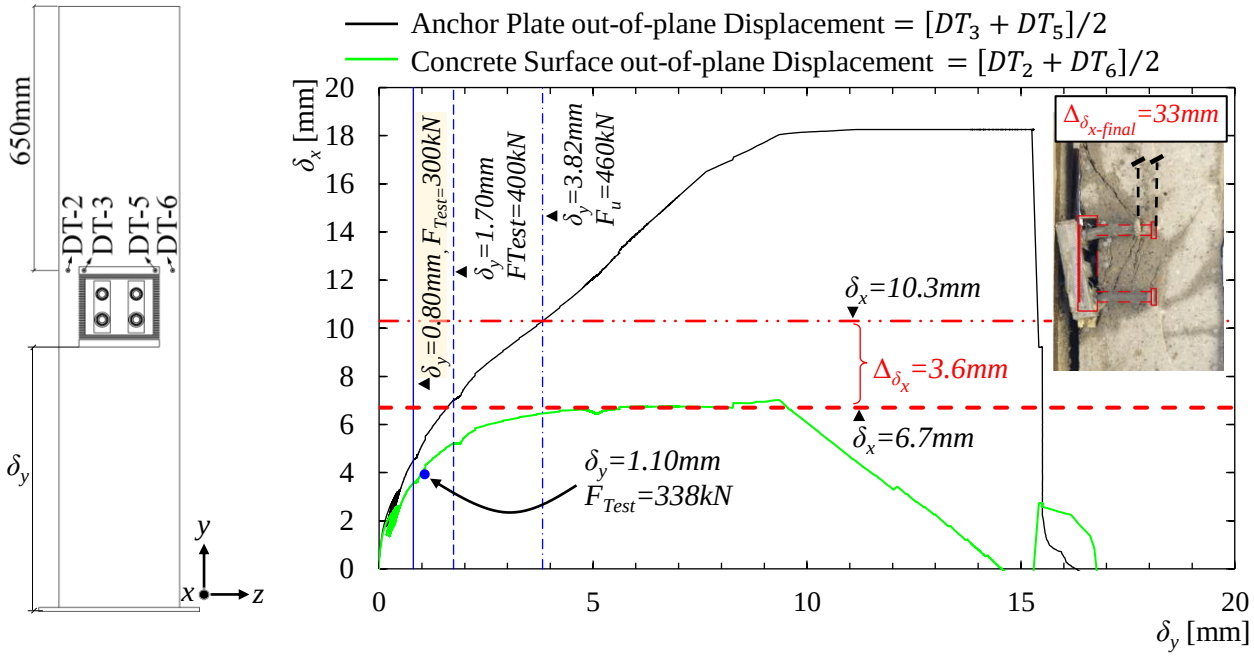

Figure 3.69: Investigation of pull-out failure / CC-02.

Similar to the first test, there was no headed-fastener failure. However, the lower row of the headed-fasteners was highly deformed. Fig. 3.70 shows the deformed state of the anchor plate after the experimental test together with the strain data and the corresponding stress resultants for the upper row of the headed-fasteners. The unloading period after the ultimate test load is excluded from the figure. The resultant forces were calculated with Eq. 3.33 based on the recorded strain data, the nominal elastic modulus [81] and the stress area ($Ø$=22) of the headed-fasteners

According to Fig. 3.70, SG-7 damaged around δ_y=8.5mm. Therefore, the data recorded by this strain-gauge is excluded from the figure after the damage instant. It could be noticed that the tension force in the anchorage was distributed equally between the upper headed-fasteners. No strain data were recorded from the lower row of the headed-fasteners. However, based on their deformed shapes, it is concluded that they were also yielded. Similar to the first test results, considering the high deformation of the lower headed-fasteners, it could be stated that the applied load initially resisted by the lower row of the headed-fasteners and by their yielding the upper row of the headed fasteners also resisted the applied load as they were also partially bent.

There was no visible deformation along the saw-tooth interface and the T-head bolts at the end of the test. Fig. 3.71 shows after test conditions for the saw-tooth surfaces of the anchor and the corbel plates. In addition, after test conditions of the T-head bolts and the variation of the tension forces in the bolts are presented in Fig. 3.72. The unloading period is excluded from the figure. At the ultimate load-level ($F_{u,CC\text{-}02}$=460kN), the tension forces in the upper row of the T-head bolts were less than their elastic load-bearing capacity calculated based on their nominal stress area ($Ø$=16) and the yield strength of the selected bolt material grade (8.8 [25]).

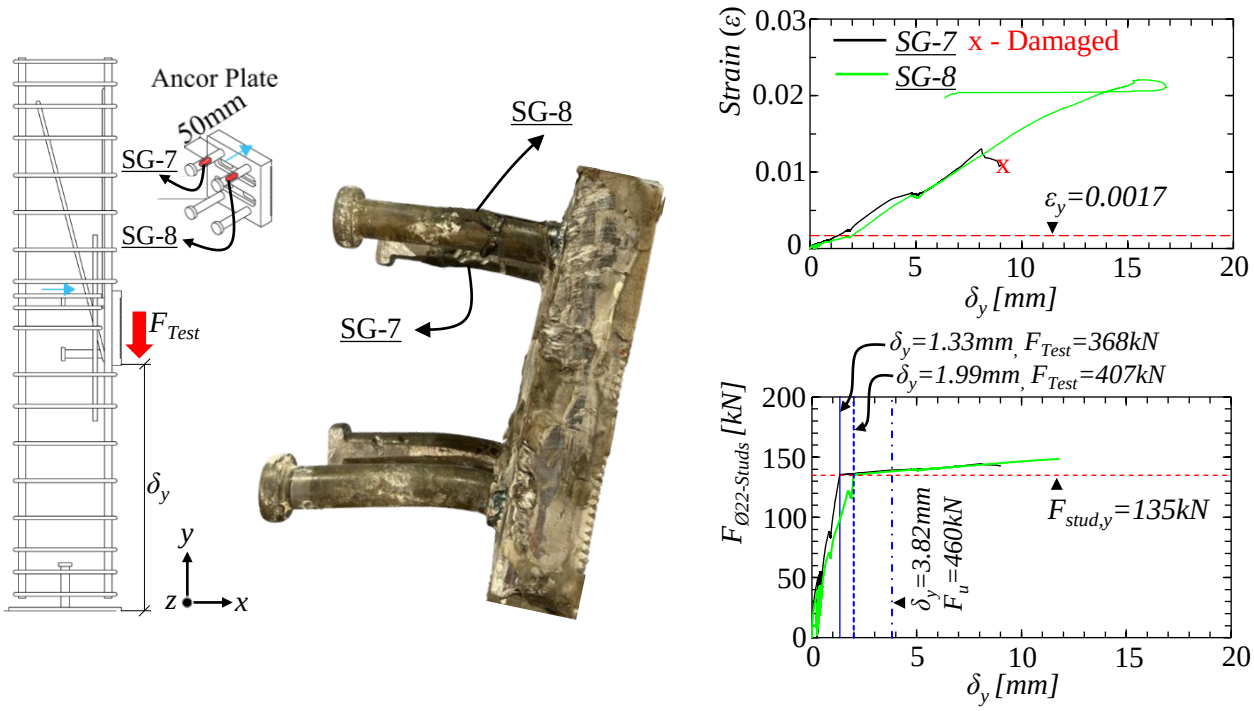

Figure 3.70: Strains and corresponding stress resultants on the upper headed-fasteners / CC-02.

a) Anchor Plate Saw-tooth Surface

b) Corbel Plate Saw-tooth Surface

Figure 3.71: After test conditions of the saw-tooth surfaces / CC-02.

The increase in the tension stress resultants in the upper row of the bolts after the ultimate load-limit of the anchorage was due to the rotation of the SMIBC which triggered the applied vertical load to be further decomposed along the *x-axis* direction as illustrated in Fig.3.71b. Consequently, neither the saw-tooth interface nor the bolts of SMIBC were damaged during the test.

a) T-head Bolts and Their Positions

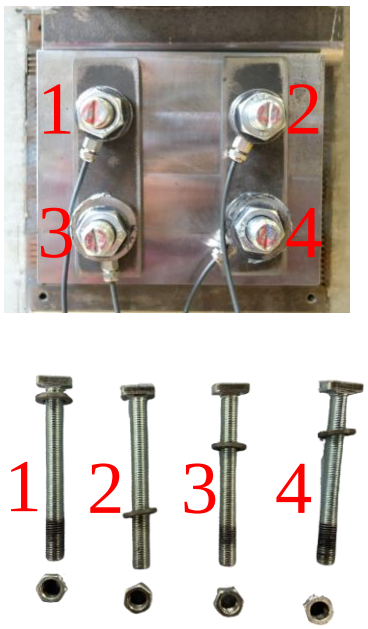

b) Variation of Tension Forces in the Bolts

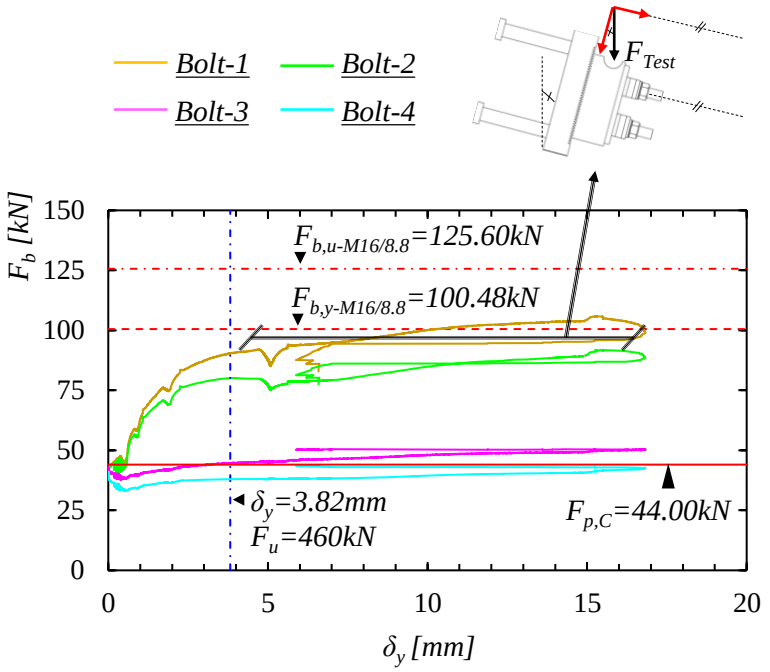

Figure 3.72: After test conditions and tension force of the T-head bolts / CC-02.

Table 3.26 summarizes the recorded test loads, i.e. F_{Test}, and the vertical anchor plate displacements, i.e. δ_y, successively together with the corresponding individual failure modes identified for the anchorage of CC-02 test specimen.

Table 3.26: Summary of the identified failure modes for the anchorage of CC-02 test specimen.

Position	Failure Modes	F_{Test} [kN]	δ_y [mm]	Identifications
Column	Concrete Pry-out	250	0.58	Initiation
Column	Concrete Cone	275	0.65	Initiation
Column	Pull-out	300	0.80	Initiation
UR Headed Stud	Yielding[1]	368	1.33	Fully Developed
Column	Pull-out	400	1.70	Partially Developed
UL Headed Stud	Yielding[1]	407	1.99	Fully Developed
Column	Pull-out	460	3.82	Fully Developed

UL: Upper Left, UR: Upper Right.

[1] The yield strength of the headed-fasteners against tensile loading calculated based on the characteristic material properties given in the product catalog [81]. Thus, they may not reflect the actual yield instant of the fasteners as it was possible to increase the loading after the yielding of both of the upper row of the headed-fasteners.

3.3.6.3 Test results and discussions / CC-03

Fig. 3.73 shows the vertical displacements of the anchor plate with respect to the applied loading. Similar to the previous test results while the load-displacement curve given in Fig. 3.73 includes the global column displacements, they are excluded from the load-displacement curve presented in Fig. 3.74 based on Eq. 3.30. The expected ultimate load-bearing capacity of the anchorage in CC-03 test specimen was 410kN , ($F_{u,exp}$=*410*). Therefore, the loading procedure and related loading steps were defined based on the expected capacity. However, the actual ultimate load-bearing capacity of the anchorage was 438kN ($F_{u,CC\text{-}03}$=*438*) to be 7% higher than the expected capacity. The expected capacity was estimated based on the numerical simulations performed prior to the experimental test. Therefore, the difference could be linked to the actual material properties of the test specimens. According to Fig. 3.59, at 311kN and 375kN load-levels there were sudden load-drops as similar to the previous test results. These drops might indicate damage initiation in the anchorage. Therefore, the reason behind these load-drops are later investigated in detail in this section.

Comparing Fig. 3.73 and Fig. 3.74, it is obvious that the assembly gaps of the test frame closed during the initial loading step (Up to 40% - $F_{u,exp}$) and the cycling loading period. Therefore, from here on, the load-displacement behavior presented in Fig. 3.74 is used for further investigation of the test results for CC-03 test specimen.

During the unloading period, the displacement transducer that measured the global vertical column displacements (DT-13 see Fig. 3.38) was stuck at the largest measurement range (10mm see Table 3.24). Therefore, the recovery of the anchor plate vertical displacements recorded during the unloading period does not represents the real behavior in Fig. 3.74.

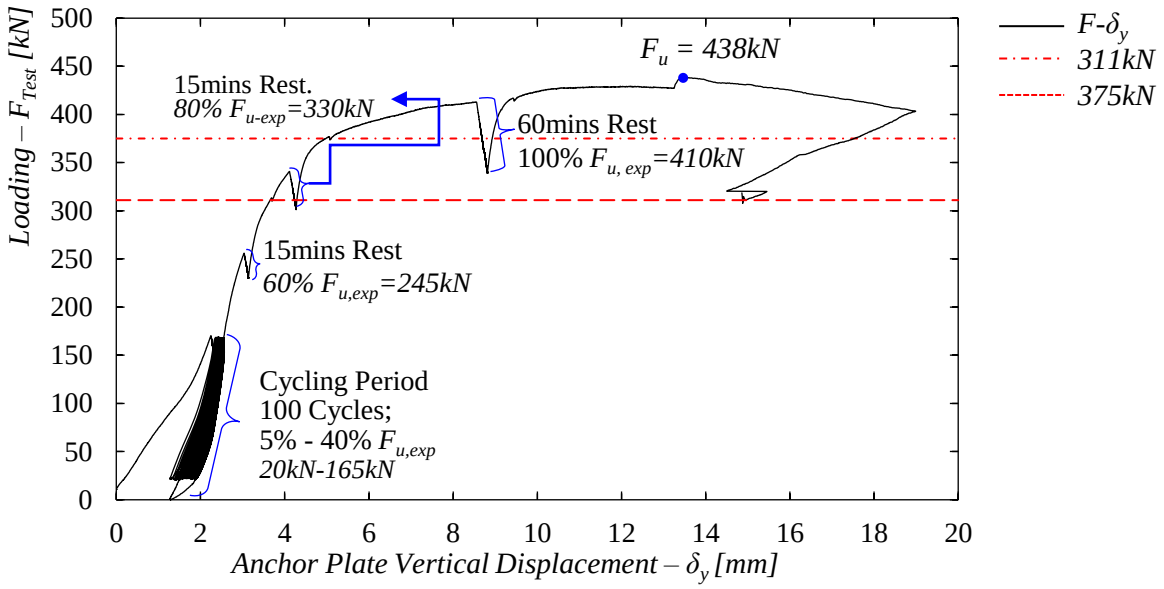

Figure 3.73: Anchor plate load-displacement behavior with the global column behavior / CC-03.

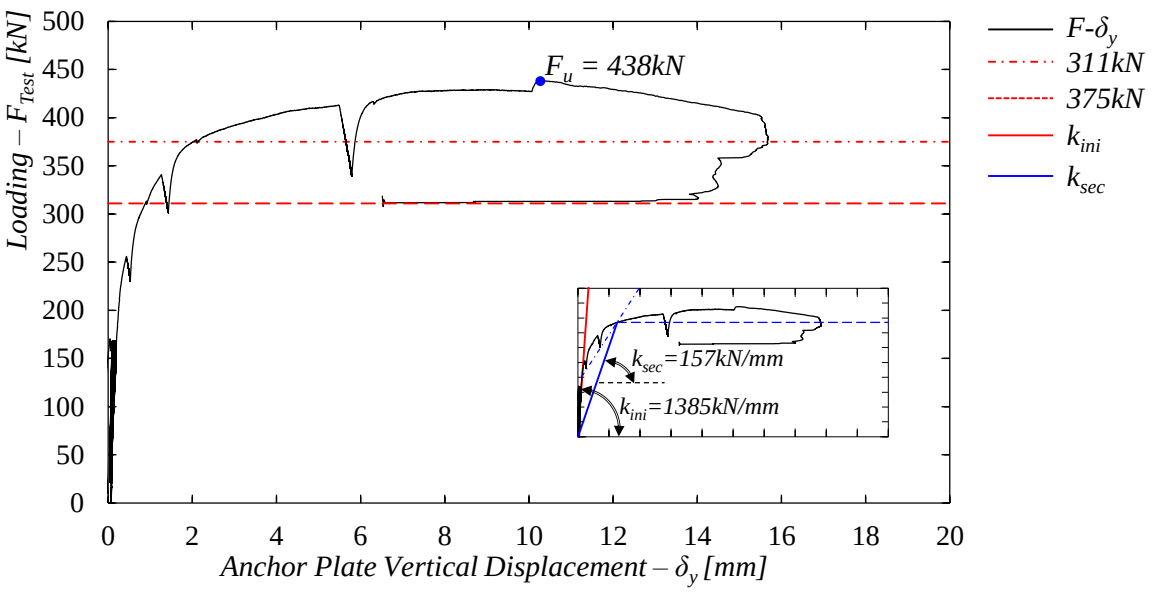

Figure 3.74: Anchor plate load-displacement behavior without the global column behavior / CC-03.

Fig. 3.75 shows the moment-rotation behavior of the anchor plate. The global column displacements were excluded from the figure by using Eq. 3.31 for the calculation of the rotation values. In addition, the cycling loading period and the unloading period after the ultimate load-level are excluded from the figure to better understand the moment-rotation behavior of the anchorage. As identical to the previous test results, the moment values were calculated by the multiplication of the applied loading with the pre-defined load eccentricity (e=32mm). The initial elastic rotational stiffness of the anchorage ($S_{j,ini}$) could not be identified from the figure. This is because the presented rotations were calculated with Eq. 3.31 by excluding the global horizontal column displacements. Therefore, the moment-rotation behaviour of the anchorage is investigated based on the output results of the numerical simulations detailed in Section 3.3.7.

Fig. 3.76 to Fig. 3.80 show the crack propagation on the test specimen with respect to the loading steps of the test procedure. During the cycling loading period, and at 245kN load-level (60% of the expected capacity - $F_{u,exp}$) no surface crack was observed; thus, no visual inspection shown for these loading periods. Furthermore, Fig. 3.81 shows the crack patterns on the third test specimen after the disassembly of the set-up components.

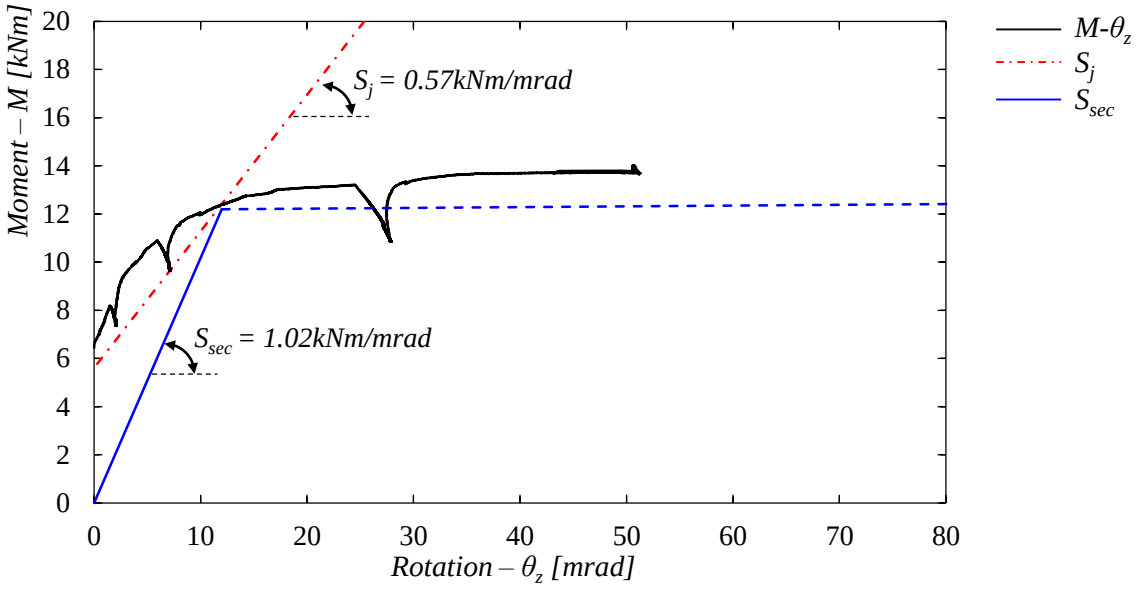

Figure 3.75: Moment-rotation behavior of the anchor plate / CC-03.

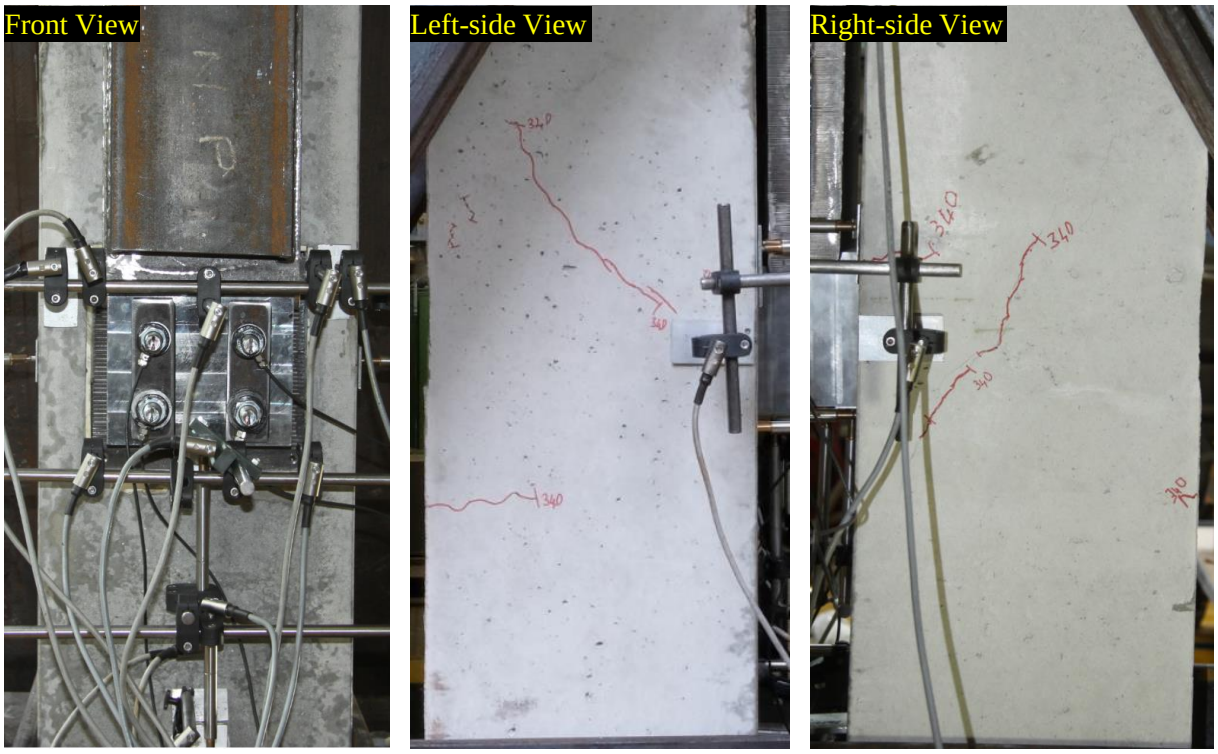

Figure 3.76: Crack patterns at 340kN (80% of $F_{u,exp}$) / CC-03.

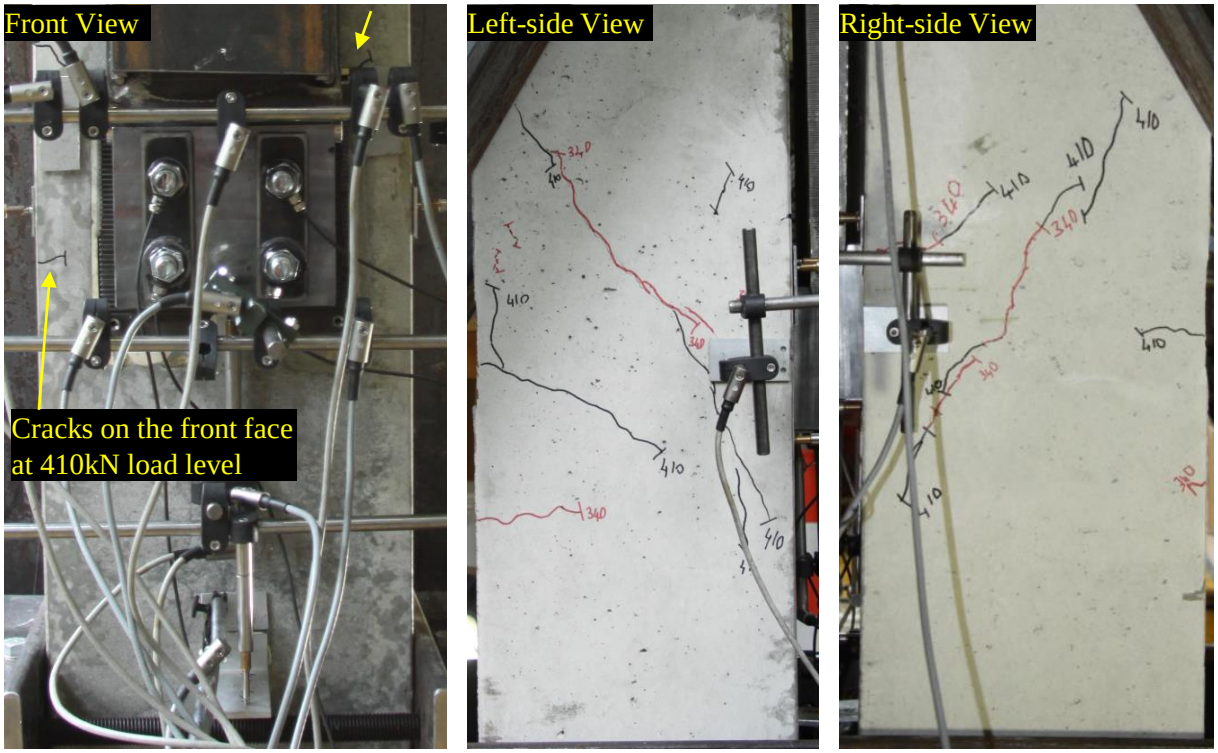

Figure 3.77: Crack patterns at 410kN (100% of $F_{u,exp}$) / CC-03.

Dashed blue lines are drawn after the test due to the safety concerns

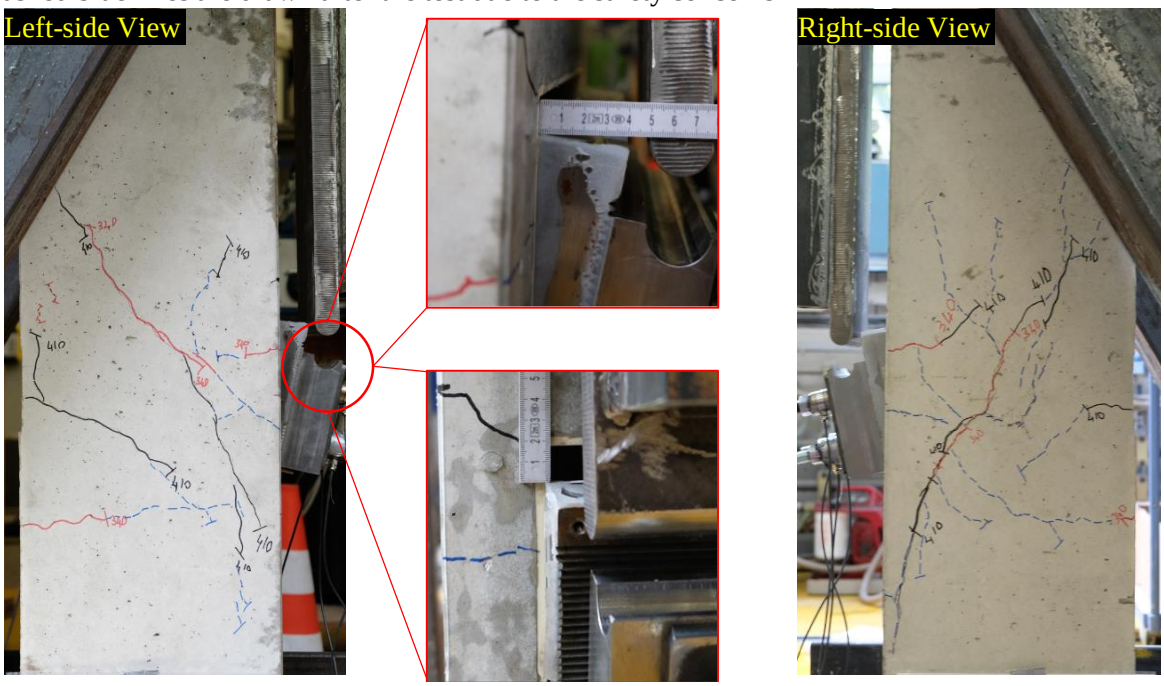

Figure 3.78: Crack patterns at the maximum displacement level / CC-03.

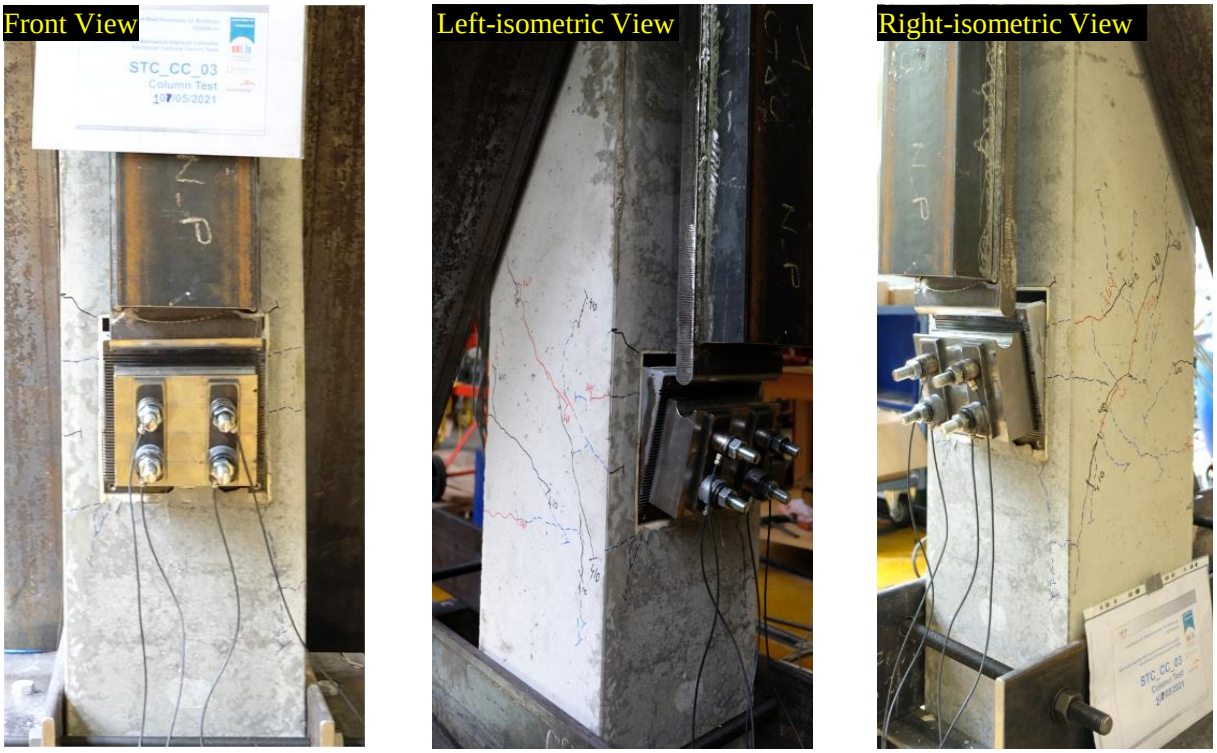

Figure 3.79: Crack patterns at the maximum displacement level - Additional views / CC-03.

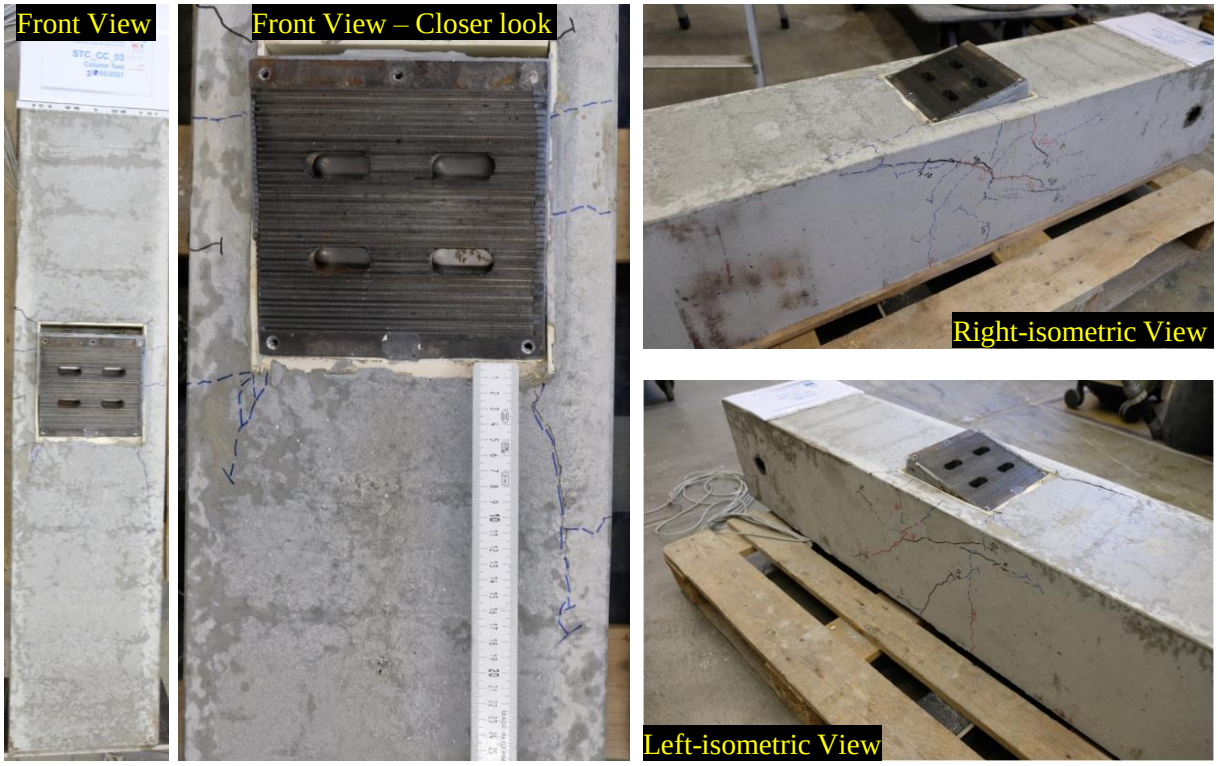

Figure 3.80: Crack patterns after the disassembly of the test set-up / CC-03.

As it could be identified from Fig. 3.76 to Fig. 3.80, the crack patterns along the side views of the column started to grow about 340kN load-level. The propagation of the crack patterns could be attributed to the concrete-cone failure mode. To have clear identification for the development of the cone-shaped concrete breakout body, Fig. 3.81 highlights the crack patterns along the side-views of the columns with respect to the corresponding loading steps. According to Fig. 3.81, a secondary cone-shaped breakout body could be identified at the end of the test. Therefore, it could be stated that the initial cone-shaped breakout body did not fully form. This statement could be validated with Fig. 3.80 as the crack patterns for the initial cone-shaped breakout body did not fully propagate along the front surface of the column. Therefore, the limiting value of the ultimate load-level (F_u=*438kN*) could not be attributed to concrete-cone failure mode, and it could be stated that the secondary cone-shaped breakout formed after the pull-out failure of the upper row of the headed-fasteners as similar to the previous test results (see Fig. 3.53 and Fig. 3.68).

Furthermore, similar to the second test results, there was no surface crack below the anchor plate. Thus, it could be stated that the special shape supplementary reinforcements of CC-03 test specimen (see Fig. 3.34c) were effective against the pry-out failure mode.

To investigate the contribution of the special shape supplementary reinforcements on the load-bearing mechanism of the anchorage, the resultant forces on the reinforcements positioned next to the anchor plate are investigated in Fig. 3.82. The resultant forces were calculated with Eq. 3.32 based on the recorded strain data, the mean elastic modulus (see Table 3.22) and the nominal cross-section area of the reinforcements (*Ø=14*). The unloading period is excluded from the figure. In addition, the data recorded by SG-5 is not shown after δ_y=*14mm* as it was damaged at this instant.

According to Fig. 3.82, at 230kN load-level, the rate of the resultant forces started to increase for the special shape supplementary reinforcements located close to the side surfaces of the column (SG-1 and SG-4). In addition, it could be noticed that at this load-level the resultant force on the stirrup reinforcements located next to the upper row of the headed-fasteners were nearly zero (SG-5 and SG-6). Thus, it could be stated that the pry-out failure mode initiated at 230kN load-level due to the crushing of the concrete volume under the headed-fasteners, and this caused the special shape supplementary reinforcements to be loaded. However, even at 410 load-level the characteristic pry-out concrete cracks close to the bottom edge of the anchor plate were not detected during the visual inspection (see Fig. 3.81). Therefore, it is concluded that the special shape supplementary reinforcements were activated against the pry-out failure, and as they were not yielded by the ultimate load-level they prevented the development of the pry-out concrete break-out body.

Furthermore, at 283 kN load-level, the stirrup reinforcements positioned next to the upper row of the headed-fasteners (SG-5 and SG-6) started to be loaded and the rate of the resultant forces on all of the special shape supplementary reinforcements increased; thus, this load-level is accepted as the initiation of the concrete-cone failure mode. However, as earlier indicated, neither full pry-out nor full cone-shaped concrete breakout bodies were detected by the visual inspection presented in Fig. 3.81, and the reinforcements positioned next to the anchor plate did not yield at the ultimate load-level. Therefore, the failure of the anchorage could not be attributed to these failure modes.

a) Right Side Views

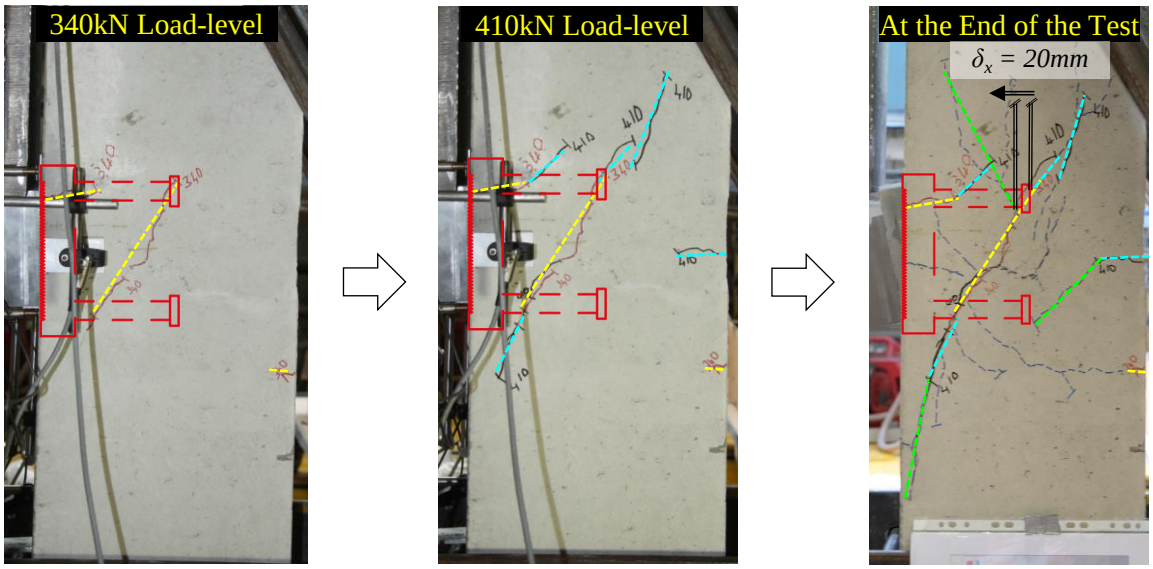

b) Left Side Views

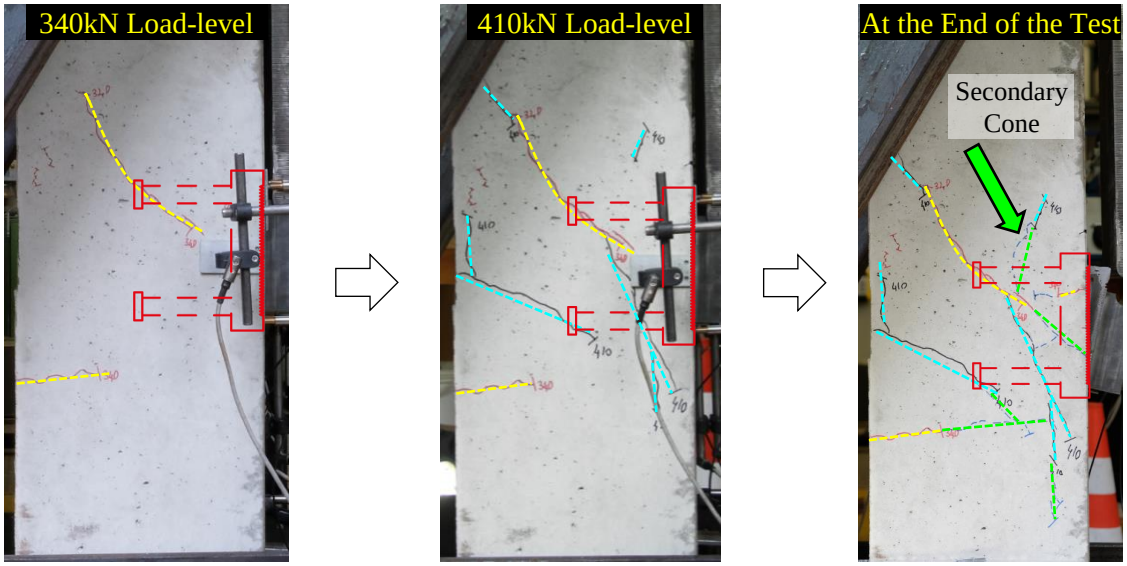

Figure 3.81: Development of cone shaped concrete breakout body / CC-03.

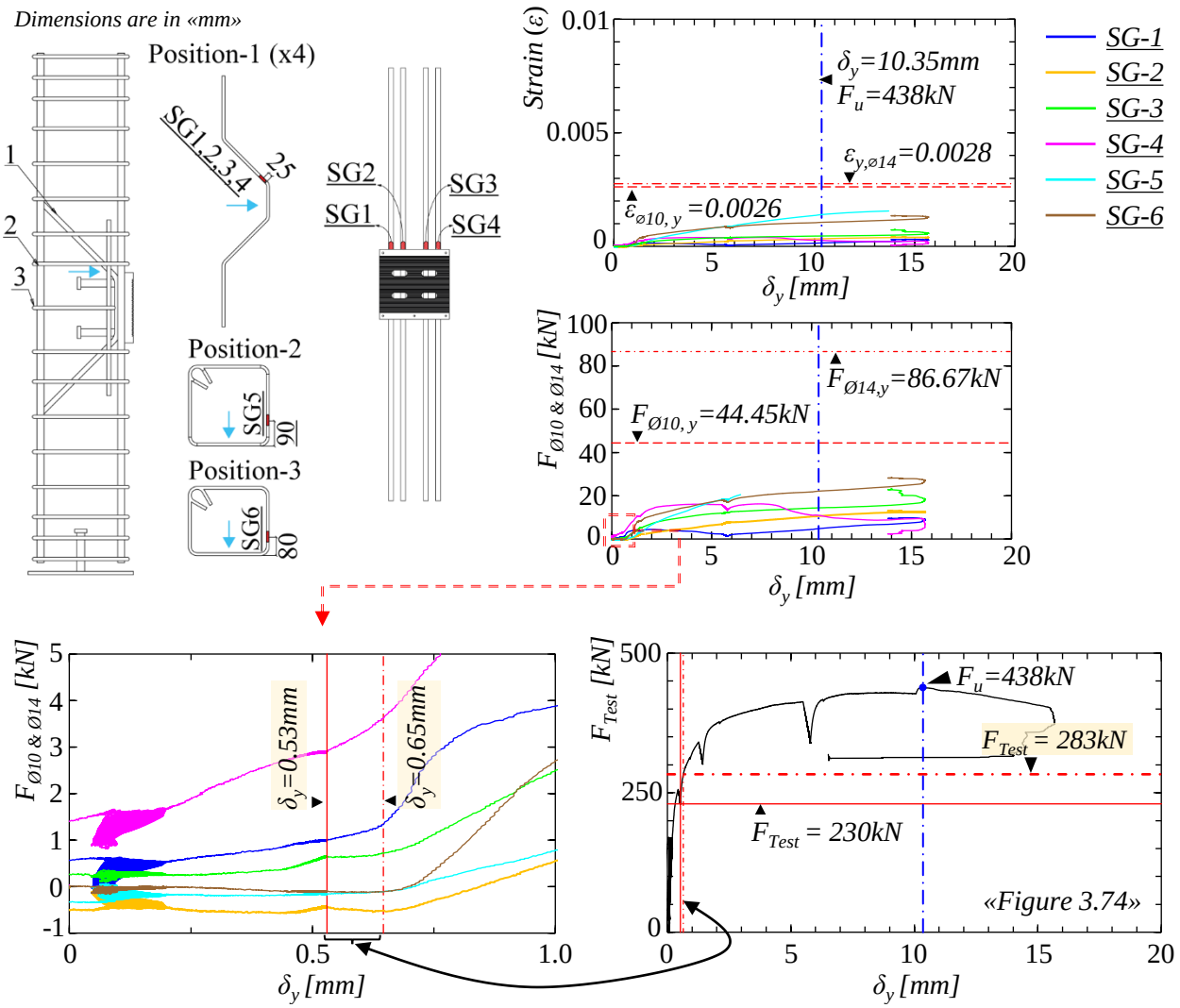

Figure 3.82: Strains and corresponding stress resultants on the reinforcements / CC-03.

Fig. 3.83 shows a section cut of the column together with the left-side column view presented in Fig. 3.78. The crack formations inside the test specimen for the initial position of the anchor plate is consisted with the crack patterns highlighted during the visual inspections at 340kN and 410kN load-levels. In addition, it could be noticed from the section cut that the cone-shaped concrete breakout body did not form at the initial position of the anchor plate. However, in Fig. 3.82b the pull-out failure of the upper row of the headed-fasteners could be clearly detected. Furthermore, a characteristic crack pattern for pry-out failure mode could be identified in Fig. 3.82c and it could be seen that this crack pattern did not fully propagate at the initial position of the upper row of the headed-studs next to the special shape supplementary reinforcement. Therefore, it is concluded that the pry-out failure of the anchorage was initiated before the pull-out failure, but it did not propagate as the supplementary reinforcements started to resist the applied load.

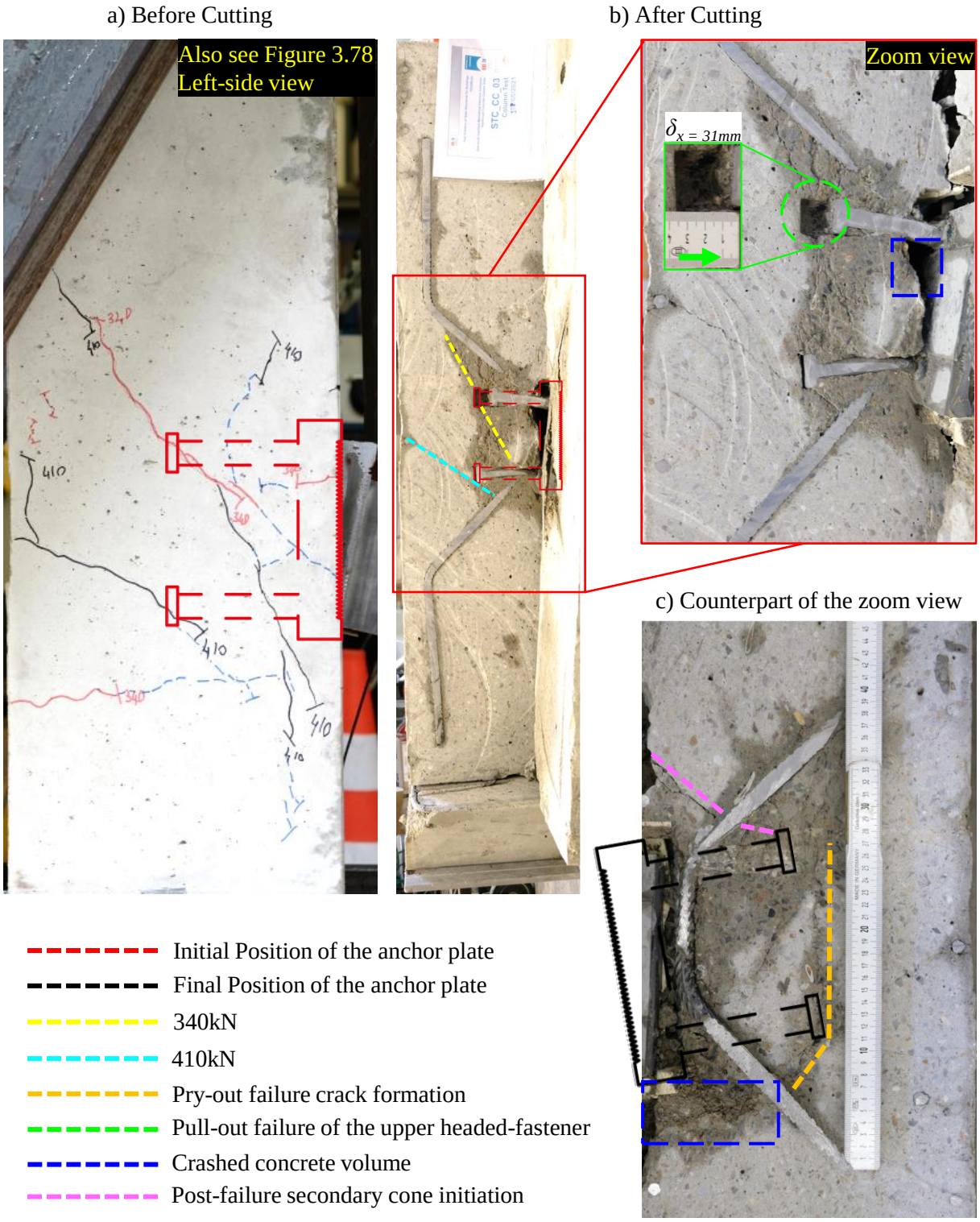

Figure 3.83: Section cut of the test specimen / CC-03.

Consequently, it could be stated that the failure of the anchorage was mainly due to the pull-out failure of the upper row of the headed-fasteners as different failure modes initiated but did not propagate for the initial position of the anchor plate. The last but not the least, it could be noticed in Fig. 3.83 that the secondary cone-shaped breakout body did not fully form unlike to the first test (see Fig. 3.53) and the second test (see Fig. 3.68). This outcome could explain the relatively high ductility of the third test specimen before attaining the ultimate load-level compared to the first and the second test results.

The pull-out failure mode is investigated in Fig. 3.84. The unloading period after the ultimate test load is excluded from the figure. At 235kN load-level the relative horizontal displacements (*x-axis* direction) between the anchor plate and the concrete surface started to increase as a result of the pull-out failure initiation. In addition, at 363kN load-level it could be noticed that the rate of the relatively displacements started to increase; thus, the second load-drop highlighted in Fig. 3.59 for F_{Test}=*375kN* could be attributed to the development of the pull-out failure. On the other hand, unlike the investigations of the pull-out failure of the previous test specimens (see Fig. 3.54 and Fig. 3.69) the initial load-drop highlighted in Fig. 3.74 for F_{Test}=*311kN* could not be linked the pull-out failure. Therefore, the load drop at F_{Test}=*311kN* is considered to be linked to the development of concrete pry-out failure mode highlighted with orange dashed lines in Fig. 3.82c.

Furthermore, it could be noticed in Fig. 3.84 that at 416kN load-level the anchor plate starts to freely displace along the out-of-plane direction as no further displacement on the concrete surface was identified. Thus, F_{Test}=*416kN* could be accepted as the instant that corresponds to the pull-out failure of the upper row of the headed-fasteners.

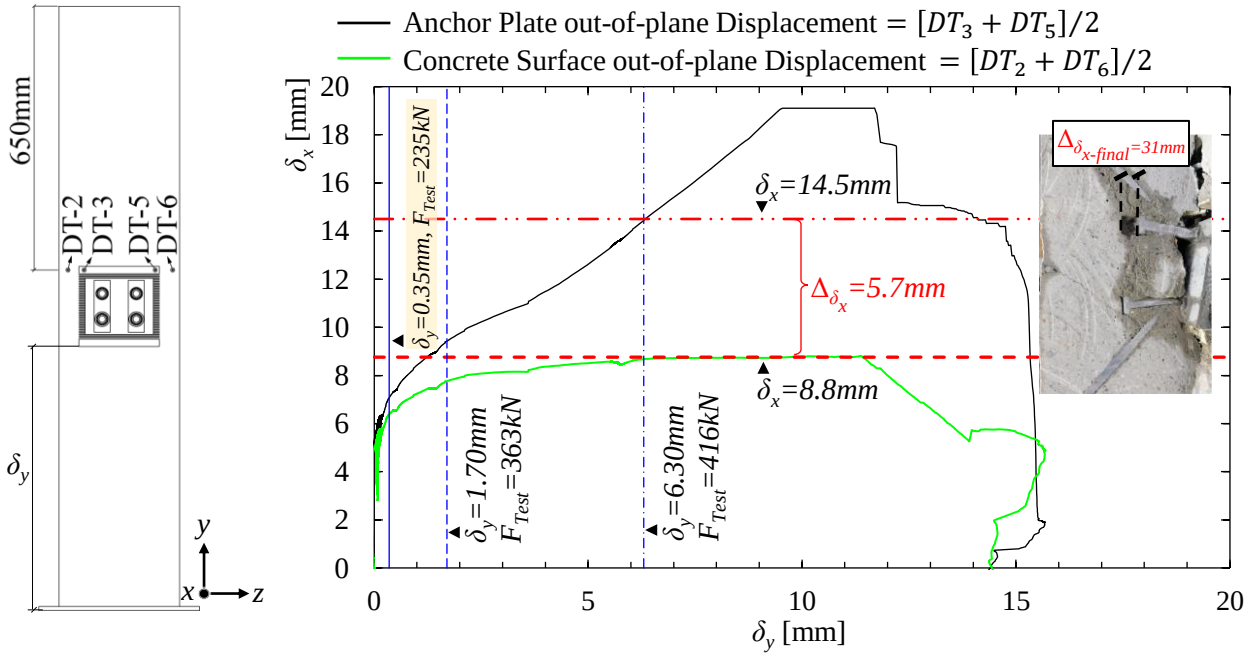

Figure 3.84: Investigation of pull-out failure / CC-03.

However, the ultimate load-level was 438kN (F_u=*438kN*) for the third test; thus, there was 22kN additional capacity after the pull-out failure. In Fig. 3.82c, the formation of the secondary cone-shaped concrete breakout body could be seen as highlighted with pink dashed line that coincides with the special shape supplementary reinforcement. Therefore, it is concluded that after the pull-out failure the special shape supplementary reinforcements were also activated against the secondary cone-shaped breakout body and provided additional capacity with high ductility. It was not possible to identify the activation of the special shape supplementary reinforcements in Fig. 3.81 as the strain-gauges were not at the crack pattern of the secondary cone-shaped breakout body. As a result, it is concluded that the special shape supplementary reinforcements increased the ductility of the anchorage by also activated at post pull-out failure stage of the anchorage.

The headed-fasteners did not fail during the test. However, as similar to the previous tests, the lower row of the headed-fasteners was highly deformed. Fig. 3.85 shows the deformed state of the anchor plate after the test together with the strain data and the corresponding stress resultants for the upper row of the headed-fasteners. The unloading period after the ultimate test load is excluded from the figure. The resultant forces were calculated with Eq. 3.33 considering the nominal elastic modulus [81] and the nominal cross-section area, (*Ø=22mm*), of the headed-fasteners, and the recorded strains.

According to Fig. 3.85, the SG-8 was damaged at δ_y=*7.4mm*. Therefore, the data recorded after the damage instant is not shown in the figure. Both of the upper headed-fasteners were yielded before the ultimate load-level. It was detected that the upper right fastener (SG-7) yielded earlier than the left one; thus, one could state an unequal load distribution between the upper row of the fasteners. However, the crack patterns presented in Fig. 3.81 were similar for the left and the right side surfaces. Therefore, this difference might be related with the shear deformation of the upper row of the fasteners as the uniformity and the compactness of the concrete volume under the fasteners might not be identical. However, considering the yield status of the upper fasteners, it is concluded that the applied loading was uniformly distributed between the headed-fasteners at the ultimate load-level. This statement could be further justified with the after test condition of the anchor plate as the deformation profiles for each row of the fasteners could be noticed to be nearly identical.

There was no visible deformation along the saw-tooth interface and the T-head bolts at the end of the test. Fig. 3.86 shows the after test conditions for the saw-tooth surfaces of the anchor and the corbel plates. In addition, after test conditions of the T-head bolts and the variation of the tension forces in the bolts are presented in Fig. 3.87. The unloading period is excluded from the figure. At the ultimate load-limit ($F_{u,CC\text{-}03}$=*438kN*) the tension force in the upper row of the T-head bolts was less than their yield strength as similar to the previous test results.

The increase in the tension stress resultants in the upper row of the bolts after the ultimate load-level was due to the rotation of the SMIBC which resulted in the applied vertical load to be decomposed further along the *x-axis* horizontal direction as illustrated in Fig. 3.87b. Consequently, neither the saw-tooth interface nor the bolts of SMIBC were damaged during the test.

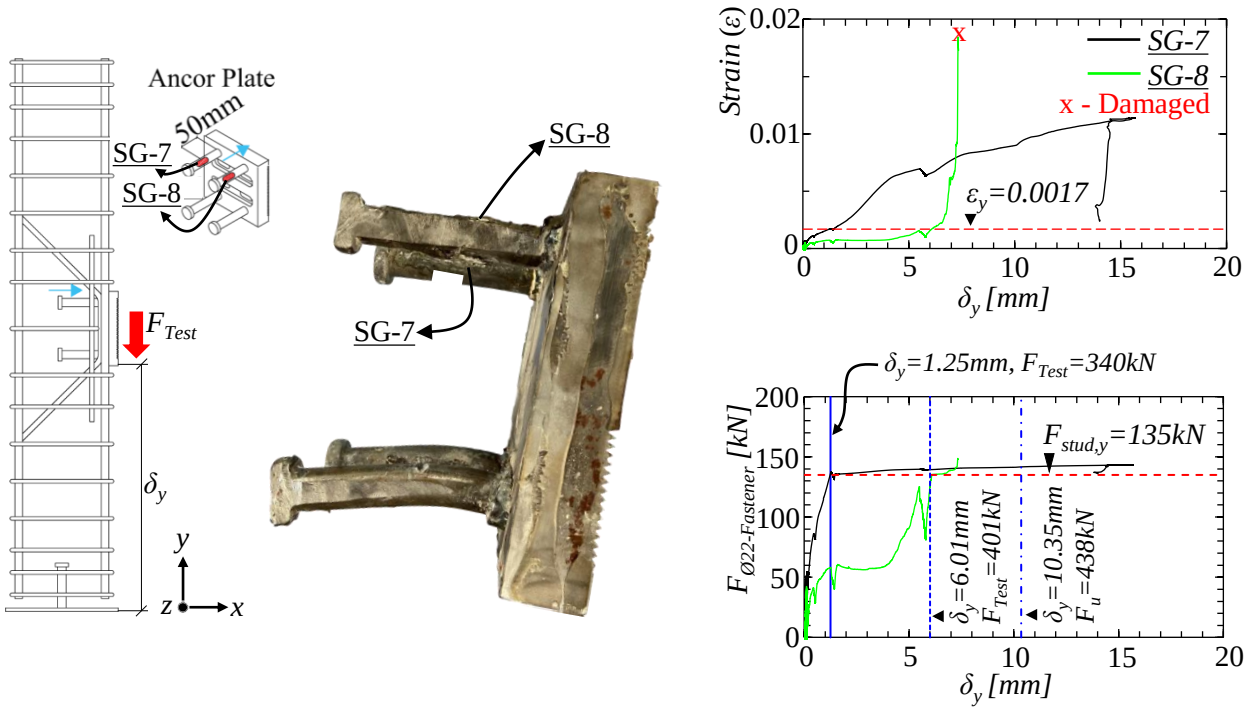

Figure 3.85: Strains and corresponding stress resultants on the upper headed-fasteners / CC-03.

a) Anchor Plate Saw-tooth Surface

b) Corbel Plate Saw-tooth Surface

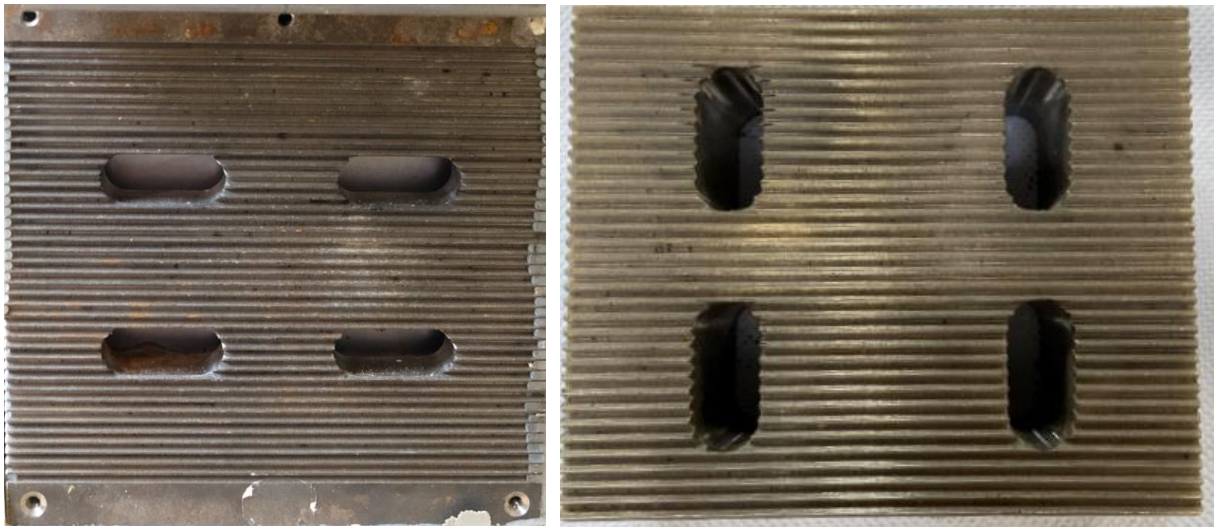

Figure 3.86: After test conditions of the saw-tooth surfaces / CC-03.

a) T-head Bolts and Their Positions

b) Variation of Tension Forces in the Bolts

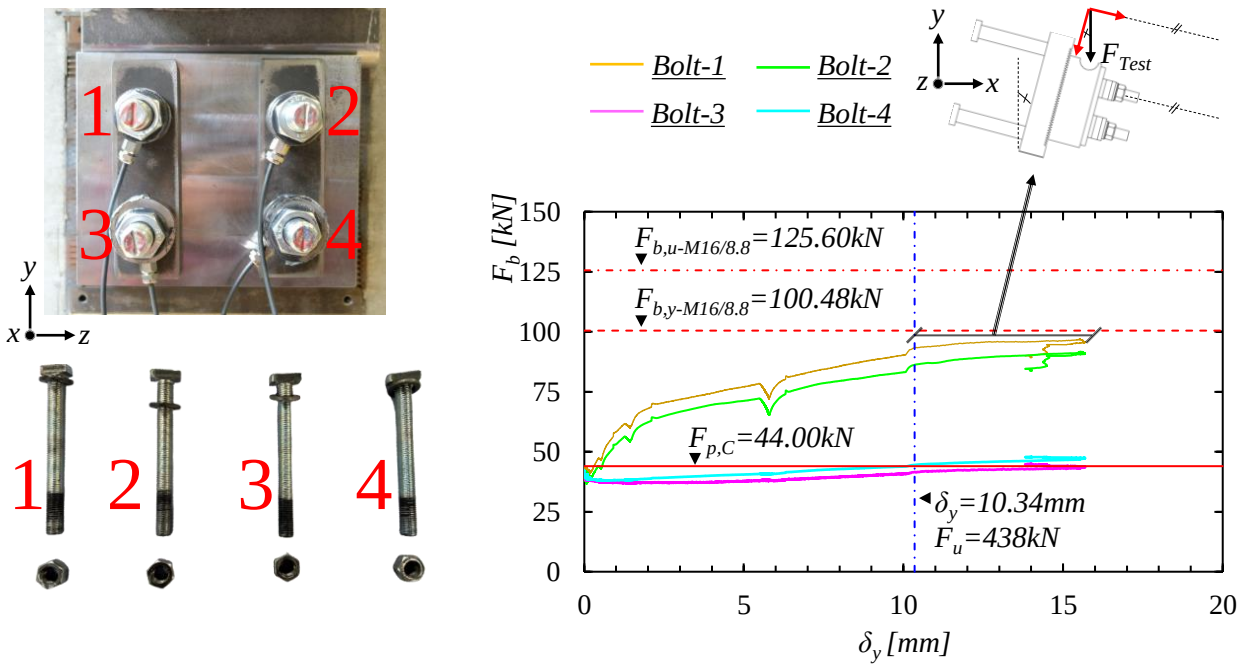

Figure 3.87: After test conditions and tension force of the T-head bolts / CC-03

Table 3.27 summarizes the recorded test loads, i.e. F_{Test}, and the vertical anchor plate displacements, i.e. δ_y, successively together with the corresponding individual failure modes identified for the anchorage of CC-03 test specimen.

Table 3.27: Summary of the identified failure modes for the anchorage of CC-03 test specimen.

Position	Failure Modes	F_{Test} [kN]	δ_y [mm]	Identifications
Column	Pull-out	235	0.35	Initiation
Column	Concrete Pry-out	230	0.53	Initiation
Column	Concrete Cone	283	0.65	Initiation
UR Headed Stud	Yielding[1]	340	1.25	Fully Developed
Column	Pull-out	363	1.70	Partially developed
UL Headed Stud	Yielding[1]	401	6.01	Fully Developed
Column	Pull-out	416	6.30	Fully Developed

UL: Upper Left, UR: Upper Right.

[1] The yield strength of the headed-fasteners against tensile loading was calculated based on the characteristic material properties given in the product catalog [81]. Thus, they may not reflect the actual yield instant of the fasteners as it was possible to increase the loading after the yielding of both of the upper row of the headed-fasteners.

3.3.6.4 Comparison of the test results

Fig. 3.88 compares the load-displacement and moment-rotation behaviors of the anchor plates. The cycling loading periods were excluded from the figure for clear comparisons. In addition, the crack patterns recorded from the side surfaces at the end of each test are compared in Fig. 3.89.

According to Fig. 3.88a, it could be stated that the load-displacement behavior of the anchorages is similar for all three tests. However, the initial translational elastic stiffness of CC-01 test specimen seems to be higher compared to CC-02 and CC-03 test specimens. This difference may be linked to the fact that Fig. 3.88a presents the load-displacement curves of the anchorages excluding the global vertical column displacements (see Eq. 3.30) to solely focus on the deformation of the anchorages. However, as the magnitudes of the displacements in the initial elastic ranges of the curves are less than 1mm and the position of the displacement transducers used for the measurement of the vertical column and anchor plate displacements were at different heights (see Fig. 3.38), the global in-plane rotation of the column for CC-01 test specimen cause misevaluation of the initial translational elastic stiffness of the anchorage. In Section 3.3.7, the accuracy of this statement is further evaluated with FEA simulations as the global column displacements in the FE-models were fully restrained with ideal boundary-conditions. In addition, the load-displacement curves of the anchorages including the global column behaviors are also presented in Section 3.3.6.1 to Section 3.3.6.3.

Furthermore, it could be noticed in Fig. 3.88a that the ultimate load-bearing capacity of the anchorage in CC-02 test specimen is about 5% higher than CC-01 and CC-03 test specimens. For all three tests, the failure mechanism of the anchorages was mainly governed by the pull-out

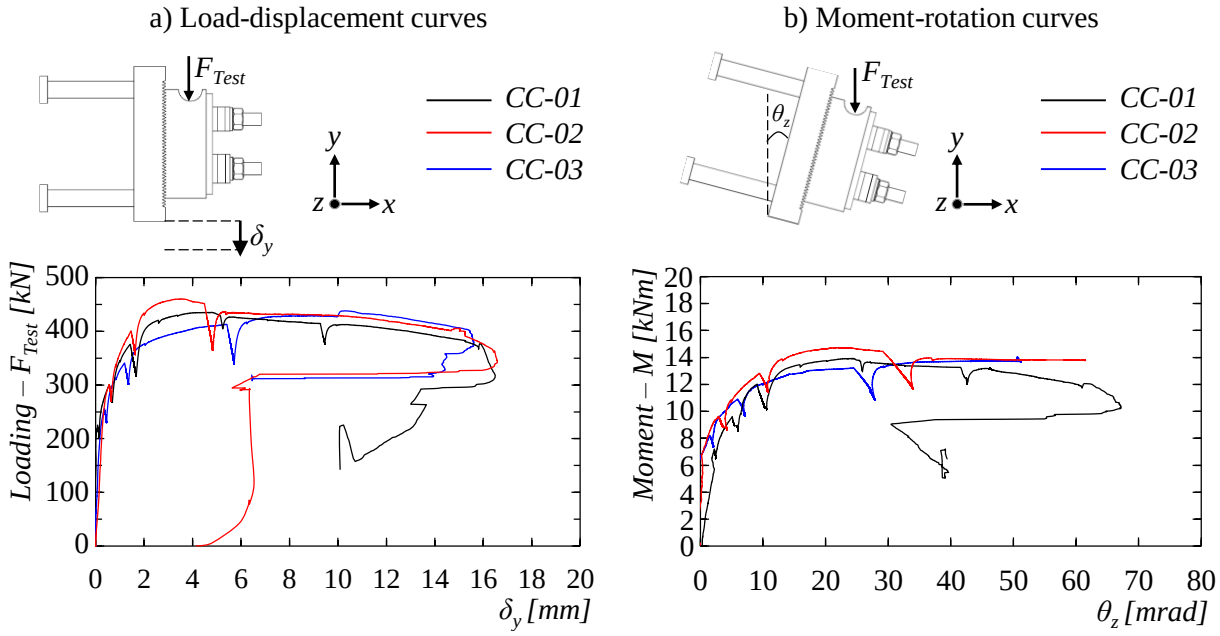

Figure 3.88: Comparison of the load-deformation behaviors of anchor plates.

a) Right Side Views

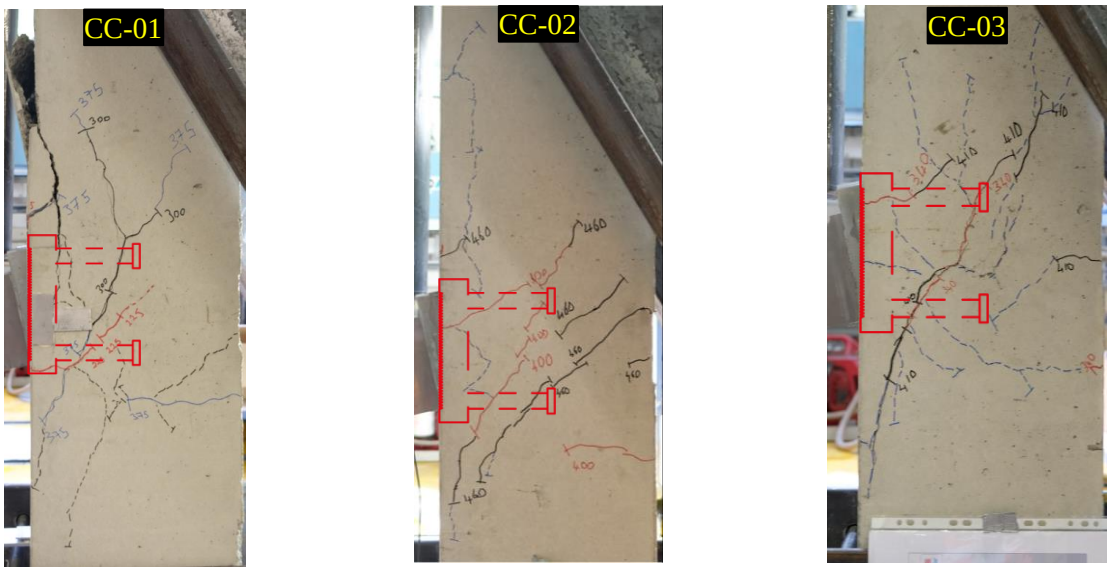

b) Left Side Views

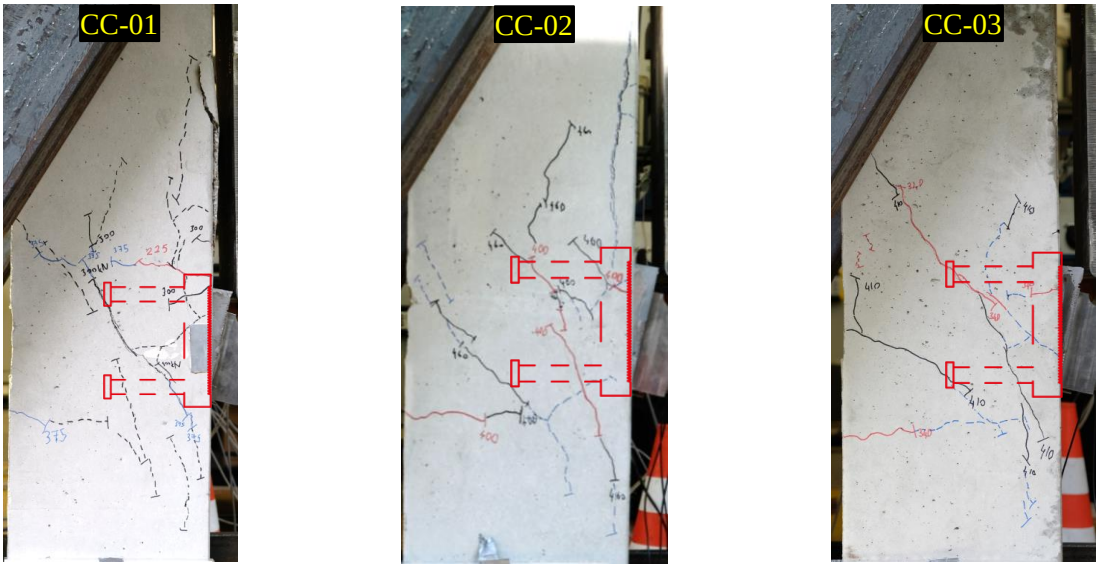

Figure 3.89: Comparison of the final crack-patterns of SMIBC-CC test specimens.

failure of the upper row of the fasteners. However, it is the fact that there was the interaction of the tensile (concrete-cone, pull-out) and the shear (pry-out) failure modes as illustrated from Section 3.3.6.1 to Section 3.3.6.3. Therefore, the higher load-bearing capacity of CC-02 test specimen could be linked to the existence of the shear supplementary reinforcement positioned under the upper row of the headed-fasteners (see Fig. 3.34b/ Pos.-5). Because, during the test CC-02, this reinforcement relatively prevented the propagation of the compression failure of the concrete volume under the shanks of the upper row of the headed-fasteners as a result of the applied load transferred to the concrete volume by the shanks. However, as earlier indicated, EN1992-4 [1] does

not explicitly consider the advantageous contribution of the shear supplementary reinforcements (see Fig. 3.34b/Pos.-5 and Pos.-6) against the pry-out failure mode; thus, the design calculations for anchorages with headed-fasteners and supplementary reinforcements for RC-column configuration under eccentric loading conditions becomes significantly conservative [13, 24, 75].

Additionally, it could be seen in Fig. 3.88a that although the load-bearing capacity of CC-01 ($F_{u,CC\text{-}01}$=*435kN*) and CC-03 ($F_{u,CC\text{-}03}$=*438kN*) test specimens were nearly identical, the hardening plateau of CC-03 test specimen had lower stiffness than CC-01 test specimen until the pull-out failure (at $F_{Test,CC\text{-}03}$=*416kN*, see also Fig. 3.84). On the other hand, as the anchorage of CC-03 test specimen was detailed with additional supplementary reinforcements (Fig. 3.34c/Pos.-7), one could expect it to have higher hardening stiffness and load-bearing capacity than CC-01 test specimen. However, the provided supplementary reinforcements of CC-03 test specimen did not have advantageous contribution to the pull-out failure of the anchorage as the characteristics of this failure mode does not depend on the existence of the supplementary reinforcements. On the contrary, the supplementary reinforcements of CC-03 test specimen reduced the concrete volume between the load bearing area of the head of the fasteners and the back surface of the anchor plate, i.e. effective height of the headed-fasteners - h_{ef} [1], and as a result the response of the anchorage for CC-03 test specimen was lower compared to the anchorages of CC-01 and CC-02 test specimens. In addition, the reduced concrete volume under the head of the fasteners also reduced the pull-out capacity of the upper row of the headed-fasteners for CC-03 test specimen. However, according to Fig. 3.89, it could be noticed that the crack patterns of CC-03 test specimen above the upper headed-fasteners did not propagate until the front surface of the column as different from CC-01 and CC-02 test specimens. Thus, it is concluded that the supplementary reinforcements applied for CC-03 test specimen reduced the load-displacement response of the anchorage while they were activated against secondary cone-shaped concrete breakout formation (see also Fig. 3.83c) and provided additional load-bearing capacity after the pull-out failure of the upper headed-fasteners.

According to Fig. 3.88b, the moment-rotation behavior of the anchorages seems to be similar but the initial rotational stiffness (S_{ini}) of the anchorage for CC-01 test specimen was relatively smaller than CC-02 and CC-03 test specimens. Therefore, it is concluded that while the applied supplementary steel reinforcements for CC-02 and CC-03 test specimens did not significantly increase the ultimate load-bearing capacity, they provided additional initial rotational stiffness. However, this outcome has to be carefully evaluated as the load-deformation behaviors of the anchorages were derived by subtracting the global column displacements from the anchor plate displacements which might cause misevaluation. Therefore, the load-deformation characteristics of the tested anchorages are later re-assessed based on the output results of the numerical simulations (see Table 3.33).

Table 3.28 and Table 3.29 summarize the comparisons for the test results of SMIBC-CC test campaign with respect to the load-deformation characteristics and the identified failure modes for the anchorages.

Table 3.28: Comparison of the load-deformation characteristics of SMIBC-CC test specimens.

Test ID	F_u [kN]	$\delta_{y,at\ F_u}$ [mm]	k_{ini} [kN/mm]	k_{sec} [kN/mm]	S_{ini} [kNm/mrad]	S_{sec} [kNm/mrad]
CC-01	435	4.60	1430	141	2.59	0.96
CC-02	460	3.82	1400	141	19.29	0.86
CC-03	438	10.35	1385	157	N/A	1.02

Table 3.29: Comparison of the identified failure modes of SMIBC-CC test specimens.

Failure Mode	Status	CC-01		CC-02		CC-03	
		F_{Test} [kN]	δ_y [mm]	F_{Test} [kN]	δ_y [mm]	F_{Test} [kN]	δ_y [mm]
Concrete-cone	Initiation	180	0.0025	275	0.65	283	0.65
Concrete Pry-out	Initiation	225	0.083	250	0.58	230	0.53
Pull-out	Initiation	345	1.03	300	0.80	235	0.35
Yielding of Fasteners	Fully Developed	375	1.83	407	1.99	401	6.01
Pull-out	Fully Developed	435	4.60	460	3.82	416	6.30

3.3.7 FEA simulations

In the previous section, it is shown that the load-bearing mechanisms of the tested anchorages were relatively complex due to the interaction between the tension and shear stress resultants. In addition, it was shown that the concrete and the steel (supplementary reinforcements) components together resist the applied loading unlike the conservative assumption of EN1992-4 [1] that considers either concrete or steel components resist the loading. Therefore, the experimental tests were simulated by means of FEA to identify the successive failure mechanisms of the tested anchorages and to understand the resistance contribution of the concrete, steel and frictional components against the applied loading.

The half-symmetric geometry of the test set-up was modelled with a commercial FEA software, Abaqus [66]. The test frame was excluded from the model and ideal boundary conditions (BCs) were applied where necessary as consistent with Fig. 3.28. The T-bolts and saw-tooth surfaces of the anchor and corbel plates were excluded from the FE-models as neither the saw-tooth interfaces nor the T-bolts of were damaged during the experimental tests. Fig. 3.90 shows the FE-model geometry, BCs, FE-types and FE-discretization of the model components.

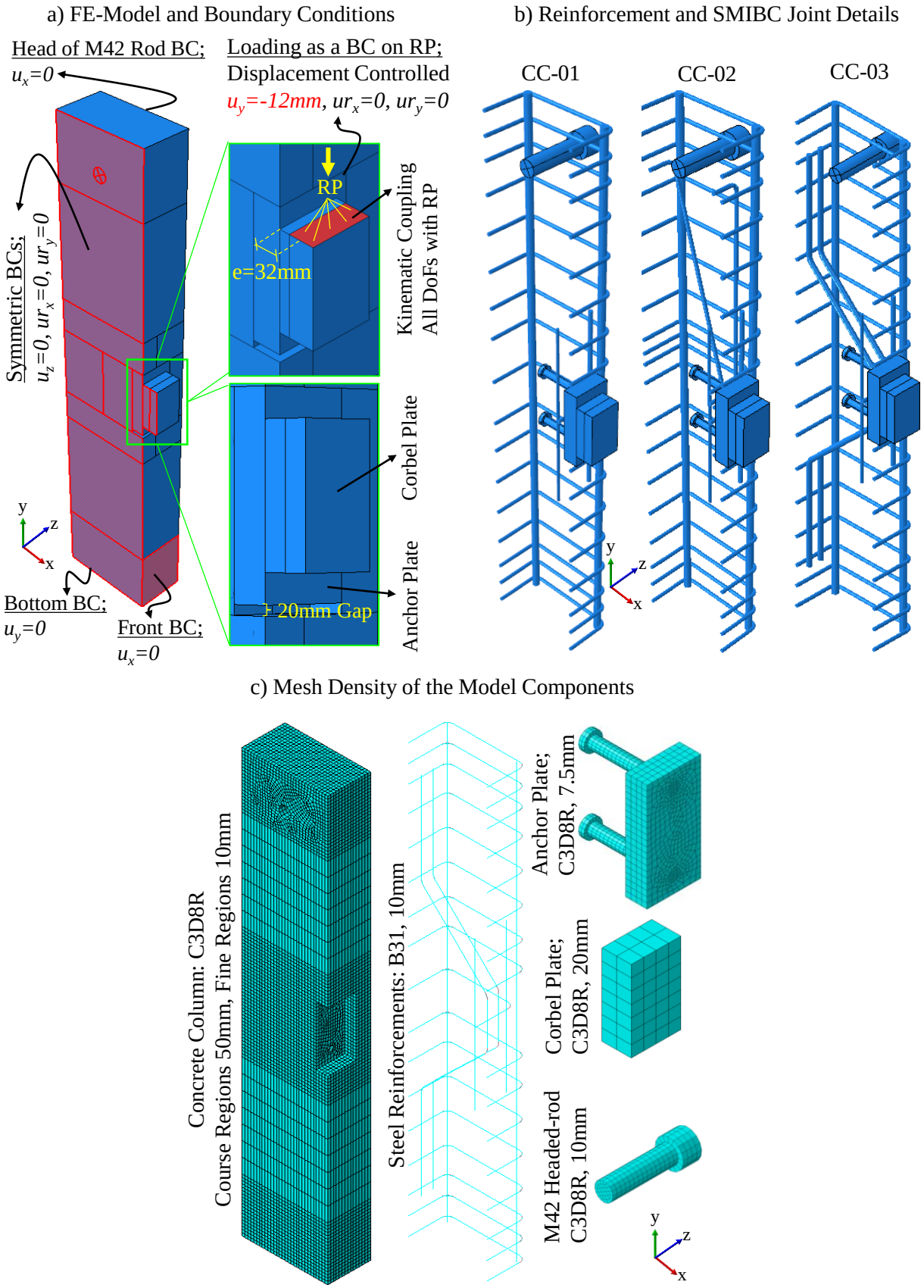

Figure 3.90: FE-Model Details of SMIBC-CC test campaign.

The constitutive material law of the concrete components was defined with concrete damage plasticity feature of the software [66]. Non-linear compressive stress-strain relation of EN1992-1-1 [72] was used for the concrete compressive behavior. Tensile stress-strain behavior and stress crack-width relation of the concrete material was defined according to the fib Model Code [3]. Fig. 3.91a illustrates the applied material model and corresponding damage parameters for the concrete components. As the experimental tests were successively executed only in six days, the material properties of concrete components assigned for the FEAs were taken as the mean values for the all of the available data for the test dates presented in Table 3.21, and identical concrete material model was used for all of the FEAs. The parameters assigned for the material model of the concrete components are given in Table 3.30 and the formulations for the corresponding properties are presented in Annex-C.

Table 3.30: Material properties of concrete FE-model components / SMIBC-CC test campaign.

Elastic		Compressive Behavior					Tensile Behavior			
E_{cm} [GPa]	ν	f_{cm} [MPa]	f_f [MPa]	ε_{c1} [‰]	ε_{cu1} [‰]	ε_f [‰]	f_{ctm} [MPa]	ε_{ctm} [‰]	w_1 [mm]	w_c [mm]
31.17	0.2	34.97	5.00	2.06	3.50	4.27	3.33	0.15	0.04	0.21
Concrete Damage Plasticity Parameters [66]										
Dilatation Angle	: 48°(CC-01), 36°(CC-03), 34°(CC-02)									
Eccentricity	: 0.1									
f_{b0}/f_{c0}	: 1.16									
K_c	: 0.667									
Viscosity Parameter	: 0.001									
Tension Recovery	: 0									
Compression Recovery	: 0									

The material laws of the steel reinforcements and the anchor plates were defined with tri-linear material model using the mean properties presented in Table 3.22. At the end of the experimental tests, no damage was identified for the corbel plates and M42-threaded rods; thus, their material laws were defined with elastic steel properties according to EN1993-1-1 [50]. The headed-fasteners were modelled with bi-linear material model without softening as there was no available data for their ultimate and fracture strains as no material characterization tests were performed for them. However, it is the fact the weld-seam between the anchor plate and headed-fasteners resists the large portion of the applied load [11] and provides additional shear resistance with high ductility. Therefore, the bi-linear material model assigned to the headed-fasteners could be accepted to be realistic. The yield and ultimate strengths of the fastener were assigned from the product specification [81]. Fig. 3.91b illustrates the material models of the steel components and

the corresponding parameters are listed in Table 3.31.

Table 3.31: Material properties of steel FE-model components / SMIBC-CC test campaign.

Component Name	Material Model	E [GPa]	ν	f_y [MPa]	f_u [MPa]	f_f[1] [MPa]	ε_u[2] [%]	ε_f[3] [%]
Anchor Plate	Tri-linear	217	0.3	383	486	309	25.17	38.17
Cover Plate	Linear-elastic	210	0.3	N/A	N/A	N/A	N/A	N/A
Headed-fasteners	Bi-linear	210	0.3	375	490	N/A	15	N/A
Reinforcements-*Ø10*	Tri-linear	216	0.3	566	651	169	15.78	25.06
Reinforcements-*Ø12*	Tri-linear	218	0.3	410	604	398	23.82	30.01
Reinforcements-*Ø14*	Tri-linear	204	0.3	562	643	441	12.81	20.06
Reinforcements-*Ø20*	Bi-linear	210	0.3	500	540	N/A	0.15	N/A
M42-threaded Rod	Linear-elastic	210	0.3	N/A	N/A	N/A	N/A	N/A

[1] The calculation for the fracture stresses, f_f, is presented in Annex-C.

[2] The calculation of the ultimate strains, ε_u, for the tri-linear material law is presented in Annex-C.

[3] The fracture strain, ε_f, corresponds to A presented in Table 3.22.

The interactions between the FE-model components are listed in Table 3.32. The reinforcements were embedded into the concrete columns, and general contact with hard and penalty friction formulations was used to define the normal and tangential interactions between the anchor plate (including the headed-fasteners) and the concrete column. The anchor and corbel plates were tied together as the load-bearing capacity of the SMIBC was much higher than the ultimate test loads.

Loading was applied with displacement control method by defining BC to the reference point kinematically coupled with top surface of the corbel plate. Smooth step function of the software [66] was used for the loading steps. The load-eccentricity (e=*32mm*) was kept identical with the experimental tests by dividing the top surface of the corbel plate similar to the loading introduction recess presented in Fig. 3.29b. Abaqus/Explicit solver was used for the solution of the FEAs. The explicit solver parameters and the energy balances of the FEAs are given in Annex-C.

Table 3.32: Interaction properties between the FE-model components of SMIBC-CC test campaign.

Connected Components	Interaction Method	Interaction Properties	
		ND	TD
Anchor Plate to Corbel Plate	Tie Constrain	N/A	N/A
Anchor Plate to Concrete Column	General Contact	Hard	Penalty Friction ($\mu = 0.5$)
Headed-fasteners to Concrete Column	General Contact	Hard	Penalty Friction ($\mu = 0.5$)
M42-Rod to Concrete Column	General Contact	Hard	Penalty Friction ($\mu = 0.5$)

ND: Normal Direction, TD: Tangential Direction

a) Constitutive Material Model for Concrete Components

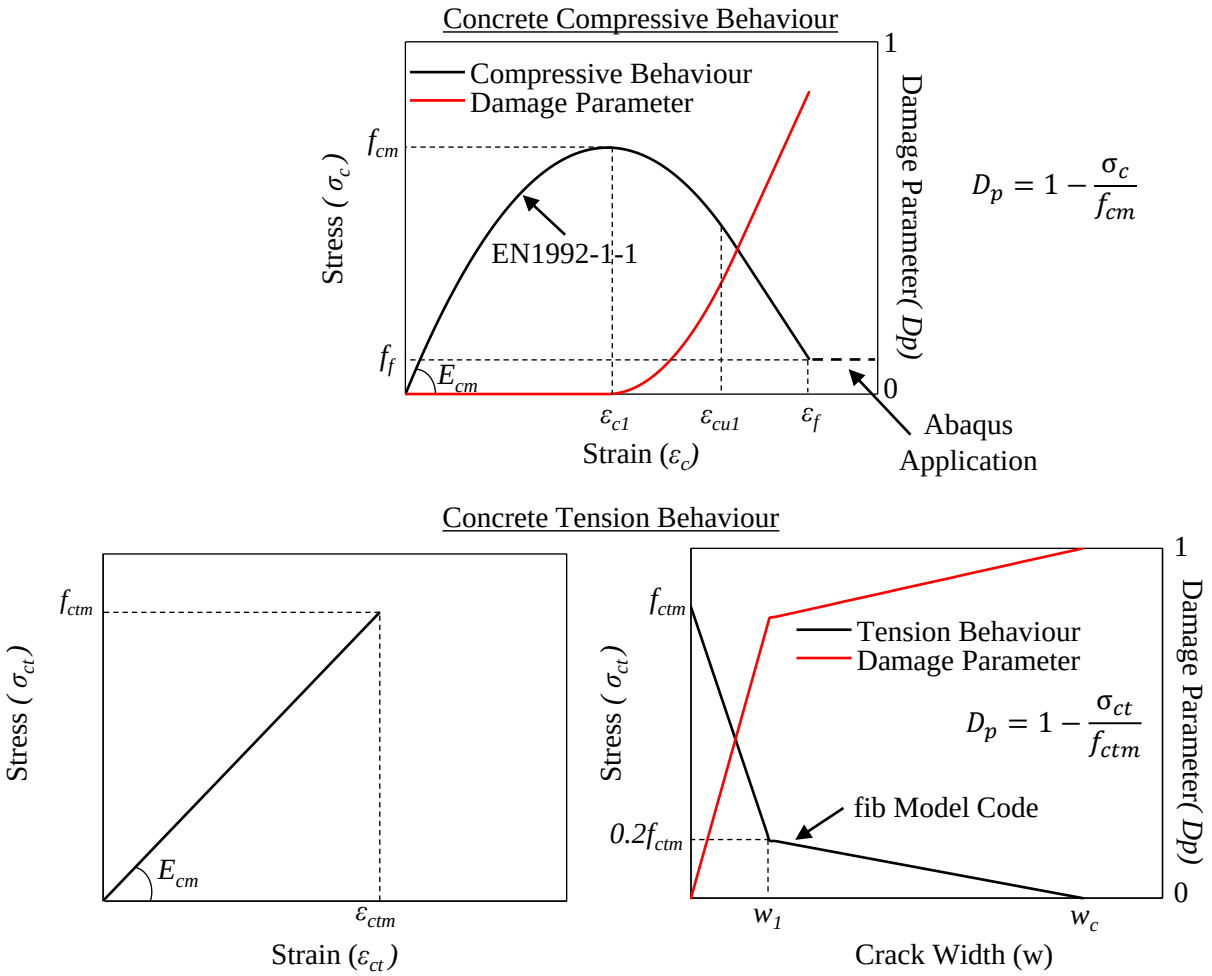

b) Constitutive Material Models for Steel Components

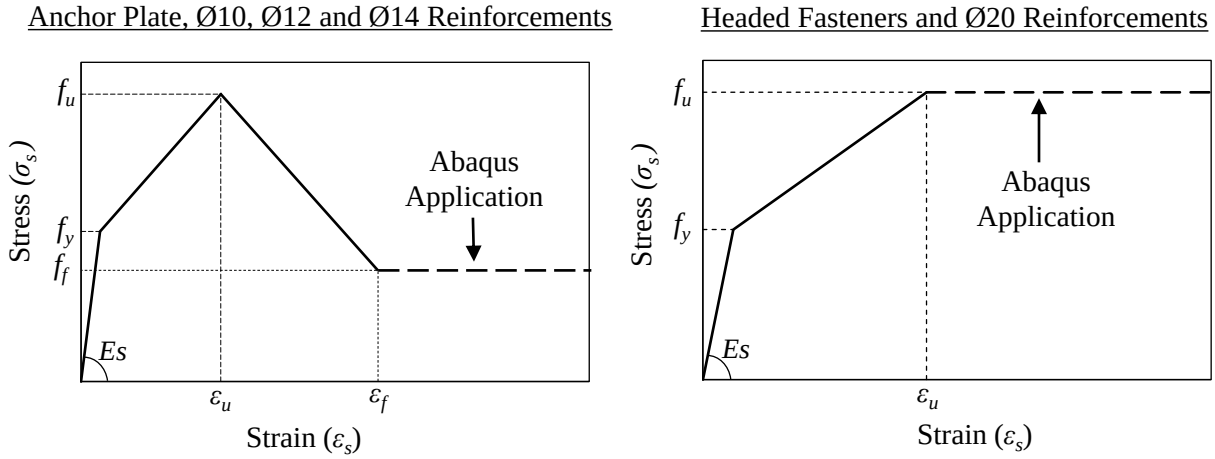

Figure 3.91: Illustration of the material laws assigned to FEA model components.

Fig. 3.92 compares the load-deformation behaviors obtained from the experimental tests with the outputs results of the FEAs. It could be noticed in Fig. 3.92b that the initial elastic rotational stiffness for CC-02 and CC-03 test specimens was higher than the corresponding FEAs. This difference is due to the fact that the experimental moment-rotation curves were derived by subtracting the global column displacements from the anchor plate displacements based on Eq. 3.31. Thus, any perturbation in the global column behavior might had impact on the presented experimental moment-rotation curves. Therefore, the translational and rotational stiffness values for the tested anchorages presented in Table 3.28 are re-assessed in Table 3.33 based on the output results of the FEAs for more precise characterization of the anchorage behaviors. Additionally, the rotation outputs of the FEAs could be noticed to last longer compared to the test results in Fig. 3.92 as the displacement transducers positioned at the upper edge of the anchor plate (see Fig. 3.38/DT-3 and DT-4) reached their measurement limits (see Table 3.24 and Figs. 3.54, 3.69, 3.84) during the tests.

Fig. 3.93 to Fig. 3.95 compare the crack patterns at the section cuts of the test specimens with the crack patterns estimated by the FEAs together with the development of the pull-out failure of the upper headed-fasteners by means of the damaged concrete volume under the head of the fasteners. It is important to note that the crack patterns of FEA in Fig. 3.93 was presented with isosurface tool of the software as the section cut from the experimental test also includes part of the side surface.

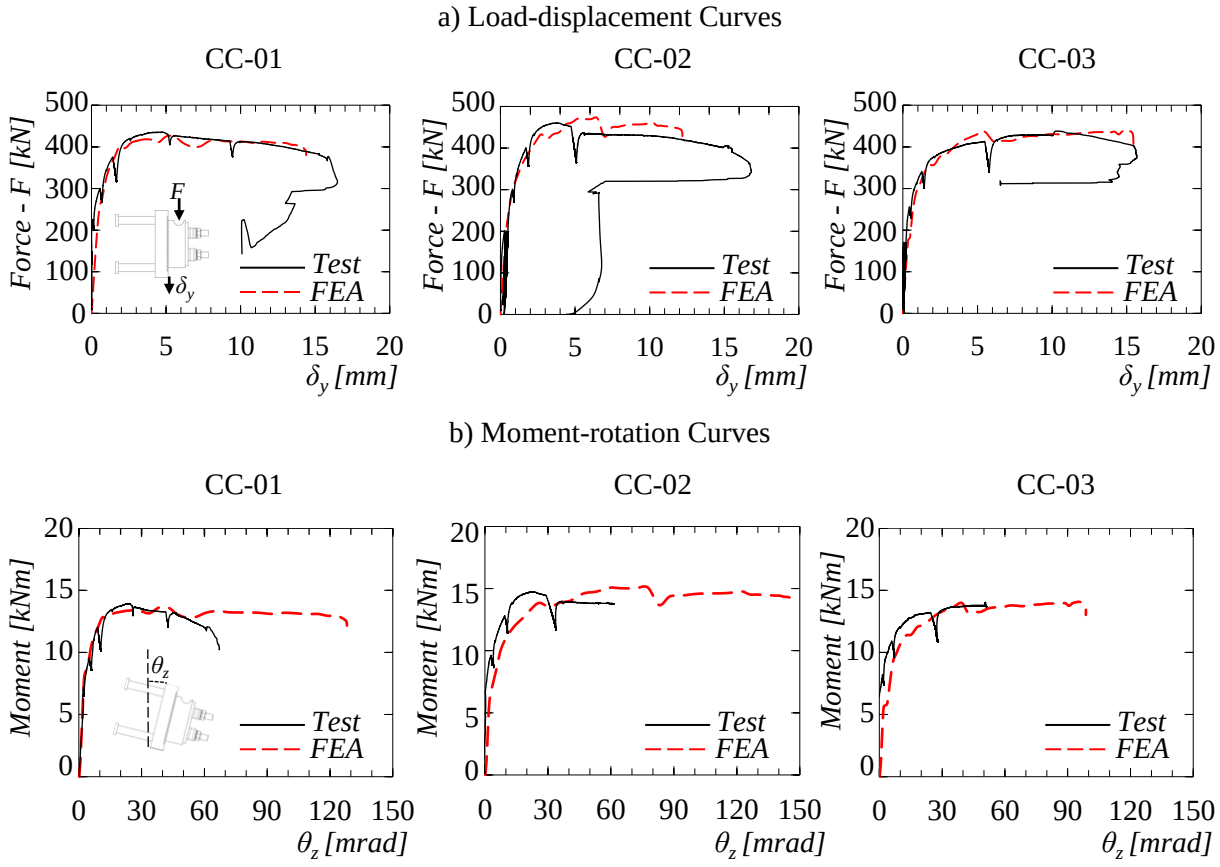

Figure 3.92: Comparison of the test results and FEAs / SMIBC-CC test campaign.

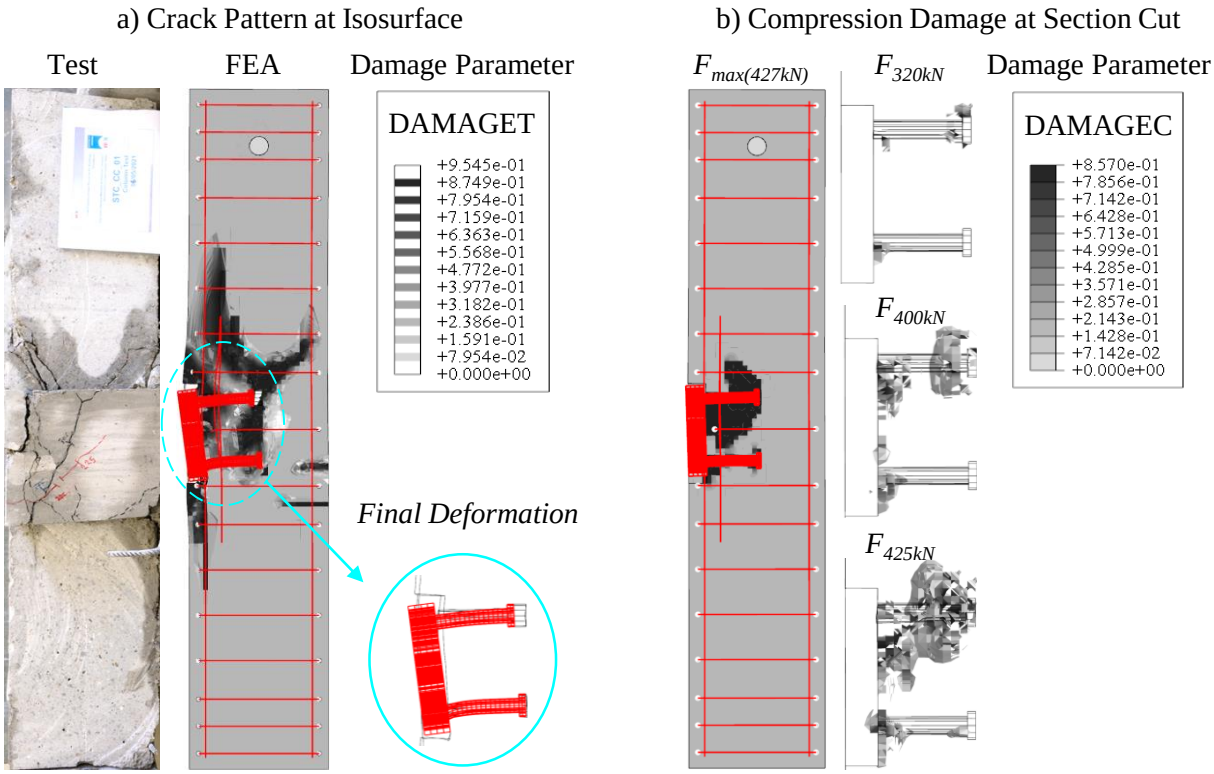

Figure 3.93: Comparison of the crack patterns and the pull-out failure mode / CC-01.

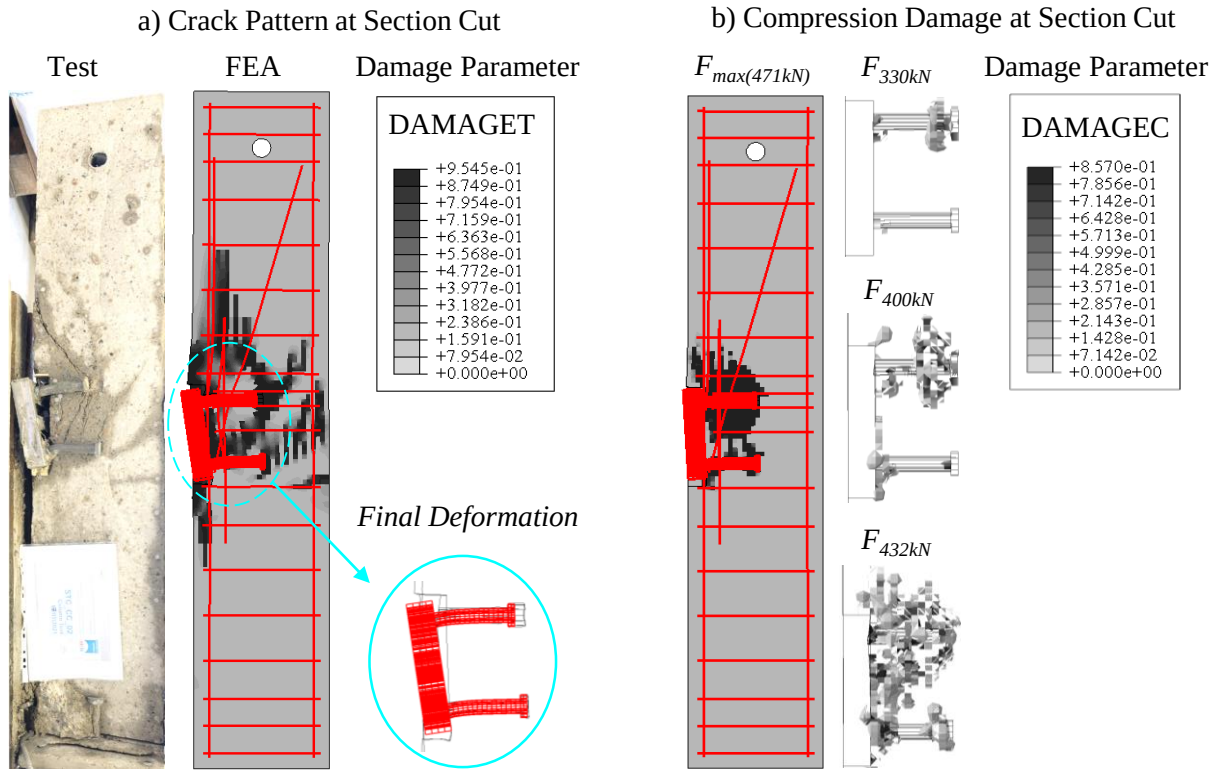

Figure 3.94: Comparison of the crack patterns and the pull-out failure mode / CC-02.

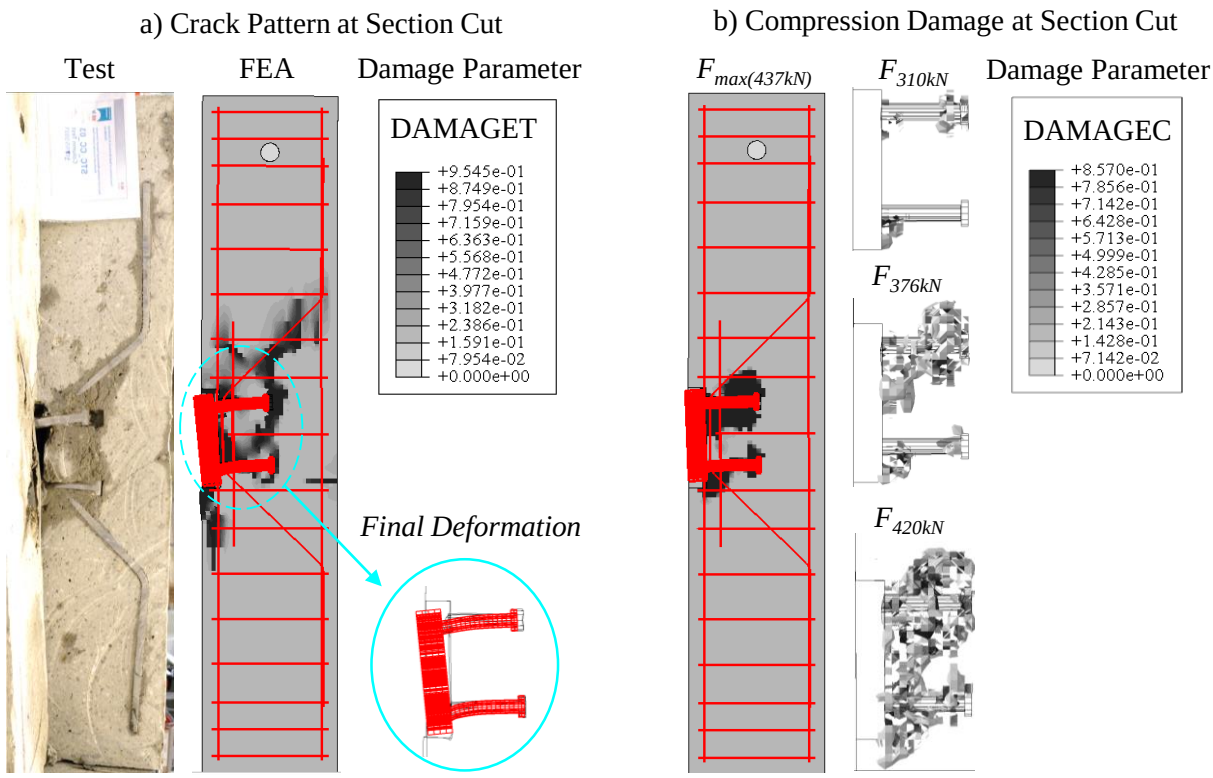

Figure 3.95: Comparison of the crack patterns and the pull-out failure mode / CC-03.

Table 3.33: Comparison of the load-deformation characteristics of SMIBC-CC test specimens.

Test ID	$F_{u,FEA}$ [kN]	$\delta_{y,at\ F_{u,FEA}}$ [mm]	$k_{ini,FEA}$ [kN/mm]	$k_{sec,FEA}$ [kN/mm]	$S_{ini,FEA}$ [kNm/mrad]	$S_{sec,FEA}$ [kNm/mrad]
CC-01	425	5.01	526	138	2.67	1.08
CC-02	472	6.50	588	109	2.67	0.55
CC-03	440	15.02	556	115	2.67	0.46

According to the presented details, it is concluded that the FE-models are capable to simulate the experimental tests with high accuracy by means of both global and local behaviours. Therefore, the FE-models of the test specimens could be used to estimate the resistance contribution of the concrete, steel and frictional components against the applied loading. Thereby, it becomes possible to investigate the load-bearing behavior of each component activated in the experimental tests and perform an assessment of design methodology presented by the current European code of practice for fastenings for use in concrete [1] as detailed in the following section.

3.3.8 Assessment of EN1992-4 with respect to SMIBC-CC test campaign

Table 3.34 presents the nominal values for the design and the mean capacities of the load-bearing components of the tested anchorages according to EN1992-4 [1]. The design capacities were calculated as consisted with EN1992-4 [1] based on the ordered material grades presented in Table 3.21 and Table 3.22. The mean capacities were calculated by using the mean material properties presented in Table 3.30 and Table 3.31 and multiplying the design equations of EN1992-4 [1] with calibration factors where necessary as defined in Table 3.34.

Comparing the tension and the shear design capacities of the headed-fasteners presented in Table 3.34 with the design capacities of the other failure modes, it could be concluded that the failure of the headed-fasteners is unlikely for the tested anchorages as the interaction for the tension and shear forces on the headed-fasteners is evaluated with an expression identical to Eq. 3.34 but by using an exponent equal to two (α=2) in EN1992-4 [1]. In fact, this outcome is deliberate as SMIBC-CC test campaign was designed to investigate the impact of the steel reinforcements positioned next to the anchor plate on the load-deformation behavior of the tested anchorages. Therefore, also considering the detailed results presented in Section 3.3.6.1 to Section 3.3.6.3, it is decided to exclude that the steel failure of the headed-fasteners for the assessment.

According to EN1992-4 [1], if the anchorage is subjected to tension and shear forces simultaneously, the design capacity of the anchorage against the interaction of the tension and shear forces could be verified with Eq. 3.34 for the failure modes other than steel failure of the fasteners. In this expression, N_{Ed} and V_{Ed} (see Fig. 3.96) correspond to the design tension and the shear forces on the anchorage while $N_{Rd,i}$ and $V_{Rd,i}$ are the minimum individual design tensile and shear resistances of the possible failure modes. In EN1992-4 [1], the exponent (α) is defined if the design of the anchorage relies on the supplementary reinforcements against tension and shear forces as follows;

$$\left(\frac{N_{Ed}}{N_{Rd,i}}\right)^{\alpha} + \left(\frac{V_{Ed}}{V_{Rd,i}}\right)^{\alpha} \leq 1 \tag{3.34}$$

- For fastenings with supplementary reinforcement against both tension and shear forces, α=1.5,
- For fastenings with supplementary reinforcement against either tension or shear forces, α=0.67 and it is required to satisfy the following conditions;

$$\frac{N_{Ed}}{N_{Rd,i}} \leq 1 \quad and \quad \frac{V_{Ed}}{V_{Rd,i}} \leq 1 \tag{3.35}$$

Furthermore, EN1992-4 [1] indicates that if the design of the anchorage relies on the supplementary reinforcements against tension or shear, or for both of them;

- $N_{Rd,i}$ or/and $V_{Rd,i}$ in Eq. 3.34 for concrete cone failure mode (tension) and concrete edge failure mode (shear) is/are replaced with corresponding value/values of the supplementary reinforcement failure resistances.

Table 3.34: The nominal values of the design and the mean capacities for the load-bearing components of the tested anchorages.

Loading	Failure Mode	Section EN1992-4 [1]	Calibration Factor[1]	Design *(Rd,i)* and Mean Capacities *(Rm,i)* [kN]					
				CC-01		CC-02		CC-03	
				Design	Mean	Design	Mean	Design	Mean
Tension[9]	Steel Failure of Fasteners [2], N_s	7.2.1.3	N/A	237	372	237	372	237	372
	Concrete Cone[3], N_c	7.2.1.4	1.25 [82]	44	89	44	89	44	89
	Pull-out[3], N_p	7.2.1.5	1.15 [83]	244	492	244	492	244	492
	Rein. Yielding[4], N_{re}	7.2.1.9.1	N/A	137[5]	178[5]	273	356	137[5,6]	178[5,6]
	Rein. Anchorage[4], N_a	7.2.1.9.2	N/A	48[5]	78[5]	111	177	48[5,6]	78[5,6]
Shear	Steel Failure of Fasteners[7], V_s	7.2.3.1	N/A	341	447	341	447	341	447
	Concrete Pry-out[3], V_{cp}	7.2.1.4	1.25 [82]	102	207	102	207	102	207
	Rein. Yielding[4], N_{re}	7.2.1.9.1	N/A	N/A	N/A	137	178	N/A[6]	N/A[6]
	Rein. Anchorage[4], V_a	7.2.2.6.3	N/A	N/A	N/A	N/A[8]	N/A[8]	N/A[6]	N/A[6]

NOTE-1: The calculations presented in this table were performed based on the geometry of the anchor plates and the headed-fasteners presented in Fig. 3.29a.

[1] The calibration factors are used to estimate the mean load-bearing capacities based on characteristic capacities calculated according to EN1992-4 [1].

[2] Only the upper row of the headed-fasteners (2 pieces) are considered to calculate the steel failure of the fasteners against tension.

[3] The calculations are performed with uncracked concrete conditions.

[4] The yield and anchorage failure capacities of the supplementary reinforcements are calculated according to EN1992-4 [1] based on the detailing presented in Fig. 3.34.

[5] Although the anchorages of CC-01 and CC-03 test specimens were not detailed with additional tension supplementary reinforcements, the regular column stirrups reinforcements positioned next to upper row of the headed-fasteners (see Fig. 3.34a - Pos.-2 and Pos.-4) are also effective against concrete-cone failure mode according to EN1992-4 [1].

[6] The load-bearing capacity contribution of the special shape supplementary reinforcements of CC-03 test specimen (see Fig. 3.34c/Pos.-7) are not considered against tension and shear forces in the anchorage as the geometry and position of them are not consisted with the supplementary reinforcement definition of EN1992-4 [1].

[7] Both the upper and the lower rows of the headed-fasteners (4 pieces) are considered to calculate the steel failure of the fasteners against shear.

[8] According to Clause 7.2.2.6.3 (1) of EN1992-4 [1] if the supplementary reinforcements are in the shape of stirrups or loops in contact with the fasteners (Fig. 3.34b - Pos.5 Pos.6) no proof of the anchorage capacity of the supplementary reinforcement is necessary.

[9] According to Clause 7.2.1.8 (1) of EN1992-4 [1] as the edge distance of the fasteners (c=*100mm* see Fig. 3.29a) is longer than the half of the effective height of the fasteners (h_{ef}=*110mm* see Fig. 3.29a), i.e. $0.5(h_{ef}=110mm) \leq c$, the blow-out failure mode is not required to be verified.

To summarize, according to EN1992-4 [1], the supplementary steel reinforcements are only considered to be effective against concrete-cone failure or/and concrete-edge failure modes. As a result, EN1992-4 [1] does not directly consider the load-bearing capacity of the shear supplementary reinforcements against the pry-out failure mode. Furthermore, EN1992-4 [1] ignores the residual load-bearing capacity of the concrete volume against concrete-cone (tension) and concrete-edge (shear) failure modes if the design relies on the supplementary reinforcements.

Having investigated the design rules of EN1992-4 [1] for the anchorages with headed-fasteners and supplementary reinforcements subjected to both tension and shear forces, Eq. 3.34 could be evaluated with respect to the experimental results of SMIBC-CC test campaign by replacing the terms that correspond to the design capacities against tension and shear forces, i.e. $N_{Rd,i}$ and $V_{Rd,i}$, with the mean capacities, i.e. $N_{Rm,i}$ and $V_{Rm,i}$, of the corresponding load bearing components.

In addition, to perform the assessment, it is also required to replace the design tension and shear forces in the anchorage, i.e. N_{Ed} and V_{Ed}, with the actual tension and shear forces, i.e. N_{Test} and V_{Test}. As consisted with EN1992-4 [1], ignoring the contribution of the frictional resistance between the concrete column and the anchor plate, the applied test load (F_{Test}) could be accepted to be equal to the actual shear force in the anchorage (V_{Test}). Furthermore, the actual tension force in the anchorage resulted due to the load-eccentricity could be estimated with a 2D simplified load-distribution defined by assuming the rigid rotation of the anchor plate (see Figs. 3.50, 3.65, 3.80) as shown in Fig. 3.96a. The height of the compression zone (h_{comp}) for the simplified load-distribution is calculated using rectangular compression stress block [72] by assuming that the quarter of the anchor plate height ($h_{anchor\text{-}plate}$=*200mm* - see Fig. 3.29a) is subjected to the compressive stresses [84]. Thereby, the magnitude of the actual tension force in the anchorage (N_{Test}) could be estimated with Eq. 3.36 as a mathematical manipulation of the applied load. The level-arm (z) that appear in Eq. 3.36 is the distance between the central axis of the upper row of the headed-studs and the central axis of the rectangular compressive stress block.

$$N_{Test} = \frac{(e + t_{anchor} + d_{studs}) \cdot F_{Test}}{z} \qquad (3.36)$$
$$N_{Test} = 0.63 \cdot F_{Test} \;\; where; \;\; F_{Test} = V_{Test}$$

Having defined the mean capacities of the individual load-bearing components in Table 3.34 and the relation between N_{Test} and V_{Test} with respect to the applied load (F_{Test}) by Eq. 3.36, the ultimate load-bearing capacity of the tested anchorages (F_u) could be estimated with Eq. 3.37. Consequently, Table 3.35 presents the assessment of EN1992-4 [1] with respect to SMIBC-CC test camping.

$$\left(\frac{0.63 \cdot F_{u,Test}}{min(N_{Rm,i})}\right)^{\alpha} + \left(\frac{F_{u,Test}}{min(V_{Rm,i})}\right)^{\alpha} = 1 \qquad (3.37)$$

- If the design relies on the supplementary reinforcements; The terms $min(N_{Rm,i})$ and $min(V_{Rm,i})$ shall be based on the anchorage or the yield capacity of the supplementary reinforcements.

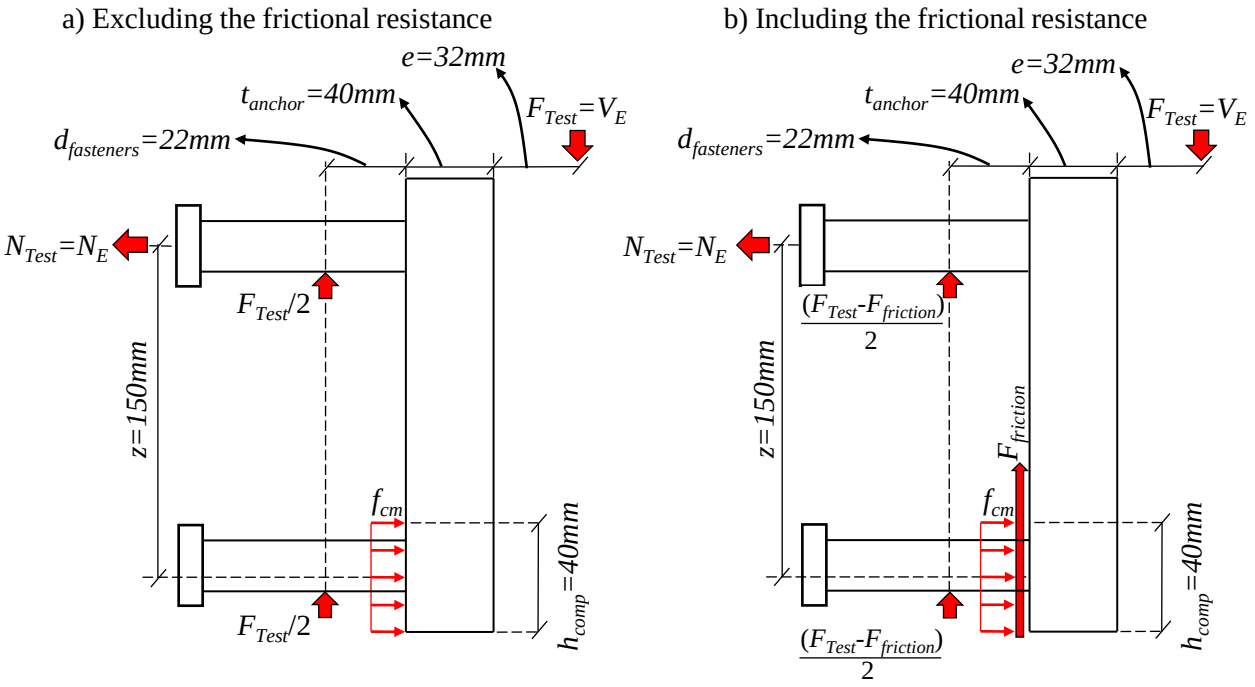

Figure 3.96: 2D - Simplified load-distribution on the anchor plate for SMIBC-CC test campaign.

Table 3.35: Assessment of EN1992-4 with respect to the experimental test results.

Loading	Assessment Criteria	CC-01	CC-02	CC-03
Tension	Tension Supp. Rein.	YES	YES	YES[1]
	Tension Failure Mode	Rein. Anchorage	Rein. Anchorage	Rein. Anchorage
	$min(N_{Rm,i\text{-}see\ Table\ 3.34})$ [kN]	78	177	78
Shear	Shear Supp. Rein.	NO	YES	NO[1]
	Shear Failure Mode	Pry-out	Pry-out [2]	Pry-out
	$min(V_{Rm,i\text{-}see\ Table\ 3.34})$ [kN]	207	207	207
N-V Interac.	Estimator	Eq. 3.37	Eq. 3.37	Eq. 3.37
	Exponent, α	0.67	1.5	0.67
	$F_{u,Test\text{-}estimated}$ [kN]	55	149	55
	$F_{u,Test\text{-}actual}$ [kN]	435	460	438
Difference: $F_{u,Test\text{-}actual} \div F_{u,Test\text{-}estimated}$		7.96	3.09	7.96

[1] The special shape supplementary reinforcements of CC-03 test specimen (see Fig. 3.34c - Pos.7) are not consisted with the supplementary reinforcement definition of EN1992-4 [1]; Thus, their resistance against tension and shear forces is not considered in the assessment.

[2] The resistance of the shear supplementary reinforcements of CC-02 test specimen (see Fig. 3.34c - Pos.5 and Pos.6), against the pry-out failure mode is not considered in EN1992-4 [1]; Thus, their resistance is not taken account for the pry-out resistance of the anchorage.

According to the ratio of the actual ultimate test loads ($F_{u,Test\text{-}actual}$) and the estimations ($F_{u,Test\text{-}estimated}$) presented in Table 3.35, it is concluded that the current European code for design of fasteners for use in concrete [1] is highly conservative.

Therefore, a modified methodology is proposed based on the output results of the FEAs presented in the previous section and the observations from the experimental tests to create a basis for further development of the design rules presented in EN1992-4 [1].

3.3.9 Modified methodology for the design of headed-fasteners for use in concrete

The previous studies showed that the frictional resistance between an anchor plate and a concrete member plays a crucial role in the ultimate load-bearing capacity of an anchorage subjected to an eccentric-loading [13, 74]. Thus, the simplified load-distribution presented in Fig. 3.96a should be revised by including the frictional resistance against the applied loading as shown in Fig. 3.96b. Thereby, the total shear force in the anchorage (V_{Test}) could be re-defined with Eq. 3.38. It is important to note that the non-linear relation between the frictional resistance ($F_{friction}$) and the tension force in the upper row of the headed-fasteners (N_{Test}) is not taken into account for the simplicity. In addition, the frictional resistance between the fasteners and the concrete is also ignored. It also important to mention that the lever arm (z) defined in Fig. 3.96 may be re-calculated with an iterative procedure to achieve further precision for the modified methodology.

$$
\begin{aligned}
V_{Test} &= F_{Test} - F_{friction} \\
&\textit{where;} \\
F_{friction} &= N_{Test} \cdot \mu_{=0.5} \\
&\textit{and;} \\
N_{Test} &= 0.63 \cdot F_{Test} \\
&\textit{thus;} \\
V_{Test} &= 0.685 F_{Test}
\end{aligned}
\tag{3.38}
$$

Having redefined the action effects in the anchorage considering the frictional resistance between the anchor plate and the column, Eq. 3.37 could be revised to estimate the ultimate test load as provided in Eq. 3.39;

$$
\left(\frac{0.63 \cdot F_{u,Test}}{min(N_{Rm,i})}\right)^{\alpha} + \left(\frac{(1 - 0.63 \cdot \mu) \cdot F_{u,Test}}{min(V_{Rm,i})}\right)^{\alpha} = 1 \tag{3.39}
$$

As it was earlier indicated in Section 3.3.2, EN1992-4 [1] does not consider the simultaneous resistance of concrete volume and supplementary steel reinforcements, and considers only the resistance of the concrete volume or the steel reinforcements in the design equations. This assumption is also adopted for the modified methodology as it is required to develop stiffness based design

concept [13] to be able to consider the load-bearing resistances of the concrete and steel components simultaneously.

On the other hand, in EN1992-4 [1], only stirrups and loop shape steel supplementary reinforcements are considered to be effective against the tension and shear forces in the anchorage. However, it is shown in Fig. 3.82 that the special shape supplementary reinforcements of CC-03 test specimen also resisted the applied loading; therefore, their contribution should be also included for the estimation of the ultimate test load of CC-03 test specimen.

Furthermore, although the anchorage resistance of the tension supplementary reinforcements are calculated to be far less than their yield strength as listed in Table 3.34, no anchorage failure of the tension supplementary reinforcements was observed before attaining the ultimate test loads. This dilemma is mainly due to the fact that EN1992-4 [1] ignores the hooks resistance of the stirrup reinforcements for their anchorage capacity calculation [75]. Therefore, the modified methodology ignores the anchorage failure of the steel reinforcements accordingly with the observations from the experimental tests.

Consequently, to precisely estimate the ultimate test load with Eq. 3.39, the mean resistance of the tested anchorages against tension ($N_{Rm,i}$) and shear ($V_{Rm,i}$) forces presented in Table 3.35 should be modified. Therefore, the output results of the FEAs were used for further investigation of the load distribution between the concrete, steel and frictional load-bearing components.

Fig. 3.97, Fig. 3.98 and Fig. 3.99 show the distribution of the tension and shear forces in the anchorages of CC-01, CC-02 and CC-03 test specimens based on their FEAs.

According to the shear force distributions presented in Figs.3.97a, 3.98a and 3.99a, the frictional resistance between the anchor plate and the concrete column against the applied loading could be clearly detected. Thus, the validity of Eq. 3.39 is verified. Furthermore, it could be noticed that the straight reinforcement bars positioned behind the anchor plate (Pos.1, Pos.2 and Pos.3) activates against the shear force in the anchorage, i.e. applied loading. Therefore, the modified methodology considers the load-bearing capacity of the straight reinforcements bars against concrete-pry failure mode if the design of the anchorage against the shear force relies on the steel reinforcements.

Figs. 3.97b, 3.98b and 3.99b present the tension force distributions in the anchorages of CC-01, CC-02 and CC-03 test specimens, respectively. According to the figures, the theoretical cone-shaped concrete breakout-body with 55° was formed for all of the test specimens. Furthermore, the stirrups (Pos.1 to Pos.3) positioned in the theoretical cone-shaped concrete breakout-body resisted the tension force imposed by the upper row of the headed-fastener. On the other hand, according to the limitation of EN1992-4 [1] presented in Fig. 3.97b, the stirrup reinforcement nominated as Pos.3 in Figs. 3.97b, 3.98b, 3.99b may not be considered to be effective against the tension forces in the anchorage as the distance between this reinforcement and the upper row of the headed fastener is higher than $0.75h_{ef}$=*110mm* (see also Fig. 3.34). However, considering the amount of the tension force resisted by this reinforcement (Pos.3) and having ignored the anchorage failure of the steel reinforcements, it is certain that the load-bearing capacity of this reinforcement (Pos.3) is required to be considered to precisely estimate the ultimate test loads. Therefore, the proposed

methodology considers the load-bearing capacity of any stirrup reinforcements against tension force in the anchorage if they are in the theoretical cone-shaped concrete breakout-body.

According to Fig. 3.97a, the load-bearing contribution of the concrete volume against the shear force in the anchorage started to drop at 229kN, which is consisted with the mean pry-out resistance of CC-01 test specimen ($V_{Rm,cp}$=*207kN* - see Table 3.34). In addition, as indicated earlier, the straight reinforcement bars positioned behind the anchor plate (Pos.1 to Pos.3) resisted continuously the shear force in the anchorage. However, it could be noticed that the larger ratio of the applied loading was resisted by the residual strength of the concrete volume and the frictional resistance, thus it is certain for CC-01 test specimen that the shear resistance of the anchorage is limited to the concrete pry-out failure capacity.

Similarly, according to Fig. 3.97b, the ultimate resistance of the concrete volume against the tension force in the anchorage was estimated to be 131kN, and it is shown in the figure that the stirrup reinforcements (Pos.1 to Pos.3) started to resist the tension force in the anchorage after the concrete volume reached its ultimate tension resistance. It could also be seen in the figure that the total tension force imposed by the upper row of the headed-fasteners to the concrete volume was resisted by these stirrup reinforcements at the maximum vertical displacement level of the anchor plate. Therefore, the concrete-cone resistance of the anchorage for CC-01 test specimen could be estimated as the total ultimate resistance of the stirrup reinforcements in the theoretical cone-shaped concrete breakout-body.

In Fig. 3.98a, it is noted the load-bearing contribution of the concrete volume against the shear force started to drop around 166kN. This load-level is 1.25 times less than the mean pry-out resistance of CC-02 test specimen ($V_{Rm,cp=207kN}$) presented in Table 3.34. This difference may be linked to the primary development of the cone-shaped concrete breakout body as presented in Fig. 3.98b. Nevertheless, it could be seen in Fig. 3.98a that both the straight reinforcement bars (Pos.1 to Pos.3) and the supplementary shear reinforcements (Pos.4 and Pos.5) continuously resisted the applied loading with increasing ratio. Therefore, the shear resistance CC-02 test specimen could be estimated as the total ultimate resistance of the straight reinforcement bars and the supplementary shear reinforcements.

According to Fig. 3.98b, as similar to CC-01 test specimen, the entire stirrup reinforcements positioned in the theoretical cone-shaped concrete breakout body activated against the tension force imposed by the upper row of the headed-fasteners after the concrete volume started to lose its load-bearing capacity against the tension force at 111kN. Therefore, the previous statement made for CC-01 specimen could be still considered to be valid and the concrete-cone resistance of the anchorage for CC-02 test specimen could be estimated as the total ultimate resistance of the stirrup reinforcements in the theoretical cone-shaped concrete breakout-body.

In Fig. 3.99a, it is shown that the load-bearing capacity of the concrete-volume against the shear force in the anchorage started to drop at 153kN before reaching the mean concrete pry-out failure capacity of CC-03 test specimen ($V_{Rm,cp}$=*207kN* - see Table 3.34). This outcome could be again attributed to primary development of the cone-shaped concrete breakout body. However,

after 153kN load-level it was possible to further increase the applied loading, thus the shear force in the anchorage was resisted by the straight reinforcement bars (Pos.1 to Pos.3) and the special shape supplementary reinforcements (Pos.4 to Pos.7) continuously. Therefore, it could be stated that the special shape supplementary reinforcements were effective against pry-out failure mode of the anchorage in contrast to EN1992-4 [1]. Consequently, the shear resistance of CC-03 test specimen could be estimated as the total ultimate resistance of the straight reinforcement bars and the special shape supplementary reinforcements. However, it is important to note that the normal force resultants in the special shape supplementary reinforcements presented in Fig. 3.99a were calculated based on the vertical direction (*y-axis*) decomposition of the force in the bend of the reinforcements. Therefore, analogically the ultimate resistance of the special shape supplementary reinforcements against to the shear stress resultants in the anchorage depends on the bend angle (45°- see Fig. 3.34c/ Pos.-7) and could be estimated with Eq. 3.40;

$$N_{Rm,u,re} = f_{u,m} \cdot A_{s,re} \cdot \sin\theta \tag{3.40}$$

$$\textit{where;}$$

$$\theta = \textit{the bend angle and equal to } 45°$$

$$f_{u,m} = \textit{the mean ultimate material strength}$$

$$A_{s,re} = \textit{Stress area of the reinforcement}$$

As a result, the bend angle of the special shape supplementary reinforcements should be determined based on the ratio of the tension and shear forces in the anchorage (see Eq. 3.39), which depends on the magnitude of the load-eccentricity (e) and the friction coefficient (μ) between the anchor plate and the concrete surface.

Finally, in Fig. 3.99b, it is shown that the load-bearing capacity of the concrete volume against the tension force in the anchorage of CC-03 specimen started to drop at 92kN. Accordingly, at this load-level, the tension forces in the stirrup reinforcements (Pos.1 to Pos.3) and the special shape supplementary reinforcements (Pos.4 to Pos.7) started to increase. Consequently, in accordance with the softening of the concrete strength against to the tension force in the anchorage, the total normal force in these reinforcements became equal to the total tension force applied to the anchorage by the upper row of the headed-fasteners. Therefore, it is concluded that the special shape supplementary reinforcements were also effective against the concrete-cone failure mode.

The normal force in the special shape supplementary reinforcements presented in Fig. 3.99b was also calculated based on the horizontal direction (*x-axis*) decomposition of the total force in the bend of the reinforcements. Thus, analogical to Eq. 3.41, the mean ultimate resistance of the special shape supplementary reinforcements against the tension stress resultants in the anchorage depends on the bend angle (45°- see Fig. 3.34c/Pos.-7) and could be estimated with Eq. 3.41;

$$N_{Rm,u,re} = f_{u,m} \cdot A_{s,re} \cdot \cos\theta \tag{3.41}$$

a) Shear force distribution between concrete, steel and frictional components

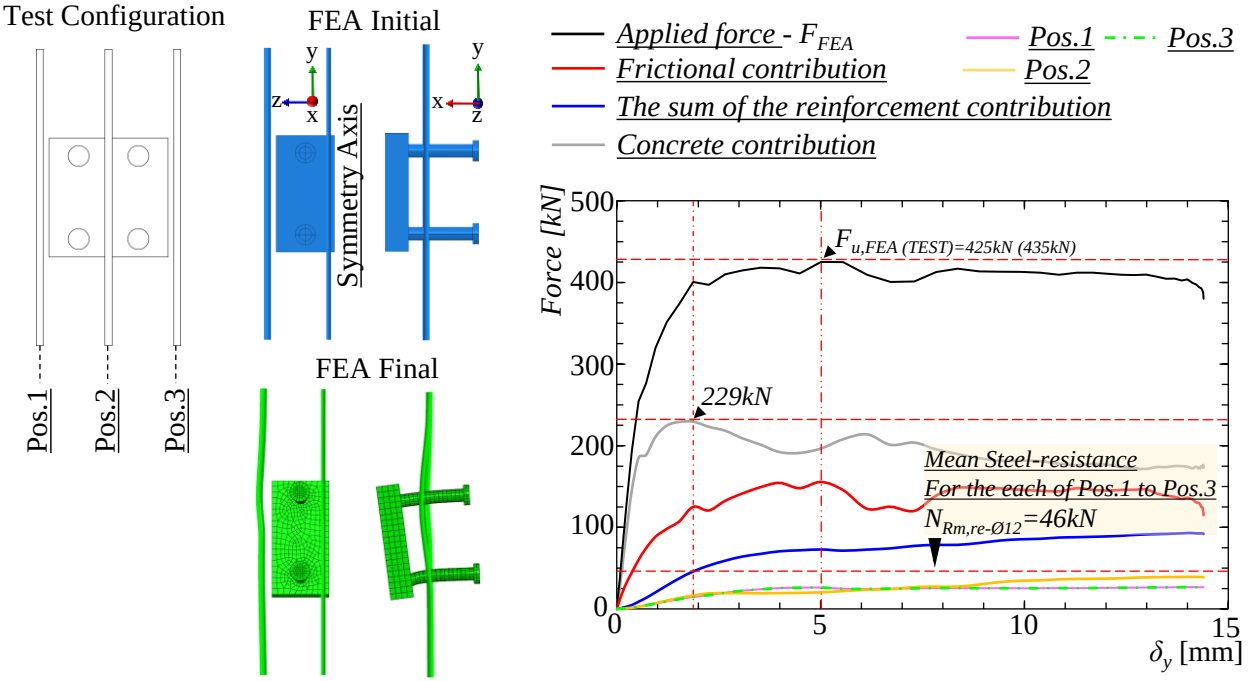

b) Tension force distribution between concrete and steel components

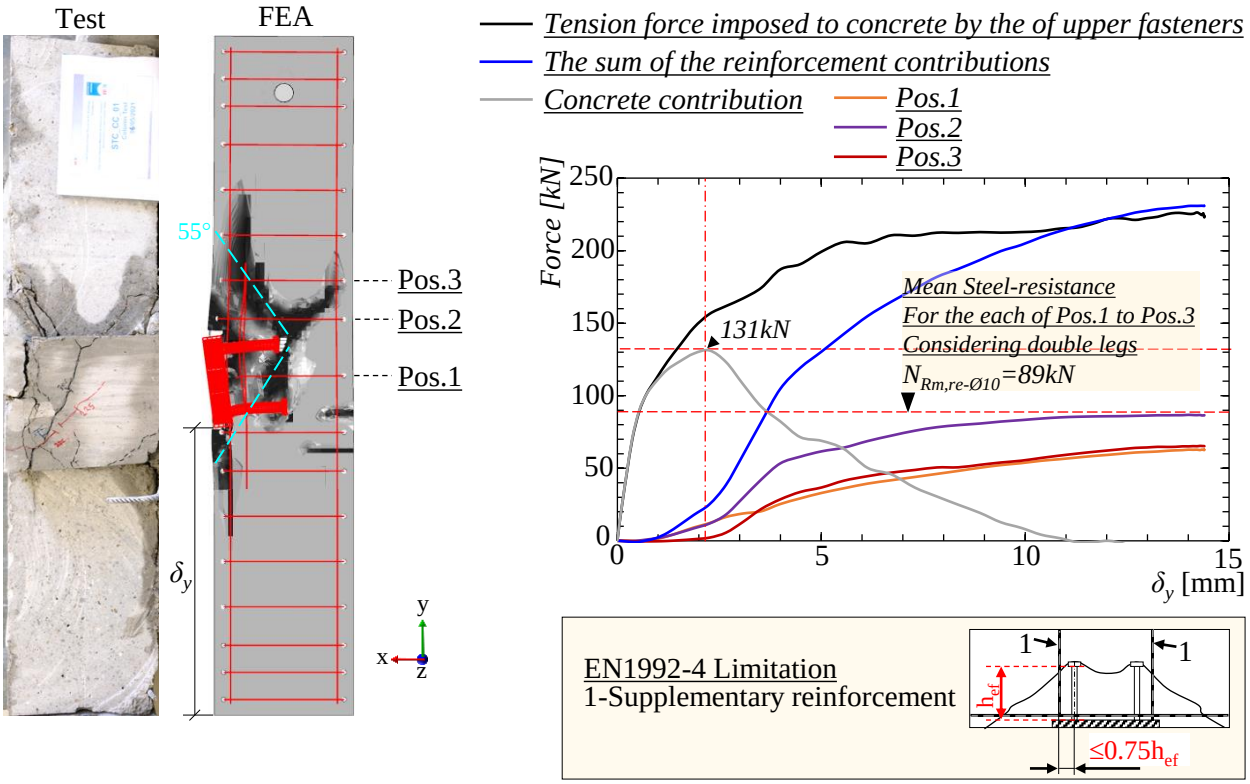

Figure 3.97: Distribution of the shear and tension forces in the anchorage / CC-01.

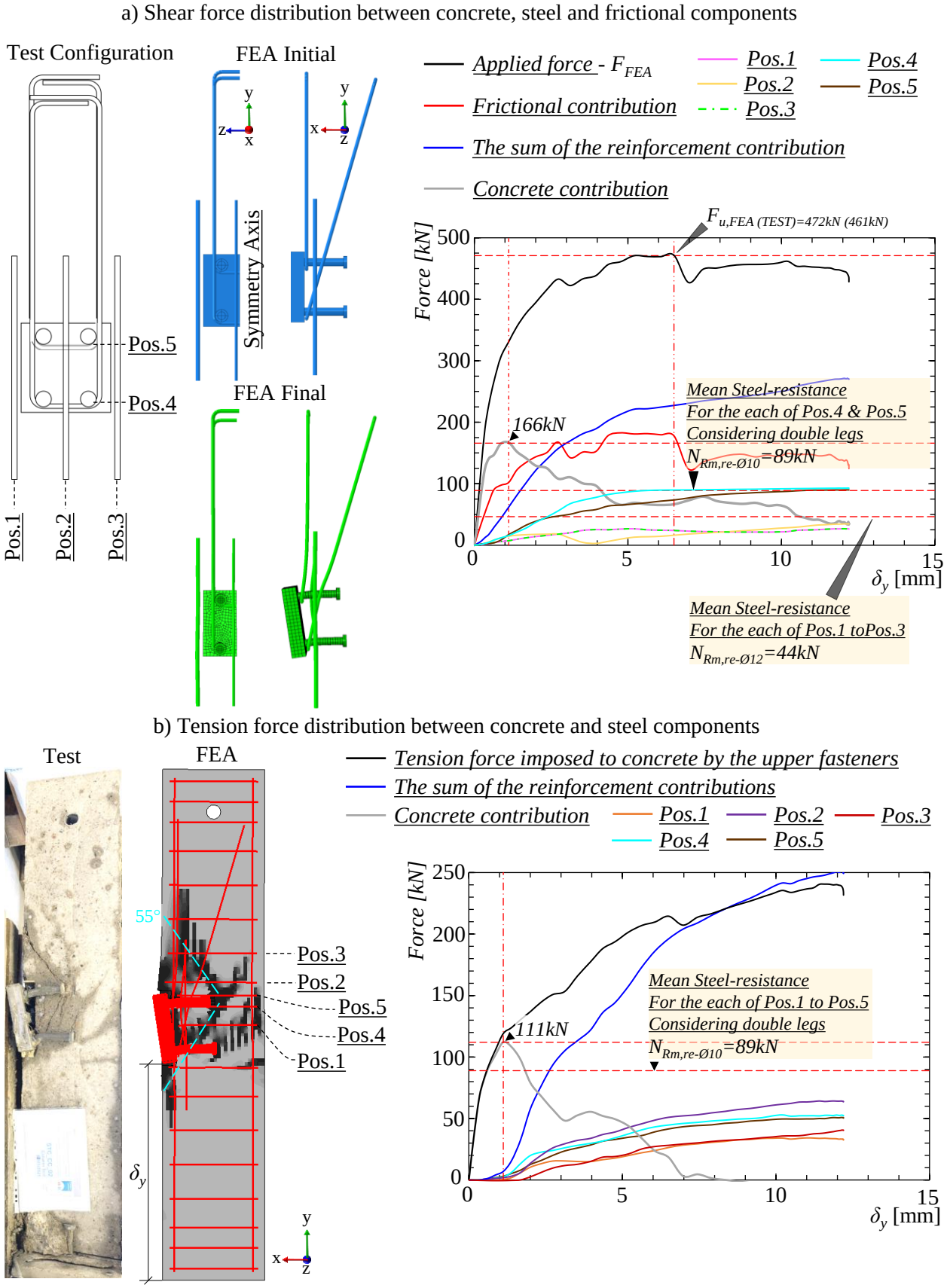

Figure 3.98: Distribution of the shear and tension forces in the anchorage / CC-02.

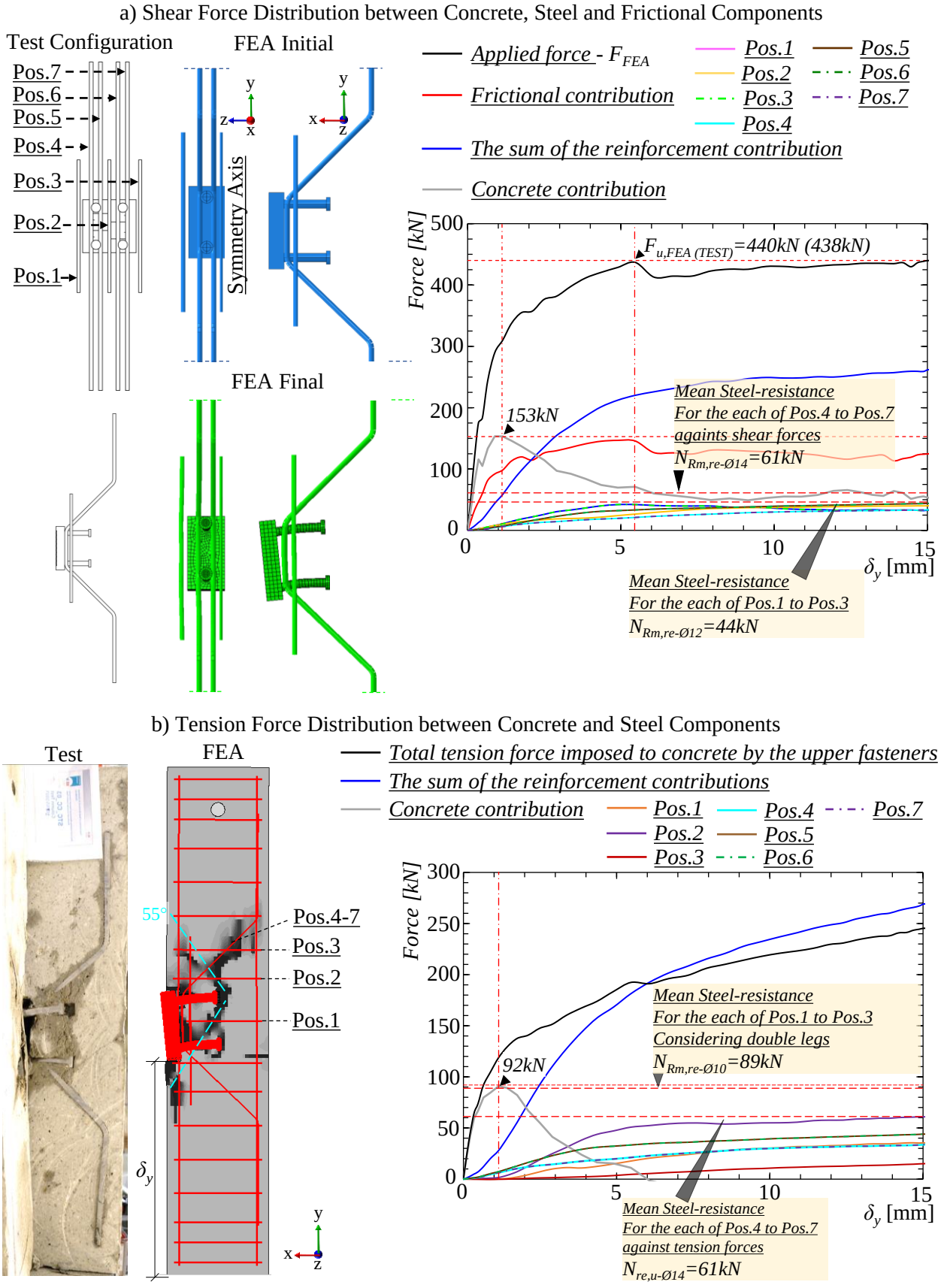

Figure 3.99: Distribution of the shear and tension forces in the anchorage / CC-03.

Identifying the tension and shear force distributions within the vicinity of the anchorage, following conclusions are defined for the application of the modified methodology;

1. Frictional resistance between an anchor plate and concrete surfaces should be taken into account in the calculations of the action effects on an anchorage.
2. Hook resistance against the anchorage failure of the stirrup reinforcements should be included in the calculations of the stirrup reinforcement anchorage capacity;

    - For the assessment of the modified methodology, the anchorage resistance of the steel reinforcements were not calculated because there was no anchorage failure of the reinforcements in the experimental tests.

3. The shear load-bearing capacity of an anchorage with respect to the pry-out failure mode should be estimated based on the higher value of the concrete pry-out capacity or the total ultimate load-bearing capacity of the steel reinforcements positioned in the theoretical pry-out concrete breakout body.
4. The tension load-bearing capacity of an anchorage with respect to the concrete-cone failure mode should be estimated based on the higher value of the concrete-cone capacity or the total ultimate load-bearing capacity of the steel reinforcements positioned in the theoretical concrete-cone breakout body.

    - In contrast to EN1992-4 [1] where the load-bearing capacity of the steel reinforcements in the anchorage is calculated based on the yield strength of the reinforcement material ($N_{Rm,re}$) if no anchorage failure of the reinforcements is expected, the modified methodology suggests calculating the load-bearing capacity of the reinforcements based on the ultimate strength of the reinforcement material ($N_{Rm,u,re}$).

According to the conclusions listed above, the nominal values of the mean capacities for the load-bearing components of the tested anchorages are presented in Table 3.36. Thereby, it becomes possible to estimate the ultimate load-bearing capacity of the tested anchorages with Eq. 3.39 and to assess the modified methodology against to the test results. Table 3.37 presents the assessment of the modified methodology with respect to the test results.

Table 3.36: The nominal values of the mean capacities for the load-bearing components of the tested anchorages according to the modified methodology.

Loading	Failure Mode	Section EN1992-4 [1]	Calibration Factor [1]	Mean (*Rm,i*) Capacities [kN]		
				CC-01	CC-02	CC-03
Tension[8]	Steel Failure of Fasteners[2], N_s	7.2.1.3	N/A	372	372	372
	Concrete Cone[3], N_c	7.2.1.4	1.25 [82]	89	89	89
	Pull-out[3], N_p	7.2.1.5	1.15 [83]	492	492	492
	Steel Failure of Rein.[4], $N_{u,re}$	7.2.1.9.1	N/A	307	511	587[5]
Shear	Steel Failure of Fasteners[6], V_s	7.2.3.1	N/A	447	447	447
	Concrete Pry-out[3], V_{cp}	7.2.1.4	1.25 [82]	207	207	207
	Steel Failure of Rein.[4], $N_{u,re}$	7.2.1.9.1	N/A	205	410	485[7]

NOTE-1: The calculations presented in this table were performed based on the geometry of the anchor plates and the headed-fasteners presented in Fig. 3.29a.

[1] The calibration factors are used to estimate the mean load-bearing capacities based on characteristic capacities calculated according to EN1992-4 [1].

[2] Only the upper row of the headed-fasteners (2 pieces) are considered to calculate the steel failure resistance of the fasteners against tension.

[3] The calculations are performed with uncracked concrete conditions.

[4] The formulation presented in EN1992-4 [1] was modified by using the ultimate material strengths of the reinforcements against the tension and shear stress resultants to calculate the ultimate resistance of the reinforcements. See Table 3.22 for the mean ultimate material strengths of the reinforcement materials.

[5] The steel failure resistance (i.e. ultimate resistance) of the special shape supplementary reinforcements against the tension stress resultants was calculated according to Eq. 3.41

[6] Both the upper and the lower rows of the headed-fasteners (4 pieces) are considered to calculate the steel failure resistance of the fasteners against shear.

[7] The steel failure resistance (i.e. ultimate resistance) of the special shape supplementary reinforcements against the shear stress resultants was calculated according to Eq. 3.40

[8] According to Clause 7.2.1.8 (1) of EN1992-4 [1] as the edge distance of the fasteners (c=100mm see Fig. 3.29a) is longer than the half of the effective height of the fasteners (h_{ef}=110mm see Fig. 3.29a), i.e. $0.5(h_{ef}=110mm) \leq c$, the blow-out failure mode is not required to be verified.

Table 3.37: Assessment of the modified methodology with respect to the experimental test results.

Loading	Assessment Criteria	CC-01	CC-02	CC-03
Tension	Tension Supp. Rein.	YES	YES	YES
	Tension Failure Mode	Steel Failure of Rein.	Pull-out Failure	Pull-out Failure
	$min(N_{Rm,i\text{-}see\ Table\ 3.36)}$ [kN]	307	492	492
Shear	Shear Supp. Rein.	YES	YES	YES
	Shear Failure Mode	Pry-out	Pry-out	Pry-out
	$min(V_{Rm,i\text{-}see\ Table\ 3.36)}$ [kN]	205	410	485
N-V Interac.	Estimator	Eq. 3.39	Eq. 3.39	Eq. 3.39
	Exponent, α	1.5	1.5	1.5
	$F_{u,Test\text{-}estimated}$ [kN]	230	425	467
	$F_{u,Test\text{-}actual}$ [kN]	435	460	438
Difference: $F_{u,Test\text{-}actual} \div F_{u,Test\text{-}estimated}$		1.89	1.08	0.94

Comparing the ratio of the estimated and the actual ultimate load-bearing capacities of the tested anchorages presented in Table 3.37 with the ones presented in Table 3.35, it is concluded that the modified methodology highly improves the design approach of EN1992-4 [1]. Therefore, it could be stated that the design of the anchorage for the use of SMIBC in joint configuration of steel-concrete building frames may be performed based on the modified methodology.

3.3.10 Summary for the investigations of anchorage details for SMIBC joint configuration

This section presented the investigation of the load-deformation behaviours for the novel *"Saw-tooth Interface Mechanical Interlock Bolted Connection - SMIBC"* joint in reinforced-concrete column configurations detailed with and without supplementary steel reinforcements positioned next to the anchor plate of SMIBC. Three different experimental tests were performed by varying the shape and the ratio of the steel reinforcements around the anchor plate. The successive developments of the failure modes identified for the anchorages were presented in detail based on the data recorded during the experimental tests. In addition, section cuts of the test specimens were presented to verify the identified failure modes. The experimental tests were simulated with computer-aided finite element analyses to estimate the distribution of the tension and shear stress resultants between the concrete, steel and frictional resistance components of the anchorages. The finite element modelling technique and solution scheme were validated against the test results. Thereby, according to the output results of the finite element analyses, it was shown that the frictional resistance between the anchor plate and the concrete column plays a crucial role in the ultimate load-bearing capacities of the tested anchorages. Furthermore, it was shown that the all steel

reinforcements positioned next to the anchor plates were activated against to the applied loading.

The experimental test results were compared with the mean ultimate load-bearing capacities of the anchorages calculated according to the formulations of EN1992-4 [1] and it was shown that the current European code of practice for fastenings for use in concrete [1] highly underestimates the ultimate load-bearing capacities of the tested anchorages. Therefore, a modified methodology was proposed based on the formulations of EN1992-4 [1] but considering the frictional resistance and the ultimate strength of the all steel reinforcements activated against to the applied loading. The modified methodology estimated the ultimate load-bearing capacities of the tested anchorages with better accuracy. Therefore, it is concluded that the design of SMIBC joint configuration for use in reinforced-concrete column and walls of steel-concrete hybrid building systems may be performed based on the modified methodology. However, it is crucial to mention that the estimations of the modified methodology were evaluated against only three experimental tests. Therefore, further investigation with variation in the geometry and the reinforcement detailing of the anchorage together with the parametrization of the concrete material properties may lead to further calibration and the statistical assessment for the estimations of the modified methodology by extending the scope this thesis. The last but not the least, this section also presented the practicality of SMIBC to accommodate the construction and manufacturing tolerances and showed that SMIBC could offer flexible solutions for the fast erection of steel beams with reinforced-concrete columns and walls of steel-concrete hybrid building systems.

CHAPTER 4

Bolt-less Plug-in Connection for Steel-concrete hybrid building systems

4.1 Introduction

Under the second work-package (WP2) of the FEOSBuild research project, on site weld-free and bolt-less plug-in connection, here on named as Plug-inC, is developed for the assembly of reinforce-concrete (RC) columns/walls and steel beams of steel-concrete hybrid building systems. The main load-bearing mechanism of Plug-inC is designed with dovetail connector which is produced with computer numerical control (CNC) production technique. Thereby, it is aimed to satisfy high geometrical accuracy for the construction site assembly of the connection components and high reliability for the load-bearing mechanism of Plug-inC.

Fig. 4.1 illustrates the nominal dimensions and overall configuration of Plug-inC together with the detailed illustrations of the connection components which are the anchor plate and the corbel plate with hub and dovetail counterparts, respectively. The dimensions of the dovetail are presented in Fig. 4.1d and listed in Table 4.1. It is important to note that the dimensions of the hub are identical with the dovetail. The joint assembly of Plug-inC is presented in Fig. 4.2. As similar to SMIBC joint assembly, the interaction between the anchor plate and the RC-members is designed to be constructed with headed-fasteners. Consequently, the joint assembly of Plug-inC (Fig. 4.2) requires to install the anchor plate into the formwork of the RC-members in an orientation that the hub of the anchor plate to be in a surface-flush position with the formwork (similar to SMIBC assembly - see Fig. 3.35). Thereby, after the removal of the formwork, the corbel plate of Plug-inC could be connected with the anchor plate by sliding the dovetail into the hub. The connection between the steel beam and the corbel plate is proposed to be realized with shop-welded threaded rods which allow to assemble the steel beams with the corbel plate through the long slotted-holes drilled at the bottom flange of the beams along the longitudinal direction of the beam. Thereby, the construction and manufacturing tolerances could be accommodated with the long slotted-holes for the fast erection of the hybrid building systems as consistent with the global scope of the research project. It is important to note that the shop-welded threaded-rods do not contribute the main load-bearing mechanism of Plug-inC and they are only proposed to securely assemble the steel beams with the corbel plate against possible accidents on the construction sites, e.g. accidental

crane lift in the erection state, and to reduce the vibrations during the erection stages of the building frames. Furthermore, additional M10 locking screws are proposed (see Fig. 4.1a) to prevent any uplift of the corbel plate during the erection stage of the building frames; but, M10 screws also do not have a contribution to the load-bearing capacity of Plug-inC.

For the development of Plug-inC, initially the preliminary design calculations were performed to determine the design action effects required to be resisted by the connection components. Having defined the design action effects, the dimensions of the hub and dovetail counterparts were designed based on the available CNC-production technologies and the results of the preliminary computer aided finite element analysis (FEA). The details for the primary design calculations and production of the hub and dovetail counterparts are given in Section 4.2. The load-displacement and moment-rotation behaviours of Plug-inC were determined with an experimental testing campaign consisting of three experimental tests which are presented in Section 4.3. Furthermore, numerical simulations of the experimental tests were executed by means of FEAs and the output results of the analyses were validated with the test data which are presented in Section 4.4. Simplified analytical resistance models are presented in Section 4.5 to estimate the elastic and ultimate load-bearing capacities of Plug-inC. In addition, the numerical simulation technique was later used in Section 4.6 to perform a parametric study which investigates the impact of the dovetail thickness, dovetail round radius, friction coefficient between the hub and dovetail counterparts and the load-eccentricity on the load-deformation behaviours of Plug-inC. Finally, in Section 4.7 the estimations of the analytical resistance models were evaluated based on the output results of the parametric study, and statistical evaluations of the analytical resistance models were performed according to EN1990, Annex-D [58] to establish partial safety factors for the analytical resistance models.

Table 4.1: Geometrical details of the dovetail and hub counterparts.

Dovetail Angle, θ [°]	45
Dovetail Ratio, $tan(\theta)$	1
Vertical Slope Angle, ϕ [°]	17.1
Vertical Slope, $cot(\phi)$	3.25
Round Radius, R [mm]	40
Thickness, t [mm]	15
Inner Height, h_{inner} [mm]	65
Central Height, h_{centre} [mm]	72.5
Outer Height, h_{outer} [mm]	80
Inner Width, w_{inner} [mm]	120
Central Width, w_{center} [mm]	135
Outer Width, w_{outer} [mm]	150
Aspect Ratio, $\frac{w_{\text{center}}}{t}$	1:9

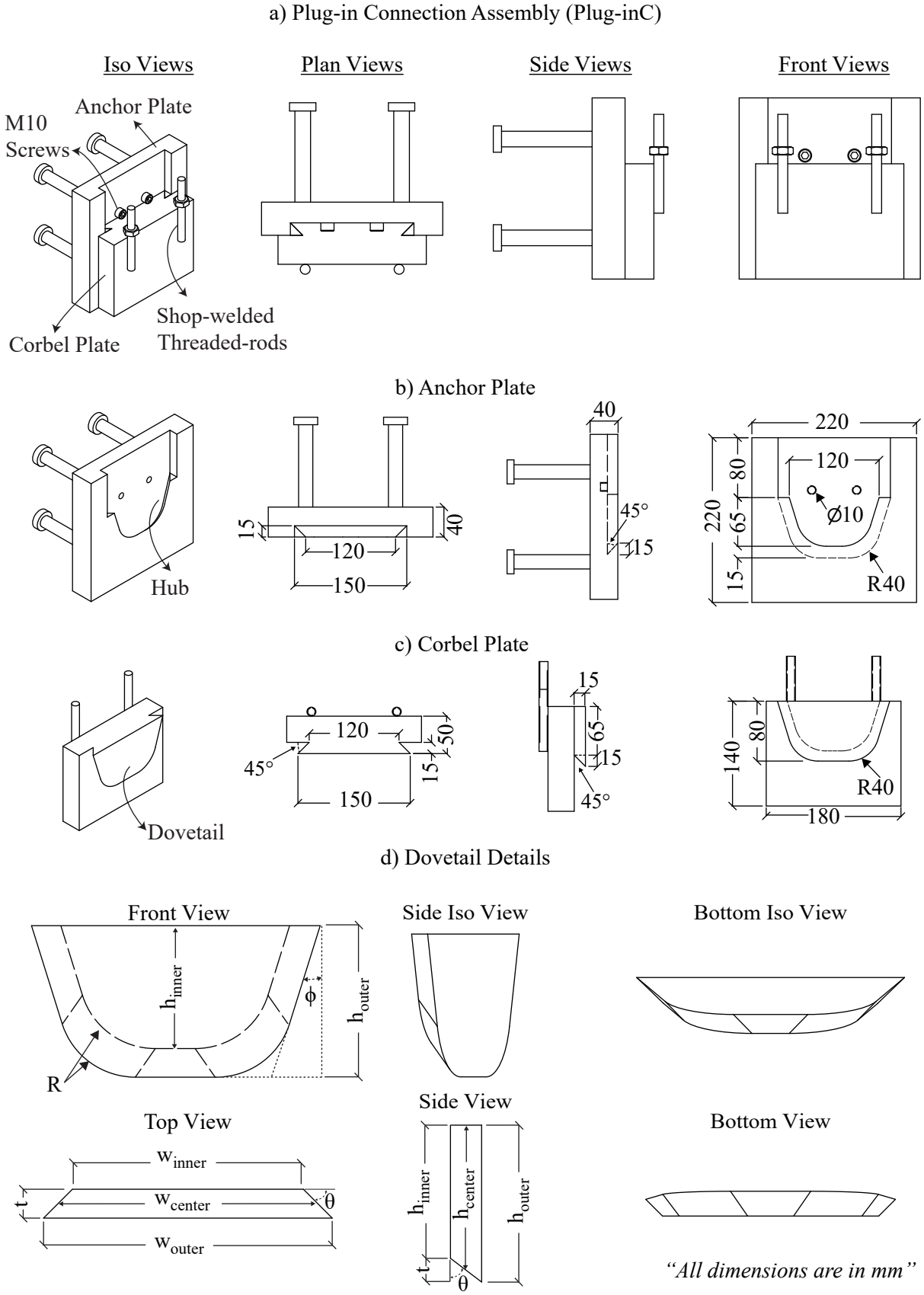

Figure 4.1: Technical drawings of Plug-inC components.

4.2 Design strategy and the production of Plug-inC components

Plug-inC is developed to assemble RC-columns/walls and the steel beams of braced steel-concrete hybrid building systems. Therefore, the minimum design load-bearing capacity of Plug-inC was determined to be higher than the design action effects at the outer boundaries of a simple supported steel-concrete composite slab system with 14m span length and 4m beam intervals. Fig. 4.2b illustrates the structural system used for the calculations of the design action effects to be resisted by Plug-inC. Accordingly, Eq. 4.1 and Eq. 4.2 presents the calculations according to EN1990:2002 [58] and EN1991-1-1 [85].

According to Eq. 4.2, the design load bearing capacity of Plug-inC shall be larger than 478kN. Therefore, for the preliminary design, considering the partial safety factors and the intrinsic lower bounding quantiles required to be applied through statistical analyses to convert the mean test results to the characteristic resistance of Plug-inC, it was decided that the mean load-bearing resistance of Plug-inC ($R_{plug\text{-}inC,m}$) shall be at least 50% higher than the minimum design requirement presented in Eq. 4.2.

$$
\begin{aligned}
L_b &= 14m \\
L_{interval} &= 4m \\
g_{k,0(IPE330)} &= 0.5kN/m \\
g_{k,1(225mm\ concrete\ slab)} &= 22.5kN/m \\
g_{k,2(finishing)} &= 5.4kN/m \\
q_{k(B-Class/C3[85])} &= 20kN/m \\
(g+q)_d = 1.35 \cdot (g_{k,0} + g_{k,1} + g_{k,2}) + 1.5 \cdot (q_k) &= 68.3kN/m
\end{aligned} \tag{4.1}
$$

Thereby;

$$
R_{plug-inC,d} > \frac{L_b \cdot (g+q)_d}{2} = \frac{14 \cdot 68.3}{2} = 478kN \tag{4.2}
$$

Consequently;

$$
\begin{aligned}
R_{plug-inC,m} &> 1.5 \cdot R_{plug-inC,d} \\
R_{plug-inC,m} &> 718kN
\end{aligned} \tag{4.3}
$$

Having defined the minimum required mean load-bearing capacity in Eq. 4.3, the geometric parameters of the hub and dovetail counterparts, which are the dovetail thickness and dovetail round radius, were determined according to the available CNC-production techniques and based on the output results of the preliminary FEAs performed with the characteristic material properties

of commonly available steel grades, i.e. S355 and S235 [50]. The details of the FE-model are presented in Section 4.4. The selection of the proper production technique and common material grades for the development of Plug-inC was crucial as the main goal of the FEOSBuild research project is to develop state-of-the-art connection systems for steel-concrete hybrid buildings that may find large market opportunities in the construction industry. Thus, if costly production techniques or uncommon material grades would be selected, the market integration of the final product would not be feasible. Fig. 4.3 shows the CNC-production of the hub and the dovetail counterparts.

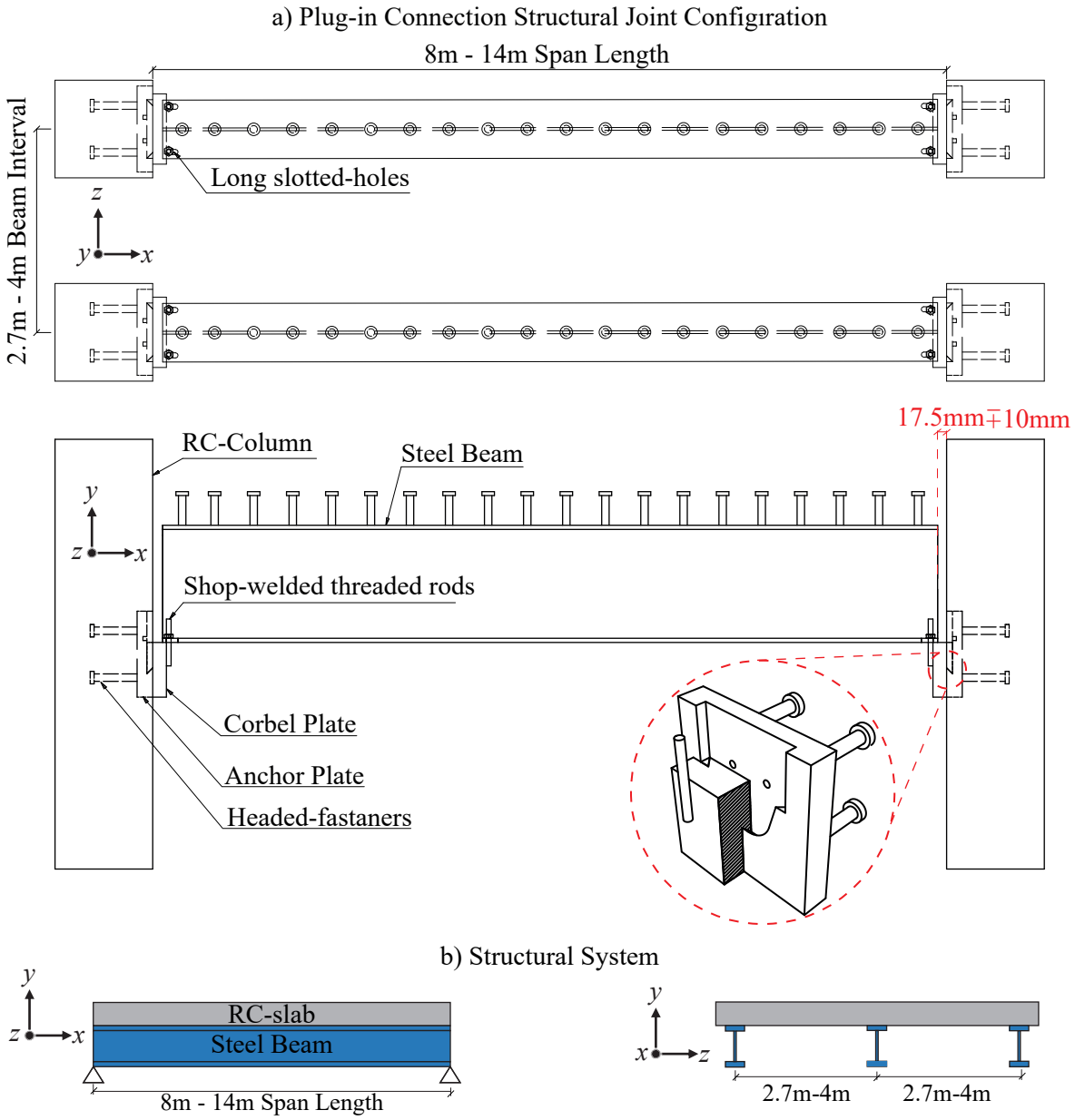

Figure 4.2: Plug-inC joint in reinforced concrete (RC) column configuration.

a) CNC-production of Dovetail Counterparts

b) CNC Inputs and Cutter

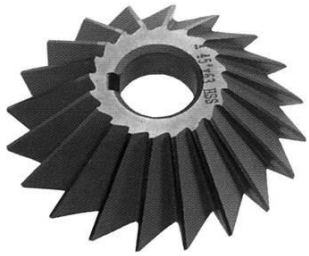

Figure 4.3: CNC-production details of the hub and the dovetail counterparts.

4.3 Experimental test campaign

To determine the load-displacement and moment-rotation behaviors of Plug-inC, three experimental tests were performed in The Structural Laboratory for the University of Wuppertal. As similar to SMIBC experimental test campaigns presented under Section 3.1, the experimental test campaign of Plug-inC was also performed based on an isolated configuration of the connection components. Thus, neither RC-components nor headed-fasteners were included in the tests.

The experimental test set-up was designed to determine the load-bearing capacity and the load-deformation behaviours of Plug-inC under pre-defined load-eccentricity which is *e=17.5mm* and corresponds to the distance between the edge of the steel beam and the concrete surface as highlighted in Fig. 4.2. A symmetric test set-up was used to perform the tests with an uni-axial testing machine. Fig. 4.4 shows the overall configuration of the test set-up together with the technical drawings and the corresponding images of the test specimens. The dimensions of the hub and dovetail counterparts presented in Fig. 4.1 were identical for the test configuration of the inner plate, which is the equivalent of the anchor plate, and the cover plates, which are the equivalent of the corbel plate.

The load-eccentricity was achieved by introducing the loading to the cover plates through M42 threaded-rod holes. The distance between the mid-length of the threaded-rod holes and the outer edge of the dovetail was designed to be equal to 17.5mm as identical to the load-eccentricity

highlighted in Fig. 4.2 (*e=17.5mm*). Furthermore, 10mm gaps were designed between the cover plates and the loading plate to resist the moment action by only the equivalent Plug-inC test configuration. It is important to note that the numerical parametric study presented in Section 4.6 also parameterize the load-eccentricity to investigate its impact on the load-deformation behaviors of Plug-inC. The dimensions and the ordered material grades of the test specimens are listed in Table 4.2.

Table 4.2: Dimensions and ordered material grades of Plug-inC test specimens.

Specimen Name	Dimensions	Ordered Grade
Inner Plates	450x220x70	S235
Cover Plates	460x180x50	S235
Loading Plate	545x140x50	S460
Threaded Rods	M42x300	HV 10.9

4.3.1 Material properties of the main test specimens

The material properties of the inner and the cover plates were determined with coupon tests according to EN ISO 6892-1 [63]. Three coupon samples were manufactured from three different inner and cover plates of each test specimens after the execution of the test campaign. Table 4.3 summarizes the material properties determined based on the coupon tests. In addition, detailed results of the coupon tests are presented in Annex-D.

Table 4.3: Material properties of main Plug-inC test specimens.

Specimen Name	Order	Sample ID	E^1 [GPa]	f_y [MPa]	f_u [MPa]	A[2] [%]
Inner Plate	S235	Plug-inC-01 (IP-1)	207	242	441	36.0
		Plug-inC-02 (IP-2)	207	243	444	35.5
		Plug-inC-03 (IP-3)	209	246	449	34.5
Mean Values			208	244	445	35.3
Cover Plates	S235	Plug-inC-01 (CP-1)	205	226	410	39.5
		Plug-inC-02 (CP-2)	209	263	488	38.0
		Plug-inC-03 (CP-3)	209	255	445	36.5
Mean Values			208	248	434	38.0

[1] Elastic modulus (E) was determined according to EN ISO 6892-1 Method A1 [63].

[2]The term A corresponds to percentage elongation of the steel coupon after the fracture [63].

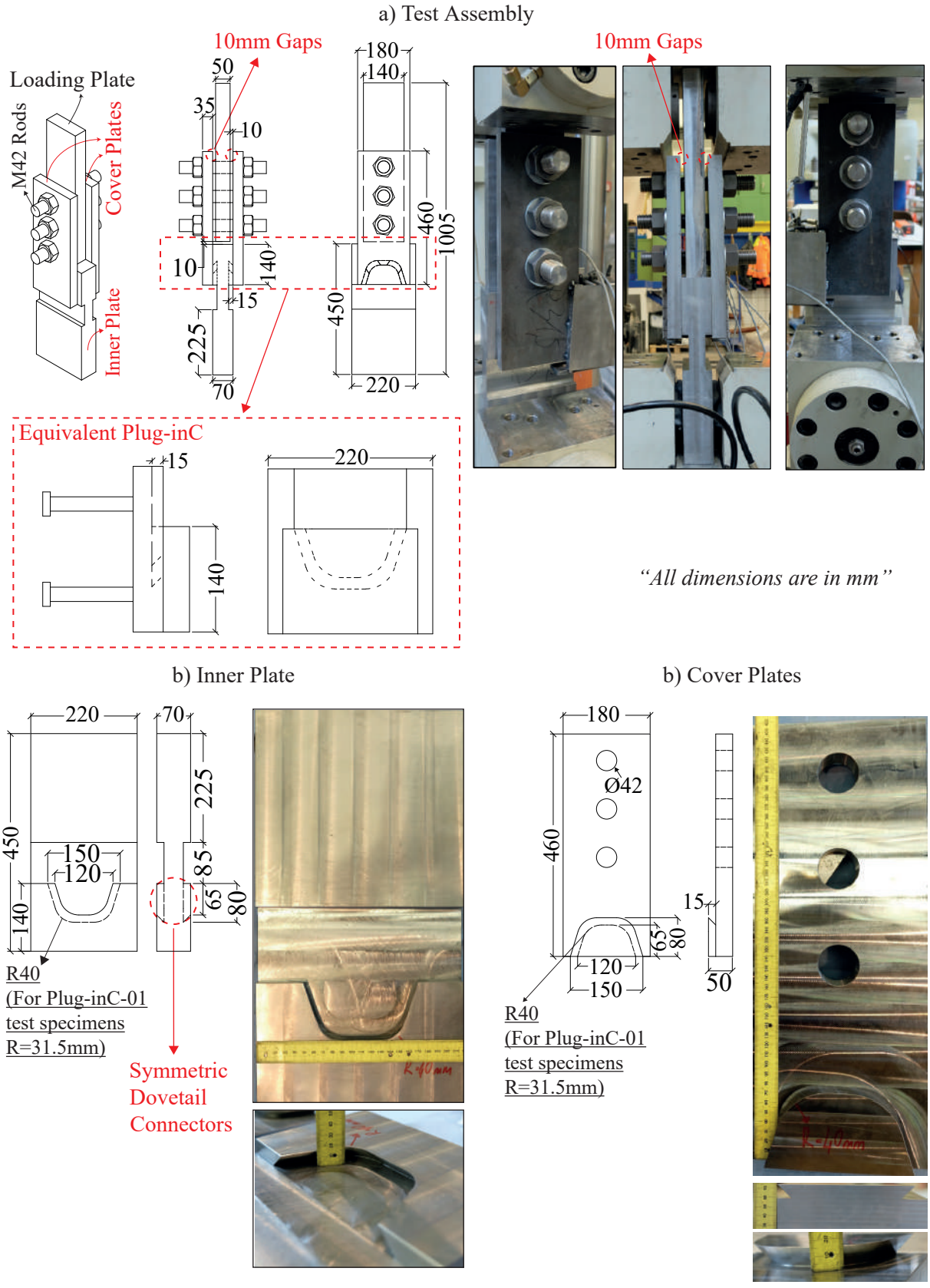

Figure 4.4: Plug-inC test set-up and the main set-up components.

4.3.2 Loading procedure

The tests were executed with a 2500kN capacity uni-axial testing machine. Fig. 4.5 illustrates the loading procedure of the experimental tests with respect to the following loading steps;

- Monotonically load up to 5% of the expected test capacity - $F_{u,exp}$ (Displacement-controlled 0.06mm/min).
- Cycling loading period between 5% - 40% of the expected test capacity (Force-controlled 0.01Hz - 25Cycles).
- Monotonically load until the ultimate test capacity - $F_{u,Test}$ (Displacement-controlled 0.06mm/min).

For the first test, the expected ultimate test capacity ($F_{u,exp}$) was estimated with FEA performed prior to the experimental tests with the characteristic material properties [50] of the ordered material grades listed in Table 4.2. The FE-model are presented in Section 4.4. For the second (Plug-inC-02) and the third (Plug-inC-03) tests the expected ultimate test capacity was taken as the ultimate test load of the first test (Plug-inC-01).

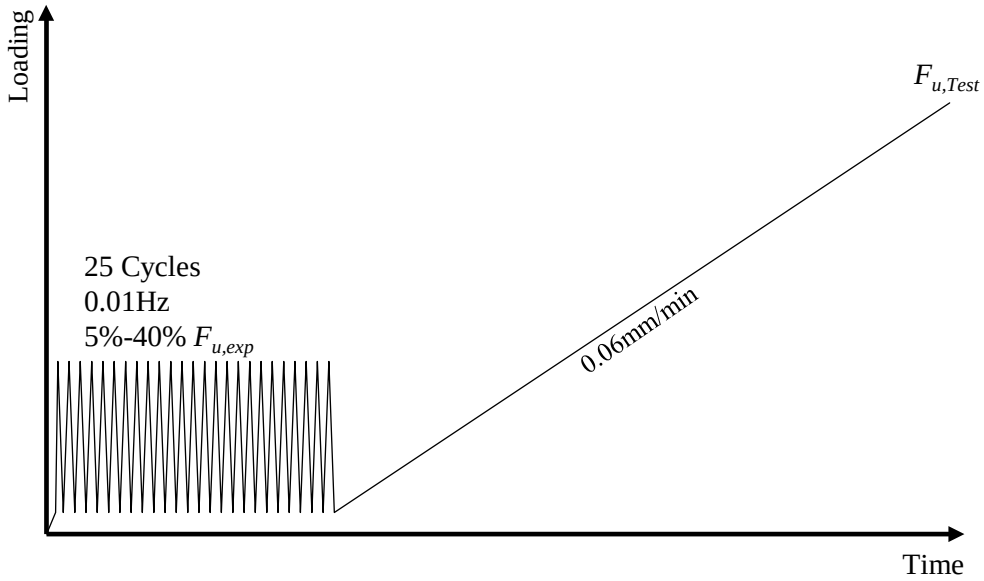

Figure 4.5: Loading procedure of Plug-inC test campaign.

4.3.3 Instrumentation of the test specimens

In total eight displacement transducers (DTs) were used to measure the relative displacements between the inner and the cover plates to determine load-displacement and moment-rotation behaviour of Plug-inC. Fig. 4.4a shows the labels and the configuration of the DTs together with images of the entire Plug-inC test set-up. The measurement ranges and the measurement alignments of the DTs are summarized in Table 4.4.

Table 4.4: Details of the displacement-transducers (DT) used in Plug-inC test campaign.

Test ID	Sensor ID	Direction	Range
Plug-inC-01 Plug-inC-02 Plug-inC-03	DT-1	Vertical (*y-axis*)	20mm[1]
	DT-2	Vertical (*y-axis*)	20mm[1]
	DT-3	Horizontal (*x-axis*)	10mm
	DT-4	Horizontal (*x-axis*)	10mm
	DT-5	Horizontal (*x-axis*)	10mm
	DT-6	Horizontal (*x-axis*)	10mm
	DT-7	Horizontal (*x-axis*)	10mm
	DT-8	Horizontal (*x-axis*)	10mm

[1] For the first test (Plug-inC-01), the displacement transducers DT-1 and DT-2 had 10mm measurement range.

As shown in Fig. 4.6, all DTs were fixed to the inner plate at the vertical symmetry axis of the test set-up. DT-1 and DT-2 were used to measure the relative vertical displacements between the inner and the cover plates. To estimate the rotations of the cover plates along the connection height ($h_{connection}$=*140mm*) of the equivalent Plug-inC test configuration, DT-3 and DT-4 were positioned to measure the relative horizontal displacement (*x-axis* direction) between the inner and cover plates at a height that corresponds to the bottom edge of Plug-inC, while DT-7 and DT-8 were positioned

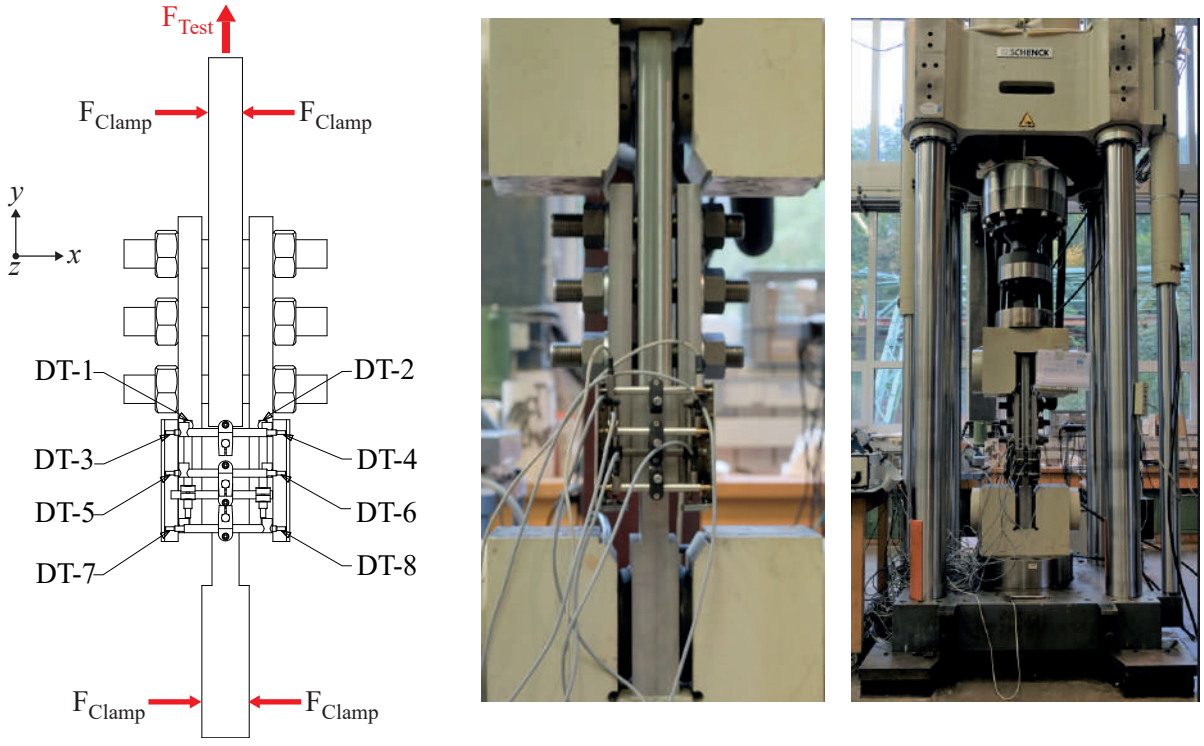

Figure 4.6: Layout and the labels of the displacement transducers (DT) of Plug-inC test campaign.

to measure the relative in-plane horizontal displacements at a height that corresponds to the top edge of the connection height of Plug-inC. In addition, DT-5 and DT-6 were positioned at the mid connection height of Plug-inC to investigate the linearity of the rotation profiles for the cover plates.

4.3.4 Test results and discussions

Fig. 4.7 shows the load-displacement and the moment-rotation curves for the symmetric Plug-inC configurations of the test specimens. The presented load values were calculated by dividing the applied loading with a factor of two as the test set-up and the loading were symmetric with respect to the central vertical axis (*y-axis*) of the test setup. The relative displacement between the inner and the cover plates (δ_y) was calculated with Eq. 4.4 as the arithmetic mean of the data recorded with DT-1 and DT-2 (see Fig. 4.6).

$$\delta_y = \frac{DT_1 + DT_2}{2} \tag{4.4}$$

The moment values were calculated with Eq. 4.5 by multiplying the half of the applied loading with the pre-defined load-eccentricity (*e=17.5mm*). The out-of-plane (*z-axis*) rotation was calculated with Eq. 4.6.

$$M = \frac{F_{Test} \cdot e}{2} \tag{4.5}$$

$$\theta_z = \arctan\left(\frac{\frac{DT_3+DT_4}{2} + \frac{DT_7+DT_8}{2}}{h_{connection} = 140mm}\right) \tag{4.6}$$

For the first test (Plug-inC-01), the displacement transducers DT-1 and DT-2 reached their gauge limits (see Table 4.4) before attaining the ultimate test load. Therefore, although the ultimate load capacity of each symmetric Plug-inC configuration was 873kN, the load-displacement curve of Plug-inC-01 presented in Fig. 4.7 terminates at 752kN load-level. Therefore, as noted in Table 4.4, DT-1 and DT-2 were replaced with a new set of devices having larger gauge limit for the second (Plug-inC-02) and the third (Plug-inC-03) tests.

It could be deduced from Fig. 4.7a that the load-bearing mechanism of the dovetail connectors activates after the accommodation of the initial fitting tolerances between the hub and dovetail counterparts during the initial loading step. This behaviour is more obvious for the first and the second tests as highlighted in the figure. On the other hand, during the cycling loading periods of the experimental tests, there was nearly no relative displacement between the inner and the cover plates. Thus, it could be concluded that the load-bearing mechanism of the equivalent Plug-inC test configuration was fully activated at the beginning of the monotonic loading steps.

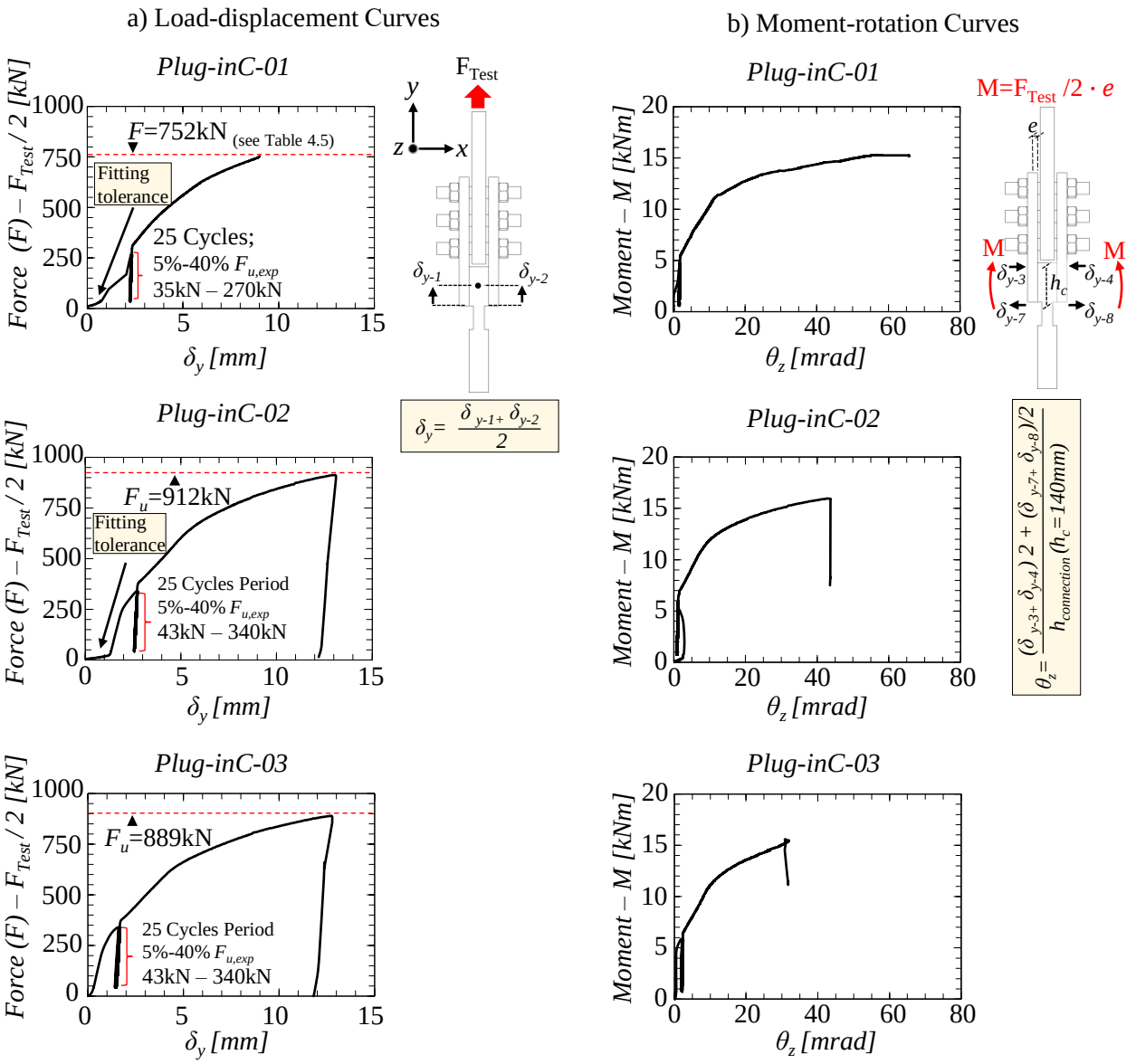

Figure 4.7: The experimental load-deformation behaviors of Plug-in Connection.

Consequently, to be able to define the translational stiffness characteristics of Plug-inC, the load-displacement curves of the experimental tests are also presented in Fig. 4.8 excluding the cycling loading periods. According to Fig. 4.8, tri-linear load-displacement behavior of Plug-inC could be noticed, and it could be deduced that the translational load-bearing characteristics of the experimental tests were similar. However, it could also be noticed that the load-displacement behavior of the first test (Plug-inC-01) followed a lower path with respect to the second and the third tests. The detailed information regarding to the tri-linear translational stiffness values of each test specimens are presented in Table 4.5.

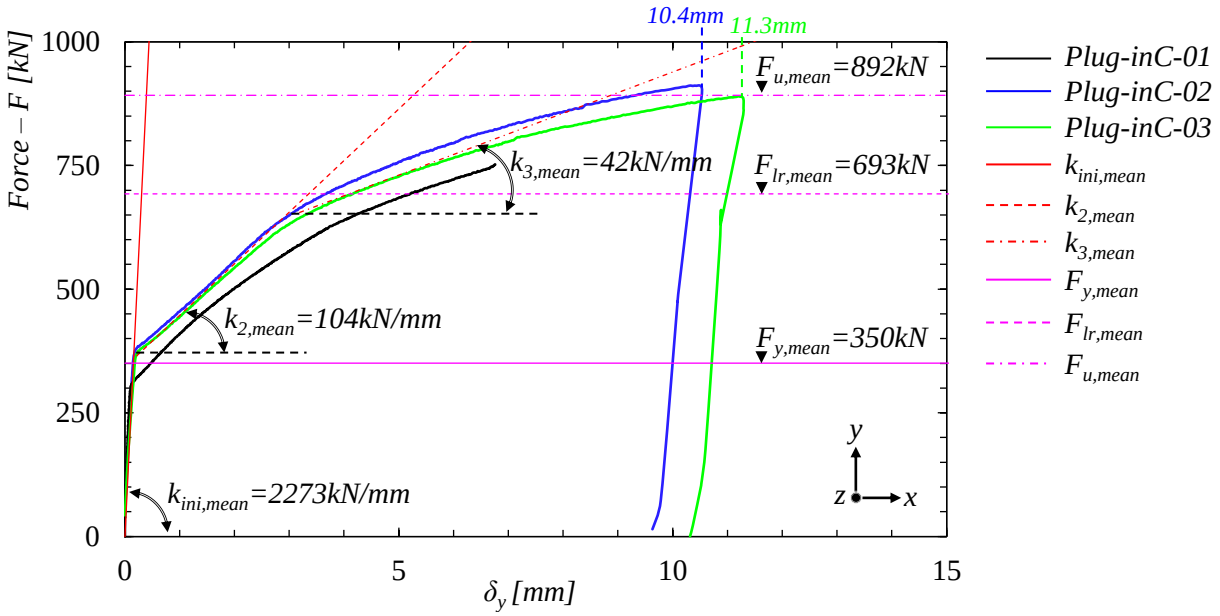

Figure 4.8: Comparison of the load-displacement curves of Plug-inC test campaign (excluding cyclic loading periods) with the identification of a tri-linear load-displacement behavior.

As indicated earlier, the relative displacements between the inner and cover plates of Plug-inC-01 were not fully recorded as the related DTs reached their gauge limits before attaining the ultimate test load. Therefore, to clarify the lower load-displacement behavior of the first test specimens, a new set of load-displacement curves was derived based on the total force and displacement data recorded by the testing machine. Fig. 4.9 compares the new set of the load-displacement curves.

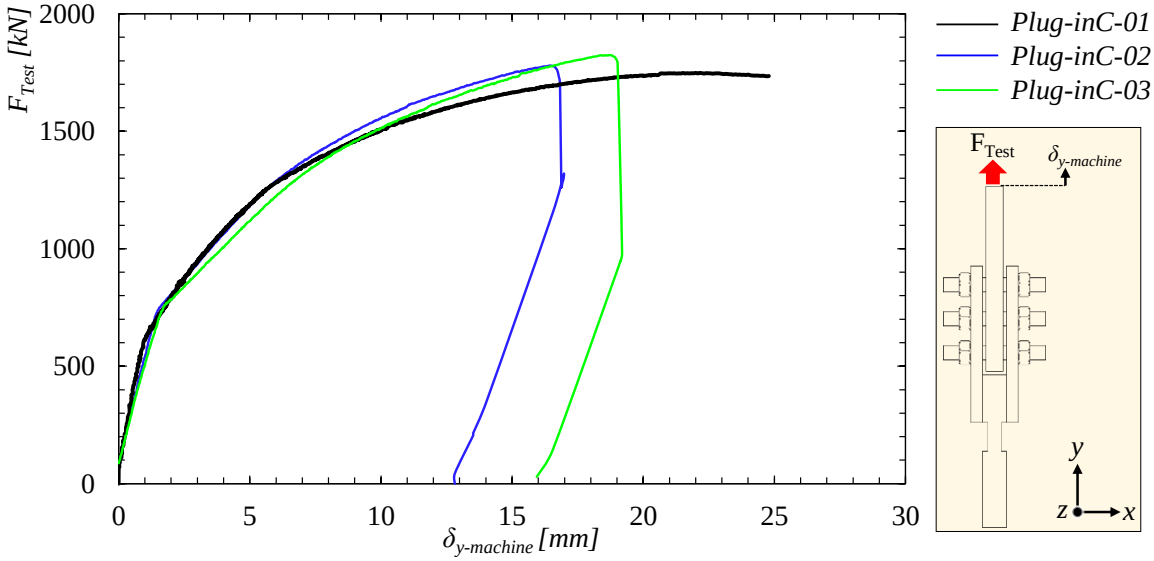

Figure 4.9: Comparison of the load-displacement curves of Plug-inC test campaign (excluding the cyclic loading periods) based on the total load-displacement data of the uni-axial test machine.

According to Fig. 4.9, similar load-bearing mechanisms of the three test specimens could be verified. Therefore, it is stated that the lower load-displacement curve of Plug-inC-01 observed in Fig. 4.8 was due to higher relative displacement between the inner and the cover plates, in other words higher slip along the hub and the dovetail counterparts of the first test specimen. In addition, it could also be noticed in Fig. 4.7b and Fig. 4.9 that the load-displacement behavior of the first test specimen was relatively more ductile. These differences could be attributed to either the lower material yield strength of the cover plates (see Table 4.3) or the different dovetail radius of the first test specimens (see Fig. 4.4). The impact of the dovetail round radius on the load-deformation behaviors of Plug-inC is further investigated as a part of the numerical parametric study presented in Section 4.6.

Fig. 4.10 presents the comparison of the moment-rotation curves of the experimental tests without the cycling loading periods. In agreement with the load-displacement behaviors, the rotational load-bearing characteristics of the experimental tests were also similar. It is important to note that the presented moment values do not include the secondary effects that may develop due to the bending and the out-of-plane rotation of the corbel plates, and they were calculated based on the assumption that the load introduction to the cover plates was at the mid-length of the M42 threaded-rod holes. Therefore, more accurate estimation of the moment action resisted by the equivalent Plug-inC test configuration is further investigated with the numerical simulations presented in Section 4.4. The detailed information regarding to the tri-linear rotational stiffness values of each test specimen is listed in Table 4.5.

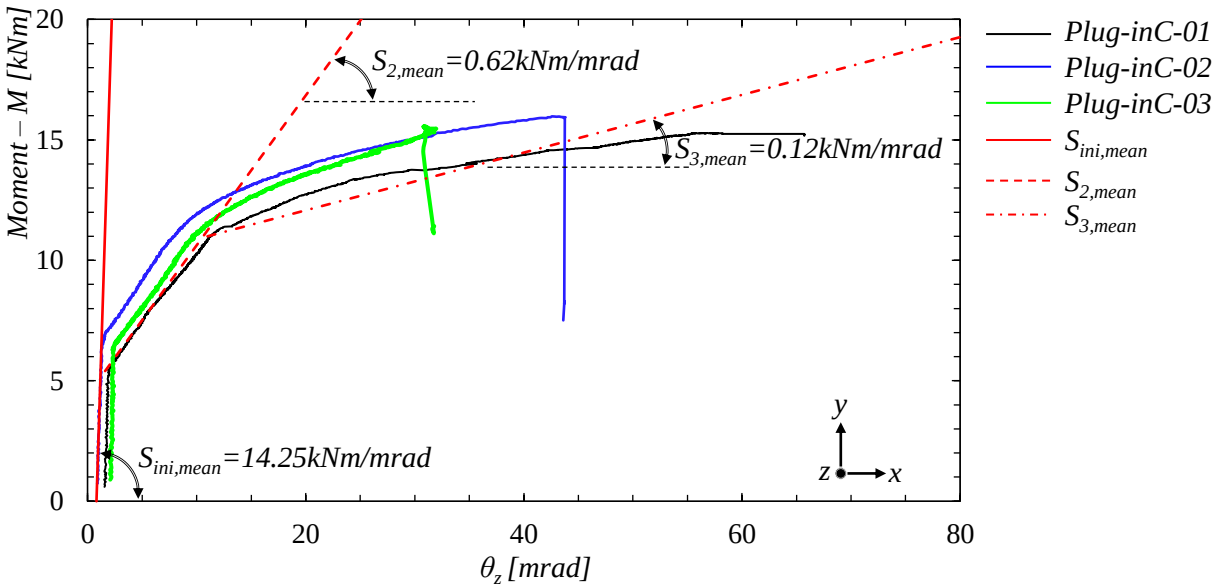

Figure 4.10: Comparison of the moment-rotation curves of Plug-inC test campaign (excluding cyclic loading periods) with the identification of a tri-linear moment-rotation behavior.

Furthermore, Fig. 4.11 presents the relative in-plane horizontal displacements (δ_x) of the cover plates along the equivalent Plug-inC connection height with respect to the inner plates. As highlighted in the figure that until a certain loading limit (F_{lr}) there were linear-like relations between the in-plane horizontal displacements of the cover plates and beyond this limit the development of nonlinear-rotation profiles could be noticed. To have a more clear understanding of this phenomenon, the rotation profiles of the cover plates along the equivalent Plug-inC connection height are also presented in Fig 4.12 at the instants that correspond to F_{lr} and the ultimate load-bearing capacity (F_u) of each symmetric Plug-inC test configurations.

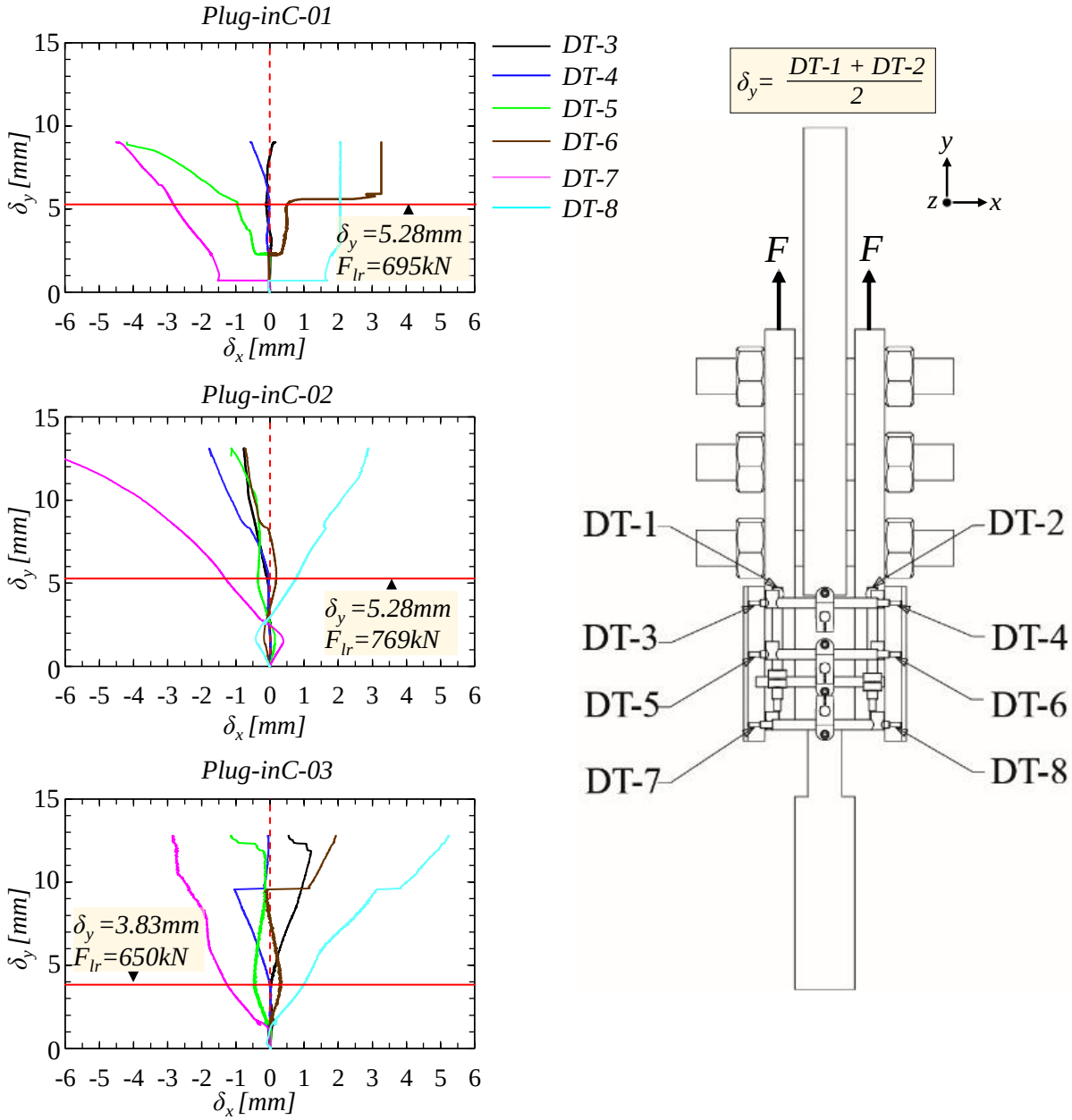

Figure 4.11: In-plane horizontal displacements of the cover plates with respect to the inner plate.

It could be deduced from Fig. 4.12 that the rotation profiles of the cover plates were almost linear at F_{lr}, thus analogically also before attaining F_{lr}. However, the significant change in the rotation profiles for the cover plates is obvious at the ultimate load-bearing capacity of each symmetric Plug-inC test configuration (F_u). Therefore, the threshold for the linear-rotation profile of the cover plates; thus the corbel plate for Plug-inC, could be defined as F_{lr}. The definition of this threshold is crucial in the development of analytical resistance models to estimate the linear and the ultimate load-bearing capacities of Plug-inC (see Section 4.5). Additionally, the final rotations of the cover plates at the end of the experimental tests are also presented in Fig. 4.13 to Fig. 4.15.

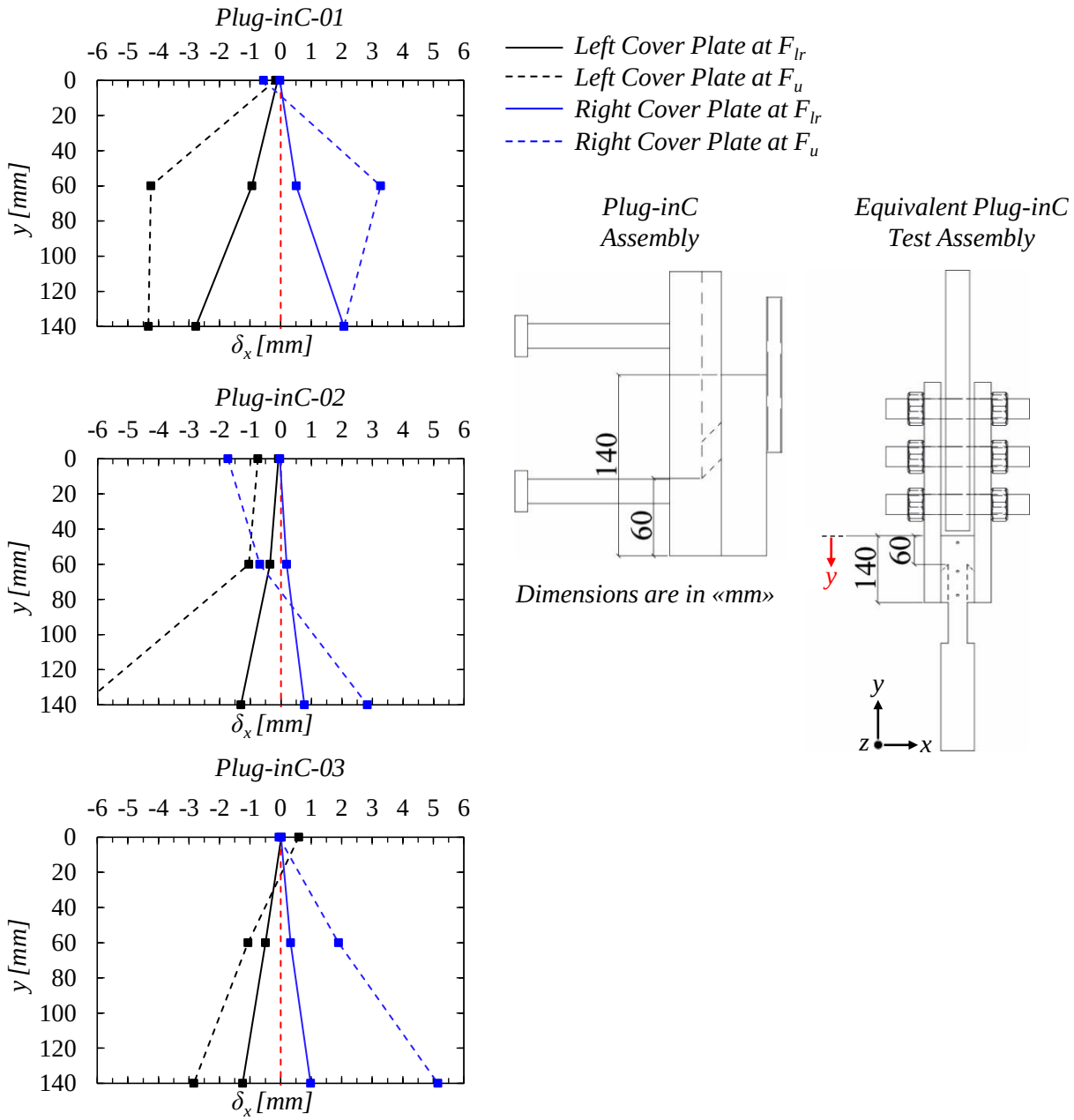

Figure 4.12: Rotation profiles of the cover plates at F_{lr} and F_u for Plug-inC test campaign.

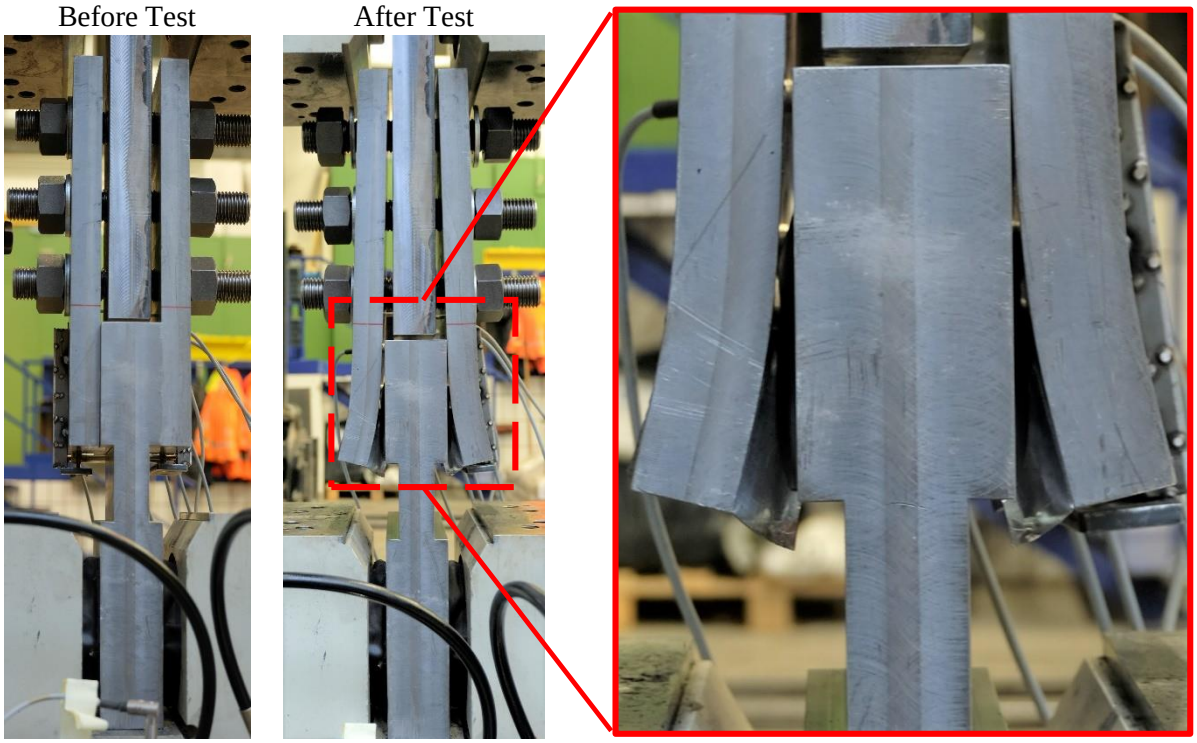

Figure 4.13: Final rotation of the cover plates / Plug-inC-01.

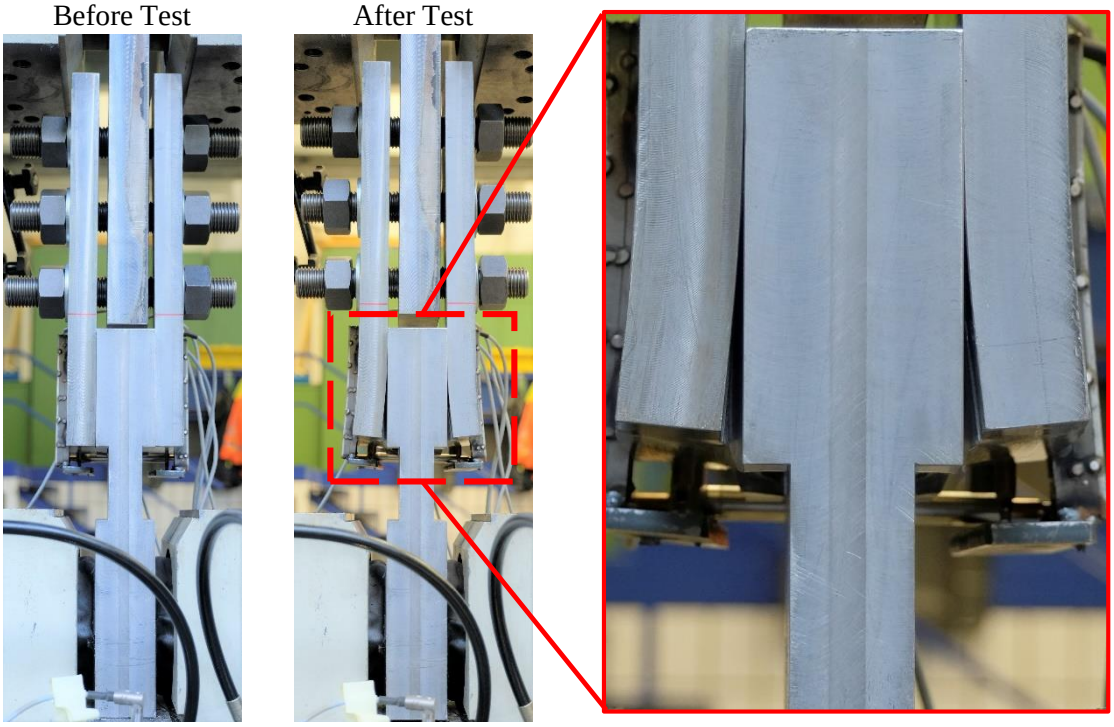

Figure 4.14: Final rotation of the cover plates / Plug-inC-02.

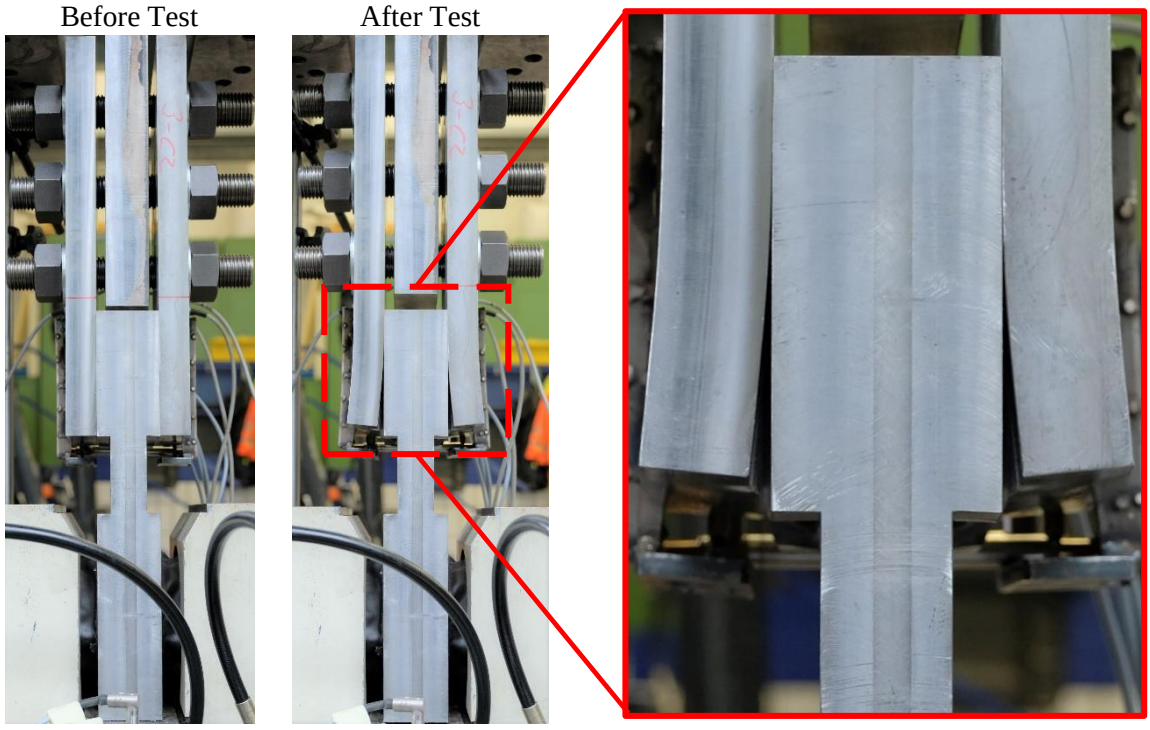

Figure 4.15: Final rotation of the cover plates / Plug-inC-03.

According to the zoomed images presented in Figs. 4.13-4.15, the nonlinear-rotation profiles along Plug-inC connection height could be recognized. In addition, as indicated earlier, the larger deformations for the hub and the dovetail counterparts of the first test specimens (Plug-inC-01) could be noticed with respect to the second and the third test specimens (see also Figs. 4.9-4.10). This difference was earlier attributed to the smaller dovetail round radius (see Fig. 4.4) and the lower material strength of the cover plates for the first test specimens (see Table 4.3) and further investigated in Section 4.4 and Section 4.6.

Fig. 4.16 compares the before and the after test conditions of the hub and the dovetail counterparts for the first test specimens to identify the stress distribution on the counterparts and to clarify the failure the mechanism of Plug-inC test configuration. The comparisons for the second and the third test specimens are presented in Annex-D. It is important to note that the deformations are only compared for the in-plane left hub and dovetail counterparts of Plug-inC test configuration as it is verified in Figs. 4.13-4.15 that the applied loading was uniformly distributed between the symmetric right and left sides of the test set-ups.

In Fig. 4.16, the high compressive deformation at the bottom surface of the dovetail and the hub counterparts, and the shear deformation of the dovetail indicate that the ultimate non-eccentric load-bearing capacity of Plug-inC mainly depends on the shear resistance of the dovetail back surface. However, it is important to note that in addition to the compressive stress resultants at the bottom surface, the part of the loading was transferred to the hub by the frictional resistance developed at the side surfaces of the dovetail. Therefore, frictional resistance between the dovetail

and the hub plays an important role for the ultimate load-bearing capacity of Plug-inC, thus the impact of the frictional resistance on the load-bearing mechanism of Plug-inC is investigated with FEAs and analytical resistance models presented in Section 4.4 and Section 4.5, respectively.

The tensile deformations of the dovetail and the hub side surfaces highlighted in Fig. 4.16 indicate that the tensile stress resultants developed due to the moment action were transferred to the hub by the side surfaces of the dovetail. In addition, it could be noticed that the entire height of the dovetail side surfaces were under tension action; thus it is concluded that the rotation center of the cover plates was above the bottom edge level of the dovetail connector. The previous outcome could verified with Figs. 4.13-4.15.

Consequently, the shear, the compression and the tension stresses developed at the inner edge of the bottom dovetail surface caused crack formations as highlighted in Fig. 4.16b. Therefore, the ultimate test loads and the brittle failure characteristics of the second (Plug-inC-02) and the third test (Plug-inC-03) could be linked to the crack formations around the inner edge of the bottom dovetail surface.

Having identified the stress distributions for the dovetail connector of Plug-inC, the summary of the test results is presented in Table 4.5 together with the tri-linear translational and rotational stiffness values of each test specimens. According to the mean ultimate load-bearing capacity of each symmetric Plug-inC test configuration ($F_{u,mean}$=892kN) it is concluded that the load-bearing capacity of Plug-inC is 24% higher than the minimum required mean resistance defined in Eq. 4.3. Therefore, it could be stated that the proposed Plug-in connection could satisfy the design requirements for simple connections between the RC-column/walls and steel beams of steel-concrete hybrid building systems presented in Fig 4.2.

On the other-hand, as indicated earlier, the actual load-eccentricity for the equivalent Plug-inC test configuration depends on the stress distribution within the M42 threaded-rod holes and the rotation of the cover plates. Therefore, it is required to investigate if the load-eccentricity of the equivalent Plug-inC test configuration was identical with the load-eccentricity of the joint configuration presented in Fig 4.2. This investigation has been detailed in Section 4.4 by means of the actual magnitude of the load-eccentricity for the equivalent Plug-inC test configuration.

Table 4.5: Comparison of Plug-inC test results.

Test ID	F_y [kN]	F_{rl} [kN]	F_u [kN]	$\delta_{y,at\ F_u}$ [mm]	${k_{ini}}^1$ $[\frac{kN}{mm}]$	${k_2}^1$ $[\frac{kN}{mm}]$	${k_3}^1$ $[\frac{kN}{mm}]$	${S_{ini}}^2$ $[\frac{kNm}{mrad}]$	${S_2}^2$ $[\frac{kNm}{mrad}]$	${S_3}^2$ $[\frac{kNm}{mrad}]$
Plug-inC-01	305	659	873	21.59	2273	111	47	16.80	0.59	0.08
Plug-inC-02	368	769	912	16.24	2273	101	42	10.00	0.63	0.12
Plug-inC-03	378	650	890	18.70	2273	99	30	16.00	0.63	0.17
Mean Values	350	693	892	18.84	2273	104	42	14.27	0.62	0.12

[1] Highlighted in Fig.4.8.

[2] Highlighted in Fig.4.10.

a) Inner Plate with Hub Counterpart at In-plane Left Side

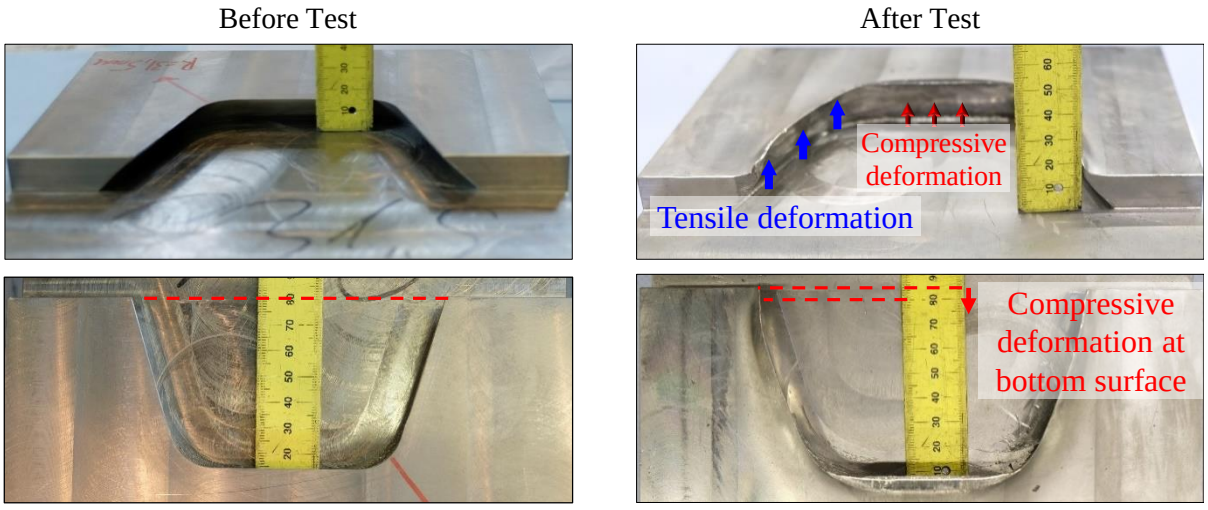

b) Cover Plate with Dovetail Counterpart at In-plane Left Side

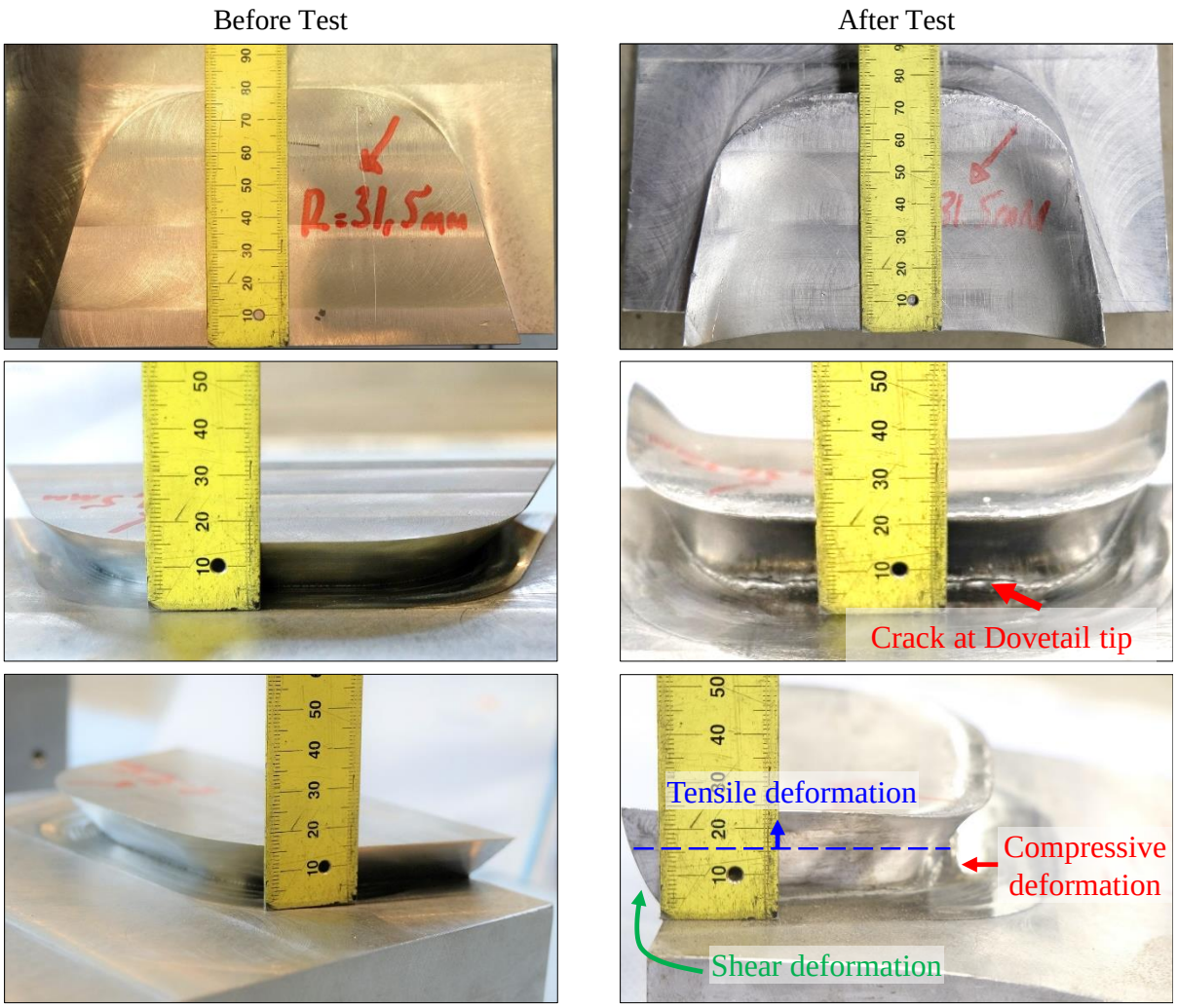

Figure 4.16: Deformation of the hub and dovetail counterparts / Plug-inC-01.

4.4 FEA simulations

A set of numerical simulations were performed with the commercial FEA software package Abaqus/CAE [66] to design the test set-ups, to clarify the failure mechanisms of Plug-inC, to investigate the load distribution between the frictional resistance and the mechanical interlock resistance of the dovetail counterparts. In addition, the impact of the dovetail round radius on the load-deformation behavior of Plug-inC was investigated with the FEAs. The FE-modelling technique and solution methodology of the FEAs were validated with respect to the experimental test results.

FE-models of Plug-inC test configurations were developed with explicit geometries of the set-up components including the entire dovetail geometry presented in Fig. 4.4. Two different FE-models of the test set-ups were developed with different round radius of the dovetail as the round radius of the first test specimens was 31.5mm while it was 40mm for the second and the third test specimens (see Fig. 4.4). The threaded regions of the M42-threaded rods and nuts were not included in the FE-models, and the rod-nut-washer assembly was modelled as a single component with circular geometry to reduce the computational effort. Only a quarter-symmetric geometry of the test set-up was modelled with symmetric boundary conditions (BCs) because the test set-up and the loading were symmetric with respect to the in-plane vertical and horizontal central axes of the test set-up. Fig. 4.17 shows the FE-model geometry, BCs, FE-types and FE-discretization and the mesh density of the model components.

The material laws of the inner plate and the cover plate were defined with tri-linear material model using the mean properties presented in Table 4.3. At the end of the experimental tests, no yielding was identified for the loading plate and M42-threaded rods; thus, the material laws of these components were defined with linear-elastic behavior with elastic steel properties defined by EN1993-1-1 [50]. The tri-linear material laws assigned to the inner and cover plates is illustrated in Fig. 4.17a, and the corresponding properties are listed in Table 4.6.

Table 4.6: Material properties assigned to FE-model components / Plug-inC test campaign.

Component Name	Material Model	E [GPa]	ν	f_y [MPa]	f_u [MPa]	f_f[1] [MPa]	ε_u[2] [%]	ε_f[3] [%]
Inner Plate	Tri-linear	209	0.3	244	445	40	30.4	35.3
Cover Plate	Tri-linear	208	0.3	248	434	40	32.0	38.0
Loading Plate	Linear-elastic	210	0.3	N/A	N/A	N/A	N/A	N/A
M42-threaded Rod	Linear-elastic	210	0.3	N/A	N/A	N/A	N/A	N/A

[1] The fracture stress has been assumed to be equal to 10% of the ultimate tensile strength as illustrated in Fig. 4.17a.

[2] The details regarding to the calculation of the ultimate strains for the tri-linear material law are presented in Annex-D.

[3] The fracture strain corresponds to the term A presented in Table 4.3.

a) FE-model components, Boundary Conditions, Load-introduction and Material Law

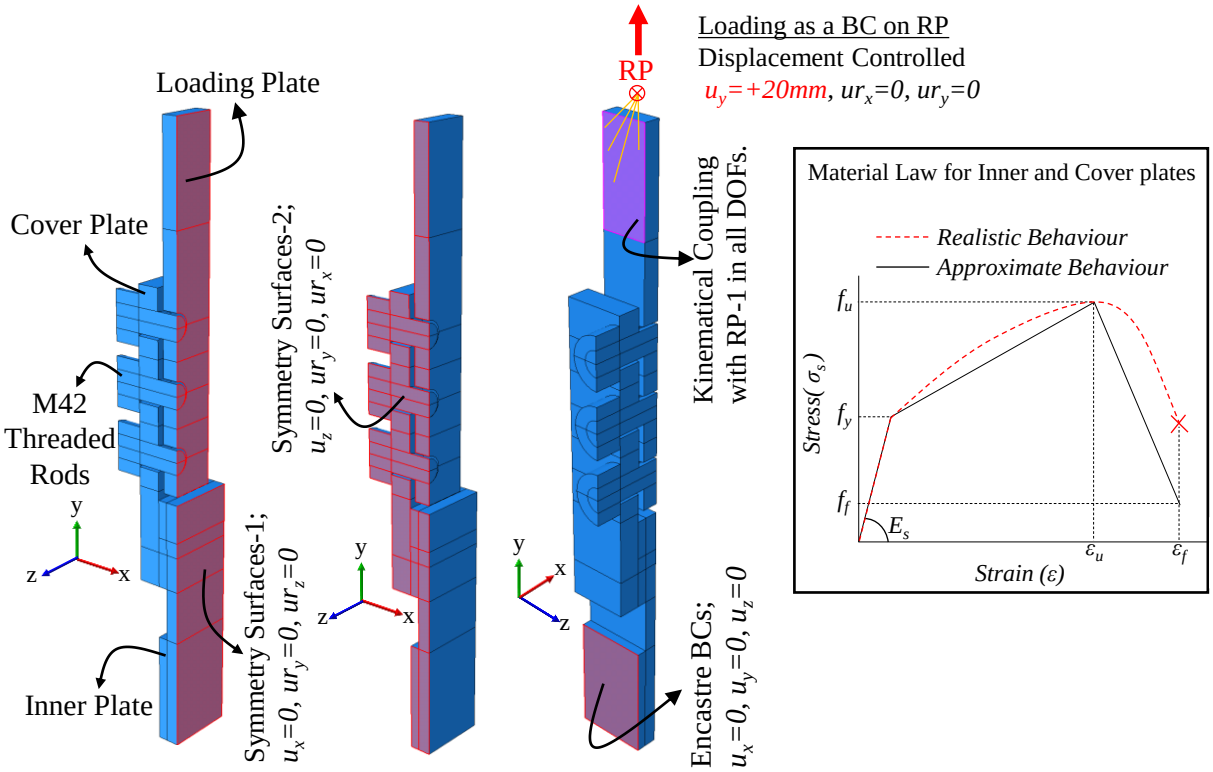

b) Mesh Density and the FE-discretization of the Model Components

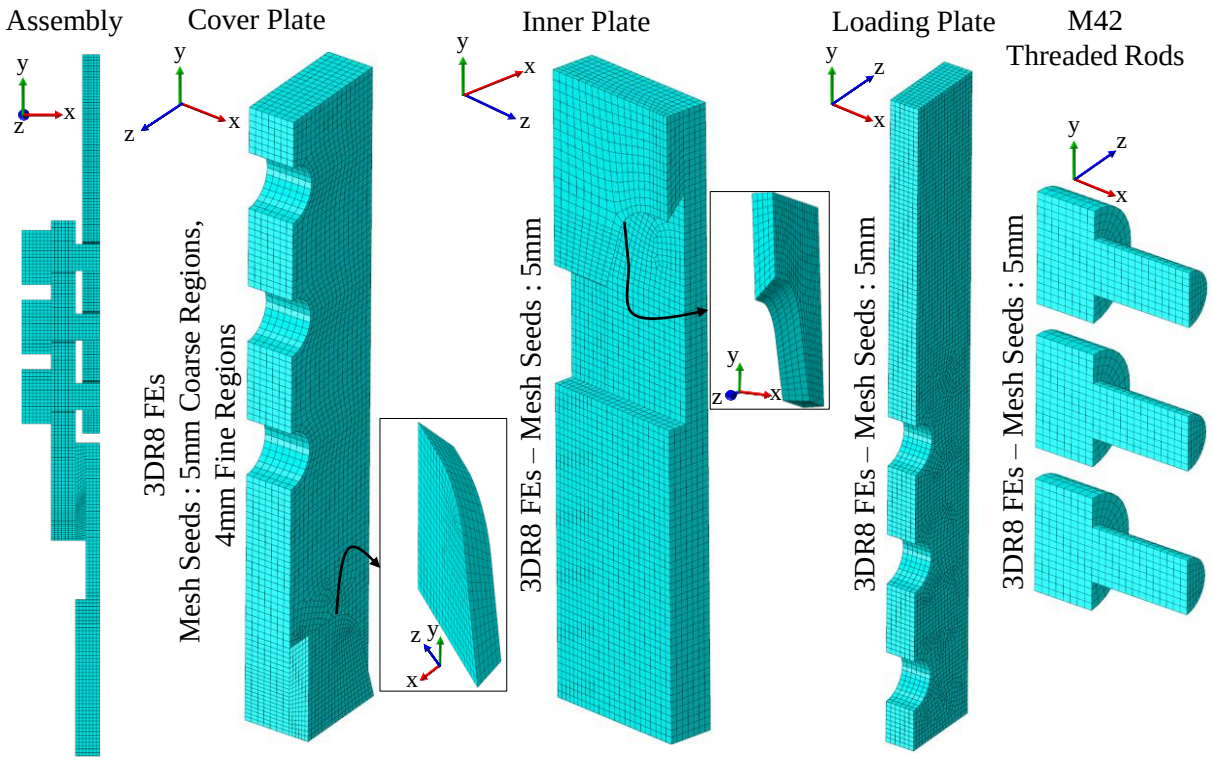

Figure 4.17: FE-model of Plug-inC test campaign.

The frictional behavior between the hub and the dovetail counterparts and the flat surfaces of the inner and the cover plates were defined with penalty friction formulation of the software [66]. The interaction properties between the FE-model components are summarized in Table 4.7.

Table 4.7: Interaction properties between the FE-model components of Plug-inC test campaign.

Connected Components	Interaction Method	Interaction Properties	
		ND	TD
Inner Plate to Cover Plate	Surface to Surface Contact	Hard	Penalty Friction (μ=*0.4*[1])
M42-rods to Loading Plate	Surface to Surface Contact	Hard	Friction-less
M42-rods to Cover Plate	Surface to Surface Contact	Hard	Friction-less

ND: Normal Direction, TD: Tangential Direction

[1] The friction coefficient between CNC-cut steel surfaces is determined with a supplementary testing campaign, see Annex-A.

The loading was applied to a reference point, which was kinematically coupled with the front top surface of the loading plate as identical to the test configuration presented in Fig. 4.4a, with displacement-controlled loading steps defined by the smooth step function of the software [66]. The details of the load-introduction are shown in Fig.4.17a.

For the solution of the FEAs, Abaqus/Standard solver was used with dynamic-implicit solution scheme [66]. The dynamic-implicit solution scheme was selected to optimize the solution time. Because, the hub and the dovetail counterparts were modelled with their explicit complex geometry which resulted the minimum characteristic length of the finite elements around the round radius to be relatively small, e.g. 0.6mm - 1.2mm; thus, if the dynamic-explicit solver was selected the maximum stable step size of the explicit solution would be relatively small and the solution of FEAs would be computationally more expensive. The parameters of the implicit solution scheme are presented in Annex-D together with internal energy - external work balance of the FEAs.

Fig. 4.18 compares the load-displacement and moment-rotation curves of the tests with the FEAs outputs. The force outputs of the FEAs correspond to the total reaction force at the surface of the inner plate restrained with the encastre boundary conditions [66] (see Fig. 4.17a). The moment outputs of the FEAs were calculated with Eq. 4.5 as identical to the test results. The comparisons show that the output results of the FEAs are in good agreement with the test results. Furthermore, no difference was observed for the load-displacement behaviours of the FEAs performed with 31.5mm dovetail round radius (*R=31.5mm*) and 40mm dovetail round radius (*R=40mm*). However, the moment-rotation behaviour of the FEA with (*R=31.5mm*) was slightly less stiff than the moment-rotation behavior of the FEA with (*R=40mm*) beyond the initial elastic stages of the curves. Therefore, it is concluded that although the dovetail round radius does not have considerable impact on the load-bearing capacity of tested Plug-inC configuration, it may effect the moment-rotation behavior. Consequently, the ultimate load-bearing capacity of Plug-inC may be impacted by the dovetail round radius if the load-eccentricity is increased. This dependency is investigated in Section 4.6.

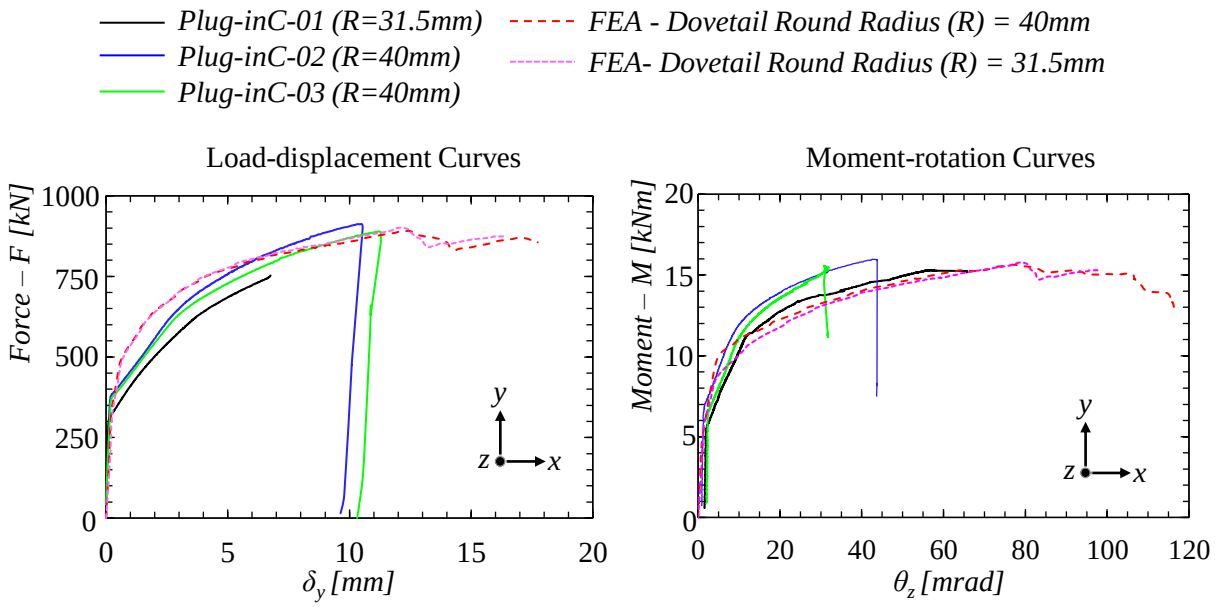

Figure 4.18: Load-deformation behaviours of Plug-inC test campaign against FEA.

Additionally, the load-displacement curves of the FEAs are observed to be more stiff compared to the corresponding test results beyond the initial elastic stages. In contrast, the moment-rotation curves of the FEAs are noticed to be less stiff than the corresponding test results. These differences are attributed to the perfect geometry of the FE-model components. In other words, although the Plug-inC test specimens were manufactured with CNC-production technique, it was necessary to provide assembly tolerances to connect the hub and the dovetail counterparts. Therefore, the geometry of the test specimens was slightly different with respect to the corresponding FE-model components as the assembly tolerances were defined by the producer and not included in the FEAs.

According to Fig. 4.18, it is concluded that the assembly tolerances of the hub and the dovetail counterparts also affect the load-deformation behaviors of Plug-inC beyond the initial elastic stage. This phenomenon could be further explained with Fig. 4.19 considering the state of the contact closure between the hub and the dovetail counterparts. It could be seen in the figure that before the yielding of the side surfaces of the dovetail, which was in full contact with the side surfaces of the hub, there was a gap (δ_{gap}) between the bottom surfaces of the counterparts. This gap was due to the assembly tolerances. However, after the yielding of the side surfaces, the dovetail slipped (δ_{slip}) in the hub with a magnitude that is equal to δ_{gap} and the contact initiated between the bottom surfaces of the hub and the dovetail counterparts. Consequently, as a result of the slip (δ_{slip}) the load-displacement behaviours of the tests were less stiff compared to the output results of the FEAs. Furthermore, due to the slip, the tension stresses started to be resisted at a lower level of the side surfaces of the hub as illustrated in Fig. 4.19. As a result, this effect provided more strength against to the rotation of the cover plate. Therefore, the moment-rotation behaviors of the tests were more stiff than their corresponding FEA output results beyond the initial elastic stages.

To summarize, as the assembly tolerances were not included in the FE-models, the entire surfaces of the dovetail and hub were in full contact at the beginning of FEAs. Therefore, there was no additional slip (δ_{slip}) between the hub and the dovetail counterparts and this difference resulted load-deformation behaviours of the tests to slightly deviate from the output results of the FEAs.

Nevertheless, it is obvious that the FEAs were estimated the initial elastic stiffness, the elastic and the ultimate load-bearing capacities of Plug-inC test configurations in a very good agreement. In addition, the FEAs also estimated sudden load-drop once the ultimate load-bearing capacity is attained. Therefore, the termination of the second and the third tests could be attributed to the safety configuration of the testing machine as it was programmed to automatically stop if a sudden load-drop occurs.

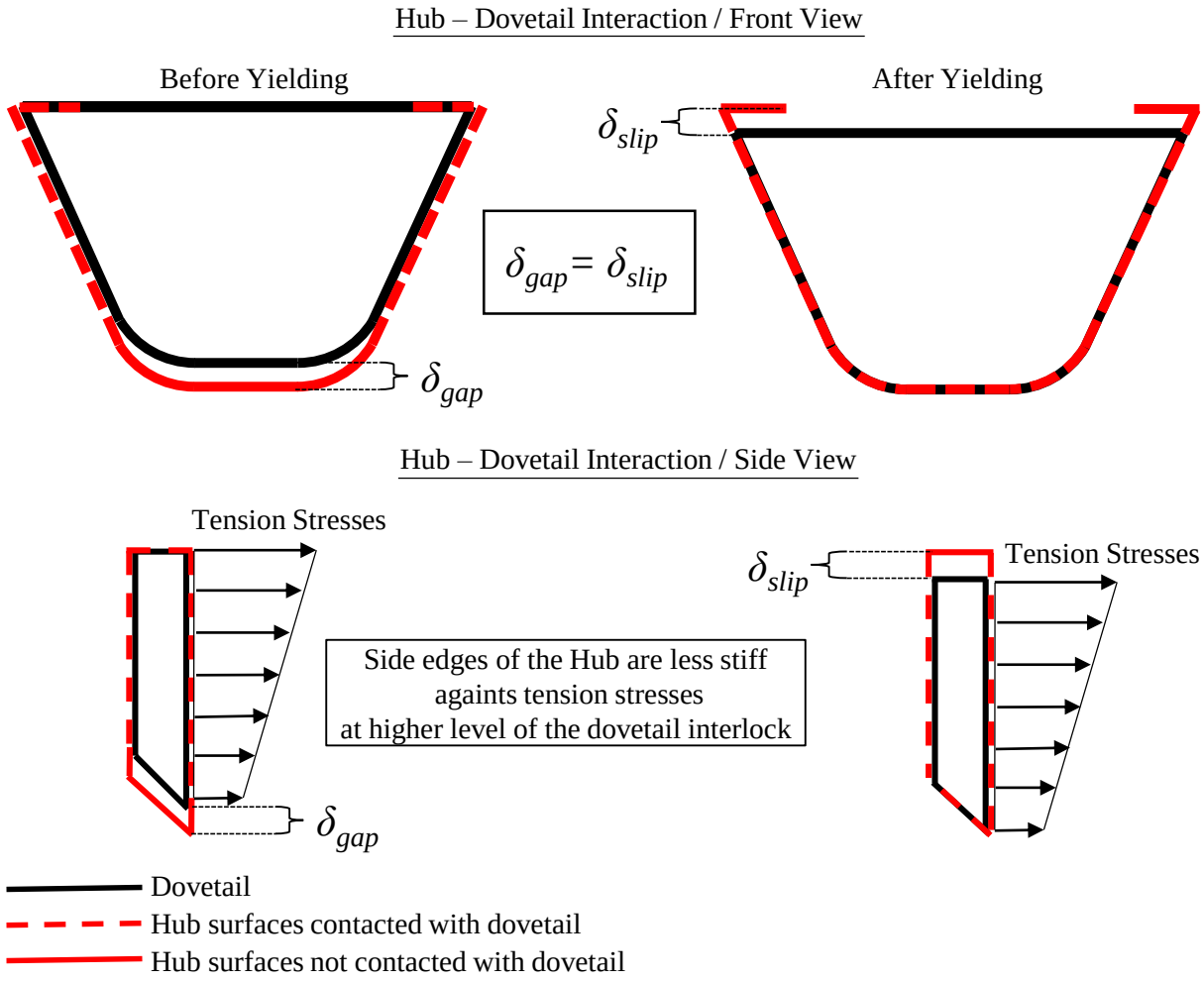

Figure 4.19: Illustration of the contact conditions between the dovetail and the hub counterparts.

After test conditions of the test assemblies and the first test specimens (Plug-inC-01) are also compared with their corresponding FEAs outputs in Fig. 4.20 and Fig. 4.21, respectively. The comparisons for the second and the third tests are presented in Annex-D. According to the presented details, the selected FE-modelling technique and the solution scheme are verified to be capable to simulate Plug-inC test campaign. Therefore, it is concluded that the output results of the FEAs could be further investigated to clarify the load-bearing mechanisms of Plug-inC and to create the basis for the development of analytical resistance models. Only the output results of FEA performed with 40mm dovetail round radius (*R=40mm*) are used for the rest of this chapter.

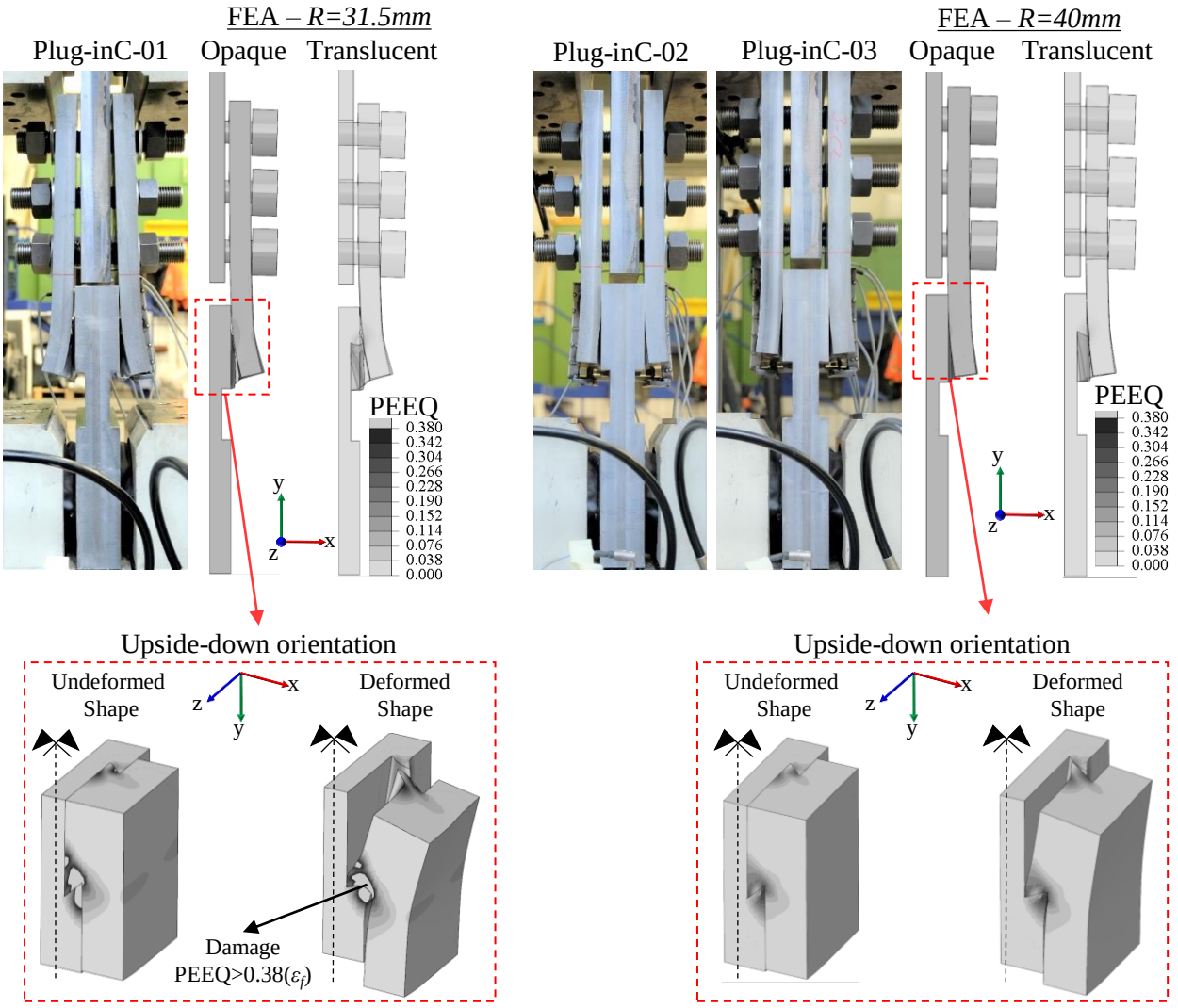

Figure 4.20: Comparison of the deformations for the test assemblies against FEAs.

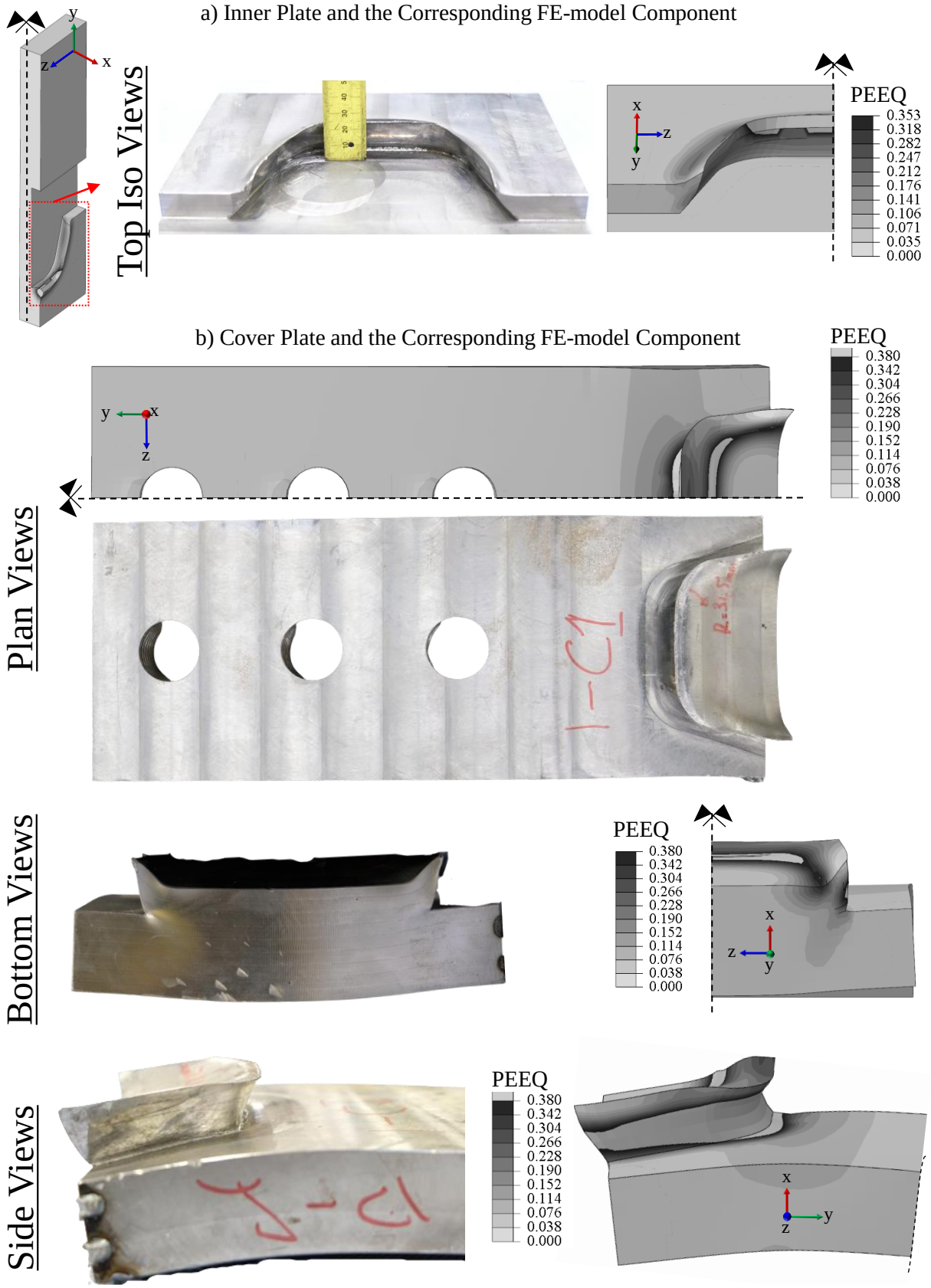

Figure 4.21: Comparison of the deformations for Plug-inC-01 test specimens against FEAs.

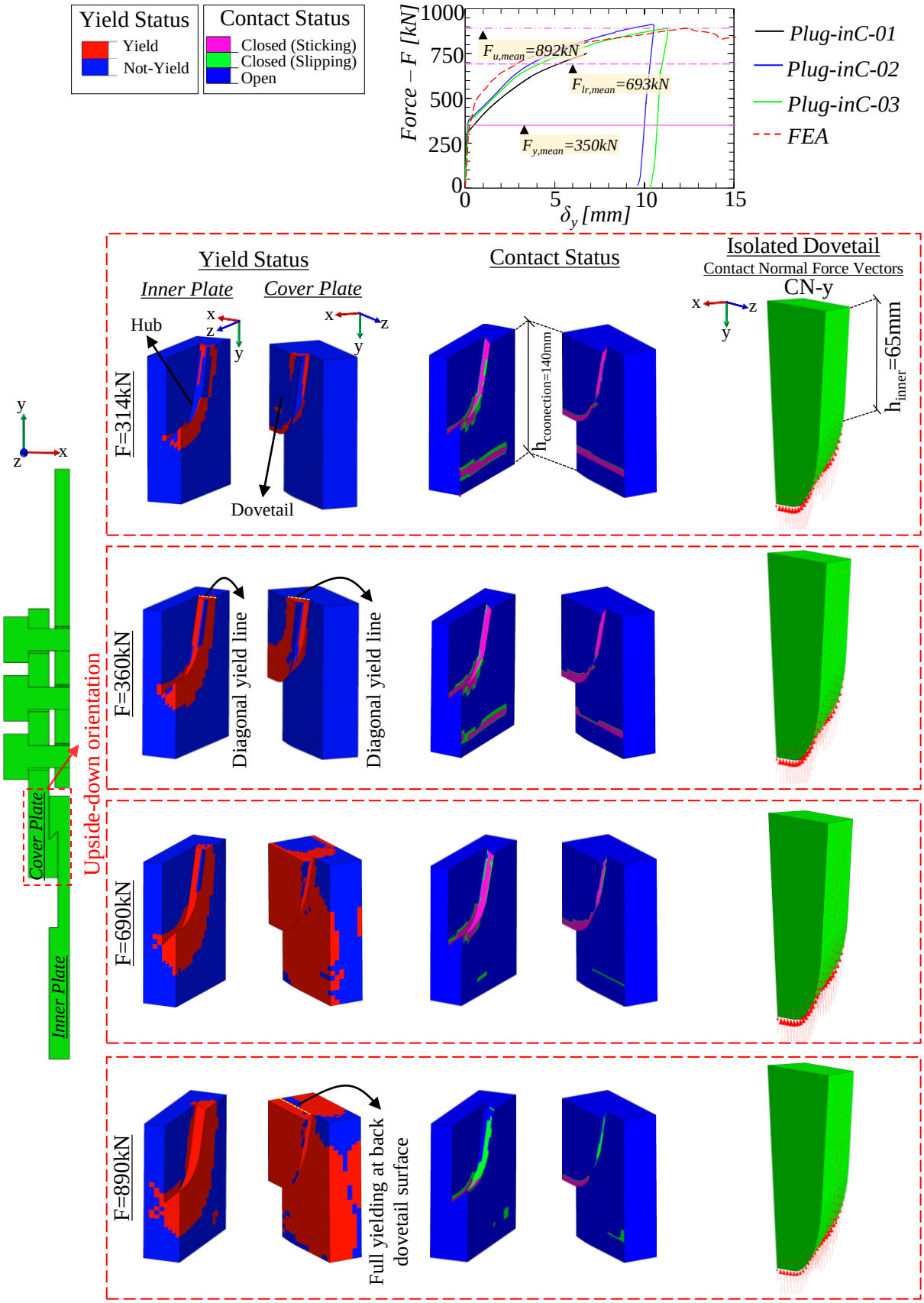

Figure 4.22: Yield and contact status of the hub and dovetail.

Fig. 4.22 shows the yield and contact status of the hub and dovetail counterparts together with the *y-axis* contact normal force vectors on the isolated image of the dovetail. According to the yield status, fully formed diagonal yield line could be noticed for both of the hub and the dovetail at 360kN load level as consistent with the mean yield load capacity of the experimental tests (see also Table 4.5 - $F_{y,mean}$=*350kN*. Therefore, it is concluded that the elastic load-bearing capacity of Plug-inC could be simply estimated as the yield capacity of the diagonal dovetail surface. Furthermore, according to the contact status, the flat surfaces of the inner and the cover plates could be noticed to be closed at the yielding of the diagonal surfaces. Thus, for the yield load-bearing capacity estimation of Plug-inC, the corbel plate (equivalent of the cover plate - see Fig. 4.4a) could be assumed to rigidly rotate around on the flat surface of the anchor plate (equivalent of the inner plate - see Fig.4.4a).

At the load-level that corresponds to the mean ultimate load-bearing capacity of the equivalent Plug-inC test configuration ($F_{u,mean}$=*892kN*), the full yielding of the dovetail back surface could be noticed. Thus, the ultimate load-bearing capacity of Plug-inC could be simply estimated as the plastic load-bearing capacity of the dovetail back surface. In addition, the contact status between the flat surfaces of the inner and the cover plates could also be noticed to be mostly open at 690kN load level which corresponds to the mean linear-rotation threshold ($F_{lr,mean}$=*693* - see also Figs. 4.11-4.12). Therefore, for the estimation of the ultimate load-bearing capacity of Plug-inC, the entire moment-action could be assumed to be transferred to the hub by only the isolated dovetail. In other words, at the ultimate load level, the connection height ($h_{connection}$) could be assumed to be equal to the inner dovetail height (h_{inner}=*65mm* - see also Fig. 4.1d).

According to the magnitudes of the *y-axis* contact force vectors presented in Fig. 4.22 for the isolated dovetail image, it is concluded that the large portion of the applied loading is transferred to the hub through the bottom dovetail surface (including the round regions) compared to the dovetail side surfaces. However, the dovetail side surfaces also transfer the applied loading to the hub through frictional resistance, in other words the contact shear force. To clarify this phenomenon, the *y-axis* contact normal and shear forces on the side dovetail surfaces are compared by the applied loading in Fig. 4.23 and it is shown that at the mean yield load-level ($F_{y,mean}$=*350kN*) the contribution of the dovetail side surface contact normal and shear forces against the applied loading were about 23.0%-(83kN) and 3.6% (13kN), respectively. Furthermore, it is also shown that the *y-axis* contact normal force does not increase at the side surfaces after attaining the yield capacity while there is only limited increase for the *y-axis* contact shear force. It could also be noticed that the ratio of the total *y-axis* force transferred to the hub by the dovetail side surfaces is also about 26% at the ultimate load-level. Thus the contribution of the side surfaces against the applied loading could be assumed to be conservatively constant about 25% for the entire loading history.

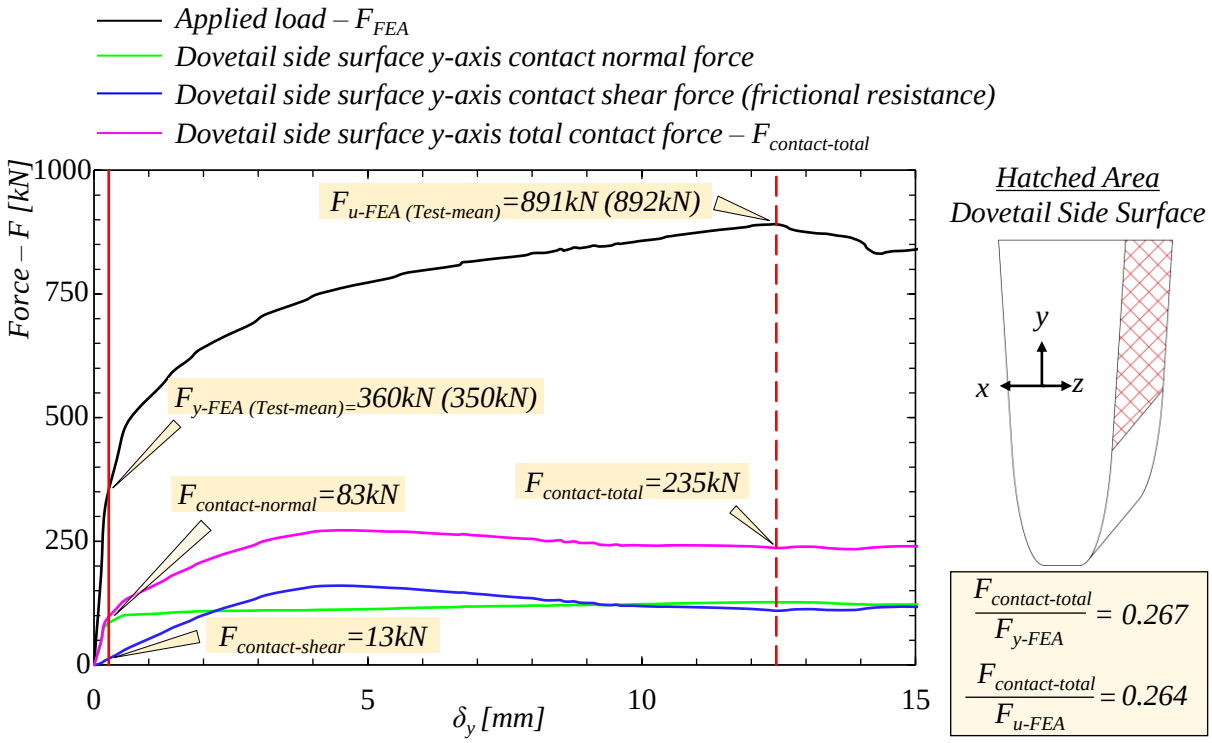

Figure 4.23: Contact normal and shear forces at the dovetail side surfaces against to the applied loading.

The last but not the least, as mentioned earlier, although the test set-up was designed to achieve 17.5mm load-eccentricity (*e=17.5mm*) the actual magnitude of the eccentricity was depending the bending and the out-of-plane rotation of the cover plates together with the stress distribution along the length of the M42 threaded-rod holes where the load was introduced to the cover plates. Therefore, Fig. 4.24 presents a section cut at the upper edge of the cover plate at the ultimate load level of the FEA and shows that the actual load-eccentricity was 12.5mm. Consequently, the magnitudes of the moments in Fig. 4.7 and Fig. 4.20 should be reduced by a factor of 1.4. Furthermore, the ultimate load-bearing capacity of Plug-inC must be re-assessed with respect to the minimum required mean resistance defined in Eq. 4.6 for the load-eccentricities larger than 12.5mm as it is presented in Fig. 4.2 that the load-eccentricity for central position of a steel-beam in Plug-inC joint configuration is 17.5mm∓10mm. This investigation is executed with a numerical parametric study presented in Section 4.6.

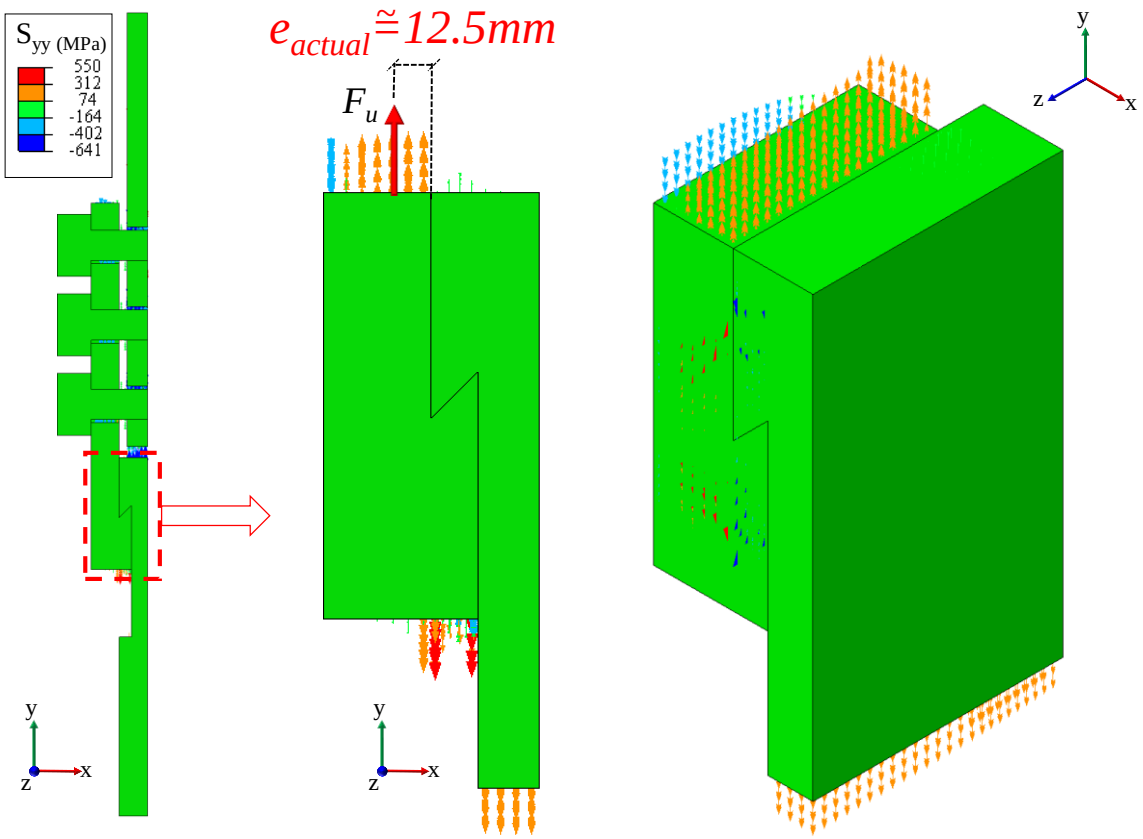

Figure 4.24: Position of the *y-axis* resultant force on a section cut of the cover plate at $F_{u,FEA}$.

4.5 Analytical resistance models for Plug-inC

Simplified analytical and *"semi-analytical"* resistance models are developed to estimate the elastic and the ultimate load-bearing capacities of Plug-inC under static loading conditions. Following assumptions are adopted for the simplification of the resistance models.

- Plane section remains in plane after the bending deformations.
- Deformations are small and they could be ignored for the analytical calculations.
- There exists full contact between the hub and the dovetail counterparts. Thus, there are no assembly gap or relative slip between the counterparts.
- Corbel plate rotates rigidly.
- The status of the contact between the flat surfaces of the anchor and cover plates is open and the entire moment-action is transferred to the anchor plate by only the dovetail at the ultimate load-level.
- The distribution of the shear stress is uniform along the entire height of the yield and failure surfaces.

For the development of the analytical resistance model, the required geometric details and the corresponding definitions are presented in Fig. 4.25. Correspondingly, the formulations for the calculation of the back surface area (A_{ba}) and the position of its geometric center (h_{GC}) is presented in Annex-D.

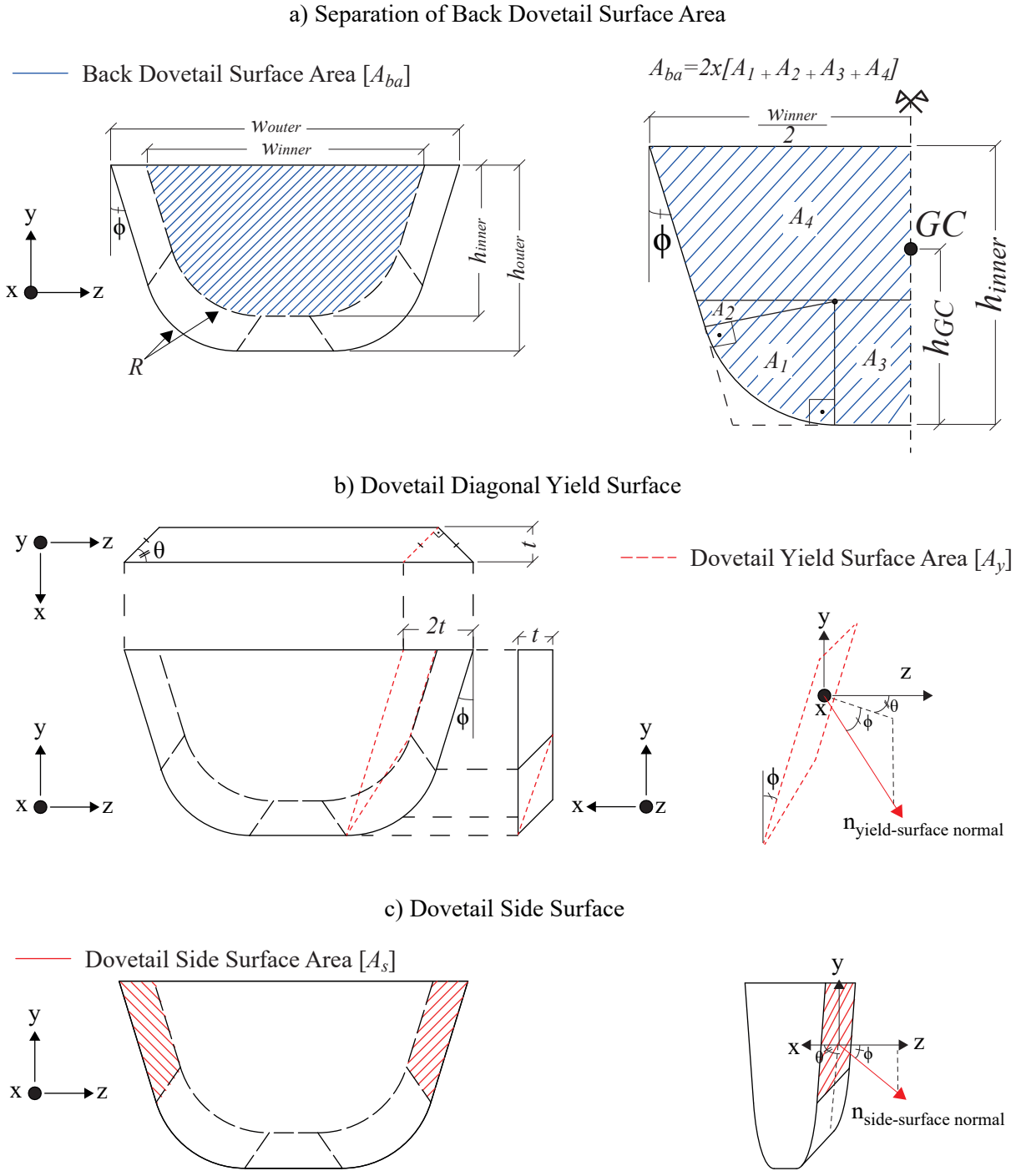

Figure 4.25: Required geometric details of the dovetail for Plug-inC analytical resistance model.

Furthermore, the area of the diagonal yield surface (A_y) which is illustrated in Fig. 4.25b could be simply estimated with Eq. 4.7. It is important to note that due to the dovetail round radius (R) the calculation of the diagonal yield surface area requires complex geometrical manipulations. Therefore, Eq. 4.7 simplifies this calculation to be consistent with the simplified approach of the analytical resistance model.

$$A_y = t\sqrt{2} \cdot \frac{\frac{h_{outer}}{\cos\phi} + \left(\frac{h_{inner}-R}{\cos\phi} + R\tan\phi\right)}{2} \tag{4.7}$$

Having defined the required geometric details, a simplified load distribution could be defined for the corbel plate as shown in Fig. 4.26 by assuming the height of the rotation centre (h_{rc}) to be equal to the quarter of the connection height ($h_{connection}$). Consequently, the static force equilibrium conditions in 2D Cartesian coordinate system could be derived for the corbel plate with Eq. 4.8 and Eq. 4.9 according to the contact normal direction of the dovetail side surfaces presented in Fig. 4.25c. The lower terms "s" and "bo" that appear in the following equations correspond to the side and bottom surfaces.

$$\sum F_{y=0} = N_{bo} \cdot \sin\theta + N_{bo} \cdot \mu \cdot \cos\theta + N_s \cdot \sin\phi + N_s \cdot \mu \cdot \cos\phi - F \tag{4.8}$$

$$\sum F_{x=0} = N_{bo} \cdot \cos\theta - N_{bo} \cdot \mu \cdot \sin\theta + N_s \cdot \cos\theta \cdot \cos\phi + N_s \cdot \mu \cdot \cos\theta - F_{comp,tail} - F_{comp} \tag{4.9}$$

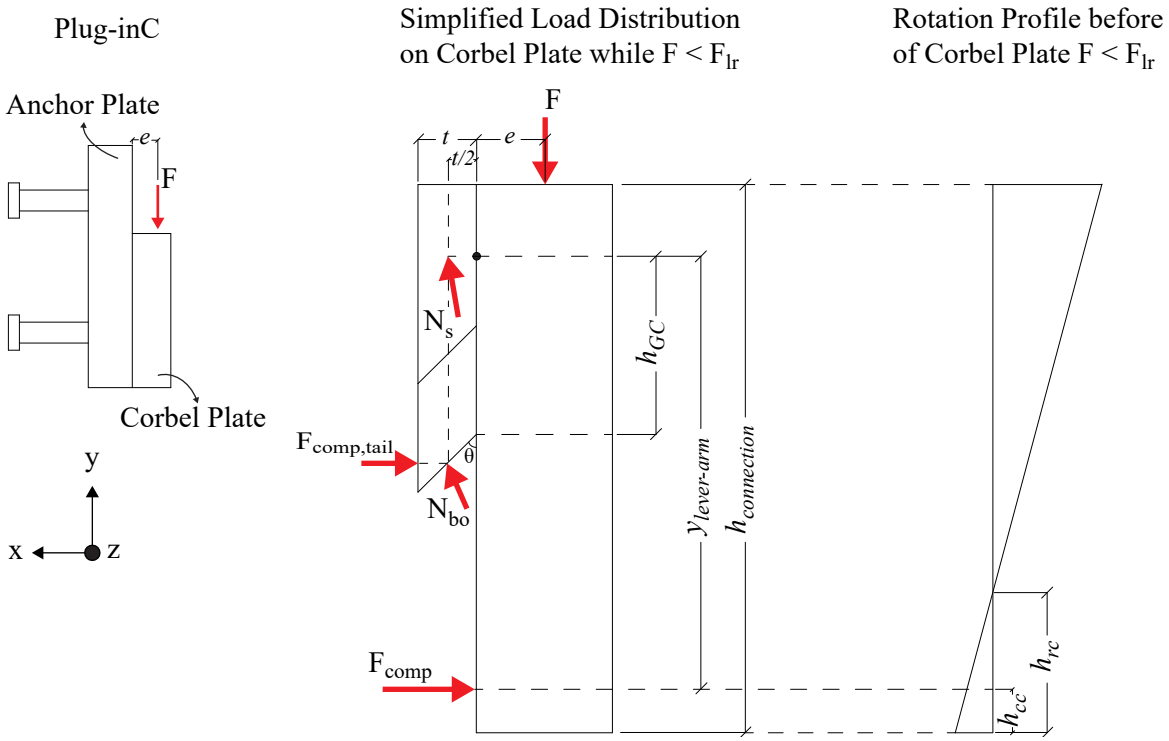

Figure 4.26: Simplified load-distribution on the corbel plate for the analytical resistance model.

Additionally, assuming the localization of the *x-axis* stresses at the bottom surface of the dovetail Eq. 4.10 could be written. Thereby, Eq. 4.9 could be simplified as formulated in Eq. 4.11;

$$F_{comp,tail} = N_{bo} \cdot \cos\theta - N_{bo} \cdot \mu \cdot \sin\theta \tag{4.10}$$

$$\sum F_{x=0} = N_s \cdot \cos\theta \cdot \cos\phi + N_s \cdot \mu \cdot \cos\theta - F_{comp} \tag{4.11}$$

As a result, the static moment equilibrium condition of the corbel plate could be derived with Eq. 4.12 with respect to the geometric center of the dovetail back surface. It is here important to note that for the simplified load distribution presented in Fig. 4.26, the *y-axis* position of the normal force at the side dovetail surfaces is assumed to coincide with the geometric centroid of the dovetail back surface area for simplicity.

$$\sum M_{z,\ about\ GC=0} = F \cdot (e + \frac{t}{2}) - (N_s \cdot \cos\theta \cdot \cos\phi + N_s \cdot \mu \cdot \cos\theta) \cdot y_{lever-arm} \tag{4.12}$$

Thus;

$$F \cdot (e + \frac{t}{2}) = (N_s \cdot \cos\theta \cdot \cos\phi + N_s \cdot \mu \cdot \cos\theta) \cdot y_{lever-arm} \tag{4.13}$$

Furthermore, by resolving the side surface normal force (N_s) in *x-axis* of the Cartesian coordinate system by Eq. 4.14, the total *x-axis* force on the dovetail side surfaces ($F_{s,x}$) could be formulated by means of the applied loading (F) with Eq. 4.15. Additionally, the total *y-axis* force in Cartesian coordinate system on the dovetail bottom surface ($F_{bo,y}$) could be derived by combining Eq. 4.8 with Eq. 4.14 and Eq. 4.15 as shown in Eq. 4.16.

$$F_{s,x} = N_s \cdot \cos\theta \cdot \cos\phi + N_s \cdot \mu \cdot \cos\theta \tag{4.14}$$

$$F_{s,x} = \frac{F \cdot (e + \frac{t}{2})}{y_{lever-arm}} \tag{4.15}$$

$$F_{bo,y} = \frac{F \cdot (e + \frac{t}{2})}{y_{lever-arm} \cdot \cos\theta \cdot (\cos\phi + \mu)} \cdot (\sin\phi + \mu \cdot \cos\phi) \tag{4.16}$$

Inputting the geometrical parameters (see Table 4.8) into Eq. 4.16 with a static friction coefficient of 0.4 (μ=*0.4*), the total *y-axis* stress resultant on the dovetail bottom surface ($F_{bo,y}$) is found to be equal to 85% of the applied loading (F); thus, it is concluded that 15% of the applied loading is resisted by the dovetail side surfaces. This result could be accepted to be consisted with the output results of the FEA presented in Fig. 4.23 considering the simplicity of the assumed load-distribution (see Fig. 4.26).

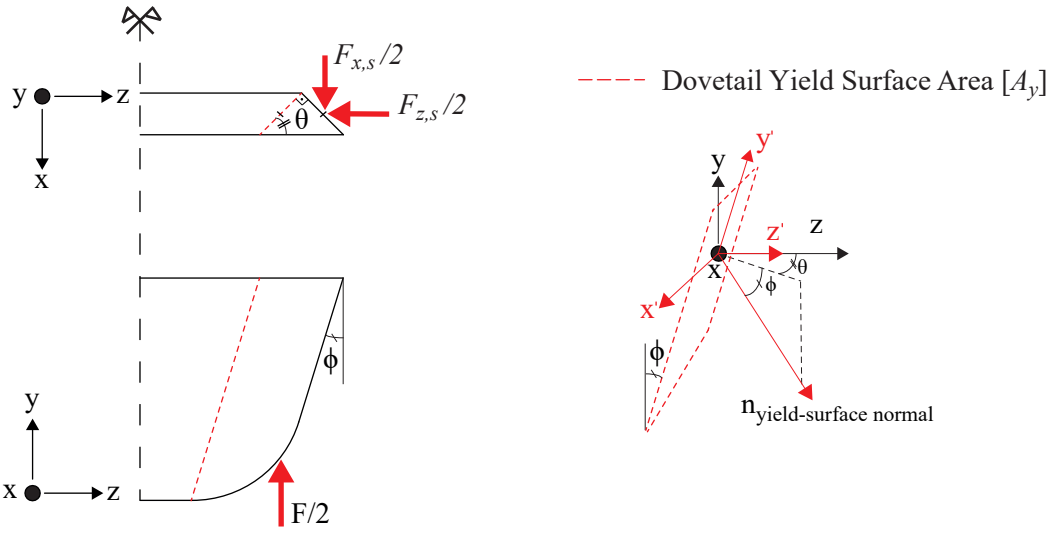

Figure 4.27: Stress resultants on the half symmetric configuration of the dovetail in Cartesian coordinate system, and the local coordinate system of the yield surface.

Consequently, having verified the simplified load-distribution, the stress resultants on the half symmetric configuration of the dovetail could be drawn in Cartesian coordinate system by means of the applied loading as illustrated in Fig. 4.27. It is important to mention that the *z-axis* stress resultant (F_z) that appears in Fig. 4.27 could be defined with Eq. 4.17 based on the side surface normal presented in Fig. 4.25c;

$$F_{s,z} = F_{s,x} \tag{4.17}$$

Thereby, the normal and shear stresses could be defined with Eq. 4.18 to Eq. 4.20 on the diagonal yield surface based on the local coordinate system presented in Fig. 4.27;

$$\sigma_{z'} = \frac{F \cdot \sin\phi}{2 \cdot A_y} \tag{4.18}$$

$$\tau_{z'x'} = \frac{F \cdot \sqrt{2} \cdot (e + \frac{t}{2})}{2 \cdot A_y \cdot y_{lever-arm}} \tag{4.19}$$

$$\tau_{z'y'} = \frac{F \cdot \cos\phi}{2 \cdot A_y} \tag{4.20}$$

Furthermore, the yield status of the diagonal yield surface could be defined with Eq. 4.21 analogical to the Von-mises yield criterion;

$$f_y = \sqrt{\sigma_{z'}^2 + 3 \cdot \left(\sqrt{\tau_{z'x'}^2 + \tau_{z'x'}^2}\right)^2} \tag{4.21}$$

Finally, by combining Eq. 4.21 with Eqs. 4.18-4.20, the elastic load-bearing capacity of Plug-inC, F_y, could be estimated with Eq. 4.22.

$$F_y = \frac{2 \cdot A_y \cdot f_y}{\sqrt{3 \cdot \left(\frac{e+\frac{t}{2}}{y_{lever-arm}}\right)^2 + 2 \cdot (\cos\phi)^2 + 1}} \tag{4.22}$$

Table 4.8 compares the estimation of Eq. 4.22 and the elastic load-bearing capacity of Plug-inC determined with the experimental tests (see also Table 4.5). According to the percentage differences between the estimations and the test results, it is concluded that the presented analytical resistance model estimates the elastic load-bearing capacity of Plug-inC with a good agreement. However, it is important to note that the estimations were nonconservative. Therefore, statistical assessment of Eq. 4.22 needs to be performed to establish partial safety factors. This investigation is presented in Section 4.7 based on the results of the numerical parametric study detailed in Section 4.6.

Table 4.8: Comparison of the test results and the estimation of the analytical resistance model for the elastic load-bearing capacity of Plug-inC.

Test ID	f_y[1] [MPa]	R [mm]	ϕ [°]	t [mm]	e[2] [mm]	$y_{lever\text{-}arm}$ [mm]	A_y [mm^2]	$F_{y,est}$[3] [kN]	$F_{y,test}$ [kN]	Diff. [%]
Plug-inC-01	226	31.5	17.1	15	12.5	99.0	1362	358	305	17.4
Plug-inC-02	263	40	17.1	15	12.5	99.5	1296	396	368	7.6
Plug-inC-03	255	40	17.1	15	12.5	99.5	1296	384	378	1.5

[1] The yield strengths of the cover plates presented in Table 4.3 were used because the elastic load-bearing capacity of Plug-inC is estimated based on the yield status of the dovetail.

[2] Although the desired load-eccentricity for the tests was *e=17.5mm*, it is shown in Fig. 4.24 that the actual load-eccentricity was e_{actual}*=12.5mm*.

[3] $F_{y,est}$ corresponds to the estimated elastic yield capacity of Plug-in with Eq. 4.22

It has been earlier shown in Fig. 4.12 that the rotation profiles of the cover plates, in other words the corbel plate, become non-linear once the loading on Plug-inC is larger than the linear rotation threshold (F_{lr}). In addition, it is shown in Fig. 4.22 that the contact status between the flat surfaces of the inner and the cover plates becomes mostly open at the ultimate load limit. Therefore, the simplified load-distribution presented in Fig. 4.26 becomes invalid for the ultimate load limit as the contact normal force on the flat surface of the corbel plate (F_{comp}) disappears. As a result, at the ultimate load limit of Plug-inC, the entire moment-action could be assumed to be resisted by only the dovetail. Therefore, a new load-distribution should be defined for the estimation of the ultimate load-bearing capacity of Plug-inC. Fig. 4.28a illustrates the new simplified load distribution for the isolated configuration of the dovetail at the ultimate load limit together with a possible 2D strain and corresponding stress distributions at the dovetail back surface.

Considering the relatively complex geometry of the dovetail, the non-linear stress-strain relation of the ductile metals beyond the yield strain and the impact of the shear stresses at the dovetail back surface, it becomes unreasonable complicated to develop closed form analytical design equation for the estimation of the ultimate load-bearing capacity of Plug-inC. Therefore, the ultimate load-bearing capacity of Plug-inC is estimated with the *"semi-analytical"* resistance model using strain limited design concept [71], which is generally used in civil engineering practice for the design of the reinforced concrete members under bending moment action. However, different from the regular strain limited design concept, the impact of the shear stress on the load-bearing capacity of Plug-inC shall be considered as it was earlier shown in Fig. 4.16 that the dovetail counterpart undergoes excessive shear deformation at the ultimate load limit. Therefore, a notional material law is proposed with reduced yield and ultimate material strengths (f_{yr} and f_{ur}) for the resistance against to the normal stresses at the back surface of the dovetail as illustrated in Fig. 4.28b. It is important to note that the utilization of a notional material law with reduced mechanical properties in case of an excessive shear loading along a cross-section is not a new concept as it has been already proposed by EN1993-1-1 [50] for the cross-sectional analysis of steel beams under bending moment and vertical shear actions. The reduced mechanical properties of the notional material law could be calculated analogical to the Von-mises yield criterion in 2D loading conditions as presented in Eq. 4.23 to Eq. 4.25. Furthermore, it is crucial to mention that the proposed notional material law also assumes perfectly plastic behavior between the ultimate strain and the fracture strain values as different from the actual stress-strain behavior of the ductile metals not to have convergence problems for the *"semi-analytical"* resistance model proposed to estimate the ultimate load-bearing capacity of Plug-inC.

$$\sigma_v = \sqrt{{\sigma_x}^2 + 3 \cdot {\tau_{xy}}^2} \tag{4.23}$$

$$f_{yr} = \sqrt{{f_y}^2 - 3 \cdot {\tau_{xy}}^2} \tag{4.24}$$

$$f_{ur} = \sqrt{{f_u}^2 - 3 \cdot {\tau_{xy}}^2} \tag{4.25}$$

The in-plane shear stress (τ_{xy}) that appears in Eqs. 4.23-4.25 could be formulated with Eq. 4.26 considering the assumptions listed at the beginning of this section and the free body diagram of the dovetail presented in Fig. 4.28.

$$\tau_{xy} = \frac{F}{A_{ba}} \tag{4.26}$$

a) Simpflied Load Distribution and Corresponding Strain-stress State for Isolated Dovetail

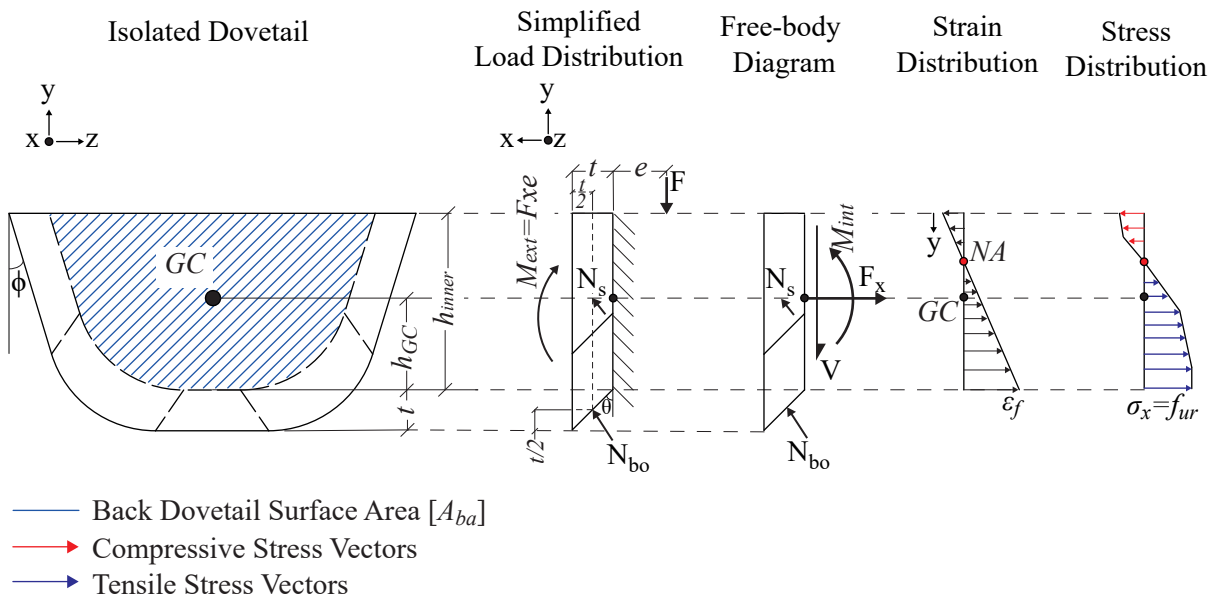

b) Simpflied Material Law and the Corresponding Notional Material Law

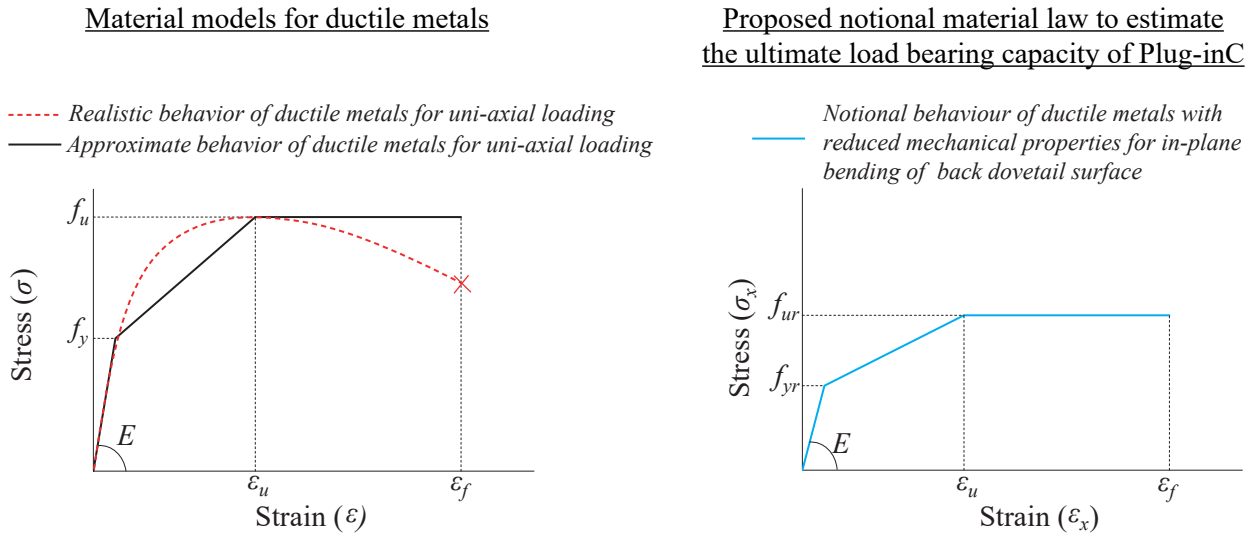

Figure 4.28: Simplified load distribution and the corresponding normal stress strain state for the isolated dovetail configuration and the illustration of the notional material law for the normal stress strain relation.

According to the free-body diagram presented in Fig. 4.28a, the force equilibrium conditions could be defined at the dovetail back surface with Eq. 4.27 and Eq. 4.29

$$\sum F_{x=0} = N_{bo} \cdot (\cos\theta - \mu \cdot \sin\theta) + N_s \cdot \sin\phi \cdot \cos\theta \cdot (1+\mu) - F_x \tag{4.27}$$

Thus;

$$F_x = N_{bo} \cdot (\cos\theta - \mu \cdot \sin\theta) + N_s \cdot \sin\phi \cdot \cos\theta \cdot (1+\mu) \tag{4.28}$$

In addition;

$$\sum F_{y=0} = N_s \cdot (\sin\phi + \mu \cdot \cos\phi) + N_{bo} \cdot (\sin\theta + \mu \cdot \cos\theta) - V \tag{4.29}$$

where;

$$N_s \cdot (\sin\phi + \mu \cdot \cos\phi) + N_{bo} \cdot (\sin\theta + \mu \cdot \cos\theta) = F \tag{4.30}$$

Thus;

$$V = F \tag{4.31}$$

It is the fact that the magnitude of F_x in Eq. 4.28 depends on the distribution of the applied loading between the side and the bottom surfaces of the dovetail, which is unknown. However, it was earlier shown in Fig. 4.23 that about 25% of the applied loading is transferred to the hub by the side surfaces of the dovetail. Therefore, for the derivation of the following equations, it is adopted that the ratio between the applied load and the resistance against the loading at the side dovetail surfaces is one quarter. Consequently, the derivation of the following equations could be considered to be *"semi-analytical"*. Based on the herein mentioned adoption, the relation between the side normal and bottom normal forces could be defined by means of the applied loading, as shown in Eq. 4.32 and Eq. 4.33.

$$N_{bo} \cdot (\sin\theta + \mu \cdot \cos\theta) = 0.75 \cdot F \tag{4.32}$$

$$N_s \cdot (\sin\phi + \mu \cdot \cos\phi) = 0.25 \cdot F \tag{4.33}$$

Thereby, combining Eq. 4.28 with Eqs. 4.32-4.33, F_x could be found as formulated in Eq. 4.34;

$$F_x = 0.25 \cdot F \cdot \frac{\sin\phi \cdot \cos\theta \cdot (1+\mu)}{\sin\phi + \mu \cdot \cos\phi} + 0.75 \cdot F \cdot \frac{(\cos\theta - \mu \cdot \sin\theta)}{\sin\theta + \mu \cdot \cos\theta} \tag{4.34}$$

Furthermore, based on the free-body diagram, the moment equilibrium with respect to the centroid of the dovetail back surface could be defined by Eq. 4.35;

$$\sum M_{z\ about\ GC=0} = F \cdot (e + \frac{t}{2}) + 0.75 \cdot F \cdot \left(\frac{\cos\theta - \mu \cdot \sin\theta}{\sin\theta + \mu \cdot \cos\theta}\right) \cdot \left(h_{GC} + \frac{t}{2}\right) - M_{int} \tag{4.35}$$

Thus;

$$M_{int} = F \cdot \left(e + \frac{t}{2}\right) + 0.75 \cdot F \cdot \left(\frac{\cos\theta - \mu \cdot \sin\theta}{\sin\theta + \mu \cdot \cos\theta}\right) \cdot \left(h_{GC} + \frac{t}{2}\right) \tag{4.36}$$

Consequently, as consisted with the free-body diagram and the normal stress distribution presented in Fig. 4.28, Eq. 4.37 and Eq. 4.38 could be defined for the dovetail back surface.

$$F_x = \int_0^{h_{inner}} \sigma_x \, dA_{ba} \tag{4.37}$$

$$M_{int} = \int_0^{h_{inner}} \sigma_x \cdot y \, dA_{ba} \tag{4.38}$$

As a result, by solving Eq. 4.37 and Eq. 4.38 together with the linear strain distribution and the notional material behaviour presented in Fig. 4.28, the ultimate load bearing capacity of Plug-inC (F_u) could be estimated. However, due to the non-linear stress distribution and the relatively complex geometry of the dovetail, the solution becomes unreasonable complicated for an engineering model. Therefore the solution is approximated based on the partition method [86]. Fig. 4.29 shows the partitioning of the dovetail back surface area and corresponding strain and stress states. The dovetail round radius is not included in the partitioning for simplicity. However, it is important to note that the impact of the round radius is taken account indirectly by Eq. 4.25 and Eq. 4.26. Thereby, the equilibrium conditions presented in Eq. 4.37 and Eq. 4.38 could be re-written based on Fig. 4.29 as presented in Eq. 4.39 and Eq. 4.40, respectively.

$$F_x = \sum_{i=1}^{n=number\ of\ parts} \sigma_{x-i} \cdot \frac{h_{inner}}{n} \cdot \left(w_{inner} - \frac{i \cdot \tan\phi \cdot h_{inner}}{n}\right) \tag{4.39}$$

$$M_{int} = \sum_{i=1}^{n=number\ of\ parts} \sigma_{x-i} \cdot \frac{h_{inner}}{n} \cdot \left(w_{inner} - \frac{i \cdot \tan\phi \cdot h_{inner}}{n}\right) \cdot \left(h_{inner} \cdot \left(1 - \frac{1}{2n} - \frac{1-i}{n}\right) - h_{gc}\right) \tag{4.40}$$

Although, the simultaneous solution of Eq. 4.39 and Eq. 4.40 is relatively simple compared with the closed form solution of Eq. 4.37 and Eq. 4.38, it is still required to perform iterative spreadsheet calculation to be able to estimate the ultimate load bearing capacity of Plug-inC due to the non-linearity of the problem.

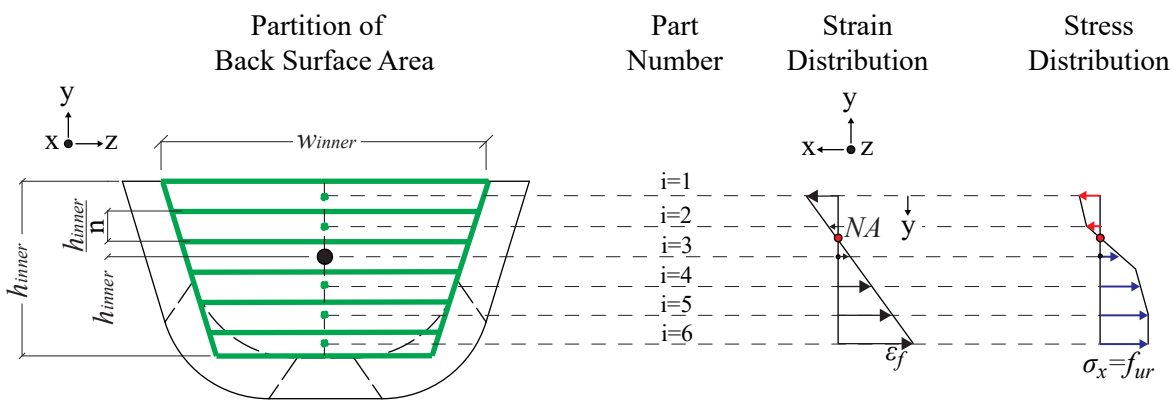

Figure 4.29: Illustration for the partition of the dovetail back surface and corresponding strain-stress relationship.

Table 4.9 presents the result of the spreadsheet calculations performed to estimate the ultimate load-bearing capacity of Plug-inC test configurations. According to the percentage difference between the estimated and actual ultimate capacities, it is concluded that the proposed *"semi-analytical"* resistance model could accurately estimate the ultimate load-bearing capacity of Plug-inC. The accuracy of the *"semi-analytical"* resistance model is also assessed based on the output results of the numerical parametric study which is presented in Section 4.6.

Table 4.9: Comparison of test results and the estimation of the *"semi-analytical"* resistance model for the ultimate load-bearing capacity of Plug-inC.

Test[1]	f_y[2] [MPa]	f_u[2] [MPa]	ε_u [%]	ε_f [%]	ϕ [°]	θ [°]	t [mm]	w_i[3] [mm]	A_{ba} [mm^2]	$F_{u,e}$[4] [kN]	$F_{u,t}$[5] [kN]	Diff. [%]
01	226	410	33.5	39.5	17.1	45	15	120	6297	822	873	5.8
02	263	488	31.8	38.0	17.1	45	15	120	6177	978	912	7.2
03	255	455	30.0	36.5	17.1	45	15	120	6177	921	890	3.5

NOTE: The actual load-eccentricity was *e=12.5mm* for all of the experimental tests as shown in Fig. 4.24.

[1] Test IDs are shorten / 01:Plug-inC-01, 02:Plug-inC-02, 03:Plug-inC-03

[2] The yield and ultimate strengths of the cover plates presented in Table 4.3 were used because the ultimate load-bearing capacity of Plug-inC is estimated based on the load-bearing capacity of the dovetail.

[3] w_i corresponds to the w_{inner}.

[4] $F_{u,e}$ corresponds to the estimated ultimate load-bearing capacity of Plug-in by simultaneous solution of Eqs. 4.39-4.40

[5] $F_{u,t}$ corresponds to the ultimate load-bearing capacity of Plug-inC determined with the experimental tests.

4.6 Numerical parametric study

The previous section presents two different resistance models to estimate the elastic and ultimate load-bearing capacities of Plug-inC. To be able to further assess the accuracy of the presented resistance models and to understand the impact of the dovetail round radius, dovetail thickness, static friction coefficient and the load-eccentric on the load-deformation behaviors of Plug-inC, a numerical parametric study was performed by means of FEAs. Table 4.10 presents the input parameters of the parametric study. To summarize, for each dovetail round radius (R) listed in Table 4.10, 54 separate FEAs were performed by varying the dovetail thickness (t), the static friction coefficient between the hub and the dovetail (μ) and the load-eccentricity (e). The variation of the load-eccentricity was selected based on the position of the steel-beam with respect to the column surface as highlighted in Fig. 4.2. In addition, one extreme case with 100mm load-eccentricity (e_6=*100mm*) was investigated together with the all other parameters listed in Table 4.10 to check the validity of the analytical resistance models for an extreme load-eccentricity. It is however important to mention that this eccentricity is not realistic for the joint configuration presented in Fig. 4.2.

A separate FE-model was created to perform the numerical parametric study. Fig. 4.30 shows the details of the FE-model. The anchor plate and the corbel plate were modelled with their half-symmetric explicit geometry presented in Fig. 4.1 and detailed in Table 4.2. It is important to mention that the headed-fasteners were excluded from the FE-model and the back surface of the anchor plate was fully restrained in all degrees of freedom (DOFs) with the encastre boundary conditions as the interaction between the Plug-inC and RC-members is out of the scope of this chapter. The material law with approximate material behavior presented in Fig. 4.17a was used for the anchor and the corbel plates with the mechanical properties presented in Table 4.6 in which the cover plate corresponds to the corbel plate and inner plate corresponds to the anchor plate. The interaction method and the interaction properties presented in Table 4.7 were kept identical but as listed in Table 4.10 the friction coefficient was parameterized. The mesh of the hub and the dovetail also kept identical with the FE-model of the experimental tests. Identical to the FEAs of the experimental tests, Abaqus/Standard solver was used with dynamic-implicit solution scheme [66].

Table 4.10: The variable parameters of the numerical parametric study of Plug-inC.

R [mm]	t [mm]	μ	e [mm]	Analysis Vector [108x1]
$\begin{bmatrix} R_1 = 31.5 \\ R_2 = 40 \end{bmatrix}$	$\begin{bmatrix} t_1 = 9 \\ t_2 = 12 \\ t_3 = 15 \end{bmatrix}$	$\begin{bmatrix} \mu_1 = 0.2 \\ \mu_2 = 0.4 \\ \mu_3 = 0.6 \end{bmatrix}$	$\begin{bmatrix} e_1 = 7.5 \\ e_2 = 12.5 \\ e_3 = 17.5 \\ e_4 = 22.5 \\ e_5 = 27.5 \\ e_6 = 100 \end{bmatrix}$	$\begin{bmatrix} R_1 t_1 \mu_1 e_1 \\ R_1 t_1 \mu_1 e_2 \\ \vdots \\ \vdots \\ R_2 t_3 \mu_3 e_5 \\ R_2 t_3 \mu_3 e_6 \end{bmatrix}$

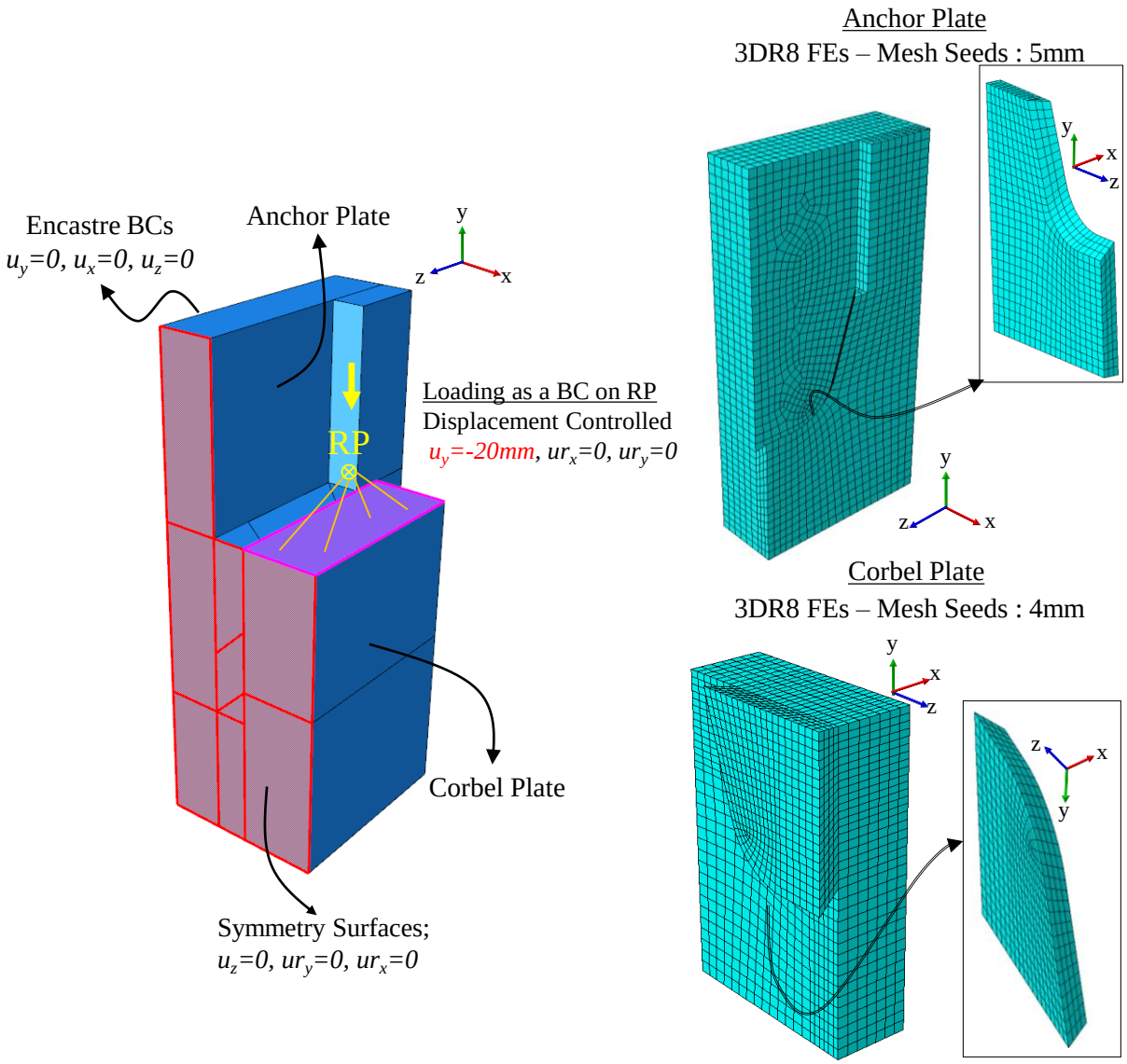

Figure 4.30: FE-Model of Plug-inC parametric study.

The load-displacement and moment-rotation curves for each FEA of the parametric study are presented in Annex-D. In addition, the comparison between the test results and the FEA performed with 12.5mm load-eccentricity (e), 15mm dovetail thickness (t), 40mm round radius (R) and 0.4 friction coefficient (μ) is presented in Fig. 4.31 to verify that the actual load-eccentricity (e_{actual}) achieved by the experimental test set-up was 12.5mm (see also Fig. 4.24). The force outputs of the FEA are taken as the total reaction force at the encastre restrained surface of the anchor plate. One could criticize that the post-failure behaviors of the FEAs presented in Fig. 4.18 differ from the one presented in Fig. 4.31. This difference could be attributed to the second order effects. In other words, the experimental tests, thus the corresponding FEAs were performed by vertically pulling the cover plates (equivalent to corbel plate) while the FEAs of the parametric study was performed

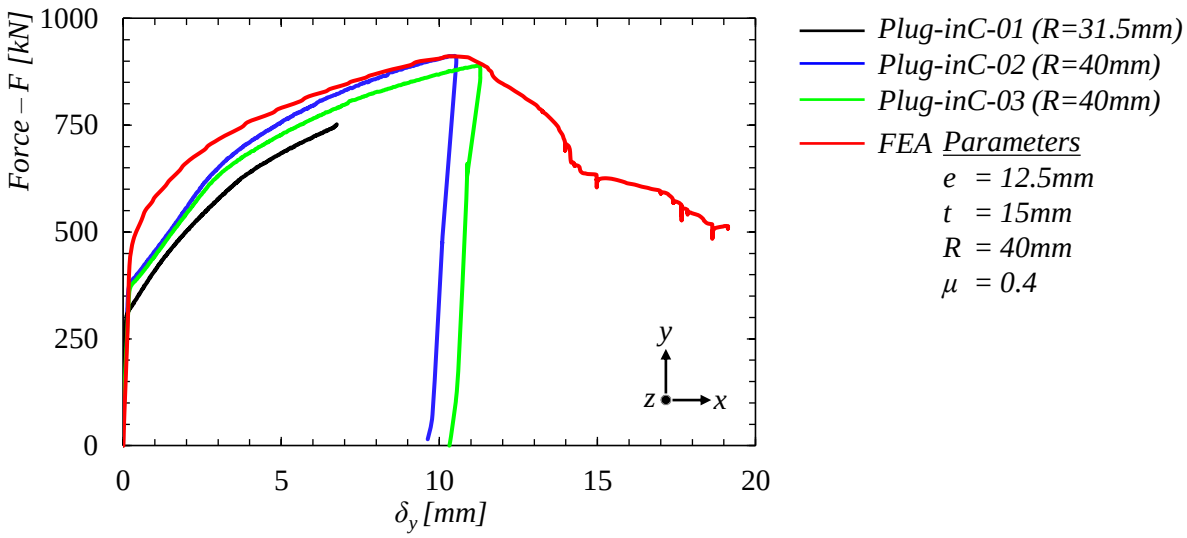

Figure 4.31: The load-displacement curves of Plug-inC test campaign against FEA of *e=12.5mm*.

by vertically pushing the corbel plate as consisted with the joint configuration of Plug-inC for gravitational loading conditions (see Fig. 4.2). Consequently, for the experimental tests the load-eccentricity was gradually reducing and the rate of the reduction significantly increases by attaining the ultimate load-bearing capacity. On the other hand, for the FEAs of the parametric study the load-eccentricity was increasing during the entire loading-history. Nevertheless, according to Fig. 4.18 it is verified that the actual load-eccentricity achieved by the experimental tests was 12.5mm.

Fig. 4.32 shows the variation of the elastic and the ultimate load-bearing capacities of Plug-inC with respect to the selected parameters. The output results of the FEAs with 100mm load-eccentricity are excluded from the figure as these analyses were performed only to investigate the accuracy of the analytical resistance models for an extreme eccentric-loading. Furthermore, there was nearly no impact of the friction coefficient on the elastic load-bearing capacity (F_y) of Plug-inC (see also Annex-D). Therefore, Fig. 4.31b presents only the results for μ=*0.4*. In fact, this outcome was expected as Eq. 4.22 does not involve the friction coefficient for the estimation of the elastic load-bearing capacity. Furthermore, it was earlier illustrated in Fig. 4.19 that the impact of the friction coefficient becomes decisive after attaining the elastic load-bearing capacity due to the relative slip between the hub and the dovetail. According to Fig. 4.32 following conclusions are can be drawn;

- The dovetail round radius does not have significant impact on the load-bearing capacities.
- The friction coefficient (μ) does not effect the elastic load-bearing capacity (see also Annex-D).
- There is a linear like relation between the load-eccentricity (e) and the elastic and ultimate load-bearing capacities.
- The relation between the dovetail thickness and the elastic and the ultimate load-bearing capacities could be defined as linear.

- The ultimate load-bearing capacity of Plug-inC linearly changes based on the magnitude of the friction coefficient (μ).

The conclusions are also consistent with the design equations formulated in Eq. 4.22, Eq. 4.39 and Eq. 4.40. Consequently, it could be stated that the analytical resistance models presented in Section 4.5 conceptually valid by means of the inclusion of the main design parameters. Furthermore, it could be noticed from Fig. 4.32b that for the proposed dovetail thickness (*t=15mm* - see Fig. 4.1) the ultimate load-bearing capacity (F_u) is always higher than the required design resistance ($R_{Plug\text{-}inC,d}$=*478kN*) presented by Eq. 4.3. Therefore, it could be stated that Plug-inC is a promising solution for the fast assembly of steel-beams and RC-members of steel-concrete hybrid buildings.

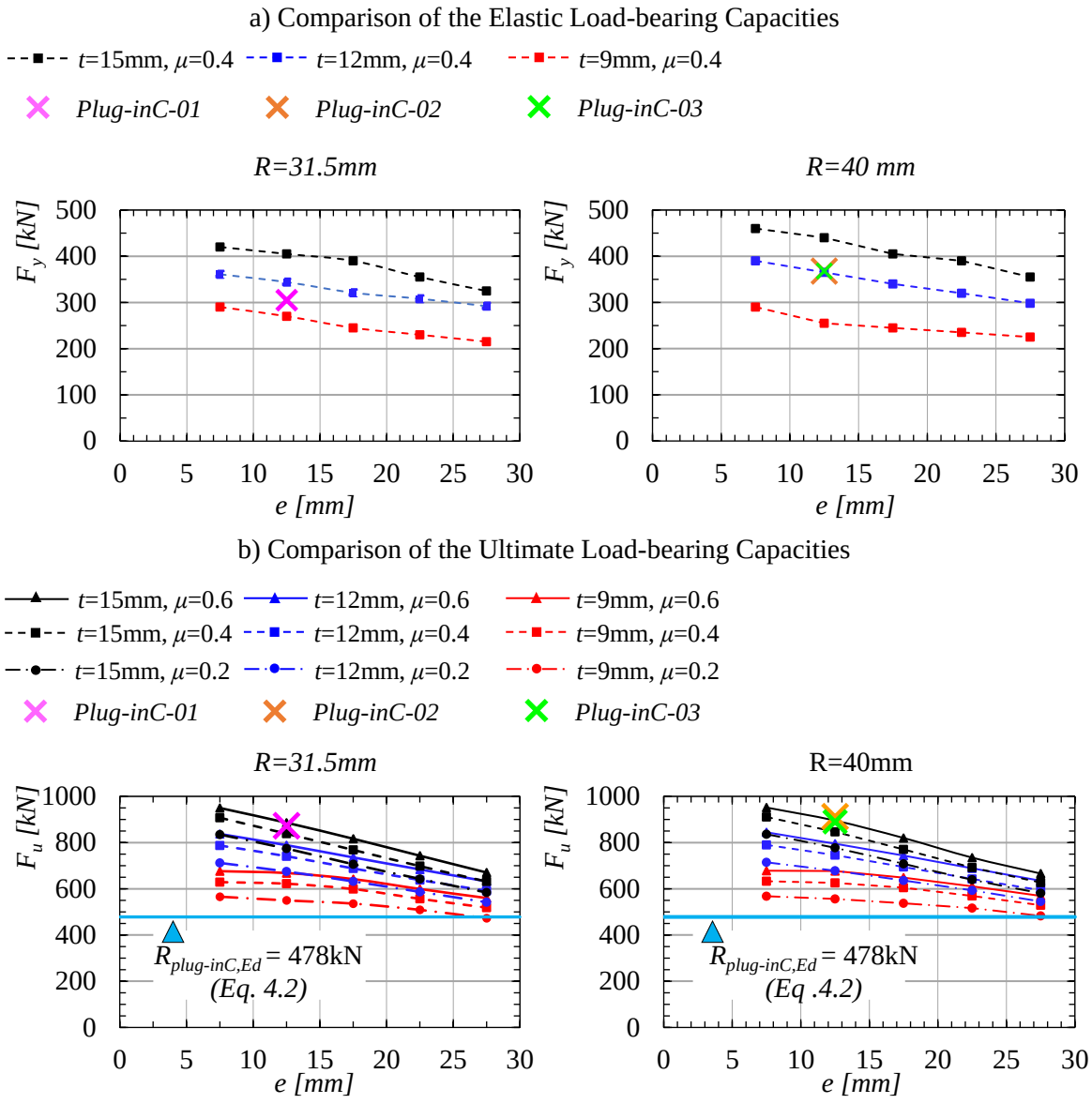

Figure 4.32: Comparisons of the output results for the numerical parametric study.

4.7 Statistical evaluation of the analytical resistance models

Fig. 4.33 compares the elastic load-bearing capacity of the parametric FEAs with the estimations of Eq. 4.22 together with the best linear fit line. As indicated in the previous section, there was no significant relation between the friction coefficient (μ) and the elastic load-bearing capacity of Plug-inC (F_y). Therefore, the estimations of Eq. 4.22 is only compared with the output results of the parametric FEAs performed with 0.4 static friction coefficient (μ=*0.4*).

Based on Fig. 4.33, it is concluded that Eq. 4.22 estimates the elastic load-bearing capacity of Plug-inC with a good accuracy. However, as expected, there is distribution around the diagonal line; thus, the estimations are not perfect. Therefore, the statistical evaluation of Eq. 4.22 was performed based on the procedure defined in EN1990, Annex D [58] to establish partial safety factors for the utilization of Eq. 4.22, in other words to calibrate the analytical resistance function of Plug-inC for the calculation of the elastic load-bearing capacity. The statistical evaluation was performed based on the data presented in Fig. 4.33. It is crucial to mention that the statistical evaluation performed in this section does not fully conform with EN 1990 Annex D [58] as the evaluation is not only based on the experimental test data but also on the output results of the FEA due to the quantity of the performed tests.

According to EN1990, Annex D [58] the coefficient of variation (CoV) of the basic variables of the resistance function (Eq. 4.22) is required to be defined based on the prior knowledge to perform the statistical evaluation. It is the fact that there is a lack of information for the statistical parameters of the basic variables. In other words, the probabilistic distribution and the related statistical parameters, i.e. the mean values and coefficient of variations, of the load-eccentricity (e), dovetail round radius (R), dovetail thickness (t), vertical slope angle (ϕ) and the material yield

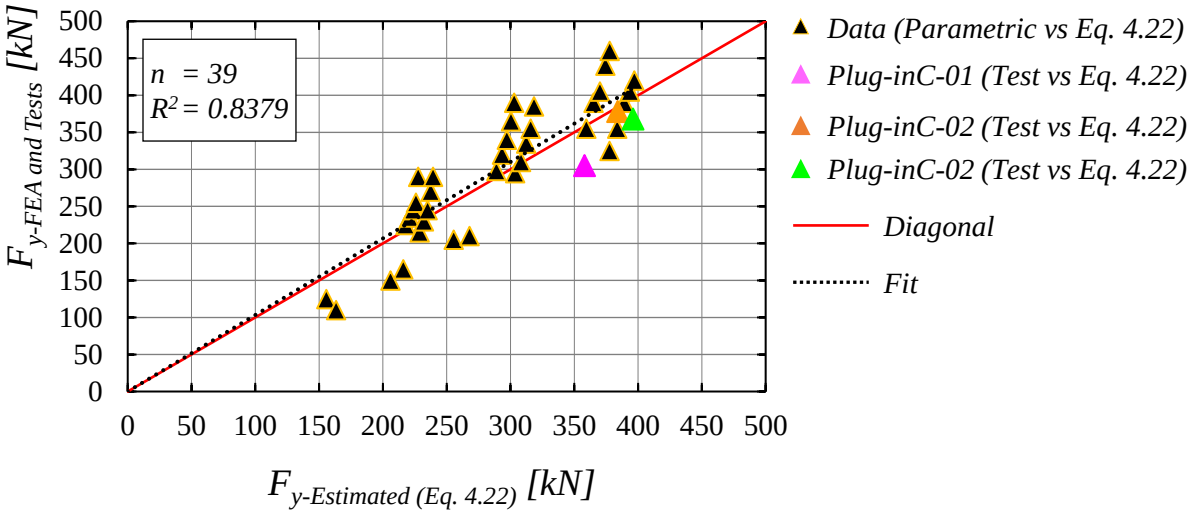

Figure 4.33: The estimated elastic load-bearing capacity of Plug-inC against the experimental tests and the parametric study.

Table 4.11: Basic variables and their statistical parameters for the statistical evaluation of Eq. 4.22

Basic Variables	Mean Values[1]	Coefficient of Variation (CoV) [%]	Distribution
f_y[2] [MPa]	246	4.7	Normal
R[3] [mm]	31.5, 40	0.6, 0.5	Normal
t[3] [mm]	9, 12, 15	2.2, 1.7, 1.3	Normal
h_{outer}[3] [mm]	80	0.2	Normal
h_{inner}[3] [mm]	65	0.3	Normal
w_{inner}[3] [mm]	120	0.2	Normal
ϕ[4] [°]	17.1	10.9	Normal
e[5] [mm]	7.5, 12.5, 17.5, 22.5, 27.5, 100	26.7, 16.0, 11.4, 8.9, 7.3, 2.0	Normal

NOTE-1: Nominal values are presented for the basic variables and their coefficient of variations.

[1]The input values presented in Table 4.10 are considered as the mean values of the corresponding basic variables for the statistical evaluation.

[2] The mean value and the coefficient of variation of the material yield strength was determined based on the entire data presented in Table 4.3 as the ordered material grade was identical (S235) for all of the inner and the cover plates.

[3] The coefficients of variation for the dimensions of the dovetail were determined based on the coarse machining tolerance of the CNC-cutting procedure and taken as 0.2mm according to the producer feedback.

[4] The coefficient of variation of the vertical slope angle (ϕ) was determined with *Monte Carlo Simulation* using the trigonometrical relation between the w_{inner} and h_{inner} - see Fig. 4.1d

[5] The coefficients of variation for the load-eccentricities were determined according to EN1090, Annex D-Table D.1.9 [59].

strength (f_y) are not known. Therefore, the statistical parameters of the basic variables are estimated based on the available information and according to the relevant literature. Table 4.11 presents the basic variables and their statistical parameters for the statistical evaluation of Eq. 4.22.

Based on the basic variables and their CoVs presented in Table 4.11, 36 separate *Monte Carlo Simulations* were performed by varying the dovetail round radius (R), dovetail thickness (t) and the load-eccentricity (e). Thereby, the CoV for the output results of Eq. 4.22 is determined as the mean of the CoVs from the 36 separate *Monte Carlo Simulations*. Having defined the CoV for the estimations of Eq. 4.22, the statistical evaluation procedure of EN1090, Annex D [58] could be finalized based on the data presented in Fig. 4.33. By the scope of this chapter, the statistical evaluation procedure of EN1990, Annex D [58] will not be not further detailed and only the input and output parameters of the procedure are presented in Table 4.12. Consequently, the comparison between the estimated elastic load-bearing capacities of Plug-inC and the output results of the numerical parametric study is shown in Fig. 4.34 together with the characteristic and design values of the estimations. Thereby, it is concluded that Eq. 4.22 could be used to estimate the elastic load-bearing capacity of Plug-inC with output parameters presented in Table 4.12 for engineering approximations.

Table 4.12: Input parameters for the statistical evaluation procedure of EN1990, Annex D (n=39 < 100) and the output parameters of the evaluation procedure for Eq. 4.22

Required Input Parameters	Assigned Values
V_δ	0.322[1]
V_{rt}	0.051[2]
k_n	1.64[3]
k_∞	1.64[3]
$k_{d,n}$	3.04[3]
$k_{d,\infty}$	3.04[3]
Output Parameters	**Output Results**
r_k	$0.776 \cdot r_t$
r_d	$0.614 \cdot r_t$
$\gamma_M = r_k / r_d$	1.262

[1] Determined according to data set presented in Fig. 4.33.

[2] Determined based on the results of the 36 *Monte Carlo Simulations*.

[3] According to EN1990, Annex D [58].

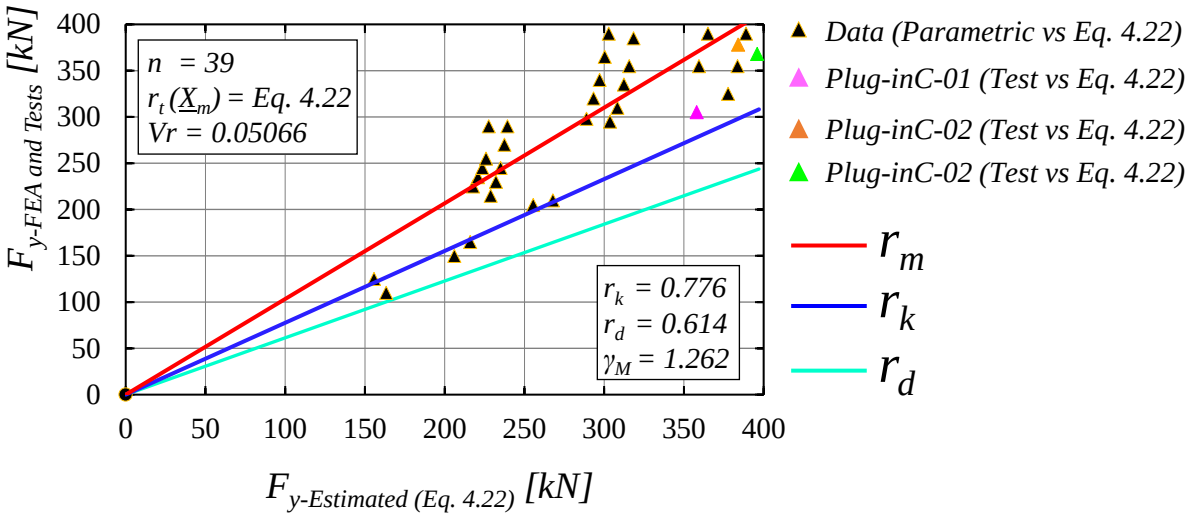

Figure 4.34: The characteristic and design partial safety factors for the analytical resistance model to estimate the elastic load-bearing capacity of Plug-inC.

As presented in Section 4.5, the ultimate load-bearing capacity of Plug-inC is estimated with a separate "*semi-analytical*" resistance model. Fig. 4.35 compares the ultimate load-bearing capacities of the parametric FEAs with the estimations of "*semi-analytical*" resistance model. It is obvious that the "*semi-analytical*" resistance model overestimates the ultimate load-bearing capacity of Plug-inC. Especially as the dovetail thickness get smaller and the friction coefficient get higher (e.g. *t=9mm*, μ*=0.6*) as shown in Fig. 4.36. This phenomenon could be linked to the second order effects developed after attaining the elastic load-bearing capacity and could be clarified with Fig. 4.37 which compares the in-plane *x-axis* displacements for two different FEAs of the parametric study at the instants that corresponds to the elastic and the ultimate load limits. It could be noticed for the FEA with *t=9mm and* μ*=0.2* that the in-plane *x=axis* displacements of the corbel plate at the ultimate load-limit were relatively larger compared to the FEA with *t=15mm and* μ*=0.6*. As a result, after attaining the elastic load-bearing capacity, the load-eccentricity: thus, the second order effects increased with higher rate for the smaller dovetail thickness. Correspondingly, due to the increased moment-action the frictional resistance at the side surfaces of the dovetail became more dominant as a result of the increase in the tension stress resultants at the dovetail side surfaces. Therefore, the errors for the estimation of the "*semi-analytical*" resistance model were higher for Plug-inC configurations with smaller dovetail thickness and higher friction coefficients as the large deformations and the second order effects were not included in the "*semi-analytical*" resistance model. Nevertheless, the proposed "*semi-analytical*" resistance model is also assessed with the statistical evaluation procedure of EN1990, Annex D [58] to establish the partial safety factors to utilize it for engineering approximations.

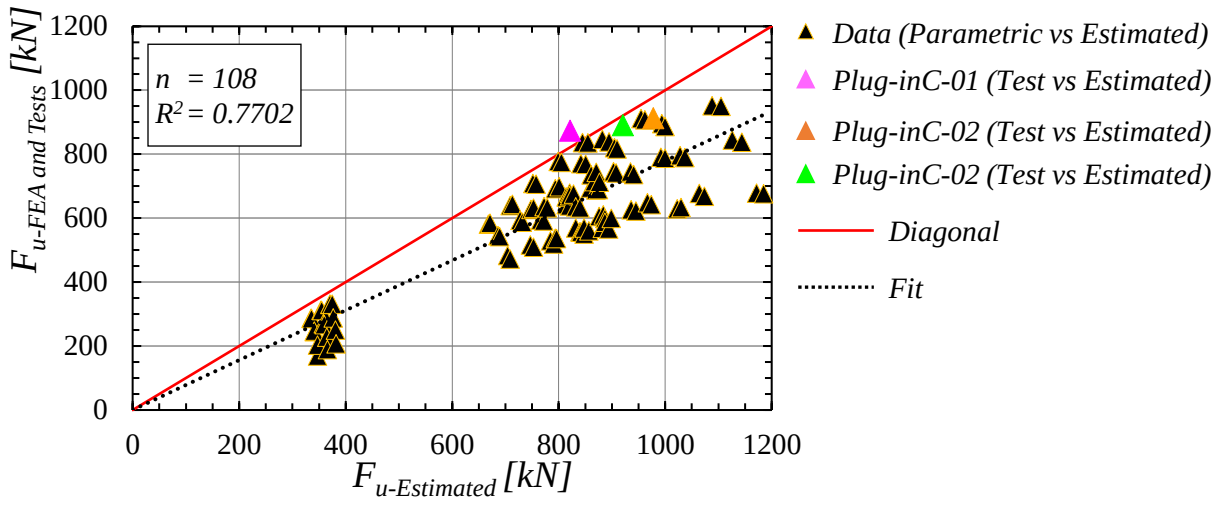

Figure 4.35: The estimated ultimate load-bearing capacity of Plug-inC against the experimental tests and the parametric study.

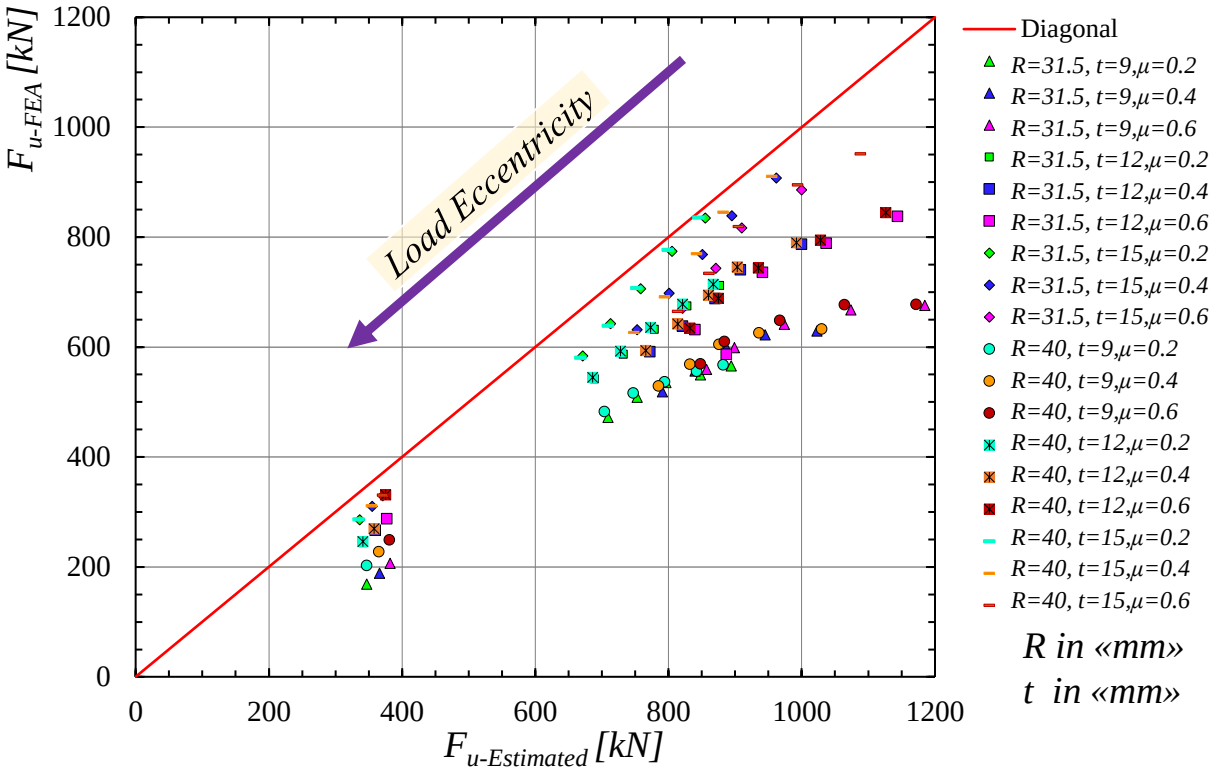

Figure 4.36: Breakdown for the estimated ultimate load-bearing capacity of Plug-inC against the parametric study.

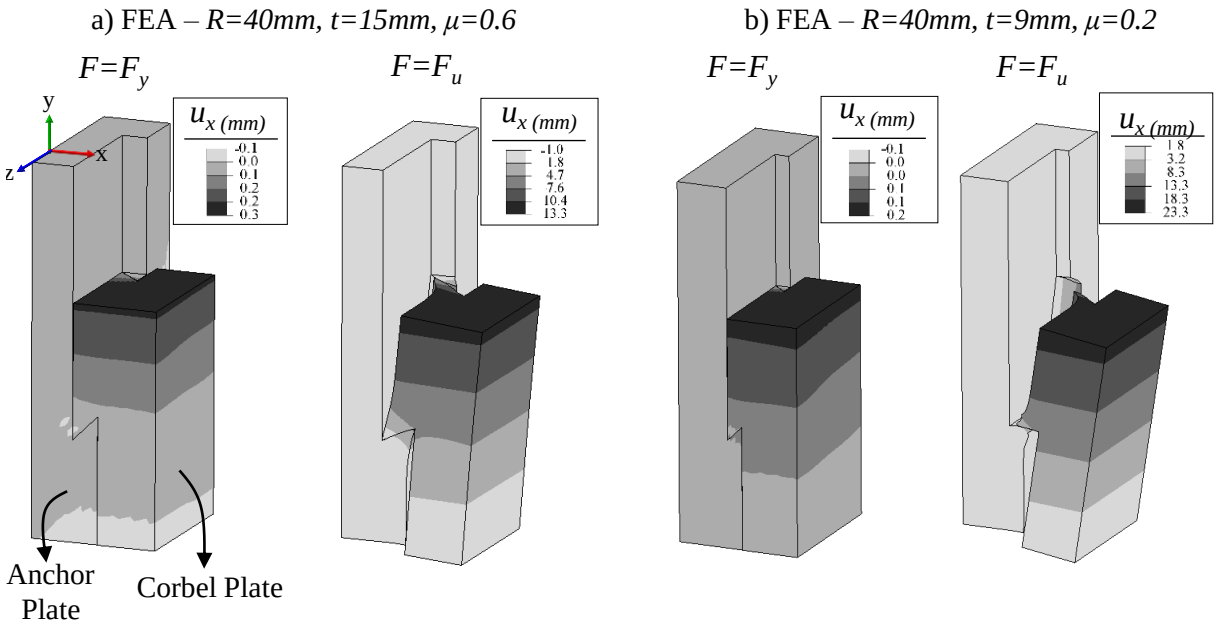

Figure 4.37: In-plane horizontal (*x-axis*) displacements for two different FEAs of the numerical parametric study.

Table 4.13: Basic Variables and their statistical parameters for the statistical evaluation of the *"semi-analytical"* resistance model.

Basic Variables	Mean Values[1]	Coefficient of Variation (CoV) [%]	Distribution
E[2] [GPa]	208	5	Normal
f_y[2] [MPa]	246	4.7	Normal
f_u[2] [MPa]	446	5.1	Normal
ε_u[3] [%]	31.1	4.2	Normal
ε_f[3] [%]	36.7	4.5	Normal
μ[4]	0.2, 0.4, 0.6	5.4	Normal
R[5] [mm]	31.5, 40	0.6, 0.5	Normal
t[5] [mm]	9, 12, 15	2.2, 1.7, 1.3	Normal
h_{outer}[5] [mm]	80	0.2	Normal
h_{inner}[5] [mm]	65	0.3	Normal
w_{inner}[5] [mm]	120	0.2	Normal
ϕ[6] [°]	17.1	10.9	Normal
θ[7] [°]	45	1.5	Normal
e[8] [mm]	7.5, 12.5, 17.5, 22.5, 27.5, 100	26.7, 16.0, 11.4, 8.9, 7.3, 2.0	Normal

NOTE-1: Nominal values are presented for the basic variables and their coefficient of variations.

[1]The input values presented in Table 4.10 are considered as the mean values of corresponding the basic variables for the statistical evaluation.

[2] The mean values and the coefficient of variations of the elastic modulus (E), yield strength (f_y) and ultimate strength (f_u) were determined based on the entire data presented in Table 4.3 as the ordered material grade was identical (S235) for all of the inner and cover plates.

[3] The mean values and the coefficient of variation of the necking strain (ε_u) and the fracture strain (ε_f) were determined based on the entire corresponding data presented in Annex-D as the ordered material grade was identical (S235) for all of the test specimens

[4] The coefficient of variation for the static friction coefficient was assumed to be identical for all different friction coefficient and determined based on the a separate test campaign presented in Annex-A.

[5] The coefficients of variation for the dimensions of the dovetail were determined based on the coarse machining tolerance of the CNC-cutting procedure, which corresponds to the standard deviation and taken as 0.2mm according to the producer feedback.

[6] The coefficient of variation of the vertical slope angle was determined with *Monte Carlo Simulation* using the trigonometrical relation between the w_{inner} and h_{inner} - see Fig. 4.1d

[7] The coefficient of variation of the dovetail angle was determined with *Monte Carlo Simulation* using the trigonometrical relation between the w_{inner}, w_{outer} and t - see Fig. 4.1d

[8] The coefficient of variation for the load-eccentricities was determined according to EN1090, Annex D Table D.1.9 [59].

Table 4.14: Input parameters for the statistical evaluation procedure of EN1990, Annex D (n=111 $>$ 100) and the output parameters of the evaluation procedure for the "*semi-analytical*" resistance model.

Required Input Parameters	Assigned Values
V_δ	0.157[1]
V_{rt}	0.056[2]
k_∞	1.64[3]
$k_{d,\infty}$	3.04[3]
Output Parameters	**Output Results**
r_k	$0.585 \cdot r_t$
r_d	$0.464 \cdot r_t$
$\gamma_M = r_k / r_d$	1.261

[1] Determined according to data set presented in Fig. 4.35. [2] Determined based on the results of the 108 *Monte Carlo Simulations*. [3] According to EN1990, Annex D [58].

Table 4.13 presents the basic variables and their statistical parameters for the statistical evaluation of the "*semi-analytical*" resistance model. Based on the presented basic variables and their CoVs, 108 separate *Monte Carlo Simulations* were performed by varying the dovetail round radius (R), dovetail thickness (t), friction coefficient (μ) and the load-eccentricity (e). Thereby, the CoV for the output results of the "*semi-analytical*" resistance model was determined as the mean of the CoVs of the 108 *Monte Carlo Simulations*. Table 4.14 presents the input and output parameters of the statistical evaluation procedure performed for the "*semi-analytical*" resistance model. Consequently, the comparison between the estimated ultimate load-bearing capacities of Plug-inC and the output results of the numerical parametric study is shown in Fig. 4.38 together with the characteristic and design values of the estimations. To conclude, the "*semi-analytical*" resistance model could be used with the output parameters in Table 4.14 for the ultimate capacity approximation of Plug-inC.

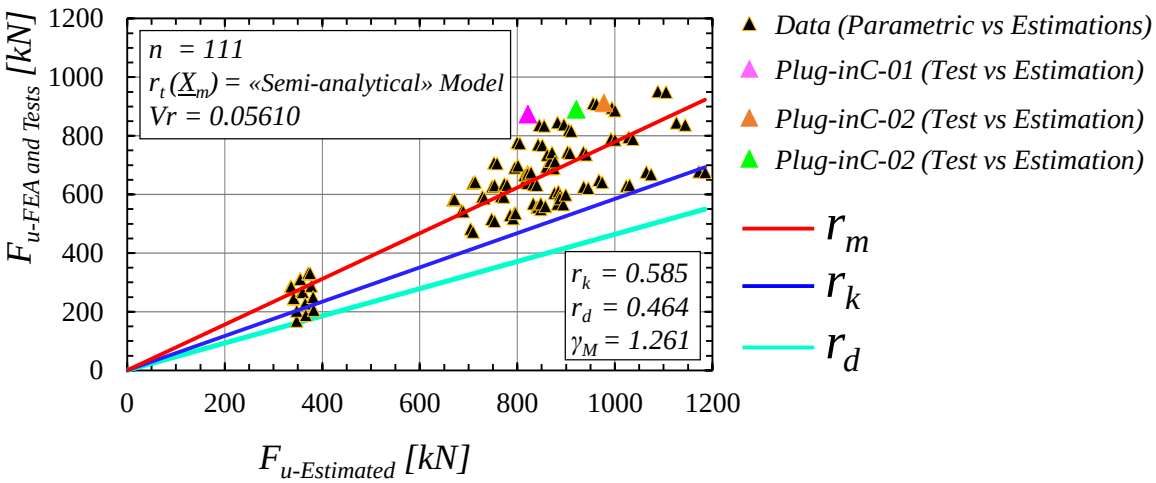

Figure 4.38: The characteristic and design partial safety factors for the "*semi-analytical*" resistance model to estimate the ultimate load-bearing capacity of Plug-inC.

4.8 Summary

This chapter presented novel *"Plug-in Connection"* for the assembly of the steel beams with RC-column/walls of steel-concrete hybrid building systems. The dimensions and the CNC-production details of Plug-inC components were presented in detail for the reproducibility of the novel connection. The load-deformation behaviors of the connection were examined with three experimental tests. The test results were investigated in detail to present the main load-bearing mechanism of the connection. The experimental tests were simulated with computer-aided finite element analysis to further investigate the load-bearing mechanism of the connection and to create basis for the development of the analytical resistance models for the estimation of the elastic and ultimate load-bearing capacities of the connection. The finite element modelling technique and solution scheme were validated against the test results. Based on the output results of the FEAs, an analytical and a semi-analytical resistance models were established to estimate the elastic and the ultimate load-bearing capacities of the connection, respectively. The estimations of the resistance models were compared with the test results and it was shown that the estimations of the models in good agreement with the test results. To further investigate the accuracy of the resistance models and to understand the load-deformation behaviour of the connection against the design parameters, a numerical parametric study was performed by means of the finite element analyses. According to the results of the parametric study, it was shown that the proposed configuration of the connection is sufficient to satisfy the required load-bearing capacity for the steel beam to RC-column/wall joint configurations of steel-concrete hybrid building systems for general beam span lengths. In addition, the estimations of the resistance models were compared with the output results of the numerical parametric study and the accuracy of the resistance models was examined. Finally, the statistical evaluation of the resistance models was performed based on the comparison of their estimations against the output results of the numerical parametric study and partial safety factors were established for the utilization of the resistance models.

CHAPTER 5

Grouted Joints for Continuous Composite Slim-floor Beams

5.1 Introduction

Steel-concrete composite beams show superior load-deformation behaviours compared to same dimensions of regular steel or regular reinforced-concrete beams as they resist tension and compression stress resultants which develop due to bending moment actions along the beam length with the most advantageous material behaviors of steel, concrete and steel reinforcements. Therefore, engineers benefit from the superior load-deformation behavior of the steel-concrete composite beams to design structural members for the large spans of multi-storey and high-rise buildings. Recently composite slim-floor beams, which consist of steel-beam, concrete encasement and concrete slab, gained importance for the construction of steel-concrete hybrid building systems [87, 88] as they increase compartment volumes by eliminating the beam down-stand under the floor and reducing the effective depth of the floor systems. Fig. 5.1 presents the cross section views for a regular and a slim-floor steel-concrete composite beams to make the distinction. It is also important to mention that the slim-floor beams are generally designed in ultimate limit state as single span beams due to the lack of knowledge about their rotational capacities [88].

In the previous two chapters two different novel connection mechanisms, SMIBC and Plug-inC, were presented for the fast erection of the steel-beams with reinforced-concrete (RC) columns and walls of the steel-concrete hybrid building systems. It is a fact that these connection mechanisms could also be used to connect the slim-floor beams with RC-column/walls as illustrated in Fig. 5.2. On the other hand, the regular or the slim-floor steel-concrete composite beams could also be designed as continuous beam over an internal support at the mid-span to eliminate the connection mechanisms as illustrated in Fig. 5.3 for the steel-concrete hybrid building systems.

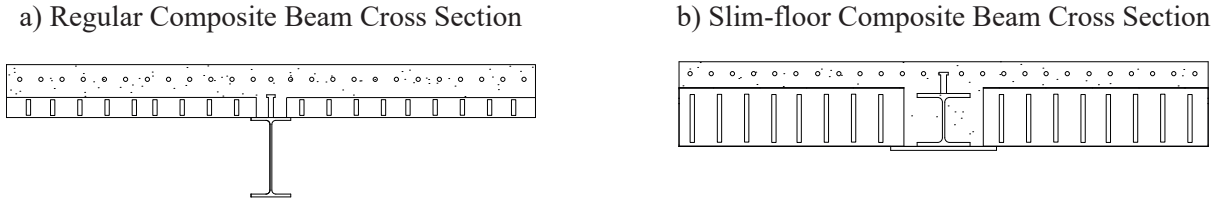

Figure 5.1: Cross-sectional views for a regular and a slim-floor steel-concrete composite beams.

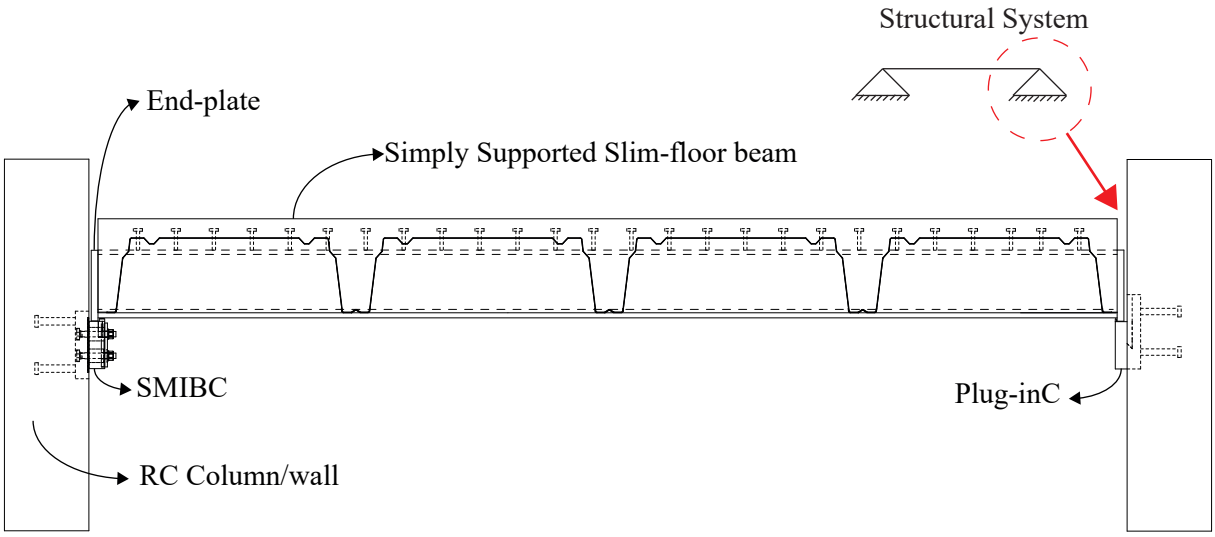

Figure 5.2: Illustration of possible SMIBC and Plug-inC joint configurations with a slim-floor beam.

The continuity over the mid-span of a continuous beam also reduces the sagging moments as a result of the statically indeterminacy added to the structural system. Thereby, more economical design of the composite beams may be achieved. However, in contrast to the reduced sagging moments, the hogging moments develop around the internal support as illustrated in Fig. 5.4. In addition, unlike to the homogeneous steel beams the hogging moment resistance of the steel-concrete composite beams are generally not equal and less than their sagging moment resistances [89].

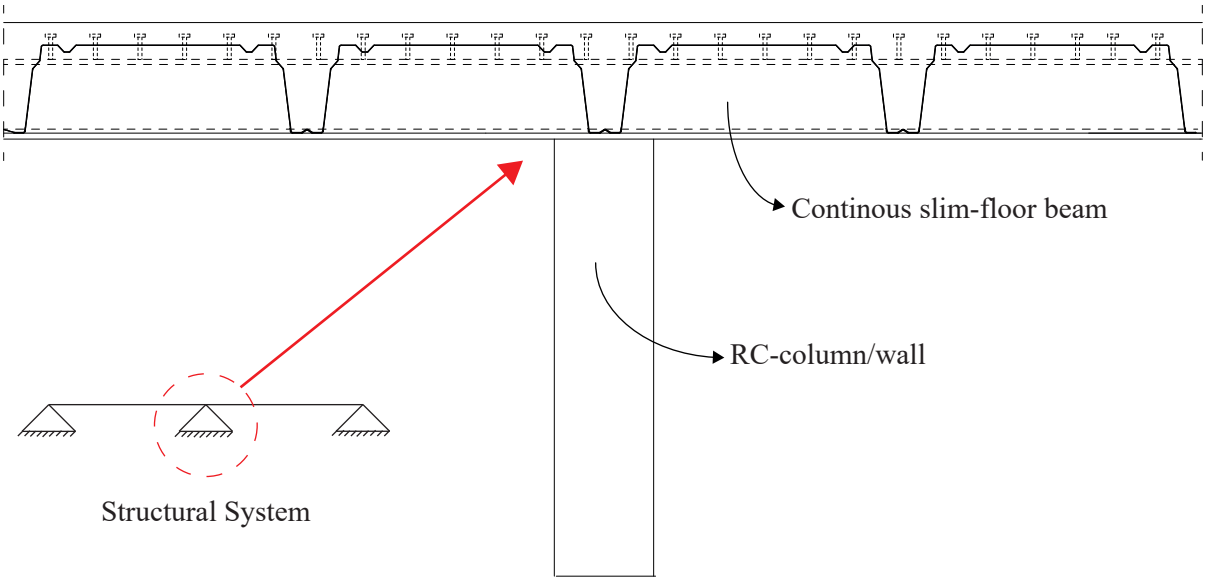

Figure 5.3: Illustration of continuous slim-floor beam of steel-concrete hybrid building systems.

As a result, magnitude of the hogging moments that develop at the internal-support of a continuous composite beam may be dominant for the determination of the cross-sectional dimensions and may result in uneconomical dimensions based on the distribution of the internal forces determined with an elastic global structural analysis. On the other hand, once the cross-section of the beam reaches its elastic load-bearing capacity, the constitutive materials of the cross-section degrade and the flexural rigidity of the structural members reduces. This phenomenon causes the hogging moments to be distributed to the sagging zone [90]. However, this impact could only be determined if a plastic non-linear structural analysis is performed as illustrated in Fig. 5.4.

It is a fact that due to the structural indeterminacy and highly non-linear material behavior of concrete under compression stress resultants, the plastic non-linear structural analysis of steel-concrete composite beams requires computer programming. As a result, it is not feasible to perform these complicated analyses for engineering solutions. Therefore, EN1994-1-1 [2] allows simplification with limited redistribution of the hogging moments, which are calculated with elastic global analysis, to the sagging zone for the regular continuous steel-concrete composite beams according to the cross-section classification of the steel beams and crack status of the concrete over an internal support. The redistribution ratios defined by EN1994-1-1 [2] depends on the rotation capacity of the steel beam and these ratios are limited based on the local buckling of the bottom flange which subjects to compression stress resultants in the hogging zone for gravitational loading conditions. On the other hand, EN1994-1-1 [2] does not provide any design rule for the redistribution of the hogging moments to the sagging zone for the continuous composite slim-floor beams. Additionally, to be able to use the moment-redistribution factors of EN1994-1-1 [2], the steel beam needs to be continuous over the internal support or special beam-to-column joint configurations should be provided to achieve continuity of the beam. Therefore, in order to apply the moment-redistribution method presented by EN1994-1-1 [2] for continuous composite slim-floor beams, it is either required to consider the non-linear material behavior of the concrete encasement for the moment-rotation behavior of a continuous slim-floor beam or to provide a composite joint which satisfies strength and stiffness requirements of EN1994-1-1 [2] to achieve full-continuity between two separate slim-floor beams over an internal support. According to EN1994-1-1 [2], a composite joint is defined as a joint between a composite member to another composite, steel or reinforced concrete member in which the longitudinal steel reinforcements of a composite beam is taken into account for the resistance and stiffness of the joint. Therefore, even the steel beam is not continuous over an internal support, the continuity of the reinforcements and concrete slab may still provide continuity as a composite joint for the continuous composite beams.

However, according to EN1994-1-1 [2], if full continuity is required for the design of a composite beam with special beam-to-column joint over an internal support, the design bending moment resistance of the joint shall be equal or higher than 1.2 times of the design bending plastic moment resistance of the connected beams ($1.2M_{b,pl,hogging,Rd} \leq M_{j,pl,Rd}$). Thereby, the joint could be considered to be a full strength joint and to have sufficient rotation capacity for the redistribution of the hogging moments to the sagging zone; thus, the composite beam could be accepted to be fully continuous

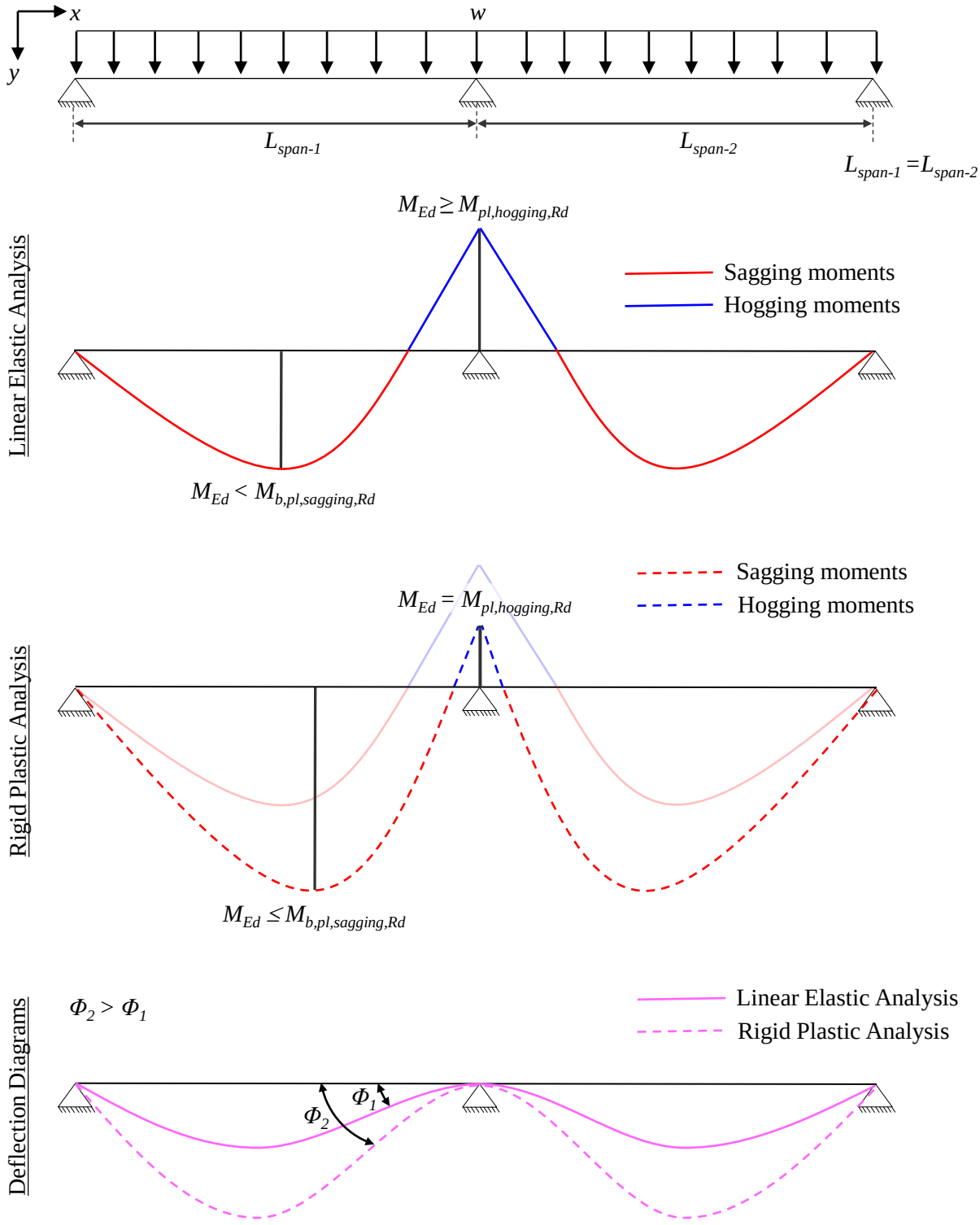

Figure 5.4: Illustration for the bending moment-distributions of continuous beam configuration for linear elastic and rigid plastic structural analysis together with the deflection profiles of the beam.

over the internal support. In contrast, as the steel beam is not continuous over the internal support, it is certain that the continuity of the steel reinforcements and concrete slab could not satisfy sufficient strength ($1.2M_{b,pl,hogging} < M_{j,pl,Rd}$) and it is required to provide special composite joint components to achieve full continuity of the beam. However, it is not practical for the fast erection of steel-structures to design a composite joint having design resistance 20% higher than a composite beam as it may require labor intensive on-site welding or use of relatively high number of structural bolts over the internal support. As a result, it becomes the question if the beam-to-column composite joints having design strength less than 1.2 times of the design plastic moment resistance of the connected beams ($M_{j,pl,Rd} < 1.2M_{b,pl,hogging,Rd}$) may still satisfy sufficient rotation capacity by sustaining their plastic moment resistance ($M_{j,pl}$) for the redistribution of the hogging moments, which are calculated by the elastic global analysis, to the sagging zone for continuous composite beams. To be able to further investigate this question, it is necessary to classify the composite joints.

Fig. 5.5 presents the classification boundaries of the composite joints based on their rotational stiffness and the strength. According to Fig. 5.5, EN1993-1-8 [25] defines joint model to be included in the global structural analysis for the calculation of the internal forces as summarized in the following items.

if a composite joint is classified;

- As a nominally-pin joint based on either the strength or stiffness clarifications, the joint could be modelled as a simple joint for the global structural analysis; thus, no hogging moments would develop over an internal support of a continuous composite beam,
- As a rigid joint based on the stiffness classification;

    1. If the joint is also classified as a full-strength joint based on the strength classification, the joint should be modelled as a continuous joint for the elastic global analysis and the moment-redistribution factors presented in EN1994-1-1 [2] may be used to calculate the design bending moment distribution based on the results of the elastic global analysis,
    2. If the joint is classified as a partial-strength joint based on the strength classification, the joint should be modelled as semi-continuous for either the elastic or the rigid-plastic global analysis. Therefore, the magnitude of the hogging moments depends on the moment-rotation behavior of the joint and the maximum magnitude of the sagging moments is limited by the ultimate rotation capacity of the joint ($\Phi_{j,u}$).

- As a semi-rigid joint based on the stiffness classification, the joint should be modelled as semi-continuous for either the elastic or the rigid-plastic global analysis. Therefore, the magnitude of the hogging moments depends on the moment-rotation behavior of the joint and the maximum magnitudes of the sagging moments is limited by the ultimate rotation capacity of the joint ($\Phi_{j,u}$).

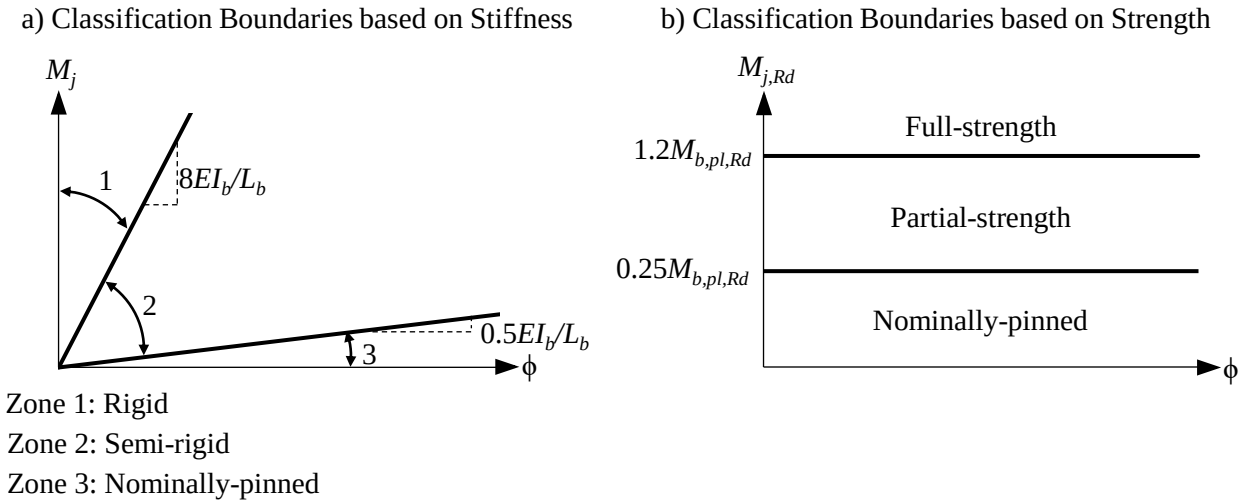

Figure 5.5: Classification boundaries of a composite joints according to EN1994-1-1 [2].

Thereby, it could be concluded that to calculate the bending moment actions on a cross-section of a continuous composite beam, in other words; to be able to economically design a continuous composite beam, the classification of the joint and the determination of the joint rotation capacity is required. Although EN1994-1-1 [2] provides analytical expressions in accordance with EN1993-1-8 [25] for the stiffness and strength calculations of the composite joints, no rules are provided for the calculation of their rotation capacity and it is assisted to demonstrate the rotation capacity of the composite joints with experimental tests or alternative calculation methods supported by the tests. Furthermore, the analytical expressions are only limited with few joint configurations and could not be applied for special composite joints, especially for the joint configurations of the continuous slim-floor beams. Therefore, it is inevitable to perform experimental investigations to accurately define the moment-rotation behavior of special composite joints for their classifications and their considerations in a global structural analysis.

This chapter presents on-site weld-free and bolt-less composite joint developed for the fast erection of slim-floor beams with RC-column/walls of steel-concrete hybrid building systems. The proposed composite joint is here on named as *Grouted Joint for Continuous Composite Slim-floor Beams (GJSFB)*. Fig. 5.6 illustrates the proposed composite joint with constitutive and constructive details designed for the fast erection of the slim-floor beams with the RC-column/walls.

In Fig. 5.6, it could be noticed that the continuity of the steel beam is proposed to be partially satisfied by the thread-rods and concrete grout above the internal support. The nuts for the upper row of the threaded-rods are positioned to resist the tension stress resultants that would develop due to the hogging bending moments over the internal support. Contrary, the nuts for the lower threaded-rods are positioned to resist the compressive stress resultants together with the concrete grout along the width of the beam-end plates. Furthermore, the integrated bearing plates in RC-column and over-sized holes on the bottom plate are designed for the fast erection of the steel-beam by accommodating the construction and manufacturing tolerances over the internal support.

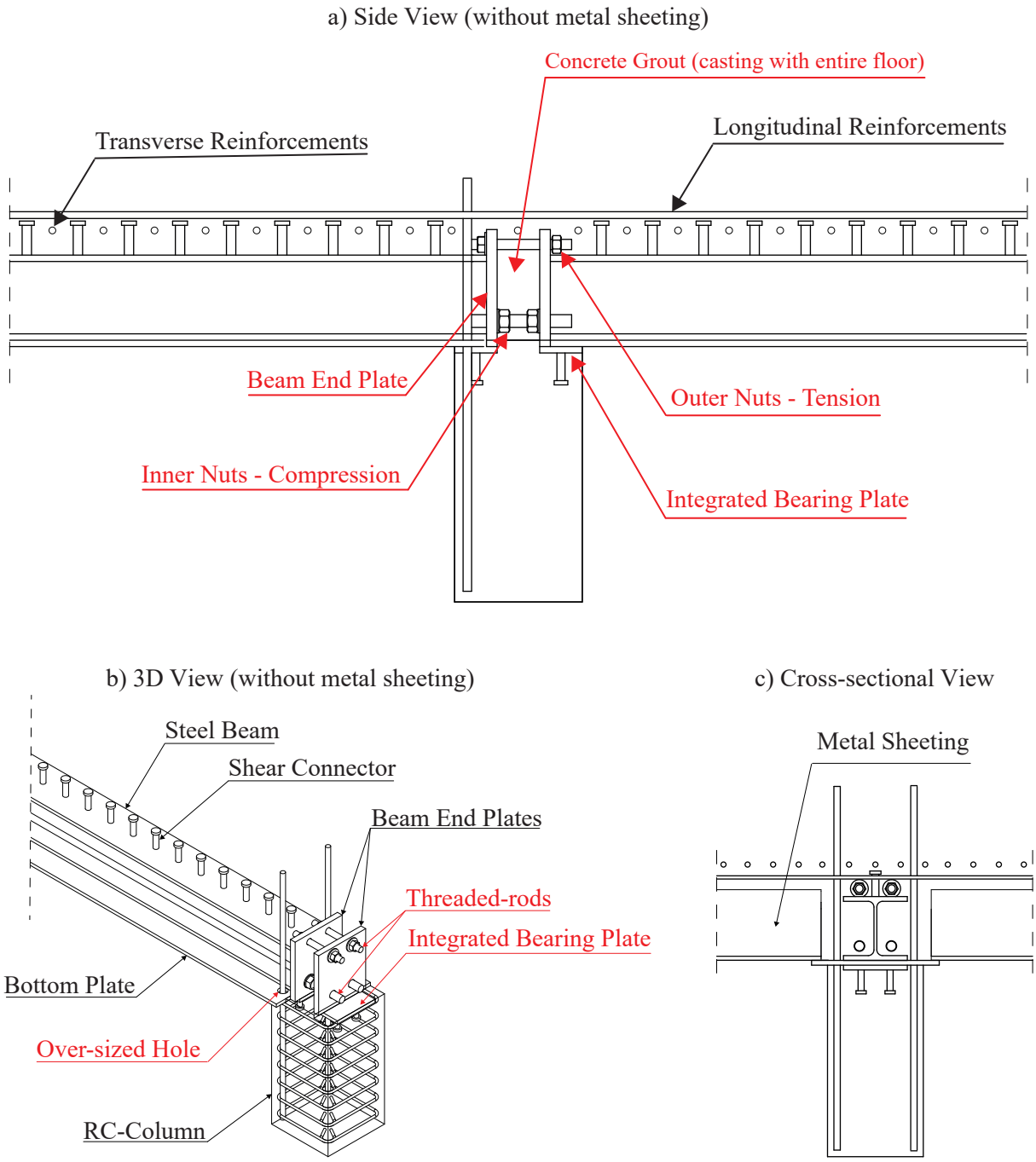

Figure 5.6: Grouted joint for composite slim-floor beams (GJSFB).

To determine the moment-rotation behavior and to examine the constructibility of the proposed composite joint an experimental testing campaign was established with two full-scale hogging zone slim-floor beam tests. The details of the testing campaign are presented in Section 5.2 together with the test results and their discussions. Additionally, the experimental tests were simulated by means of finite element analysis (FEA) with a commercial FEA software package - Abaqus/CAE [66] to

further investigate the load-bearing mechanism and the rotation capacity of the proposed joint configurations with parametric analyses. The details of the FEAs, and the discussions regarding to the output results of the FEAs are presented in Section 5.3. Thereafter, in Section 5.4, analytical models developed to estimate the ultimate bending moment and the rotation capacities of the proposed composite joint are presented. The estimations of the analytical models are compared with the test results and the output results of the FEAs for validation.

To create a basis for the development of the novel joint configurations for steel-concrete composite continuous composite slim-floor beams, a separate literature review that focuses on the investigations regarding to the joint behaviors of the steel-concrete composite beams is prepared as presented in the following paragraphs.

Nethercot et al. [91] performed analytical investigations based on cross-sectional moment-curvature relation of steel-concrete composite beams to determine magnitude of the joint rotation required to achieve desired degree of moment-redistribution from the hogging zone to the sagging zone of semi-continuous composite beams. They demonstrated that the required rotation capacity is independent from the moment-rotation characteristics of the joints. Furthermore, they also highlighted that the available degree of the moment-redistribution can be 30% or higher (as much as 56%) if the rotation capacity of the joint is larger than 20mrad. One of the most important findings in their study was that the available degree of moment-redistribution is a function of the span lengths of a continuous composite beam. Accordingly, they noted that shorter span beams allow larger degrees of moment-redistribution for a constant available rotation capacity of the composite joint. Furthermore, they also demonstrated that the degree of moment-redistribution is a function of the loading condition and single point loading condition allows the maximum degree of moment-redistribution while the two-point loading condition allows the minimum degree of moment-redistribution, and the degree of the moment-redistribution for a uniformly distributed loading condition is between the single-point and the two-point loading conditions. The last but not the least, they also highlighted that to be able to utilize the ultimate moment resistance capacities in both the sagging and hogging zone of a regular continuous steel-concrete composite beam it is required to have at least 36mrad-50mrad ultimate available rotation capacity over an internal support.

Kemp et al. [92] conducted theoretical and experimental studies to investigate the required and the available rotation capacities in the vicinity of the internal joints of double-span continuous steel-concrete composite and plain steel beams to estimate the plastic capacity utilization ratio at the sagging zone of the beams. They concluded that the rotation capacity over an internal support required to turn the sagging zone to plastic mechanism, i.e. plastic collapse, is much larger for the continuous composite beams compared to the continuous plain steel beams. Furthermore, they also noted that asymmetry in the span lengths and uniformity of the loading decrease the demand for the required rotation capacity at the joint vicinity for full plastic capacity utilization at the sagging zone of the composite beams. The results of their experimental test campaign demonstrated that the utilization of a higher longitudinal steel reinforcement ratio results in lower inelastic

rotation capacity for the composite cross-section subjected to hogging moment actions because the proportion between the height of the tension and the compressive stress blocks increases to balance the tension in the longitudinal steel reinforcements. Consequently, they suggested a relatively small amount of longitudinal steel reinforcements be used together with a semi-rigid end connection (special composite joint) to overcome the reduced ductility.

On the other hand, Odenbreit [93] showed that steel-concrete composite joints with only mesh reinforcements were not able to develop plastic capacity due to the limited ductility of the mesh reinforcements and showed brittle failure characteristics. Therefore, he suggested not to include the resistance contribution of the mesh reinforcement in the design calculation of the composite joints. Furthermore, Odenbreit [93] provided a conservative approach to estimate the required rotation capacity which allows full plastic capacity utilization at the sagging zone of continuous composite beams and calculated the required rotation capacity as 80mrad to be independent from the moment-rotation behaviour of the joints by using allowable maximum mid-span deflection at the ultimate limit state of the beams to be equal to one-fifty of the span length. Although the estimation of Odenbreit [93] for the required rotation capacity was highly conservative compared to the findings of Nethercot et al. [91], the simplicity of his suggestion for the required rotation capacity (i.e. 80mrad) provides a global threshold to design ductile composite joints.

Bode et al. [94] performed experimental studies to investigate semi-rigid behavior of welded, end-plate, fin plate, contact plate, and bolt-less steel-work steel-concrete beam-to-column composite joints with five different experimental test campaigns. According to their test results, they concluded that the behavior of the composite joints mainly depends on the structural detailing of the steel reinforcements, and the deformation capacity of the composite joints can be increased until a certain limit by utilizing higher ratio of longitudinal steel reinforcement that have ductile stress-strain behavior. They also highlighted that the lower strength joints requires larger rotation capacity for the full capacity utilization at the sagging zone by the redistribution of the hogging moments. Their experimental test campaigns also provided information regarding the influence of the longitudinal shear connectors on the load-deformation behavior of the composite joints as the degree of the longitudinal shear connector influences the crack pattern of the continuous concrete slab (i.e. concrete flanges).

Chen and Jia [95] reported that the available moment-redistribution from the hogging zone to the sagging zone of continuous composite beams might be higher than the ones determined with the pre-defined factors of design regulations depending on the reinforcement ratio in the hogging zone as consisted with the results of Nethercot et al. [91]. Therefore, they highlighted that the load-deformation behaviour and the load-bearing capacity of composite joints should be investigated in detail to achieve optimized design strategy for continuous composite beam configurations.

Jiang et al. [96] conducted experimental testing program together with theoretical investigations for moment-redistribution in partially encased continuous steel-concrete composite beams and regular continuous composite beams. One of the most important result of their experimental

program was that the redistribution of the bending moments from hogging zone to sagging zone decreases as the steel section forms plasticity in the sagging zone and the moments redistributed back to the hogging zone. In addition, they proposed simple formulations to calculate the plastic-rotation capacity of composite beams based on their moment-curvature relations. Nie and Cai [97] reported that the slip between the steel beam and concrete slab might reduce 17% the flexural rigidity of the sagging zone despite the utilization of full shear connection for composite behaviour; thus their research supports the findings of Jiang et al. [96] and also provides additional supports regarding to the findings of Bode et al. [94].

Pop et al. [98] numerically and experimentally studied the connection of composite beam to reinforced-concrete wall under quasi-static loading conditions and they deduced that the dominant failure mode of the joint was the rupture of the longitudinal steel reinforcements in tension although steel decks sustained large deformations.

Thai et al. [99] investigated moment-rotation behavior of blind bolted end-plate composite connection under static loading conditions by differentiating the geometry of the connection components such as using flush and extended end-plates for rectangular and circular concrete filled tubular columns. They conducted four full-scale experimental tests with a test set-up that represents the hogging zone of continuous composite beams. They kept the longitudinal and transverse reinforcement ratios, the longitudinal shear connector distribution, the dimensions and the material properties of the test specimens identical to solely focus on the impact of the end-plates and the column geometries on the moment-rotation behavior of the blind bolted end-plate composite connection. Due to the limitations of their testing facility they turned the test specimens in upside down orientation around the longitudinal axis of the beams and applied the loading as a compression force for simply supported beam configuration to achieve negative bending moment at the joint. They classified their composite joints as semi-rigid joint and they highlighted that the composite joints consist of blind bolted end-plate connection show highly ductile behavior. They identified two different failure modes for their test specimens as the loss of the bond between the longitudinal steel reinforcements and the concrete slab, and the local buckling at the flange and the web of the steel beam. According to the results of their experimental results, they concluded that the use of the extended end-plate limits the crack width in the concrete slab and leads to increased moment resistance and initial stiffness compared to the use of the flush end-plate. Additionally, they also mentioned that the use of circular columns instead of rectangular columns may increase the moment capacity and the initial stiffness of composite joints with blind bolted end-plate connection by 13.5% and 18.3%, respectively.

Duarte da Costa et al. [100] presented results of comprehensive experimental, numerical and analytical investigations [89] performed to investigate the moment-rotation behavior of beam-to-column joints, which comprise bolt-less and bolted (4 pieces - M24 Grade 10.9 structural bolts) flush end-plate connections, between steel-concrete composite continuous slim-floor beams and steel columns. The ratio and the diameter of the longitudinal steel reinforcements and the existence of the bolts for the flush end-plate were taken as the variable parameters of their investigations.

They performed in total seven experimental tests that represent the hogging zone of symmetric double span continuous beam configuration for plain steel beams with bolted flush end-plate connection and for steel-concrete composite slim-floor beams with and without bolted flush end-plate connections [101]. Their experimental test with the plain steel beam was performed to be a reference test to investigate the contribution of the concrete encasement and the reinforced-concrete slab on the moment-rotation behavior of the bolted flush end-plate beam-to-column connection. Their experimental test campaign could be accepted to be state-of-the-art as it was the first test campaign which investigated the bolted flush end-plate connection for slim-floor composite beams in continuous beam configuration. The results of their experimental test campaign showed that the composite joints with higher longitudinal steel reinforcement ratio and larger reinforcement diameter have larger rotation capacity compared to the joints with lower longitudinal steel reinforcement ratio and smaller reinforcement diameter. Additionally, they noted that the rotation capacities of their composite joint configurations were higher than 95mrad. Therefore, it could be said that their composite joint configurations allow full plastic capacity utilization at the sagging zone of steel-concrete composite continuous slim floor beams for the ultimate limit state with respect to the conservative required rotation capacity (80mrad) derived by Odenbreit [93]. The results of their experimental test campaign also showed that the initial stiffness of their composite joint configuration is mainly impacted by the ratio of the steel reinforcements while the existence of the structural bolts does not significantly influence the moment-rotation characteristics of their joint configurations. Duarte da Costa et al. [100] also performed a set of computer aided-finite element analysis to conduct numerical parametric study to further investigate the influence of the reinforcement ratio and the elongation capacity of the reinforcement materials on the rotation capacity of their composite joint configurations. Their parametric study showed that the elongation capacity of the reinforcement material plays a crucial role in the magnitude of the ultimate rotation capacity of their joint configurations. Finally, Duarte da Costa et al. [100] also proposed an analytical resistance model based on component method [2, 25] to predict the initial stiffness and the rotation capacity of their composite joint configurations for different concrete grades, reinforcement ratios and reinforcement material elongation capacities. The predictions of their analytical expressions showed a good agreement with the results of their experimental and numerical investigations. Thus, their analytical expressions could be used for design purposes of their joint configurations.

According to the literature presented above, the load-deformation behaviors of semi-rigid beam-to-column composite joints and the mechanical response of structural systems for continuous beam configuration where the composite joints are used could be concluded to be relatively complex for the ultimate limit states. Because, the geometry of the beam end-plates, the shape of the columns, the ratio and the diameter of the longitudinal steel reinforcements, the deformation capacity of the individual joint components, the bond strength between the reinforcements and the concrete slab, the degree of the longitudinal shear connectors, the span length, the loading conditions have impact on both the load-deformation behaviours of the joint and the structural system.

Additionally, it has been demonstrated in the presented literature that most of the existing

research effort has been focused on the development of novel composite beam-to-column joints for traditional steel-concrete composite continuous beams and steel or concrete-filled tubular steel columns. There exist only a few investigations regarding the beam-to-column joints of steel-concrete composite continuous slim-floor beams [89, 102] with steel columns. To the best of the author's knowledge, no joint configuration has been proposed yet for the composite continuous slim-floor beams in connection with reinforced-concrete columns.

Therefore, it is inevitable to conduct experimental, numerical and analytical investigations to be able to establish novel beam-to-column composite joints that enable the fast erection of steel structures for steel-concrete hybrid building systems.

5.2 Experimental test campaign

Two separate full-scale experimental tests were performed to investigate the moment-rotation behavior of GJSFB under negative, i.e. hogging, moments. In addition, during the construction of the test specimens, the constructibility of GJSFB is examined.

To be able to simulate the hogging moments over the internal support of a continuous composite slim-floor beam, a structural system presented in Fig. 5.7 was designed with a point load configuration over the mid-span, where the GJSFB presents, of a simply supported beam. It is crucial to mention that due to the limitations of the testing facility, it was only possible to apply compression (push) forces with the hydraulic jack. Therefore, the test specimens were positioned on the roller supports in the upside-down orientation. Thereby, it became possible to simulate the negative hogging moment effects along the entire length of the test specimens.

The upside-down turning operations of the test specimens were carried carefully with temporary longitudinal timber supports connected to the test specimens before the initiation of the turning operations. Fig. 5.8 shows the installations of the timber supports, and the turning operations of the test specimens.

The test specimens were designed to reflect the hogging zone of double span continuous composite slim-floor beams. Therefore, the distance between the point load and the roller support was aimed to be equal to the hogging zone of $16m + 16m$ equal length double span continuous composite slim-floor beam subjected to uniformly distributed loading. According to EN1994-1-1 [2], the length of the hogging zone for a double span continuous composite beam could be estimated as 15% of the span on each side of the internal support. Consequently, for 16m span length, the hogging zone could be calculated to be equal to 2.4m on each side of the internal support for equal length double span continuous composite slim-floor beam. However, due to the limitations of the strong floor grid, where the roller supports are fixed, the distance between the central-axis of the roller supports and the central axis of the test specimens was designed to be 2.4225m. In addition, due to the height limitations of the hydraulic jack, the composite cross section was terminated 225mm before the roller supports, and the test specimens were positioned on the roller support in contact with the bearing plates welded at the top flange of the steel beam. Thereby, 90mm vertical distance was gained to be able to position the specimens under the hydraulic jack. On the other hand, this detail reduced the length of the composite section to 2.2m on each side of the central axis of the test specimens. As a result, the composite section was in total 0.4m shorter than the hogging zone of 32m equal length double span continuous composite slim-floor beam subjected to uniformly distributed loading. Nevertheless, the configurations of the test specimens could be considered to be highly similar to the actual hogging zone of a double span continuous composite slim-floor beam. The width of the test specimens was designed to be equal to 2m as consisted with EN1994-1-1 [2] for the effective width of a 32m equal length double span continuous composite beam. Fig. 5.9 presents the overall dimensions of the test set-up.

a) Illustritration of the Structural System

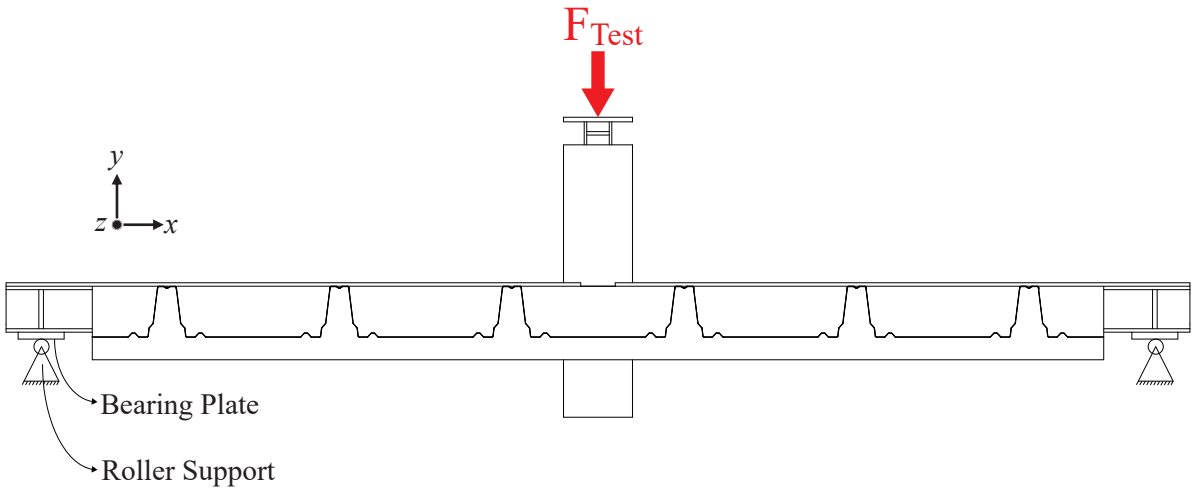

b) Test Environment

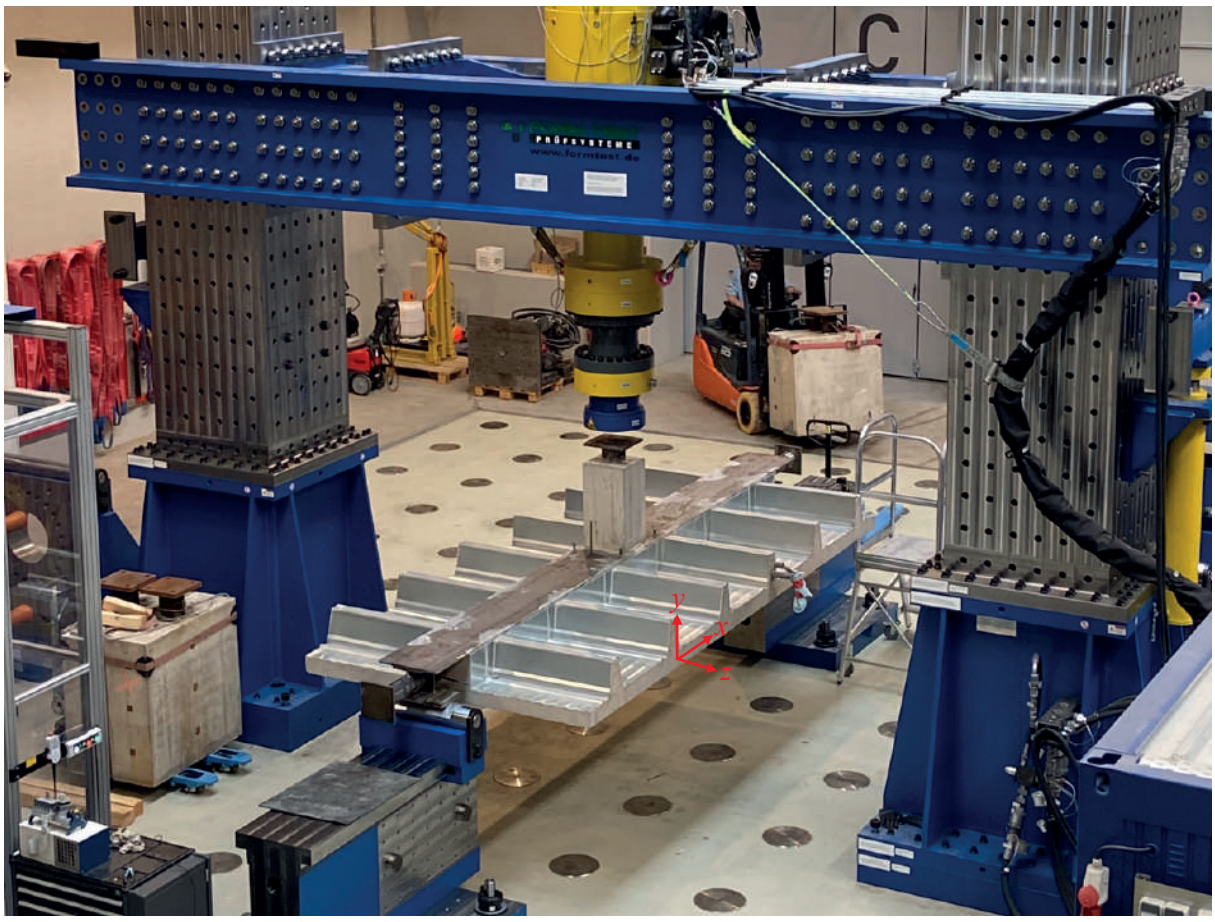

Figure 5.7: Structural system of GJSFB experimental test campaign.

The loading was introduced to the test specimen with a load-introduction assembly embedded to the RC-column above the mid-span. Fig. 5.10 presents the technical drawings of the load-introduction assembly which was identical for both experimental tests. Further details regarding to the test specimens are presented in the next section.

a) Installation of the Temporary Timber Supports

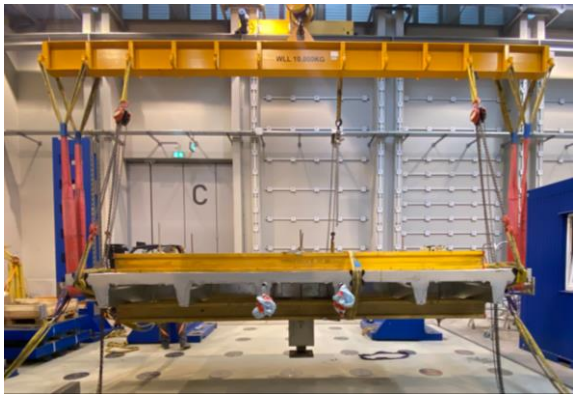

b) Upside-down Turning of the Test Specimens

Figure 5.8: Upside-down turning operation of the test specimens.

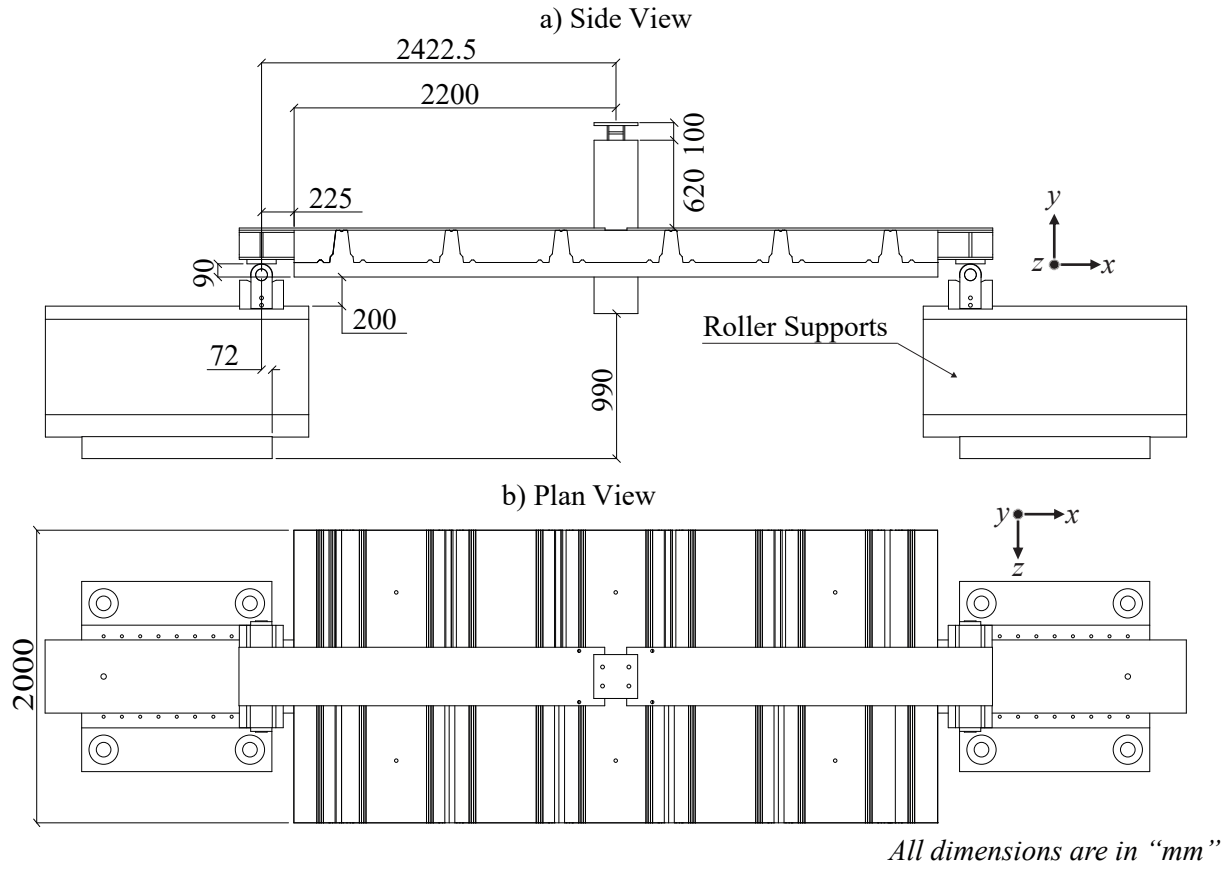

Figure 5.9: Overall dimensions of the test set-up for GJSFB test campaign.

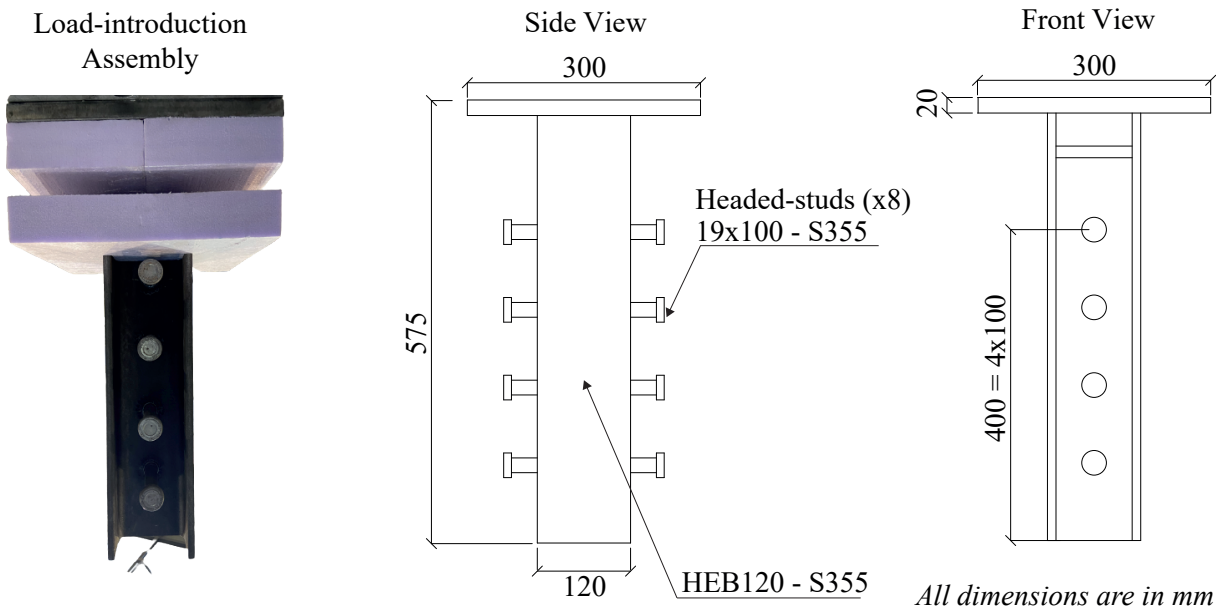

Figure 5.10: Load-introduction assembly of GJSFB test campaign.

5.2.1 Test specimens

Fig. 5.11 presents the cross-sectional view of the tested composite slim-floor beams. The composite action between the steel beam and the flat concrete slab was achieved with headed-fasteners (e.g. shear-studs) by using full shear connection stud distribution determined according to EN1994-1-1 [2]. The total height of the cross-section was kept to be equal to 340mm as consisted with the slim-floor design concept. The longitudinal steel reinforcements were positioned 30mm below the top surface of the flat slab. It could be noticed that the longitudinal reinforcements were not uniformly distributed above the steel-beam. This was necessary to be able to position the longitudinal steel reinforcements of the RC-column (see Fig. 5.13).

Fig. 5.12a presents the technical details of GJSFB joint configuration for the first test specimen, which is here on named as GJSFB-01. The threaded-rods of GJSFB were omitted for the first test specimen and relatively low longitudinal reinforcement ratio ($\rho = 1.29$) was applied for the composite cross-section. Thereby, a possible lower boundary for the moment-rotation behavior of GJSFB was aimed to be determined for a regular slim-floor beam cross-section.

Fig. 5.12b presents the technical details of GJSFB configuration for the second test specimen, here on named as GJSFB-02. The second test specimen was detailed with high-strength threaded-rods of grade 12.9, which is the common highest material grade for the structural applications in the building frames. The longitudinal reinforcement ratio for the effective width of the composite cross-section was kept relatively high ($\rho = 2.30$) considering the flat slab thickness (i.e. 105mm) and the total composite cross-section height (i.e. 340mm). By this means, it was aimed to define a possible upper boundary for the moment-rotation behavior of GJSFB for a regular slim-floor beam cross-section.

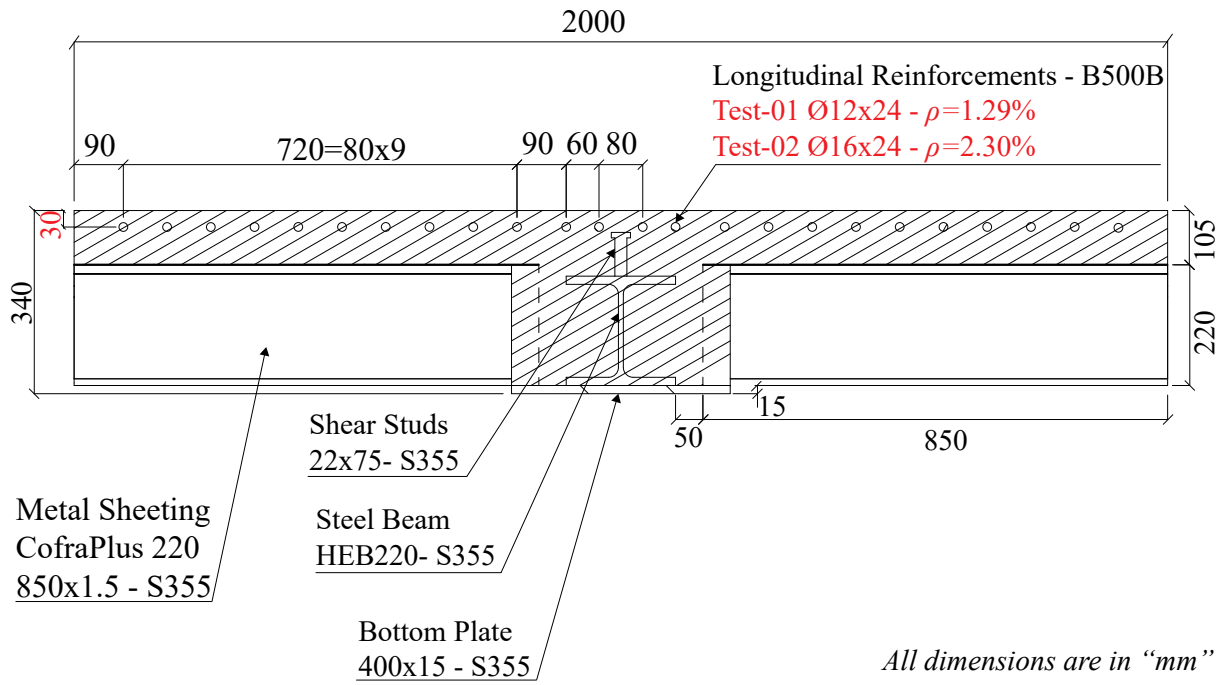

Figure 5.11: Cross-sectional view of the tested composite slim-floor beams.

Table 5.1 compares the GJSFB joint details of the test specimens. All the other technical and constructive details of the test specimens were identical, in other words the cross-sectional details, the RC-column, the load-introduction assembly, the beam end plates, the integrated bearing plates, the transverse shear reinforcements, the configurations of the shear connectors (i.e. shear studs), the metal sheeting (Cofraplus 220) and the reinforcement details in the rib of the metal sheeting.

Fig. 5.13 presents the reinforcement and steel-beam details of the test specimens. The longitudinal reinforcements were positioned under the transverse shear reinforcements as suggested in the literature [89]. The shear-studs were uniformly distributed with 120mm intervals but the number of the stud rows doubled close to the roller supports.

Table 5.1: Comparison of tested GJSFB joint configurations

Variable Test Parameters	GJSFB-01	GJSFB-02
Diameter of the Longitudinal Reinforcements [mm]	12	16
Longitudinal Reinforcements Ratio [%]	1.29	2.30
Upper row of the Threaded-rods[1]	N/A	2xM24-12.9 (DIN976-A [62])
Lower row of the Threaded-rods[1]	N/A	2xM30-12.9 (DIN976-A [62])

[1] The positions are given based on the configurations before the upside-down turning of the test specimens.

a) Technical Details of GJSFB Joint Configuration of the First Test Specimen (GJSFB-01)

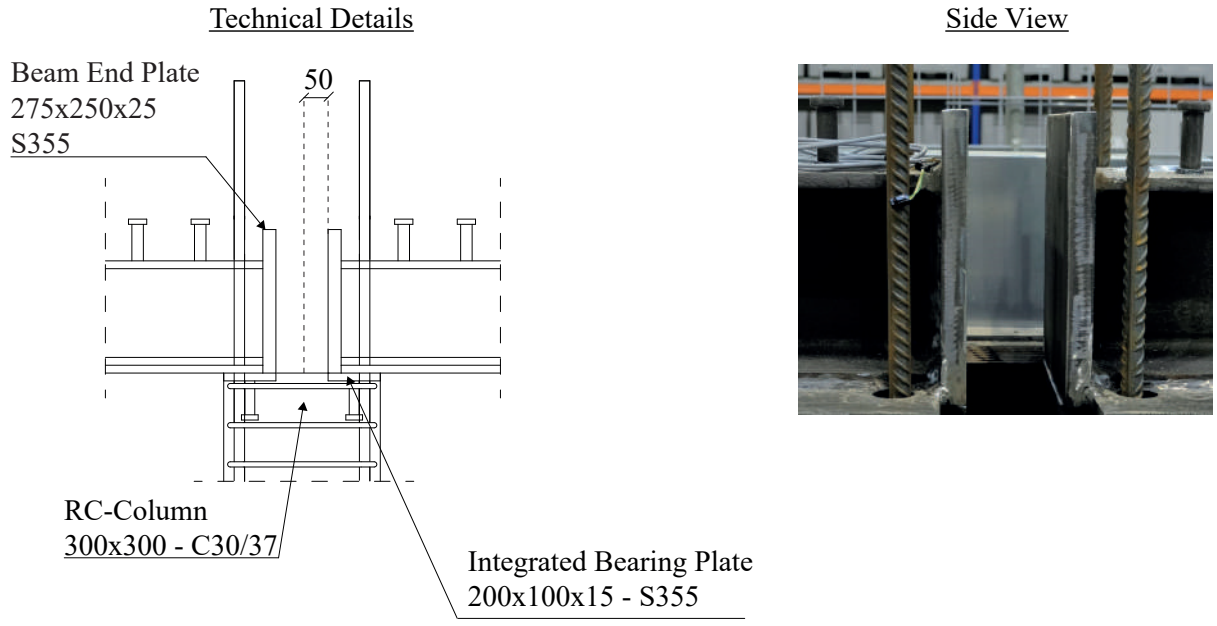

b) Technical Details of GJSFB Joint Configuration of the Second Test Specimen (GJSFB-02)

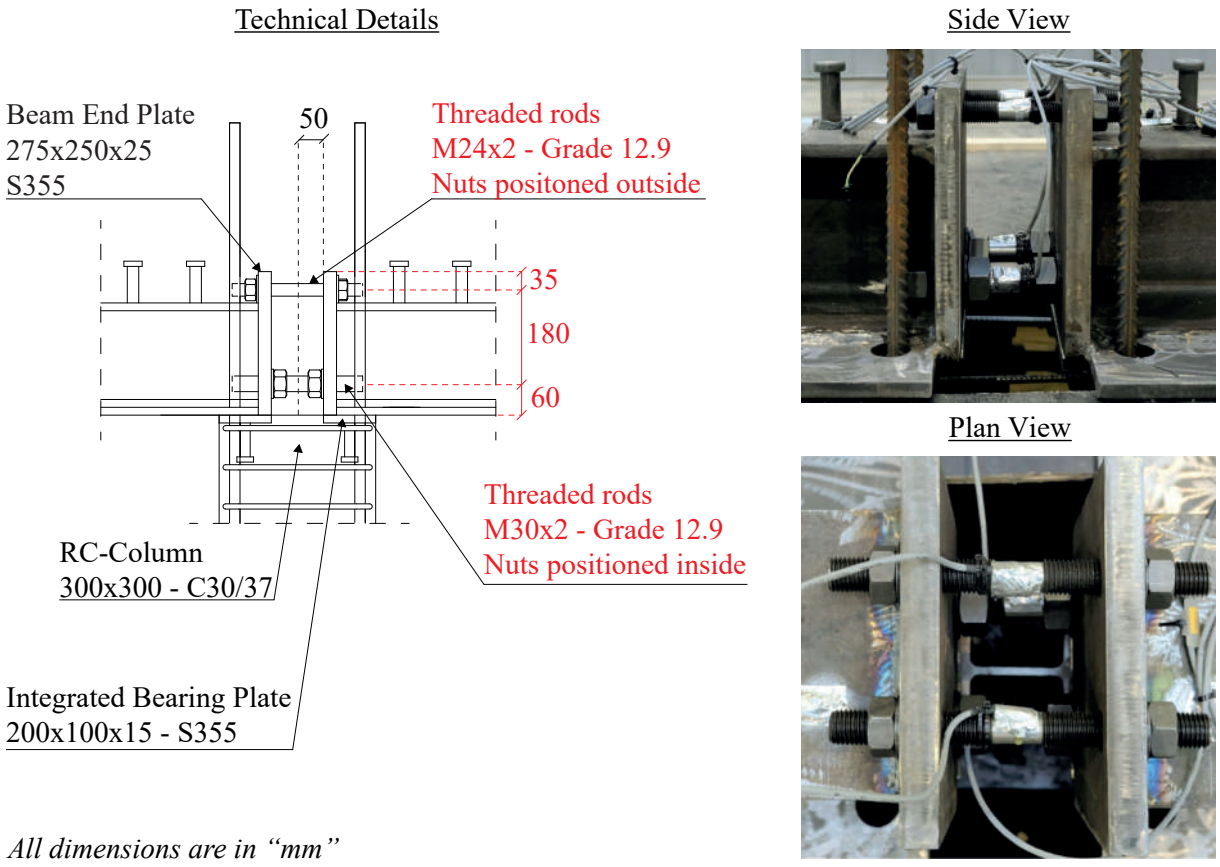

Figure 5.12: Technical details of the tested GJSFB joint configurations.

a) Reinforcement Details of the Test Specimens

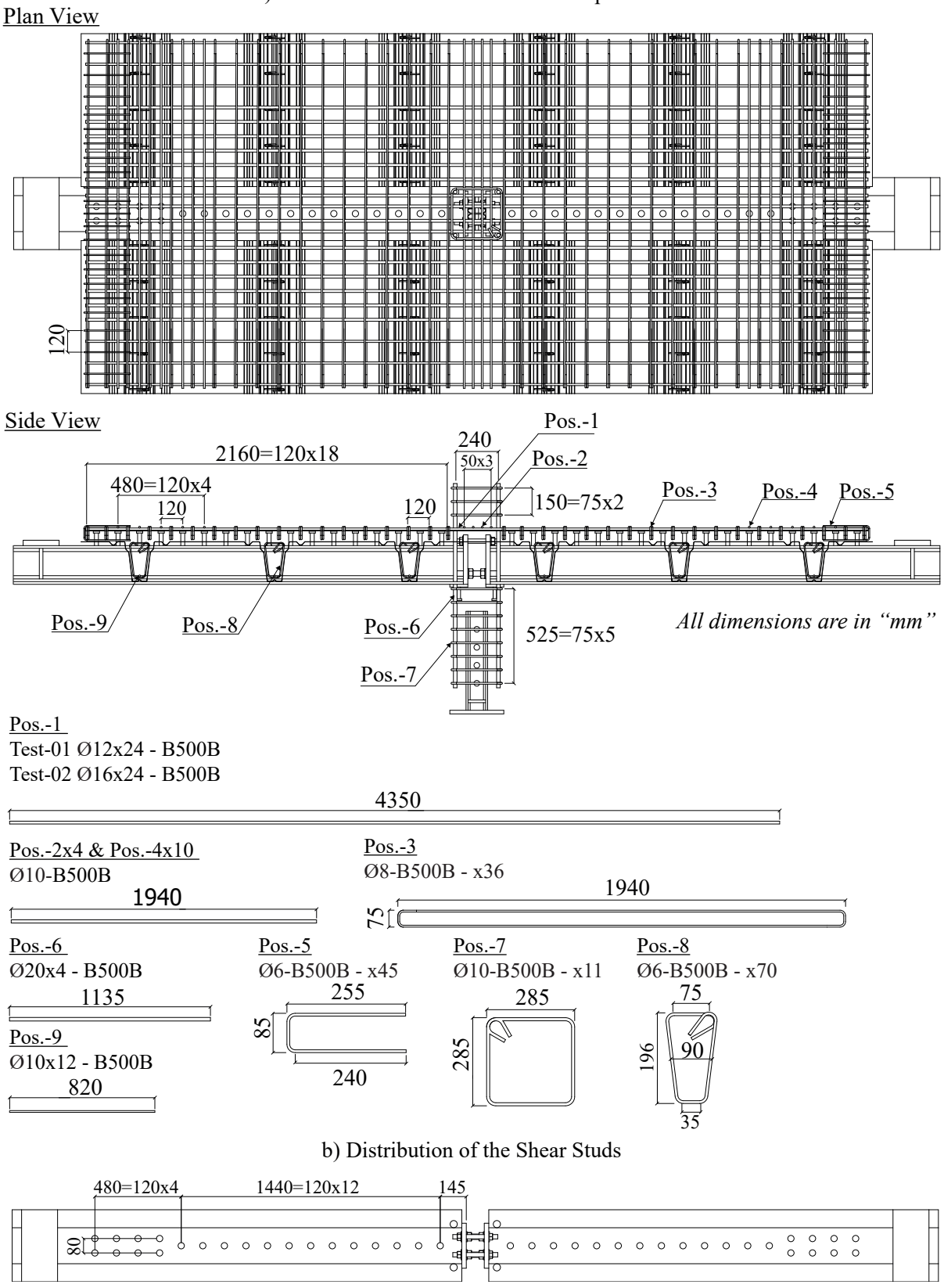

b) Distribution of the Shear Studs

Figure 5.13: Reinforcement details and shear stud distribution of the test specimens.

5.2.2 Production of the test specimens

To produce both test specimens (2x2mx6m) at the same time in a laboratory hall, a temporary platform was constructed inside the Structural Testing Laboratory of the University of Luxembourg. The elevation of the platform was necessary for the production of the concrete column down-stand under the composite slim-floor beam before the upside-down turning of the test specimens. After the construction of the temporary platforms, the steel beams were laid on the platform. Thereafter, the metal sheeting was fixed with the bottom plate and the formwork was installed around the metal sheeting initially. The reinforcements were tied after the installation of the form-work and finally the concrete casting was performed with the same delivery truck for both test specimens. Figs. 5.14-5.15 present the production stages of the test specimens. Additional images are presented in Annex-E.

Temporary Platform

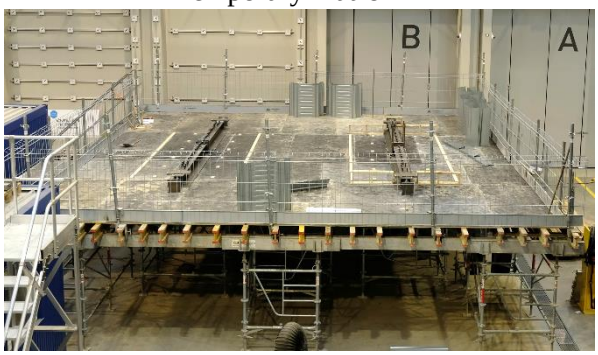

Positioning of Beams

Positioning of Metal Sheeting (CofraPlus220)

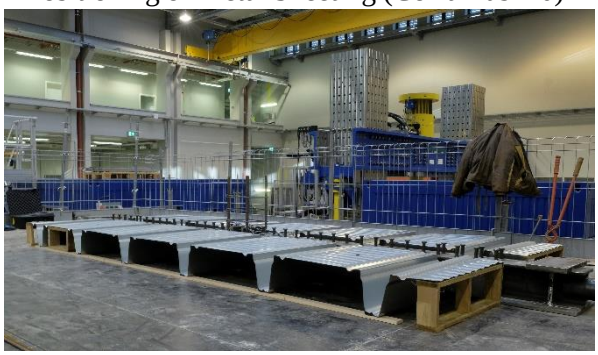

Form-work

Reinforcement Details / GJSFB – 01

Reinforcement Details / GJSFB – 02

Figure 5.14: Production of the test specimens / GJSFB test campaign.

Down-stand Concrete Column Reinforcements

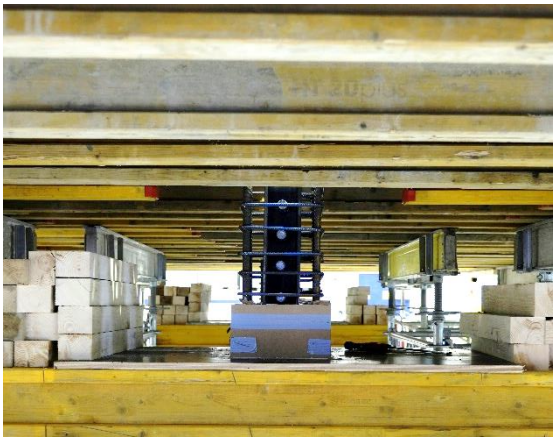

Concrete Pouring

Removal of Form-works and Casting Upper Part of Column

Figure 5.15: Additional images for the production of the test specimens / GJSFB test campaign.

5.2.3 Material properties of the test specimens

Twelve cylindrical (150x300mm) and 9 cubic (150x150mm) concrete samples were cast together with the test specimens. The elastic modulus and the compressive strength of the concrete material were determined according to EN12390-3 [78] and EN12390-13 [79] at 28 days after the concrete casting and at the test dates. Table 5.2 summarizes the results of the material characterization tests of the concrete samples.

The material properties of the steel beam, bottom plate, longitudinal steel reinforcements and the threaded-rods were determined with steel coupon tests performed according to EN ISO 6892-1 [63]. Table 5.3 summarizes the results of the material characterization tests of the steel coupon samples. Detailed results are also presented in Annex-E.

It is important to mention that although the ordered material grade of the Ø12 and Ø16 longitudinal steel reinforcements was B500B, the yield strength (f_y) and the ultimate strength (f_u) of these reinforcements were determined to be less than the minimum specified requirements for the nominated material grade [103]. Therefore, the plastic moment capacity, the ultimate-rotation capacity, and the stiffness and strength classifications of GJSFB joint configurations presented based

on the experimental test results (see Section 5.2.5) and the estimations of the finite element analyses (see Section 5.3) should be investigated considering this inconsistency. The material supplier and the laboratory management have been informed about this inconsistency.

Table 5.2: Material properties of the concrete samples of GJSFB test campaign.

Order Class **C30/37**	Sample Number	E^1 [GPa]	$f_{c,cylinder}$ [MPa]	$f_{c,cube}$ [MPa]	$f_{ctm}{}^2$ [MPa]	$\rho_{cylinder}$ [kg/dm^3]	ρ_{cube} [kg/dm^3]
Age:28 Days	Ref[3]	N/A	40.0	N/A	3.02	2.34	N/A
	1	30.0	39.2	44.0	2.97	2.33	2.29
	2	31.2	38.4	41.6	2.92	2.32	2.31
	3	31.0	38.9	42.8	2.95	2.33	2.31
Mean Values		30.7	39.1	42.8	2.97	2.33	2.30
GJSFB-01 Age:58 Days	Ref[3]	N/A	46.3	N/A	3.41	2.33	N/A
	1	33.4	44.6	46.1	3.31	2.33	2.32
	2	33.7	46.5	48.8	3.42	2.33	2.31
	3	33.0	45.3	48.5	3.35	2.33	2.31
Mean Values		33.4	45.7	47.8	3.37	2.33	2.32
GJSFB-02 Age:65 Days	Ref[3]	N/A	47.7	N/A	3.49	2.33	N/A
	1	33.8	47.5	48.9	3.48	2.32	2.31
	2	32.6	46.5	50.7	3.42	2.32	2.29
	3	33.3	47.0	50.5	3.45	2.32	2.34
Mean Values		33.2	47.2	50.0	3.46	2.32	2.31
Cement		: CEM I 42.5N					
Exposition Class		: XC4,XD1,XF1,XA1,XM1(2)					
Consistency Class		: F3					
Aggregate Size		: 8mm					

[1] Elastic modulus was determined according to EN12390-13 Method A [79] with cylindrical samples.

[2] The mean tensile strength was determined based on the formulations proposed by EN1992-1-1 [72]-Table 3.1 using the cylindrical compressive strengths ($f_{c,cylinder}$).

[3] A reference cylindrical sample for each material characterization test series was tested to initially determine a reference value for the compressive strength of the cylindrical samples required to be used in the test procedure of EN12390-13 Method A [79] to determine the elastic modulus.

Table 5.3: Material properties of the steel specimens of GJSFB test campaign.

Specimen Name	Ordered Grade	Sample ID	E^1 [GPa]	f_y [MPa]	f_u [MPa]	A[2] [%]
Steel Beam	S355	Flange-1 (F-1)	207	381	517	34.0
		Flange-2 (F-2)	207	385	514	35.0
		Web-1 (W-1)	203	418	538	28.5
Mean Values			206	395	524	32.5
Bottom Plate	S355	BP-1	212	470	538	33.0
		BP-2	210	475	538	32.5
		BP-3	204	459	533	32.5
Mean Values			209	468	536	32.7
Reinforcement-*Ø12*	B500B	*Ø12*-1	208	448	570	32.0
		Ø12-2	206	470	572	29.5
		Ø12-3	225	426	586	24.5
Mean Values			213	448	576	28.7
Reinforcement-*Ø16*	B500B	*Ø16*-1	206	383	560	31.0
		Ø16-2	212	384	559	31.5
		Ø16-3	213	414	560	33.5
Mean Values			204	394	560	32.0
Threaded-rods-*Ø24*	12.9	*Ø24*-1	201	1210	1311	13.0
		Ø24-2	207	1212	1313	13.0
		Ø24-3	203	1209	1314	12.0
Mean Values			204	1210	1313	12.7
Threaded-rods-*Ø30*	12.9	*Ø30*-1	205	1120	1216	15.0
		Ø30-2	224	1099	1194	14.0
		Ø30-3	201	1108	1204	13.5
Mean Values			210	1109	1205	14.2

[1] Elastic modulus (E) was determined according to EN ISO 6892-1 Method A1 [63].

[2]The term A corresponds to percentage elongation of the steel coupon after the fracture [63].

5.2.4 Instrumentation of the test specimens

The tension stress resultants resisted by the longitudinal steel reinforcements, and the threaded-rods of GJSFB-02 test specimen were measured by using strain-gauges. Due to the symmetry of the test specimens, only quarter symmetric positions of the reinforcements were instrumented with strain-gauges. Fig. 3.37 shows the position of the strain-gauges on the steel reinforcements and the threaded-rods. It is important to note that the positions of the strain-gauges are presented for configurations of the test set-ups before the upside-down turning operations. The strain-gauge distribution of the steel reinforcements was identical for both test specimens.

In addition, the steel beams at both sides of the mid-span were also equipped with strain-gauges at their flanges and webs. Fig. 5.16 also shows the position of the strain-gauges on the steel beams and the threaded-rods. The strain-gauge distributions of the steel beams were also identical for both test specimens.

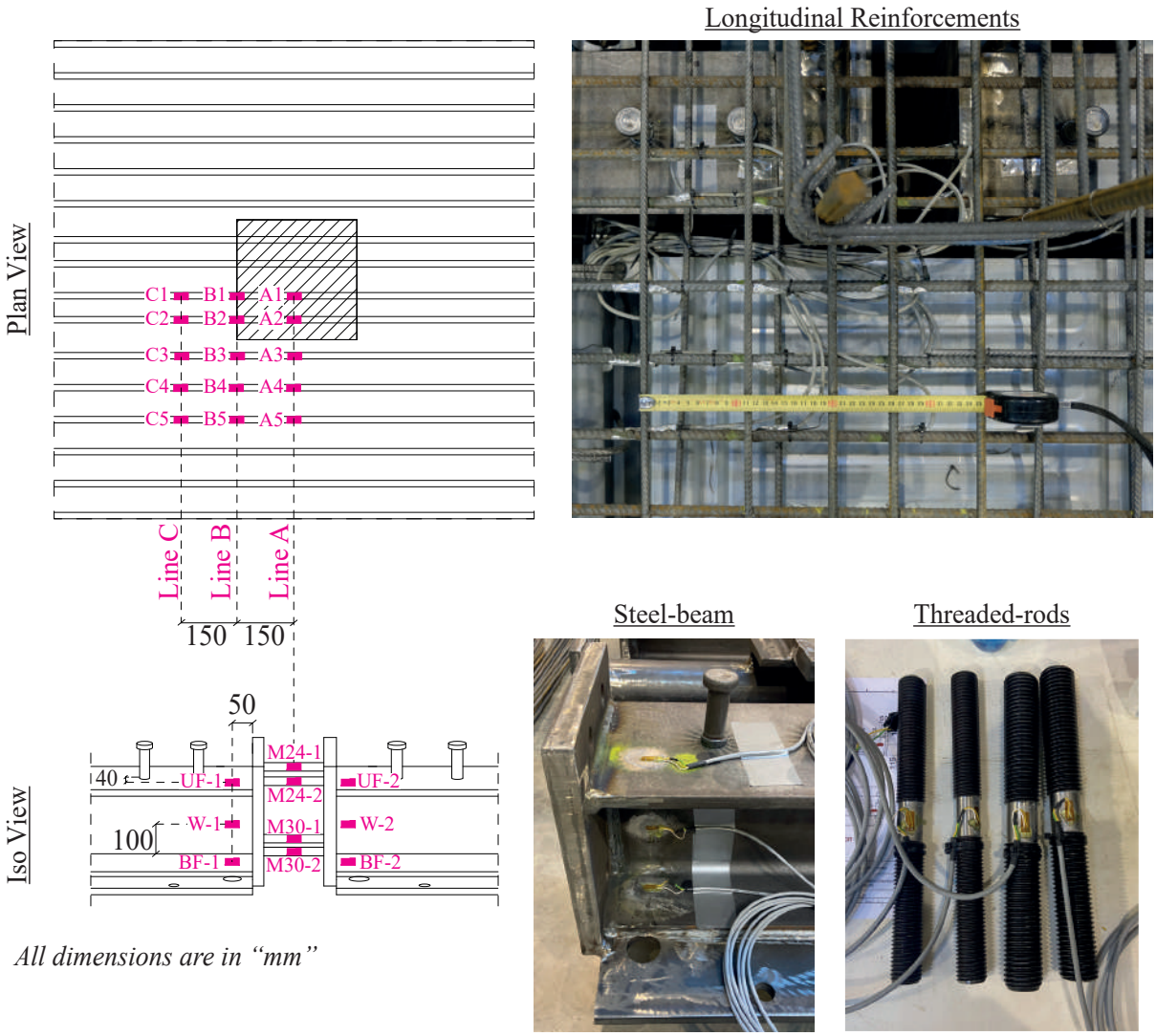

Figure 5.16: Strain-gauge distribution of the test specimens / GJSFB test campaign.

The test specimens were also equipped with 27 linear variable displacement transducers (DTs). Fig. 5.17 shows the position of the displacement transducers and their measurement orientations with measurement ranges. Identical configurations were applied for both tests except the measurement ranges of the some of the transducers. In addition, their installation purpose is summarized below;

- DT-1 & DT-8, DT-15 & DT-16 measure rotational displacements at column surfaces,

- DT-2 & DT-9 , DT-3 & DT-10, DT-4 & DT-11, DT-5 & DT-12, DT-6 & DT-13, DT-7 & DT-14 measure crack width,
- DT-20, DT-21, DT-22 (mid-span), DT-23, DT-24, DT-25 measure vertical displacements,
- DT-17 & DT-18, DT-26 & DT-27 measure slippage between the concrete encasement and the steel beams.

All dimensions are in "mm"

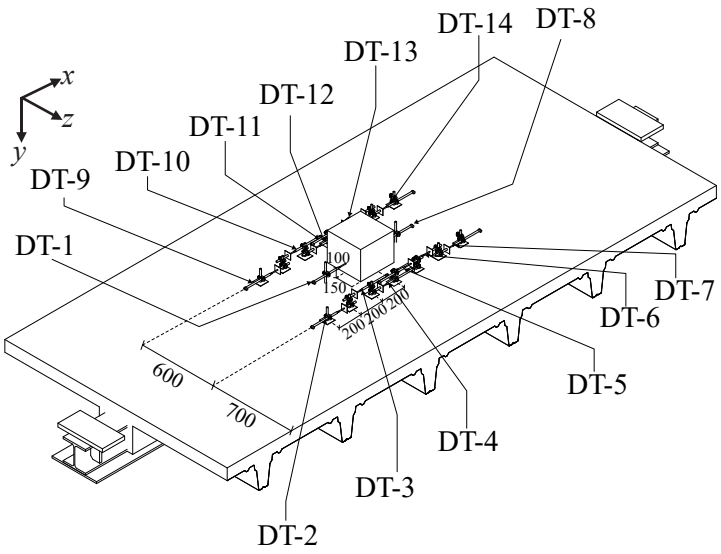

Sensor ID	Measurement Range		Direction
	GJSFB-01	GJSFB-02	
DT-1	50mm	50mm	Horizontal
DT-2	20mm	20mm	Vertical
DT-3	20mm	20mm	Vertical
DT-4	50mm	50mm	Vertical
DT-5	50mm	50mm	Vertical
DT-6	20mm	20mm	Vertical
DT-7	20mm	20mm	Vertical
DT-8	50mm	50mm	Horizontal
DT-9	20mm	20mm	Vertical
DT-10	20mm	20mm	Vertical
DT-11	50mm	50mm	Vertical
DT-12	50mm	50mm	Vertical
DT-13	20mm	20mm	Vertical
DT-14	20mm	20mm	Vertical
DT-15	50mm	50mm	Horizontal
DT-16	50mm	50mm	Horizontal
DT-17	10mm	10mm	Horizontal
DT-18	10mm	10mm	Horizontal
DT-19	10mm	10mm	Vertical
DT-20	50mm	50mm	Vertical
DT-21	50mm	50mm	Vertical
DT-22	100mm	100mm	Vertical
DT-23	50mm	50mm	Vertical
DT-24	50mm	50mm	Vertical
DT-25	10mm	10mm	Vertical
DT-26	10mm	10mm	Horizontal
DT-27	10mm	10mm	Horizontal

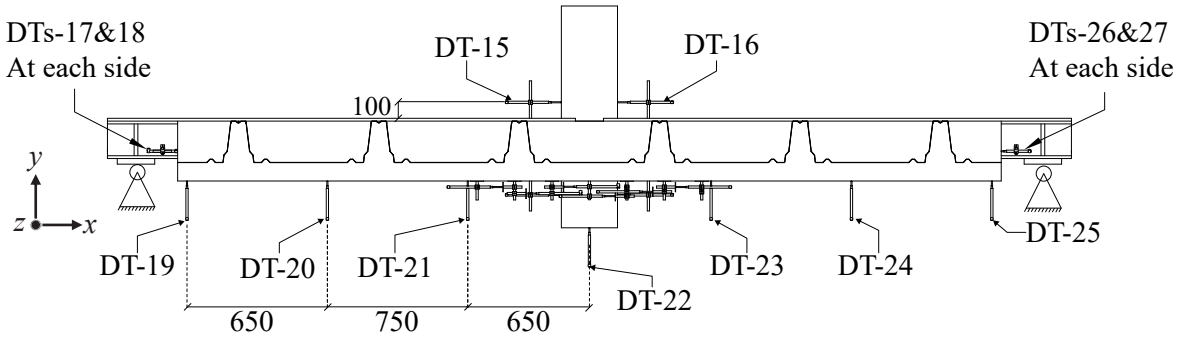

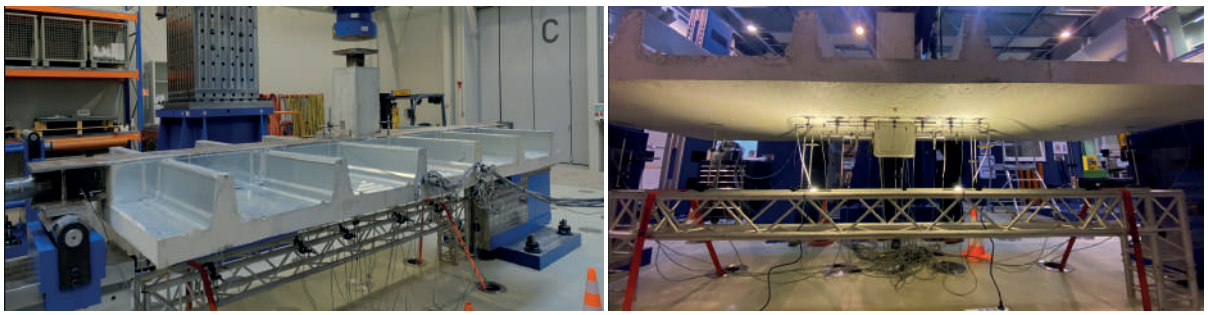

Figure 5.17: Displacement transducers (DTs) / GJSFB test campaign.

5.2.5 Execution of GJSFB test campaign

The tests were performed in The Structural Laboratory of the University of Luxembourg with 4000kN hydraulic jack (see Fig. 5.7). The force from the hydraulic jack and the data from the measurement devices presented in the previous section were continuously recording with 100Hz data acquisition speed during the tests. The loading procedure was adopted from Hanswille [80]. Fig. 5.18 presents the loading procedure having the loading steps listed below. Due to the limitations of the hydraulic jack, the cyclic loading period was also applied with displacement-controlled method based on the displacements recorded during the first loading step.

- Load up to 40% of the expected capacity - $F_{u,exp}$ (Displacement-controlled 0.6mm/min),
- Rest 15 minutes (Displacement-controlled),
- Cycling period between 5% - 40% of the expected capacity (Displacement-controlled 0.05Hz - 25 Cycles),
- Total unload at the end of the cycling period (Displacement-controlled 2mm/min),
- Load up to 60% of the expected capacity (Displacement-controlled 0.6mm/min),
- Rest 15 minutes (Displacement-controlled),
- Load up to 80% of the expected capacity (Displacement-controlled 0.6mm/min),
- Rest 15 minutes (Displacement-controlled),
- Load up to 100% of the expected capacity (Displacement-controlled 0.6mm/min),
- Rest 60 minutes (Displacement-controlled),

1. If there is no failure at the expected capacity (100%);
   (a) Total unload (Displacement-controlled 2mm/min),
   (b) Load up to 120% of the expected capacity (Displacement-control 0.6mm/min),
   (c) Rest 15 minutes (Displacement-control),
   (d) If there is no failure at the 120% of the expected capacity;
      i. Total unload (Displacement-controlled 2mm/min),
      ii. Load until the ultimate load capacity - $F_{u,Test}$ (Displacement-controlled 1.2mm/min).

The expected test capacities were determined with FEAs performed prior to the experimental tests based on the mean material properties of the ordered concrete material and the characteristic material properties of the steel reinforcements according to EN1992-1-1 [72], characteristic material properties of the steel materials according EN1993-1-1 [50], and the characteristic material properties of the threaded-rods and the shear-studs according to their producer catalogs [62, 81]. The details of the FE-models are presented in Section 5.3.

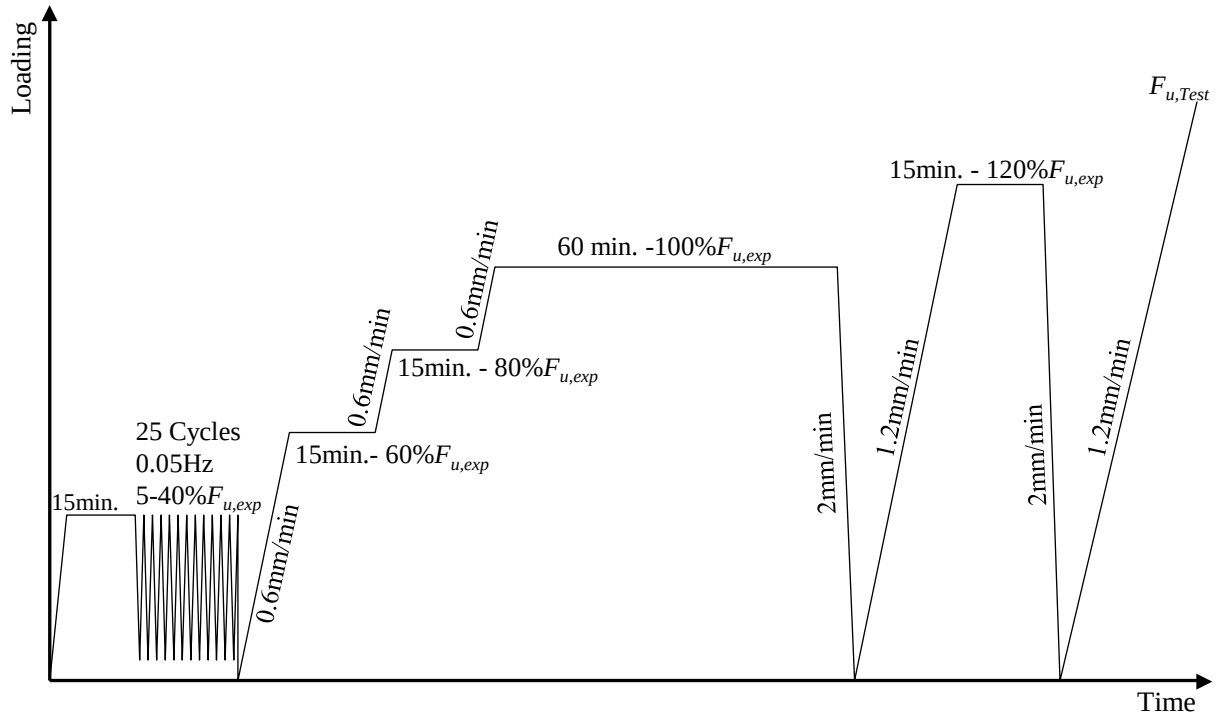

Figure 5.18: Loading procedure of GJSFB test campaign.

5.2.5.1 Test Results and Discussions / GJSFB - 01

Fig. 5.19 presents the load mid-span deflection curve of the first test specimen. The test was deliberately terminated about 90mm vertical mid-span deflection (δ_y=90mm) to protect the displacement transducers as nearly all of them were positioned under the test specimen (see Fig. 5.17) and it was decided that further deflection might damage them. Therefore, it is important to note that the rotation capacity of GJSFB-01 joint configuration presented in this section might not reflect the full rotation capacity as the test specimen might further deflect if the test was not deliberately terminated. On the other hand, as it could be clearly detected in Fig. 5.19 that the ultimate load-bearing capacity of the joint was attained during the test as there was nearly perfect plastic behavior between δ_y=60mm to δ_y=90mm.

The expected test capacity was estimated as 200kN ($F_{u,exp}$=200kN) before the test. However, the ultimate test load was recorded to be equal to 363kN ($F_{u,Test}$=363kN) as 80% higher than the expected capacity. Therefore, according to the test procedure presented in Fig. 5.18, the test specimen was unloaded and reloaded two times at 100% and 120% of the expected capacity. In addition, it could be noticed that there was relaxation of the test specimen during the waiting periods (pause) of the test procedure. It is the fact that the load-bearing mechanism of the joint was fully activated during the initial loading step and the cycling loading period.

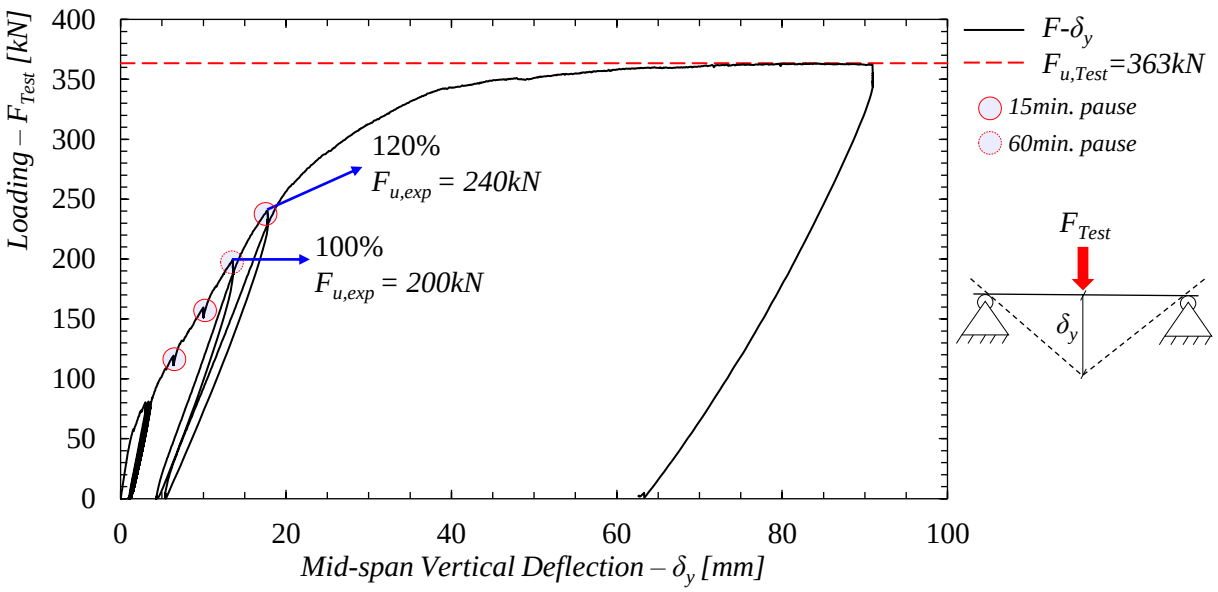

Figure 5.19: Load mid-span deflection behavior of GJSFB-01 test specimen.

To derive the moment-rotation behavior of GJSFB-01 joint configuration, it is initially required to define a calculation methodology for the determination of the joint rotations and the moments. In this study, the bending moments at the joint was calculated at the contact section between the concrete grout and the beam-end-plate. Fig. 5.20 illustrates the distance between the roller support and the beam-end-plate above the concrete-column for the symmetric half of the test specimen, and Eq. 5.1 formulates the calculation of the bending moments at the joint. The joint rotations were calculated based on the mid-span deflection [52, 89] as formulated with Eq. 5.2. Although the test specimen was instrumented with displacement transducers to record rotational displacements of the joint with respect to the RC-column surfaces (see Fig. 5.17 / DT-1 & DT-8, DT-15 & DT-16), cracks were identified on the column as shown in Fig. 5.21; therefore, the data recorded at the column surfaces were considered not to be reliable to evaluate the joint rotations and omitted.

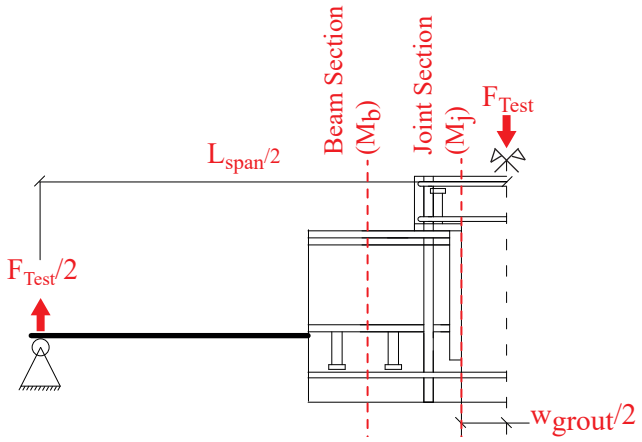

Figure 5.20: The illustration of the lever-arm between GJSFB and the roller support.

Figure 5.21: Tensile crack formation for GJSFB-01 test specimen.

$$M_j = \left(\frac{L_{span} - w_{grout}}{2} \right) \cdot \frac{F_{Test}}{2} \tag{5.1}$$

$$\Phi_j = \arctan\left(\frac{2 \cdot \delta_y}{L_{\text{span}}} \right) \tag{5.2}$$

Based on Eq. 5.1 and Eq. 5.2, Fig. 5.22 presents the moment-rotation behavior of GJSFB-01 test specimen with rotational stiffness characterizations. The initial load-step and the cycling loading period were excluded from the figure for clear identification of the moment-rotation characteristics of GJSFB-01 joint configuration. The softening of the joint stiffness at 115kNm joint moment ($M_{j,1}$=115kNm) could be attributed to the propagation of the tensile cracks.

For further investigation of the tensile crack phenomenon of the test specimen, Fig. 5.23 presents the data recorded by the displacement transducers positioned to measure the openings of the tensile cracks, in other words the crack-width for a single crack, with respect to the joint rotations. The critical crack-width (w_c=*0.2168mm*), which corresponds to the tensile load-bearing limit of the utilized concrete material and calculated according to fib Model Code [3] based on the mean values presented in Table 5.2, was also noted in the figure. The formulations for the calculation of the critical crack-width are presented in Annex-C. The unloading period was excluded from the figure for clear visualization. However, the initial load-step and the cycling loading period of the test procedure was included in the figure to accurately assess the crack status of the test specimen. It could be deduced from Fig. 5.23 that once the mean crack-openings measured by DT-4 and DT-11 reached the critical limit at 1.4mrad joint rotation (Φ_j=*1.4mrad*) then the moment-rotation behavior of GJSFB-01 joint configuration started soften. Furthermore, around 6.0mrad joint rotation (Φ_j=*6.0mrad*) the mean crack-openings measured by all of the displacement transducers reached

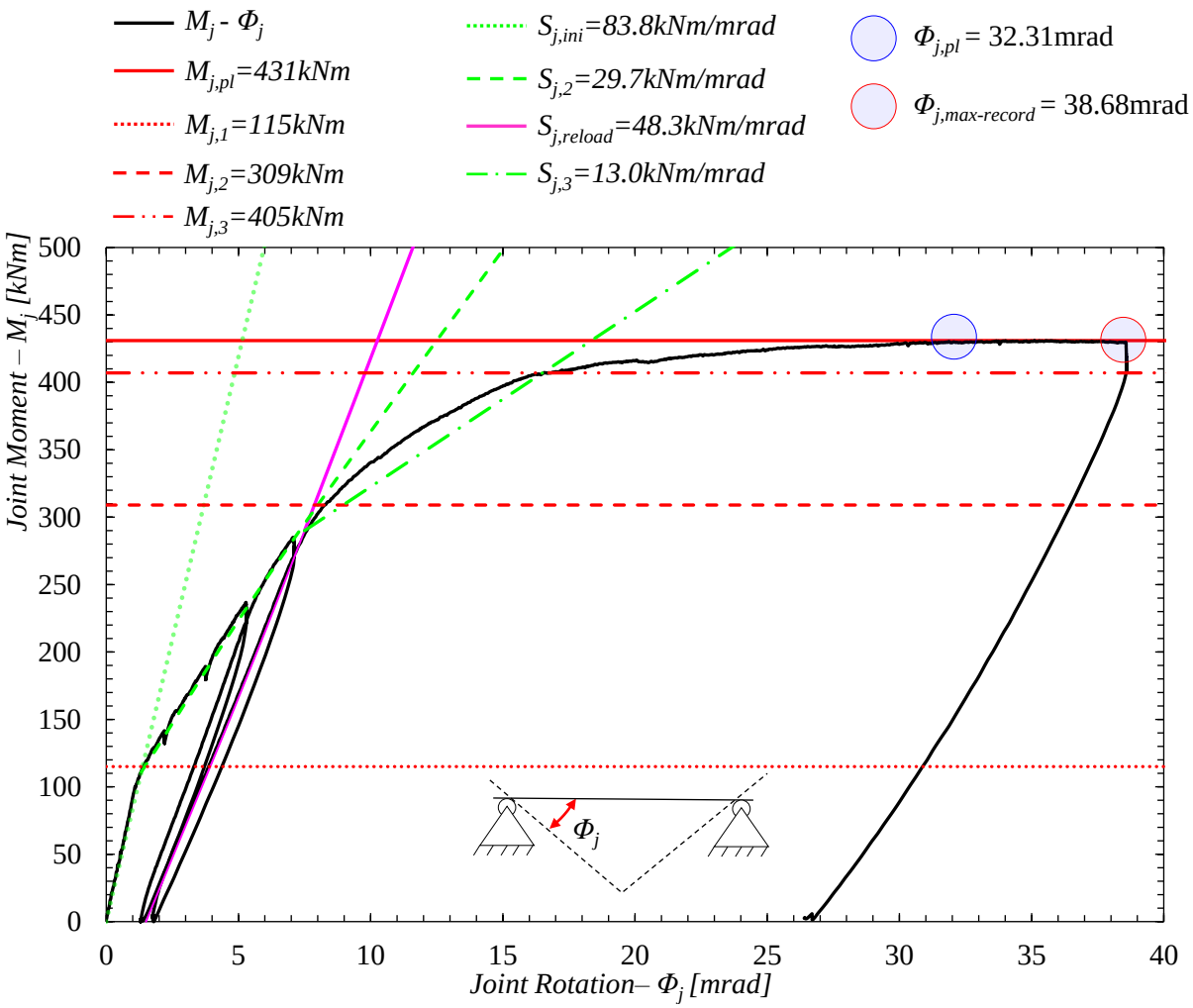

Figure 5.22: Moment-rotation behaviour of GJSFB-01 joint configuration.

the critical crack-width. Thus, it is concluded that the continuous concrete slab lost its load-bearing capacity against the tension stress resultants developed due to the bending moment actions along the effective length of the joint at 6.0mrad joint rotation. On the other hand, it could also be noticed from the figure that the moment-rotation behavior of the joint further softened at 7.5mrad joint rotation (Φ_j=*7.5mrad*) having the rotational stiffness of 13kNm/mrad (see also Fig. 5.22 - $S_{j,3}$=*13kNm/mrad*). Considering the fact that there was no further tensile capacity of the concrete slab after 6.0mrad joint rotation, the further softening at 7.5mrad joint rotation could be linked to the initiation for the yielding of the longitudinal steel reinforcements close to the joint region.

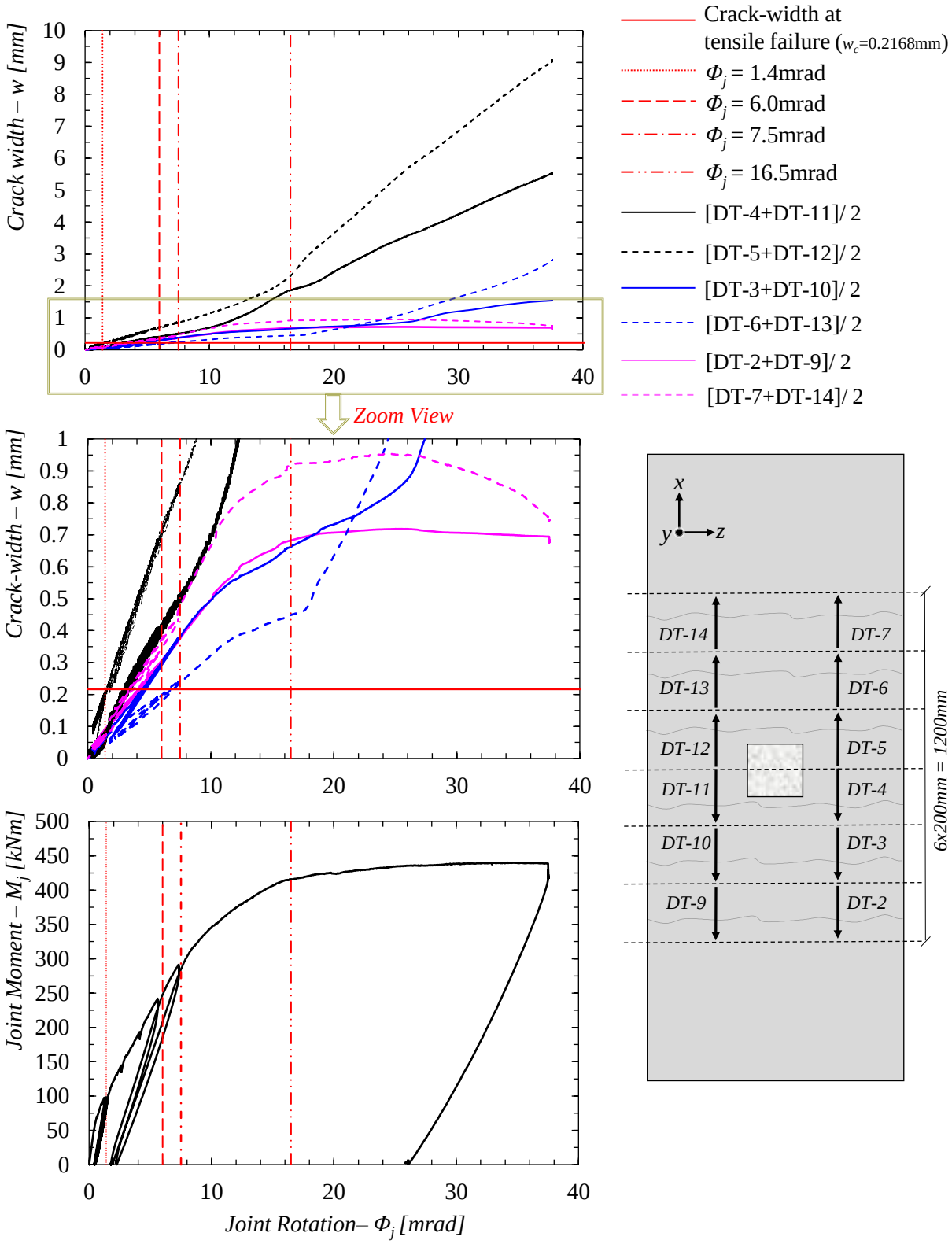

Figure 5.23: Investigation of the crack widths for GJSFB-01 test specimen.

Additionally, it could also be noticed from Fig. 5.23 that the crack-opening rate next to the joint (DT-4 & DT-11, DT5 & DT-12) started to increase significantly around 16.5mrad joint rotation (Φ_j=*16.5mrad*) and the moment-rotation behavior of the joint further softened at this instant which also corresponds to 405kNm joint moment (see also Fig. 5.22 - $M_{j,3}$=*405kNm*) as 94% of the plastic-moment capacity of GJSFB-01 joint configuration. Consequently, it is concluded that all of the longitudinal steel reinforcements of the composite cross section (see Fig. 5.11) yielded about 16.5mrad joint rotation. It is important to note that the 6% additional bending moment capacity of GJSFB-01 joint configuration after the yielding of the entire longitudinal steel-reinforcements could be linked to the strain-hardening of the reinforcement material. The yielding of the longitudinal steel reinforcements later investigated based on the recorded strain data. However, before the investigation of the strain data, further results could be deduced from Fig. 5.23 as listed below;

- The rate of the crack-openings measured between 200mm to 400mm distance from the mid-span along the *x-axis* direction also increased suddenly around 16.5mrad joint rotation; thus it could be stated that the longitudinal reinforcements were yielded at several positions between the mid-span and 400mm distance from the mid-span along the *x-axis* direction.
- The crack-openings measured between 400mm to 600mm distance from the mid-span along the *x-axis* direction started to stabilize around 16.5mrad joint rotation. Therefore, it could be deduced that the effective joint length (L_j), which corresponds to the distance between the composite joint and the restrained-end of the longitudinal steel reinforcements subjected to the tensile stress resultants [89], may be estimated to be around 600mm. The effective joint lengths of GJSFB joint configurations are further investigated in Section 5.4,
- The applied loading was equally distributed to the roller-supports based on the crack-opening histories presented with respect to the central symmetry axis of the test set-up.

Fig. 5.24 and Fig. 5.25 show the crack-patterns for GJSFB-01 test specimen.

a) Before the Test

b) At the Ultimate Load

Figure 5.24: Crack patterns next to the mid-span / GJSFB-01.

a) Crack Patterns / View-01

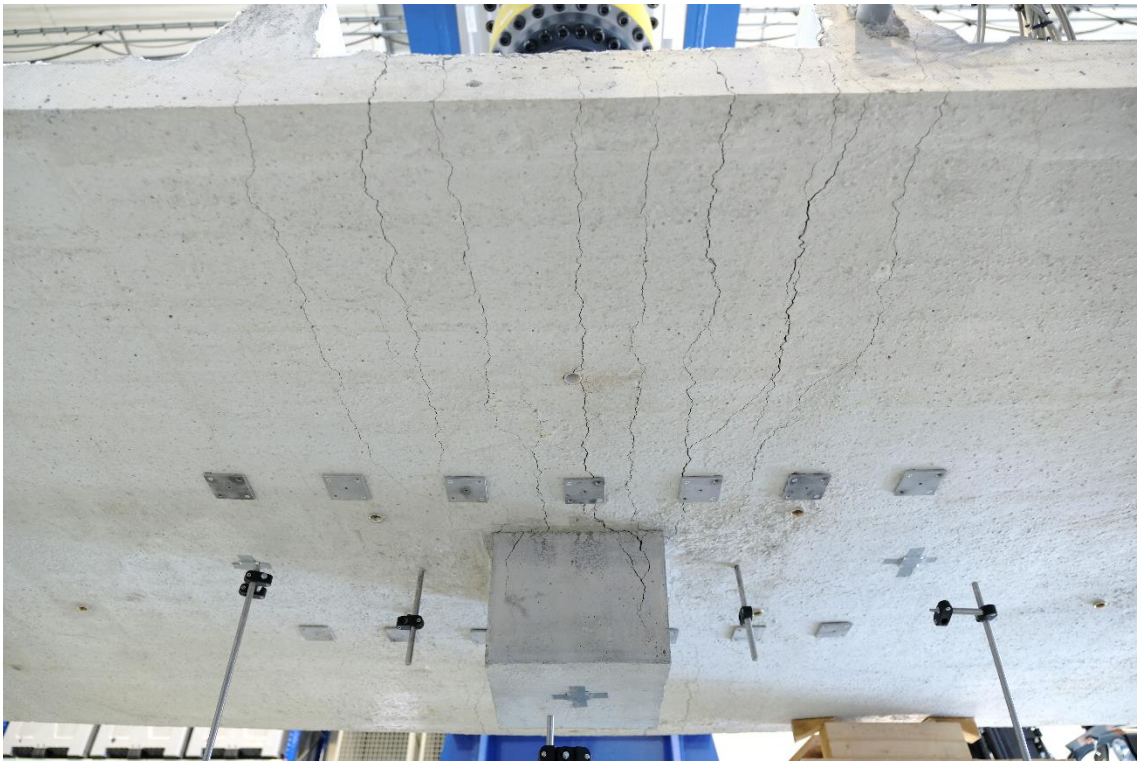

b) Crack Patterns / View-02

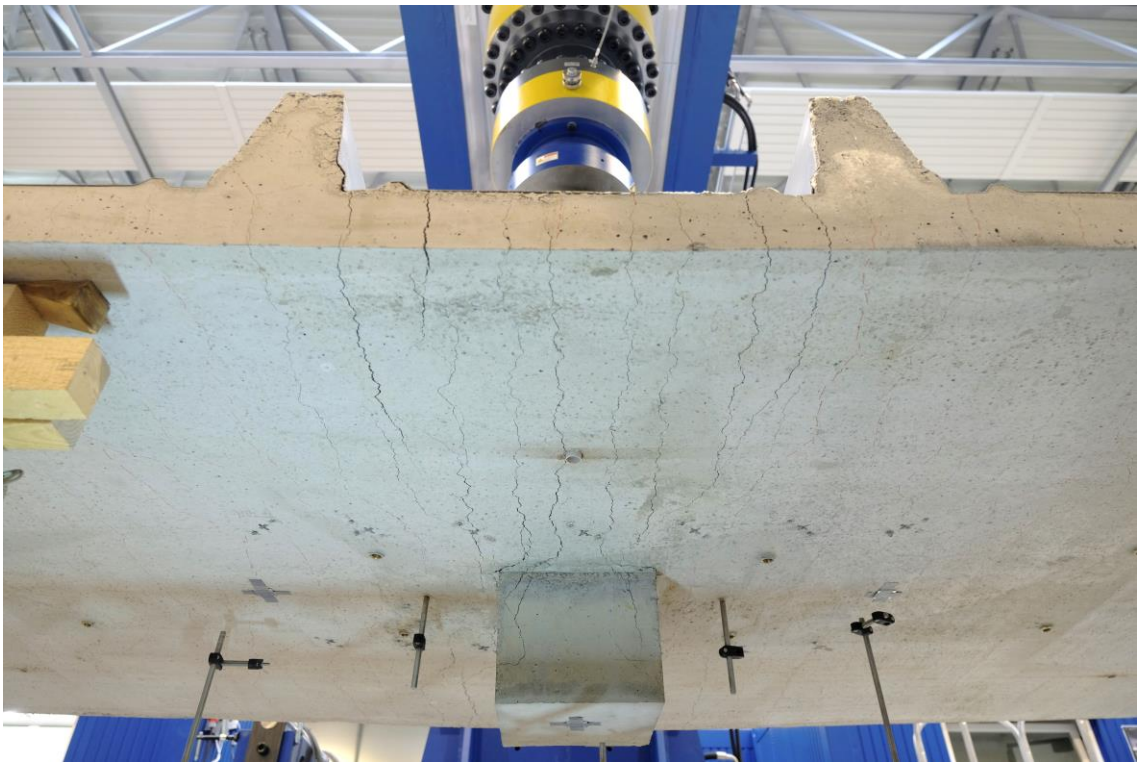

Figure 5.25: Crack patterns along the continuous slab / GJSFB-01.

As indicated earlier, several softening phases were detected for the moment-rotation behavior of GJSFB-01 joint configuration. The softening characteristics between 1.4mrad-6mrad joint rotations earlier attributed to the propagation of the tensile cracks within the 600mm longitudinal distance at both sides of the mid-span. In addition, the softening phase between 7.5mrad and 16.5mrad were linked to yielding of the longitudinal steel reinforcements. To investigate the yield status of the longitudinal steel reinforcements Fig. 5.26 presents the data recorded by the strain-gauges positioned on the longitudinal steel reinforcements together with the corresponding stress resultants. The resultant forces are presented based on the strain data recorded at the mid-span and they were calculated according to well known Hooke's law as formulated in Eq. 5.3 using the nominal cross-section area ($Ø$=*12mm*), the mean elastic modulus (E_m), the mean yield strength ($f_{y,m}$) and the corresponding strain ($\varepsilon_{y,m}$), the mean ultimate strength ($f_{u,m}$) and the corresponding strain ($\varepsilon_{u,m}$) of the longitudinal steel reinforcements. The aforementioned mean values are presented in Table 5.3. The unloading period was excluded from the figure. The strain gauges nominated as A5 and A2 were damaged at the beginning of the test and around 32mrad joint rotation, respectively.

$$F_{Ø_{re}\ or\ Ø_{th}} = \begin{cases} \frac{E_{mean}\cdot\varepsilon\cdot(Ø)^2\cdot\pi}{4} & \varepsilon \leq \varepsilon_{y,m} \\ \\ \frac{E_{mean}\cdot\varepsilon_y\cdot(Ø)^2\cdot\pi}{4} + \frac{(f_{u,m}-f_{y,m})}{(\varepsilon_{f,m}-\varepsilon_{y,m})}\cdot\frac{(\varepsilon-\varepsilon_{y,m})\cdot(Ø)^2\cdot\pi}{4} & \varepsilon > \varepsilon_{y,m} \end{cases} \tag{5.3}$$

Based on Fig. 5.26, it is clear that all of the instrumented longitudinal reinforcements were yielded at several positions about 7.5mrad joint rotation. This instant very well matches with the softening of the moment-rotation behavior having the rotational stiffness of 13kNm/mrad (see Fig. 5.22 - $S_{j,3}$=*13kNm/mrad*). Thus, it is concluded that the plastic-hinge formation for GJSFB-01 joint configuration started at 7.5mrad joint rotation which corresponds to 309kNm joint moment (see Fig. 5.22 - $M_{j,2}$=*309kNm*). Additionally, it could also be noticed from Fig. 5.22 that the softening phase with $S_{j,3}$=*13kNm/mrad* continued until 16.5mrad joint rotation, thus it is concluded that all of the longitudinal steel reinforcements were successively yielded between 7.5mrad-16.5mrad joint rotations as the moment-rotation behavior of the joint further softened at 16.5mrad joint rotation (see Fig. 5.22 - $M_{j,3}$=*405kNm*). This outcome could also be verified with Fig. 5.23 based on the sudden increase in the rate of the crack-openings at 16.5mrad joint rotation. Therefore, it is concluded that the theoretical full plastic-hinge formation of GJSFB-01 joint configuration developed at 16.5mrad joint rotation with plastic moment capacity to be equal to 405kNm. However, it could be observed in Fig. 5.22 that GJSFB-01 joint configuration turned to full plastic hinge about 32.3mrad joint rotation ($\Phi_{j,pl}$=32.3mrad) by sustaining the 431kNm plastic bending moment capacity ($M_{j,pl}$=*431kNm*). Consequently, the joint had about 6% additional bending moment capacity compared to the possible theoretical limit. This difference could be linked to the ductile strain-hardening of the longitudinal steel reinforcements. In addition, the measured maximum rotation capacity of the joint was 38.6mrad ($\Phi_{j,max\text{-}record}$=*38.6mrad*) to be 134% higher than the rotation at the joint for the initiation of the theoretical plastic-hinge formation.

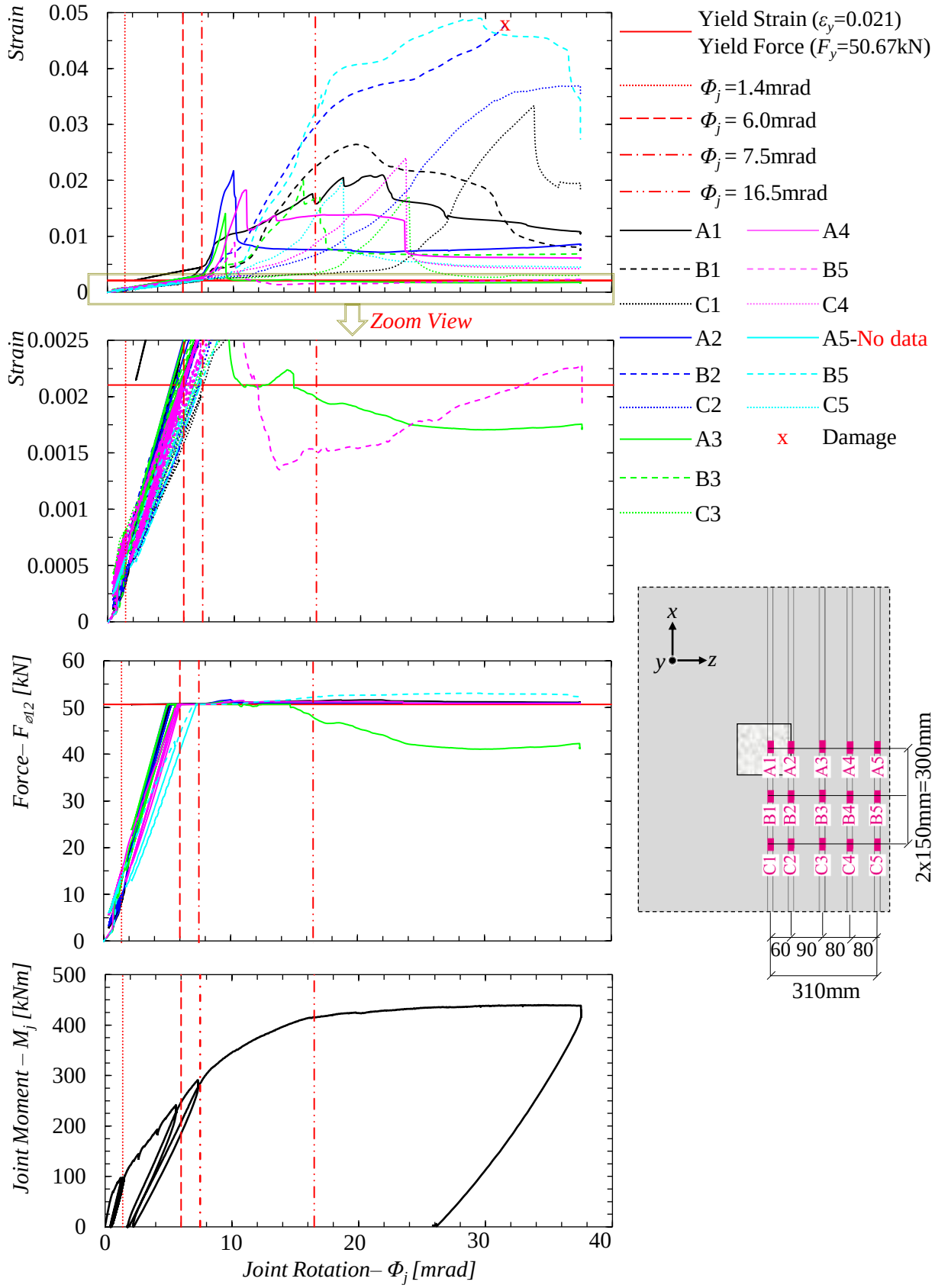

Figure 5.26: Yield status of the longitudinal steel reinforcements / GJSFB-01 test specimen.

It is crucial to note that the experimental test was deliberately terminated at 38.6mrad joint rotation due to the large deformation of the test specimen. Therefore, one could expect the ultimate rotation capacity of GJSFB-01 joint configuration to be larger than 38.6mrad as it could also be seen in Fig. 5.26 that the magnitudes of the strains for the instrumented longitudinal steel reinforcements were far less than the magnitudes of their fracture strains presented in Table 5.3 ($Ø12$-ε_f).

On the other hand, it is the fact that the threaded-rods were omitted for GJSFB-01 joint configuration (see Fig. 5.12a); thus, it could be stated that the compressive stress resultants developed due to the bending moment in the joint was only resisted by the concrete grout. Therefore, the cross-section for GJSFB-01 joint configuration could be considered to be analogically identical to a continuous reinforced-concrete T-beam. As a result, it would be expected that the crushing of the concrete grout under the compressive stress resultants limits the rotation capacity of GJSFB-01 joint configuration. Although, there was no sign of the crushing of the concrete grout during the test according to moment-rotation behaviour presented in Fig. 5.22. The status of the concrete grout was investigated after the test by removing a part of the metal sheeting at the mid-span of the test specimen as shown in Fig. 5.27. Contrary to the moment-rotation behavior in Fig. 5.22, partial crushing of the concrete grout and the tensile cracks could be clearly identified from the figure together with the position of the neutral axis. According to this outcome, it can be concluded that the ultimate plastic rotation capacity of GJSFB-01 joint configuration could not be much larger than 38.6mrad as there was already partial crushing developed until the side surfaces of the concrete grout. However, as the test was deliberately terminated the possible limit for the plastic rotation capacity of GJSFB-01 joint configuration is also investigated with the numerical simulations and the analytical resistance model presented in Section 5.3 and Section 5.4, respectively.

Fig. 5.28 presents the yield status of the steel beams with respect to the joint rotations. The yield strains of the flanges ($\varepsilon_{y,f}$) and the web ($\varepsilon_{y,w}$) were calculated based on the yield strengths and the elastic modules of the related components presented in Table 5.3. It is important to note that the upside-down orientation of the beams should be considered while investigating the strain data as the test specimen was turned 180° around the longitudinal axis of the beams (see Fig. 5.8). According to the presented strain data, it is concluded that the steel beams were deformed elastically during the test. In addition, the strain data of the steel beams also supports the previous statement that indicates the applied loading was uniformly distributed between the roller supports.

Partial concrete cracks were observed around the shear studs at the end of the composite section near to the roller supports. Fig. 5.29 shows these crack patterns. The relative end-slip between the steel beams and the concrete encasement was also recorded during the test. Fig. 5.30 presents the relative end-slip with respect to the joint rotations. The negative values of the end-slip indicate divergence of the steel-beam and the concrete encasement. Very small negative end-slip was observed to be less than 0.3mm for both sides of the test specimen. Thus, it is concluded that the concrete encasement around the steel beams was also resisting the bending moment actions along the entire span-length. It is important to note that the presented slips do not correspond to the relative slip between the continuous concrete slab and the steel beams.

a) Test Specimen after the Test / Front View

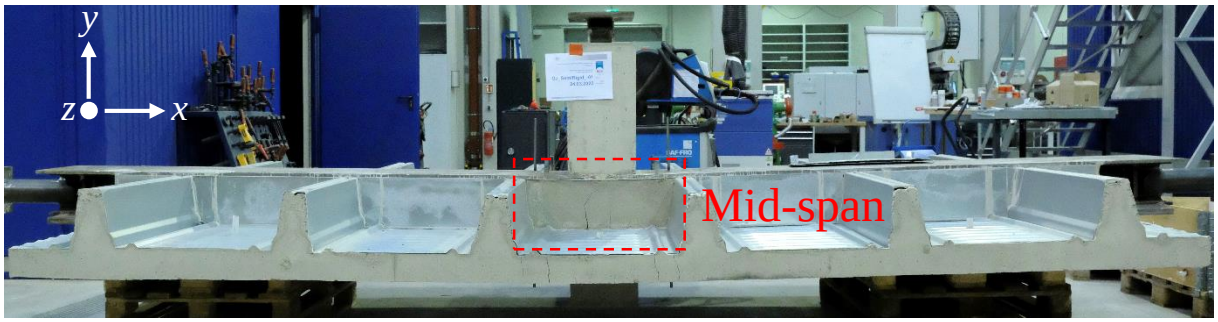

b) Status of the Concrete Grout at Mid-span / Front View

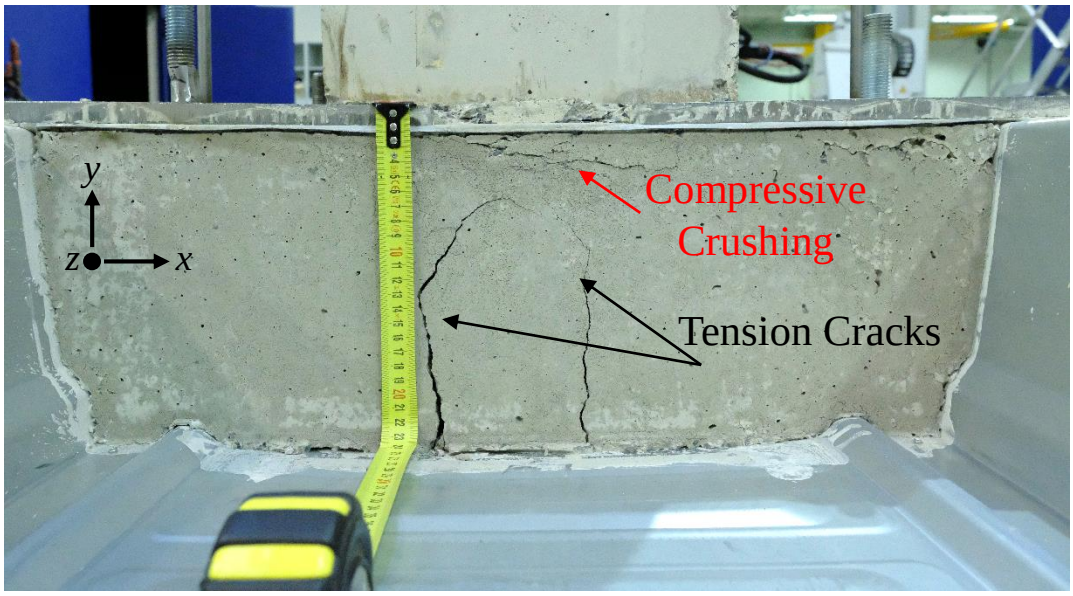

c) Status of the Concrete Grout at Mid-span / Back View

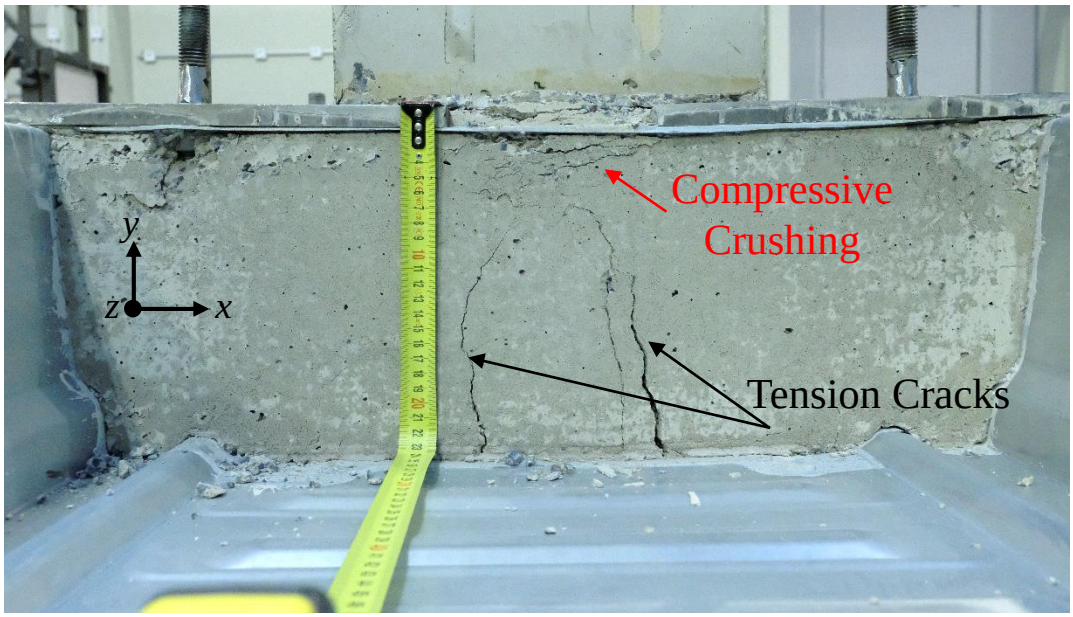

Figure 5.27: Status of the concrete grout at the mid-span of GJSFB-01 test specimen.

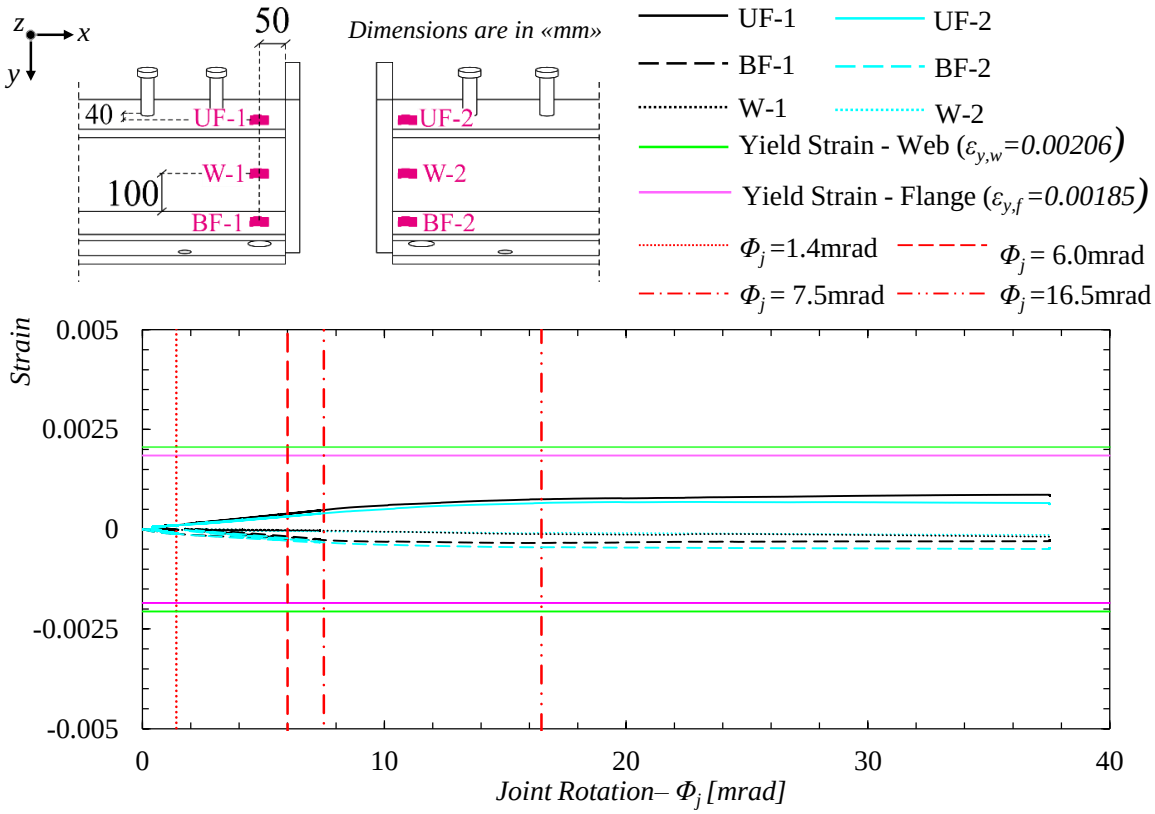

Figure 5.28: Yield status of the steel beams / GJSFB-01 test specimen.

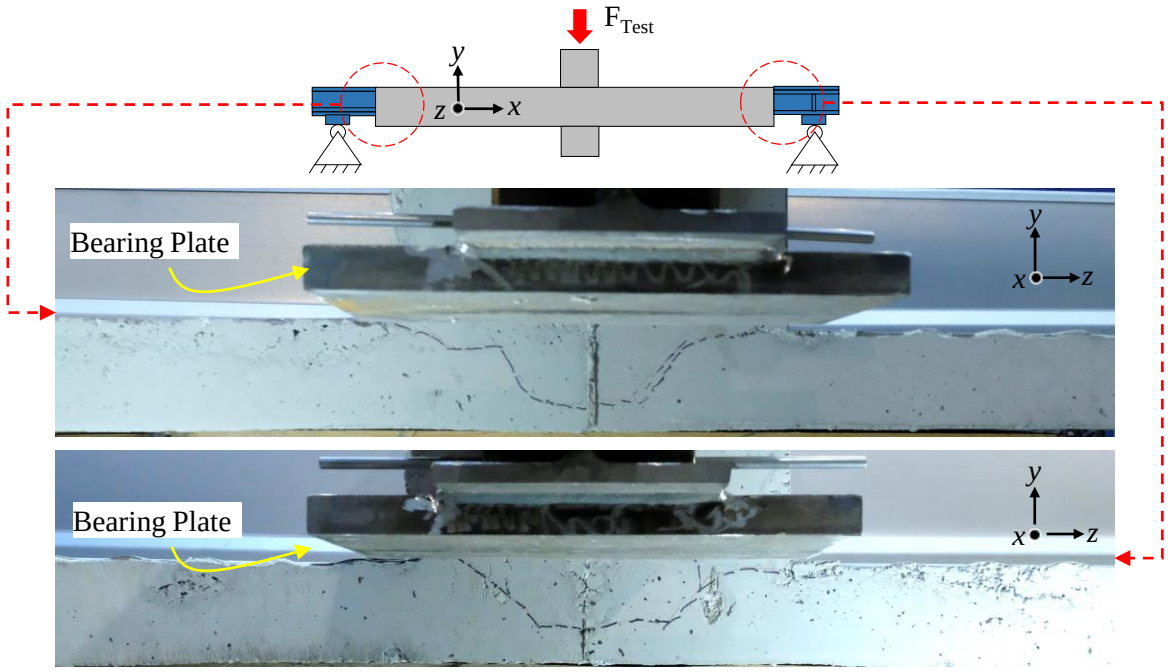

Figure 5.29: Crack patterns observed next to the roller supports / GJSFB-01 test specimen.

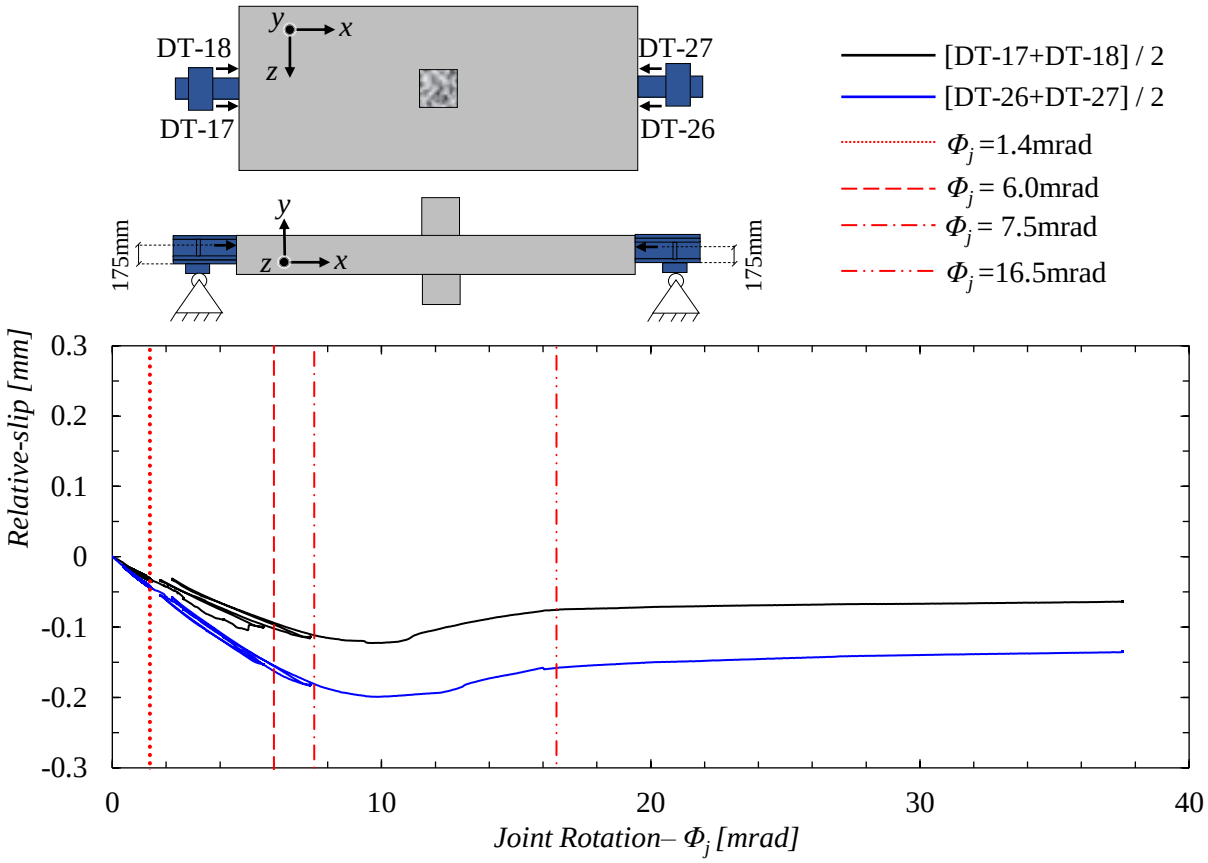

Figure 5.30: End-slip between the steel beams and concrete encasement/ GJSFB-01 test specimen.

Fig. 5.31 presents the final deformed shape of the test specimen, together with the data recorded by the displacement transducers positioned to record the vertical deflection of the test specimen along the entire span length. In Fig. 5.31c, the discontinuity at the ultimate load-level could be observed for the displacement profile of the test specimen. However, as it could be deduced from Fig. 5.31a that this was not the real behavior as the displacement transducers DT-21 and DT-23 (see also Fig. 5.17) reached their maximum measurement range before the termination of the test. Therefore, they were replaced with higher range displacement transducers in the second test.

Table 5.4 summarizes the identified test results presented in this section.

Table 5.4: Summary of GJSFB-01 test results.

Test ID	$F_{u,Test}$ [kN]	$\delta_{y,at\ F_{u,Test}}$ [mm]	$M_{j,pl}$[1] [kNm]	$\Phi_{j,pl}$ [mrad]	$\Phi_{j,max\text{-}record}$ [mrad]	$S_{j,ini}$ $[\frac{kNm}{mrad}]$	$S_{j\,2}$ $[\frac{kNm}{mrad}]$	$S_{j,3}$ $[\frac{kNm}{mrad}]$
GJSFB-01	363	90.95	431	32.31	38.68	83.8	29.7	13.0

[1] $M_{j,pl}$ corresponds to the joint moment when the moment-rotation behavior of the test specimen starts to show full plastic behavior; thus, it should be distinguished from the theoretical plastic moment-capacity that is calculated based on the yield status of the longitudinal steel reinforcements.

a) Deformed Shape of the Test Specimen

b) End Rotation at the Roller Support

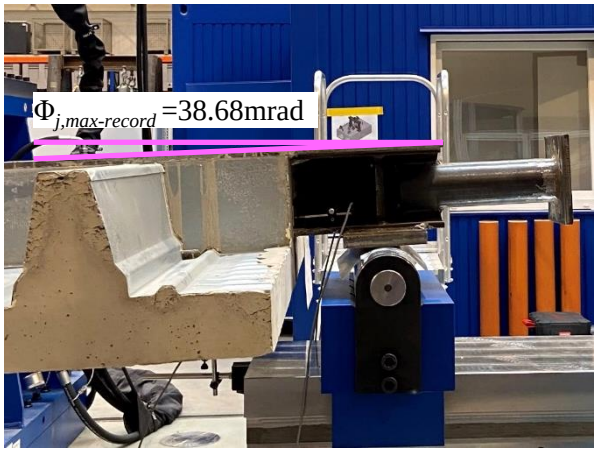

c) Displacement Profile of the Test Specimen

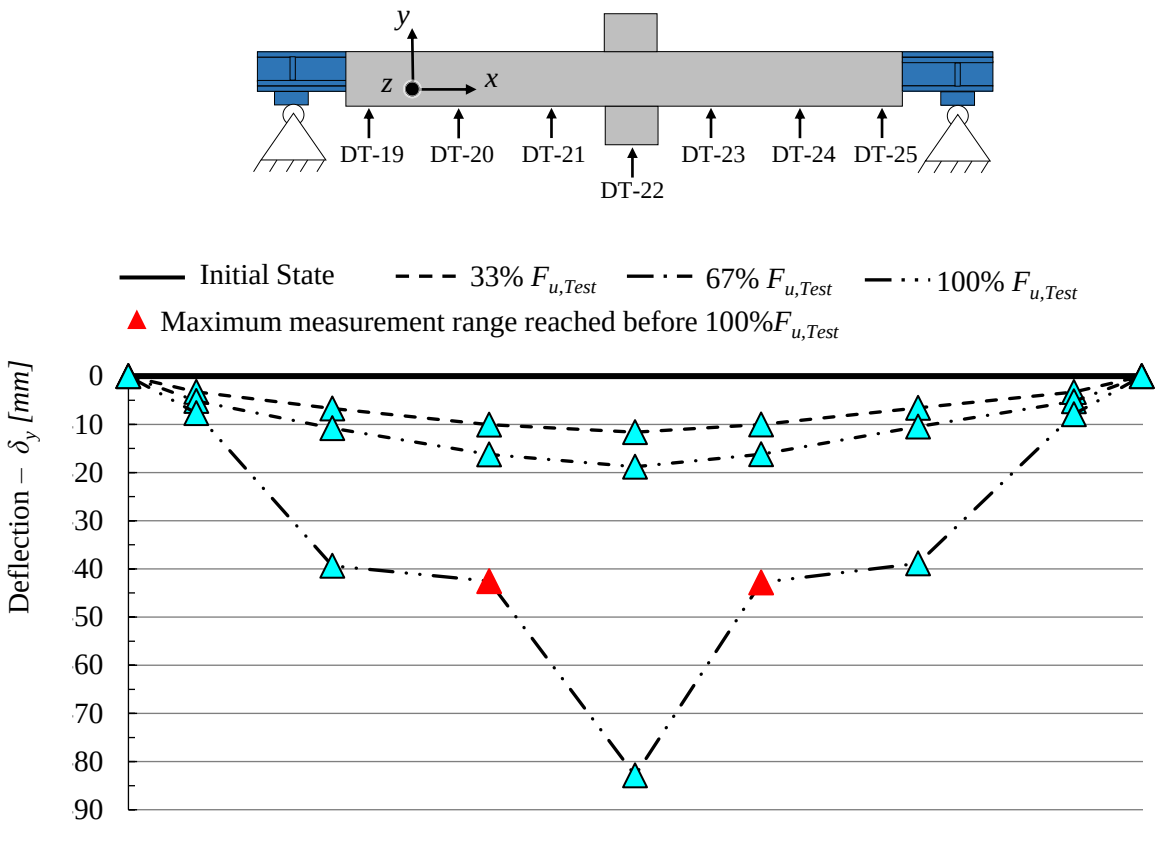

Figure 5.31: Deflection profiles of GJSFB-01 test specimen.

5.2.5.2 Test Results and Discussions / GJSFB - 02

Fig. 5.32 presents the load mid-span deflection curve of the second test specimen. There was a sudden failure about 55mm vertical mid-span deflection (δ_y=55mm). The expected test capacity was estimated as 500kN ($F_{u,exp}$=*500kN*) before the test. The ultimate test load was recorded to be equal to 512kN ($F_{u,Test}$=*512kN*) as only about 2% higher than the expected capacity. However, as consisted with the test procedure presented in Fig. 5.18, the test specimen was unloaded and reloaded at 100% of the expected capacity. The relaxation of the test specimen could be observed during the waiting periods (pause) of the test procedure. It could be deduced from Fig. 5.32 that the load-bearing mechanism of the joint was fully activated during the initial loading step and the cycling loading period.

At the ultimate test load, longitudinal shear failure was observed between the steel beams and the concrete slab at the end of the composite section near to the roller supports. Therefore, the test was deliberately terminated after the sudden load-drop at 512kN load-level. Fig. 5.33 shows the longitudinal shear failure. On the other hand, prior to the test, the ultimate load-bearing capacity of GJSFB-02 joint configuration was estimated to be only 2% lower than the ultimate test load. Therefore, it is suspicious if the test specimen initially failed due to the longitudinal shear failure or if the failure of the joint propagated the longitudinal shear failure. Consequently, the maximum joint rotation recorded during the test might not reflect the real ultimate rotation capacity of the joint if the test specimen was initially failed due to the longitudinal shear failure. This section investigates in detail the moment-rotation behavior of GJSFB-02 joint configuration and brings clarification to the reasons behind the sudden failure characteristic of the test specimen. In addition, further investigations regarding to the sudden failure of the test specimen are also presented in Section 5.3 the numerical simulation of the experimental test.

Fig. 5.34 presents the moment-rotation behavior of GJSFB-02 test specimen with rotational stiffness characterizations. The initial load-step and the cycling loading period were excluded from the figure for clear identification of the moment-rotation characteristics of GJSFB-02 joint configuration. The moments and the corresponding rotation values were calculated with Eq. 5.1 and Eq. 5.2, respectively. It is important to note that as the test specimen suddenly failed with longitudinal shear cracks, the ultimate joint moment attained in the test may not reflect the ultimate plastic moment-capacity of the joint considering the lack of the ductile yielding plateau.

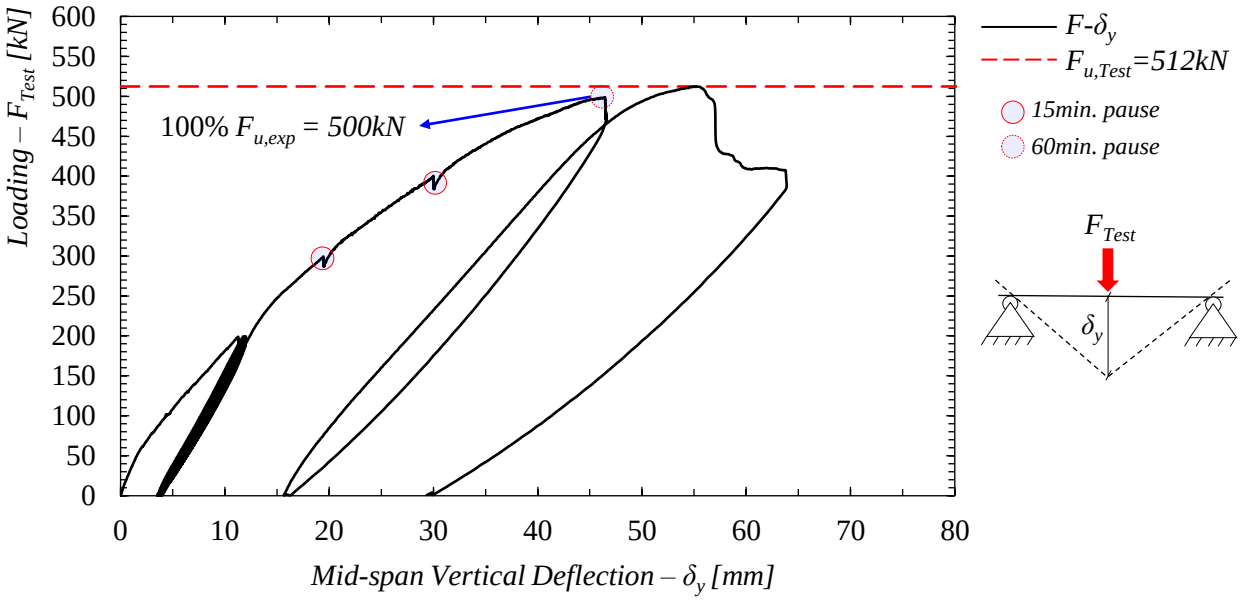

Figure 5.32: Load mid-span deflection behavior of GJSFB-02 test specimen.

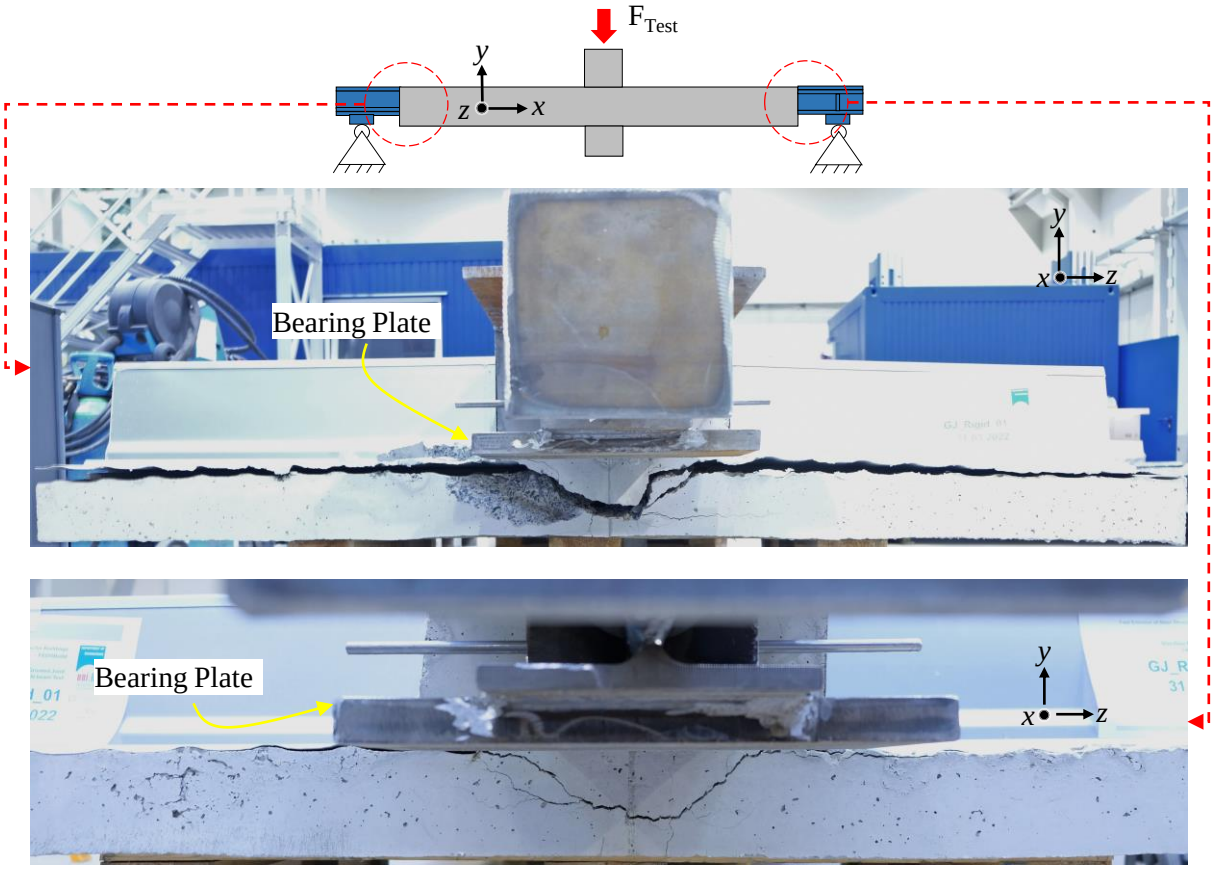

Figure 5.33: Longitudinal shear failure next to the roller supports / GJSFB-02 test specimen.

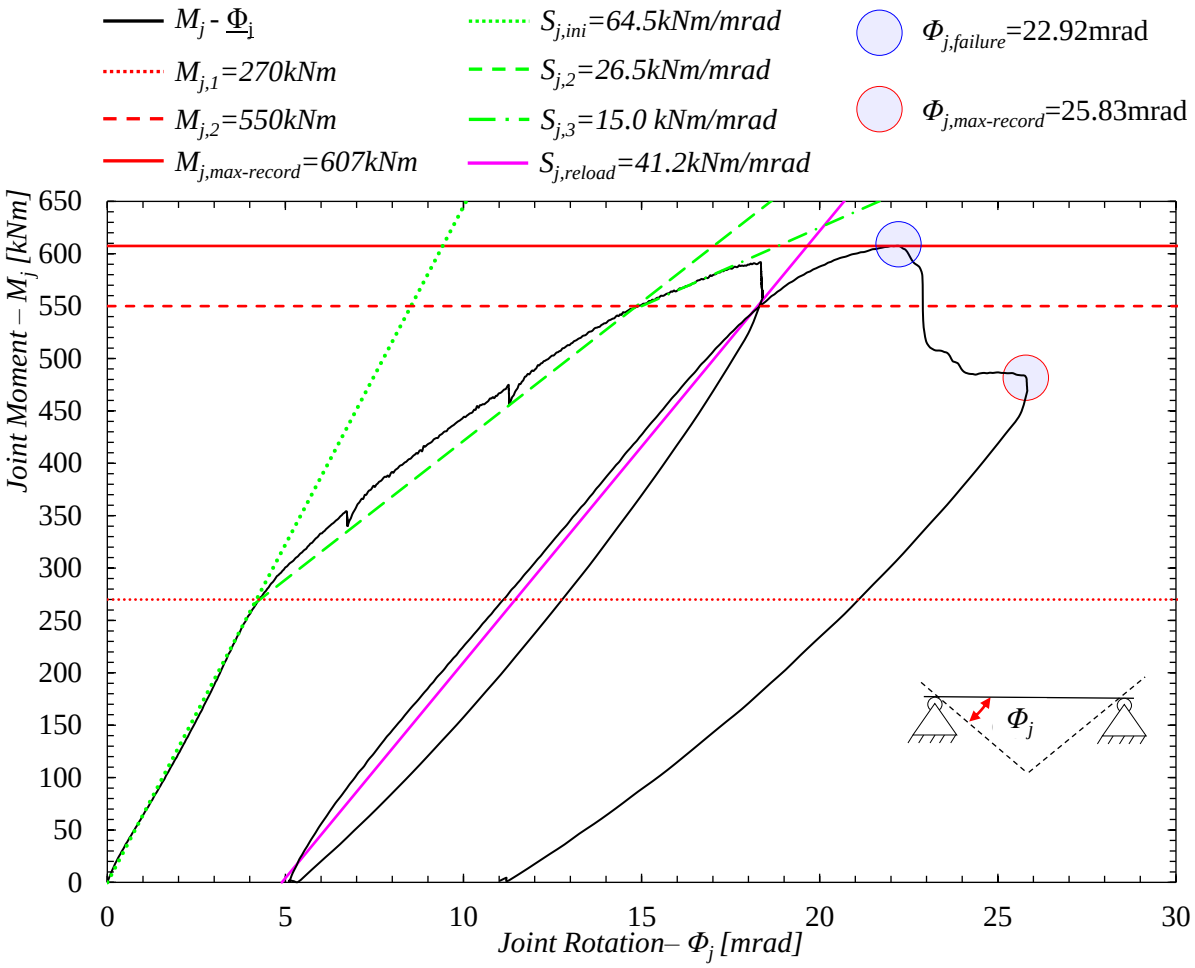

Figure 5.34: Moment-rotation behaviour of GJSFB-02 joint configuration.

Furthermore, according to Fig. 5.34, the initial softening of the moment-rotation behavior could be noticed to start around 270kNm joint moment ($M_{j,1}$=270kNm). This behavior could be attributed to the propagation of the tensile cracks. In addition, around 550kNm joint moment ($M_{j,2}$=550kNm) there were further softening of the moment-rotation behavior having the rotational stiffness of 15kNm/mrad ($S_{j,3}$=15kNm/mrad). The second softening phase of the moment-rotation behavior may indicate the initiation of the yielding for either the M24 threaded-rods, which were positioned to resist the tension stress resultants for GJSFB-02 joint configuration, or the longitudinal steel reinforcements. To clarify the softening phases of GJSFB-02 joint configuration, the tensile cracking status of the continuous slab and the yield status of the longitudinal steel reinforcements and the threaded-rods are investigated in the following paragraphs.

Fig. 5.35 presents the data recorded by the displacement transducers positioned to measure the openings of the tensile cracks, in other words the crack-width for a single crack, with respect to the joint rotations. The critical crack-width (w_c=0.2111mm), which corresponds to the tensile load-bearing limit of the utilized concrete material and is calculated according to fib Model Code

[3] based on the mean values presented in Table 5.2, is also noted in the figure. The formulations for the calculation of the critical crack-width are presented in Annex-C. The unloading period was excluded from the figure for clear visualization. However, the initial load-step and the cycling loading period of the test procedure were included in the figure to accurately assess the crack status of the test specimen. It could be deduced from Fig. 5.35 that the critical crack limit was attained nearly most of the measurement locations during the cycling loading period. Therefore, the moment-rotation behavior presented in Fig. 5.34 should be assessed by considering the fact that the continuous concrete slab was partially cracked at the beginning of the monotonic loading-history. On the other hand, the width of the cracks was relatively small compared to GJSFB-01 test specimen (see Fig. 5.23) for the entire loading history. This difference could be attributed to the higher longitudinal reinforcement ratio and threaded-rods of GJSFB-02 test specimen.

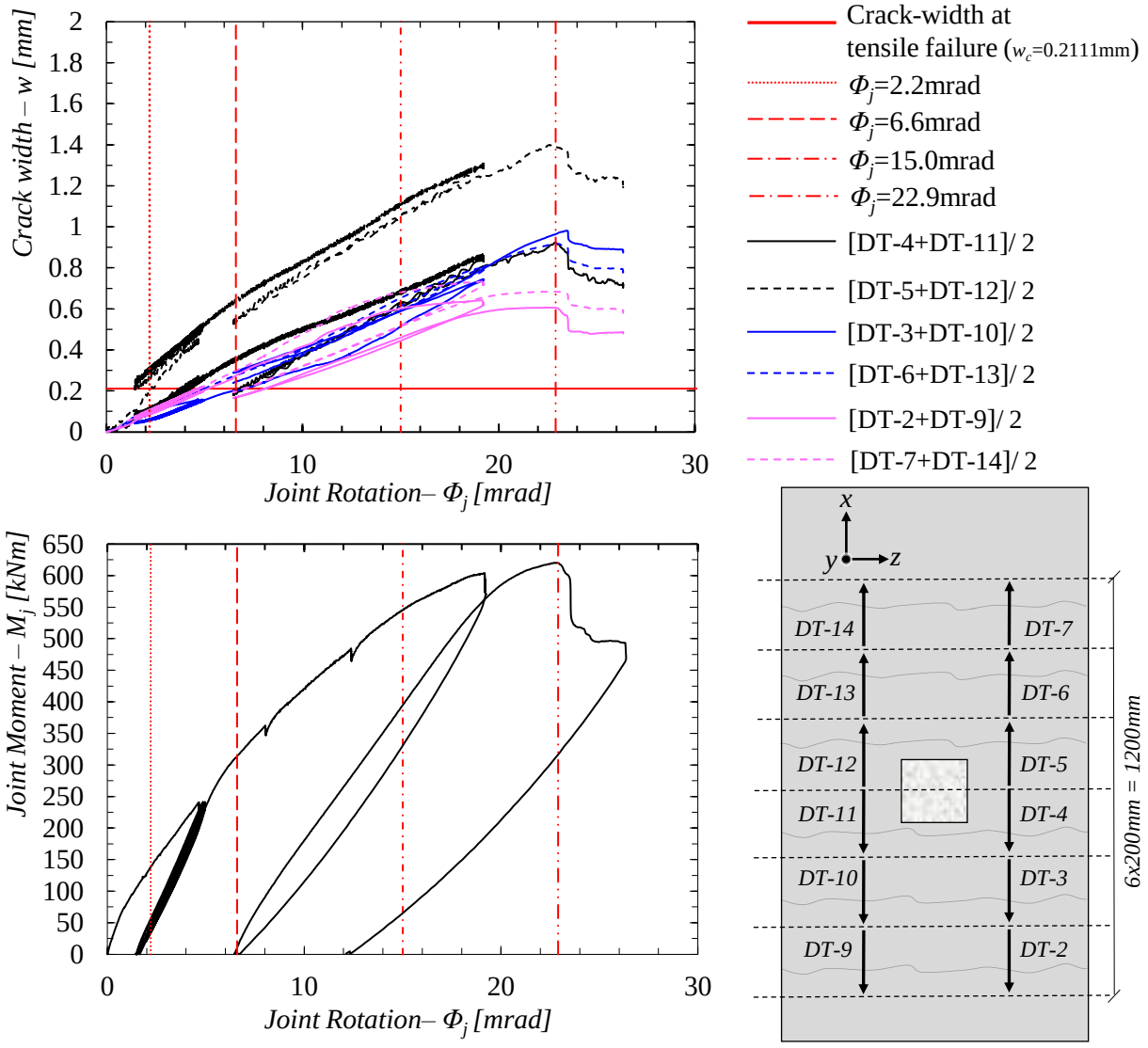

Figure 5.35: Tensile crack formation for GJSFB-02 test specimen.

Additionally, based on Fig. 5.35, around 6.6mrad joint rotation (Φ_j=*6.6mrad*) the mean crack-openings measured by all of the displacement transducers reached the critical crack-width (w_c=*0.2111mm*). Thus, it is concluded that the continuous concrete slab lost its load-bearing capacity against the tension stress resultants developed due to the bending moment actions along the effective length of the joint at 6.6mrad joint rotation. This outcome is also consisted with the moment-rotation characteristics of GJSFB-02 joint configuration as the moment-rotation behavior of the joint started to soften about 6mrad joint rotation which corresponds to 270kNm joint moment (see also Fig. 5.34 - $M_{j,1}$=*270kNm*). Furthermore, it was earlier shown in the previous section that the moment-rotation behavior of GJSFB-01 joint configuration was also softened at 6mrad joint rotation. Considering the fact that the test specimens were produced with same concrete delivery by one truck and they were tested in 7 days time interval, the load-bearing capacity of the continuous slabs for both test specimens would be expected to be similar against the tension stress resultants developed due to the bending moment actions. As a result, it is concluded that the moment-rotation behavior of GJSFB-02 joint configuration was mainly governed by the tensile behavior of the continuous concrete slab until 6.6mrad joint rotation. The further softening of the moment-rotation behavior of GJSFB-02 joint configuration was started about 15mrad joint rotation (Φ_j=*15mrad*). Considering the fact that there was no additional contribution of the continuous concrete slab against to the tensile load-bearing capacity of the joint at this rotation level, the softening at 15mrad joint rotation could be linked to the yielding of the longitudinal steel reinforcements or the M24 threaded-rods at the mid-span. The yield status of the aforementioned components will be investigated in the following paragraphs but before this investigation further information could be deduced from Fig. 5.35 as listed below;

- In contrast to the first test results, there was no sudden increase in the rate of the crack-openings. Therefore, it could be concluded that the entire longitudinal steel reinforcements did not yield for GJSFB-02 test specimen.
- The crack-openings measured between 400mm to 600mm distance from the mid-span along the *x-axis* direction started to stabilize around 15mrad joint rotation. Therefore, it could be deduced that the effective joint length (L_j), which corresponds to the distance between the composite joint and the restrained-end of the longitudinal steel reinforcements subjected to the tensile stress resultants [89], may be estimated to be around 600mm. The effective joint lengths of GJSFB joint configurations are further investigated in Section 5.4.
- The applied loading was equally distributed to the roller-supports based on the presented crack-opening histories with respect to the central symmetry axis of the test set-up.

Fig. 5.36 and Fig. 5.37 show the identified crack-patterns which were highlighted after the test as the magnitude of the crack-openings was less than 1mm for the most of measurement positions as consisted with the data presented in Fig. 5.35.

a) Before the Test

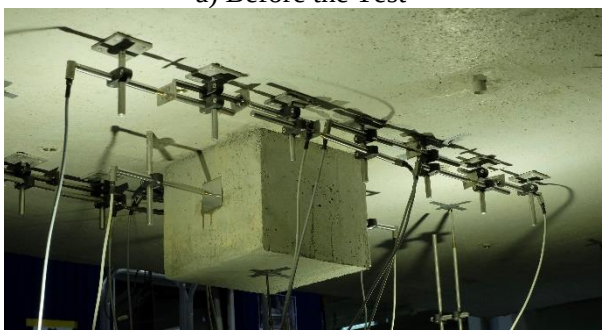

b) At the Ultimate Load

Figure 5.36: Status of the continuous concrete slab next to the mid-span / GJSFB-02.

Condition of the concrete slab before drawing the crack pattern identification lines

Dashed lines were drawn after the test for the identification of the crack patterns

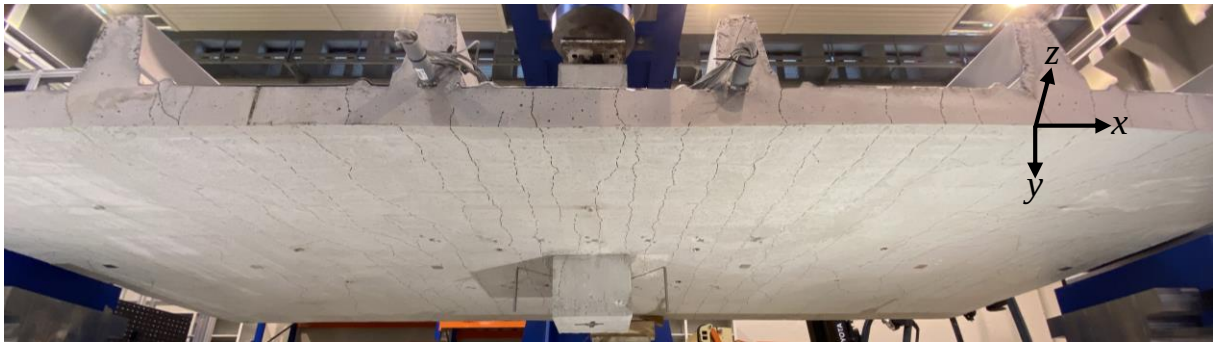

Figure 5.37: Crack patterns along the continuous slab / GJSFB-02.

Fig. 5.38 presents the strain and the corresponding stress resultants for the instrumented longitudinal steel reinforcements of GSJFB-02 test specimen to investigate their yield status. The resultant forces are presented based on the strain data recorded at the mid-span and they were calculated with Eq. 5.3 using the nominal cross-section area (*Ø=16mm*), the mean elastic modulus (E_m), the mean yield strength ($f_{y,m}$) and the corresponding strain ($\varepsilon_{y,m}$), the mean ultimate strength ($f_{u,m}$) and the corresponding strain ($\varepsilon_{u,m}$) of the longitudinal steel reinforcements presented in Table 5.3. The unloading period was excluded from the figure.

According to Fig. 5.38, all of the instrumented longitudinal steel reinforcement were yielded about 15mrad joint rotation which corresponds to 550kNm joint moment (see Fig. 5.34 - $M_{j,2}$*=550kNm*). Therefore, the plastic-hinge formation of GJSFB-02 joint configuration could be accepted to start at 15mrad joint rotation. This instant also very well matches with the softening of the moment-rotation behavior with rotational stiffness of 15kNm/mrad (see Fig. 5.34 - $S_{j,3}$*=15kNm/mrad*). On the other hand, as presented earlier in Fig. 5.35, there was no sudden increase in the rate of the crack-openings during the entire loading-history and it is obvious from Fig. 5.34 that the full plastic-hinge formation of the joint did not develop at the sudden load-drop before the termination of the test. Therefore, it is concluded that although the non-instrumented reinforcements started to successively yield between 15mrad to 22.9mrad joint rotations, they were not fully yielded during the test. Consequently, assuming that the test specimen did not fail due to the longitudinal shear failure between the concrete slab and the steel beams, either the crushing of the concrete grout or the failure of the M30 threaded-rods positioned to resist the compressive stress-resultants at the mid-span might cause the sudden failure of the test specimen and limits the bending moment-capacity and the rotation-capacity of GJSFB-02 joint configuration.

Fig. 5.39 presents the strain data and the corresponding stress resultants for the threaded-rods to investigate their yield status. The resultant forces were calculated with Eq. 5.3 based on the nominal cross-section areas (*Ø=24mm, Ø=30mm*) of the threaded rods and the mean values presented in Table 5.3. The upside-down orientation of the threaded-rods should be considered while investigating the presented data as the test specimen was turned 180°around the longitudinal axis of the beams (see Fig. 5.8). The compressive stress resultants are shown with negative values as consisted with the strain data. The strain-gauge nominated as M30-1 was damaged at the beginning of the test; thus, no output shown for this strain-gauge. The unloading period was also excluded from the figure.

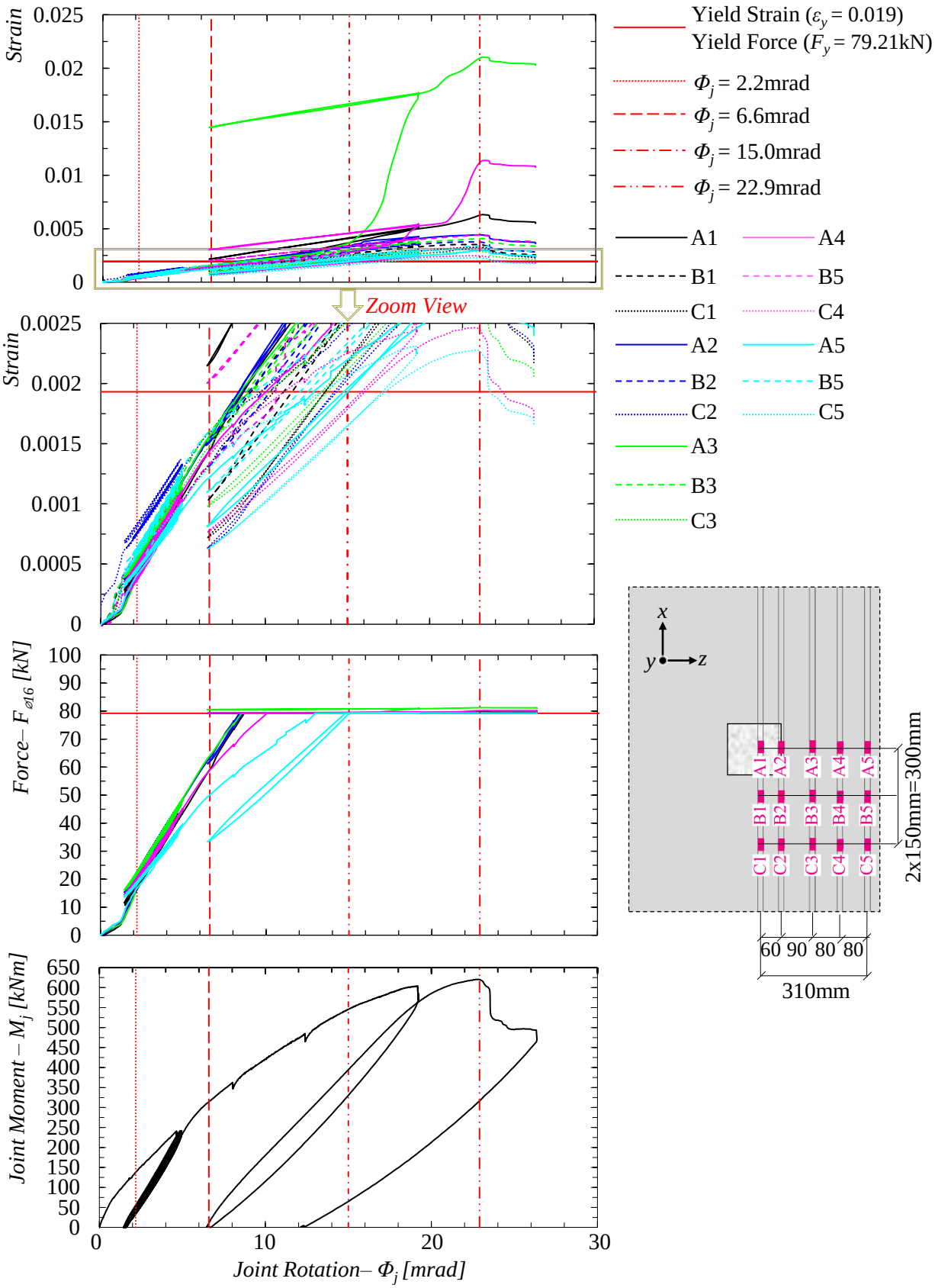

Figure 5.38: Yield status of the longitudinal steel reinforcements / GJSFB-02 test specimen.

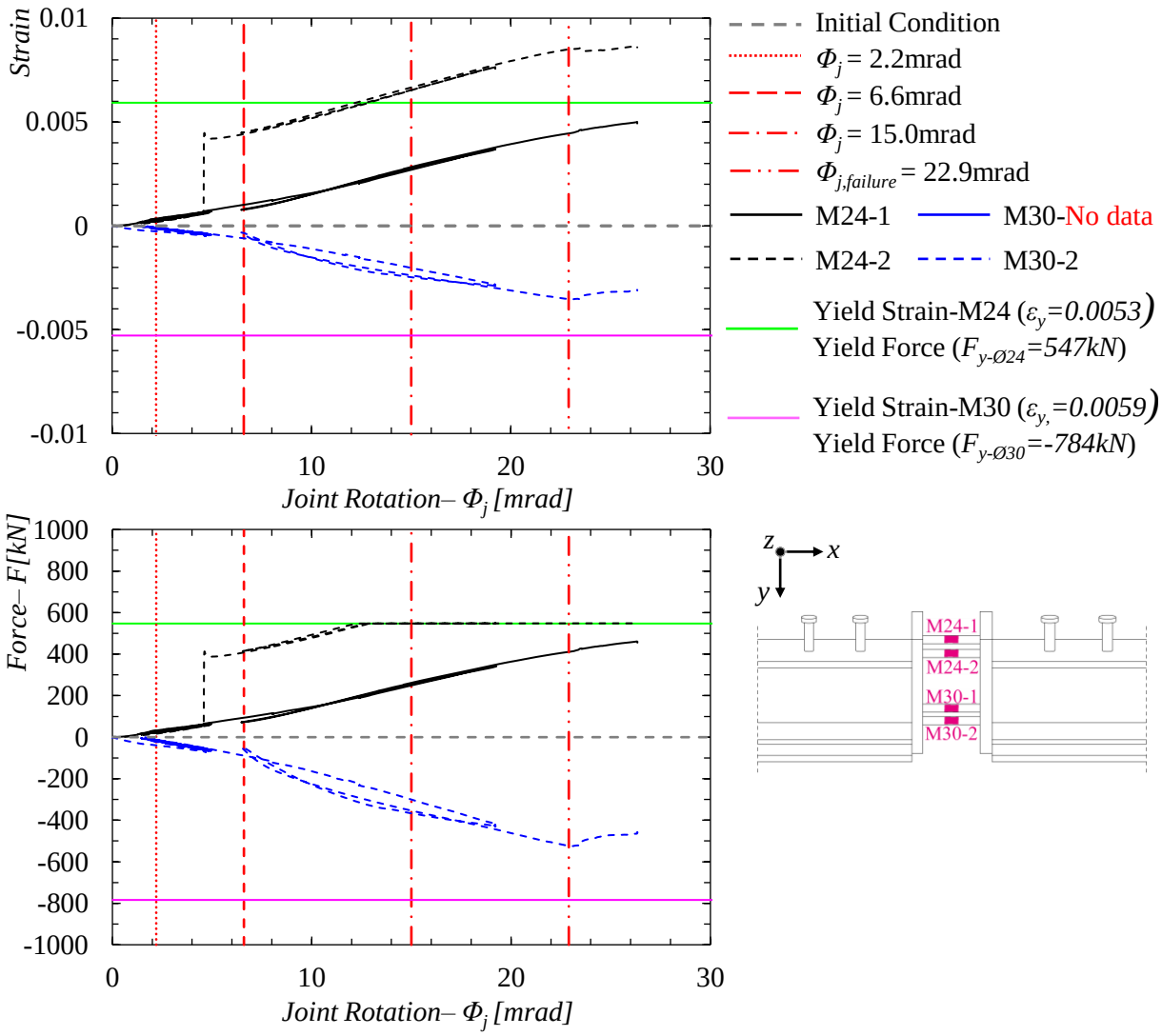

Figure 5.39: Yield status of the threaded-rods / GJSFB-02 test specimen.

According to the Fig. 5.39, it is concluded that the threaded-rods was activated against the bending moments developed in the joint. Furthermore, it could be noticed that the load bearing capacity of the M24 threaded-rods was nearly fully utilized as one of them was yielded and the other one was resisting the force by 75% ($F_{Ø,24\text{-}2}$=431kN) of its yield capacity at the joint rotation that corresponds to the failure instant ($\Phi_{j,failure}$=22.9mrad). No indication was identified for the moment-rotation behaviour of GJSFB-02 joint configuration at the sudden increase of the strain recorded on the second M24 threaded-rod (M24-2). Based on the available data from one of the M30 threaded-rods, it is also concluded that the proposed joint configuration with nuts positioned between the beam end plates (see Fig. 5.12) was effective against the compressive stress resultants developed due to the bending moments in the joint. These outcomes prove the effectiveness of the proposed GJSFB joint for continuous composite slim-floor beams. Furthermore, it could be concluded that the failure of the test specimen was not due to the joint failure as the second M30

thread-rod (M30-2) was resisting the force by 67% ($F_{Ø,30\text{-}2}$=*524kN*) of its yield capacity at the joint rotation that corresponds to the failure instant ($\Phi_{j,failure}$=*22.9mrad*). The one could indicate that the sudden failure might be also propagated by the crushing of the concrete grout under the compressive stress resultants in the joint. On the other hand, if this would be the case a sudden increase in the strain data would be expected for the data recorded by M30-2 strain-gauge. For further clarification of the reason behind the sudden failure of the test specimen the status of the concrete grout was investigated after the test by removing a part of the metal sheeting at the mid-span of the test specimen as shown in Fig. 5.40. Based on the visual inspection there was no sign of compressive crushing of the concrete grout at the mid-span. Therefore, it is concluded that GJSFB-02 test specimen was failed due to the longitudinal shear failure between the steel beam and the concrete slab (see Fig. 5.33). As a result, the ultimate moment-capacity recorded during the test (see Fig. 5.34 - $M_{j,max\text{-}record}$=*607kNm*) should be carefully evaluated as GJSFB-02 joint configuration might have further moment-capacity considering the facts that not all of the longitudinal steel reinforcements were yielded based on the magnitude and the rate of the crack-openings (see Fig. 5.35), and the threaded-rods in the joint were not 100% utilized based on their yield status (see Fig. 5.39). Accordingly, it is also concluded that the joint rotation measured at the failure instant of the test specimen ($\Phi_{j,failure}$=*22.9mrad*) does not also correspond to the ultimate rotation capacity of GJSFB-02 joint configuration.

On the contrary, it was earlier indicated that the ultimate test load was only 2% higher than the expected test capacity, and it was shown that all of the instrumented longitudinal steel reinforcements were yielded at 550kNm joint moment where the moment-rotation behavior of the joint was softened having relatively low rotational stiffness of 15kNm/mrad. Therefore, it might be expected that the plastic moment-capacity of GJSFB-02 joint configuration not to be much higher than the maximum joint moment recorded during the test ($M_{j,max\text{-}record}$=*607kNm*). Nevertheless, it was not possible to measure the plastic moment and the rotation capacities of GJSFB-02 joint configuration with the experimental test due to the longitudinal shear failure of the test specimen. Therefore, a numerical simulation of the experimental test was performed by manipulating transverse shear reinforcement ratio of the test specimen to estimate the plastic moment and rotation capacities of GJSFB-02 joint configuration by postponing the longitudinal shear failure. The corresponding numerical simulation is presented in Section 5.3.

To further investigate the effectiveness of the threaded-rods, Fig. 5.41 compares the total force resisted by the longitudinal steel reinforcements positioned near to the joint and the M24 threaded-rods. It is crucial note that the strain data from the reinforcements were collected only from the symmetric half of the test specimen; thus, for fair comparison, the force data for the longitudinal steel reinforcement presented in Fig. 5.38 was multiplied with factor of two considering the symmetry of the test set-up and the loading. Consequently, the comparison should be only considered as informative result to assess the effectiveness of GJSFB-02 joint configuration. According to Fig. 5.38, it could be noticed that the M24 threaded-rods were as effective as the longitudinal steel reinforcements to resist the tension stress resultants at the mid-span.

a) Test Specimen after the Test / Front View

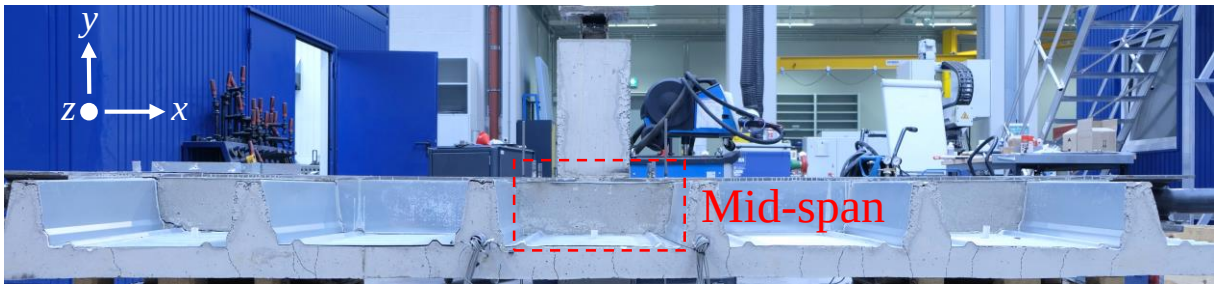

b) Status of the Concrete Grout at Mid-span / Front View

Dashed lines were drawn after the test for the identification of crack patterns

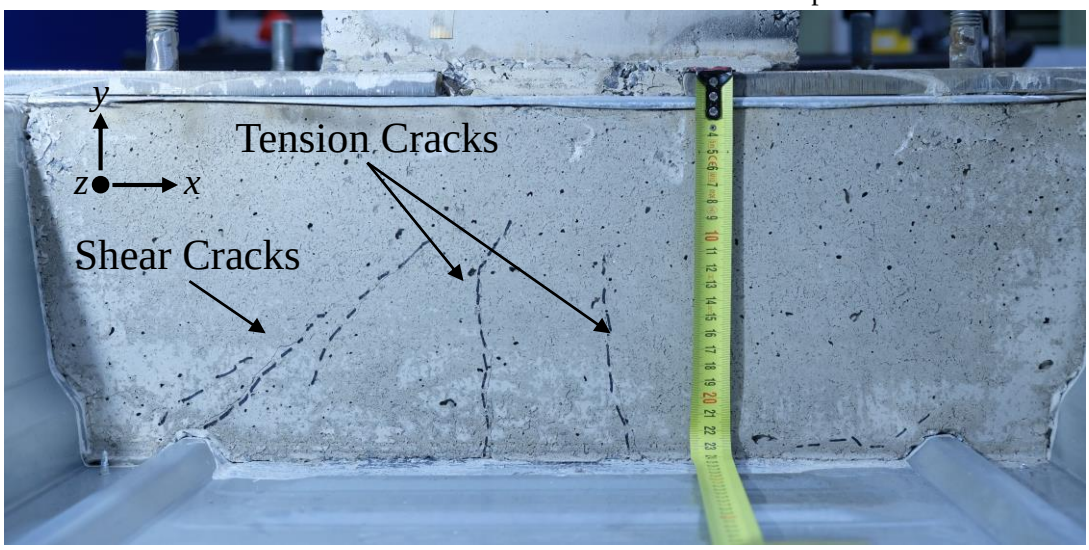

c) Status of the Concrete Grout at Mid-span / Back View

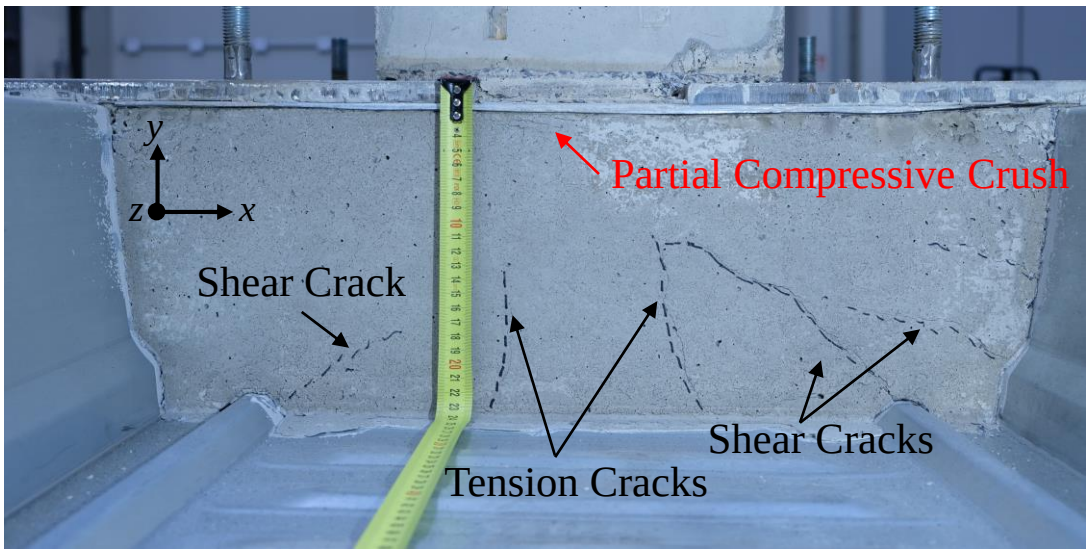

Figure 5.40: Status of the concrete grout at the mid-span of GJSFB-02 test specimen.

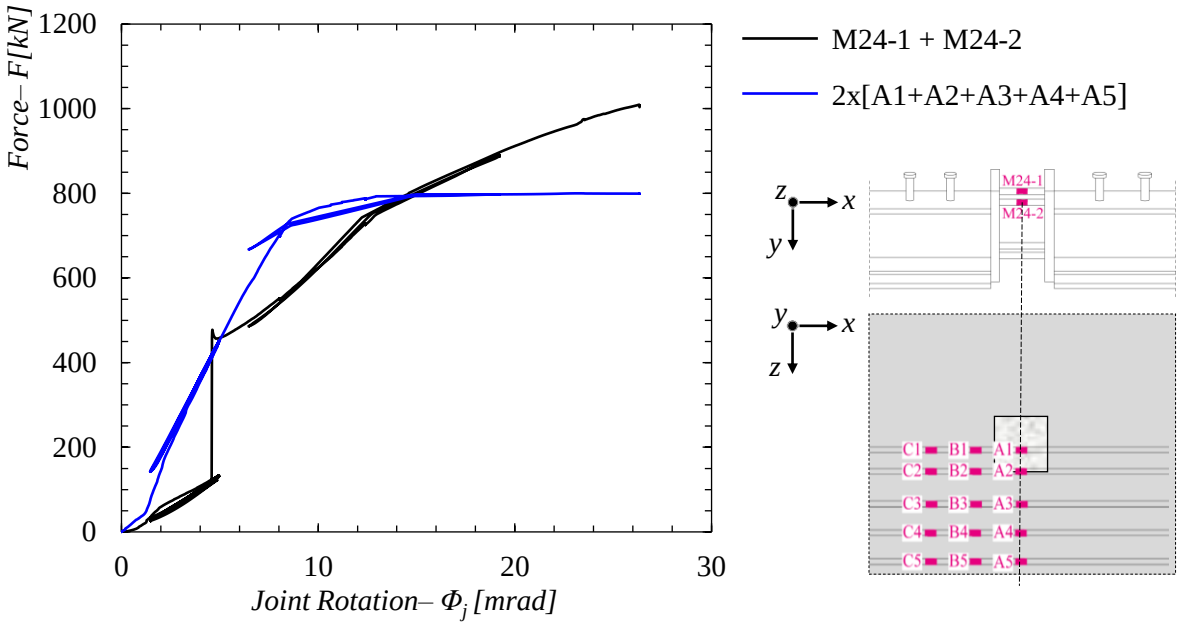

Figure 5.41: Comparison of the total tensile force resisted by the M24 threaded-rods and the longitudinal steel reinforcements.

Fig. 5.42 presents the yield status of the steel beams with respect to the joint rotations. The yield strains of the flanges ($\varepsilon_{y,f}$) and the web ($\varepsilon_{y,w}$) were calculated based on the yield strengths and the elastic modules of the related components presented in Table 5.3. It is important to note that the upside-down orientation of the beams should be considered while investigating the strain data as the test specimen was turned 180° around the longitudinal axis of the beams (see Fig. 5.8). According to the presented strain data, it is concluded that the steel beams were deformed mostly in their elastic range during the test. Only the upper flange of the beam positioned at the right side of the mid-span was yielded after attaining the ultimate test load. Therefore, it is concluded that the deformations of the steel beams did not significantly affect the moment-rotation behavior of GJSFB-02 joint configuration. In addition, based on the presented strain data of the steel beams it is also concluded that the applied loading was uniformly distributed between the roller supports.

The relative end-slip between the steel beams and the concrete encasement was also recorded during the test. Fig. 5.43 presents the slip with respect to the joint rotations. The negative values of the end-slip indicate divergence of the steel-beam and the concrete encasement. Very small end-slip was observed to be less than 0.3mm for both sides of the test specimen. Therefore, it is concluded that the concrete encasement around the steel beams was also resisting the bending moment actions along the entire span-length. It is crucial to mention that the presented slips do not correspond to the relative end-slip between the concrete slab and the steel beams.

Fig. 5.44 shows the final deformed shape of the test specimen, together with the deformation profiles of the test specimens at 33%, 67% and 100% of the ultimate test load ($F_{u,Test=512kN}$).

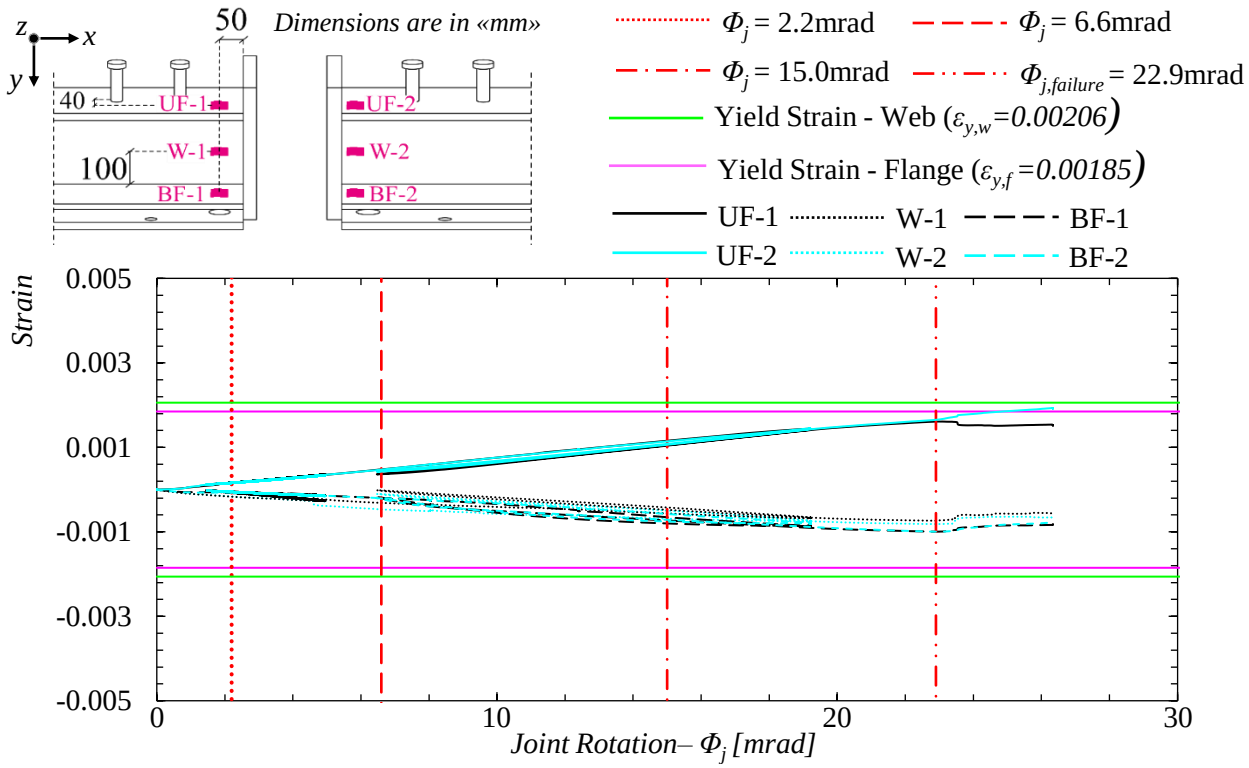

Figure 5.42: Yield status of the steel beams / GJSFB-02 test specimen.

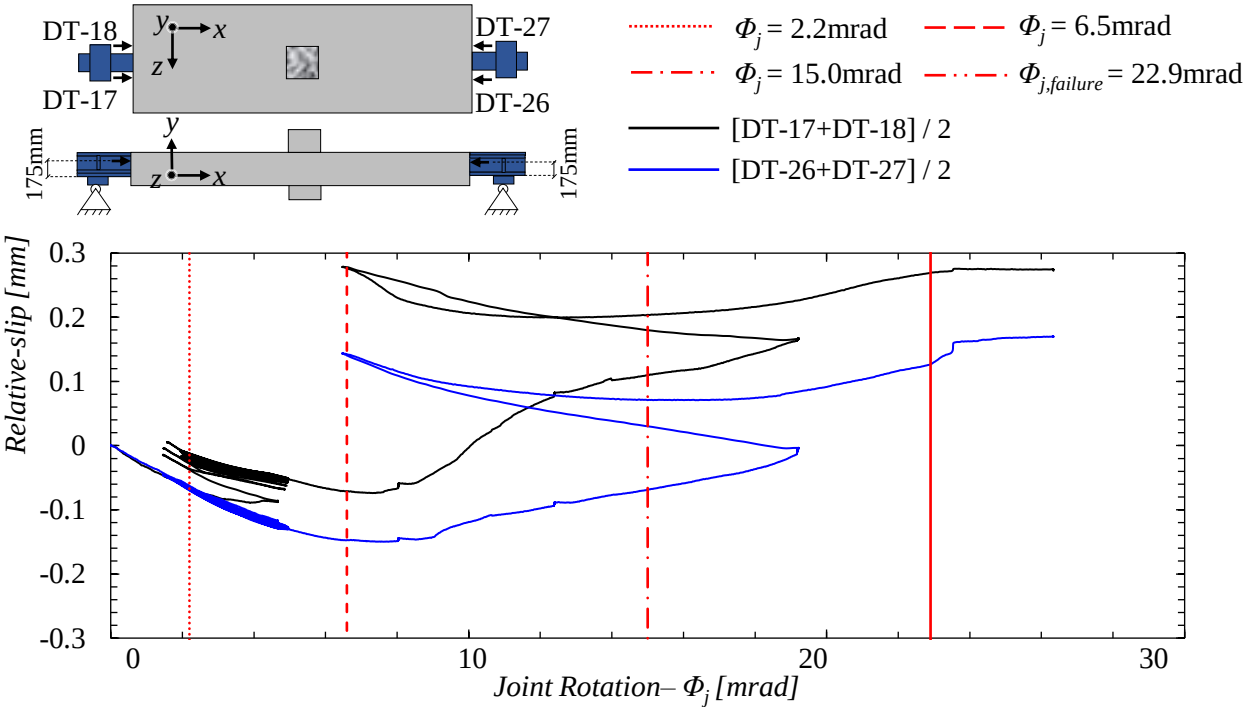

Figure 5.43: End-slip between the steel beams and concrete encasement/ GJSFB-02 test specimen.

Having investigated the all of the test data and clarified the reason behind the sudden failure of GJSFB-02 test specimen, Table 5.5 summarizes the identified test results presented in this section.

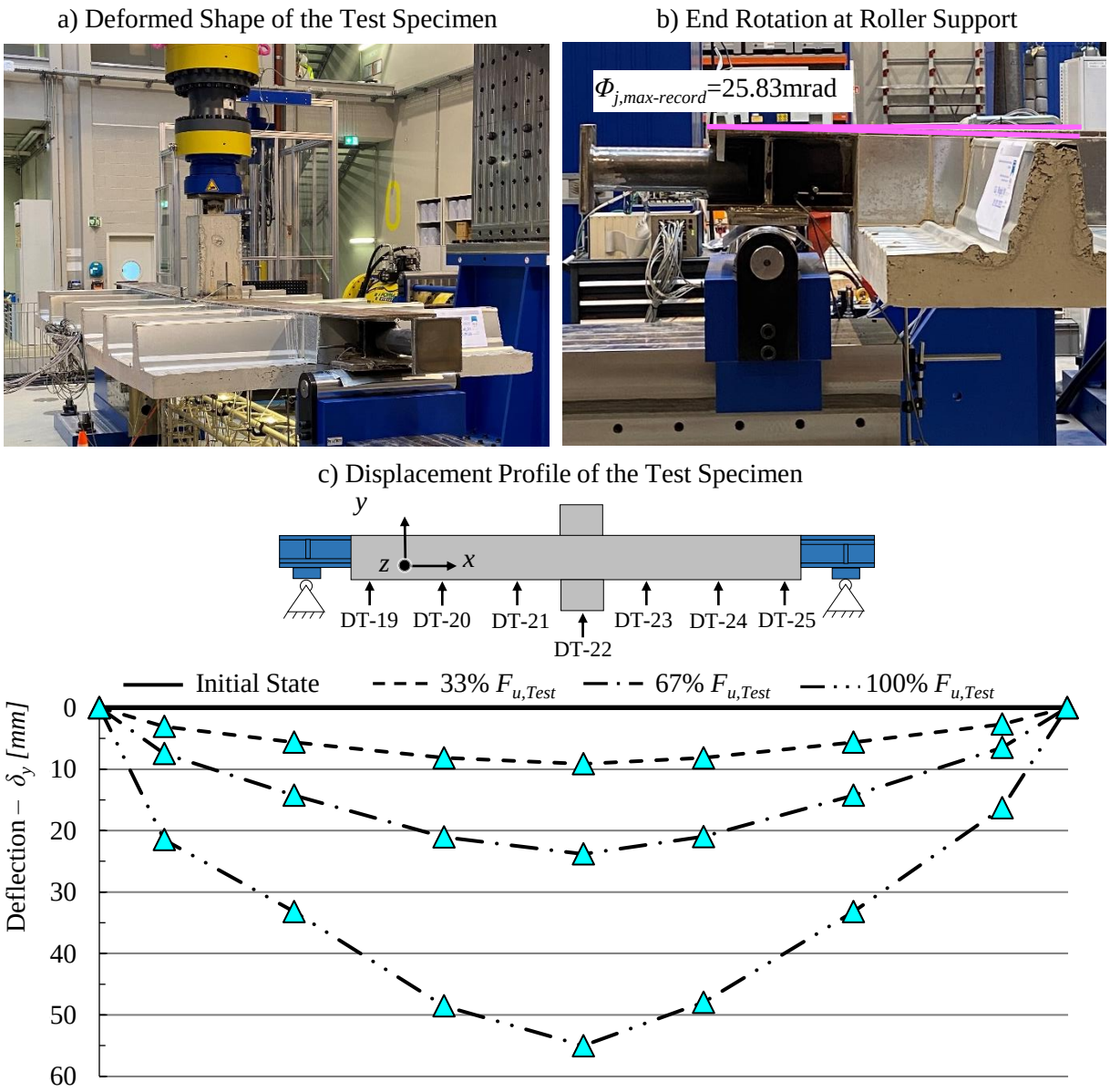

Figure 5.44: Deflection profiles of GJSFB-02 test specimen.

Table 5.5: Summary of GJSFB-02 test results.

Test ID	$F_{u,Test}$ [kN]	$\delta_{y,at\ F_{u,Test}}$ [mm]	$M_{j,max\text{-}record}$ [kNm]	$\Phi_{j,failure}$ [mrad]	$\Phi_{j,max\text{-}record}$ [mrad]	$S_{j,ini}$ $[\frac{kNm}{mrad}]$	$S_{j\,2}$ $[\frac{kNm}{mrad}]$	$S_{j,3}$ $[\frac{kNm}{mrad}]$
GJSFB-02	512	54.64	607	22.92	25.83	64.5	26.5	15.0

5.2.5.3 Comparison of the test results and the classification of GJSFB joint configurations according to EN1994-1-1

As it was earlier indicated that the purpose of the experimental tests was to define possible upper and lower boundaries for the moment-rotation behavior of GJSFB joint configurations to be used for the composite joints of regular continuous composite slim-floor beams. In this context, although the diameter and the ratio of the longitudinal steel reinforcements were different for the experimental tests, Fig. 5.45 compares the moment-rotation curves of GJSFB-01 and GJSFB-02 joint configurations including and excluding the cycling loading periods.

It could be noticed from Fig. 5.45a that the initial rotational stiffness for both joint configurations was nearly identical if the cycling loading periods were included in the comparison. On the other hand, in Fig. 5.45b the initial rotational stiffness of GJSFB-02 joint configuration could be noticed to be lower than the GJSFB-01 joint configuration when the cycling loading periods are excluded. The reason behind this difference was due to the fact that the continuous concrete slab for the experimental test of GJSFB-02 joint configuration was partially cracked during the cycling loading period (see Fig. 5.35). Consequently, the initial rotational stiffness of GJSFB-02 joint configuration presented in Table 5.5 was lower than the initial rotational stiffness of GJSFB-01 joint configuration presented in Table 5.4. Furthermore, the rotational stiffness values determined after the initial softening of the moment-rotation behavior without the consideration of the cycling loading periods presented in Table 5.4 and Table 5.5 for GJSFB-01 ($S_{j,2}$=*29.7*) and GJSFB-02 ($S_{j,2}$=*26.5*) joint configurations could also be noticed to be close to each others. As a result, it could be concluded that the rotational stiffness of the joints was also identical after the full cracking of the continuous concrete slab along the effective lengths of the joints. This outcome also supports the partial cracking condition of the continuous concrete slab during the cycling loading period of the experimental test performed for GJSFB-02 joint configuration. Consequently, the initial rotational stiffness of GJSFB-02 joint configuration presented in Table 5.5 reflects the moment-rotation characteristic of GJSFB joint configurations for partially cracked concrete conditions of the continuous concrete slab. Accordingly, it becomes necessary to identify the moment-rotation characteristics of GJSFB joint configurations based on the cracking condition of the continuous concrete slab and the yield status of the longitudinal steel reinforcements.

Table 5.6 presents the moment-rotation characteristics of tested GJSFB joint configurations based on the cracking condition of the continuous concrete slab. According to the presented results, it could be concluded that the moment-rotation characteristics of GJSFB joint configurations are independent from the ratio of the longitudinal steel reinforcements and the existence of the threaded rods for uncracked and cracked concrete conditions. However, it is the fact that the joint moments that corresponds to the fully cracked concrete condition of continuous concrete slab for GJSFB-02 joint configuration (see Fig. 5.34 - $M_{j,1}$=*270kNm*) 135% higher compared to the GJSFB-01 joint configuration (see Fig. 5.22 $M_{j,1}$=*115kNm*). This outcome was due to the higher longitudinal reinforcement ratio and the existence of the threaded-rods for GJSFB-02 joint configuration.

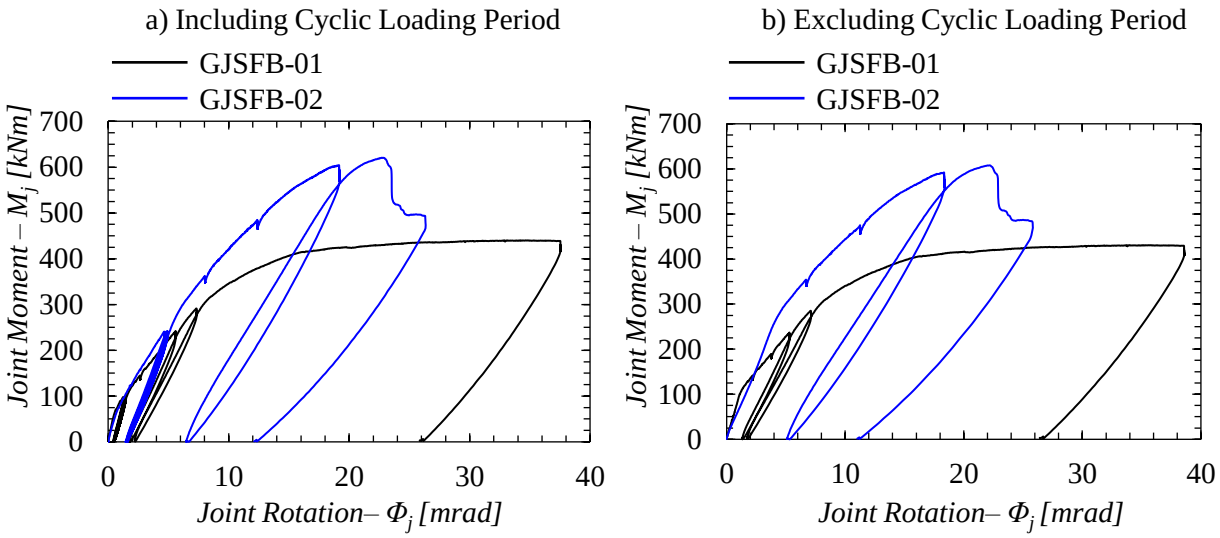

Figure 5.45: Comparison of the moment-rotation behaviors of the tested GJSFB joint configurations.

As it could be deduced from Table 5.6 that there are many parameters affecting the determination of the initial rotational stiffness of composite joints such as the cracking condition of continuous concrete slab and the loading-history. Therefore, according to EN1994-1-1 [2] the initial rotational stiffness of composite joints for elastic global analysis could be defined based on the design plastic moment capacity of the joints and the design moment actions in the joints. Fig. 5.46 presents the definition of the initial rotational stiffness of composite joints according to the provisions of EN1994-1-1 [2]. Analogically, the initial rotational stiffness of GJSFB joint configurations could be defined based on Fig. 5.46 considering the maximum joint moments recorded during the experimental tests as shown in Fig. 5.47. However, it is crucial to note that the maximum joint moment and corresponding joint rotation for GJSFB-02 joint configuration (see Fig. 5.34 - $M_{j,max\text{-}record}$=*607kNm and* $\Phi_{j,failure}$=*22.92kNm*) may not correspond to the plastic moment-capacity and plastic joint rotation as

Table 5.6: Comparison of the initial rotational stiffness values for the GJSFB joint configurations based on the moment-rotation curves obtained from the experimental tests.

Test ID	$S_{j,ini,uncracked}$[1] $[\frac{kNm}{mrad}]$	$S_{j,ini,partial\text{-}cracked}$[2] $[\frac{kNm}{mrad}]$	$S_{j,ini,cracked}$[3] $[\frac{kNm}{mrad}]$
GJSFB-01	106.7	83.3	29.7
GJSFB-02	106.7	62.7	26.5

[1] The magnitude of the initial rotational-stiffness for uncracked concrete conditions was determined based on the moment-rotation curves including the cyclic loading periods presented in Fig. 5.45a.

[2] The magnitude of the initial rotational-stiffness for partially cracked concrete conditions was determined based on the moment-rotation curves excluding the cyclic loading periods presented in Fig. 5.45b.

[3] The magnitude of the initial rotational-stiffness for cracked concrete conditions was determined based on the initial softening phase of the moment-rotation curves including the cyclic loading periods presented in Fig. 5.45a.

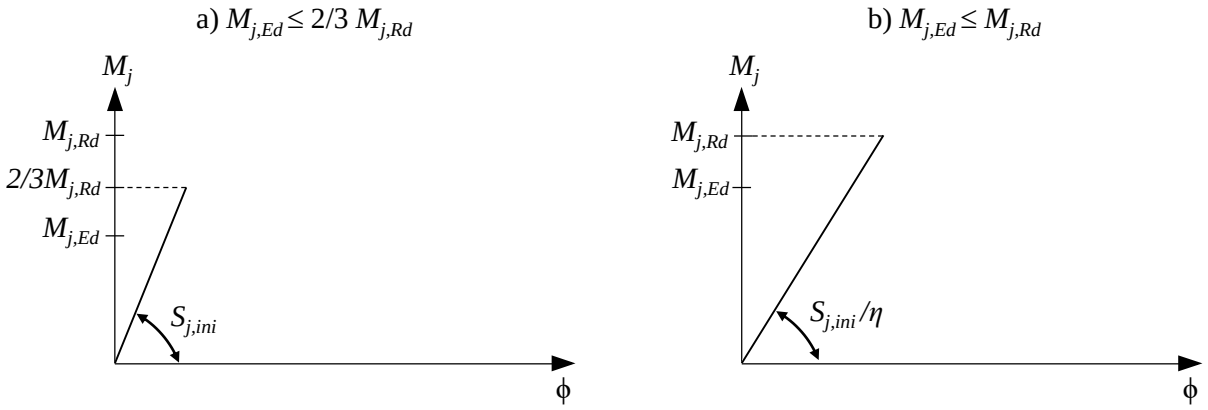

Figure 5.46: Rotational stiffness to be used in elastic global analysis based on EN1994-1-1 [2].

the test specimen was failed due to the longitudinal shear failure between the concrete slab and the steel beams before the yielding of the entire longitudinal steel reinforcements and one of the M24 threaded-rods. Therefore, the stiffness values presented in Fig. 5.47 should be only considered as informative. The actual plastic moment-capacity and the corresponding joint rotation for GJSFB-02 joint configuration later estimated with computer aided finite element analysis (FEA) in Section 5.3 and the results presented in Fig. 5.47 modified in the corresponding section. Nevertheless, considering the fact that the estimated load-bearing capacity of GJSFB-02 joint configuration was only 2% less than the ultimate test load, Fig. 5.47 could be further used to compare the moment-rotation characteristics of GJSFB joint configurations and to classify them with respect to EN1994-1-1 [2].

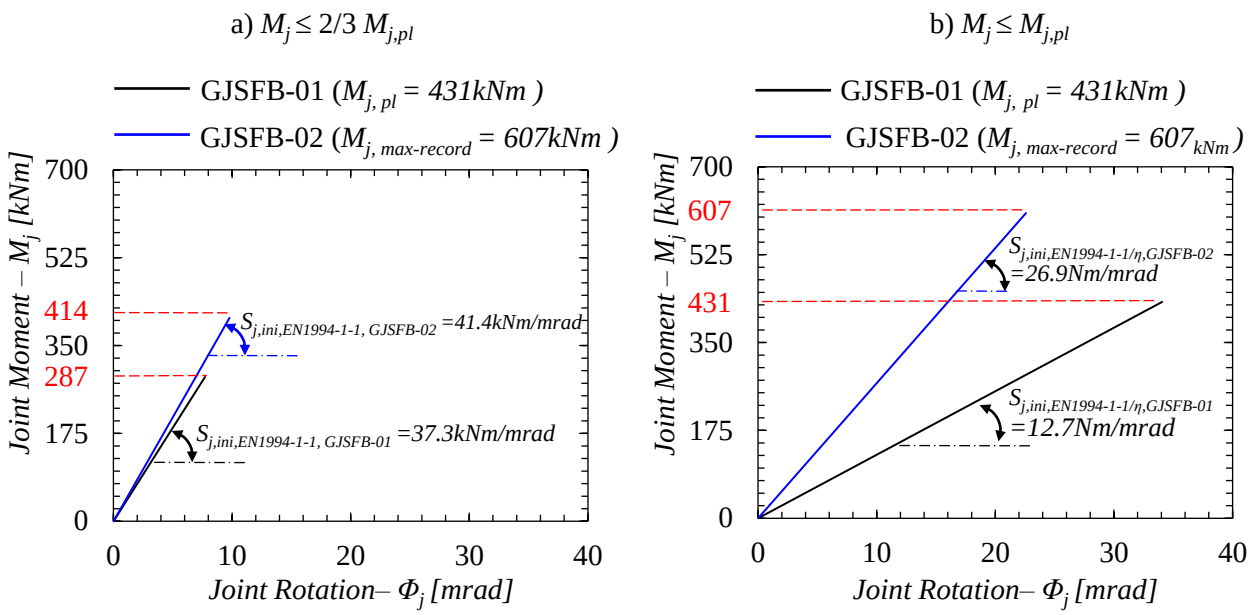

Figure 5.47: Rotational stiffness of the tested GJSFB joint configurations for elastic global analysis of continuous composite slim-floor beams.

Table 5.7 compares the initial ($S_{j,ini,EN1994\text{-}1\text{-}1}$) and the secant rotational stiffness values ($S_{j,ini,EN1994\text{-}1\text{-}1/\eta}$) presented in Fig. 5.47 and defines the stiffness modification factor (η) for the GJSFB joint configurations. Based on the magnitude of the stiffness modification factos, GJSFB-01 and GJSFB-02 joint configurations could be identified as beam-to-beam and beam-to-column joints according to the stiffness modification factors presented in EN1993-1-8 [25].

Having defined the initial elastic stiffness ($S_{j,ini}$) of the tested GJSFB joint configurations, their classification could be performed based on the classification boundaries presented in Fig. 5.5. It is important to note that the classification of the joints were performed based on the test results; therefore, the classification boundaries were determined based on the mean material properties presented in Section 5.2.3.

Fig. 5.48 presents the classification of GJSFB joint configurations according to EN1994-1-1 [2] and based on the tested composite slim-floor beams. The span length of the beams (L_b) was considered to be equal to 16m as consisted with the experimental test set-up which corresponds to the hogging zone of 16m equal length double span continuous composite slim-floor beam. The flexural stiffness of the tested composite slim-floor beam (EI_b) was calculated with well known modular ratio method [104] using the cross-section of the test specimens (see Fig. 5.11) for uncracked concrete condition and by excluding the metal sheeting. The plastic moment-capacity of the tested composite slim-floor beams were calculated with strain limited design concept [71]. The concrete encasement of the steel beams were included for the calculations of the plastic moment-capacity of the beams as small relative end-slips were recorded between the steel beams and the concrete encasement during the experimental tests (see Fig. 5.30 and Fig. 5.43).

According to Fig. 5.48, both of GJSFB-01 and GJSFB-02 joint configurations are classified as semi-rigid and partial-strength joints for the tested composite slim-floor beams. Although, both of the joint configurations were classified as semi-rigid and partial strength joint these classifications depend on the rotational stiffness and the plastic moment capacity of the connected beams where the proposed joint configurations are used to create continuity over an internal support. Consequently, it is crucial note that the proposed joint configurations might be classified differently if they are applied in different slim-floor beams.

Table 5.7: Comparison of the initial and the secant stiffness of the tested GJSFB joint configurations determined according to EN1994-1-1 [2].

Test ID	$S_{j,ini,EN1994\text{-}1\text{-}1}$ $[\frac{kNm}{mrad}]$	$S_{j,ini,EN1994\text{-}1\text{-}1/\eta}$ $[\frac{kNm}{mrad}]$	η
GJSFB-01	37.3	12.7	2.94
GJSFB-02	41.4	26.9	1.54
Ratio	0.9	0.47	1.91

a) Classification of GJSFB-01 Joint Configuration

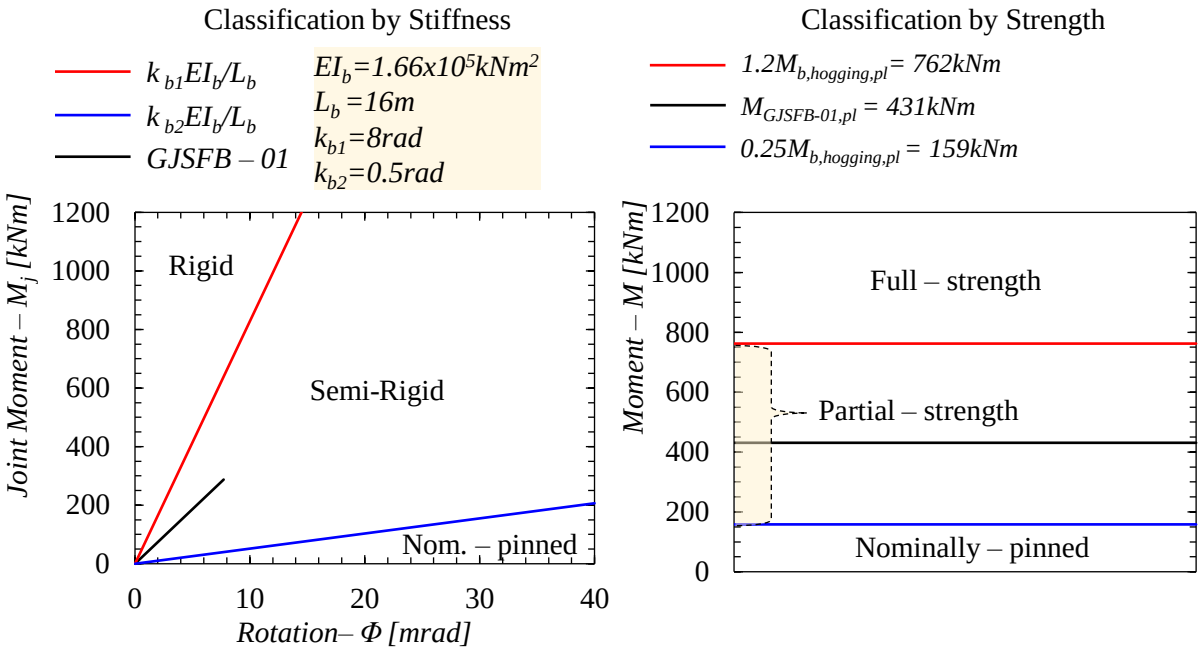

b) Classification of GJSFB-02 Joint Configuration

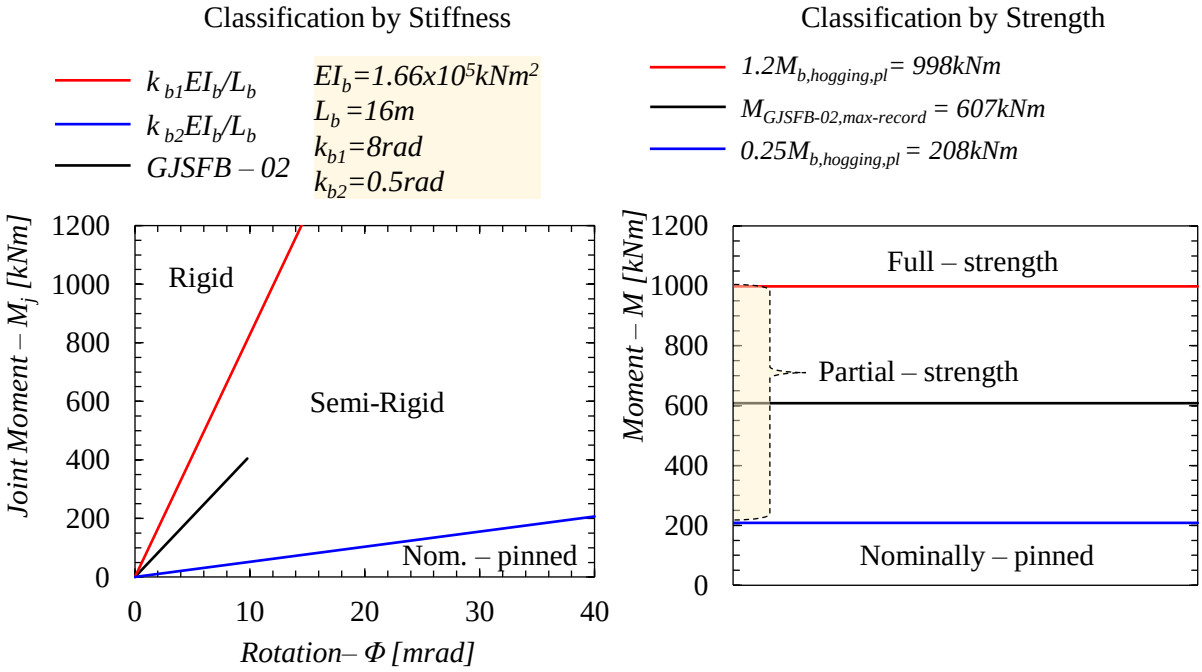

Figure 5.48: Classification of the tested GJSFB joint configurations according to EN1994-1-1 [2]

.

5.3 FEA Simulations

The moment-rotation behaviors of tested GJSFB joint configurations are presented in Section 5.2 based on two full-scale experimental tests. On the other hand, it was not possible to determine the ultimate plastic rotation capacity of GJSFB joint configurations as the first test was deliberately terminated due to the excessive deflection of the test specimen and the second test specimen was failed due to the longitudinal shear failure between the concrete slab and the steel beam. Furthermore, the diameter and the ratio of the longitudinal steel reinforcements were different for the test specimens. Consequently, although the possible upper and lower boundaries were established for the moment-rotation behavior of GJSFB (see Fig. 5.45), it was not possible to identify the contribution of the threaded-rods to GJSFB joint configuration against the hogging bending moments over the internal support of the continuous composite slim-floor beams. Therefore, the experimental tests were simulated by means of FEAs to predict the ultimate rotation capacities of the tested GJSFB joint configurations, to perform parametric analyses and to create basis for the analytical models to estimate the ultimate load-bearing and rotation capacities of GJSFB joint configurations.

The quarter-symmetric geometries of the test specimens were modelled using symmetric boundary boundary conditions (BCs) in a commercial FEA software, Abaqus [66]. Fig. 5.49 and Fig 5.50 show the FE-model geometry, BCs, FE-types and FE-discretization of the model components for GJSFB-01 and GJSFB-02 test specimens, respectively. As consisted with the experimental test of GJSFB-01 joint configuration, the threaded-rods were omitted for the corresponding FE-model. The threaded-rods of GJSFB-02 joint configuration included in the corresponding FE-model but the threaded regions of the rods were omitted from the model for computational efficiency. In addition, as no local buckling phenomenon was observed during the tests for the bottom plates near to the over-sized holes (see Fig. 5.12), the oversized holes on the bottom plates of both models were also omitted to increase the mesh quality. Further simplifications were adopted by omitting the round radius of the steel beams and excluding the metal sheeting from the FEA-models to simplify numerical models and to increase the computational efficiency. The steel beam and the bottom plate were modelled as a single part, but they were separated under the part module of the software to assign them different material properties. The shear-studs were modelled based on their explicit geometries. The concrete volumes where they overlap with the steel beam, shear studs, beam end plate and the threaded-rods were deleted with merge part instances tool of the software [66]. However, the integrated bearing plate and the steel reinforcements were embedded in the concrete volumes. The load-introduction assembly (see Fig. 5.10) was also omitted in the FE-models, and the loading was applied with displacement control method by defining BC to the reference point kinematically coupled with top surface of the column. The loading rate was kept as 0.33mm/s. Smooth step function of the software [66] was used for the loading steps. Abaqus/Explicit solver was used with mass-scaling technique for the solution of the FEAs. The explicit solver parameters and the energy balances of the FEAs are given in Annex-E.

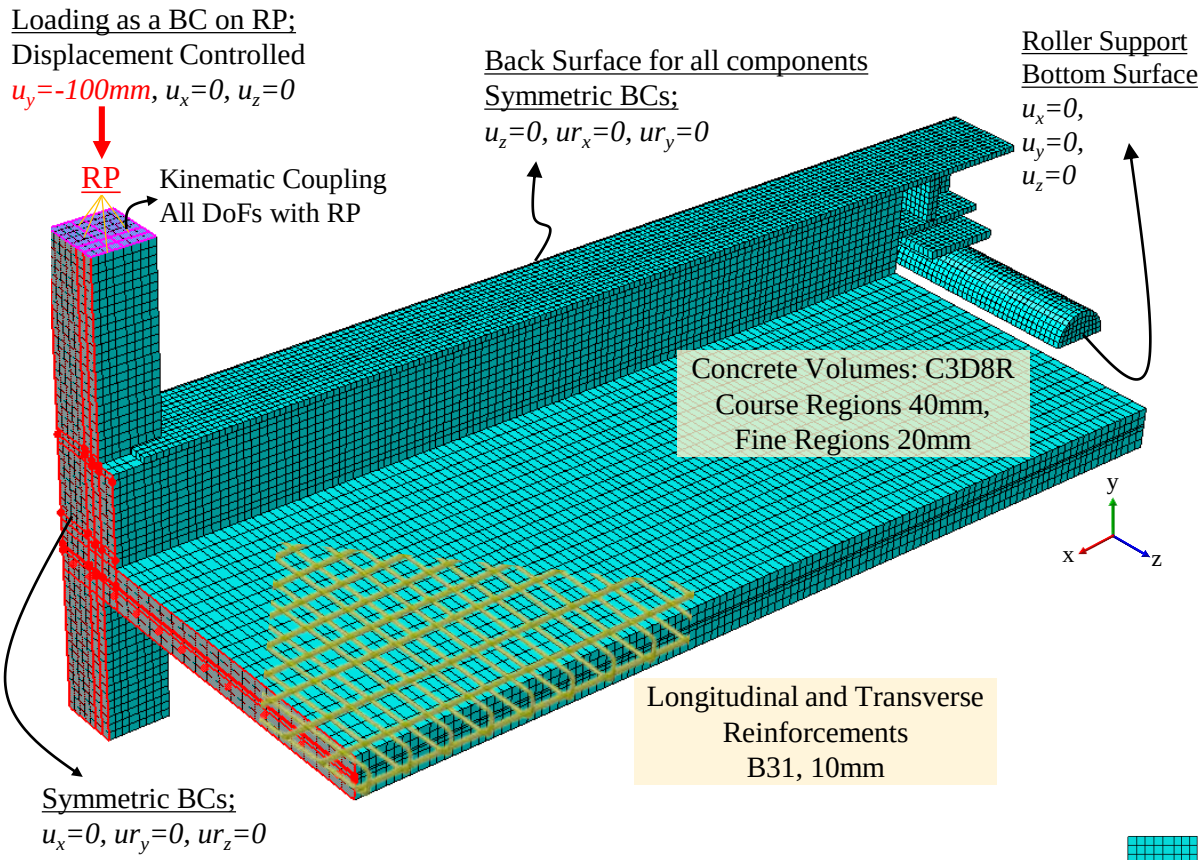

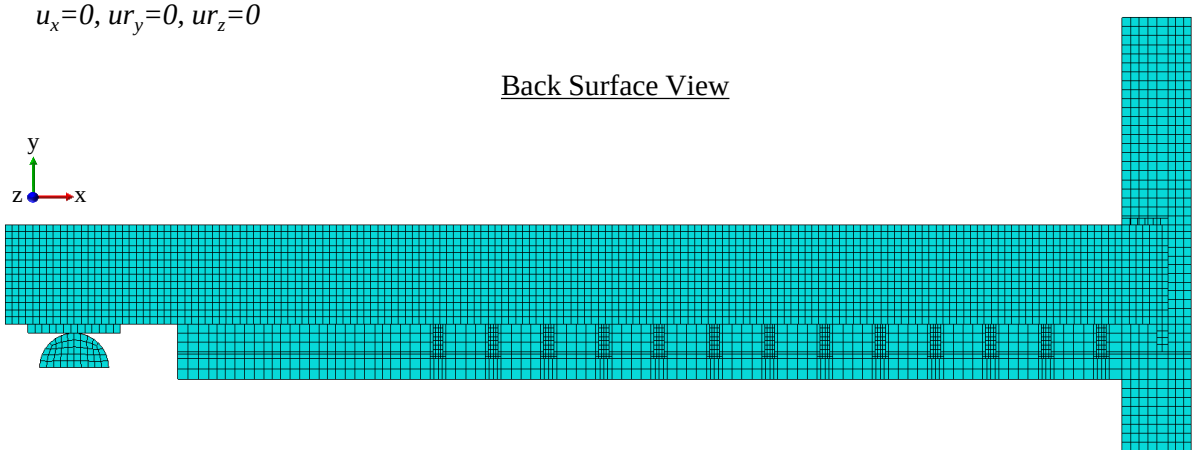

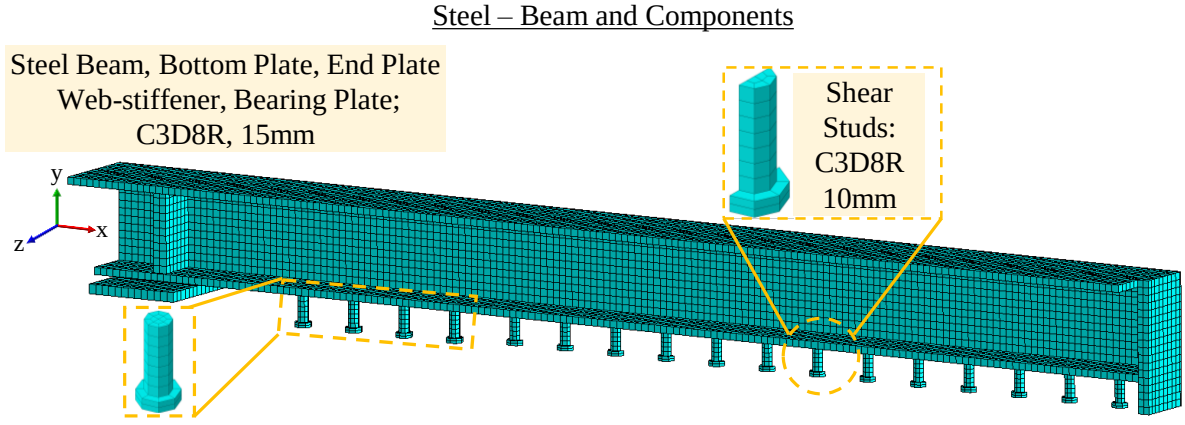

Figure 5.49: FE-Model Details of GJSFB-01 test specimen.

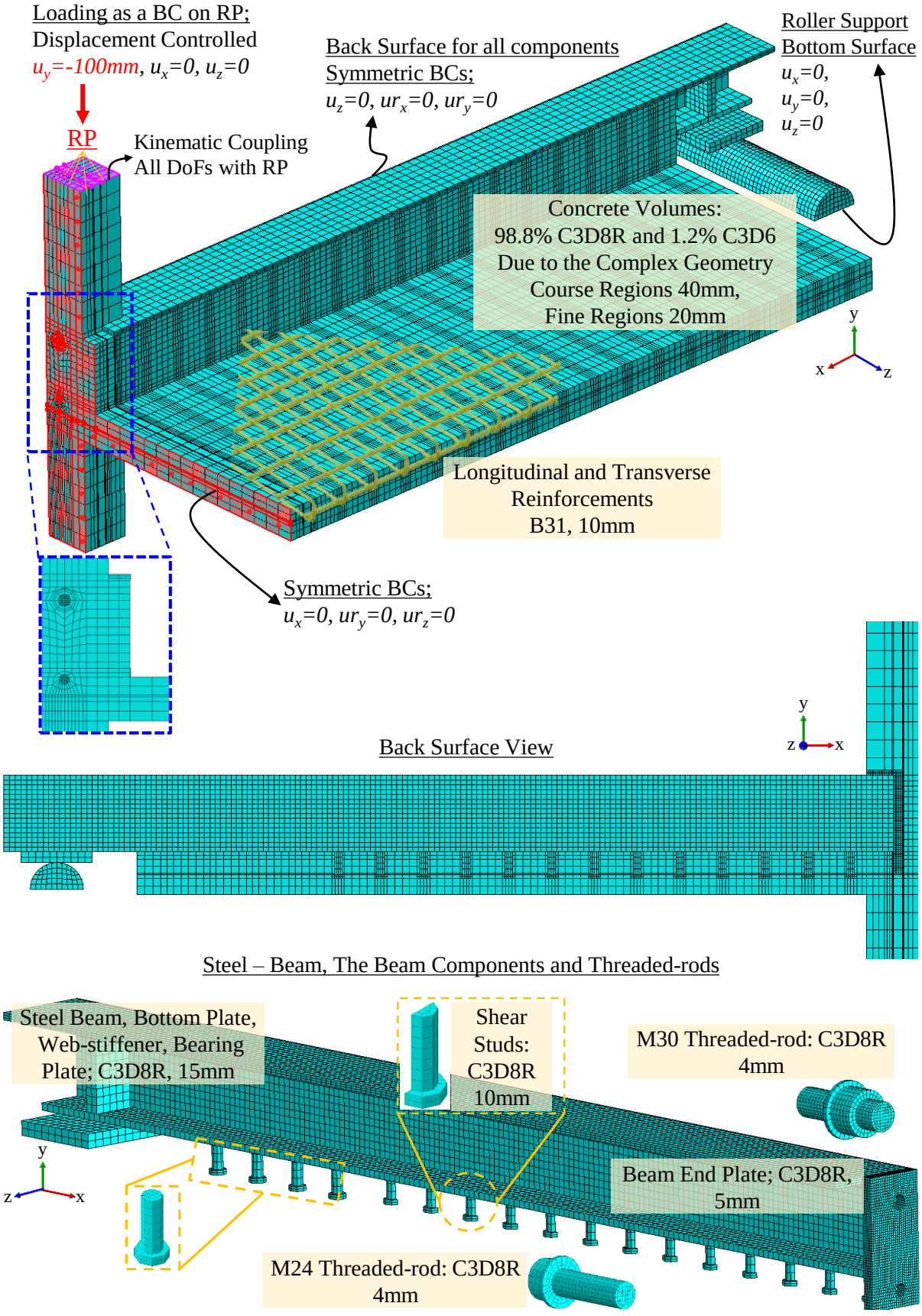

Figure 5.50: FE-Model Details of GJSFB-02 test specimen.

The material law of the concrete components was defined with concrete damage plasticity feature of the software [66]. Compressive stress-strain behavior of concrete material was defined with non-linear stress-strain relation of EN1992-1-1 [72]. Tensile stress-strain behavior of concrete material was defined as linear elastic until tensile strength. The tensile softening behavior, in other words stress crack-width relation, of the concrete material was defined according to fib Model Code [3]. Fig. 5.51a illustrates the material model and corresponding damage parameters applied for the concrete components. The formulations regarding to the calculation of the stress-strain and stress crack-width relations of concrete material are presented in Annex-C. The material properties of concrete components assigned for the FEAs were taken as the mean values presented in Table 5.2. The parameters assigned for the concrete material models of the FEAs are listed in Table 5.8.

Table 5.8: Material properties of concrete FE-model components / GJSFB test campaign.

Model ID	Elastic		Compressive Behavior					Tensile Behavior			
	E_{cm} [GPa]	ν	f_{cm} [MPa]	f_f [MPa]	ε_{c1} [‰]	ε_{cu1} [‰]	ε_f [‰]	f_{ctm} [MPa]	ε_{ctm} [‰]	w_1 [mm]	w_c [mm]
GJSFB-01	33.4	0.2	45.7	5.00	2.28	3.50	3.88	3.37	0.15	0.04	0.22
GJSFB-02	33.2	0.2	47.2	5.00	2.28	3.50	3.76	3.46	0.15	0.04	0.21
Concrete Damage Plasticity Parameters [66]											
Dilatation Angle	: 48°										
Eccentricity	: 0.1										
f_{b0}/f_{c0}	: 1.16										
K_c	: 0.667										
Viscosity Parameter	: 0.001										
Tension Recovery	: 0										
Compression Recovery	: 0										

The material laws of the steel reinforcements, threaded-rods, steel beams, bottom plates and the beam end-plates were defined with tri-linear material model using the mean properties presented in Table 5.3. The material properties of the beam end-plates were assigned as identical with the bottom plate as no material characterization test was performed for this component. The web-stiffeners and the bearing plates were modelled with elastic steel properties according to EN1993-1-1 [50] as they did not yield during the tests.

The shear-studs were modelled with bi-linear material model without material softening. It is the fact the weld-seam between the beam and the studs resists the large portion of the applied load [11] and provides additional resistance with high ductility. Therefore, the bi-linear material model of the studs could be accepted to be realistic. The yield and the ultimate strengths of the stud material were taken from the product specification [81] as the characteristic values [67]. The

transverse reinforcements of the composite beams and the reinforcements of the concrete columns were modelled with bi-linear material model without material softening using the characteristic properties of B500B grade reinforcement material according to EN1992-1-1 [72].

Fig. 5.51b illustrates the material models of the FE-model components, and the corresponding parameters are listed in Table 5.9.

Table 5.9: Material properties of the steel FE-model components / GJSFB test campaign.

Component Name	Material Model	E [GPa]	ν	f_y [MPa]	f_u [MPa]	f_f[1] [MPa]	ε_u[2] [%]	ε_f[3] [%]
Steel Beam	Tri-linear	206	0.3	395	524	354	22.1	32.5
Beam End Plate	Tri-linear	209	0.3	468	536	335	25.0	32.7
Bottom Plate	Tri-linear	209	0.3	468	536	335	25.0	32.7
M24-threaded Rod	Tri-linear	204	0.3	1210	1313	945	10.5	12.7
M30-threaded Rod	Tri-linear	210	0.3	1109	1205	760	13.1	14.2
Reinforcements-*Ø12*[4]	Tri-linear	213	0.3	448	576	426	22.8	28.7
Reinforcements-*Ø16*[5]	Tri-linear	210	0.3	394	560	374	24.5	32.0
Reinforcements-*Ø8*[6]	Bi-linear	200	0.3	500	540	N/A	15.0	N/A
Reinforcements-*Ø10*[7]	Bi-linear	200	0.3	500	540	N/A	15.0	N/A
Reinforcements-*Ø20*[7]	Bi-linear	200	0.3	500	540	N/A	15.0	N/A
Shear-studs	Bi-linear	210	0.3	375	490	N/A	15.0	N/A
Bearing Plate	Linear-elastic	210	0.3	N/A	N/A	N/A	N/A	N/A
Web-stiffener	Linear-elastic	210	0.3	N/A	N/A	N/A	N/A	N/A

[1] The magnitudes of the fracture stresses (f_f) are the mean values of the data presented in Table E.1, Table E.2 and Table E.3.

[2] The calculation of the ultimate strains (ε_u) for the tri-linear material law is presented in Annex-B.

[3] The fracture strain (ε_f) corresponds to the term A presented in Table 5.3.

[4] Longitudinal steel reinforcements of GJSFB-01 test specimen.

[5] Longitudinal steel reinforcements of GJSFB-02 test specimen.

[6] Transverse steel reinforcements of GJSFB-01 and GJSFB-02 test specimens.

[7] Longitudinal and stirrup steel reinforcements of concrete columns for GJSFB-01 and GJSFB-02 test specimens.

The interactions between the FE-model components are listed in Table 5.10. The general contact with hard and penalty friction formulations was used to define the normal and the tangential interactions between the FE-model components. The bearing plate, the web-stiffener, beam-end-plate and shear-studs were tied with steel beams for both of the FE-models.

a) Constitutive Material Model for Concrete Components

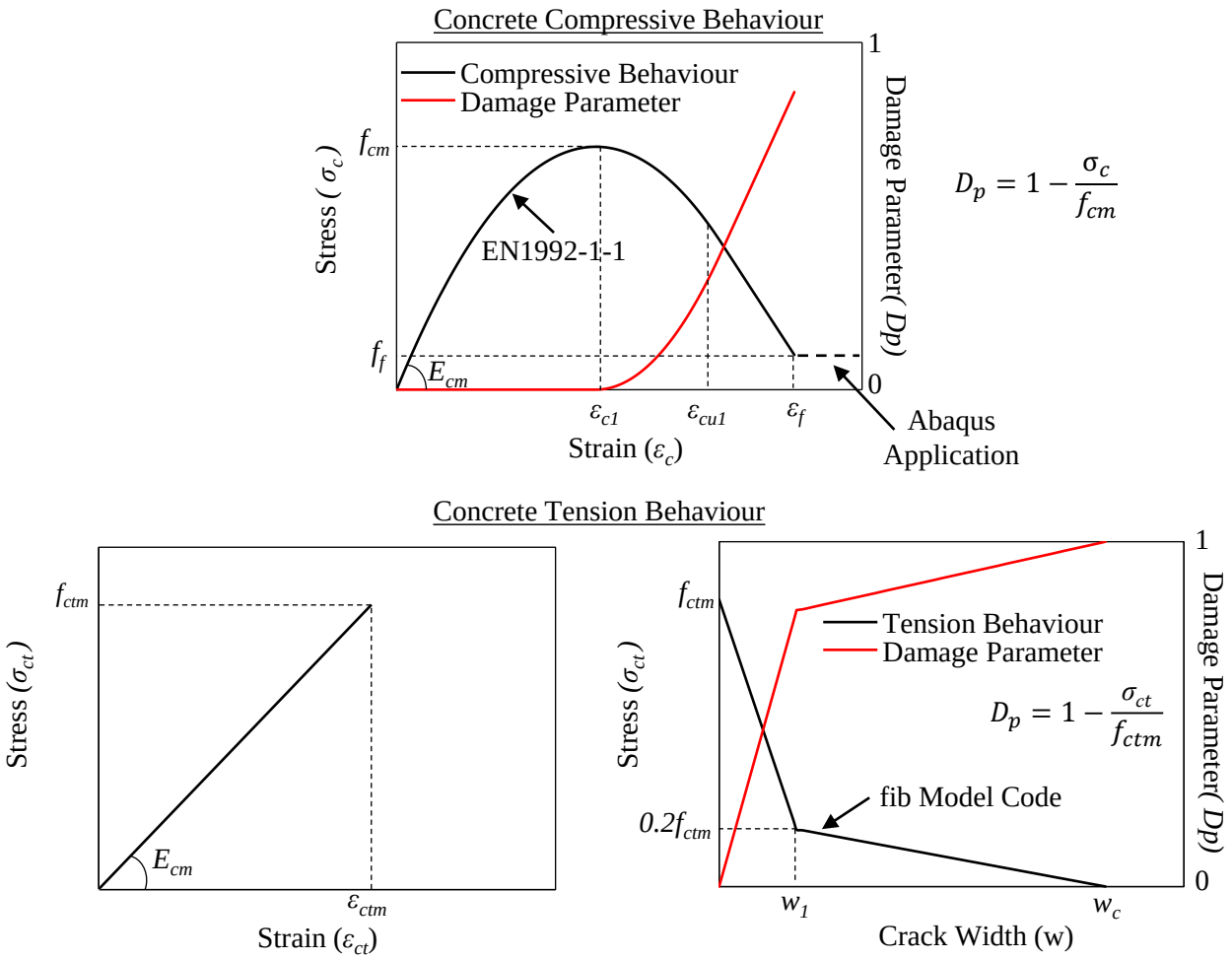

b) Constitutive Material Models for Steel Components

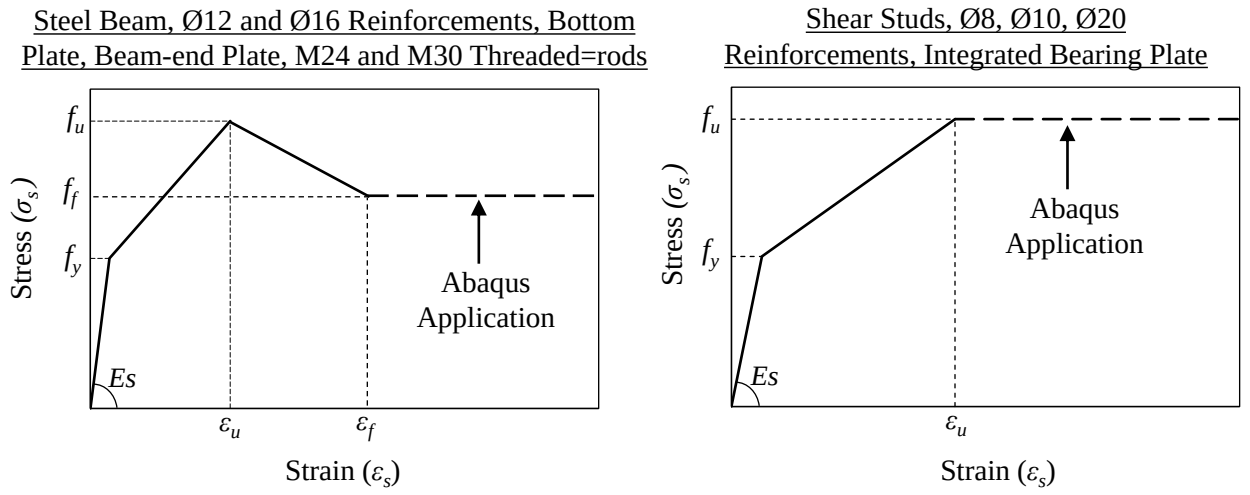

Figure 5.51: Illustration of the material laws assigned to FEA model components.

Table 5.10: Interaction properties between the FE-model components of GJSFB test campaign.

Connected Components	Interaction Method	Interaction Properties	
		ND	TD
Shear-studs to Steel Beam	Tie Constrain	N/A	N/A
Beam End Plate to Steel Beam	Tie Constrain	N/A	N/A
Bearing Plate to Steel Beam	Tie Constrain	N/A	N/A
Web-stiffener to Steel Beam	Tie Constrain	N/A	N/A
Bearing Plate to Roller Support	General Contact	Hard	Frictionless
Steel Beam to Concrete Slab	General Contact	Hard	Penalty Friction ($\mu = 0.5$)
Shear Studs to Concrete Slab	General Contact	Hard	Penalty Friction ($\mu = 0.5$)
M30-Rod to Concrete Column	General Contact	Hard	Penalty Friction ($\mu = 0.5$)
M24-Rod to Concrete Column	General Contact	Hard	Penalty Friction ($\mu = 0.5$)
M30-Rod to Beam End Plate	General Contact	Hard	Penalty Friction ($\mu = 0.3$)
M24-Rod to Beam End Plate	General Contact	Hard	Penalty Friction ($\mu = 0.3$)

ND: Normal Direction, TD: Tangential Direction

Fig. 5.52 compares the moment-rotation curves of the experimental tests with the output results of the FEAs. The moment and corresponding rotations at the joints for the FEAs were also calculated with Eq. 5.1 and Eq. 5.2 for the consistency of the comparisons. The longitudinal shear failure was also the reason for the sudden load-drop in the FEA of GJSFB-02 test specimen. Fig. 5.53 shows the compressive damage for the concrete slab of GJSFB-02 test specimen at the analysis instants before and after the sudden failure. Thus, the reason behind the failure of the test specimen (see Section 5.2.5.2) also verified with the FEA. This outcome also validates the accuracy of the FEAs.

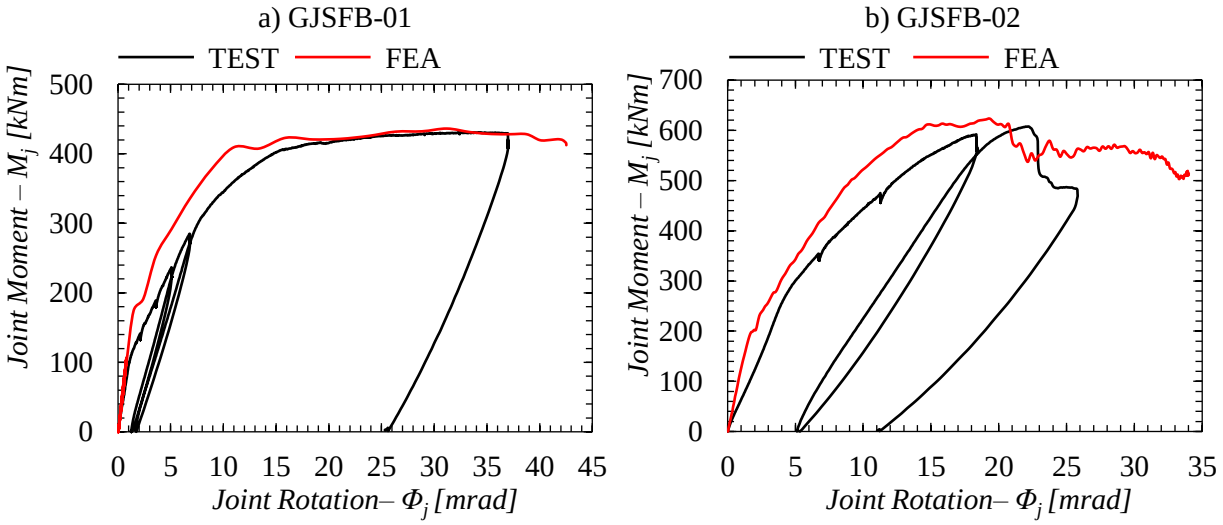

Figure 5.52: The moment-rotation behaviours of GJSFB joint configurations against FEAs.

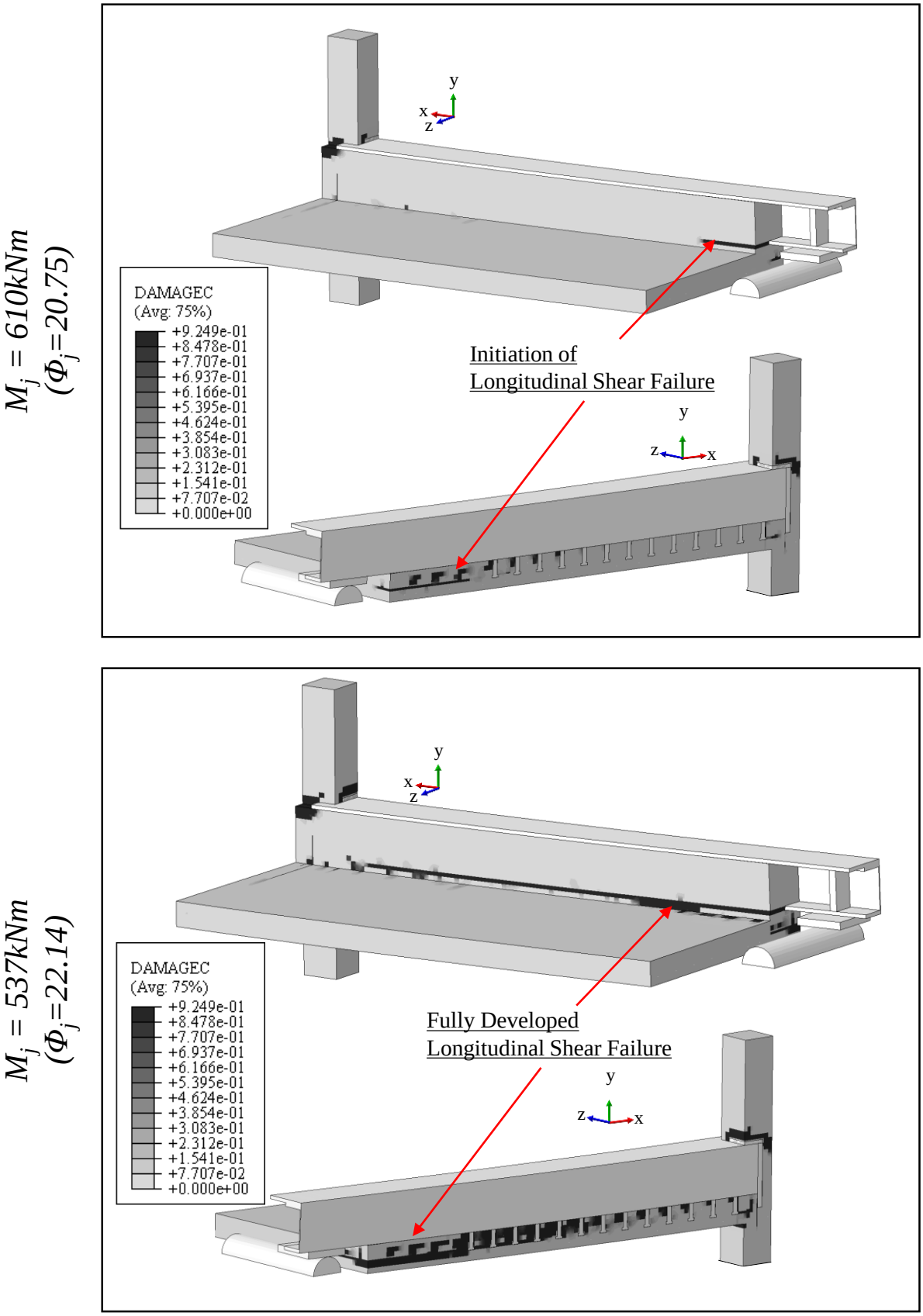

Figure 5.53: Longitudinal shear failure of GJSFB-02 test specimen.

Fig. 5.54 compares the tensile crack patterns identified after the experimental tests with the corresponding FEAs for the analysis instants that correspond to the maximum joint rotations recorded during the tests ($\Phi_{j,max\text{-}record,GJSFB\text{-}01}$=*38.68mrad* and $\Phi_{j,max\text{-}record,GJSFB\text{-}02}$=*25.83mrad*). It is important to note that the minimum colour contour limit for the tensile damage parameter was set to 0.5 in Fig. 5.54a to identify only the severe cracks. According to the presented details, it is concluded that the FE-models are capable to simulate the experimental tests with high accuracy by means of both global and local behaviours.

On the other hand, in Fig. 5.52a it could be noticed that although the FEA was estimating the initial rotational stiffness of GJSFB-01 joint configuration with high accuracy the initial softening of the moment-rotation behavior (see Fig. 5.22 - $M_{j,1}$=*115kNm*) was estimated by the FEA around 180kNm joint moment which is 57% higher than the test result. This difference was mainly due to the tensile material model applied in the software [66] as it was not possible to include the strain hardening plateau for the concrete tensile behavior together with the tensile stress crack-width definition. This phenomenon may be explained with Fig. 5.56 based on the concrete tensile material model of fib Model Code [3]. According to Fig. 5.56 the secant modulus of elasticity for the concrete material of GJSFB-01 test specimen could be calculated with Eq. 5.4 based on the mean tensile strength for concrete material of GJSFB-01 test specimen presented in Table 5.8. Thereby, it could be concluded that the elastic modulus of the concrete material applied in the FEAs was about 50% higher than the secant modulus calculated based on fib Model Code [3]. Thereby the reason behind the difference for the estimation of the initial softening of moment-rotation behavior could be directly linked to the selected tensile material model. The one could indicate that the software [66] also enables a user to define their own material model with UMAT subroutine [66] but these methodology was out of the scope of this thesis.

$$E_{cm,sec} = \frac{f_{ctm}}{\varepsilon_{ctm,fibModelCode}}$$

$$E_{cm,sec,GJSFB-01} = \frac{3.35MPa}{0.0015} \tag{5.4}$$

$$E_{cm,sec,GJSFB-01} = 22.33GPa$$

a) GJSFB-01

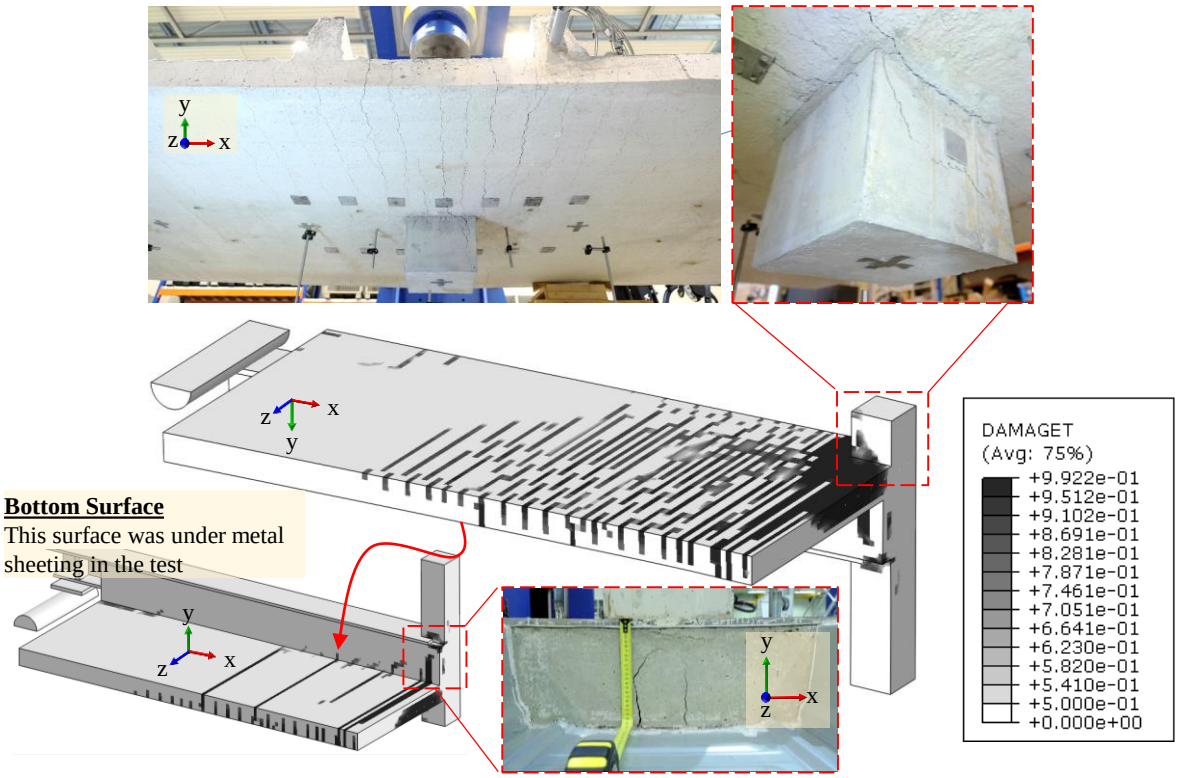

b) GJSFB-02

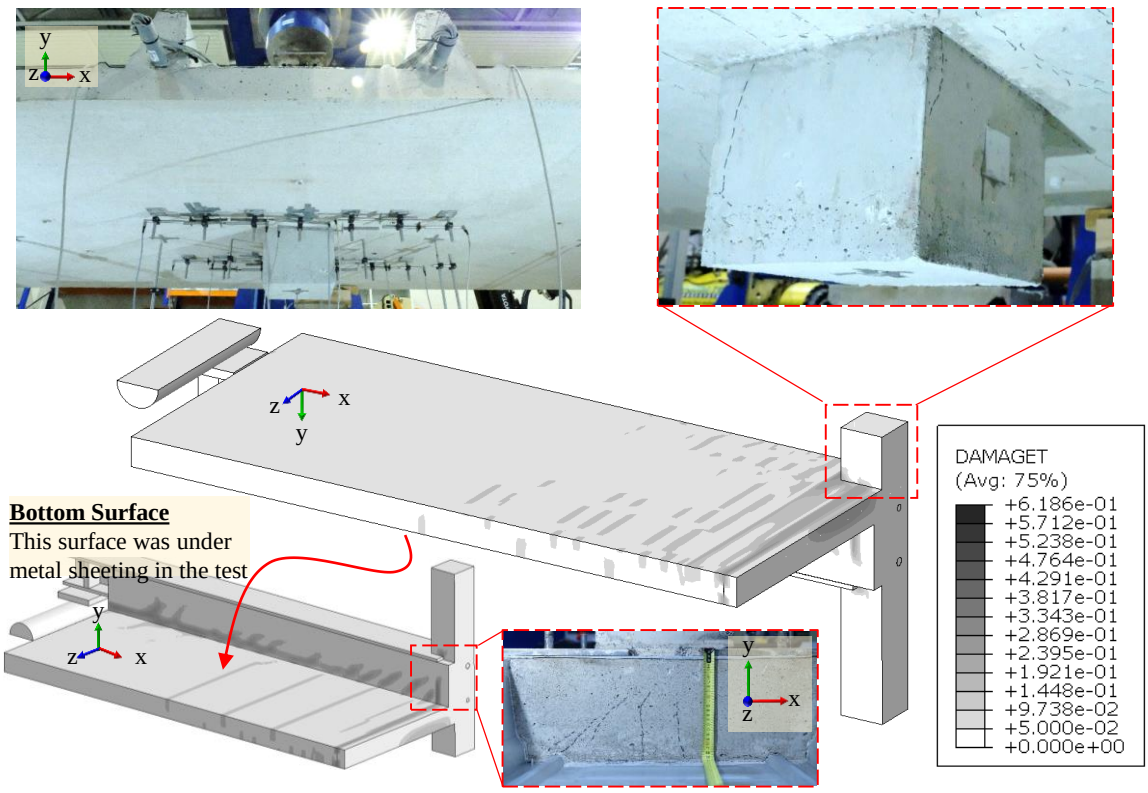

Figure 5.54: Comparisons of the crack patterns of the test specimens with the corresponding FEAs.

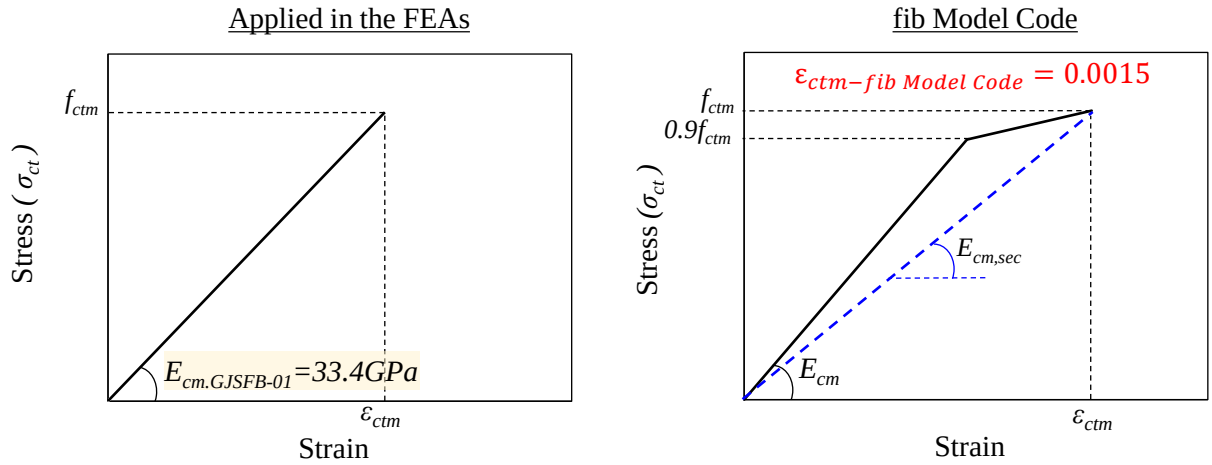

Figure 5.55: Comparisons of the tensile material models of concrete applied in the FEAs and suggested by fib Model Code [3].

In addition, it could be noticed in Fig. 5.52b that FEA of GJSFB-02 estimated the initial rotational stiffness of GJSFB-02 joint configuration higher than the test result. This difference was mainly due to the tensile crack formations for GJSFB-02 test specimen during the cyclic loading period (see Fig. 5.35 and Table 5.6). Accordingly, GJSFB-02 test specimen was partially damaged at the beginning of the monotonic loading steps. As a result, the initial rotational stiffness estimated by the FEA was higher than the corresponding test result. To further investigate this phenomenon, a cyclic loading period identical to the loading procedure of the experimental test (see Fig. 5.18) was added to the FEA of GJSFB-02 and the analysis was re-executed. Fig. 5.56 compares the monotonic part of the moment-rotation behaviour of GJSFB-02 joint configuration against FEAs including and excluding the cyclic loading period. The impact of the cyclic loading-period on the initial rotational stiffness is clear. Thus, the higher initial rotational stiffness estimation of the FEA for GJSFB-02 joint configuration is concluded to be due to the loading history. The FEA with cyclic loading-period was executed using at the HPC facilities of the University of Luxembourg [105].

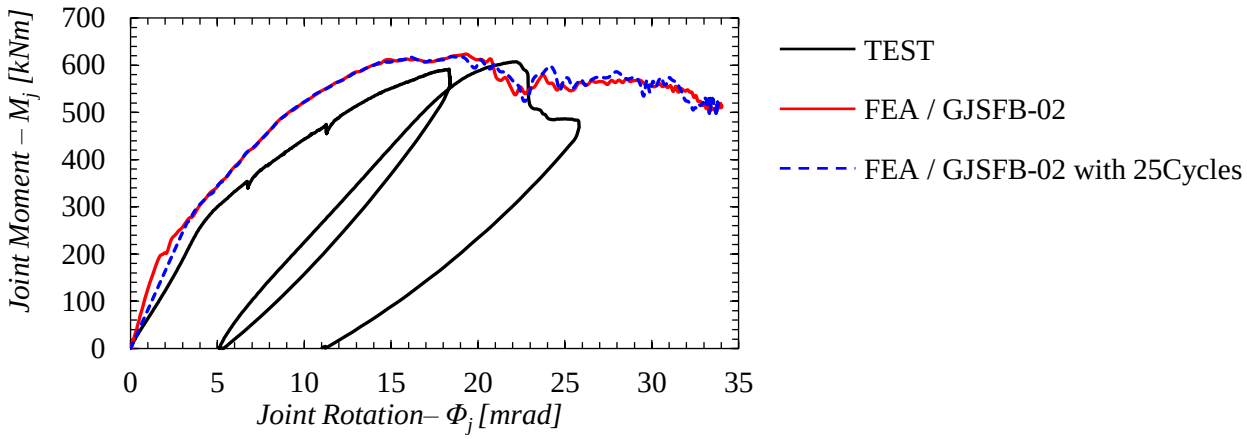

Figure 5.56: Impact of the cyclic loading period on the moment-rotation behaviour of GJSFB-02.

Having validated the accuracy of the presented FE-modelling technique and the selected solution scheme, additional four FEAs were performed. The details of the additional FEAs are explained in the following items and summarized in Table 5.11;

- GJSFB-01-ED: To estimate the ultimate rotation capacity of GJSFB-01 joint configuration, the vertical displacement applied to the reference point (see Fig. 5.49) was increased to 200mm without changing any other property of the FEA model of GJSFB-01 test specimen.
- GJSFB-02-MTR: To estimate the plastic moment-capacity and the ultimate rotation capacity of GJSFB-02 joint configuration. The ratio of the transverse reinforcement of GJSFB-02 test specimen was manipulated with a factor of two to cancel out the longitudinal shear failure between the concrete slab and the steel beam without changing the rotational behavior of the joint.
- GJSFB-01-ITH: To estimate the contribution of the threaded-rods against the bending moments in the joint, threaded rods were included in the FE-model of GJSFB-01 test specimen.
- GJSFB-02-ETH: To estimate the contribution of the threaded-rods against the bending moments in the joint, threaded rods were excluded in the FE-model of GJSFB-02 test specimen.

Table 5.11: Summary of the additional FEAs performed for GJSFB joint configurations.

FEA Model ID	GJSFB-01-ED	GJSFB-01-ITH	GJSFB-02-ETH	GJSFB-02-MTR
Displacement [mm]	200	300	300	300
Threaded Rods	NO	YES	NO	YES
Transverse Reinforcement Manipulation Factor	N/A	N/A	N/A	2

Fig. 5.57a compares the experimental moment-rotation behavior of GJSFB-01 joint configuration with the output results of the FEA nominated as GJSFB-01-ED in Table 5.11. According to the aforementioned FEA, the ultimate rotation capacity of GJSFB-01 joint configuration is estimated to be equal to 47.95mrad ($\Phi_{j,u,GJSFB\text{-}01}$=*47.95mrad*) as highlighted in the figure and it is shown in Fig. 5.57b that the crushing of the concrete grout at the joint is the limiting mechanism for the ultimate rotation capacity of GJSFB-01 joint configuration. In addition, Fig. 5.57c presents the yield status of the longitudinal steel reinforcements at the analysis instants that corresponds to 300kNm and 406kNm joint moments. It could be deduced from Fig. 5.57c that the longitudinal steel reinforcements started to yield about 300kNm joint moment and this result very well fits with the previous identifications made in Fig. 5.22. Furthermore, at 406kNm joint moment it is clear that all of the longitudinal steel reinforcements yielded; thus, the theoretical plastic hinge mechanism of GJSFB-01 joint configuration could be excepted to be fully developed at 406kNm joint moment, this outcome also very well matches with the experimental investigations presented in Section 5.2.5.1.

a) Comparison of Moment-rotation Curves

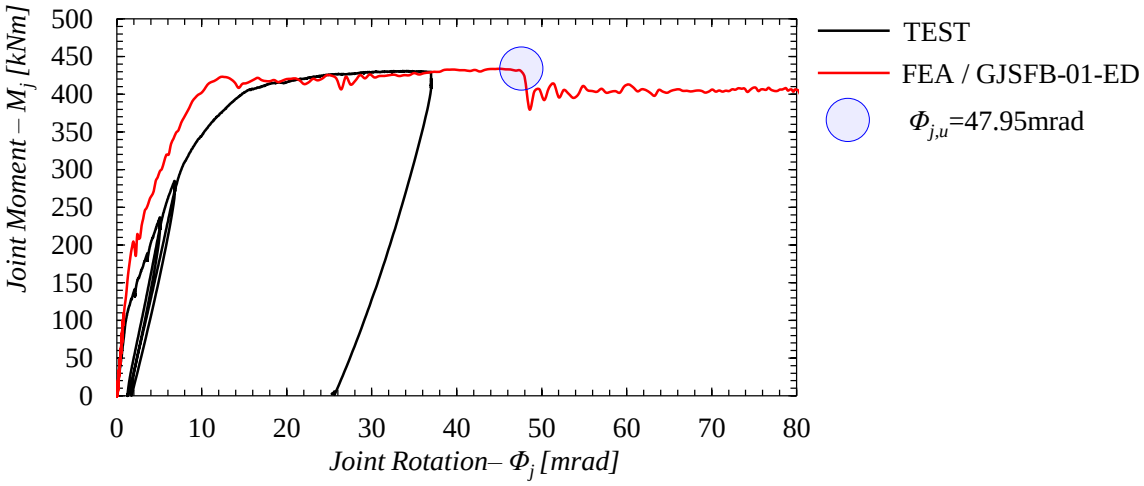

b) Status of Concrete Grout at the Joint before and after the Failure Instants

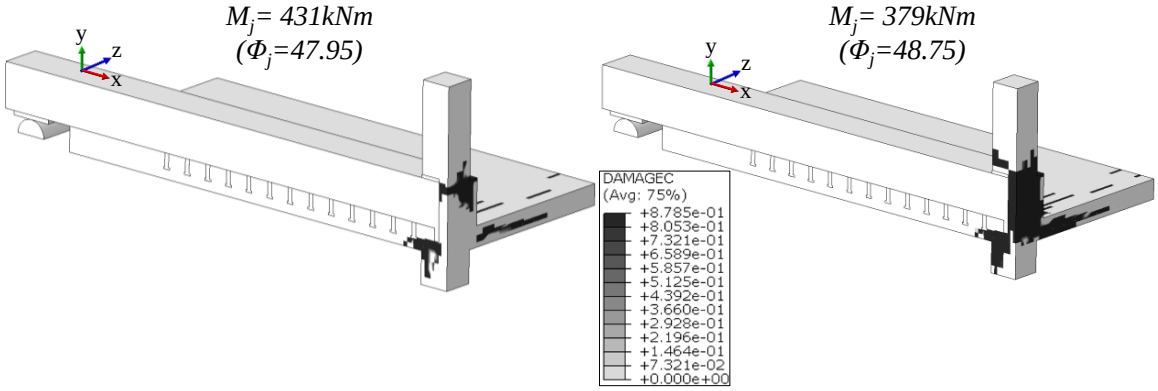

c) Yield Status of the Longitudinal Steel Reinforcements

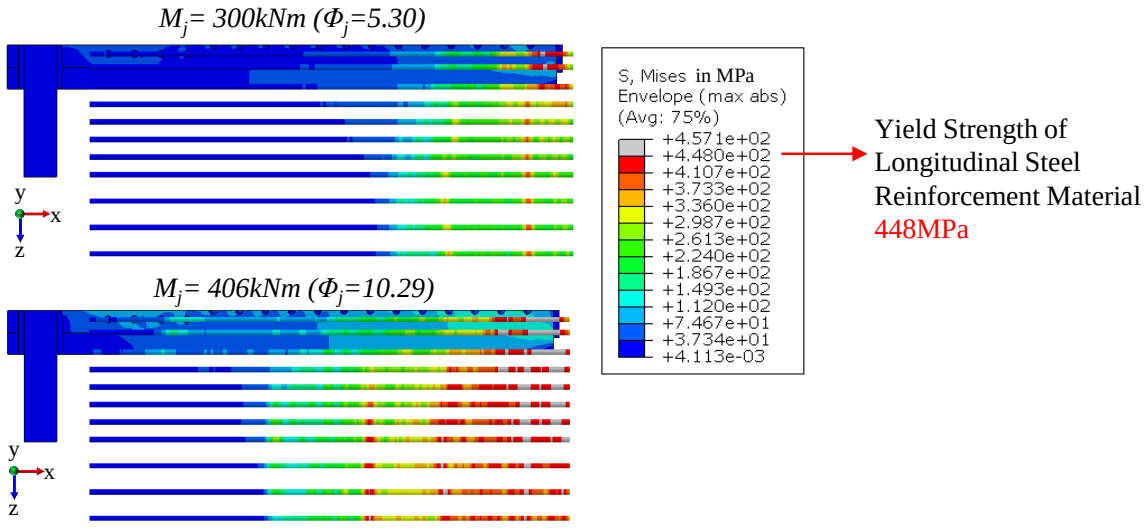

Figure 5.57: The ultimate rotation capacity of GJSFB-01 joint configuration and the limiting mechanisms of the rotation and the plastic moment capacities based on the FEA of GJSFB-01-ED.

Fig. 5.58a compares the experimental moment-rotation behavior of GJSFB-02 joint configuration with the output results of the FEA nominated as GJSFB-02-MTR in Table 5.11. The moment-rotation curve of the FEA presented in Fig. 5.52b also included in the figure to show that the magnification of the transverse reinforcement ratio successfully canceled-out the longitudinal shear failure of GJSFB-02 test specimen without impacting the moment-rotation behavior of the joint. According to the output results of GJSFB-02-MTR finite element analysis, the plastic-moment capacity and the ultimate rotation capacity of GJSFB-02 joint configuration are estimated to be equal to 695kNm ($M_{j,pl,GJSFB-02}$=*695kNm*) and 71.21mrad ($\Phi_{j,u,GJSFB-02}$=*71.21mrad*), respectively. The limiting factor for the rotation capacity of GJSFB-02 joint configuration was determined as the necking of the M24 threaded-rods. Fig. 5.57b shows the status of the concrete grout and the plastic-equivalent strain (PEEQ) distribution of the threaded-rods for the joint rotations at the analysis instant that corresponds to the fully crashed state for the concrete grout and at the analysis instant once the ultimate rotation capacity is attained. According to the presented details, it is concluded that the joint was able to rotate more than 17mrad by sustaining the plastic moment-capacity after the crushing of the concrete grout as the M30 threaded-rod was resisting the compressive stress resultants developed in the joint. However, once the M24 threaded-rod reached the plastic strain limit by means of PEEQ (see also Table 5.9) , the ultimate rotation capacity of GJSFB-02 joint configuration was attained.

Furthermore, the yield status of the longitudinal steel reinforcements is presented in Fig. 5.58c at the analysis instants that corresponds to 448kNm and 568kNm joint moments. Unlike to GJSFB-01 joint configuration, the moment-rotation behavior of GJSFB-02 joint configuration did not soften by the initiation of the longitudinal steel reinforcement yielding. This difference was mainly due to the existence of the M24 threaded-rods as they were resisting the relatively high amount of the tensile stress resultants developed in the joint due to the bending moment (see also Fig. 5.41). Furthermore, at 568kNm joint moment it is clear that all of the longitudinal steel reinforcements yielded. This instant was earlier identified with the experimental test data in Fig. 5.34 and it was earlier highlighted with Fig. 5.38 that this instant could be accepted as the initiation of the plastic hinge formation for GJSFB-02 joint configuration. However, the plastic moment capacity of GJSFB-02 joint configuration was estimated to be 695kNm about 26% higher than the joint moment by the initiation of the plastic hinge formation. Thus, it is concluded that, the existence of the threaded-rods highly increases the plastic moment capacity for GJSFB joint configurations and postpones the initiation of the plastic hinge formation until the yielding of the all longitudinal steel reinforcements. In addition, while the ultimate plastic moment capacity of GJSFB-01 joint configuration was only 6% higher than the joint moment that corresponds to the theoretical plastic hinge formation, this difference was 26% for GJSFB-02 joint configuration. Thus, it is concluded that the application of the threaded-rods highly increases the ultimate load-bearing capacity of the proposed composite joint and may be considered as a promising solution for continuous composite slim-floor beams.

a) Comparison of Moment-rotation Curves

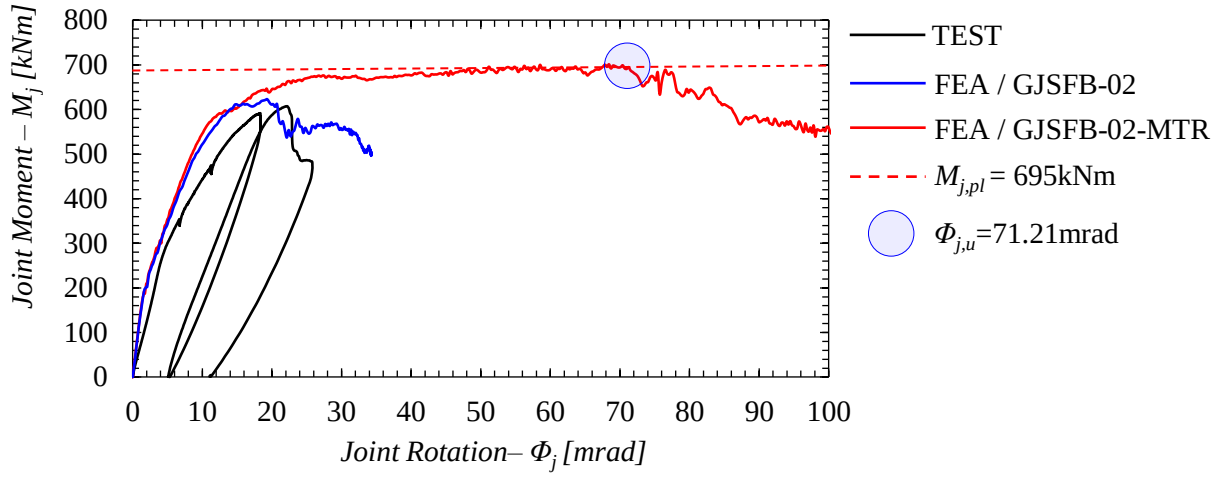

b) Damage Status of the Concrete Grout and the Necking of the M24 Threaded Rod

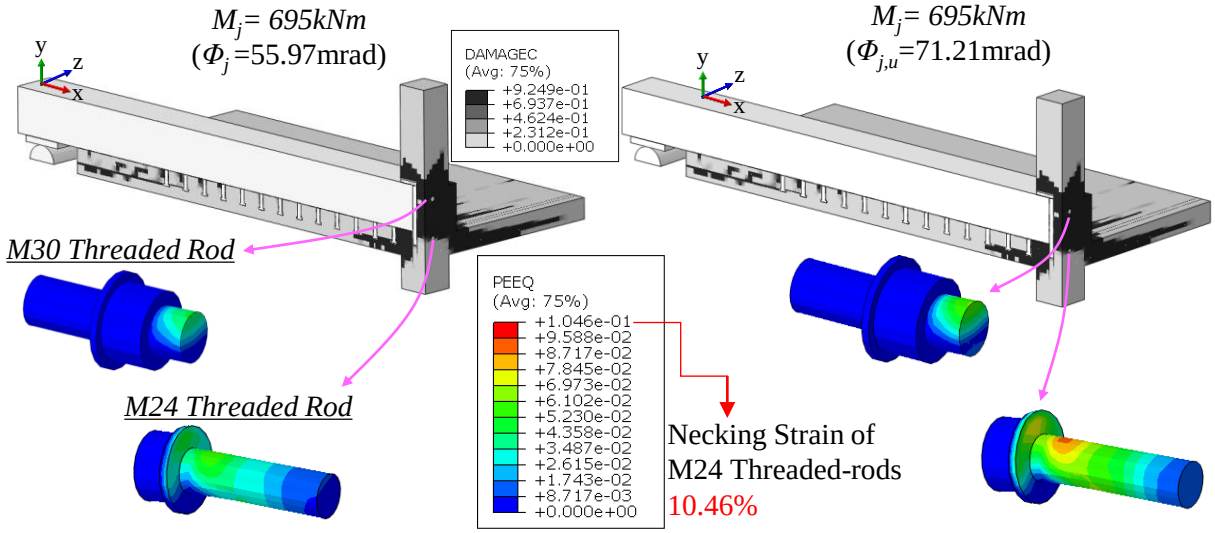

c) Yield Status of the Longitudinal Steel Reinforcements

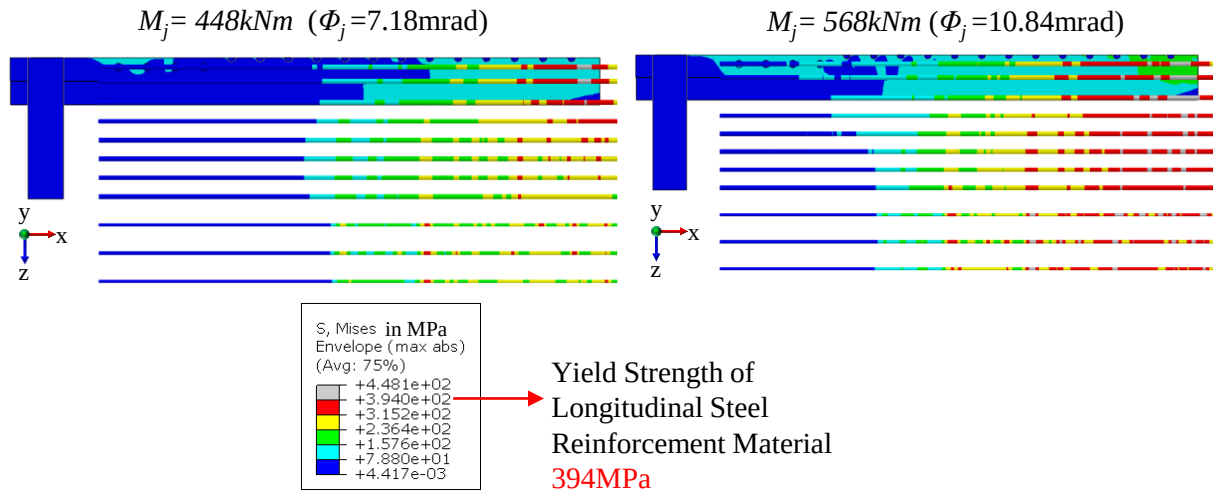

Figure 5.58: The ultimate rotation capacity of GJSFB-02 joint configuration and the limiting mechanisms of the rotation and the plastic moment capacities based on the FEA of GJSFB-02-MTR.

Although the effectiveness of the threaded-rods for the proposed joint configuration was clearly as summarized in the previous paragraph, two additional FEAs were performed (GJSFB-01-ITH and GJSFB-02-ETH see Table 5.11) to further investigate the contribution of the threaded-rods to the plastic moment-capacity and the ultimate rotation-capacity of the proposed joint details with respect to the different longitudinal reinforcement ratio of the test specimens (see also Fig. 5.11 and Table 5.1). Fig. 5.59 compares the moment-rotation behavior of the experimental tests with the FEAs performed including and excluding the threaded-rods in the joints. For both of the investigated reinforcement ratios, if the threaded-rods were not applied in the joints the failures were due to the crushing of the concrete grout (see also Fig. 5.57b) while the application of the threaded rods changed the failure modes to necking of the M24 threaded rods (see also Fig. 5.58b).

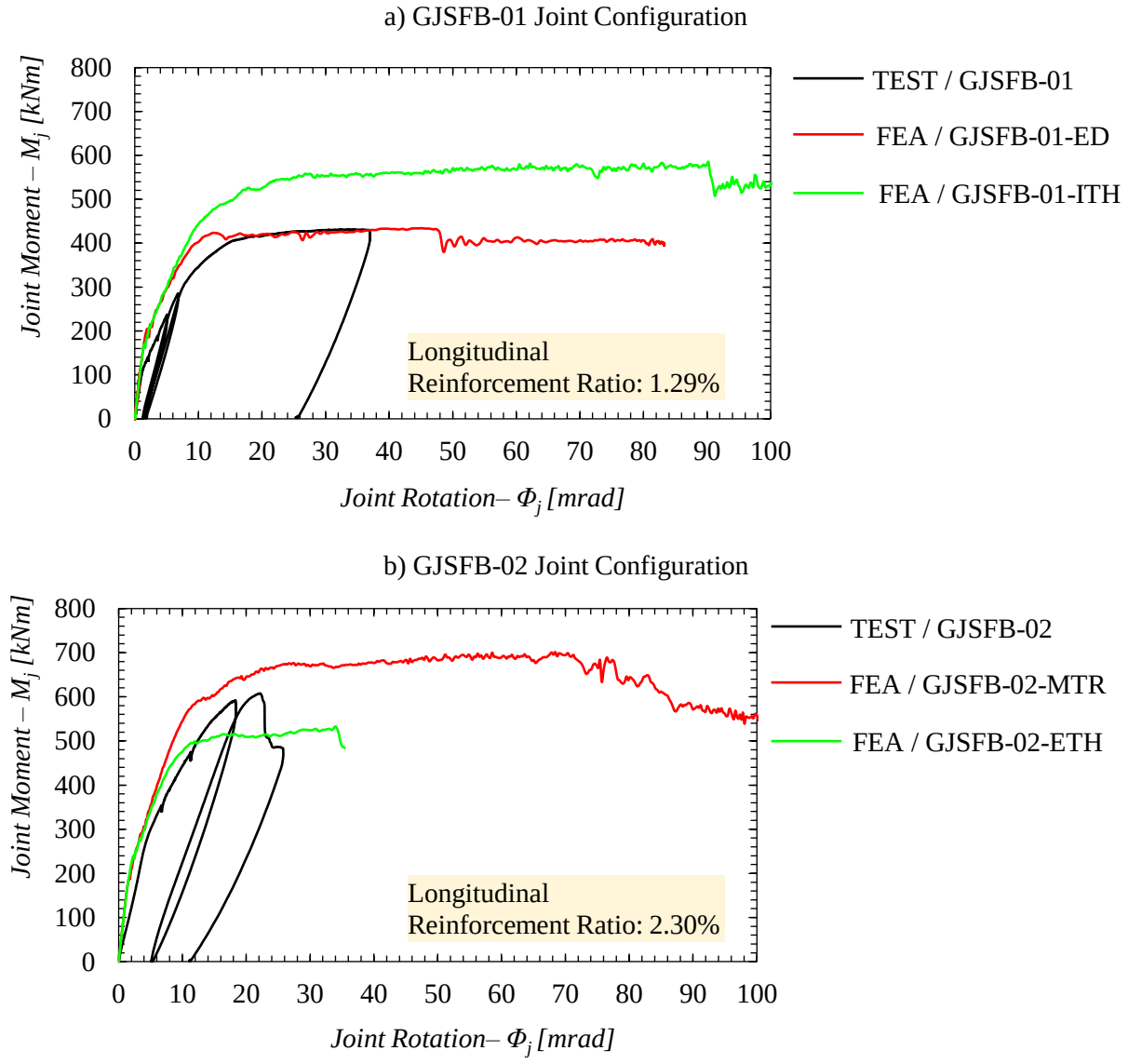

Figure 5.59: The impact of the threaded-rods to the plastic moment-capacity and the ultimate rotation-capacity of GJSFB joint configurations for different longitudinal reinforcement ratios.

Table 5.12 summarizes the results presented in Fig. 5.59 for clear comparisons for the output results of the parametric FEAs.

Table 5.12: The impact of the threaded-rods on the plastic-moment capacity and the rotation capacity of GJSFB joint configurations.

FEA Model ID	GJSFB-01-ED	GJSFB-01-ITH	GJSFB-02-ETH	GJSFB-02-MTR
[1] Rein. Diameter [mm]	12	12	16	16
[1] Rein. Ratio [%]	1.29	1.29	2.30	2.30
Threaded Rods	NO	YES	NO	YES

FEA Model ID	Plastic Moment Capacity ($M_{j,pl}$) [kNm]	Ultimate Rotation Capacity ($\Phi_{j,u}$) [mrad]
GJSFB-01-ED	431	47.95
GJSFB-01-ITH	570	90.21
Difference [%]	32.3	88.70
GJSFB-02-ETH	532	34.38
GJSFB-02-MTR	695	71.21
Difference [%]	30.6	107.12

[1] The longitudinal reinforcements.

According to Table 5.12, the following conclusions could be derived;

- The application of the threaded-rods for the proposed joint configuration increases the plastic moment-capacity of the joint by about 30-33%.
- The application of the threaded-rods for the proposed joint configuration increases the ultimate rotation-capacity of the joint by about 88-107%.
- The contribution of the threaded-rods to the plastic moment-capacity of the proposed joint configuration is very similar for different longitudinal reinforcement ratios and about 2% higher for the longitudinally less reinforced composite slim-floor beam cross-section.
- The contribution of the threaded-rods to the ultimate rotation-capacity of the proposed joint configuration is about 20% higher for the longitudinally more reinforced slim-floor beam cross-section.

By defining the plastic moment-capacity and the rotational stiffness of GJSFB-02 joint configuration, Fig. 5.47b and Fig. 5.48b could be revised as they were earlier determined based on the maximum joint moment recorded during the test instead of the plastic moment-capacity of the joint as the test specimen was failed due to longitudinal shear failure. Fig. 5.30 presents the

revised rotational stiffness values and the classifications of GJSFB-02 joint configuration based on the output results of the FEA (see Fig. 5.58a) with respect to EN1994-1-1 [2].

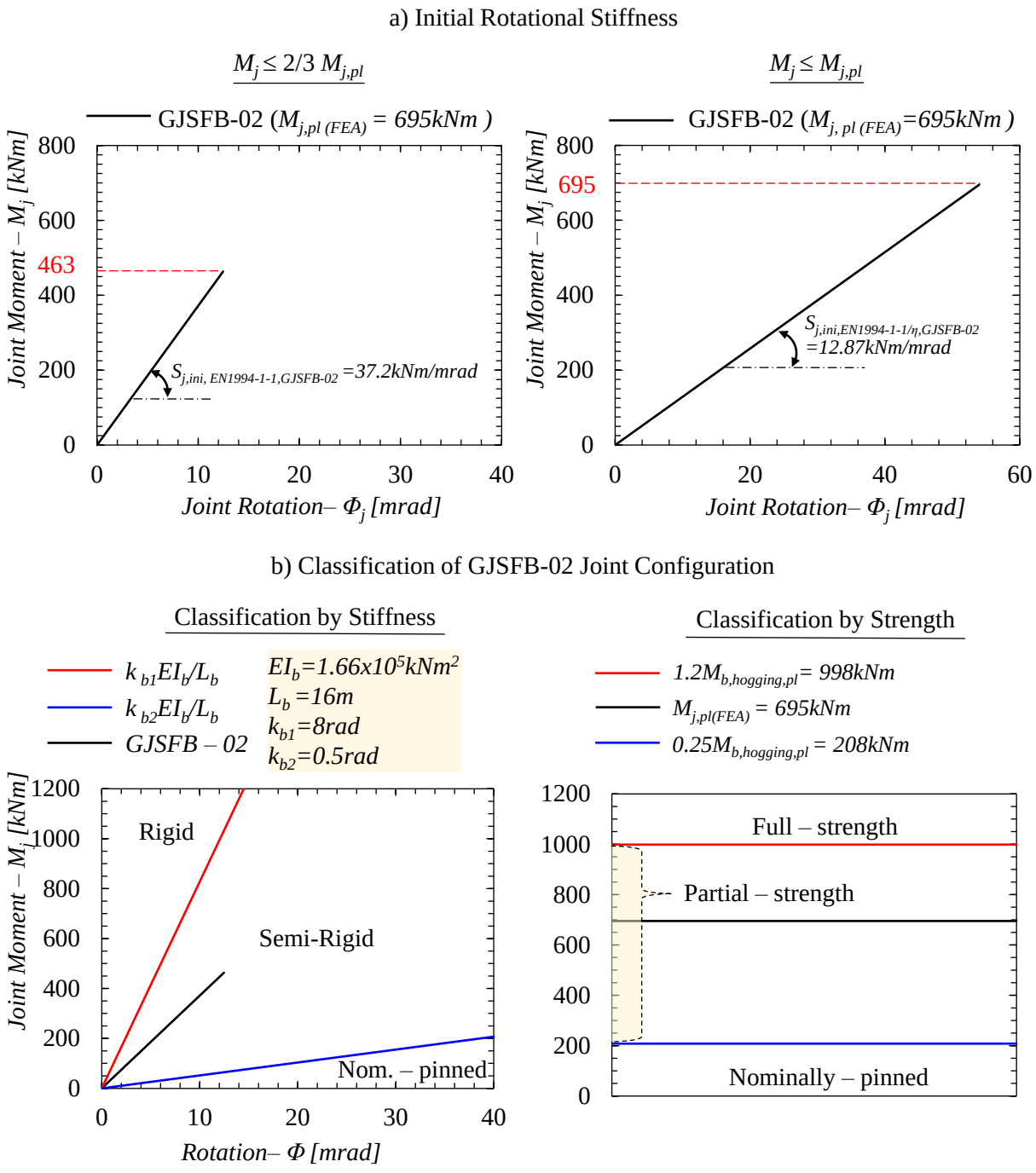

Figure 5.60: Revised initial and secant rotational stiffness and revised classification of GJSFB-02 joint configuration according to EN1994-1-1 [2].

The last but not the least, Table 5.13 compares the rotational stiffness of the tested GJSFB joint configurations considering the revised rotational stiffness values presented for GJSFB-02 joint configuration in Fig. 5.60. Based on the comparison given in Table 5.13, it is concluded that the initial rotational stiffness and the secant stiffness of GJSFB joint configurations determined according to EN1994-1-1 [2] are nearly independent from the reinforcement ratio and the existence of the threaded-rods. It is important to highlight that this outcome was also derived based on the direct investigation of the moment-rotation curves of the tested joint configurations as earlier presented in Table 5.6.

Table 5.13: Comparison of the initial and the secant stiffness of the tested GJSFB joint configurations determined according to EN1994-1-1 [2].

Test ID	$S_{j,ini}$ $[\frac{kNm}{mrad}]$	$S_{j,ini}/\eta$ $[\frac{kNm}{mrad}]$	η[1]
GJSFB-01 (Based on Test)	37.3	12.7	2.94
GJSFB-02 (Based on FEA)	37.2	12.9	2.89
Ratio	1.0	0.98	1.02

[1] The stiffness modification factor (η) corresponds to the ratio of the initial and the secant rotational stiffness of a joint $\left(\frac{S_{\text{j,ini,EN1994-1-1}}}{S_{\text{j,sec,EN1994-1-1}}}\right)$ according to EN1994-1-1 [2] based on the definition presented in Fig. 5.46.

5.4 Analytical models for the estimations of the plastic-moment and rotation capacities of GJSFB joint configurations

The previous sections presented experimental and numerical methodologies to determine the moment-rotation behavior of GJSFB joint configurations. It is the fact that the numerical simulations are much more cost efficient compared to the experimental tests considering the accuracy of their estimations for the ultimate load-bearing and deformation capacities of the proposed joint configurations. On the other hand, to execute the numerical simulations, it is required to have prior knowledge for the development of the simulation models with a specific software together with high computational power due to the geometrical and material nonlinearities at the ultimate limit state of the joints. Therefore, it is necessary to establish an analytical resistance model for the engineering capacity approximation of GJSFB joint configurations. This section presents the analytical resistance and rotation models to estimate the plastic moment-capacity and the ultimate rotation capacity of GJSFB joint configurations.

a) Cross-sectional Analysis of GJSFB-01 Joint Configuration

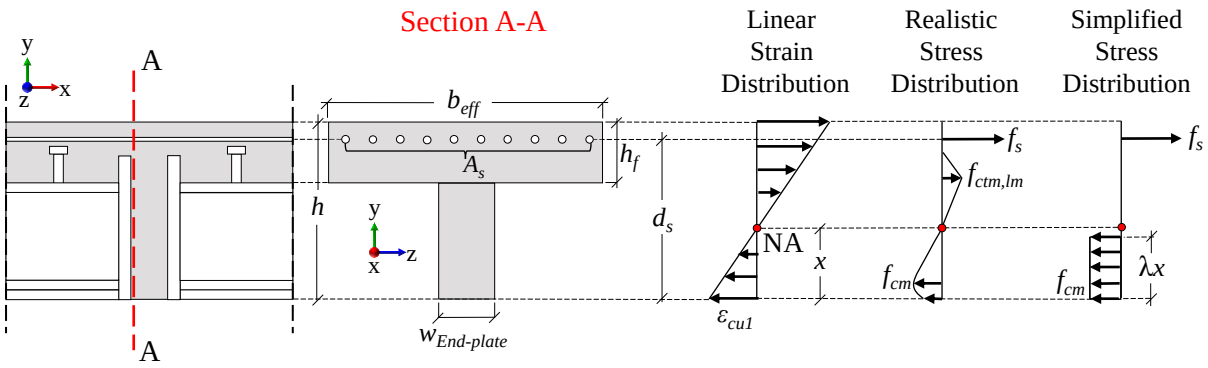

b) Cross-sectional Analysis of GJSFB-02 Joint Configuration

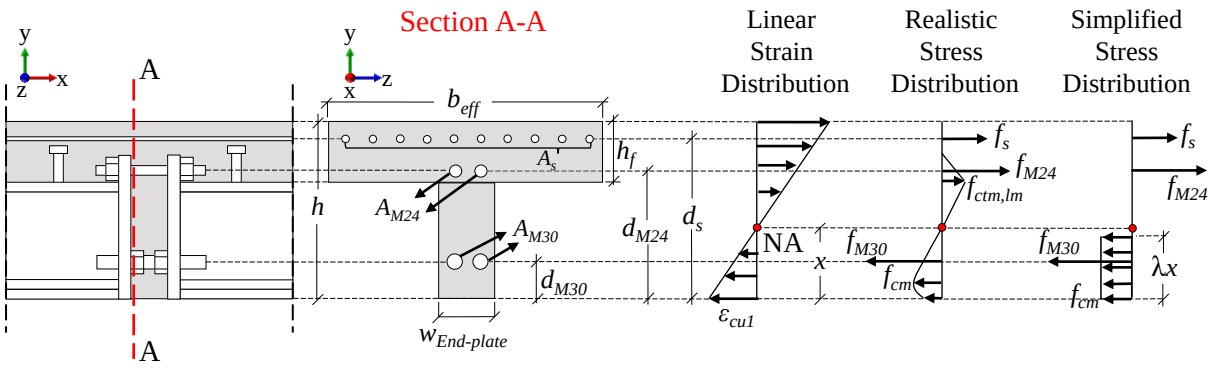

Figure 5.61: Cross-sectional analyses of GJSFB joint configurations.

Considering the fact that the steel beams at both sides of an internal support are not continuous for GJSFB joint configurations, the cross-section at the joints over an internal support could be assumed to be analogically identical to the cross-section of a reinforced-concrete (RC) T-beam. Thereby, the strain-limited design concept defined by EN1992-1-1 [72] could be used to estimate the plastic moment-capacity of the proposed joint configurations. Fig. 5.61 presents the cross-sectional analysis for the ultimate limit states of GJSFB-01 and GJSFB-02 joint configurations performed considering the linear strain distributions across the cross-section according to the Euler-Bernoulli beam theory [70], which indicates that the plain-section remains in plane after bending, and by conservatively assuming that the width of the compressive zone to be equal to the width of the beam-end-plate ($w_{End\text{-}plate}$).

Consequently, the plastic moment-capacity of GJSFB joint configurations could be estimated based on the simplified stress distributions presented in Fig. 5.61 by defining the equilibrium of internal forces and by the summing the moments of the internal forces with respect to the neutral axis (NA) of the cross-section. It is important to highlight that the tensile resistance of concrete is ignored for the aforementioned simplified stress distributions presented in Fig. 5.61.

Eq. 5.5 to Eq. 5.7 formulate the calculations to estimate the plastic-moment capacity of GJSFB-01 joint configuration;

$$\sum F_x = f_{s,m} \cdot A_s - f_{cm} \cdot \lambda \cdot x \cdot w_{End-plate} = 0 \tag{5.5}$$

where;

- $f_{s,m}$ is the mean yield strength of the longitudinal steel reinforcement material,
- A_s is the total nominal area of the longitudinal steel reinforcements,
- f_{cm} is the mean compressive strength of the concrete material,
- λ is the effective height factor for rectangular stress distribution and equal to 0.8 [72].
- $w_{End\text{-}plate}$ is the nominal width of the beam-end-plate.

Thereby, the position of the neutral axis (x) with respect to the lower-most compressed concrete fiber could be determined with Eq. 5.6 for GJSFB-01 joint configuration;

$$x = \frac{f_{s,m} \cdot A_s}{f_{cm} \cdot \lambda \cdot w_{End-plate}} \tag{5.6}$$

Having defined the position of the neutral axis (x), the plastic moment capacity of GJSFB-01 joint configuration could be estimated with Eq. 5.7;

$$M_{j,pl,GJSFB-01} = f_{s,m} \cdot A_s \cdot \left(d_s - \frac{\lambda \cdot x}{2} \right) \tag{5.7}$$

where;

- d_s is the distance between the center of the longitudinal steel reinforcement and the lower most compressed concrete fiber.

Similarly, Eq. 5.8 to Eq. 5.11 formulate the calculations to estimate the plastic-moment capacity of GJSFB-02 joint configuration. It is crucial to mention that due to the relatively high material strength of the threaded-rods (i.e. grade 12.9), it would not be expected the M30 threaded-rods to yield once the lower most compressed concrete fiber reaches its crushing strain (ε_{cu1}) according to the linear strain distribution presented in Fig 5.61b. As a result, the magnitude of the compressive stress; thus, the corresponding stress resultant for the M30 threaded-rods depends on the position of the neutral axis (x). Therefore, the solution of the proposed analytical resistance model to estimate the plastic moment-capacity of GJSFB-02 joint configuration becomes non-linear and requires iterative procedure to determine the position of the neutral axis.

$$\sum F_x = f_{s,m} \cdot A_s + f_{M24,m} \cdot A_{M24} - E_{M30,m} \cdot \varepsilon_{M30} \cdot A_{M30} - f_{cm} \cdot \lambda \cdot x \cdot w_{End-plate} = 0 \tag{5.8}$$

where;

- $f_{M24,m}$ is the mean yield strength of the M24 threaded-rod material,
- $f_{M30,m}$ is the mean elastic stress in M30 threaded-rods and calculated with Eq. 5.9;

$$f_{M30,m} = E_{M30,m} \cdot \varepsilon_{M30} \tag{5.9}$$

- $E_{M30,m}$ is the mean elastic modulus for the M30 threaded-rod material,
- ε_{M30} is the magnitude of the strain in the M30 threaded-rods once the lower most compressed concrete fiber reaches its strain limit (ε_{cu1}) and calculated with Eq. 5.10;

$$\varepsilon_{M30} = \frac{\varepsilon_{cu1} \cdot (x - d_{M30})}{x} \tag{5.10}$$

- d_{M30} is the distance between the M30 threaded-rods and the lower most compressed concrete fiber.
- A_{M24} is the total nominal area of the M24 threaded-rods,
- A_{M30} is the total nominal area of the M30 threaded-rods.

Thereby, the position of the neutral axis with respect to the lower most compressed concrete fiber (x) could be determined iteratively with Eq. 5.11 for GJSFB-02 joint configuration;

$$x = \frac{f_{s,m} \cdot A_s + f_{M24,m} \cdot A_{M24}}{\frac{E_{M30,m} \cdot \varepsilon_{cu1} \cdot (x - d_{M30}) \cdot A_{M30}}{x^2} + f_{cm} \cdot \lambda \cdot w_{end-plate}} \tag{5.11}$$

Having defined the position of the neutral axis (x), the plastic moment capacity of GJSFB-02 joint configuration could be estimated with Eq. 5.12;

$$M_{j,pl,GJSFB-02} = f_{s,m} \cdot A_s \cdot (d_s - x) + f_{M24,m} \cdot A_{M24} \cdot (d_{M24} - x) + E_{M30,m} \cdot \varepsilon_{M30} \cdot A_{M30} \cdot (x - d_{M30}) + f_{cm} \cdot w_{End-plate} \cdot \lambda \cdot x \cdot \left(x - \frac{\lambda^2 \cdot x^2}{2} \right) \tag{5.12}$$

where;

- d_{M24} is the distance between the M24 threaded-rods and the lower most compressed concrete fiber.

It is crucial to note that the upper row of the threaded-rods (M24 threaded-rods) could only resist the tension stress resultants while the bottom row of the threaded rods (M30) could only resist the compressive stress resultants due to the positions of the nuts (see also Fig. 5.12b). Therefore, this information should be considered for the iterative solution of Eq. 5.11 and for the plastic-moment capacity estimation of GJSFB-02 joint configuration with Eq. 5.12 using the following supplementary statements;

$$F_{M24} = \begin{cases} 0 \ , \ if \ d_{M24} \leq x \\ \\ f_{M24,m} \cdot A_{M24} \ , \ otherwise \end{cases} \tag{5.13}$$

$$F_{M30} = \begin{cases} 0 \ , \ if \ x \leq d_{M30} \\ \\ E_{M30,m} \cdot \varepsilon_{M30} \cdot A_{M30} \ , \ otherwise \end{cases} \tag{5.14}$$

where;

- F_{M24} is the total force in the M24 threaded-rods.
- F_{M30} is the total force in the M30 threaded-rods.

Fig 5.62 compares the plastic moment-capacity of GJSFB joint configurations calculated with Eq. 5.7 and Eq. 5.12 with the output results of the FEAs presented in Table 5.12. It could be noticed that the estimations of the presented analytical resistance model are in good agreement for GJSFB-02 joint configurations, in other words for the joints with the threaded-rods. However, the estimations for GJSFB-01 joint configurations, in other words for the joints without the threaded-rods, could be noticed to be conservative. This is mainly due to the fact that the presented analytical model conservatively considers the width of the compressive zone for concrete grout to be equal to the

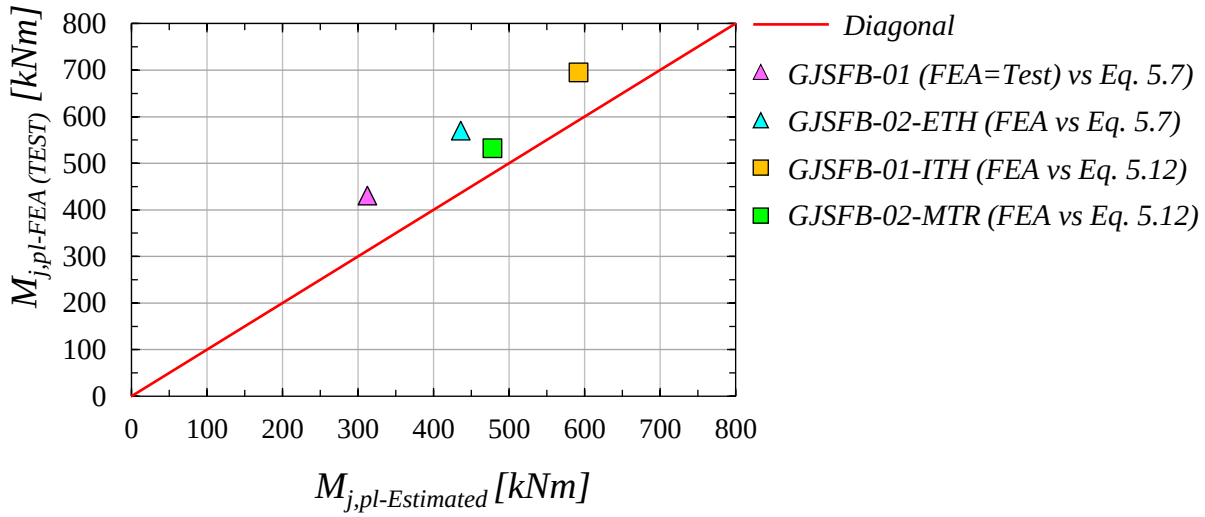

Figure 5.62: Comparison of the plastic moment-capacity estimations of the analytical resistance model with respect to the output results of the FEAs.

width of the beam-end-plate and the impact of this conservative assumption is more obvious for GJSFB-01 joint configuration as the concrete grout is the only component that resist the compressive stress resultants of the bending moments in the joint. Nevertheless, the estimations are shown to be conservative in good agreement with respect to the output results of the FEAs. Therefore, it is concluded that the presented analytical resistance model is suitable to estimate the plastic moment-capacity of GJSFB joint configurations for engineering approximations.

It is important to mention that if the presented analytical equations will be used for design purposes, it is required to replace the mean material properties that appear in Eq. 5.5 to Eq. 5.14 with the design material properties.

It has been earlier demonstrated that the rotation capacity of the composite joints could be estimated by calculating the area under the curvature diagram of a structural system over the effective length of the joint (L_{eff}) at the ultimate limit state of the critical cross-section, which is the cross-section at the joint for this study, by means of the deformation limits, i.e. strain limits of the joint components [106]. In other words, the rotation capacity of a joint could be calculated by integrating the curvatures of the cross-sections along the effective length of the joint. It is the fact that this relation is the result of Euler-Bernoulli beam theory [70] as the curvature (κ) and the rotation (Φ) at an arbitrary point along the longitudinal axis of the beam is defined with Eq. 5.15 for infinitesimal beam length subjected to transverse loading as illustrated in Fig. 5.63;

$$\Phi = \int_0^{dx} \kappa \, dx \tag{5.15}$$

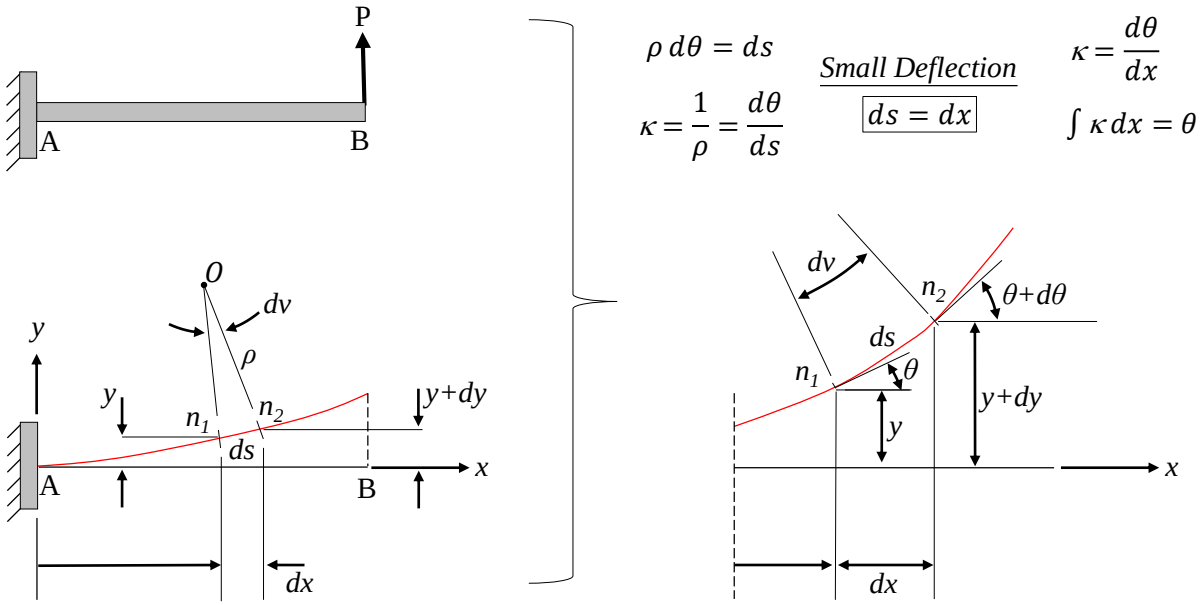

Figure 5.63: Relation between rotation and curvature.

Analogically, the ultimate rotation capacity of GJSFB joint configurations could be estimated with Eq.5.16;

$$\Phi_{j,u,GJSFB} = \int_0^{L_{j,eff}} \kappa(x)\, dx \tag{5.16}$$

where;

- $L_{j,eff}$ is the effective joint length in which the plastic hinge formation develops, in other words the reinforcements of a composite joint yields, thus the most of the sectional curvature is accumulated at the ultimate deformation limit of the joint along this length.
- κ is the curvature.

The accumulation of the curvatures along the effective joint length is illustrated in Fig. 5.64 together with deflection profile of a continuous beam for better explanation of the relation between the curvature and the joint rotation.

Thereby, if the effective length of the joint is defined for the deformation limit, i.e. strain limit, along the cross-section of the joint and by assuming the curvature of the joint to be constant along the effective joint length, the ultimate rotation capacity of GJSFB joint configurations could be estimated algebraically with Eq. 5.17.

$$\Phi_{j,u,GJSFB} = L_{j,eff} \cdot \kappa_{j,lim,GJSFB} \tag{5.17}$$

where;

- $\kappa_{j,lim,GJSFB}$ is defined with Eq. 5.18 based on the linear strain distribution at the cross-section of the joint for the strain limit of the critical joint component.

$$\kappa_{j,lim,GJSFB} = \frac{\varepsilon_{lim}}{d_{NA}} \tag{5.18}$$

- ε_{lim} is the limiting strain for the deformation of the critical joint component (e.g. crushing strain of the concrete grout, necking strain of the steel reinforcements or the threaded-rods).
- d_{NA} is the distance between the cross-sectional point where the limiting strain is attained and the neutral axis of the joint cross-section.

There has been many attempts to define the effective joint length of composite joints based on the diameter and the ratio of the longitudinal steel reinforcements [89, 91] and based on the total depth of the composite cross-section [96]. In addition, EN1994-1-1 [2] indirectly defines this length as the half width of the column where the composite joint is connected. However, it was shown by Duarte da Costa [89], the definition of EN1994-1-1 [2] is not sufficient to estimate the ultimate rotation capacity of the composite joints. In addition, the proposed GJSFB joint configurations are also not consisted with the composite joint definition of EN1994-1-1 [2]. Therefore, there is a need for a new definition of the effective joint length for the estimation of the ultimate rotation capacity of GJSFB joint configurations.

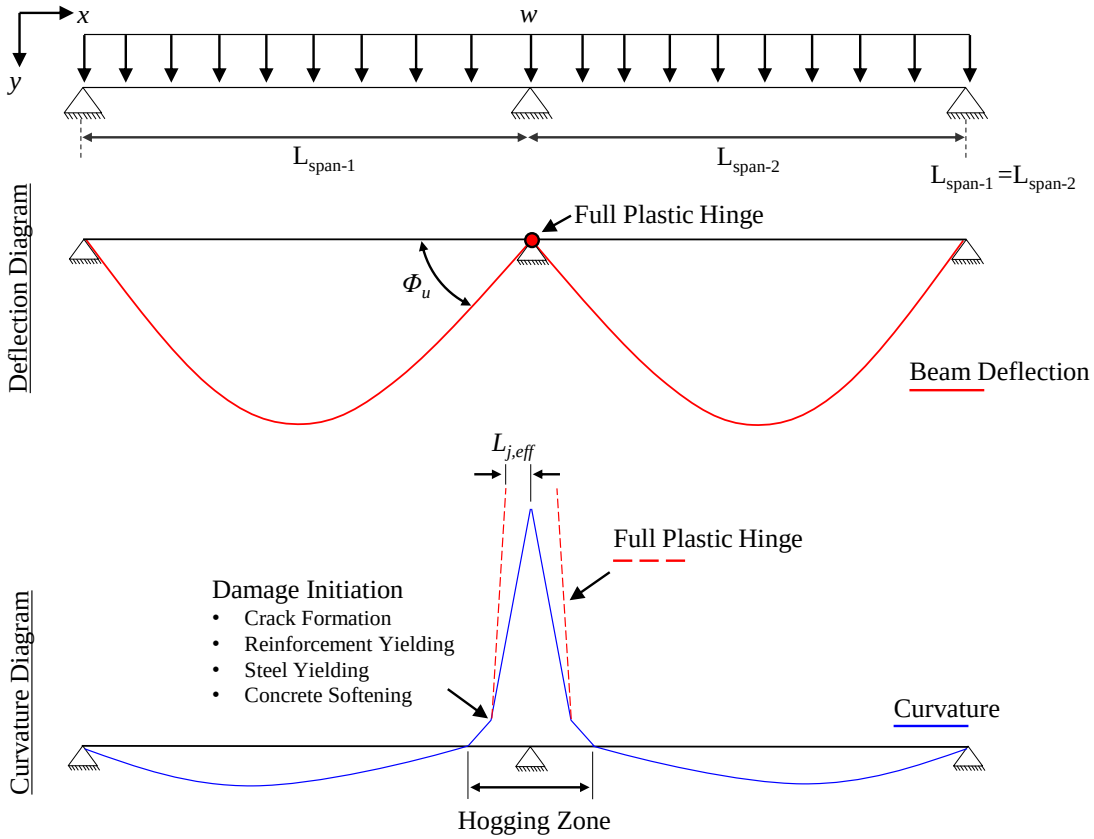

Figure 5.64: Curvature diagram of a continuous composite beam at the ultimate deflection limit.

In this thesis, the effective joint length is proposed to be equal to the distance between the internal support of a continuous composite beam and the last fully cracked section along the depth of the concrete slab. Fig. 5.65 illustrates this definition. It is the fact that the crack formations along the longitudinal axis of the composite beams develops at several locations at the ultimate deformation limit of the joint and it was shown that there is a limit distance with respect to the mid-span of the test specimen for the development of the cracks (see Fig. 5.23 and Fig. 5.35). Furthermore, it was also shown in the previous sections that the longitudinal steel reinforcements yield not only at one position but at several positions along the longitudinal axis of the composite beam (see Fig. 5.26 and Fig. 5.57, Fig. 5.38 and Fig. 5.58). Therefore, it is concluded from the observations of the experimental tests and the detailed investigations of the numerical simulations that the distance between the internal support and the last fully developed tensile crack along the depth of the concrete slab could be accepted as the effective joint length for GJSFB joint configurations.

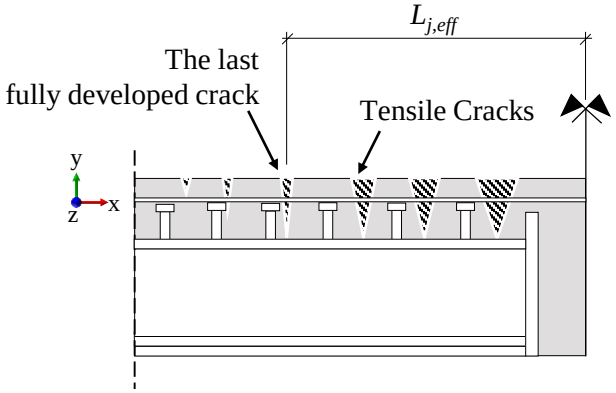

Figure 5.65: Illustration of the effective joint length for the proposed GJSFB joint configurations.

The position of the last full crack along the depth of the concrete slab for the hogging zone of a continuous composite beam at the ultimate deformation limit of the joint could also be estimated based on the strain limited design concept for which the limiting strain is set to be equal to the flexural tensile cracking strain of the concrete at the lower most concrete fiber of the slab. Fig. 5.66 illustrates the strain and simplified stress distribution for a cross-section of the composite slim-floor beam. According to Fig. 5.66, which ignores the compressive and tensile strength of concrete encasement and the web of the steel beam and assumes uniform stress distribution along the depth of the bottom plate and the beam flanges, and assuming that all of the components along the cross-section at their elastic stages the equilibrium condition along the cracked cross-section (*A*-*A*) could be defined with Eq. 5.19;

$$\sum F_x = f_{s,m} \cdot A_s + f_{uf} \cdot A_{uf} - f_{lf} \cdot A_{lf} - f_{bp} \cdot A_{bp} = 0 \tag{5.19}$$

where;

- A_s is the total cross-sectional area of the longitudinal reinforcements.

- A_{uf} is the cross-sectional area of the upper flange.
- A_{lf} is the cross-sectional area of the lower flange.
- A_{lf} is the cross-sectional area of the bottom plate.

In addition, the magnitude of the stresses that appear in Eq. 5.19 could be determined with following expressions;

$$f_s = E_{s,m} \cdot \varepsilon_s \cdot A_s \tag{5.20}$$

$$f_{upper-flange} = E_{b,m} \cdot \varepsilon_{uf} \cdot A_{uf} \tag{5.21}$$

$$f_{lower-flange} = E_{b,m} \cdot \varepsilon_{lf} \cdot A_{lf} \tag{5.22}$$

$$f_{bottom-plate} = E_{bp,m} \cdot \varepsilon_{bp} \cdot A_{bp} \tag{5.23}$$

where;

- $E_{s,m}$ is the mean modulus of elasticity of the steel material for longitudinal reinforcements.
- $E_{b,m}$ is the mean modulus of elasticity of the steel material for beam.
- $E_{bp,m}$ is the mean modulus of elasticity of the steel material for bottom plate.
- ε_s is the strain at the centroid of the longitudinal reinforcements.
- ε_{uf} is the strain at the centroid of the upper flange.
- ε_{lf} is the strain at the centroid of the lower flange.
- ε_{bp} is the strain at the centroid of the bottom plate.

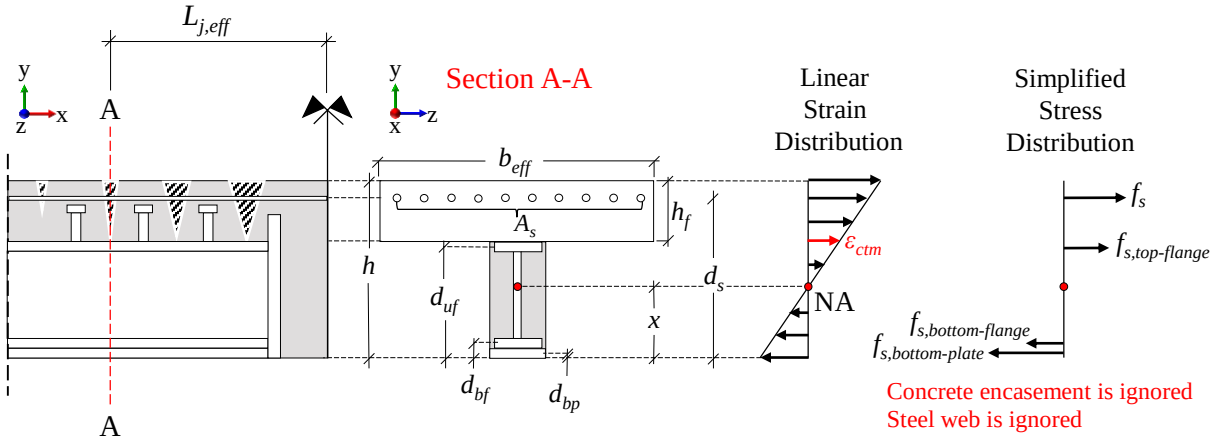

Figure 5.66: Strain and corresponding stress states for the cross-section at the last full crack.

Furthermore, the strain at the geometric center of the longitudinal reinforcements, upper flange, lower flange and the bottom plate could be calculated with Eq. 5.24 to Eq. 5.27 based on the position of the neutral axis (x);

$$\varepsilon_s = \frac{\varepsilon_{ctm} \cdot (d_s - x)}{h - x - h_f} \tag{5.24}$$

$$\varepsilon_{uf} = \frac{\varepsilon_{ctm} \cdot (d_{uf} - x)}{h - x - h_f} \tag{5.25}$$

$$\varepsilon_{lf} = \frac{\varepsilon_{ctm} \cdot (x - d_{lf})}{h - x - h_f} \tag{5.26}$$

$$\varepsilon_{bp} = \frac{\varepsilon_{ctm} \cdot (x - d_{bp})}{h - x - h_f} \tag{5.27}$$

where;

- ε_{ctm} is the tensile strain limit for the initiation of the cracks and formulated with Eq. 5.28;

$$\varepsilon_{ctm} = \frac{f_{ctm,fl}}{E_{cm}} \tag{5.28}$$

- $f_{ctm,fl}$ is the mean flexural tensile strength of concrete calculated according to EN1992-1-1 [72].
- E_{cm} is the mean modulus of elasticity of concrete.

Thereby, the equilibrium condition presented in Eq. 5.19 could be re-written using the expression presented in Eq. 5.20 to Eq. 5.28 to estimate the position of the neutral axis;

$$\begin{aligned} \sum F_x = \frac{\varepsilon_{ctm}}{h - x - h_f} \cdot \big(& E_{s,m} \cdot (d_s - x) \cdot A_s + E_{b,m} \cdot (d_{uf} - x) \cdot A_{uf} \\ & - E_{b,m} \cdot (x - d_{lf}) \cdot A_{lf} - E_{bp,m} \cdot (x - d_{bp}) \cdot A_{bp} \big) = 0 \end{aligned} \tag{5.29}$$

Furthermore, assuming modulus of elasticity for all of the steel components (reinforcements, beam, bottom plate) to be identical and equal to $E_{s,m}$, Eq. 5.29 reduces to Eq. 5.30;

$$(d_s - x) \cdot A_s + (d_{uf} - x) \cdot A_{uf} - (x - d_{lf}) \cdot A_{lf} - (x - d_{bp}) \cdot A_{bp} = 0 \tag{5.30}$$

Solving Eq. 5.30, the position of the neutral axis (x) could be determined for the investigated cross-section (see Fig. 5.66 - Section A-A) where the last full tensile crack develops along the longitudinal axis of the beams. Thereafter, the internal moment at the cross-section could be calculated with Eq. 5.31;

$$M_{A-A,int} = E_{s,m} \cdot \frac{\varepsilon_{ctm}}{h - x - h_f} \cdot \left((d_s - x)^2 \cdot A_s + (d_{uf} - x)^2 \cdot A_{uf} + (x - d_{lf})^2 \cdot A_{lf} + (x - d_{bp})^2 \cdot A_{bp} \right) \tag{5.31}$$

In addition, the external moment action at the location of the last full cracked cross-section could also be calculated with Eq. 5.32 using the equivalent simply supported beam configuration of the hogging zone identical to the test set-up at the ultimate load-bearing limit of GJSFB joint configurations as illustrated in Fig. 5.67.

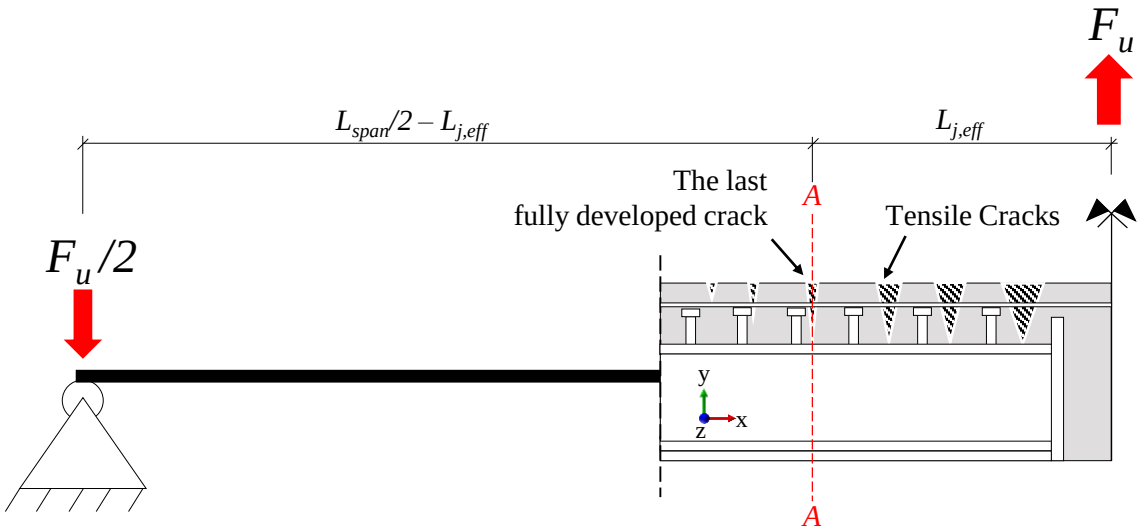

Figure 5.67: Equivalent simply supported beam configuration of the hogging zone with the illustration of the effective joint length ($L_{j,eff}$)

.

$$M_{A-A,ext} = \frac{2 \cdot M_{pl,j-GJSFB} \cdot \left(\frac{L_{span}}{2} - L_{j,eff} \right)}{L_{span}} \tag{5.32}$$

Finally, equating Eq. 5.31 and Eq. 5.32, the effective joint length for GJSFB joint configurations could be expressed analytically with Eq. 5.33;

$$L_{j,eff} = \frac{L_{span}}{2} - \frac{\frac{L_{span} \cdot E_{s,m} \cdot \varepsilon_{ctm}}{h - x - h_f} \cdot \left((d_s - x)^2 \cdot A_s + (d_{uf} - x)^2 \cdot A_{uf} + (x - d_{lf})^2 \cdot A_{lf} + (x - d_{bp})^2 \cdot A_{bp} \right)}{2 \cdot M_{j,pl,GJSFB}} \tag{5.33}$$

where;

- L_{span} is the span-length of the equivalent simply supported beam configuration of the hogging zone for a continuous composite beam.
- $M_{pl,j,GJSFB}$ is the plastic moment-capacity of a GJSFB joint configuration.

The formulations for the calculation of the plastic moment-capacity of GJSFB joint configurations ($M_{j,pl,GJSFB}$) that appear in Eq. 5.33 were earlier presented with Eq. 5.7 and Eq. 5.12.

Having defined the effective joint length, Eq. 5.17 could be used to estimate the ultimate rotation capacity of GJSFB joint configurations. It is the fact that the limit curvature ($\kappa_{j,lim,GJSFB}$) that appears in Eq. 5.17 was earlier defined for GJSFB-01 joint configuration in Fig. 5.61a based on the crushing state of the lower-most compressed concrete fiber. Thereby, the ultimate rotation capacity of GJSFB-01 joint configurations could be estimated with Eq. 5.34;

$$\Phi_{j,u,GJSFB-01} = L_{j,eff} \cdot \frac{\varepsilon_{cu1}}{x} \tag{5.34}$$

where;

- ε_{cu1} is the ultimate compressive strain in the concrete grout at the joint and determined according to EN1992-1-1 [72] for the mean properties of the concrete material used in the test (see Table 5.2).
- x is the position of the neutral axis with respect to the lower-most compressed concrete fiber at the cross-section of the joint and calculated with Eq. 5.6.

Although, it was earlier shown in Fig. 5.58c that the limiting mechanism for the rotation capacity of GJSFB-02 joint configuration was the necking of the M24 threaded-rods that resist the tensile stress resultants of the bending moment in the joint, this limiting mechanism could only be achieved if the tensile strength of the concrete grout, the residual compressive strength of the concrete grout and the plastic distribution of the compressive stresses along the entire volume of the concrete grout could be taken into account (also see Fig. 5.58b) as it is otherwise not possible to satisfy the force equilibrium in the cross-section of the joint. As a result, for the analytical calculations, it is not feasible to consider the entire stress state at the joint that allows the deformation state for the threaded-rods to reach their necking strain. Therefore, to be able to estimate the ultimate rotation capacity of GJSFB-02 joint configuration with strain-limited design concept, an ultimate deformation state along the cross-section of GJSFB-02 joint configuration is defined based on the

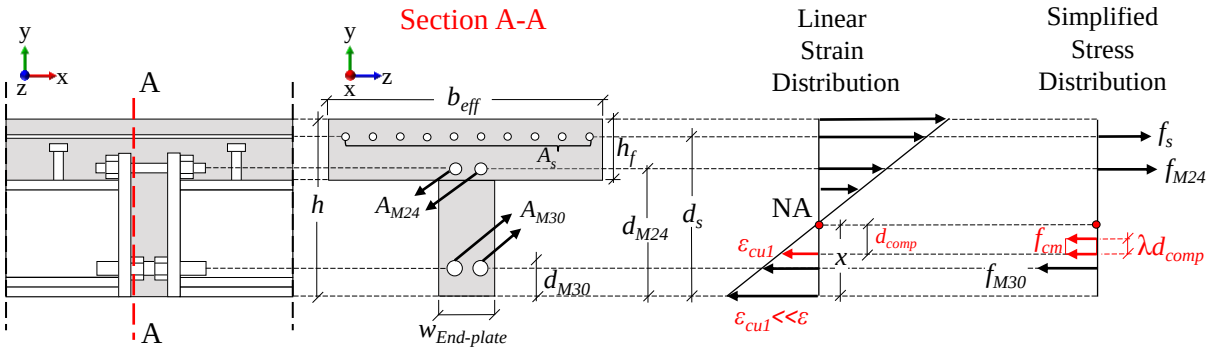

Figure 5.68: Ultimate deformation state based on the force equilibrium for the simplified stress distribution for the cross-section of GJSFB-02 joint configuration.

equilibrium of the forces for which the M24 and M30 threaded-rods, and the longitudinal steel reinforcements yield and assuming that the lower-most concrete grout has already crushed. Fig. 5.68 shows the cross-sectional analysis for the assumed ultimate deformation state. According to the presented linear strain distribution, it could be seen that the strain limit for the concrete grout is defined at an arbitrary position nominated as d_{comp} with respect to the neutral axis (NA). Considering this position as the ultimate deformation limit of the cross-section as the further strain increment would cause the reduction in the moment-capacity of the joint if the equilibrium condition for the simplified stress distribution is defined with Eq. 5.35;

$$\sum F_x = f_{s,m} \cdot A_s + f_{M24,m} \cdot A_{M24} - f_{M30,m} \cdot A_{M30} - f_{cm} \cdot \lambda \cdot d_{comp} \cdot w_{End-plate} = 0 \tag{5.35}$$

Thereby, the arbitrary position of the concrete fiber at the limiting strain for the ultimate deformation state of the joint cross-section could be expressed with Eq. 5.36;

$$d_{comp} = \frac{f_{s,m} \cdot A_s + f_{M24,m} \cdot A_{M24} - f_{M30,m} \cdot A_{M30}}{f_{cm} \cdot \lambda \cdot w_{End-plate}} \tag{5.36}$$

where;

- $f_{M30,m}$ is the mean yield strength of the M30 threaded-rod material,;
- d_{comp} is the distance between the neutral axis and the concrete fiber that reached the limiting strain.

Having defined the distance between the neutral axis and the concrete fiber of the strain limit. The curvature at the cross-section of GJSFB-02 joint configuration for the ultimate deformation state could be defined with Eq. 5.37

$$\kappa_{j,u,GJSFB-02} = \frac{\varepsilon_{cu1}}{d_{comp}} \tag{5.37}$$

Finally, the ultimate rotation capacity of GJSFB-02 joint configuration could be estimated by substituting Eq. 5.33 and Eq. 5.37 into Eq. 5.17 as presented in Eq. 5.38

$$\Phi_{j,u,GJSFB-02} = L_{j,eff} \cdot \frac{\varepsilon_{cu1}}{d_{comp}} \tag{5.38}$$

Fig. 5.69 compares the ultimate rotation capacity of GJSFB joint configurations calculated with Eq. 5.34 and Eq. 5.38 with the output results of the FEAs presented in Table 5.12. It could be noticed that the estimations of the presented analytical rotation model are in good agreement for both GJSFB-01 and GJSFB-02 joint configurations. Therefore, it is concluded that the presented analytical rotation model is promising to estimate the ultimate rotation capacity of GJSFB joint configurations for engineering approximations considering the simplicity of the proposed methodology.

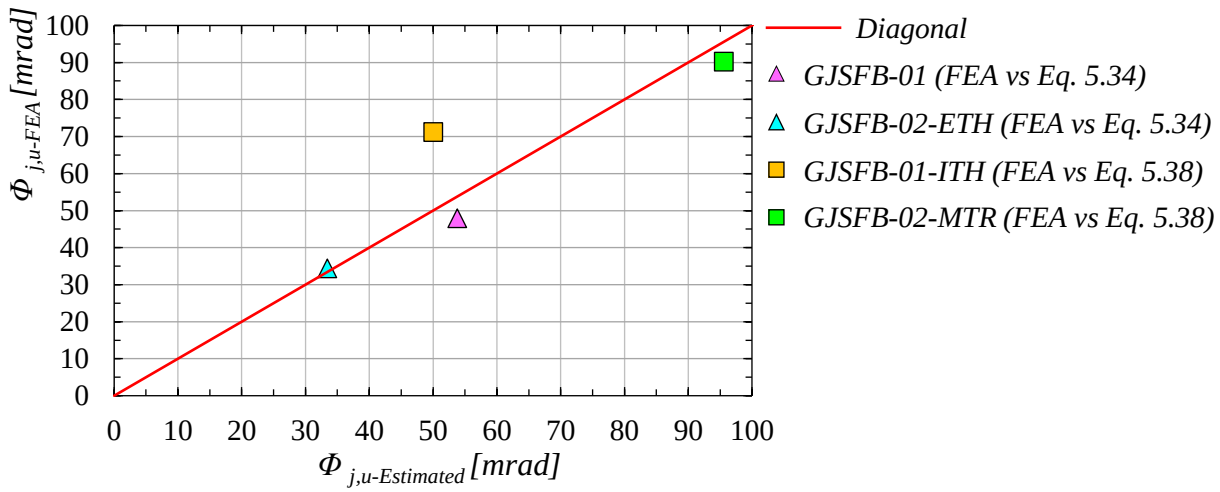

Figure 5.69: Comparison of the ultimate rotation capacity estimations of the analytical rotation model with respect to the output results of the FEAs.

It is important to note that the analytical expressions presented in this section were developed for symmetric continuous slim-floor beams by means of both geometry and loading. In addition, full bond was assumed between steel reinforcements and the concrete slab. Therefore, the application of the analytical expressions is limited to the scope of this thesis and it is required to further validate them with additional test results.

5.5 Summary

This chapter presented the investigations performed to determine the moment-rotation behaviors of the novel joints, *"Grouted Joints for Continuous Slim-floor Beams"*, proposed for the steel-concrete hybrid building systems.

Two separate full-scale experimental tests were performed and the moment-rotation behaviors of the proposed joint configurations were established for the equivalent hogging moment zones of symmetric steel-concrete continuous slim-floor beams. The ratio of the continuous longitudinal steel reinforcements and the existence of the threaded-rods at the joint was selected as the variable parameters of the experimental tests. According to the test results, the reasons behind the softening of the moment-rotation behaviors for each of the joint configurations were explained in detail and it was shown that the development of the tensile cracks for the continuous concrete slab determines the moment-rotation characteristics of the proposed joint configurations at the beginning of the loading history. According to this outcome, it was also shown that the initial rotational stiffness of the proposed joint configurations is nearly independent of the ratio of the longitudinal reinforcements and the existence of the threaded-rods. On the other hand, the test results showed that the ultimate load-bearing capacity of the proposed joint configurations highly depends on the ratio of the longitudinal steel reinforcements and the existence of the threaded-rods.

The experimental tests were simulated with computer-aided finite element analyses to estimate the ultimate rotation capacity of the proposed joint configurations as the tests were deliberately terminated due to the high deformations and the longitudinal shear failure of the test specimens before attaining the ultimate rotation capacities of the proposed joint configurations. The finite element modelling technique and the dynamic-explicit solution scheme of the finite element analyses were validated against the experimental test results. Thereby, additional finite element analyses were performed by varying the test parameters to be able to further understand the impact of the selected parameters on the load-bearing and the rotation capacities of the proposed joint configurations. Based on the output results of the finite element analyses, it was shown that the plastic moment capacity of the proposed joint configurations was attained once all of the longitudinal steel reinforcements along the effective cross-sectional width were yielded and the ultimate rotation capacity of the joint was limited to the crushing of the concrete grout if the threaded-rods were omitted. On the contrary, it was also shown that the plastic moment capacity and the rotation capacity of the proposed joint configurations were limited to the ultimate load-bearing and the deformation capacities of the threaded-rods if they were included in the joint.

According to the experimental tests and the output results of the finite element analyses, the proposed joint configurations were classified as *"Semi-rigid"* and *"Partial-strength"* joints based on the stiffness and the strength classification boundaries of EN1994-1-1 [2] for the tested cross-section of the steel-concrete composite slim-floor beams.

Based on the observations made during the experimental tests and the output results of the finite element analyses, analytical resistance models were developed to estimate the ultimate load-bearing and the rotation capacities of the proposed joint configurations. The estimations of the analytical resistance and rotation models were shown to be in good agreement with the test results and the output results of the finite element analyses. Therefore, it was concluded that the analytical resistance and rotation models could be used for engineering approximations for the capacity estimation of the proposed joint configurations to be used in steel-concrete hybrid building systems.

It is important to highlight that the experimental tests, the numerical simulations and the corresponding analytical expressions presented in this chapter were based on the equivalent hogging moment zone of the symmetric double span continuous steel-concrete composite slim-floor beams. Therefore, the constructibility of the proposed joint configurations and the estimations of the analytical resistance and rotation models should be further investigated with full-scale experimental tests including the sagging zone and considering the various loading conditions with different cross-sectional details of continuous slim-floor beams.

CHAPTER 6

Conclusion and Recommendations for Further Research

6.1 Conclusion

This thesis presents three novel structural joint configurations for the fast erection of steel beams with reinforced-concrete columns and walls of steel-concrete hybrid building systems. It has been shown that the proposed joint configurations eliminate on-site welding, minimize the use of structural bolts and allow the accommodation of the construction and manufacturing tolerances for the assembly of the steel beams with the reinforced concrete columns and walls of steel-concrete hybrid building systems.

The load-deformation behaviors of the proposed joint configurations were determined with different experimental test campaigns. In total twenty-eight experimental tests were conducted under six different experimental test campaigns as summarized below;

1. *Saw-tooth Interface Mechanical Interlock Bolted Connection (SMIBC)*
    - *SMIBC load-bearing capacity tests without load-eccentricity - 6 Tests (SMIBC-E0)*
    - *SMIBC load-bearing capacity tests with load-eccentricity - 9 Tests (SMIBC-E1)*
    - *SMIBC anchorage tests for reinforced-concrete columns - 3 Tests (SMIBC-CC)*
    - *CNC-cut saw-tooth surfaces slip-factor determination tests - 5 Tests*
2. *Bolt-less Plug-in Connection (Plug-inC)*
    - *Plug-inC load-bearing capacity tests with load-eccentricity - 3 Tests (Plug-inC)*
3. *Grouted Joints for Continuous Composite Slim-floor Beams (GJSFB)*
    - *Grouted Joint without threaded-rods load bearing capacity test - 1 Test (GJSFB-01)*
    - *Grouted Joint with threaded-rods load bearing capacity test - 1 Test (GJSFB-02)*

All of the test specimens for the aforementioned test campaigns were produced by industrial companies using the existing production methodologies. Thereby, it has been proven that the components of the proposed joint configurations are suitable for mass production with the equipment and methods now in use by industrial producers and general construction contractors.

All of the aforementioned experimental test campaigns except the slip-factor determination tests were modelled with the computer aided finite element analysis method to further investigate the failure mechanisms of the joint components and to clarify the load distribution between the joint components. The output results of the finite element analyses were validated against the experimental tests and they were used to determine the ultimate deformation limits for each component of the proposed joint configurations. Furthermore, numerical parametric studies were carried out using the validated finite element models to determine the impacts of the basic geometrical, material, and contact parameters of the joint components as well as the load-eccentricity on the load-deformation behaviors of the proposed joint configurations.

According to the results of the experimental tests and the finite element analyses, simplified analytical models were developed to estimate the load-bearing capacities of the proposed joint configurations. The estimations of the analytical models were shown to be in good agreement with the results of the experimental tests and the parametric finite element analyses. Furthermore, statistical evaluations were performed for the analytical resistance models of SMIBC and Plug-inC to establish partial safety factors for the analytical resistance model of these joint configurations. In addition, a separate analytical model was developed to predict the ultimate rotation capacities of GJSFB joint configurations in order to enable engineers to use GJSFB joint configurations for the elastic and rigid plastic global structural analyses of continuous composite slim-floor beams.

6.2 Summary and recommendations for further research

The followings are the summary of the outcomes from the experimental, numerical, and analytical investigations executed as part of this thesis together with the suggestions for further research for each of the proposed joint configurations:

Saw-tooth Interface Mechanical Interlock Bolted Connection (SMIBC)

1. The experimental, numerical and analytical investigations of SMIBC were performed with 8.8 Grade HR-bolts. The load-bearing capacity of SMIBC under loading with an eccentricity larger than 15mm was shown to be governed by the load-deformation behavior and the ultimate load-bearing capacity of the bolts. It was also shown that the use of HR-bolts results in brittle failure of SMIBC under loading with an eccentricity larger than 15mm. Therefore, further research is required with different bolt grades and bolt types (e.g. HV-bolts) to determine the load-deformation behavior of SMIBC with different structural bolts.
2. Although it was demonstrated with SMIBC-E1 test campaign that the level of the initial bolt pre-tension is not decisive for the ultimate load-bearing capacity of SMIBC under static loading conditions, it is crucial to mention that a certain pre-tension load is required to secure the saw-tooth interface of SMIBC. Therefore, loss of the initial bolt pre-tension load during

the service life of SMIBC should be investigated to determine the level of the initial bolt pre-tension load required to be applied for SMIBC.

3. The load-deformation behavior of SMIBC for different load-eccentricities was investigated with a numerical parametric study. However, SMIBC-E1 test campaign was conducted with a single load-eccentricity. Therefore, further experimental investigation is required to determine the load-deformation behavior of SMIBC under different load-eccentricities and to validate the estimations of the numerical models and the predictions of the analytical design model.
4. The load-deformation behaviour of SMIBC was determined under static loading applied with and without load-eccentricity. However, no investigation was provided to determine the structural integrity and the load-deformation behavior of the saw-tooth interface under seismic actions, fire, and cyclic loading conditions. Therefore, further research is required to investigate the reliability of SMIBC under different loading conditions.
5. The magnitude of the static friction coefficient between the saw-tooth surfaces of the anchor and corbel plates was shown to be an important parameter of the ultimate load-bearing capacity of SMIBC under static loading applied with load-eccentricity. The impact of the friction coefficient on the load-deformation behavior of SMIBC for static loading applied with load-eccentricity was investigated with a numerical parametric. However, the impact of the surface finishing for the saw-tooth surfaces on the load-deformation behavior of SMIBC needs to be further investigated to guarantee the reliability of SMIBC for different surface conditions.
6. The connection between a steel beam and SMIBC is designed to be a simple, i.e. pin, connection without any moment transfer from the beam to the reinforced concrete column and walls. However, the joint configuration of SMIBC could be modified by the addition of a contact plate between the steel beam and the anchor plate and by extending the longitudinal steel reinforcements of the reinforced-concrete slab into the column and wall. Accordingly, further research may enable SMIBC joint configuration to be developed as semi-rigid or rigid joints.
7. SMIBC-CC test campaign demonstrated the constructability of SMIBC joint configurations for reinforced-concrete columns and the success of SMIBC to accommodate construction and manufacturing tolerances. However, neither experimental tests nor numerical simulations were performed for the anchorage of SMIBC joint configuration with reinforced-concrete walls. Therefore, additional experimental studies may be required to determine the anchorage details of SMIBC joint configuration with reinforced-concrete walls.
8. Although different reinforcement details were tested for the anchorage of SMIBC in SMIBC-CC test campaign, neither the headed-fasteners nor the concrete class was parameterized for the experimental and the numerical investigations. Therefore, additional research effort with the parametrization of the headed-fasteners and the concrete material properties may enable further development of the anchorages for SMIBC joint configuration and the calibration of the modified methodology proposed to determine the ultimate load-bearing capacity of

anchorages with headed-fasteners for use in concrete.

9. Further research is required to establish analytical expressions for the prediction of the load-deformation characteristics (i.e. translational and rotational stiffness) and the ultimate deformation limits of SMIBC and SMIBC joint configurations.

Bolt-less Plug-in Connection (Plug-inC)

1. For Plug-inC experimental test campaign, the components of equivalent Plug-inC test specimens were assembled without the need for special tools, on-site welding, structural bolts or specially trained construction workers. Thus, the simplicity of the assembly of Plug-inC components was demonstrated.
2. Only a limited number of experimental tests (3 tests) were performed to determine the load-deformation behaviors of Plug-inC. In addition, only a single material grade was used for the experimental and numerical investigations performed to determine the load-deformation behaviors of Plug-inC. Therefore, additional experimental tests may be necessary to determine the load-deformation behaviors of Plug-inC with different material grades of the connection components.
3. The experimental tests showed that the fitting tolerances between the hub and the dovetail components significantly affect the initial load-bearing characteristics of Plug-inC. Therefore, the fitting tolerances may be reduced, and the surface finishing of the hub and dovetail components may be carried out with special attention to minimize the impact of the fitting tolerances on the load-deformation behaviors of Plug-inC.
4. The experimental, numerical and analytical investigations showed that there is a relatively high difference between the elastic and the ultimate load-bearing capacities of Plug-inC. Therefore, the impact of Plug-inC deformations on the mechanical response of a structural system, where Plug-inC is used to assemble the beams and columns, needs to be investigated.
5. The load-deformation behaviors of Plug-inC for different load-eccentricities were investigated with a numerical parametric study. However, Plug-inC test campaign was conducted with a single load-eccentricity. Therefore, further experimental research is required to determine the load-deformation behaviors of Plug-inC under different load-eccentricities and to validate the estimations of the numerical models and the predictions of the analytical design models.
6. It was demonstrated by a numerical parametric study that the magnitude of the static friction coefficient between the hub and the dovetail components of Plug-inC significantly impacts the ultimate load-bearing capacity of Plug-inC under static loading applied with eccentricity. Therefore, the impact of the surface finishing for the hub and the dovetail on the load-deformation behaviors of Plug-inC needs to be further investigated to guarantee the reliability of Plug-inC for different surface conditions.

7. The load-deformation behaviours of Plug-inC were determined under static loading applied with eccentricity. However, no investigation was provided to determine the structural integrity and the load-deformation behaviors of the hub-dovetail interaction under seismic actions, fire, and cyclic loading conditions. Therefore, further research is required to investigate the reliability of Plug-inC under different loading conditions.
8. Although it is possible to use anchorage details similar to the ones used in SMIBC-CC test campaign for Plug-inC joint configurations, no experimental, numerical and analytical investigations were performed for the anchorage of Plug-inC with reinforced-concrete columns and walls. Therefore, further research is necessary to determine the load-deformation behaviors of the anchorages in reinforced-concrete columns and walls for Plug-inC joint configurations.
9. The connection between a steel beam and Plug-inC is designed to be a simple, i.e. pin, connection without any moment transfer from the beam to the reinforced concrete column and walls. However, the joint configuration of Plug-inC could be modified by the addition of the contact plate between the steel beam and the anchor plate and by extending the longitudinal steel reinforcements of the reinforced-concrete slab into the column and wall. Accordingly, further research may enable Plug-inC joint configuration to be developed as semi-rigid or rigid joints.
10. Further research is required to establish analytical expressions for the prediction of the load-deformation characteristics (i.e. translational and rotational stiffness) and the ultimate deformation limits of Plug-inC.

Grouted Joints for Continuous Composite Slim-floor Beams (GJSFB)

1. The construction of GJSFB test specimens was executed by a construction contractor in the structural laboratory hall of the University of Luxembourg without the need of special tools, on-site welding, structural bolts, pre-tension application or specially trained construction workers. In addition, the proposed joint configurations were shown to be successful to accommodate the construction and the manufacturing tolerances. Therefore, GJSFB joint configurations could be considered to be practical solutions for the assembly of continuous composite slim-floor beams with the reinforced-concrete columns and walls of steel-concrete hybrid building systems.
2. The experimental, numerical and analytical investigations of GJSFB joint configurations were performed for symmetric span and loading conditions of the continuous slim-floor beams. Therefore, it is also required to perform the aforementioned investigations with unsymmetric span and loading conditions to be able to understand the load-deformation behaviors of GJSFB joint configurations under the unsymmetric conditions and to investigate the structural reliability of GJSFB joint configurations.

3. The ultimate rotation capacities of the tested GJSFB joint configurations were determined with numerical simulations due to the deliberate terminations of the experimental tests as a result of excessive deformation (GJSFB-01) and longitudinal shear failure (GJSFB-02) of the test specimens. Therefore, it may be required to perform additional experimental tests to validate the prediction of the numerical simulations in terms of the ultimate rotation capacities of the tested GJSFB joint configurations.
4. Cast-in-situ concrete was used for the grout of GJSFB joint configurations. However, to resist the compression stress resultants at the joint under hogging moments, it may be possible to use different grout materials such as high-performance cast-in-situ fibre-reinforced cement or to install a contact plate between the beam-end plates for GJSFB joint configurations. Consequently, additional research may enable further development of GJSFB joint configurations in terms of both strength and ductility.
5. The existence of the threaded-rods and the ratio of the longitudinal steel reinforcements were shown to have a very low influence on the initial rotational stiffness of GJSFB. However, further experimental, numerical and analytical investigations are required to validate these observations as some of the previous research in the literature has shown the impact of these parameters on the stiffness of the composite joints for continuous composite slim floor beams.
6. The loading history and the cracking condition of the reinforced-concrete slabs were shown to have significant influences on the initial rotational stiffness of GJSFB joint configurations. Therefore, additional experiments with different loading conditions may enable to further understanding of the load-deformation behaviors of GJSFB joint configurations.
7. The load-deformation behaviours of GJSFB joint configurations were determined under static loading conditions. No investigation was provided to determine the structural response of the GJSFB joint configurations under seismic actions, fire, and cyclic loading conditions. Therefore, further research is required to investigate the structural reliability of GJSFB joint configurations under different loading conditions.
8. The GJSFB joint configurations investigated in this thesis were classified as ”Semi-rigid” and ”Partial-strength” joints based on the stiffness and the strength classification boundaries of EN1994-1-1 [2] for the cross-sections of the tested composite slim-floor beams. On the other hand, utilization of different grout materials, installation of a contact plate between the beam-end plates, and usage of different reinforcement ratios with a different cross-section of steel beam may result in GJSFB joint configurations to be classified as ”Nominally-Pin” or ”Rigid” joints. Thus, it is required to perform further experimental, numerical and analytical parametric studies and define engineering design charts to achieve large-scale market integration of GJSFB joint configurations in the construction industry.

ANNEX A

Determination of slip-factor between CNC-cut saw-tooth surfaces of steel plates

To be able to determine the slip-factor between the CNC-cut saw-tooth surfaces of Saw-tooth Mechanical Interlock Bolted Connection (SMIBC) presented in Chapter 3, a slip factor determination test campaign was established according to EN1090, Annex G [59]. The results presented under this annex is also published as a separate research paper [4].

A.1 Slip factor determination tests

Five experimental tests were performed according to EN1090-2, Annex G [59] to determine the slip factor between the CNC-cut saw-tooth surfaces prepared from S355J2 grade steel plates. The geometry of the saw-tooth threads were kept identical with the saw-tooth threads of SMIBC presented in Fig. 3.1. In addition the production methodology of the saw-tooth surfaces was also kept identical with the production of the saw-tooth surfaces for SMIBC test specimens (see Fig. 3.2). The overall geometry and the technical drawings of the test set-up, the test specimens and the configuration of the measurement devices are presented in Fig. A.1. 10.9-grade bolts were selected for the test campaign as EN1090-2, Annex G [59] states that the characteristic slip factor determined with 10.9-grade bolts may also be used for bolted connections designed with 8.8-grade bolts. Nevertheless, the previous studies showed that the selected bolt size and the material grade of the bolts do not have a significant impact on the slip factor.

EN1090-2, Annex G [59] proposes two different sets of dimensions for the specimens of slip-factor determination tests based on the diameter of the bolts (M20 and M16). For the presented study, the dimensions of the test specimens were selected with M16-bolt [65], -nut [65],-washer [107] configurations of EN1090-2, Annex G [59] to be consistent with the diameter of the bolts used to secure the saw-tooth interface of SMIBC. However, due to the coupling of the saw-tooth surfaces and considering the height of the saw-tooth threads (see Fig. 3.1b) the thickness of the cover plate was selected to be 12mm instead of 8 mm which is the dimension of the cover plates suggested by EN1090-2, Annex G [59] for M16-bolt configuration. In addition, due to the available plate dimensions the inner plates were produced from 15mm thick plates instead of the 16mm thickness indicated by EN1090-2, Annex G [59]. Consequently, the total thickness between the outer

surfaces of the cover plates was 0.657mm more than the test configuration of M16-bolts defined by EN1090-2, Annex G [59]. This difference was considered insignificant for the determination of the slip factor [108].

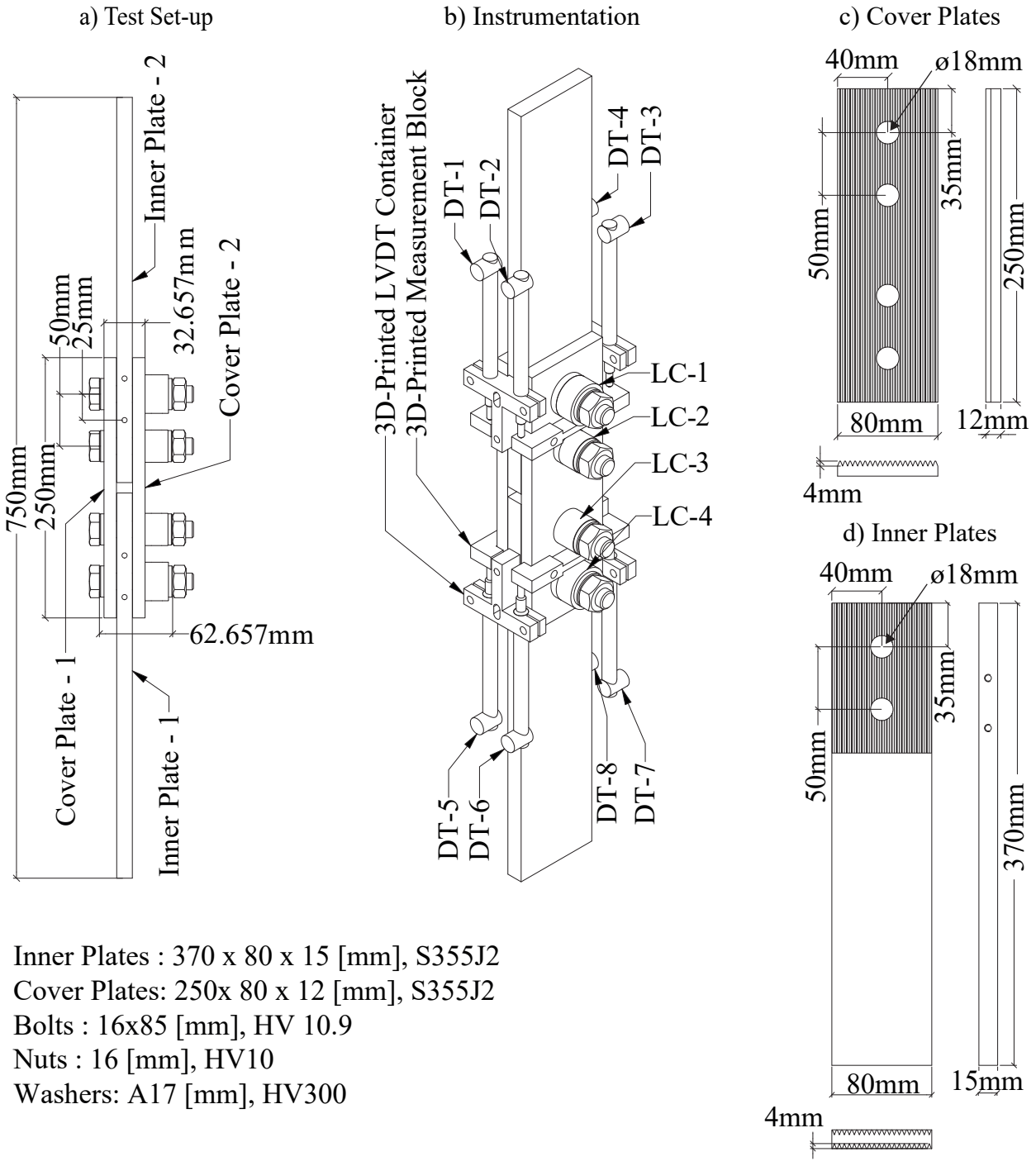

Figure A.1: Technical drawings of the test set-up and the test specimens together with the nominations of the measurement devices [4].

The experimental tests were executed with a 400kN uni-axial testing machine provided by the structural laboratory of The University of Luxembourg. The test specimens and the load cells (LCs) were assembled on a preparation bench. 110kN pre-tension was applied to the bolts while the assembly was clamped to the preparation bench. The pre-tension level was calculated according to EN1090-2 [59] with Eq. A.1;

$$F_{p,C} = 0.7 \cdot f_{ub} \cdot A_s \tag{A.1}$$

where;

- f_{ub} is the characteristic ultimate capacity of the selected bolt material.
- A_s is the stress area of the selected bolt size.

A calibrated torque wrench was used to apply the pre-tension and the level of the pre-tension was recorded during the entire torquing procedure to have accurate initial conditions for the slip factor determination tests. Once the 110kN pre-tension level was achieved for all of the bolts, the test assembly was carried into the testing machine. Fig. A.2 shows the test specimens and their assembly procedure. The assembly procedure was repeated for all of the test set-ups separately.

a) Test Specimens and Their Assembly

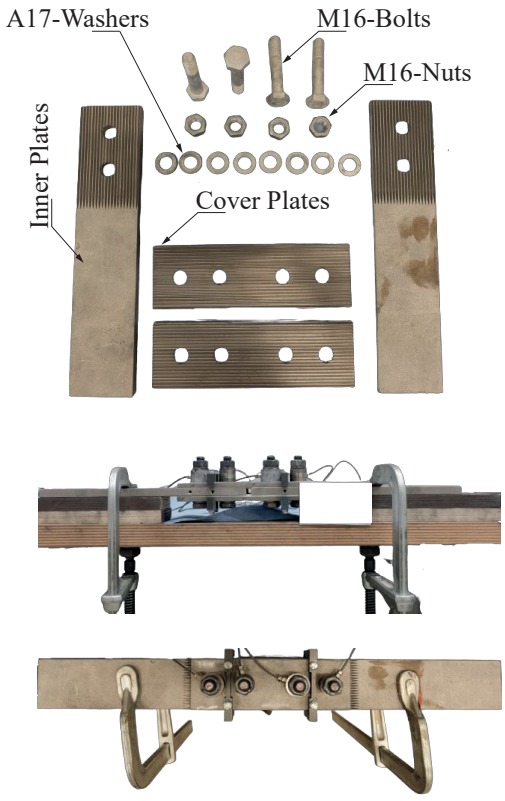

b) Installation of the Test Set-up

Figure A.2: Assembly of the test specimens and installation of the test set-up [4].

Linear variable displacement transducers (DTs) were positioned once the test assembly was clamped to the testing machine. As consistent with the provisions of EN1090-2 [59] the relative displacements between the inner and the cover plates, i.e., slip, were measured at the centre of the bolt groups for all of the four faying surfaces (see Fig. A.1a). To be able to measure the slip at the pre-defined position with high accuracy, 3D-printed DT containers and measurement blocks were produced (see Fig. A.1b), and the DT containers were fixed to the test assembly with screws at the centre of the bolt groups.

The first four tests were performed with normal test speed that corresponds to 10 to 15 minutes test duration according to EN1090-2, Annex G [59]. To comply with this limitation a displacement-controlled quasi-static monotonic loading procedure with 0.01mm/second loading speed was selected. However, it is important to note that the previous studies showed that the test speed, thus the test duration does not have an impact on the slip factor [109].

The fifth test was performed to measure the creep behaviour of the serrated interface and here on named the creep test. The following loading procedure defined by EN1090-2, Annex G [59] was applied for the creep test;

- Initially, 90% of the mean slip-load calculated based on the results of the first four tests was applied with the displacement-controlled loading procedure of the first four tests.
- Thereafter, a static loading period was applied for three hours at a loading level defined in the previous step.
- Finally, after the three hours of the static loading period, the displacement-controlled loading procedure of the initial step was continued until attaining the pre-defined slip-criterion of EN1090-2, Annex G [59] for both the upper and the lower ends.

A.1.1 Results of the test campaign

EN1090-2, Annex G [59] defines the individual slip load for the upper and lower ends of the test assembly as the load recorded at an instant that corresponds to 0.15 mm mean relative displacement between the inner and the cover plates (δ_{i} = 0.15 mm). Eq. A.2 and Eq. A.3 define the slip for the upper and the lower ends of the test assembly based on the DT configuration presented in Fig. A.1b

$$\delta_{i,upper} = \frac{\sum_{n=1}^{4} DT_n}{4} \tag{A.2}$$

$$\delta_{i,lower} = \frac{\sum_{n=5}^{8} DT_n}{4} \tag{A.3}$$

Fig. A.3a presents the load-slip curves for the upper and the lower ends of the test assemblies together with the pre-defined slip-criterion of EN1090-2, Annex G [59]. In addition, the variations of the bolt pre-tension levels are presented in with respect to the slip of the corresponding ends.

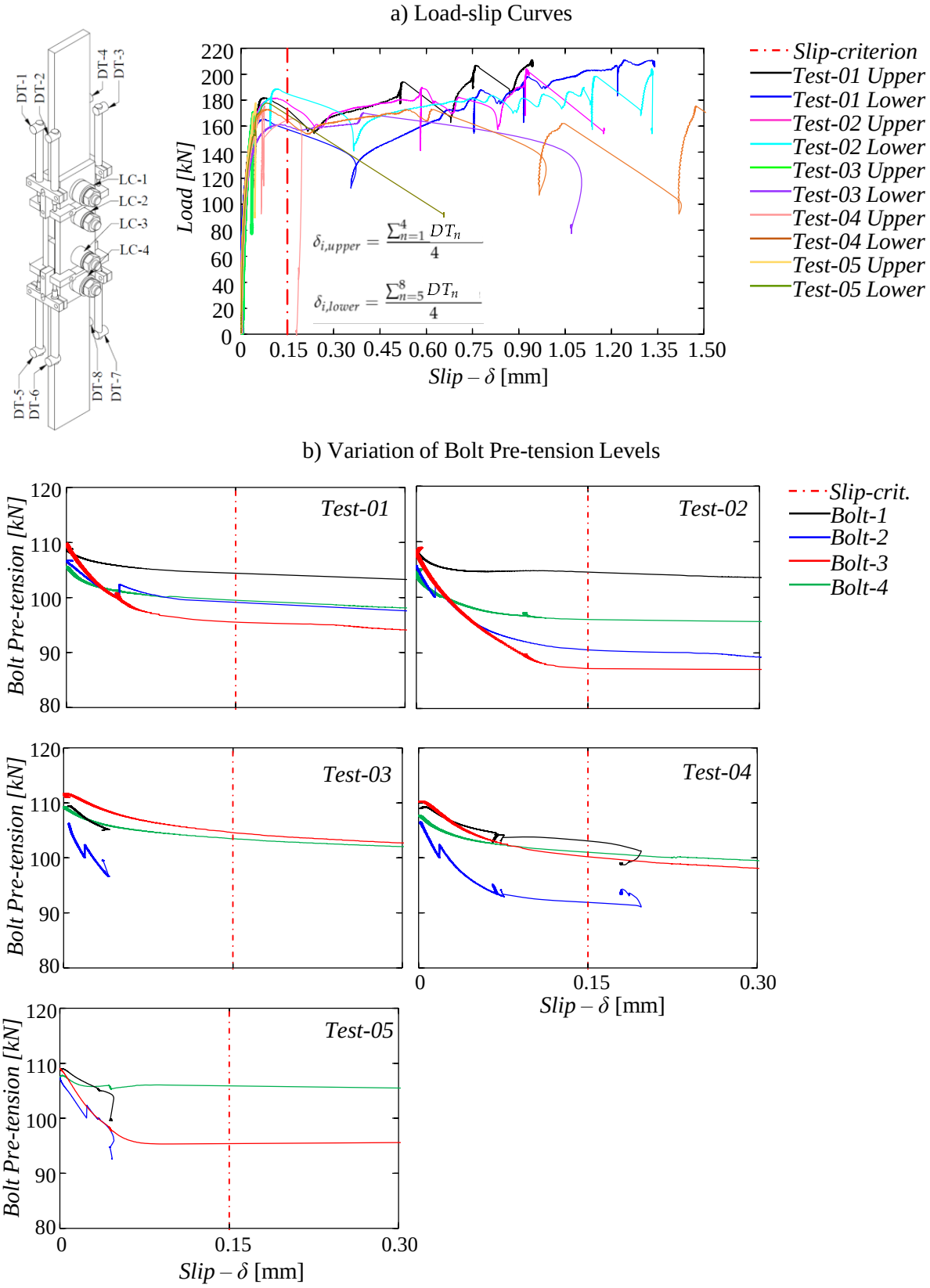

Figure A.3: Test results [4].

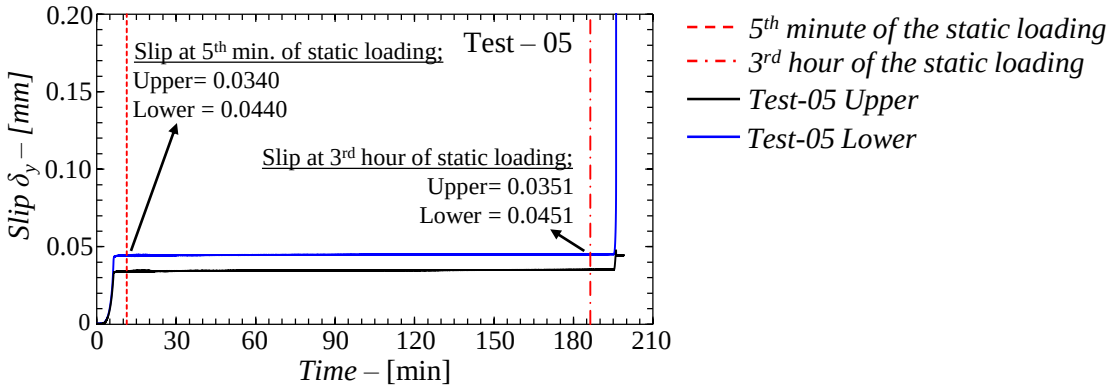

Figure A.4: Slip between the inner and cover plates during the static loading period of the creep test (Test-05) [4].

EN1090-2, Annex G [59] also defines a delayed slip-criterion, here on named as creep criterion-$\delta_{\text{creep, criterion}}$, for the creep test (Test-05) as 0.002mm slip between the fifth minutes and third hours of the static loading period defined in the loading procedure of the test campaign. Fig. A.4 presents the slip curves for the upper and the lower ends of the creep test assembly with respect to the test duration and Table A.1 presents the results of the creep tests for the evaluation of the creep behaviour against the pre-defined creep criterion ($\delta_{\text{creep, criterion}}$=0.002mm).

Table A.1: Summary of the results for Test-05 with respect to the pre-defined creep-criterion [4].

Test ID	DTs	$\delta_{\text{creep,criterion}}$	Slip [mm]		
			5th minute	**3rd hour**	**Delayed slip**
Test-05	Upper	0.002	0.0340	0.0351	0.0011
	Lower	0.002	0.0440	0.0451	0.0011

According to Table A.1 it is concluded that the delayed slip is lower than the pre-defined creep criterion for both of the upper and the lower ends of the test assembly. Therefore, the slip loads recorded at 0.15 mm slip of the creep test could also be used together with the results of the first four tests to determine the mean slip factor [59].

EN1090-2, Annex G [59] states that the individual slip factor could be calculated based on the nominal initial bolt pre-tension level and formulates the calculation of the individual slip factor for the upper and the lower ends of the test assembly with Eq. A.4.

$$\mu_{i,\ nominal} = \frac{F_{si}}{4 \cdot F_{p,C,initial}} \tag{A.4}$$

where;

- F_{si} is the individual slip-load,

- $F_{p,C,initial}$ is the initial nominal bolt pre-tension (see Eq. A.1).

On the other hand, previous studies showed that the initial bolt pre-tension level ($F_{p,\,C,initial}$) reduces by the initiation of the upright loading mainly due to lateral contraction orthogonal to the direction of the upright loading [108, 110]. Therefore, to more precisely define the slip-resistant load-bearing behaviour of CNC-cut serrated steel surfaces, the actual slip factors were determined for both the upper and the lower ends of the test assembly with Eq. A.5. Therefore, to calculate the actual slip factors, the actual bolt pre-tension levels ($F_{p,\,C,\,actual}$) at the pre-defined slip instant (δ_{i} = 0.15 mm) were used.

$$\mu_{i,\,actual} = \frac{F_{si}}{4 \cdot F_{p,C,actual}} \tag{A.5}$$

EN1090-2, Annex G [59] also defines a statistical evaluation procedure to decide if further test are required to establish the characteristic slip factor. Eqs. A.6-A.9 define the statistical evaluation parameters according to EN1090-2, Annex G [59].

$$F_{sm} = \frac{\sum F_{si}}{n} \tag{A.6}$$

$$s_{F_s} = \sqrt{\frac{(F_{si} - F_m)^2}{(n-1)}} \tag{A.7}$$

$$\mu_m = \frac{\sum \mu_i}{n} \tag{A.8}$$

$$s_{\mu} = \sqrt{\frac{(\mu_i - \mu_m)^2}{(n-1)}} \tag{A.9}$$

where;

- F_{sm} is the mean slip-load,
- s_{F_s} is the standard deviation for the distribution of the slip loads,
- μ_m is the mean slip factor,
- s_{μ} is the standard deviation for the distribution of the slip factors,

Finally, Table A.2 presents the test results by means of the individual slip load for the upper and the lower ends of the test assemblies, the initial nominal bolt pre-tension levels and the actual bolt pre-tension levels at the pre-defined slip instant, the nominal and the actual slip factors calculated with Eq. A.4 and Eq. A.5, respectively. In addition, the statistical evaluation parameters for the slip factor formulated with Eqs.A.6-A.9 are also listed in Table A.2.

Table A.2: Summary of the test results [4].

Test ID	LVDTs	$\delta_{criterion}$ [mm]	F_{si} [kN]	$F_{p,C}$—Bolt Pre-tension [kN]					μ—Slip factor	
				Nom.	Bolt-1	Bolt-2	Bolt-3	Bolt-4	$\mu_{i,nominal}$	$\mu_{i,actual}$
Test-01	Upper	0.15	158.08	110	104.28	98.78	-	-	0.359	0.389
	Lower	0.15	172.90	110	-	-	95.53	98.78	0.393	0.443
Test-02	Upper	0.15	177.47	110	104.52	90.55	-	-	0.403	0.455
	Lower	0.15	184.47	110	-	-	87.20	95.99	0.419	0.503
Test-03	Upper	0.15	N/A	110	N/A	N/A	-	-	N/A	N/A
	Lower	0.15	160.38	110	-	-	104.66	103.46	0.365	0.385
Test-04	Upper	0.15	162.16	110	102.80	91.91	-	-	0.369	0.416
	Lower	0.15	164.60	110	-	-	100.23	100.98	0.374	0.409
Test-05	Upper	0.15	N/A	110	N/A	N/A	-	-	N/A	N/A
	Lower	0.15	170.02	110	-	-	95.74	105.06	0.386	0.423
	F_{sm}[1] [kN]		168.76					**μ_m[1]**	0.384	0.428
	s_{Fs}[1] [kN]		9.15					**s_μ[1]**	0.021	0.039
	CoV_{Fs}[2] [%]		5.42					**Cov_μ[3] [%]**	5.424	9.044

[1] The results from the upper ends of Test-03 and Test-05 are not considered for the calculation of the statistical parameters.

[2] CoV_{Fs} is the coefficient of variation of the slip-loads.

[3] CoV_μ is the coefficient of variation of the slip factors.

It could be noticed from Fig. A.3 that the pre-defined slip-criterion of EN1090, Annex G [59] (δ_i = 0.15mm) was not attained for the upper ends of Test-03 and Test-05. Because these tests were automatically terminated as the testing machine was configured to stop if more than 50% load-drop occurs instantly. During Test-03 and Test-05, there were sudden slips at the lower ends of the test assemblies which triggered more than 50% load drops instantly, thus the testing machine stopped automatically for these tests. Consequently, it was not possible to further measure the slip for the upper ends of Test-03 and Test-05 test assemblies. Therefore, in Table A.2 the slip factors for the upper ends of these tests were not specified and the statistical parameters defined through Eq. A.6 to Eq. A.9 were calculated based on the eight values.

ANNEX B

Complementary results for SMIBC-E0/E1 Test Campaigns

B.1 Tensile coupon tests

The material properties of the inner and cover plates, and the M16-bolts used in SMIBC-E0 and SMIBC-E1 test campaigns were determined according to EN ISO 6892-1 Method A1 [63].

Fig. B.1 shows the technical drawing of the steel coupons produced from the inner and the cover plates utilized in the aforementioned test campaigns. The technical drawing of the steel coupons for M16-bolts are also presented in Fig. B.2. The results of the steel coupon tests for SMIBC-E0 and SMIBC-E1 test campaigns are presented in Table B.1 and Table B.2 according to EN ISO 6892-1 [63]. Furthermore, Fig. B.3 and Fig. B.4 show the before and the after test conditions of the steel coupons for the specimens of SMIBC-E0 and SMIBC-E1 test campaigns.

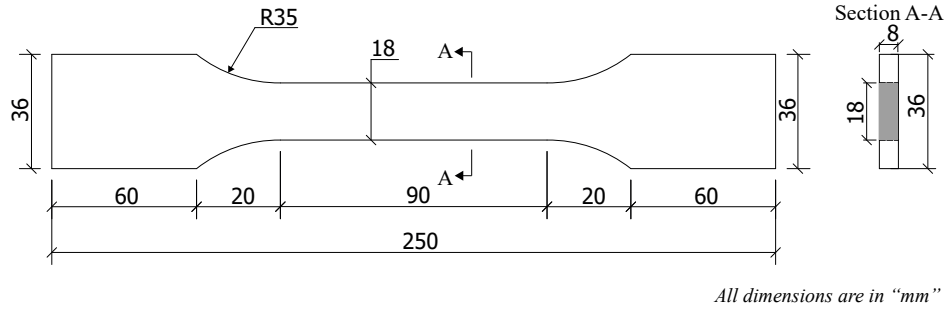

Figure B.1: Technical drawing of rectangular steel coupons / SMIBC-E0/E1 test campaigns.

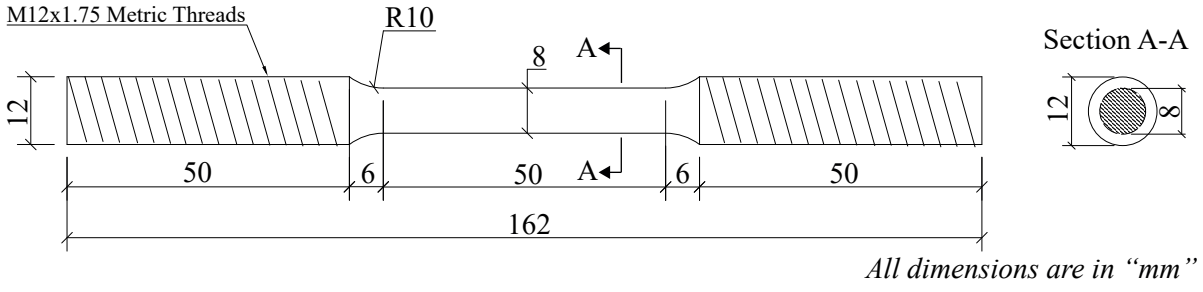

Figure B.2: Technical drawing of round steel coupons / SMIBC-E0/E1 test campaigns.

Table B.1: Tensile coupon test results / SMIBC-E0 test campaign.

Specimen Number	1	2	3	4	5	6	7	8	9
Specimen ID	IP-1	IP-2	IP-3	CP-1	CP-2	CP3	UPE-1	UPE-2	UPE-3
Material Grade	S235	S235	S235	S235	S235	S235	S355	S355	S355
Total Length of Test Piece, L_t [mm]	250	250	250	250	250	250	250	250	250
Original Gauge Length, L_o [mm]	67.8	67.8	67.8	67.8	67.8	67.8	67.8	67.8	67.8
Gauge Thickness, t_o [mm]	8.03	8.07	8.02	8.02	8.05	8.03	8.05	8.02	8.02
Gauge Width, w_o [mm]	18.09	18.09	18.06	18.05	18.05	18.03	18.03	18.05	18.03
Original Cross-sectional Area, S_o [mm^2]	145.20	146.00	144.89	144.80	145.27	144.73	145.16	144.71	144.66
Elastic Modulus, E [GPa]	194.4	195.7	194.8	207.2	206.5	208.1	204.6	205.3	205.3
Proof Strength, R_p [MPa]	218	181	181	N/A	N/A	N/A	380	386	381
Lower Yield Strength, R_{eL} [MPa]	N/A	N/A	N/A	253	268	309	N/A	N/A	N/A
Upper Yield Strength, R_{eH} [MPa]	N/A	N/A	N/A	265	273	333	N/A	N/A	N/A
Tensile Strength, R_m [MPa]	406	406	406	463	459	474	534	537	535
Total Machine Travel at Tensile Strength, δ_m [mm]	21.86	20.13	19.69	17.06	17.13	16.44	13.60	13.31	13.27
Maximum Load, F_m[1] [kN]	59.0	59.2	58.9	67.1	66.7	68.6	77.5	77.7	77.3
Failure Load, F_f[2] [kN]	59.0	59.2	58.9	67.1	66.7	68.6	77.5	77.7	77.3
Percentage Elongation after Fracture, A [%]	35.5	36.0	40.0	33.0	35.0	31.5	28.5	29.0	32.5
Percentage Reduction of Area after Fracture, Z [%]	71.40	72.91	72.84	68.96	69.00	67.20	70.03	70.10	N/A[3]
Rupture Position	1/3	1/3	1/3	1/3	1/2	1/3	1/3	1/2	1/3

[1] The maximum load corresponds to the force output from the testing machine once the necking of the steel coupon occurs.

[2] The fracture load corresponds to the force output from the testing machine once the fracture of the steel coupon occurs.

[3] The test sample of UPE-3 did not delivered by the testing laboratory of the coupon tests. Therefore, the percentage reduction of the area after the fracture could not be measured. However, the percentage elongation after fracture of UPE-3 test sample was available in the test report delivered by the testing laboratory.

Table B.2: Tensile coupon test results / SMIBC-E1 test campaign.

Specimen Number	1	2	3	4	5	6	7	8	9
Specimen ID	IP-1	IP-2	IP-3	CP-1	CP-2	CP3	M16-1	M16-2	M16-3
Material Grade	S235	S235	S235	S235	S235	S235	8.8	8.8	8.8
Total Length of Test Piece, L_t [mm]	250	250	250	250	250	250	162	162	162
Original Gauge Length, L_o [mm]	67.8	67.8	67.8	67.8	67.8	67.8	40.0	40.0	40.0
Original Gauge Thickness, a_o [mm]	8.03	7.98	8.04	7.87	7.98	7.85	N/A	N/A	N/A
Original Gauge Width, b_o [mm]	18.05	18.06	18.06	18.05	18.04	18.01	N/A	N/A	N/A
Original Gauge Diameter, d_o [mm]	N/A	N/A	N/A	N/A	N/A	N/A	8.00	8.00	7.99
Original Cross-sectional Area, S_o [mm^2]	144.97	144.17	145.12	141.93	143.94	141.33	50.30	50.30	50.18
Elastic Modulus, E [GPa]	205.9	204.0	208.8	211.4	204.3	204.1	211.7	208.0	214.8
Proof Strength, R_p [MPa]	N/A	N/A	N/A	N/A	N/A	N/A	869	865	855
Lower Yield Strength, R_{eL} [MPa]	245	244	244	259	235	282	N/A	N/A	N/A
Upper Yield Strength, R_{eH} [MPa]	255	250	258	283	250	308	N/A	N/A	N/A
Tensile Strength, R_m [MPa]	386	386	387	452	451	458	929	923	918
Total Machine Travel at Tensile Strength, δ_m [mm]	21.11	20.56	21.43	16.88	17.27	16.55	5.30	5.40	5.17
Maximum Load, F_m[1] [kN]	56.0	55.6	56.1	64.2	65.0	64.8	46.7	46.4	46.0
Fracture Load, F_f[2] [kN]	33.6	33.9	34.5	45.2	45.3	44.4	25.0	23.8	24.4
Percentage Elongation after Fracture, A [%]	41.0	40.0	39.0	30.5	28.5	28.5	18.5	20.0	19.0
Percentage Reduction of Area after Fracture, Z [%]	74.53	74.77	76.44	61.96	64.28	63.67	71.72	72.46	72.39
Rupture Position	1/2	1/2	1/3	1/3	1/3	1/3	1/3	1/3	1/3

[1] The maximum load corresponds to the force output from the testing machine once the necking of the steel coupon occurs.

[2] The fracture load corresponds to the force output from the testing machine once the fracture of the steel coupon occurs.

The ultimate strains, which correspond to the tensile strengths of the steel coupons (ε_u) and were used for the finite element analyses of SMIBC-E0 and SMIBC-E1 test campaigns, could not be determined with the coupon tests as the extensometer, the device that measures the elongation of the coupons along the original gauge length (L_o), was removed before the necking of the steel coupons not to damage the device. Therefore, the ultimate strains (ε_u) were estimated based on the total travel of the testing machine at the maximum load (F_m) with equation Eq. B.1;

$$\epsilon_u = \frac{\delta_m}{L_o} \tag{B.1}$$

a) SMIBC-E0 / Steel Coupons of Inner Plates (IP)

Before Test

After Test

b) SMIBC-E0 / Steel Coupons of Cover Plates (CP)

Before Test

After Test

c) SMIBC-E0 / Steel Coupons of Cover Plates (UPE)

Before Test

After Test

Figure B.3: Before and after test conditions of steel coupons / SMIBC-E0 test campaign.

a) SMIBC-E1 / Steel Coupons of Inner Plates (IP)

Before Test

After Test

b) SMIBC-E1 / Steel Coupons of Cover Plates (CP)

Before Test

After Test

c) SMIBC-E1 / Steel Coupons of M16-bolts (M16)

Before Test

After Test

Figure B.4: Before and after test conditions of steel coupons / SMIBC-E1 test campaign.

B.2 After test conditions of SMIBC-E0 and SMIBC-E1 test specimens

After test condition of the saw-tooth interfaces, the deformations for the saw-tooth surfaces of the inner and cover plates, and the deformations of the M16-bolts were recorded after the experimental tests of SMIBC-E0 and SMIBC-E1 test campaigns. Fig. B.4 and Fig. B.5 show the after test conditions for the aforementioned test specimens.

Figure B.5: After test condition for the test specimens of SMIBC-E0 test campaign.

Figure B.6: After test condition for the test specimens of SMIBC-E1 test campaign.

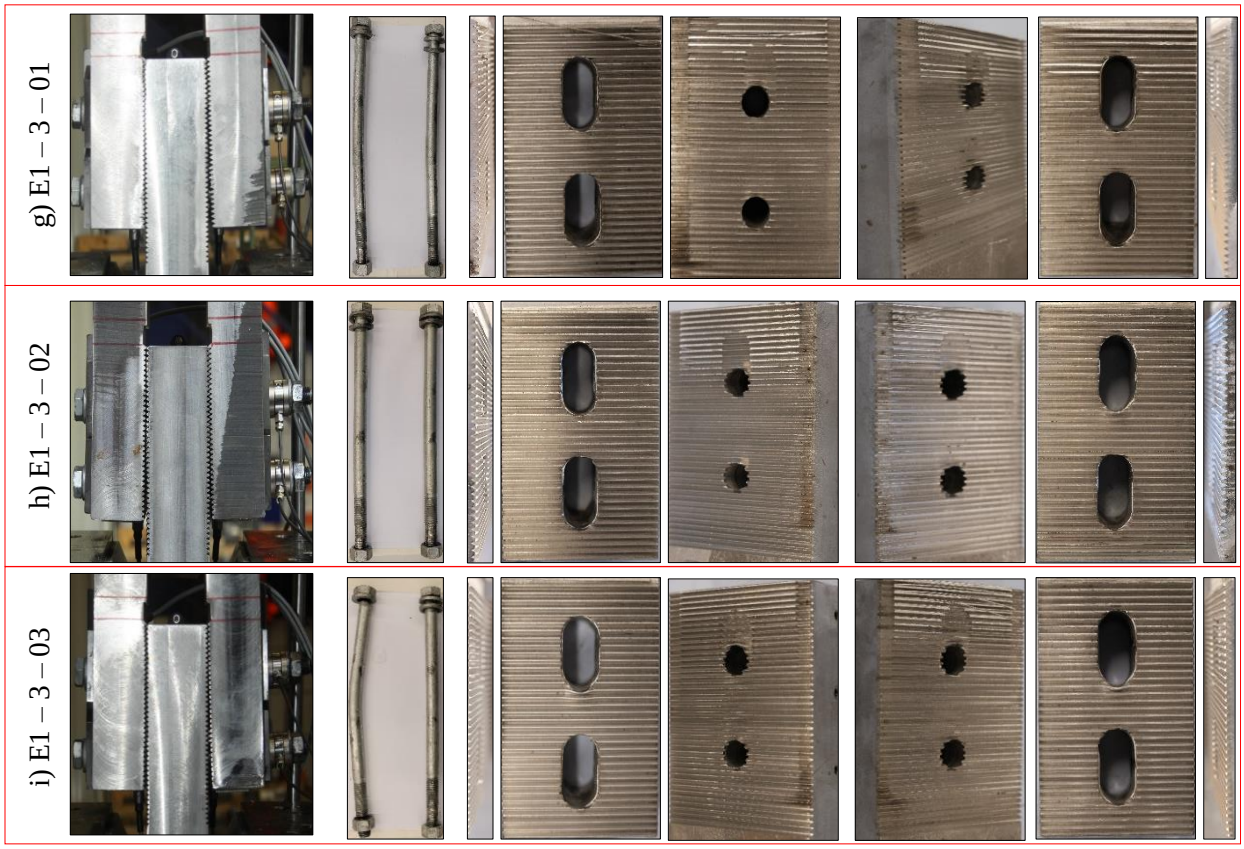

Figure B.7: Fig. B.6 cont.

B.3 Solver parameters and energy balances of the FEAs

Table B.3 presents the static and dynamic-implicit solver parameters used for the two-step finite element analysis of SMIBC-E0 and SMIBC-E1 test campaigns.

The energy balances for the corresponding analyses are also presented in Fig. B.8 for each FEA performed presented under Section 3.2.3.2.

Table B.3: FEA solver parameters of SMIBC-E0 and SMIBC-E1 test campaigns

FEA Model ID	SMIBC-E0-1		SMIBC-E0-2		SMIBC-E1-1		SMIBC-E1-2		SMIBC-E1-3	
Solution Step	Step-1	Step-2	Step-1	Step-2	Step-1	Step-2	Step-1	Step-2	Step-1	Step-2
Solver	Static	Dyn-imp.[1]	Static	Dyn-imp.	Static	Dyn-imp.	Static	Dyn-imp.	Static	Dyn-imp.
Step Time Period	1	1	1	1	1	1	1	1	1	1
Nlgeom[2]	YES									
Initial Increment Size	0.1									
Min Increment Size	10^{-8}									
Max Increment Size	0.1	Default	0.1	Default	0.1	Default	0.1	Default	0.1	Default
Matrix Storage	Sym.[3]	Unsym.[4]	Sym.	Unsym.	Sym.	Unsym.	Sym.	Unsym.	Sym.	Unsym.
Solution Technique	Full Newton									
Other Parameters	Default									

[1] Dyn-imp corresponds to dynamic-implicit solution scheme.

[2] Nlgeom corresponds to geometrical nonlinearities.

[3] Sym. corresponds to symmetric matrix storage.

[4] UnSym. corresponds to unsymmetric matrix storage.

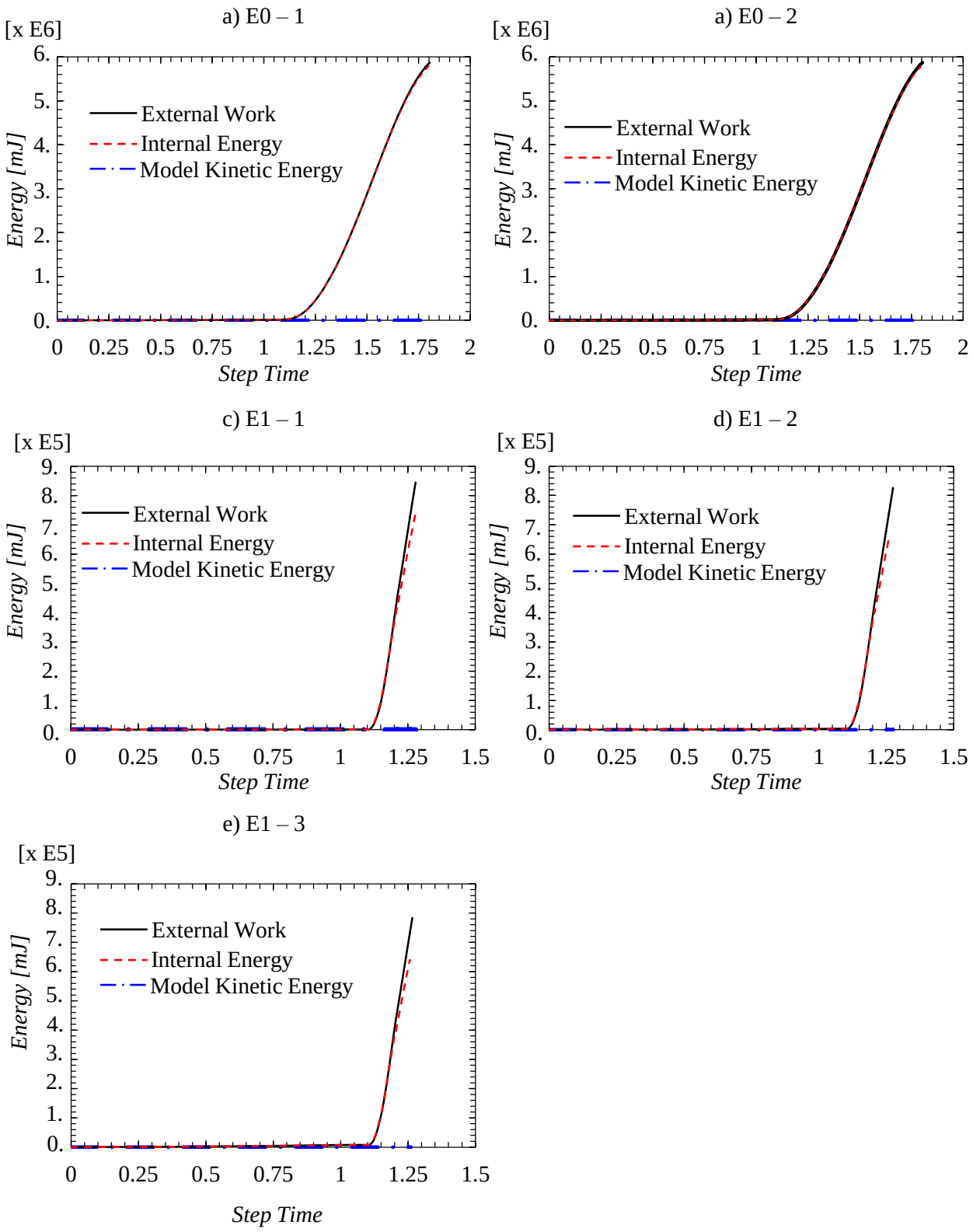

Figure B.8: Energy balance for the FEAs of SMIBC-E0 and SMIBC-E1 test campaigns.

B.4 Load-displacement curves of the numerical parametric study

The load-displacement behaviors of SMIBC for the FEAs performed under the numerical parametric study presented in Section 3.2.5.2 are given in Fig. B.9.

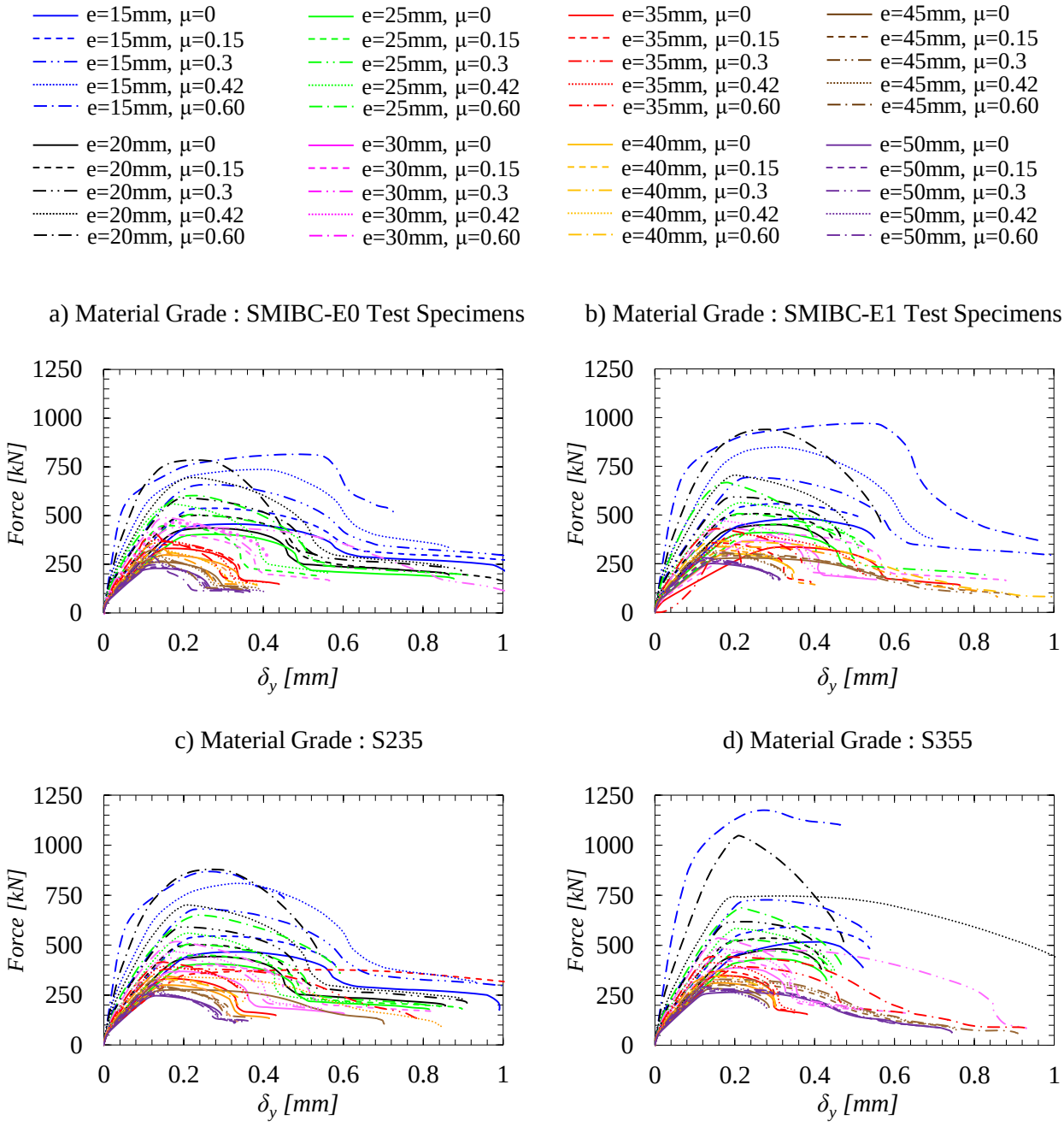

Figure B.9: Load-displacement curves for the FEAs of the numerical parametric study.

ANNEX C

Complementary results for SMIBC-CC Test Campaign

C.1 Tensile coupon tests

Fig. C.1 shows the technical drawings of the round steel coupons of the steel reinforcements positioned next to the anchorages of SMIBC-CC test specimens. The results of the round steel coupon tests are presented in Table C.1 according to EN ISO 6892-1 [63]. The technical drawing of the rectangular steel coupons for the anchor plates are presented in Fig. C.2 and the corresponding test results for them are listed in Table C.2 according to EN ISO 6892-1 [63]. Fig. C.3 and Fig. C.4 show the before and the after test conditions of the steel coupons.

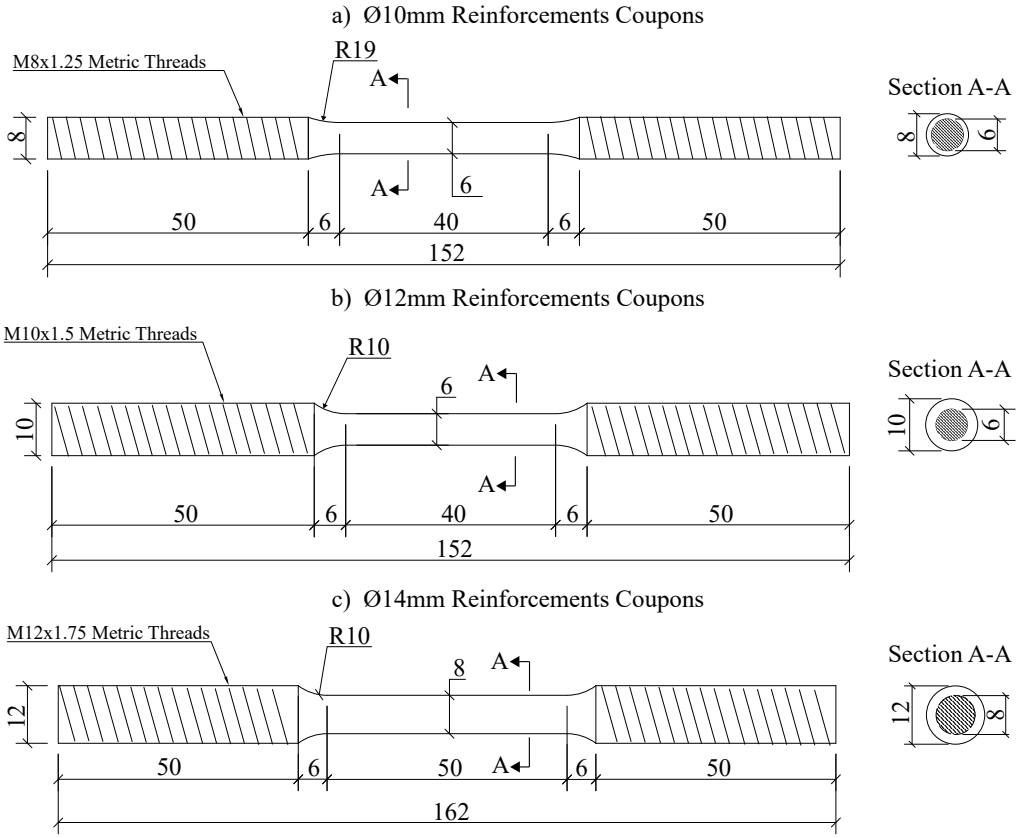

Figure C.1: Technical drawings of the round steel coupons / SMIBC-CC test campaign.

Table C.1: Round coupons tensile test results / SMIBC-CC test campaign.

Specimen Number	1	2	3	4	5	6	7	8	9
Specimen ID	*Ø10-1*	*Ø10-2*	*Ø10-3*	*Ø12-1*	*Ø12-2*	*Ø12-3*	*Ø14-1*	*Ø14-2*	*Ø14-3*
Reinforcement Diameter [mm]	10	10	10	12	12	12	14	14	14
Material Grade	B500B	B500B	B500B	B500B	B500B	B500B	B500B	B500B	B500B
Total Length of Test Piece, L_t [mm]	152	152	152	152	152	152	162	162	162
Original Gauge Length, L_o [mm]	25	25	25	30	30	30	40	40	40
Original Gauge Diameter, d_o [mm]	4.99	4.98	5.00	5.98	5.98	5.98	8.00	7.99	8.00
Original Cross-sectional Area, S_o [mm^2]	19.55	19.50	19.66	28.06	28.09	28.09	50.32	50.12	50.31
Elastic Modulus, E [GPa]	251.4	198.6	198.2	237.5	216.7	202.2	207.6	204.7	200.4
Proof Strength, R_p [MPa]	563	573	562	N/A	N/A	N/A	579	573	536
Lower Yield Strength, R_{eL} [MPa]	N/A	N/A	N/A	432	342	457	N/A	N/A	N/A
Upper Yield Strength, R_{eH} [MPa]	N/A	N/A	N/A	441	496	472	N/A	N/A	N/A
Tensile Strength, R_m [MPa]	649	655	650	593	605	613	656	651	622
Total Machine Travel at Tensile Strength, δ_m [mm]	3.95	4.06	3.87	7.56	7.12	6.76	5.08	5.12	5.18
Maximum Load, F_m[1] [kN]	12.7	12.8	12.8	16.6	17.0	17.2	33.01	32.6	31.3
Fracture Load, F_f[1] [kN]	8.6	8.9	8.3	10.3	10.8	11.2	22.2	22.2	20.8
Percentage Elongation after Fracture, A [%]	26.0	23.5	25.0	32.5	29.5	30.0	20.5	19.5	23.0
Percentage Reduction of Area after Fracture, Z [%]	63.76	59.19	65.63	68.90	69.55	66.40	59.83	61.14	69.93
Rupture Position	1/3	1/2	1/3	1/2	1/2	1/3	1/2	1/3	1/2

[1] The maximum load corresponds to the force output from the testing machine once the necking of the steel coupon occurs.

[2] The fracture load corresponds to the force output from the testing machine once the fracture of the steel coupon occurs.

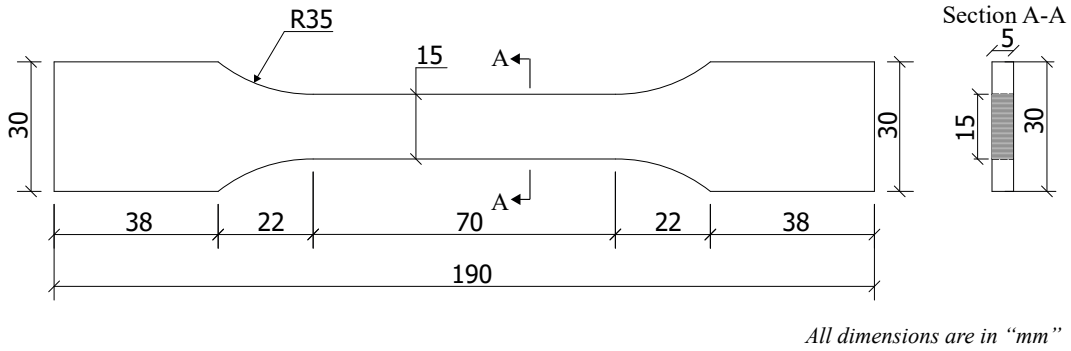

Figure C.2: Technical drawing of the rectangular coupons / SMIBC-CC test campaign.

Table C.2: Rectangular coupons tensile test results / SMIBC-CC test campaign.

Specimen Number	1	2	3
Specimen ID	AP-1	AP-2	AP-3
Material Grade	S235	S235	S235
Total Length of Test Piece, L_t [mm]	190	190	190
Original Gauge Length, L_o [mm]	50	50	50
Original Gauge Thickness, a_o [mm]	4.94	4.94	4.95
Original Gauge Width, b_o [mm]	15.05	15.06	15.06
Original Cross-sectional Area, S_o [mm^2]	74.34	74.45	74.46
Elastic Modulus, E [GPa]	216.9	221.4	212.0
Lower Yield Strength, R_{eL} [MPa]	386	383	381
Upper Yield Strength, R_{eH} [MPa]	458	470	468
Tensile Strength, R_m [MPa]	486	489	484
Total Machine Travel at Tensile Strength, δ_m [mm]	12.83	12.37	12.56
Maximum Load, F_m[1] [kN]	36.1	36.4	36.0
Fracture Load, F_f[2] [kN]	20.7	20.6	20.2
Percentage Elongation after Fracture, A [%]	39.0	36.5	38.5
Percentage Reduction of Area after Fracture, Z [%]	67.65	70.07	71.32
Rupture Position	1/2	1/2	1/3

[1] The maximum load corresponds to the force output from the testing machine at the necking of the steel coupon.

[2] The fracture load corresponds to the force output from the testing machine once the fracture of the steel coupon occurs.

The ultimate strains (ε_u) and the fracture stresses (f_f), which were used for the finite element analyses of SMIBC-CC test campaign in Section 3.3.7, were calculated with Eq. B.1 and Eq. C.1 according to the data presented in Table C.1 and Table C.2.

$$f_f = \frac{F_f}{S_o} \tag{C.1}$$

a) Ø10 Reinforcement Coupons

Before Test

After Test

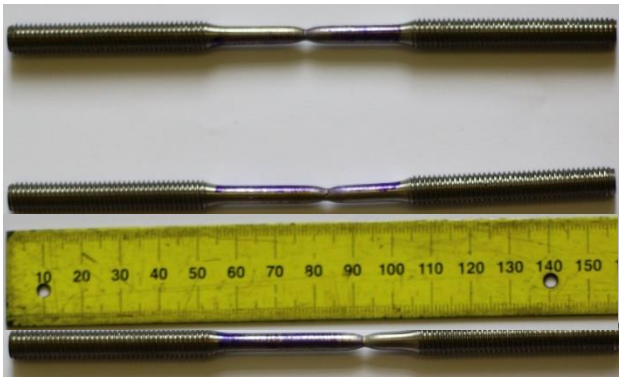

b) Ø12 Reinforcement Coupons

Before Test

After Test

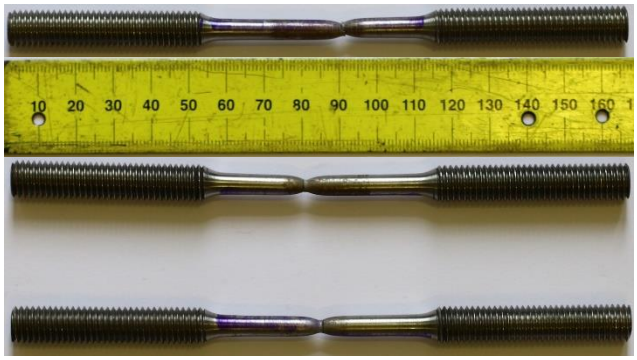

c) Ø14 Reinforcement Coupons

Before Test

After Test

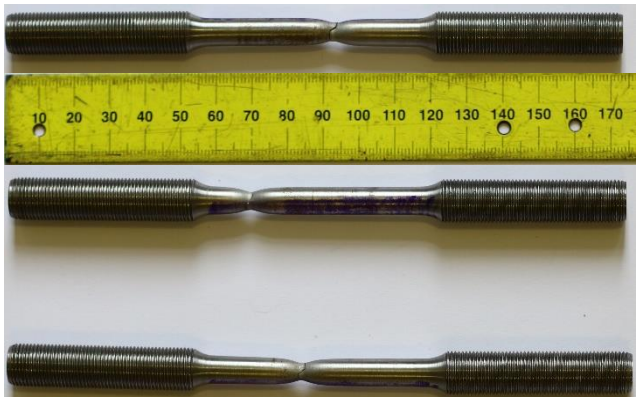

Figure C.3: Before and after test conditions of round coupons / SMIBC-CC test campaign.

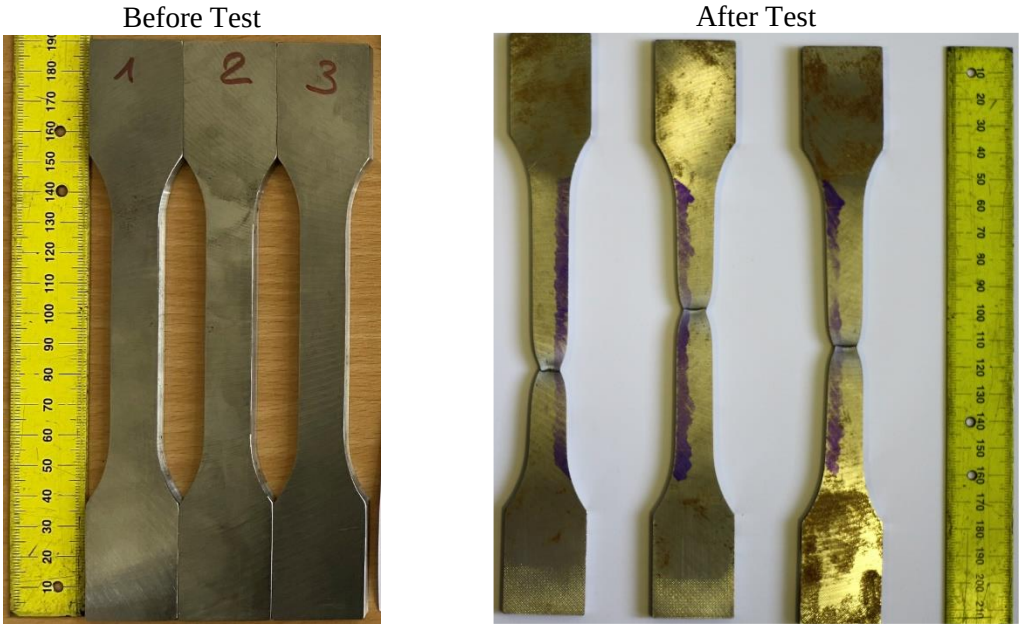

Figure C.4: Before and after test conditions of rectangular steel coupons / SMIBC-CC test campaign.

C.2 Formulations for the concrete constitutive material models of FEAs

The uni-axial compressive and the uni-axial tensile crack-width stress behaviors for the constitutive material models of the concrete components of finite element models presented under Section 3.3.7 were defined according to EN1992-1-1 [72] and fib Model Code [3], respectively.

Fig. C.5a shows the aforementioned uni-axial compressive material model for the concrete FE-model components, and Eq. C.2 presents the relation between the uni-axial compression stress (σ_c) and the compressive strain (ϵ_c) in the concrete.

$$\frac{\sigma_c}{f_{cm}} = \frac{k\eta - \eta^2}{1 + (k-2)\eta} \tag{C.2}$$

where

- $\eta = \frac{\epsilon_c}{\epsilon_{c1}}$;
  - ϵ_c= Compressive strain in the concrete;
  - ϵ_{c1}= Compressive strain in the concrete at the peak stress;
- $k = 1.05 E_{cm} \times |\epsilon_{c1}| / f_{cm}$;
  - E_{cm} is the secant modulus of elasticity of concrete;
  - f_{cm} is the mean value of concrete cylinder compressive strength.

According to EN1992-1-1 [72], the expression presented by Eq. C.2 is valid for $0 < |\epsilon_c| < |\epsilon_{c1}|$. However, to be able to simulate the concrete damage progression in the FEAs, the upper boundary

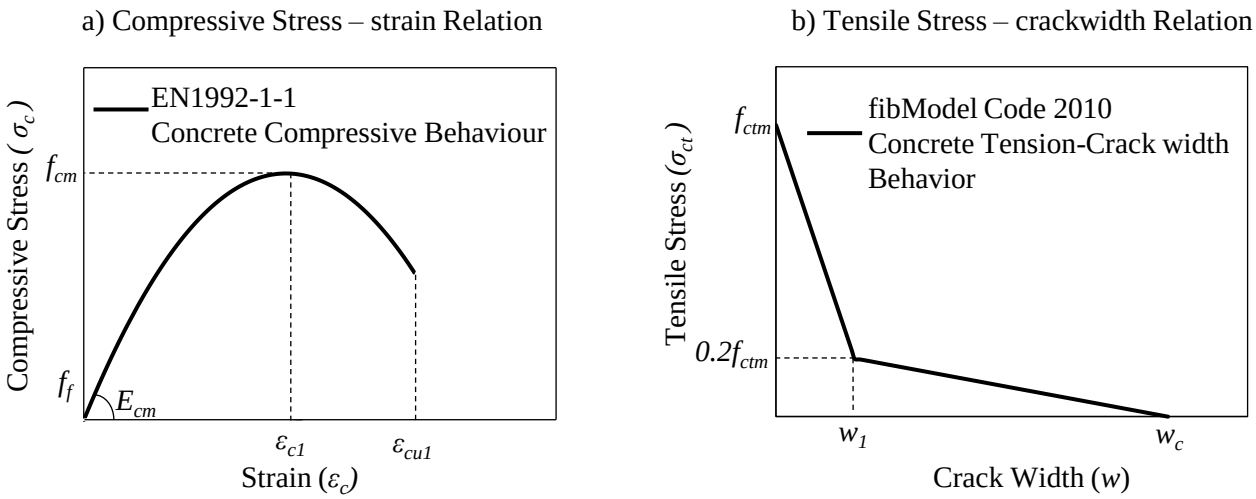

Figure C.5: Uni-axial compressive stress-strain and uni-axial tensile stress crack width relation of concrete material.

of the strain limits were extended as earlier presented in Fig. 3.91 and Table 3.32 (see also Fig. 5.51 and Table 5.8).

Fig. C.5b shows the uni-axial tensile crack-width stress material model for the concrete FE-model components, and Eqs. C.3-C.4 presents the relation between the uni-axial tensile stress (σ_{ct}) and the crack-width (w) in the concrete.

$$\sigma_{ct} = f_{ctm} \cdot (1 - 0.8 \cdot \frac{w}{w_1}) \; for \; w \leq w_1 \tag{C.3}$$

$$\sigma_{ct} = f_{ctm} \cdot (0.25 - 0.05 \cdot \frac{w}{w_1}) \; for \; w_1 < w \leq w_c \tag{C.4}$$

where

- w is the crack opening in mm;
- w_1=G_F/f_{ctm} in mm when $\sigma_{ct} = 0.20 \cdot f_{ctm}$;
- w_c=$5 \cdot G_F/f_{ctm}$ in mm when $\sigma_{ct} = 0$;
- G_F is the fracture energy in N/mm and calculated as follows;
  - $G_F = 73 \cdot {f_{cm}}^{0.18}$
  - f_{cm} is the mean compressive strength in MPa.
- f_{ctm} is the tensile strength in MPa.

C.3 Solver parameters and the energy balances of the FEAs

Table C.3 presents the explicit solver parameters [66] of FEAs performed under Section 3.3.7. In addition, the energy balances of the FEAs are presented in Fig. C.5.

Table C.3: FEA solver parameters of SMIBC-CC test campaign

FEA Model ID	CC-01	CC-02	CC-03
Solution Step	Step-1	Step-1	Step-1
Solver	Dynamic Explicit		
Time Period	50 [second]		
Geometrical Nonlinearities	YES		
Type	Automatic		
Stable Increment Estimation	Global		
Maximum Time Increment	Unlimited		
Time Scaling Factor	1		
Mass Scaling Factor	Whole Model:10000		
Linear Bulk Viscosity Parameter	0.06		
Quadratic Bulk Viscosity Parameter	0.12		

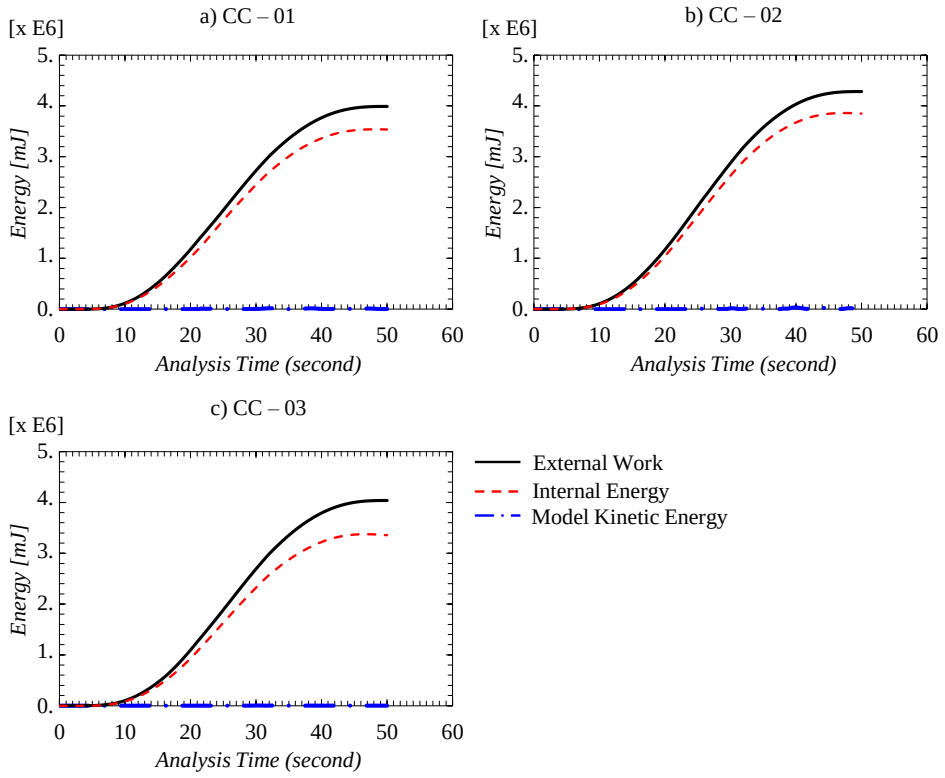

Figure C.6: Energy balance for the FEAs of SMIBC-CC test campaign.

ANNEX D

Complementary results for Plug-inC Test Campaign

D.1 Tensile coupon tests

The material properties of the inner and cover plates used in Plug-inC test campaign were determined according to EN ISO 6892-1 Method A1 [63].

Fig. D.1 shows the technical drawing of the steel coupons produced from the inner and the cover plates utilized in the aforementioned test campaign. The results of the steel coupon tests are presented in Table D.1 and Fig. D.2 shows the before and the after test conditions of the steel coupons.

The ultimate strains (ε_u), which were used for the finite element analyses of Plug-inC test campaign presented in Section 4.4, were calculated with Eq. B.1 according to the data presented in Table D.1.

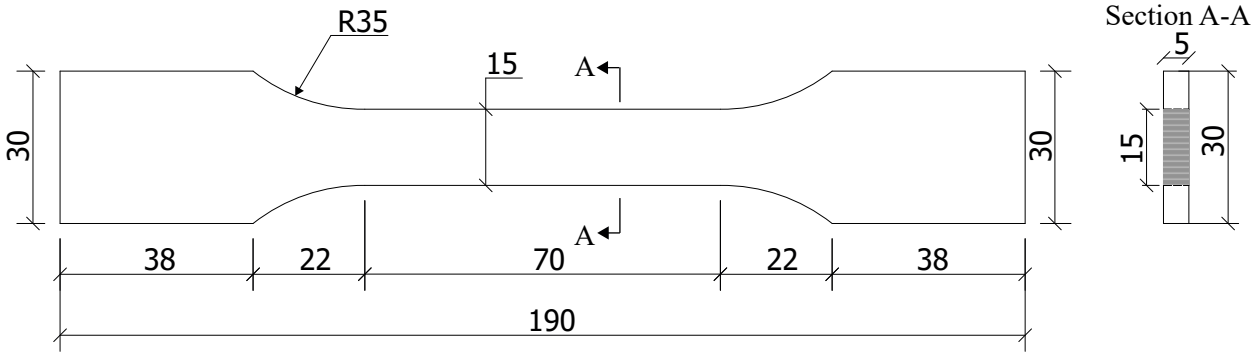

All dimensions are in "mm"

Figure D.1: Technical drawings of the steel coupons / Plug-inC test campaign.

Table D.1: Tensile coupon test results / Plug-inC test campaign.

Specimen Number	1	2	3	4	5	6
Specimen ID	IP-1	IP-2	IP-3	CP-3	CP-3	CP-3
Material Grade	S235	S235	S235	S235	S235	S235
Total Length of Test Piece, L_t [mm]	190	190	190	190	190	190
Original Gauge Length, L_o [mm]	50	50	50	50	50	50
Original Gauge Thickness, a_o [mm]	5.031	5.035	5.037	5.027	5.029	5.033
Original Gauge Width, b_o [mm]	15.021	15.003	15.051	15.077	15.054	15.031
Original Cross-sectional Area, S_o [mm^2]	75.58	75.54	75.81	75.80	75.71	75.65
Elastic Modulus, E [GPa]	206.7	206.8	206.7	209.4	205.0	209.2
Lower Yield Strength, R_{eL} [MPa]	242	243	246	263	226	255
Upper Yield Strength, R_{eH} [MPa]	250	256	267	305	244	281
Tensile Strength, R_m [MPa]	441	444	449	448	410	445
Total Machine Travel at Tensile Strength, δ_m [mm]	15.22	14.75	15.57	15.94	16.78	15.23
Maximum Load, F_m[1] [kN]	33.4	33.6	34.1	33.4	31.1	33.6
Fracture Load, F_f[2] [kN]	22.7	22.8	23.8	22.8	20.5	21.9
Percentage Elongation after Fracture, A [%]	36.0	35.5	34.5	38.0	39.5	36.5
Percentage Reduction of Area after Fracture, Z [%]	62.6	64.8	60.1	67.7	66.7	67.1
Rupture Position	1/2	1/2	1/2	1/2	1/3	1/2

[1] The maximum load corresponds to the force output from the testing machine at the necking of the steel coupon.

[2] The fracture load corresponds to the force output from the testing machine once the fracture of the steel coupon occurs.

a) Plug-inC / Steel Coupons of Inner Plates (IP)

Before Test | After Test

b) Plug-inC / Steel Coupons of Cover Plates (CP)

Before Test | After Test

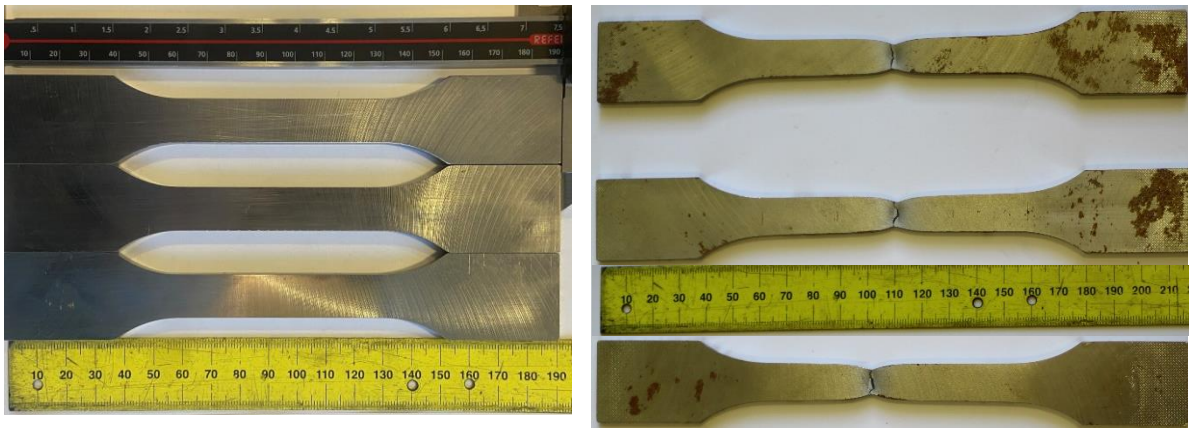

Figure D.2: Before and after test conditions of steel coupons / Plug-inC test campaign.

D.2 Before and after test conditions of Plug-inC-02 and Plug-inC-03 test specimens

Fig. D.3 and Fig. D.4 compare the before and the after test conditions of the hub and the dovetail counterparts for the second (Plug-inC-02) and the third test specimens (Plug-inC-03) for Plug-inC test campaign. It is important to note that the deformations are only compared for the in-plane left hub and dovetail counterparts of Plug-inC test configuration according to Fig. 4.6.

a) Inner Plate with Hub Counterpart at In-plane Left Side

Before Test

After Test

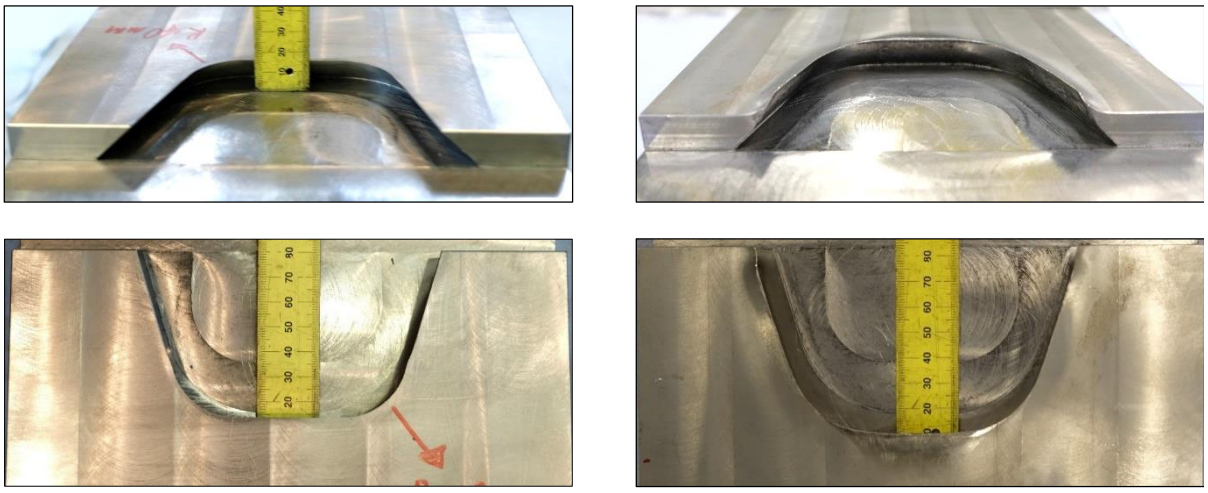

b) Cover Plate with Dovetail Counterpart at In-plane Left-side

Before Test

After Test

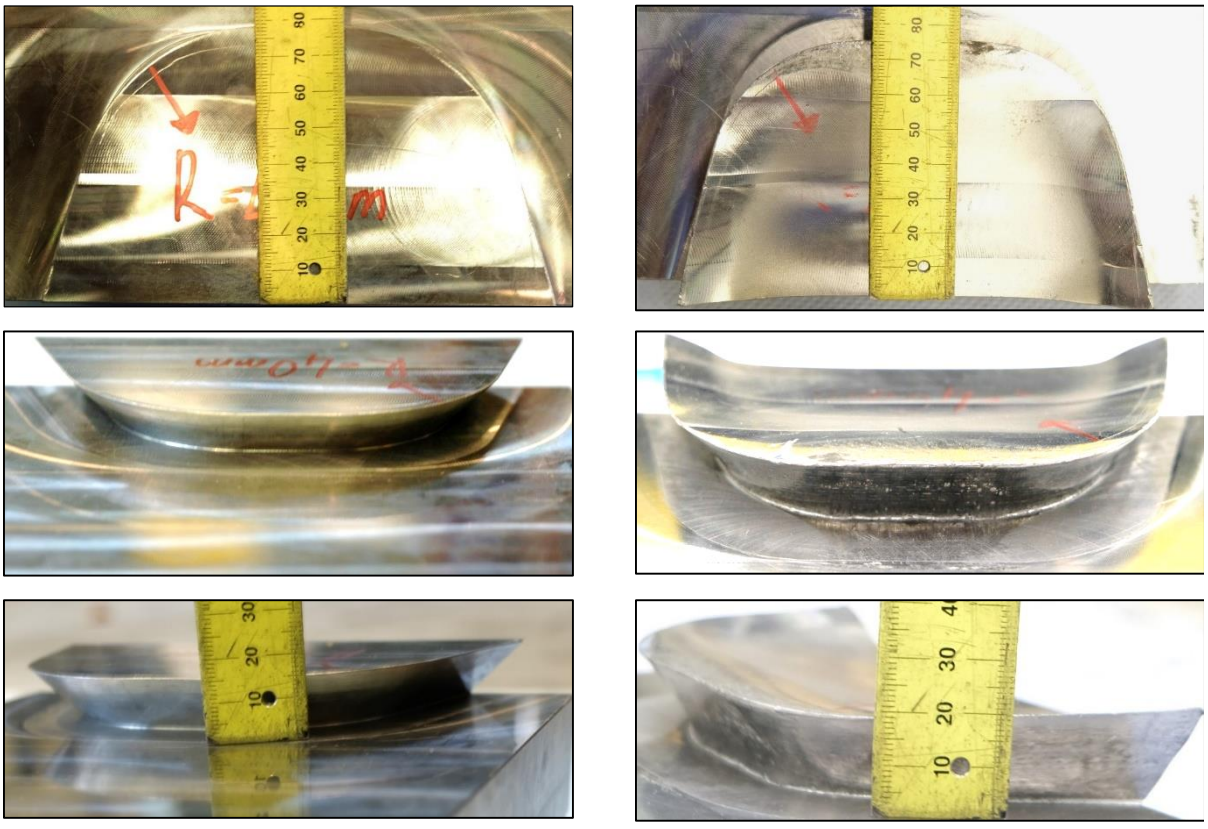

Figure D.3: Deformation of the hub and dovetail counterparts / Plug-inC-02.

a) Inner Plate with Hub Counterpart at In-plane Left Side

Before Test

After Test

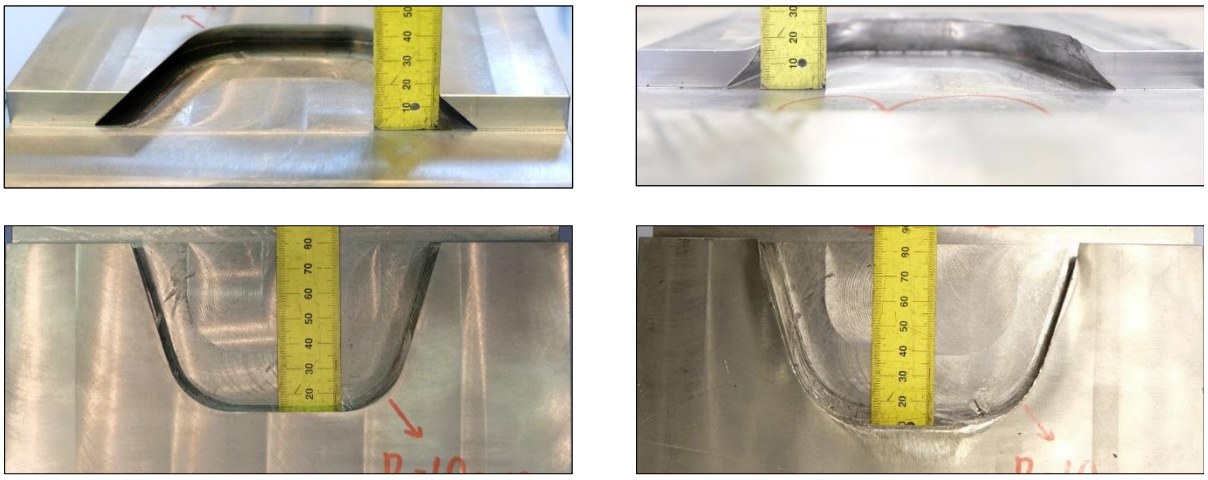

b) Cover Plate with Dovetail Counterpart at In-plane Left-side

Before Test

After Test

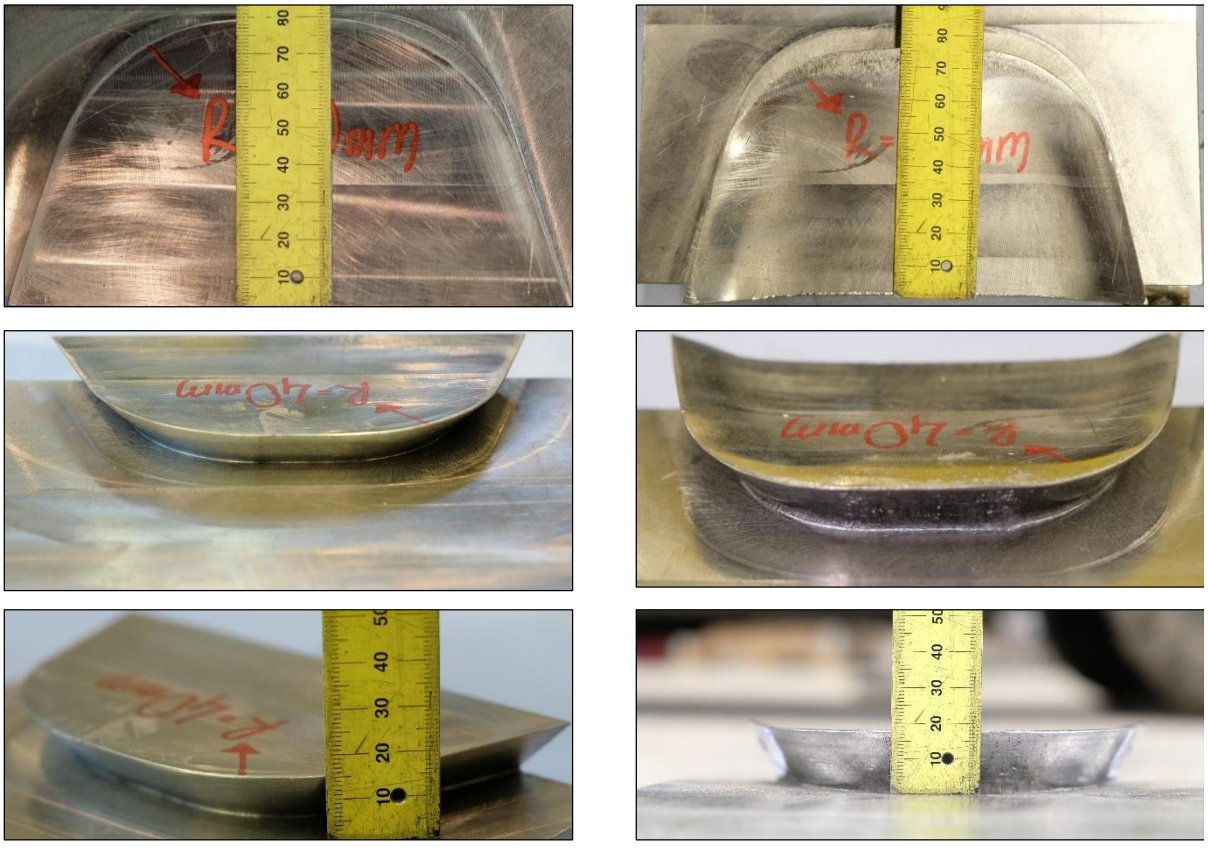

Figure D.4: Deformation of the hub and dovetail counterparts / Plug-inC-03.

D.3 Additional FEAs results, solver parameters and energy balances of the FEAs

After test conditions of the second (Plug-inC-02) and the third test specimens (Plug-inC-03) are compared with their corresponding FEAs outputs in Fig. D.5 and Fig. D.6, respectively.

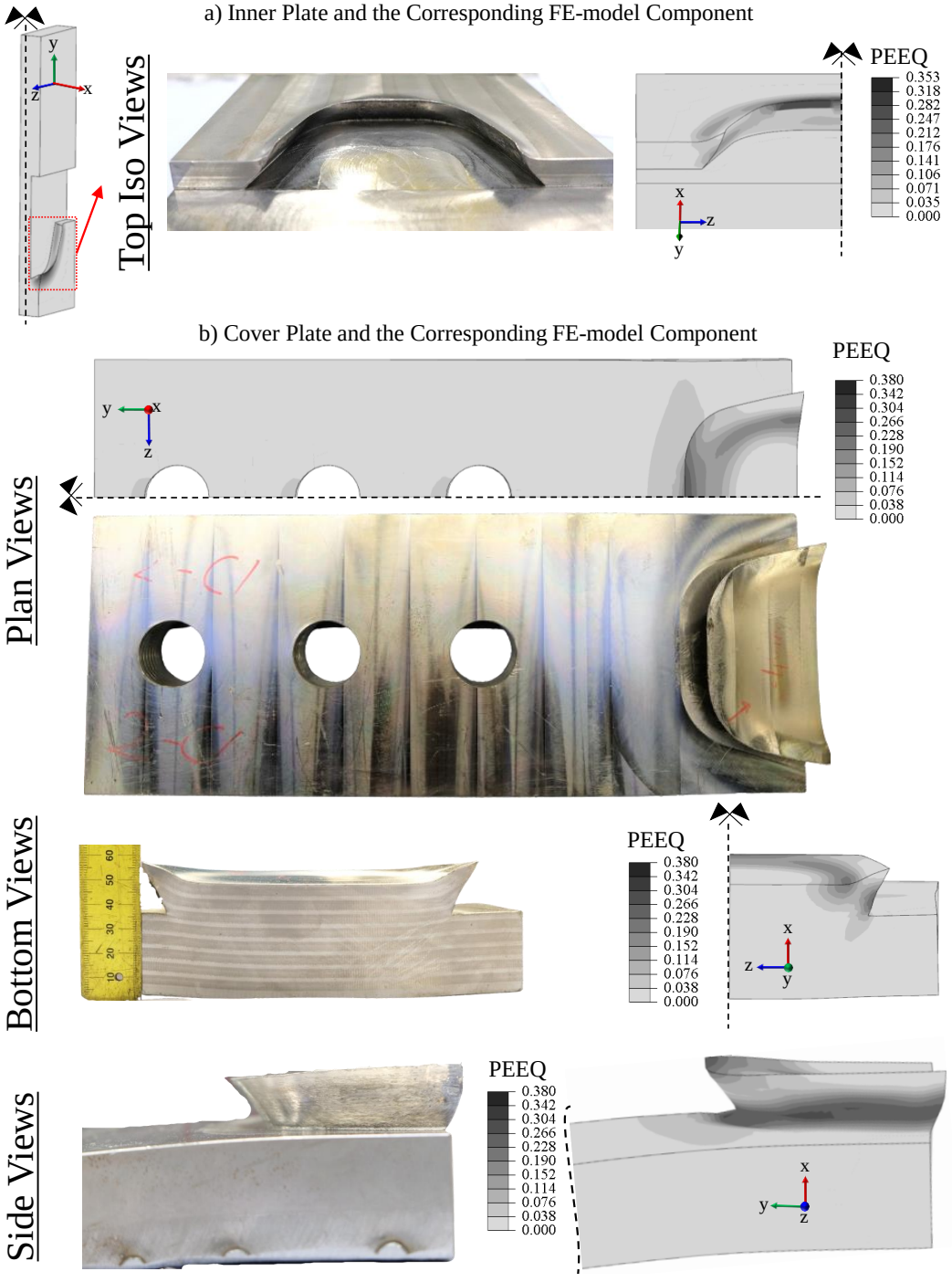

Figure D.5: Comparison of the deformations for Plug-inC-02 test specimens against FEA.

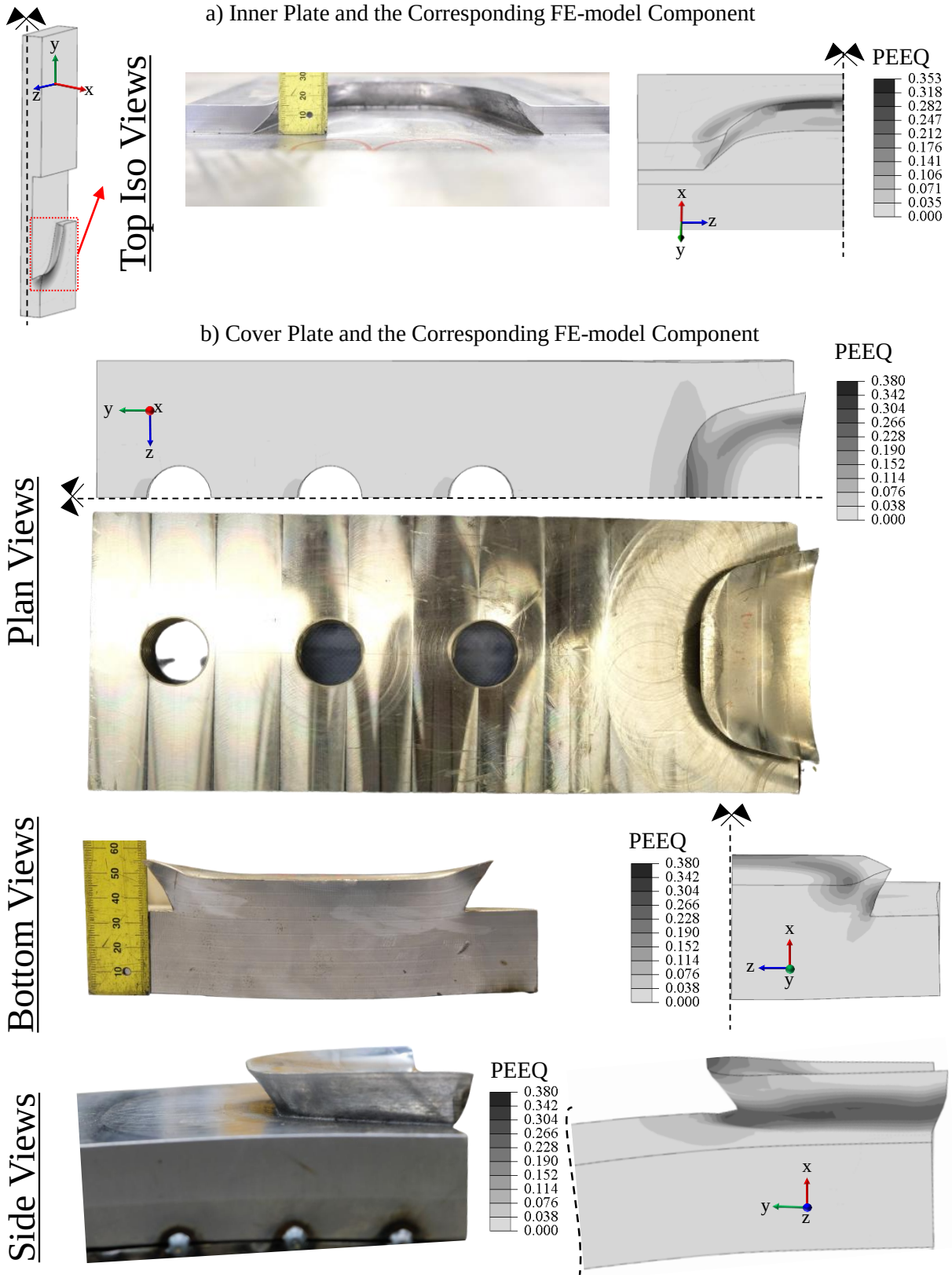

Figure D.6: Comparison of the deformations for Plug-inC-03 test specimens against FEA.

Table D.2 presents the dynamic-implicit solver parameters for the FEAs of Plug-inC test campaign. The energy balances of the corresponding FEAs are also presented in Fig. D.7.

Table D.2: FEA solver parameters of Plug-inC test campaigns

FEA Model ID	Plug-inC-01	Plug-inC-02	Plug-inC-03
Solution Step	Step-1		
Solver	Dynamic-implicit		
Step Time Period	1		
Geometrical Nonlinearities	YES		
Initial Increment Size	0.1		
Min Increment Size	10^{-8}		
Max Increment Size	0.1		
Matrix Storage	Unsymmetric		
Solution Technique	Full Newton		
Other Parameters	Default		

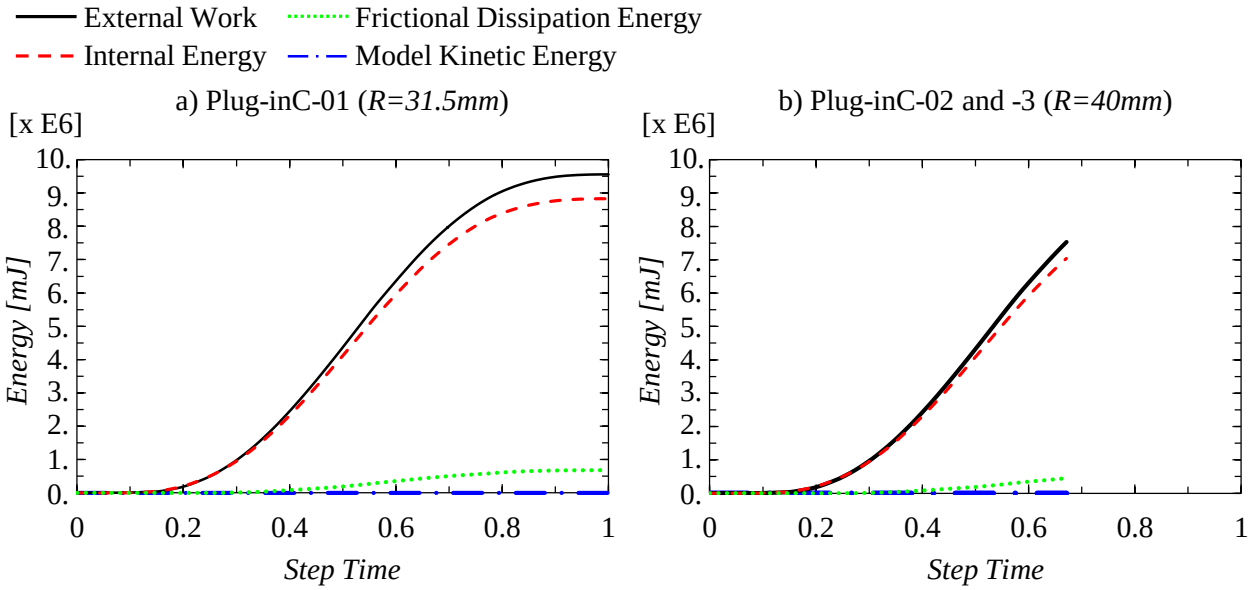

Figure D.7: Energy balance for the FEAs of Plug-inC test campaign.

D.4 Load-deformation behaviors of the numerical parametric study

The load-displacement and moment-rotation curves of the FEAs performed under the numerical parametric study presented in Section 4.6 are given in Fig. D.8 and Fig. D.9 for the dovetail round radius 31.5mm (*R=31.5mm*) and 40mm dovetail round radius (*R=40mm*), respectively.

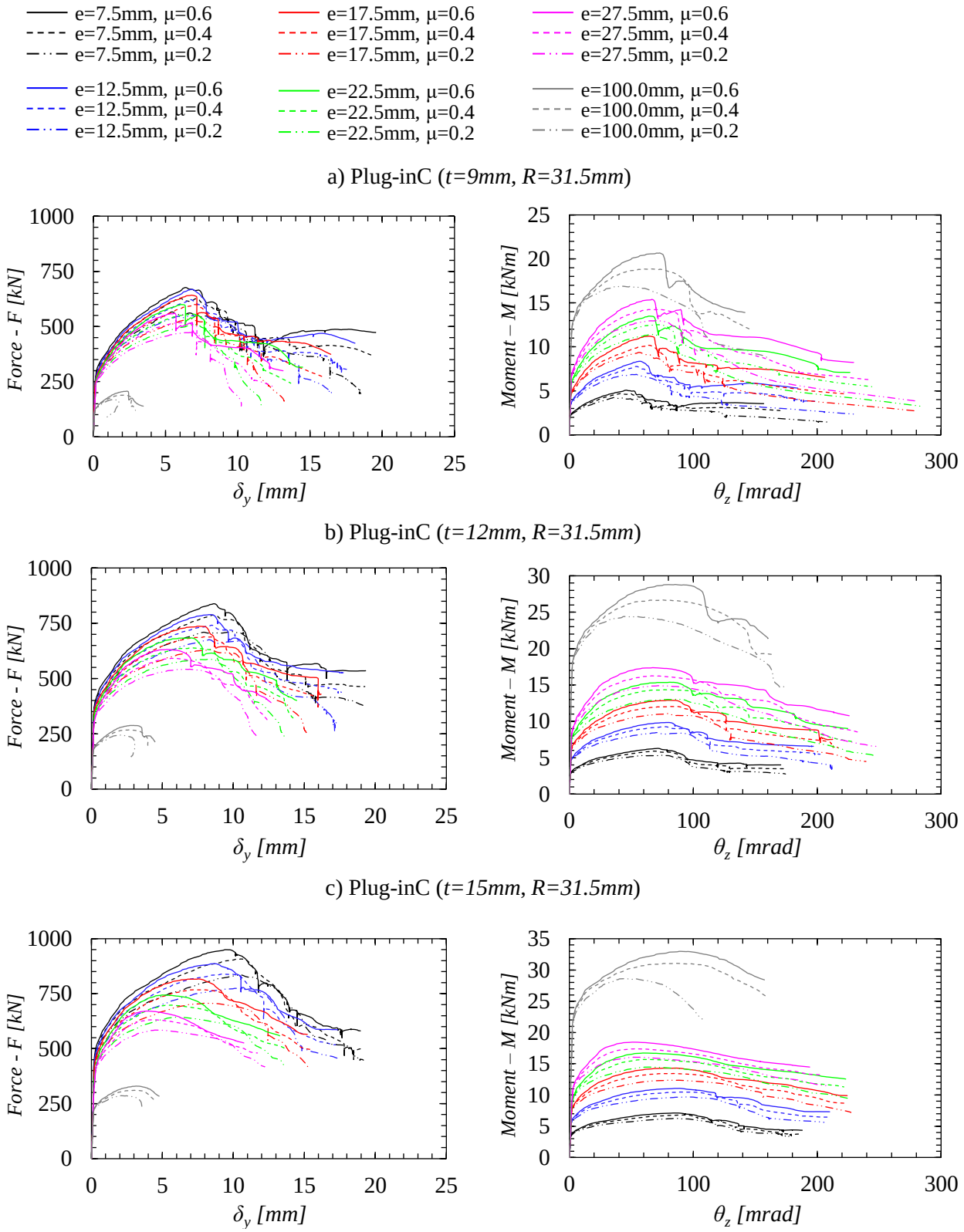

Figure D.8: Load-displacement and moment-rotation curves for the FEAs of the numerical parametric study with 31.5mm dovetail round radius (*R=31.5mm*).

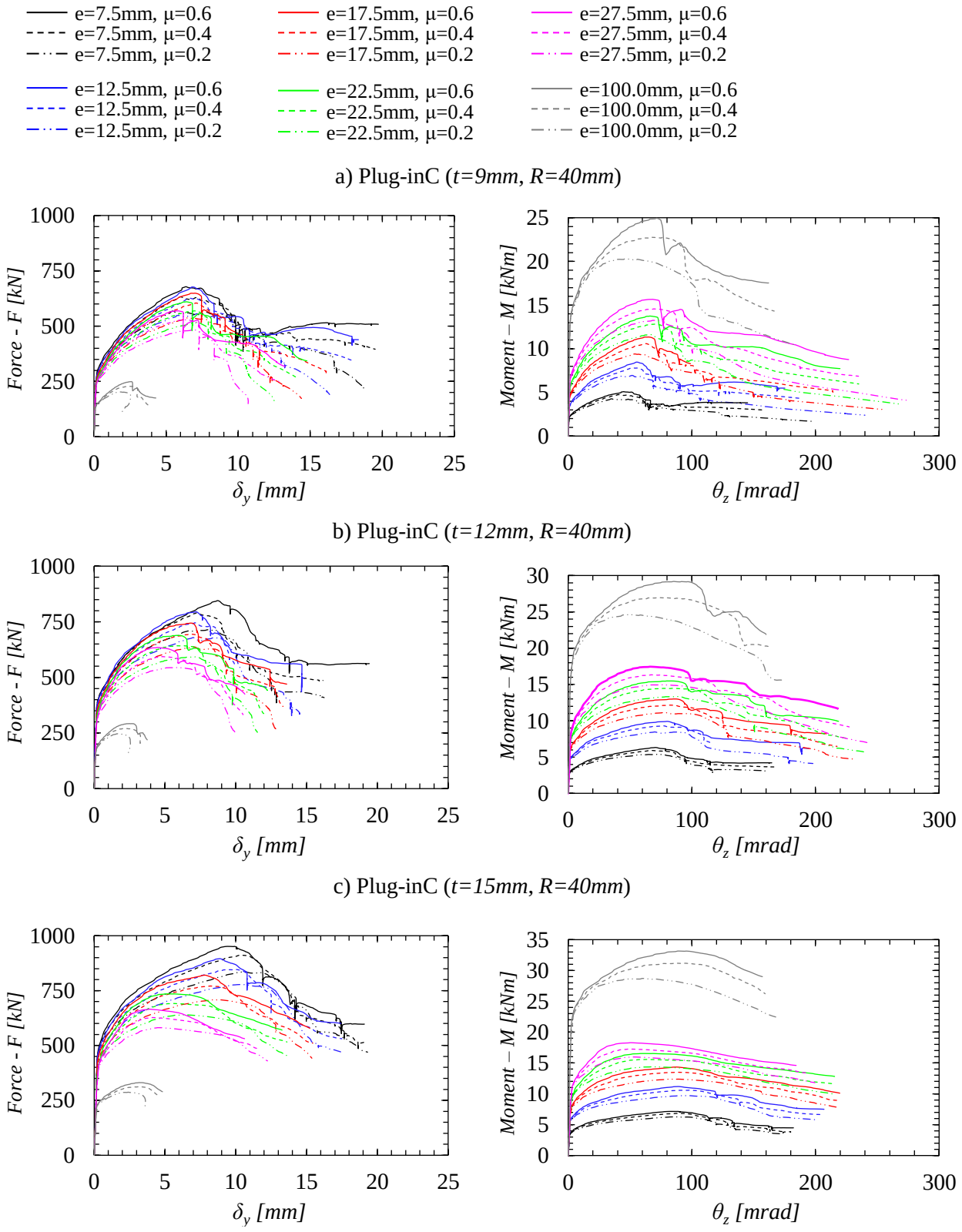

Figure D.9: Load-displacement and moment-rotation curves for the FEAs of the numerical parametric study with 40mm dovetail round radius (*R=40mm*).

D.5 Calculation of dovetail back surface area and its geometric center

The back surface area of the dovetail can be calculated with Eq. D.1;

$$A_{ba} = 2 \cdot [A_1 + A_2 + A_3 + A_4] \tag{D.1}$$

where;

$$A_1 = \frac{\frac{\Pi}{180} \cdot (90 - \phi) \cdot R^2}{2} \tag{D.2}$$

$$A_2 = \frac{R^2 \cdot \tan\phi}{2} \tag{D.3}$$

$$A_3 = \frac{R \cdot w_{inner}}{2} - R^2 \cdot \left(\frac{w_{inner}}{2 \cdot h_{inner}} - \tan\phi \right) - \frac{R^2}{\cos\phi} \tag{D.4}$$

$$A_4 = (h_{inner} - R) \cdot \left(\frac{w_{inner}}{2} + \frac{R \cdot w_{inner}}{4 \cdot h_{inner}} - \frac{\tan\phi}{2} \right) \tag{D.5}$$

Thereby, *y-axis* position of the geometric center of the back dovetail surface, h_{GC}, could be calculated with Eq. D.6;

$$h_{A_{ba}-GC} = \frac{\sum_{i=1}^{i=4} A_i \cdot h_{A_i-GC}}{A_{ba}} \tag{D.6}$$

where;

$$h_{A_1-GC} = R - 2R \cdot \left(\frac{\sin\frac{(90-\phi)}{2}}{3 \cdot \frac{\Pi}{180} \cdot (90 - \phi)} \right) \cdot \cos\frac{(90 - \phi)}{2} \tag{D.7}$$

$$h_{A_2-GC} = R \cdot \left(1 - \frac{\sin\phi}{3} \right) \tag{D.8}$$

$$h_{A_3-GC} = \frac{R}{2} \tag{D.9}$$

$$h_{A_4-GC} = \frac{(h_{inner} - R) \cdot \left(R \cdot \left(\frac{w_{inner}}{2 \cdot h_{inner}} - \tan\phi \right) + w_{inner} \right)}{3 \cdot \left(\frac{w_{inner}}{2} + R \cdot \left(\frac{w_{inner}}{2 \cdot h_{inner}} - \tan\phi \right) \right)} \tag{D.10}$$

ANNEX E

Complementary results for GJSFB Test Campaign

E.1 Tensile coupon tests

The material properties of the steel beams, bottom plates, longitudinal steel reinforcements and the threaded rods (M24 and M30) used in GJSFB test campaign were determined according to EN ISO 6892-1 Method A1 [63]. Fig. E.1 shows the technical drawing of the rectangular steel coupons produced from the steel beams and the bottom plate. Fig. E.2 shows the technical drawing of the round steel coupons produced from the longitudinal steel reinforcements and the threaded-rods. The results of the rectangular steel coupon tests are presented in Table E.1. The results of the round steel coupon tests of the steel reinforcements are presented in Table E.2 and the results of the round steel coupon tests of the threaded-rods are presented in Table E.3. Fig. E.3 and Fig. E.4 present the before and the after test conditions of the steel coupons.

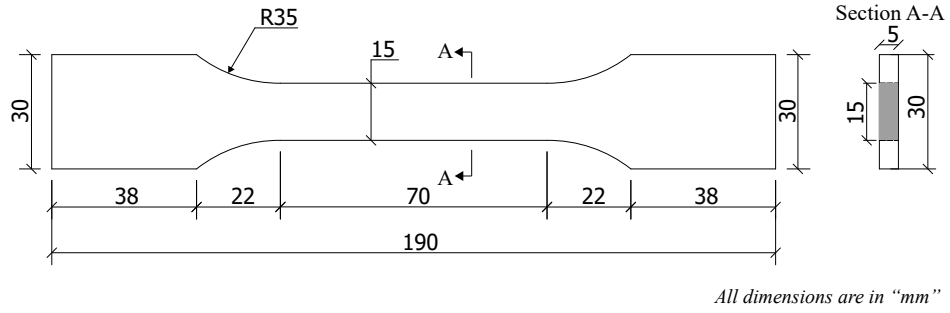

Figure E.1: Technical drawing of the rectangular steel coupons / GJFSB test campaign.

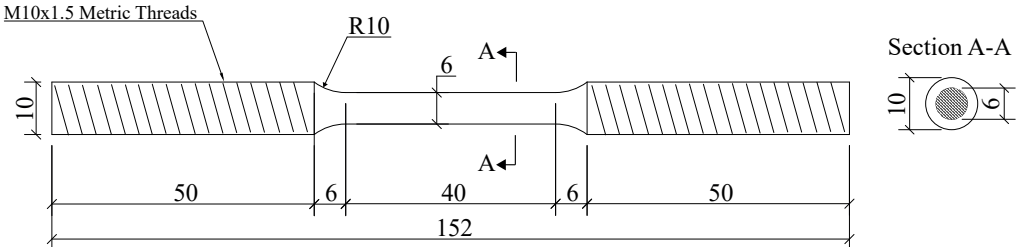

Figure E.2: Technical drawing of the round steel coupons / GJFSB test campaign.

Table E.1: Rectangular coupon tensile test results / GJSFB test campaign.

Specimen Number	1	2	3	4	5	6
Specimen ID	F-1	F-2	W-1	BP-1	B1-2	BP-3
Material Grade	S355	S355	S355	S355	S355	S355
Total Length of Test Piece, L_t [mm]	190	190	190	190	190	190
Original Gauge Length, L_o [mm]	50	50	50	50	50	50
Original Gauge Thickness, a_o [mm]	5.030	5.060	5.025	5.032	5.036	5.036
Original Gauge Width, b_o [mm]	15.045	15.041	15.045	15.029	15.035	15.034
Original Cross-sectional Area, S_o [mm^2]	75.68	76.11	75.60	75.62	75.72	75.71
Elastic Modulus, E [GPa]	206.5	207.4	203.1	212.3	210.1	204.3
Proof Strength, R_p [MPa]	N/A	N/A	418	N/A	N/A	N/A
Lower Yield Strength, R_{eL} [MPa]	358	358	N/A	395	396	391
Upper Yield Strength, R_{eH} [MPa]	381	385	N/A	470	475	459
Tensile Strength, R_m [MPa]	517	514	538	538	538	533
Total Machine Travel at Tensile Strength, δ_m [mm]	12.42	11.95	8.77	11.94	12.47	13.03
Maximum Load, F_m[1] [kN]	39.1	39.1	40.7	40.7	40.7	40.3
Fracture Load, F_f[2] [kN]	26.6	26.0	28.3	25.2	25.5	25.4
Fracture Stress, f_f [MPa]	351.5	341.6	374.3	333.2	336.8	335.5
Percentage Elongation after Fracture, A [%]	34.0	35.0	28.5	33.0	32.5	32.5
Percentage Reduction of Area after Fracture, Z [%]	60.0	67.6	54.4	64.2	62.7	68.8
Rupture Position	1/2	1/2	1/2	1/2	1/2	1/2

[1] The maximum load corresponds to the force output from the testing machine at the necking of the steel coupon.

[2] The fracture load corresponds to the force output from the testing machine once the fracture of the steel coupon occurs.

Table E.2: Round coupon tensile test results for the reinforcements / GJSFB test campaign.

Specimen Number	1	2	3	4	5	6
Specimen ID	*Ø12-1*	*Ø12-2*	*Ø12-3*	*Ø16-1*	*Ø16-2*	*Ø16-3*
Material Grade	B500B	B500B	B500B	B500B	B500B	B500B
Total Length of Test Piece, L_t [mm]	152	152	152	152	152	152
Original Gauge Length, L_o [mm]	30	30	30	30	30	30
Original Gauge Diameter, d_o [mm]	5.965	5.997	5.998	5.998	5.998	5.995
Original Cross-sectional Area, S_o [mm^2]	27.95	28.25	28.25	28.26	28.26	28.23
Elastic Modulus, E [GPa]	207.8	205.6	225.2	205.5	212.3	212.6
Proof Strength, R_p [MPa]	N/A	N/A	426	383	384	N/A
Lower Yield Strength, R_{eL} [MPa]	404	363	N/A	N/A	N/A	364
Upper Yield Strength, R_{eH} [MPa]	448	470	N/A	N/A	N/A	414
Tensile Strength, R_m [MPa]	570	572	586	560	556	560
Total Machine Travel at Tensile Strength, δ_m [mm]	7.46	7.25	5.76	7.28	7.45	7.33
Maximum Load, F_m[1] [kN]	15.9	16.1	16.6	15.8	15.8	15.8
Fracture Load, F_f[2] [kN]	11.9	11.9	12.2	10.7	10.5	10.5
Fracture Stress, f_f [MPa]	425.8	421.2	431.9	378.6	371.5	371.9
Percentage Elongation after Fracture, A [%]	32.0	29.5	24.5	31.0	31.5	33.5
Percentage Reduction of Area after Fracture, Z [%]	57.8	55.9	57.9	64.3	68.4	65.3
Rupture Position	1/2	1/2	1/2	1/2	1/2	1/2

[1] The maximum load corresponds to the force output from the testing machine at the necking of the steel coupon.

[2] The fracture load corresponds to the force output from the testing machine once the fracture of the steel coupon occurs.

Table E.3: Round coupon tensile test results for the threaded-rods / GJSFB test campaign.

Specimen Number	1	2	3	4	5	6
Specimen ID	*Ø24-1*	*Ø24-2*	*Ø24-3*	*Ø30-1*	*Ø30-2*	*Ø30-3*
Material Grade	12.9	12.9	12.9	12.9	12.9	12.9
Total Length of Test Piece, L_t [mm]	152	152	152	152	152	152
Original Gauge Length, L_o [mm]	30	30	30	30	30	30
Original Gauge Diameter, d_o [mm]	6.010	6.009	5.993	5.988	6.000	5.980
Original Cross-sectional Area, S_o [mm^2]	28.37	28.36	28.21	28.16	28.28	28.09
Elastic Modulus, E [GPa]	201.1	206.8	203.4	204.9	223.7	201.0
Proof Strength, R_p [MPa]	1210	1212	1209	1120	1099	1108
Tensile Strength, R_m [MPa]	1311	1313	1314	1216	1194	1204
Total Machine Travel at Tensile Strength, δ_m [mm]	3.31	3.36	3.31	4.10	3.80	3.94
Maximum Load, F_m[1] [kN]	37.2	37.2	37.1	34.2	33.8	33.8
Fracture Load, F_f[2] [kN]	27.0	26.9	26.5	21.4	21.3	21.5
Fracture Stress, f_f [MPa]	951.7	948.5	934.4	759.9	753.2	765.4
Percentage Elongation after Fracture, A [%]	13.0	13.0	12.0	15.0	14.0	13.5
Percentage Reduction of Area after Fracture, Z [%]	45.7	48.6	49.6	60.6	60.5	60.0
Rupture Position	1/2	1/3	1/3	1/3	1/3	1/3

[1] The maximum load corresponds to the force output from the testing machine at the necking of the steel coupon.

[2] The fracture load corresponds to the force output from the testing machine once the fracture of the steel coupon occurs.

The ultimate strains (ε_u), which were used for the finite element analyses of GJSFB test campaign presented in Section 5.3, were calculated with Eq. B.1 according to the data presented in Table E.1, Table E.2 and Table E.3 for the corresponding FE-model components.

a) GJSFB / Steel Coupons of Beam (F-1, F2 and W-1)

Before Test

After Test

b) GJSFB / Steel Coupons of Bottom Plate (BP)

Before Test

After Test

Figure E.3: Before and after test conditions of the rectangular steel coupons / GJSFB test campaign.

a) Ø12 Reinforcement Coupons

Before Test

After Test

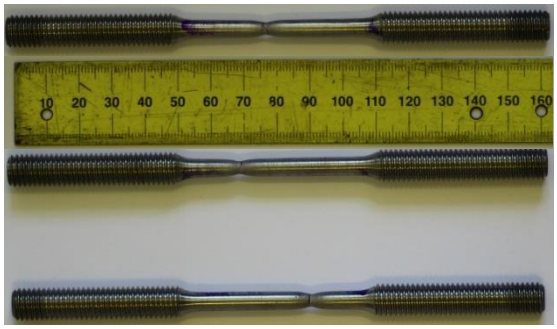

b) Ø16 Reinforcement Coupons

Before Test

After Test

c) Ø24 Threaded-rod Coupons

Before Test

After Test

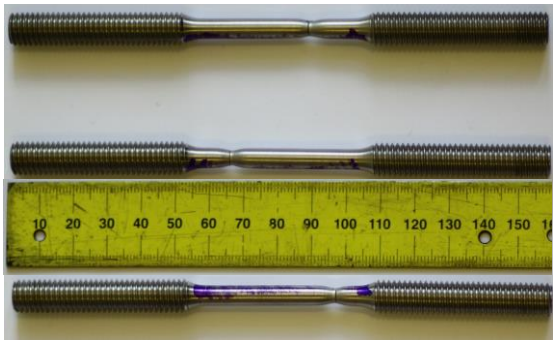

b) Ø30 Threaded-rod Coupons

Before Test

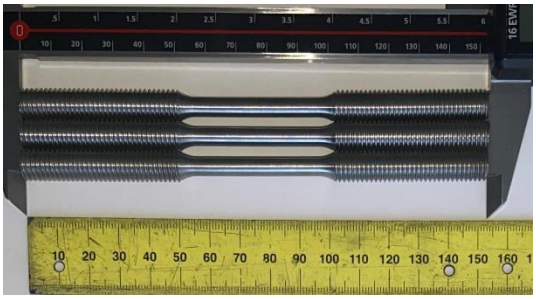

After Test

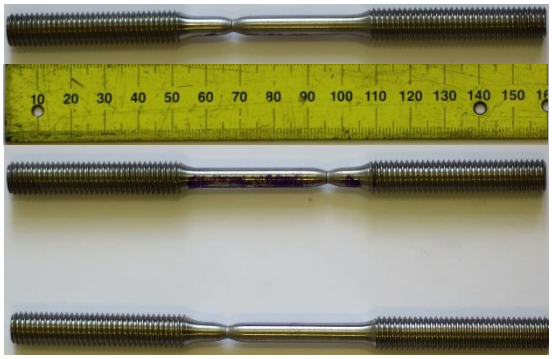

Figure E.4: Before and after test conditions of the round steel coupons / GJSFB test campaign.

E.2 Additional images for the production of GJSFB test specimens.

Fig. E.5 to Fig. E.8 present additional images for the production of GJSFB test specimens.

Positioning of Steel Beams and the End-diagram for the Metal Sheeting

Positioning of Steel Metal Sheeting

Shear Connectors and Weld-seem of a Sheer Connector

Figure E.5: Additional images for the production of GJSFB test specimens-1.

Formwork of the Test Specimens

Concreting of the Test Specimens

Couplers Installed to Carry the Test Specimens

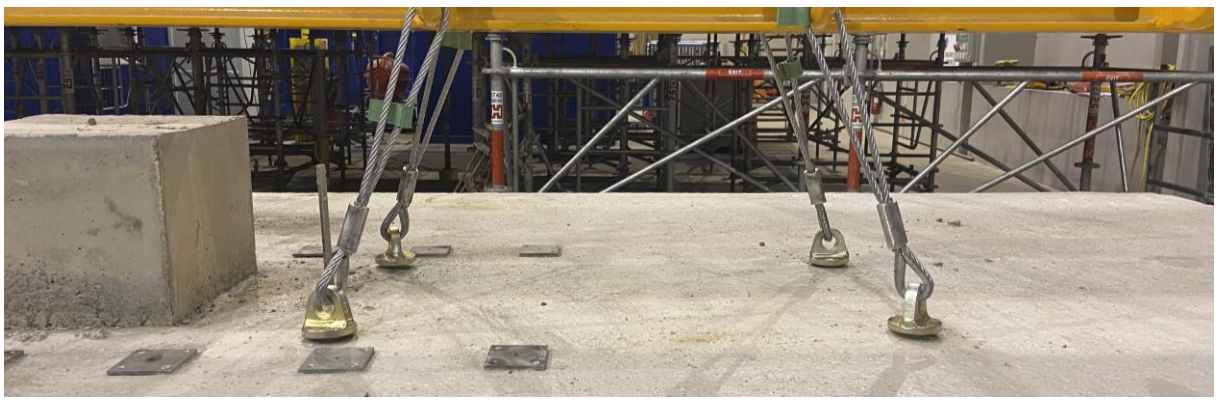

Figure E.6: Additional images for the production of GJSFB test specimens-2.

Lifting Operation of the Test Specimens

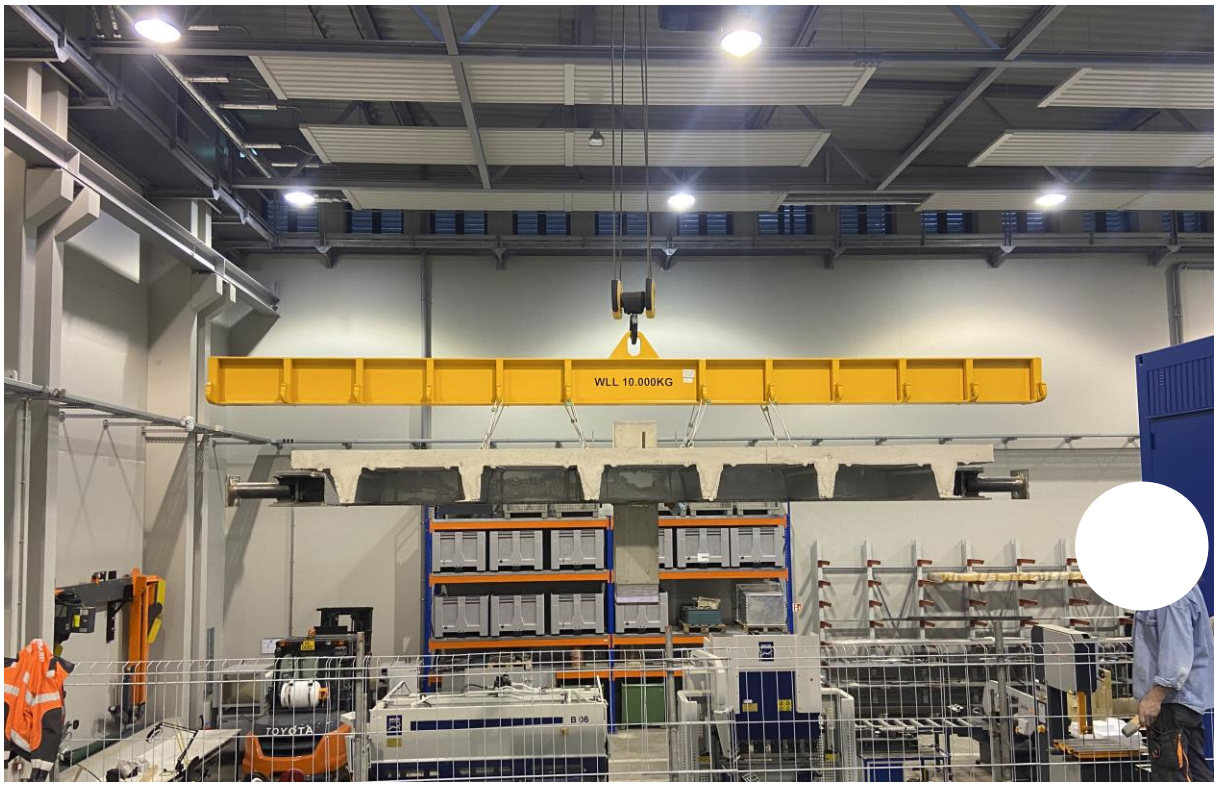

Installation of the Temporary Supports and the Preparation for the Upside-down Turning Operation

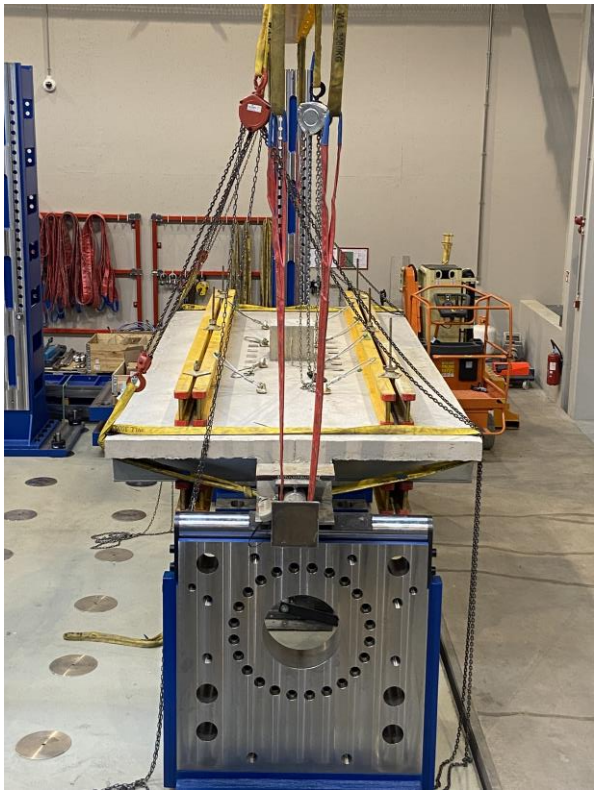

Figure E.7: Additional images for the production of GJSFB test specimens-3.

Upside-down Turning Operation of the Test Specimens

Concrete Samples and Their Storage for the Material Characterization Tests

Figure E.8: Additional images for the production of GJSFB test specimens-4.

E.3 Solver parameters and the energy balances of the FEAs

Table E.4 presents the explicit solver parameters [66] of FEAs performed under Section 5.3. In addition, the energy balances of the corresponding FEAs are presented in Fig. E.9.

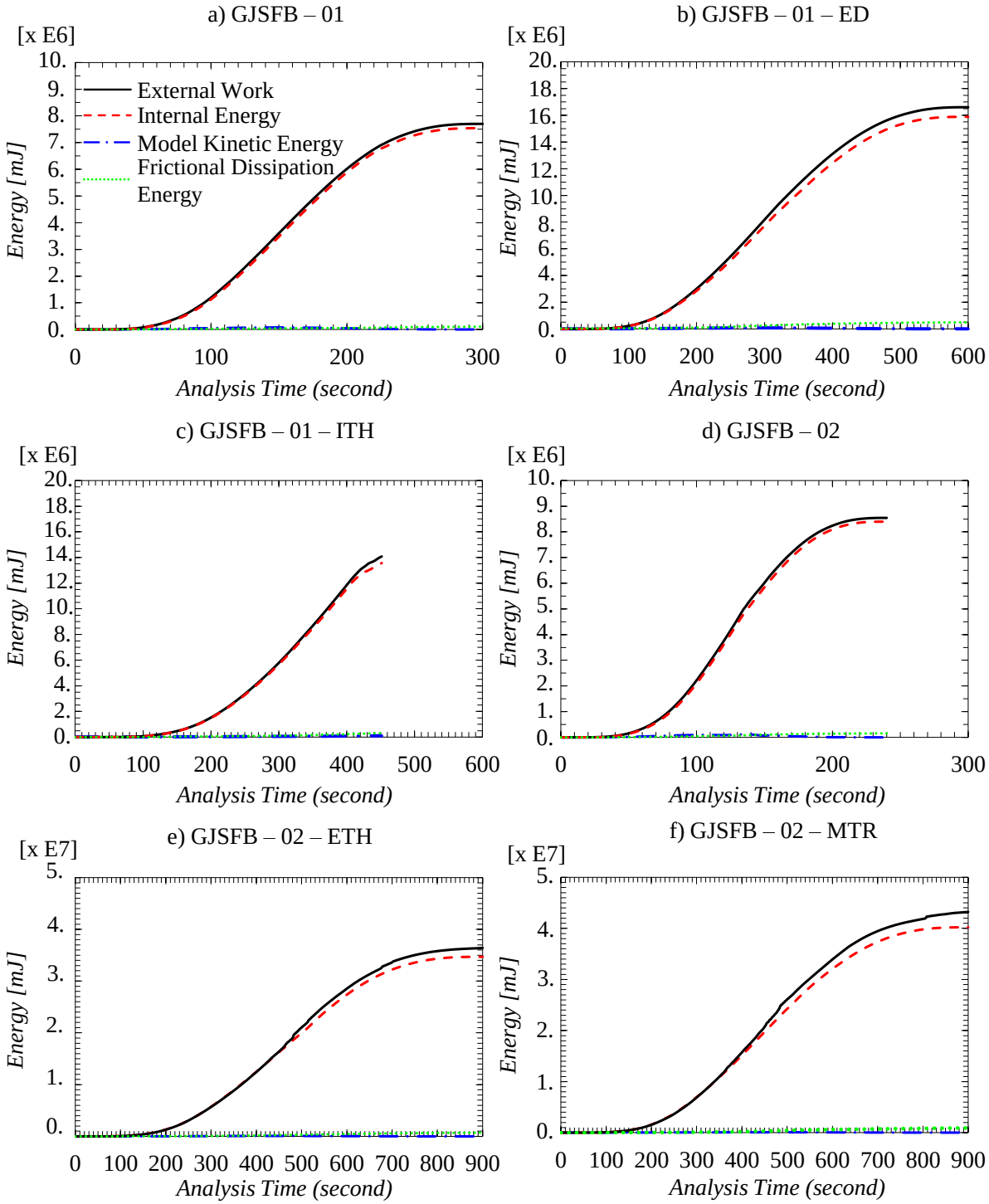

Figure E.9: Energy balance for the FEAs of GJSFB test campaign.

Table E.4: FEA solver parameters of GJSFB test campaign

FEA Model ID	GJSFB-01	GJSFB-01-ED	GJSFB-01-ITH	GJSFB-02	GJSFB-02-Cyclic		GJSFB-02-ETH	GJSFB-02-MTR
Solution Step	Step-1	Step-1	Step-1	Step-1	Step-1	Step-2	Step-1	Step-1
Solver	Dynamic Explicit							
Time Period (second)	300	900	900	300	15000	300	900	900
Geometrical Nonlinearities	YES							
Type	Automatic							
Stable Increment Estimation	Global							
Maximum Time Increment	Unlimited							
Time Scaling Factor	1							
Mass Scaling Factor	Whole Model:10^6							
Linear Bulk Viscosity Parameter	0.06							
Quadratic Bulk Viscosity Parameter	0.12							

BIBLIOGRAPHY

[1] European Committee for Standardization (CEN). *EN1992-4:2018: Design of concrete structures - Part:4 Design of fastenings for use in concrete.* Brussels, Belgium, 2018.

[2] European Committee for Standardization (CEN). *EN1994-1-1: Eurocode 4 - Design of composite steel and concrete structures. Part 1-1: General rules and rules for buildings.* Brussels, Belgium, 2010.

[3] International Federation for Structural concrete (fib). *fib Model Code for Concrete Structures 2010*. Wilhelm Ernst Sohn, Berlin, Germany, 2010.

[4] T.F. Yolacan and M. Schäfer. Determination of slip factor between cnc-cut serrated surfaces of s355j2 grade steel plates. *MDPI Buildings*, 46(4):32–42, 2022.

[5] R. Roger-Bruno. Industrialised building systems: Reproduction before automation and robotics. *Automation in Construction*, 14:442–451, 2005.

[6] H. Zabihi, F. Habib, and L. Mirsaeedie. Definitions, concepts and new directions in Industrialized Building Systems (IBS). *KSCE Journal of Civil Engineering*, 17:1199–1205, 2013.

[7] A.W. Lacey, C. Wensu, H. Hao, and K. Bi. New interlocking inter-module connection for modular steel buildings:Simplified structural behaviors. *Engineering Structures*, 227:111409, 2021.

[8] Hon. D. Alfred A. Yee. Structural and economic benefits of precast/prestressed concrete construction. *PCI Journal*, 46(4):32–42, 2001.

[9] L. Jaillon and C.S. Poon. Sustainable construction aspects of using prefabrication in dense urban environment: a hong kong case study. *Construction Management and Economics*, 26:953–966, 2008.

[10] A.S.H. Suwaed and T. L. Karavasilis. Novel Demountable Shear Connector for Accelerated Disassembly, Repair, or Replacement of Precast Steel-Concrete Composite Bridges. *Journal of Bridge Engineering*, 28(9):397–410, 2017.

[11] Marko Pavloviç. *Resistance of Bolted Shear Connectors in Prefabricated Steel-Concrete Composite Decks*. PhD Dissertation, University of Belgrade, Belgrade, 2013.

[12] J. Wang, B. Uy, H.-T. Thai, and D. Li. Behaviour and design of demountable beam-to-column composite bolted joints with extended end-plates. *Journal of Constructional Steel Research*, 144:221–235, 2018.

[13] U. Kuhlmann, W. Frantisek, J. Hofmann, and et al. *New Market Chances for Steel Structures by Innovative Fastening Solutions between Steel and Concrete (INFASO): Design of Steel-to-Concrete Joints Design Manual I.* European Convention for Constructional Steelwork, Prague, Stuttgart, Coimbra, and Brussels, 2014.

[14] Y. A. Al-Salloum, M.A. Alrubaidi, , H.M. Elsanadedy, T.H. Almusallam, and R.A. Iqbal. Strengthening of precast RC beam-column connections for progressive collapse mitigation using bolted steel plates. *Engineering Structures*, 161:146–160, 2018.

[15] U. Ersoy and T. Tankut. Precast Concrete Members With Welded Plate Connections Under Reversed Cyclic Loading. *PCI Journal*, 38:94–100, 1993.

[16] D.N. Suzanne, E.E. Robert, and L.P. Juergen. Ductile Connectors for a Precast Concrete Frame. *PCI Journal*, 39:46–59, 1994.

[17] J. Bujnak, W. Roeser, S. Matiasko, and M. Böhm. Experimental assessment of an innovative beam to column connection. In D.A. Hordijk and M. Luković, editors, *High Tech Concrete: Where Technology and Engineering Meet*, pages 983–988, Cham, 2018. Springer International Publishing.

[18] H. Wang, E. M. Marino, , P. Pan, H. Liu, and X. Nie. Experimental study of a novel precast prestressed reinforced concrete beam-to-column joint. *Engineering Structures*, 156:68–81, 2018.

[19] N.B. Eghbali and S.R. Mirghaderi. Experimental investigation of steel beam to rc column connection via a through-plate. *Journal of Constructional Steel Research*, 133:125–140, 2017.

[20] W. Li, Q.-n. Li Li, W.-s. Jiang, and L. Jiang. Seismic performance of composite reinforced concrete and steel moment frame structures – state-of-the-art. *Composites Part B: Engineering*, 42(2):190–206, 2011.

[21] G. Abbiati, E. Cazzador, S. Alessandri, O.S. Bursi, F. Paolacci, and S. De Santis. Experimental characterization and component-based modeling of deck-to-pier connections for composite bridges. *Journal of Constructional Steel Research*, 150:31–50, 2018.

[22] H. Zhao, X. Nie, D. Zhu, and M.X. Tao. Mechanical properties of novel out-of-plane steel beam–concrete wall pinned joints with t-shaped steel connectors under monotonic tension load. *Engineering Structures*, 192:71–85, 2019.

[23] J.R. Henderson. *The Design of Cast-in Plates*. The Steel Construction Institute (SCI), Berkshire, UK, 2017.

[24] Stephan Fromknecht. *Contribution to the load-bearing capacity of anchor plates with headed studs in reinforced concrete columns*. PhD Dissertation, University of Luxembourg, Luxembourg, 2009.

[25] European Committee for Standardization (CEN). *EN1993-1-8: Eurocode 3 - Design of steel structures. Part 1-8: Design of joints.* Brussels, Belgium, 2005.

[26] A. Ožbolt, U. Kuhlmann, J. Henriques, and L.S. da Silva. Behaviour of steel-to-concrete joints. *Steel Construction*, 5(3):145–150, 2012.

[27] J. Henriques, L.S. da Silva, and I.B. Valente. Numerical modeling of composite beam to reinforced concrete wall joints part i: Calibration of joint components. *Engineering Structures*, 52:747–761, 2013.

[28] D. Konertz, G.K. Kocur, F. Häusler, and P. Mark. Longitudinal shear transmission of anchor channels into concrete—an experimental approach. *Structural Concrete*, 22(2):1–13, 2020.

[29] HALFEN-GmbH. *HALFEN HUC Universal Connection Technical Product Information, HUC 10-US*. HALFEN GmbH, Germany, 2012.

[30] PEIKKO GROUP. *Technical Manual, PCs® CORBEL - Hidden Corbel for Supporting Beams, PEIKKO GROUP 04/2019*. PEIKKO GROUP, 2019.

[31] Deutsches Institut für Bautechnik (DIBt). *Peikko PCs Konsole zum Anschluss von Balken an Wande und Stützen, DIBt: Z-21.8-2076*. Deutsches Institut für Bautechnik (DIBt), Berlin, Germany, 2022.

[32] PEIKKO GROUP. *Technical Manual, DELTABEAM® Composite Beams - Slim Floor Structure with integrating fireproofing, PEIKKO GROUP 03/2021*. PEIKKO GROUP, 2021.

[33] P. Kyriakopoulos, S. Peltonen, I. Vayas, C. Spyrakos, and M.V. Leskela. Experimental and numerical investigation of the flexural behavior of shallow floor composite beams. *Engineering Structures*, 231:111734, 2021.

[34] PEIKKO GROUP. *Technical Manual, PCs® Beam Shoe - Hidden beam shoe for corbel system, PEIKKO GROUP 05/2022*. PEIKKO GROUP, 2022.

[35] C. Fiala, J. Hejl, V. Tomalova, V. Bilek, T. Pavlu, T. Vlach, M. Volf, M. Novotna, and P. Hajek. Structural design and experimental verification of precast columns from high performance concrete. *Advanced Materials Research*, 1106:110–113, 2015.

[36] Joakim Kvist and Daniel Näkne. *FE-Analysis of a beam-column connection in composite structures exposed to fire.* Master's Thesis 2011:67, Chalmers University of Technology, Sweden, 2011.

[37] N.D. Perreira, R.B. Fleischman, B.V. Viscomi, and Le-Wu Lu. *Automated construction and ATLSS connections; Development, analysis, experimentation, and implementation of ATLSS connections for automated construction*. Lehigh University, Bethlehem, PA, 1993.

[38] B.V. Viscomi, W.D. Michalerya, and Le-Wu Lu. Automated construction in the atlss integrated building systems. *Automation in Construction*, 3:35–43, 1993.

[39] D.D. Viana, I.D. Tommelein, and C.T. Formoso. Using modularity to reduce complexity of industrialized building systems for mass customization. *MDPI Energies*, 10(10):1622, 2017.

[40] R.B. Fleischman, B.V. Viscomi, and Le-Wu Lu. Development, analysis, experimentation and implementation of atlss connections for automated construction. In *Proceedings of 1993 National Steel Construction Conference*. American Institute of Steel Construction (AISC), 1993.

[41] Richard B. Garlock. *ATLSS Connections with Moment Capacity*. Lehigh University, Bethlehem, PA, 1993.

[42] Kali E. Wyncott. *Behaviour of frames with partially restrained composite connections using the ATLSS connector*. Lehigh University, Bethlehem, PA, 1996.

[43] A.M. Rosa, Le-Wu Lu, and B.V. Viscomi. Atlss connectors in semi-rigid composite connections. In *Proceedings of Structures Congress XII*. The American Society of Civil Engineers (ASCE), 1994.

[44] Anstar Oy. *Design Manual, A-BEAM S®, Version 11/2021*. Anstar Oy, Erstantie, FINLAND, 2021.

[45] Anstar Oy. *AEP Steel Bracet Manual, Version 1/2015*. Anstar Oy, Erstantie, FINLAND, 2015.

[46] American Institute of Steel Construction (AISC). *Prequalified Connections for Special and Intermediate Steel Moment Frames for Seismic Applications, including Supplement No.1 - ANSI/AISC 358-16, ANSI/AISC 358s1-18*. United States of America, 2016.

[47] A. Rezaeian, M. Jamal-Omidi, and F. Shahidi. Seismic behavior of conxl rigid connection in box-columns not filled with concrete. *Journal of Constructional Steel Research*, 97:79–104, 2014.

[48] Y. Chao, J.F. Yang, M.Z. Su, and Liu C.Z. Numerical study on seismic behaviours of conxl biaxial moment connection. *Journal of Constructional Steel Research*, 121:185–201, 2016.

[49] E.M. Shemshadian, A.E. Schultz, J.L. Le, R. Labbane, D.F. Laefer, S. Al-Sabah, L. Truong-Hong, M.P. Huynh, P. McGetrick, T. Martin, and P. Matis. Amass: Advanced manufacturing for the assembly of structural steel. *Practice Periodical on Structural Design and Construction*, 26 (1):04020052, 2021.

[50] European Committee for Standardization (CEN). *EN1993-1-1: Eurocode 3 - Design of steel structures. Part 1-1: General rules and rules for buildings.* Brussels, Belgium, 2005.

[51] W.A.H. Mashrah, Z. Chen, and H. Liu. Numerical and theoretical study on mechanical behaviors of new dovetail joint system (ndjs) subjected to tensile, compressive, and out-of-plane bending moment forces. *International Journal of Steel Structures*, 21(3):1108–1133, 2021.

[52] W.A.H. Mashrah, Z. Chen, H. Liu, and M.A. Amer. Static performance of novel steel dovetail joints for single-layer grid shells under out-of-plane bending moments. *Journal of Constructional Steel Research*, 187:106988, 2021.

[53] H.-K. Choi, Y.-C. Choi, and C.-S. Choi. Development and testing of precast concrete beam-to-column connections. *Engineering Structures*, 56:1820–1835, 2013.

[54] H.H. Ghayeb, H.A. Razak, and N.H.R. Sulong. Seismic performance of innovative hybrid precast reinforced concrete beam-to-column connections. *Engineering Structures*, 202:109886, 2020.

[55] Y. Zhong, F. Xiong, J. Chen, A. Deng, W. Chen, and X. Zhu. Experimental study on a novel dry connection for a precast concrete beam-to-column joint. *MDPI Sustainability*, 11 (17):4543, 2019.

[56] J. Esmaeili and N. Ahooghalandary. Introducing an easy-install precast concrete beam-to-column connection strengthened by steel box and peripheral plates. *Engineering Structures*, 205:110006, 2020.

[57] S.I. Evans, J. Wang, J. Qin, Y. He, P. Shepherd, and J. Ding. A review of waam for steel construction – manufacturing, material and geometric properties, design, and future directions. *Structures*, 44:1506–1522, 2022.

[58] European Committee for Standardization (CEN). *EN1990:2002: Eurocode - Basis of Structural Design*. Brussels, Belgium, 2002.

[59] European Committee for Standardization (CEN). *EN1090-2: Execution of steel structures and aluminium structures. Part 2: Technical requirements for the execution of steel structures.* Brussels, Belgium, 2008.

[60] European Committee for Standardization (CEN). *EN10025-2:2004: Hot rolled products of structural steel Part 2: Technical delivery conditions for non-alloy structural steels.* Brussels, Belgium, 2004.

[61] European Committee for Standardization (CEN). *Hexagon head bolts - Product grades A and B (ISO4014:2000).* Brussels, Belgium, 2000.

[62] Deutsches Institut Fur Normung (DIN) E.V. *Fasteners - Stud - bolts - Part 1: Metric thread*. Germany, 2016.

[63] International Organization for Standardization (ISO). *Metallic materials - Tensile testing - Part 1: Method of test at room temperature (ISO 6892-1:2009*. 2009.

[64] M. D"Aniello, D. Cassiano, and R. Landolfo. Simplified criteria for finite element modelling of European preloadable bolts. *Steel and composite Structures*, 24(6):643–658, 2017.

[65] European Committee for Standardization (CEN). *EN14399-4:2005: High strength structural bolting assemblies for preloading - Part 4: System HV Hexagon bolt and nut assemblies.* Brussels, Belgium, 2005.

[66] ABAQUS. *User Manual, Version 6.14.* DS SIMULIA Corp, Providence, RI, USA, 2015.

[67] European Committee for Standardization (CEN). *EN1993-1-5: Eurocode 3 - Design of steel structures. Part 1-5: Plated structural elements.* Brussels, Belgium, 2006.

[68] International Organization for Standardization (ISO). *Mechanical properties of fasteners made of carbon steel and alloy steel - Part 1: Bolts, screws and studs with specified property classes - coarse thread and fine pitch thread (ISO 898-1:2009*. 2009.

[69] A.-T. Akono and F.-J. Ulm. Scratch test model for the determination of fracture toughness. *Engineering Fracture Mechanics*, 78(2):334–342, 2011.

[70] O. A. Bauchau and J. I. Craig. Euler-bernoulli beam theory. In O. A. Bauchau and J. I. Craig, editors, *Structural Analysis*, pages 173–221. Springer Netherlands, Dordrecht, 2009.

[71] Qingjie Zhang. *Moment and longitudinal resistance for composite beams based on strain limited design method*. PhD Dissertation, University of Luxembourg, Luxembourg, 2020.

[72] European Committee for Standardization (CEN). *EN1992-1-1: Eurocode 2 - Design of concrete structures. Part 1-1: General rules and rules for buildings.* 2004.

[73] HS Montagetechnik GmbH. *HS-lieferprogramm-2022-01*. HS Montagetechnik GmbH, Freiberg, Germany, 2022.

[74] A. Sharma, R. Eligehausen, and J. A Asmus. A new model for concrete edge failure of multiple row anchorages with supplementary reinforcement-Reinforcement failure. *Journal of Structural Concrete*, 18:893–901, 2017.

[75] A. Sharma, R. Eligehause, J. Asmus, and J. Bujnak. Anchorages with supplementary reinforcement under tension, shear and interaction loads – experimental database. In *Proceedings of the fib Symposium 2019: Concrete - Innovations in Materials, Design and Structures*. The International Federation for Structural Concrete (fib), 2019.

[76] R. Eligehause, A. Sharma, and J. Asmus. Behaviour and design of fastenings with headed-studs with supplementary reinforcement close to an edge under shear loads perpendicular to the edge. *J. Otto-Graf, Journal on Research and Testing of Materials.*, 18:65–78, 2019.

[77] Ruopp Jakob. *Untersuchungen zum Tragverhalten von Ankerplatten mit Kopfbolzen zur Abtragung von Zug- und Querkräften*. Number Nr. 2020-3. PhD Dissertation, Universität Stuttgart, Germany, 2020.

[78] European Committee for Standardization (CEN). *EN12390-3: Testing Hardened Concrete - Part 3 : Compressive strength of test specimens*. Brussels, Belgium, 2019.

[79] European Committee for Standardization (CEN). *EN12390-13: Testing Hardened Concrete - Part 13 : Determination of secant modulus of elasticity in compression*. Brussels, Belgium, 2013.

[80] Gerhard Hanswille and Markus Porsch. *Forschung für die Praxis P 487 - Lasteinleitung bei ausbetonierten Hohlprofilverbund-stützen mit normal- und hochfesten Betonen*. Düsseldorf, Germany, 2004.

[81] Deutsches Institut für Bautechnik (DIBt). *European Technical Assessment, ETA-03/0039*. Deutsches Institut für Bautechnik (DIBt), 2018.

[82] Rasoul Nilforoush. *Achorage in concrete structure*. PhD Dissertation, Lulea University of Technology, Sweden, 2017.

[83] Johannes Furche. *Load-bearing and displacement of headed anchors under axial tension loading*. PhD Dissertation, University of Stuttgart, Germany, 1994.

[84] Kahlmeyer Eduard. *Stahlbau, Träger - Stützen - Verbindungen*. Werner-Verlag GmbH, Düsseldorf, Germany, 1990.

[85] European Committee for Standardization (CEN). *EN1991:2002: Eurocode 1: Actions on structures - Part 1-1: General actions - Densities, self-weight, imposed loads for buildings*. Brussels, Belgium, 2002.

[86] Robert Alexander Adams and Christopher Essex. *Calculus - A complete course*. Pearson Education Canada, 7th edition, 2009.

[87] Matthias Braun. *Investigation of the load-bearing behavior of CoSFB-Dowels*. PhD Dissertation, University of Luxembourg, Luxembourg, 2018.

[88] Ulrike Kuhlmann. *Stahlbau Kalender, Verbundbau; Fertigung*. Wilhelm Ernst Sohn publishing house for architecture and technology, Berlin, Germany, 2018.

[89] Job Duarte da Costa. *Structural properties of steel-concrete composite joints*. PhD Dissertation, University of Luxembourg, Luxembourg, 2018.

[90] T.F. Yolaçan and M. Schäfer. Investigation of the moment redistribution for steel – concrete continuous composite beams. *ce/papers*, 3:251–256, 2019.

[91] D.A. Nethercot, T.Q. Li, and B. S. Choo. Required rotations and moment redistribution for composite frames and continuous beams. *Journal of Constructional Steel Research*, 35(2):121–163, 1995.

[92] A.R. Kemp, N.W. Dekker, and P. Trinchero. Differences in inelastic properties of steel and composite beams. *Journal of Constructional Steel Research*, 34(2-3):187–206, 1995.

[93] Christoph Odenbreit. *Zur Ermittlung der Tragfähigkeiten, der Steifigkeiten und der Schnittgrößen von Verbundträgern mit halbsteifen, teiltragfähigen Verbundanschlüssen*. PhD Dissertation, Technical University of Kaiserslautern, Germany, 2000.

[94] H. Bode, W. Ramm, S. Elz, and H.J. Kronenberger. Composite connections - experimental results. In *IABSE Report (75) - Proceedings of IABSE Colloquium Istanbul 1996 - Semi-Rigid Structural Connections*, pages 31–41. International Association for Bridge and Structural Engineering (IABSE), 1996.

[95] S. Chen and Y. Jia. Required and available moment redistribution of continuous steel–concrete composite beams. *Journal of Constructional Steel Research*, 64(2):167–175, 2008.

[96] Y. Jiang, X. Hu, W. Hong, and B. Wang. Experimental study and theoretical analysis of partially encased continuous composite beams. *Journal of Constructional Steel Research*, 117:152–160, 2016.

[97] J. Nei and C.S. Cai. Steel-concrete composite beams considering shear slip effects. *Journal of Structural Engineering*, 129(4).

[98] M. Pop, Z. Kiss, and P. Pernes. Joint configuration of composite beams to reinforced concrete wall. *Procedia Technology*, 22:108–114, 2006.

[99] H.T. Thai, B. Uy, Yamesri, and F. Aslani. Behaviour of bolted endplate composite joints to square and circular cfst columns. *Journal of Constructional Steel Research*, 131:68–82, 2017.

[100] J. Duarte de Costa, R. Obiala, and C. Odenbreit. Rotation capacity of composite joints for slim-floor beams. *Stahlbau*, 88:675–684, 2019.

[101] J. Duarte de Costa, R. Obiala, and C. Odenbreit. Experimental investigations on semi-continuous encased composite joints. *ce/papers*, 1(2-3):530–539, 2017.

[102] Mikko Malaska. *Behavior of a semi-continuous beam-column connection for composite slim floors*. PhD Dissertation, Helsinki University of Technology, Finland, 2000.

[103] International Organization for Standardization (ISO). *Steel for the reinforcement of concrete - Part 2: Ribbed bars (ISO 6935-2:2007)*. 2007.

[104] Russell Charles Hibbeler. *Mechanics of Materials Edition*. Pearson Prentice Hall, Boston, United States of America, 8th edition, 2011.

[105] S. Varrette, P. Bouvry, H. Cartiaux, and F. Georgatos. Management of an academic HPC cluster: The UL experience. In *Proc. of the 2014 Intl. Conf. on High Performance Computing & Simulation (HPCS 2014)*, pages 959–967, Bologna, Italy, July 2014. Institute of Electrical and Electronics Engineers (IEEE).

[106] G. Hanswille and M. Schäfer. Zur praktischen ermittlung der verformungen von verbundträgern und flachdeckensystemen unter berücksichtigung der nachgiebigkeit der verbundfuge. *Stahlbau*, 76:845–854, 2007.

[107] European Committee for Standardization (CEN). *EN14399-6:2005: High strength structural bolting assemblies for preloading - Part 6: Plain chamfered washers.* Brussels, Belgium, 2005.

[108] N. Stranghöner, N. Afzali, de P.A. Vries, E. Schedin, J. Pilhagen, and S. Cardwell. Slip-resistant bolted connections of stainless steel. *Steel Construction*, 10:333–343, 2017.

[109] N. Stranghöner and et al. *Execution and Reliability of Slip Resistant Connections for Steel Structures Using CS and SS (SIROCO)-Final Report*. Publication office of the European Union: Luxembourg, 2019.

[110] C. Otter and J. Maljaars. Preload loss of stainless steel bolts in aluminium plated slip resistant connections. *Thin-Walled Structures*, 157:106984, 2020.